# Advances in Image-Guided Urologic Surgery

Joseph C. Liao
Li-Ming Su
*Editors*

Springer

# Advances in Image-Guided Urologic Surgery

Joseph C. Liao • Li-Ming Su
Editors

# Advances in Image-Guided Urologic Surgery

Springer

*Editors*
Joseph C. Liao, MD
Department of Urology
Stanford University School of Medicine
Stanford, CA
USA

Li-Ming Su, MD
Department of Urology
University of Florida College of Medicine
Gainesville, FL
USA

ISBN 978-1-4939-1449-4 ISBN 978-1-4939-1450-0 (eBook)
DOI 10.1007/978-1-4939-1450-0
Springer New York Heidelberg Dordrecht London

Library of Congress Control Number: 2014950792

*In loving memory of my father Lienjin, who taught me audacity*
Joseph C. Liao

# Preface

Advances in imaging technologies have been a key source of innovation in modern medicine and surgery. In the preoperative setting, computed tomography (CT), magnetic resonance imaging (MRI), and ultrasound (US) play indispensable roles in clinical diagnosis and surgical planning. Modern endoscopy and minimally invasive surgery can trace their foundation to the invention of *Lichtleiter* by Bozzini in 1806 and the first laparoscopic procedures a century later. In urological surgery and beyond, patients and their surgeons today strive for precise surgical treatments in the least invasive manner while minimizing collateral damage to surrounding organs.

*Advances in Image-Guided Urologic Surgery* is a compendium of the emerging field of image-guided surgery and intervention in urology. The book is divided into four sections. The first section focuses on optical imaging technologies including wide-field fluorescence, optical coherence tomography, and endomicroscopy. The second section addresses the current applications of intraoperative ultrasound. The third section focuses on the integration of CT- and MRI-guided surgical interventions, particularly for prostate and kidney cancer. The fourth section introduces other emerging applications including augmented reality, simulators, and molecular imaging.

The intended audience of this book includes urological surgeons and trainees, biomedical engineers, and imaging scientists interested in technology translation. We are grateful for the contribution of a group of international experts who are among the foremost leaders in this emerging field. Ultimately, we share the common goal that by being able to "see" better, we will deliver better surgical outcomes for our patients.

Stanford, CA, USA — Joseph C. Liao, MD
Gainesville, FL, USA — Li-Ming Su, MD

# Acknowledgments

We are indebted to our families for their love and support. We thank our mentors and students for their inspiration. We are grateful to the many authors for their time and dedication in the preparation of their chapters. A special acknowledgment goes to Margaret Burns at Springer for her expert assistance in making this book a reality.

# Contents

# Contributors

**Mohamad E. Allaf, MD** Departments of Urology, Oncology, and Biomedical Engineering, Johns Hopkins Brady Urological Institute, Baltimore, MD, USA

**Jamin V. Brahmbhatt, MD** Department of Urology, The PUR Clinic, South Lake Hospital in Partnership with Orlando Health, Clermont, FL, USA

**M.T.J. Bus, MD, MSc** Department of Urology, Academic Medical Center Amsterdam, Amsterdam, The Netherlands

**Jeffrey A. Cadeddu, MD** Department of Urology, UT Southwestern Medical Center, Dallas, TX, USA

**Janet Laura Colli, MD** Department of Urology, University of Tennessee, Memphis, TN, USA

**D.M. de Bruin, MSc** Department of Urology, Academic Medical Center Amsterdam, Amsterdam, The Netherlands

Department of Biomedical Engineering & Physics, Academic Medical Center Amsterdam, Amsterdam, The Netherlands

**J.J.M.C.H. de la Rosette, MD, PhD** Department of Urology, Academic Medical Center Amsterdam, Amsterdam, The Netherlands

**Th.M. de Reijke, MD, PhD** Department of Urology, Academic Medical Center Amsterdam, Amsterdam, The Netherlands

**Laura Findeiss, MD, FSIR, FAHA** Department of Radiology, University of Tennessee Graduate School of Medicine, Nashville, TN, USA

**Robert L. Galloway Jr., PhD** Department of Urologic Surgery, Vanderbilt University Medical Center, Nashville, TN, USA

Department of Neurosurgery, Vanderbilt University Medical Center, Nashville, TN, USA

Department of Biomedical Engineering, Vanderbilt University Medical Center, Nashville, TN, USA

**Michael J. Glamore, MD** Herbert Wertheim College of Medicine, Florida International University, University Park, FL, USA

**Ali S. Gözen, MD** Department of Urology, SLK Kliniken Heilbronn, University of Heidelberg, Heidelberg, Germany

**Ahmet Gudeloglu, MD** Department of Urology, The PUR Clinic, South Lake Hospital in Partnership with Orlando Health, Clermont, FL, USA

**Mohit Gupta, MD** Department of Urology, University of Florida College of Medicine, Gainesville, FL, USA

**Axel Häcker, MD** Department of Urology, Medical School Mannheim, University of Heidelberg, Heidelberg, Germany

**Harry W. Herr, MD, FACS** Department of Urology, Memorial Sloan-Kettering Cancer Center, New York, NY, USA

**S. Duke Herrell, MD, FACS** Department of Urologic Surgery, Vanderbilt University, Nashville, TN, USA

Department of Biomedical Engineering, Vanderbilt University, Nashville, TN, USA

**Mark Hsu, MD** Department of Urology, Stanford University School of Medicine, Stanford, CA, USA

**Johannes Huber, MD** Department of Urology, Medical School, Technical University of Dresden, Dresden, Germany

**Manu Jain, MD** Department of Pathology and Laboratory Medicine, Weill Medical College of Cornell University, New York, NY, USA

**Jan Klein, MD** Department of Urology, SLK Kliniken Heilbronn, University of Heidelberg, Heidelberg, Germany

**Jaime Landman, MD** Department of Urology, University of California Irvine, Orange, CA, USA

**Benjamin R. Lee, MD** Departments of Urology and Oncology, Tulane University School of Medicine, New Orleans, LA, USA

**Raymond J. Leveillee, MD, FRCS-G** Department of Urology, University of Miami Miller School of Medicine, Miami, FL, USA

**Joseph C. Liao, MD** Department of Urology, Stanford University School of Medicine, Stanford, CA, USA

VA Palo Alto Health Care System, Palo Alto, CA, USA

**Estevao Lima, MD** Department of Urology, Medical School Braga, University of Braga, Braga, Portugal

**Daniel J.A. Margolis, MD** Department of Radiological Sciences, UCLA Geffen School of Medicine, Los Angeles, CA, USA

**Surena F. Matin, MD** Department of Urology, The University of Texas MD Anderson Cancer Center, Houston, TX, USA

**Toru Matsugasumi, MD** Department of Urology, Norris Cancer Center, University of Southern California, Los Angeles, CA, USA

**Kathleen F. McGinley, DO** Division of Urology, Department of Surgery, Duke University Medical Center, Durham, NC, USA

**Hans-Peter Meinzer, PhD** Division of Medical and Biological Informatics, German Cancer Research Center, Heidelberg, Germany

**Michael I. Miga, PhD** Departments of Neurological Surgery, Vanderbilt University, Nashville, TN, USA

Departments of Radiology and Radiological Sciences, Vanderbilt University, Nashville, TN, USA

Departments of Biomedical Engineering, Vanderbilt University, Nashville, TN, USA

**Sushmita Mukherjee, PhD, MS** Department of Biochemistry, Weill Medical College of Cornell University, New York, NY, USA

**Annika Mulaney** Intern, The PUR Clinic, South Lake Hospital in Partnership with Orlando Health, Clermont, FL, USA

**Michael Müller, PhD** Division of Medical and Biological Informatics, German Cancer Research Center, Heidelberg, Germany

**Ephrem O. Olweny, MD** Department of Urology, University of Texas Southwestern Medical Center, Dallas, TX, USA

**Michael Ordon, MD, MSc, FRCSC** Division of Urology, Department of Surgery, University of California, Irvine, CA, USA

**Ying Pan, PhD** Department of Urology, Stanford University School of Medicine, Stanford, CA, USA

**Sijo J. Parekattil, MD** Department of Urology, The PUR Clinic, South Lake Hospital in Partnership with Orlando Health, Clermont, FL, USA

**Phillipe Pereira, MD** Department of Radiology, SLK Kliniken Heilbronn, University of Heidelberg, Heidelberg, Germany

**Bogdan Petrut, MD** Department of Urology and Oncology, Medical School Cluj, University of Cluj, Cluj-Napoca, Romania

**Bryce W. Polascik** Division of Urology, Department of Surgery, Duke University Medical Center, Durham, NC, USA

**Thomas J. Polascik, MD, FACS** Division of Urology, Department of Surgery, Duke University Medical Center, Durham, NC, USA

**Sima Porten, MD, MPH** Department of Urology, The University of Texas MD Anderson Cancer Center, Houston, TX, USA

**Jens Rassweiler, MD** Department of Urology, SLK Klinikum Heilbronn, Heilbronn, Germany

**Marie-Claire Rassweiler, MD** Department of Urology,
Medical School Mannheim, University of Heidelberg, Heidelberg, Germany

**Manuel Ritter, MD** Department of Urology, Medical School Mannheim,
University of Heidelberg, Heidelberg, Germany

**Ashley E. Ross, MD, PhD** Departments of Urology, Oncology, Pathology,
Johns Hopkins Brady Urological Institute, Baltimore, MD, USA

**Thomas Scagnelli, MD, FSIR** Department of Interventional Radiology,
Baptist Cardiac and Vascular Institute, Doctor's Hospital, Miami, FL, USA

**Douglas S. Scherr, MD** Department of Urology, Weill Medical College
of Cornell University, New York, NY, USA

**Jason Cheng-En Sea, MD** Department of Urology,
Indiana University, Indianapolis, IN, USA

**Sunao Shoji, MD, PhD** Department of Urology,
Tokai University Hachioji Hospital, Hachioji, Japan

**Geoffrey A. Sonn, MD** Department of Urology,
Stanford University School of Medicine, Stanford, CA, USA

**Dan Stoianovici, PhD** Departments of Urology, Mechanical Engineering,
and Neurosurgery, Johns Hopkins Brady Urological Institute,
Baltimore, MD, USA

**Li-Ming Su, MD** Division of Robotic and Minimally Invasive Urologic
Surgery, Department of Urology, University of Florida
College of Medicine, Gainesville, FL, USA

**Chandru P. Sundaram, MD** Department of Urology,
Indiana University, Indianapolis, IN, USA

**Dogu Teber, MD** Department of Urology, Medical School Heidelberg,
University of Heidelberg, Heidelberg, Germany

**Katherine J. To'o, MD** Department of Radiology,
VA Palo Alto Health Care System, Palo Alto, CA, USA

Department of Radiology, Stanford University School of Medicine,
Stanford, CA, USA

**Osamu Ukimura, MD, PhD** Department of Urology, Norris Cancer
Center, Keck School of Medicine, University of Southern California,
Los Angeles, CA, USA

**Raghu Vikram, MD** Department of Diagnostic Radiology,
The University of Texas MD Anderson Cancer Center, Houston, TX, USA

**Guan Wu, MD, PhD** Departments of Urology, Pathology, and Oncology,
University of Rochester Medical Center, Rochester, NY, USA

**Ingmar Wegner, PhD** Division of Medical and Biological Informatics,
German Cancer Research Center, Heidelberg, Germany

# Part I

# Optical Imaging Technologies

# 1 Endoscopic Fluorescence Imaging of Bladder Cancer: Photodynamic Diagnosis and Confocal Laser Endomicroscopy

Mark Hsu and Joseph C. Liao

Bladder cancer is the second most common genitourinary cancer and the fifth most common cancer overall in the United States. In 2014, there are projected 72,570 new cases and 15,210 cancer-related deaths [1]. Modern white-light cystoscopy (WLC), the standard approach to evaluate the lower urinary tract and manage non-muscle-invasive bladder cancer (NMIBC), has been the result of sequential landmark innovations over the last two centuries [2]. Despite significant advances, WLC and WL-guided transurethral resection (TUR) have numerous limitations that can affect accurate detection and staging of bladder cancer, including differentiation of nonpapillary urothelial carcinoma from inflammatory lesions and delineation of tumor borders [3]. While histology is the standard for definitive cancer diagnosis, it is not available intraoperatively in real time to guide surgical intervention. The inherent subjective nature and operator dependence of WLC can lead to incomplete resection, thereby increasing the risk of tumor persistence, recurrence, and progression [4]. Thus, there has been great interest in developing optical imaging technologies that can enhance the diagnostic accuracy of WLC, improve completeness of TUR, and thereby improve surgical and cancer outcomes.

Fluorescence imaging that utilizes exogenous contrast agents is emerging as a useful adjunct for intraoperative guidance across different surgical disciplines, including urology [5]. With ease of access, the bladder is a well-suited target organ amenable to intraoperative fluorescence imaging. Imaging strategies typically combine a fluorescence illumination source in combination with exogenous contrast agents. Currently, three fluorescent contrast agents are approved for clinical use: protoporphyrin IX precursor hexaminolevulinate (HAL), fluorescein, and indocyanine green (ICG). This chapter focuses on the approved endoscopic fluorescence imaging technologies for bladder cancer: photodynamic diagnosis (PDD) and confocal laser endomicroscopy (CLE). Considerations including optical specifications, ease of OR integration, available clinical evidence, and suggested future directions will be highlighted.

## Photodynamic Diagnosis

PDD provides wide-field fluorescence imaging of the bladder mucosa with a field of view comparable to WLC (i.e., ~cm). Also known as fluorescence cystoscopy or blue-light cystoscopy,

M. Hsu, MD
Department of Urology, Stanford University School of Medicine, Stanford, CA, USA
e-mail: markhsu@stanford.edu

J.C. Liao, MD (✉)
Department of Urology, Stanford University School of Medicine, Stanford, CA, USA

VA Palo Alto Health Care System, Palo Alto, CA, USA
e-mail: jliao@stanford.edu

J.C. Liao, L.-M. Su (eds.), *Advances in Image-Guided Urologic Surgery*,
DOI 10.1007/978-1-4939-1450-0_1, © Springer Science+Business Media New York 2015

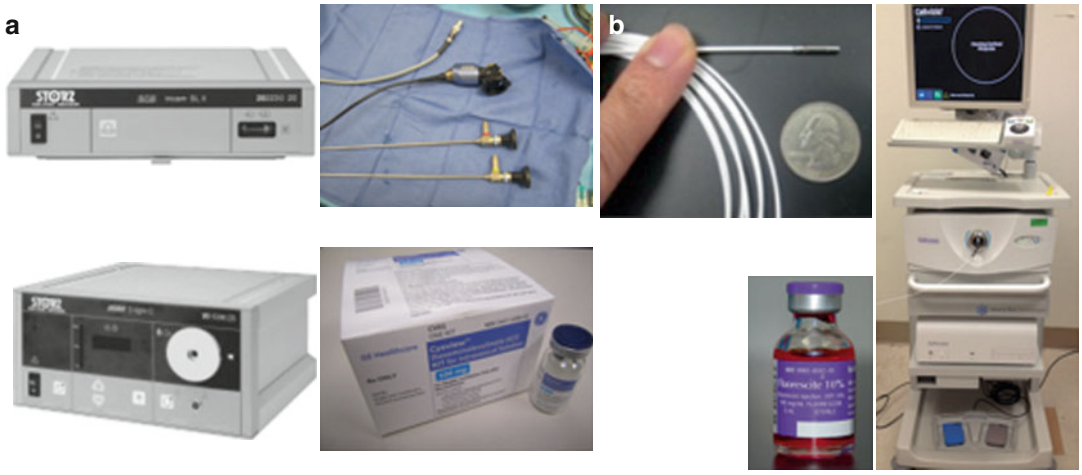


**Fig. 1.1** Endoscopic fluorescence imaging systems for bladder cancer. (**a**) Photodynamic diagnosis (PDD) composed of a blue-light source, specialized camera head and lens, and hexaminolevulinate as the contrast agent. (**b**) Confocal laser endomicroscopy (CLE) composed of a 2.6-mm fiberoptic imaging probe, fluorescein as the contrast agent, and the laser scanning unit

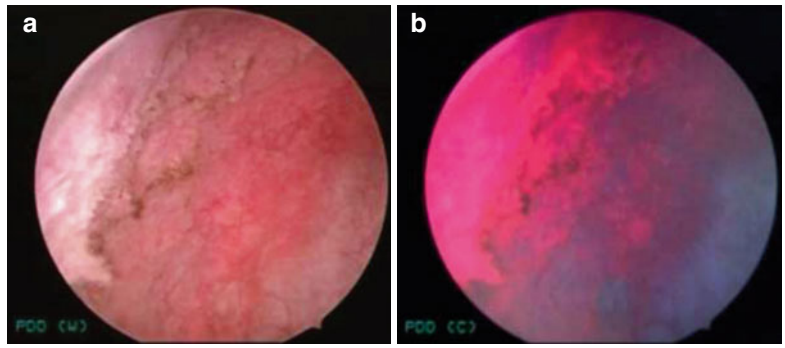


**Fig. 1.2** PDD of bladder cancer. (**a**) White-light image of a large flat lesion at the right bladder wall showing indistinct borders and (**b**) the corresponding PDD image. The region was confirmed to be carcinoma in situ (*CIS*) (From Hsu et al. [27], with permission)

PDD uses photosensitive protoporphyrin IX precursor as the contrast agent, a blue-light source that illuminates at 375–440 nm, and a specialized lens and camera (Fig. 1.1a). The protoporphyrin, introduced intravesically, accumulates preferentially in neoplastic tissues and emits red fluorescence under blue light (Fig. 1.2). In the bladder, two protoporphyrin analogues, 5-aminolevulinic acid (5-ALA) and hexaminolevulinate (HAL), have been investigated. HAL is the more potent lipophilic ester analogue of 5-ALA and is approved for clinical use in Europe and the United States for patients with suspicion for or known bladder cancer. Due to increased potential for increased false positives, it is currently approved for single administration after 90 days following intravesical bacillus Calmette-Guerin (BCG).

Integration in the OR environment is overall straightforward. HAL is solubilized and instilled intravesically by either the surgical team or nursing staff via a catheter 1–3 h prior to cystoscopy and TUR. Fluorescence imaging is switched on and off dynamically through the press of a button on the camera head. Fluorescence imaging is used for generalized survey of the urothelium as well as in conjunction with standard TUR, with improved contrast-enhanced visualization of both papillary and flat (i.e., carcinoma in situ, CIS) lesions.

In diagnostic cystoscopy, PDD is reported to have a sensitivity and specificity ranging from 87

to 97 % and 43 to 76 %, respectively [4]; a meta-analysis demonstrated that 5-ALA and HAL had similar sensitivity and specificity rates [6]. PDD has been shown to have an improved rate of initial detection of papillary and CIS lesions compared to WLC [7–9]. A meta-analysis of three phase III studies concluded that HAL had a higher CIS detection rate than WLC [10]. In addition, several meta-analyses have found significantly reduced residual tumor rates with PDD, with odds ratio of residual tumor being 0.28 (95 % CI, 0.15–0.52) compared to WLC [11] and the RR of residual tumor being 2.77-fold higher (95 % CI, 1.47–5.02; $p=0.002$) with WLC versus PDD [12].

However, the overall recurrence rate of PDD-guided TUR of bladder tumor for NMIBC remains to be determined. One extensive meta-analysis compiled 1,345 patients across six studies with known or suspected NMIBC comparing HAL to WLC, with significant additional lesions detected ($p<0.001$) and a significantly lower recurrence rate at 12 months in the HAL group versus WLC group (34.5 % vs 45.4 %; $p=0.006$). When stratified by subgroup, recurrence rates were lower for patients with T1/CIS ($p=0.052$) and Ta disease ($p=0.04$) and high-risk ($p=0.05$) and low-risk ($p=0.029$) subgroups [13]. On the other hand, two studies found no significant difference in decreasing recurrence risk or progression-free survival with fluorescence cystoscopy [7, 9]. Further randomized trials with longer follow-up time periods will be needed to validate the long-term efficacy of PDD in determining a significant benefit in recurrence-free and progression-free survival.

## Confocal Laser Endomicroscopy

CLE provides dynamic, high-resolution, subsurface imaging of the mucosa. While conventional confocal microscopes are bulky instruments widely used in laboratory settings [14–16], recent advances in instrument miniaturization have led to the development of flexible, fiberoptic endomicroscopes that can be passed through the working channel of standard endoscopes. Similar to confocal microscopy, in CLE, the illuminating light from a fiber is focused by an objective lens onto a tissue. Whereas scattered light from the in-focus tissue plane converges back into the fiber, the light from out-of-focus planes is inefficiently collected.

Of the different imaging technologies available clinically, CLE provides the highest spatial resolution (1–5 μM). Optical sectioning is performed using a 488-nm laser as the light source. Fluorescein, an FDA-approved drug, is used as the contrast agent. CLE has been approved for gastrointestinal and pulmonary endoscopic applications, with recent approval for the urinary tract.

The primary clinical system (Cellvizio, Mauna Kea Technologies) (Fig. 1.1b) uses imaging probes ranging from 0.85 to 2.6 mm in diameter that are passed through the working channels of standard endoscopes to examine the urinary tract. Images are acquired as video sequences at 12 frames/s, which allows real-time dynamic imaging of physiologic processes such as vascular flow. The images are reminiscent of standard histopathology with microarchitecture and cellular features.

In vivo applications of CLE in bladder surgery involve intravesical or intravenous administration of fluorescein with minimal systemic toxicity (Fig. 1.3) [17]. After an initial pilot study demonstrating the feasibility of using CLE in ex vivo bladders after cystectomy [18], CLE was conducted in 27 patients undergoing cystoscopy under anesthesia and TUR [19]. The ability to differentiate normal/benign mucosa from cancer (low- and high-grade lesions) was demonstrated (Fig. 1.4). Features of low-grade disease include densely packed cells and presence of fibrovascular stalks; on the other hand, high-grade disease exhibits a more distorted microarchitecture with pleomorphic, irregularly shaped shells with loss of cellular cohesiveness, indistinct cell borders, and disorganized vasculature. Carcinoma in situ (CIS) also contains a population of pleomorphic cells and indistinct cell borders but may also have extensive acellular areas that may be secondary to areas of denuded urothelium. In contrast, inflammatory sites (from processes such as post-BCG granulomatous

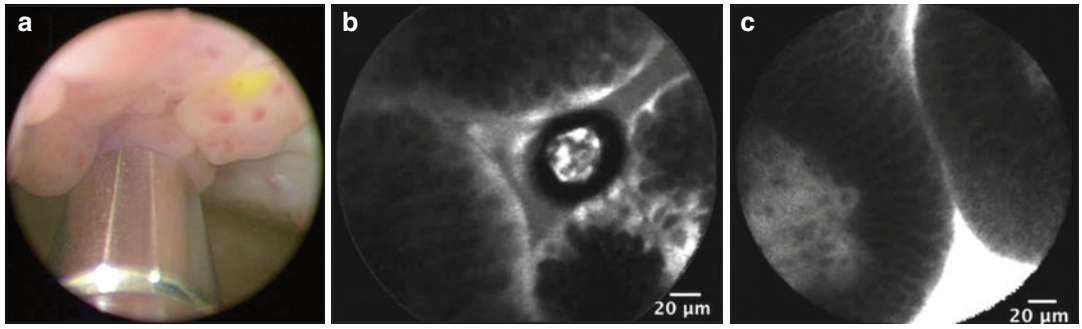


**Fig. 1.3** Representative images from WLC and CLE with intravesical or intravenous administration of fluorescein. (**a**) WLC with intravesically stained papillary tumor. 2.6-mm imaging probe is visible at the bottom of the image. (**b**) CLE of intravesically stained papillary tumor. (**c**) CLE of intravenously stained papillary tumor (From Chang et al. [17], with permission)

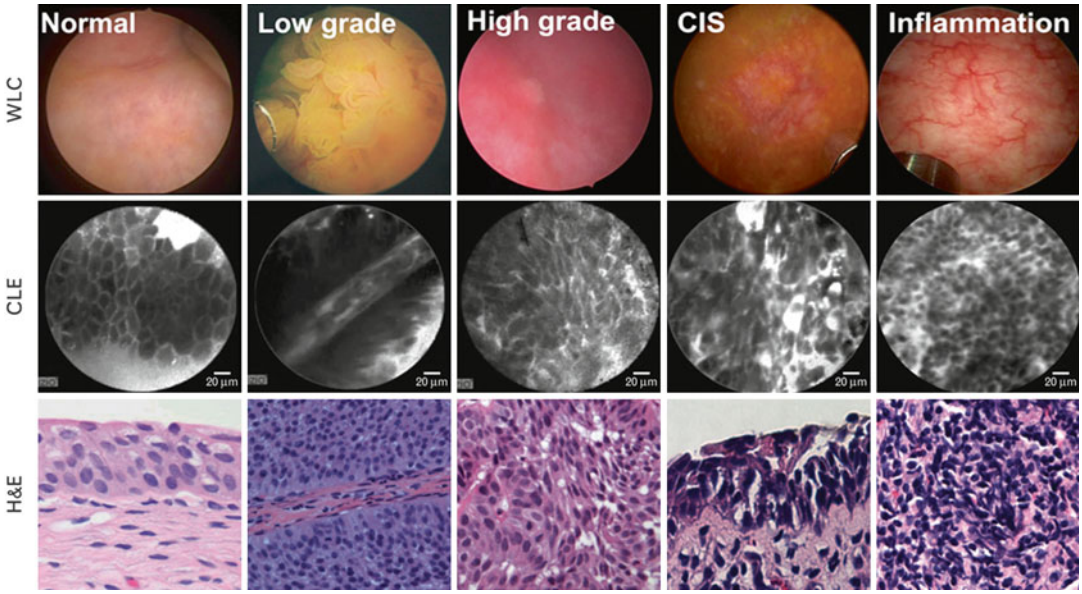


**Fig. 1.4** Probe-based optical biopsy with CLE of the bladder. CLE of normal, low/high-grade papillary bladder cancer, carcinoma in situ (*CIS*), and inflammation are shown with their corresponding white-light cystoscopy images and hematoxylin and eosin (H&E) staining from the subsequent biopsy site. Low-grade cancer shows characteristically organized papillary structures, in contrast to high-grade cancer and CIS which display pleomorphic cells and distorted microarchitecture. The inflammatory setting shows lymphocytic infiltrates (From Hsu et al. [27], with permission)

reaction, Foley catheter reaction, urinary tract infection, scarring from prior resection) contain loose aggregations of small monomorphic cells consistent with local recruitment of leukocytes in the lamina propria. Similar to histopathology, the superficial umbrella cell layer is commonly absent in cancerous lesions.

An imaging atlas was created to establish criteria for CLE diagnosis of bladder cancer [20]. Distinguishing anatomic features were documented among the various parts of the urinary tract, including the kidney (ex vivo), ureter (ex vivo), bladder, urethra, and prostate. In addition, the image process technique of mosaicing was used, allowing for juxtaposition of overlapping images into a composite, panoramic image. This application enables expansion of the field of view while preserving image fidelity.

More recently, an interobserver agreement study of CLE was conducted among novice and experienced CLE users. CLE was found to be a highly adoptable tool for cancer diagnosis and in novice CLE observers with moderate interobserver agreement. Experienced CLE observers, on the other hand, attained substantial levels of agreement for cancer diagnosis that was higher than for WLC alone [21].

## Conclusion/Future Studies

PDD and CLE hold promise in redefining the urologist's approach to examining the lower urinary tract with cystoscopy. While both technologies have potential implications in improving diagnosis and treatment, they also have inherent limitations that one must be aware of and also have costs in terms of instrumentation, contrast agents, and additional operative time. For example, with PDD, false fluorescence can result if the light source is applied tangentially to the area of interest [12, 22], and an up to 30 % false-positive rate has been reported, particularly in patients with prior BCG treatment and during the practitioner's learning curve [23]. On the other hand, CLE's maximal depth of penetration is only about 120 μM. In the case of the bladder, it is insufficient to provide information about muscle invasiveness as it can only provide anatomic detail to the level of the lamina propria. In addition, CLE requires that the probe be in direct contact with the target tissue, thus precluding imaging of the entire urothelium in a single instance given its narrow field of view. To try to improve on this drawback, CLE may be combined with other imaging modalities to help with localization, including PDD (Fig. 1.5), but the combination of HAL and CLE precluded histologic analysis by CLE because of the excitation/emission spectra of HAL [24]. Other fluorochromes are being investigated for their potential in this strategy of readily identifying lesions with real-time histologic confirmation. Future studies will focus on the diagnostic accuracy of CLE for bladder cancer, particularly the challenging flat, erythematous lesions. In addition, CLE may be expanded to other urologic applications, including the upper urinary tract and during laparoscopic and robotic-assisted surgery.

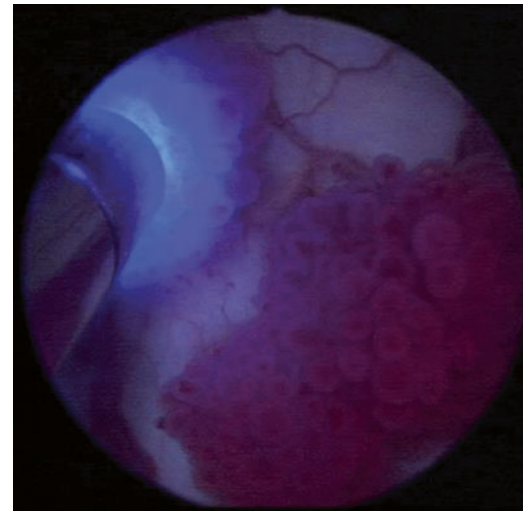

**Fig. 1.5** CLE combined with PDD in in vivo cystoscopy for bladder tumor. PDD blue light identifies red fluorescence that can guide the CLE probe to the target area (From Chang et al. [17] with permission)

Another future direction for both PDD and CLE lies in molecular imaging. It is possible to couple this modality with fluorescently labeled peptides or antibodies targeted to tumor-specific surface antigens. In recent years, preliminary studies demonstrating this concept were illustrated in the gastrointestinal tract. In colon cancer, a synthetic peptide was found to bind with greater affinity to dysplastic colonocytes compared to normal cells [25]. When conjugated to fluorescein, CLE was able to detect fluorescent signals in areas of dysplastic tissue (Fig. 1.6). A similar study was done with CLE endoscopy to identify areas of Barrett's esophagus that were specifically bound to a fluorescently labeled peptide [26]. Future studies developed in parallel to the cystoscopy setting with molecular markers for bladder cancer can guide the urologist to improved diagnosis and resection in TURBT, promising better cancer-specific and overall outcomes.

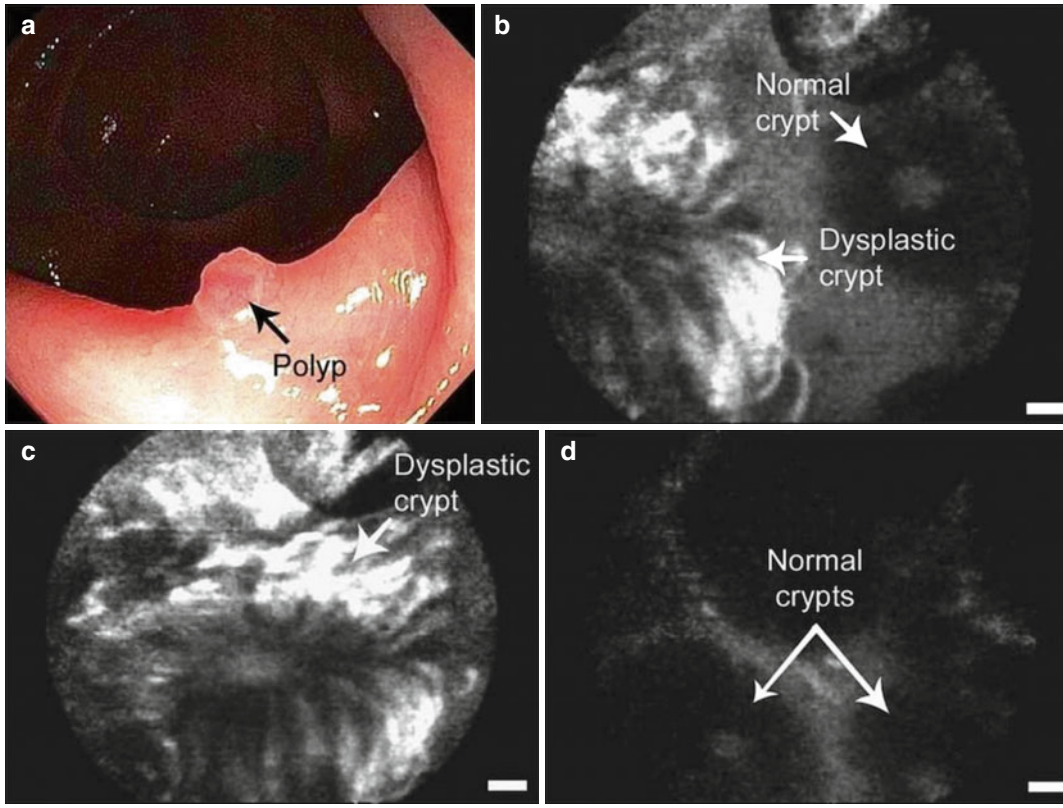


**Fig. 1.6** Confocal endomicroscopy of colonic dysplasia using a target peptide. (**a**) Area with dysplastic colonocytes that exhibit fluorescence consistent with bound peptide. (**b**) Normal mucosa treated with peptide shows relatively decreased fluorescence, with peptide collecting in regions between colonic crypts. (**c**) Hematoxylin and eosin (H&E) staining confirming dysplastic crypts. (**d**) H&E staining confirming normal crypts (From Hsiung et al. [25], with permission)

## References

1. Siegel R, Ma J, Zou Z, Jemal A. Cancer statistics, 2014. CA Cancer J Clin. 2014;64:9–29.
2. Herr HW. Early history of endoscopic treatment of bladder tumors from Grunfeld's polypenkneipe to the Stern-McCarthy resectoscope. J Endourol. 2006;20:85–91.
3. Lee CS, Yoon CY, Witjes JA. The past, present and future of cystoscopy: the fusion of cystoscopy and novel imaging technology. BJU Int. 2008;102:1228–33.
4. Liu JJ, Droller MJ, Liao JC. New optical imaging technologies for bladder cancer: considerations and perspectives. J Urol. 2012;188:361–8.
5. van den Berg NS, van Leeuwen FW, van der Poel HG. Fluorescence guidance in urologic surgery. Curr Opin Urol. 2012;22:109–20.
6. Mowatt G, N'Dow J, Vale L, Nabi G, Boachie C, Cook JA, et al. Photodynamic diagnosis of bladder cancer compared with white light cystoscopy: systematic review and meta-analysis. Int J Technol Assess Health Care. 2011;27:3–10.
7. Schumacher MC, Holmang S, Davidsson T, Friedrich B, Pedersen J, Wiklund NP. Transurethral resection of non-muscle-invasive bladder transitional cell cancers with or without 5-aminolevulinic Acid under visible and fluorescent light: results of a prospective, randomised, multicentre study. Eur Urol. 2010;57:293–9.
8. Grossman HB, Gomella L, Fradet Y, Morales A, Presti J, Ritenour C, et al. A phase III, multicenter comparison of hexaminolevulinate fluorescence cystoscopy and white light cystoscopy for the detection of superficial papillary lesions in patients with bladder cancer. J Urol. 2007;178:62–7.
9. Stenzl A, Burger M, Fradet Y, Mynderse LA, Soloway MS, Witjes JA, et al. Hexaminolevulinate guided fluorescence cystoscopy reduces recurrence in patients with nonmuscle invasive bladder cancer. J Urol. 2010;184:1907–13.
10. Lerner SP, Liu H, Wu MF, Thomas YK, Witjes JA. Fluorescence and white light cystoscopy for detection of carcinoma in situ of the urinary bladder. Urol Oncol. 2012;30:285–9.

11. Kausch I, Sommerauer M, Montorsi F, Stenzl A, Jacqmin D, Jichlinski P, et al. Photodynamic diagnosis in non-muscle-invasive bladder cancer: a systematic review and cumulative analysis of prospective studies. Eur Urol. 2010;57:595–606.
12. Shen P, Yang J, Wei W, Li Y, Li D, Zeng H, et al. Effects of fluorescent light-guided transurethral resection on non-muscle-invasive bladder cancer: a systematic review and meta-analysis. BJU Int. 2012; 110:E209–15.
13. Burger M, Grossman HB, Droller M, Schmidbauer J, Hermann G, Dragoescu O, et al. Photodynamic diagnosis of non-muscle-invasive bladder cancer with hexaminolevulinate cystoscopy: a meta-analysis of detection and recurrence based on raw data. Eur Urol. 2013;64:846–54.
14. Minsky M. Memoir on inventing the confocal scanning microscope. Scanning. 1988;10:128–38.
15. Minsky M. Microscopy apparatus. Patent US3013467; 1961. https://www.google.com/patents/US3013467.
16. Pawley J. Handbook of biological confocal microscopy. New York: Springer; 2006.
17. Chang TC, Liu JJ, Liao JC. Probe-based confocal laser endomicroscopy of the urinary tract: the technique. J Vis Exp. 2013;10:e4409.
18. Sonn GA, Mach KE, Jensen K, Hsiung PL, Jones SN, Contag CH, et al. Fibered confocal microscopy of bladder tumors: an ex vivo study. J Endourol. 2009;23:197–201.
19. Sonn GA, Jones SN, Tarin TV, Du CB, Mach KE, Jensen KC, et al. Optical biopsy of human bladder neoplasia with in vivo confocal laser endomicroscopy. J Urol. 2009;182:1299–305.
20. Wu K, Liu JJ, Adams W, Sonn GA, Mach KE, Pan Y, et al. Dynamic real-time microscopy of the urinary tract using confocal laser endomicroscopy. Urology. 2011;78:225–31.
21. Chang TC, Liu JJ, Hsiao ST, Pan Y, Mach KE, Leppert JT, et al. Interobserver agreement of confocal laser endomicroscopy for bladder cancer. J Endourol. 2013;27:598–603.
22. Jichlinski P, Guillou L, Karlsen SJ, Malmstrom PU, Jocham D, Brennhovd B, et al. Hexyl aminolevulinate fluorescence cystoscopy: new diagnostic tool for photodiagnosis of superficial bladder cancer – a multicenter study. J Urol. 2003;170:226–9.
23. Ray ER, Chatterton K, Khan MS, Chandra A, Thomas K, Dasgupta P, et al. Hexylaminolaevulinate fluorescence cystoscopy in patients previously treated with intravesical bacille Calmette-Guerin. BJU Int. 2010; 105:789–94.
24. Bonnal JL, Rock Jr A, Gagnat A, Papadopoulos S, Filoche B, Mauroy B. Confocal laser endomicroscopy of bladder tumors associated with photodynamic diagnosis: an ex vivo pilot study. Urology. 2012;80(1162):e1–5.
25. Hsiung PL, Hardy J, Friedland S, Soetikno R, Du CB, Wu AP, et al. Detection of colonic dysplasia in vivo using a targeted heptapeptide and confocal microendoscopy. Nat Med. 2008;14:454–8.
26. Sturm MB, Joshi BP, Lu S, Piraka C, Khondee S, Elmunzer BJ, et al. Targeted imaging of esophageal neoplasia with a fluorescently labeled peptide: first-in-human results. Sci Transl Med. 2013;5:184ra61.
27. Hsu M, Gupta M, Su LM, Liao JC. Intraoperative optical imaging and tissue interrogation during urologic surgery. Curr Opin Urol. 2014;24:66–74.

# Narrow Band Imaging for Urothelial Cancer

2

Harry W. Herr

Urothelial carcinoma occurs most commonly in the bladder and is detected by conventional white-light imaging (WLI) cystoscopy. Modern cystoscopy began with Nitze's invention of the first practical cystoscope in 1877 [1]. Since then, cystoscopy has evolved from wire filaments and incandescent bulbs to fiberoptics, rod lens systems, and digital chip cameras. Each technical innovation aims to bring brighter white-light illumination within the bladder and upper urinary tracts, permitting improved recognition of a multitude of maladies, including urothelial tumors. Detection of urothelial neoplasms is critical to their diagnosis, staging, and successful treatment. White-light imaging cystoscopy sometimes fails to detect bladder or upper tract tumors, especially flat or subtle papillary lesions disguised within normal-appearing urothelium [2]. Limitations of white-light imaging cystoscopy have helped to fuel the development of a new generation of optical methods designed to enhance white-light visualization [3]. One of these new methods is narrow band imaging (NBI) cystoscopy, which has recently been introduced into clinical practice, particularly in the management of bladder tumors.

H.W. Herr, MD, FACS
Department of Urology, Memorial Sloan-Kettering Cancer Center, New York, NY, USA
e-mail: herrh@mskcc.org

## Narrow Band Imaging

Narrow band imaging (NBI) is a powerful optical image enhancement technology that improves the visibility of blood vessels and epithelium comprising the bladder mucosa. Urothelial neoplasms are hypervascular owing to microvessel density. Narrow band imaging exploits the angiogenic features of urothelial tumors. Narrow band imaging filters white light into two discrete bands of light, one blue at 415 nm and one green at 540 nm. Both bands are absorbed by hemoglobin. The shorter wavelength in NBI is 415 nm light, which penetrates only the superficial layers of the mucosa. This is absorbed by superficial capillary vessels and shows up brownish to black on the video image. The second NBI wavelength is 540 nm light, which penetrates deeper into the bladder wall. It is absorbed by blood vessels located in the deep mucosa and submucosal layers and appears green on imaging. Narrow band blue light displays surface mucosal capillaries, and green light highlights vessels in the deep mucosa and submucosal vessels defining fronds of papillary tumors.

Figure 2.1 shows the NBI filter technology. Figure 2.2 shows cystoscopic appearance of normal bladder mucosa by white-light imaging (WLI) cystoscopy and narrow band imaging (NBI) cystoscopy. NBI highlights the superficial (brown) and underlying deep mucosa and submucosal (green) vasculature. NBI improves visualization of tumors by enhancing the contrast between well-vascularized lesions and normal

J.C. Liao, L.-M. Su (eds.), *Advances in Image-Guided Urologic Surgery*,
DOI 10.1007/978-1-4939-1450-0_2, 

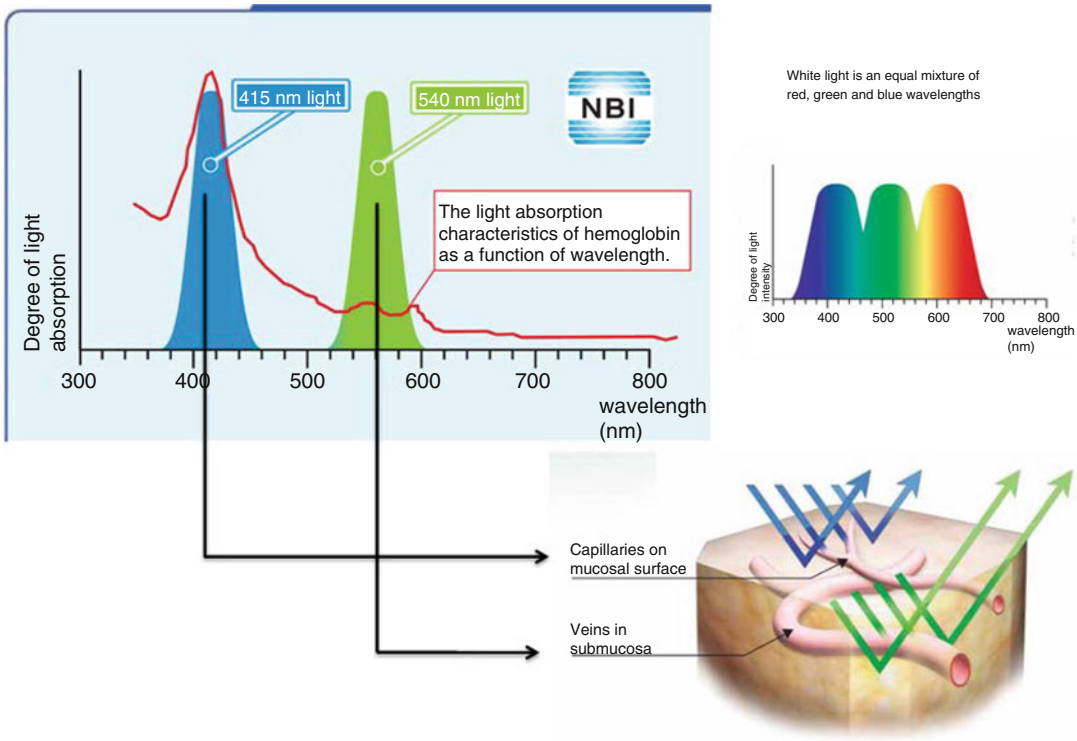


**Fig. 2.1** Narrow band imaging filter technology. Light source and video processor are used to deliver high-definition light through the cystoscope (Courtesy of Olympus)

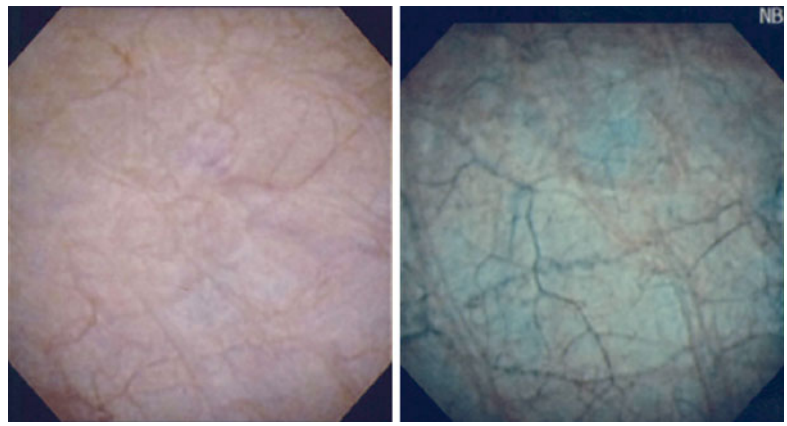


**Fig. 2.2** Normal bladder. White-light imaging (WLI) cystoscopy (*left*) and narrow band imaging (*right*). Mucosa is bland on WLI cystoscopy; NBI shows prominent green submucosal vessels and brown superficial capillaries, but no evidence of concentrated enhancement (neovascularity) (From Herr [27], with permission)

pink-white mucosa. Papillary tumors appear dark green or brownish green, owing to enhanced visualization of the submucosal fibrovascular stalk. They are usually quite distinct and contrast sharply with the adjacent normal mucosa (Fig. 2.3). However subtle or "missed" lesions on white-light imaging cystoscopy can also be detected by NBI (Fig. 2.4). Flat lesions, such as carcinoma in situ, are capillary dense and appear dark brown (Fig. 2.5). The contrast between the

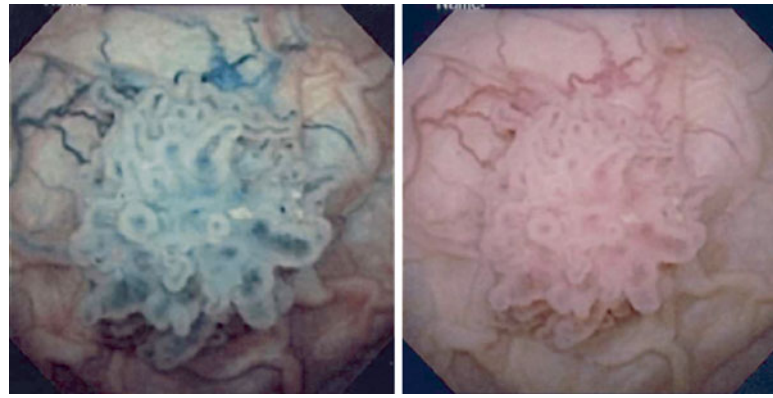

**Fig. 2.3** Papillary tumor shown by NBI cystoscopy (*left*) and WLI cystoscopy (*right*) (From Herr [27], with permission)

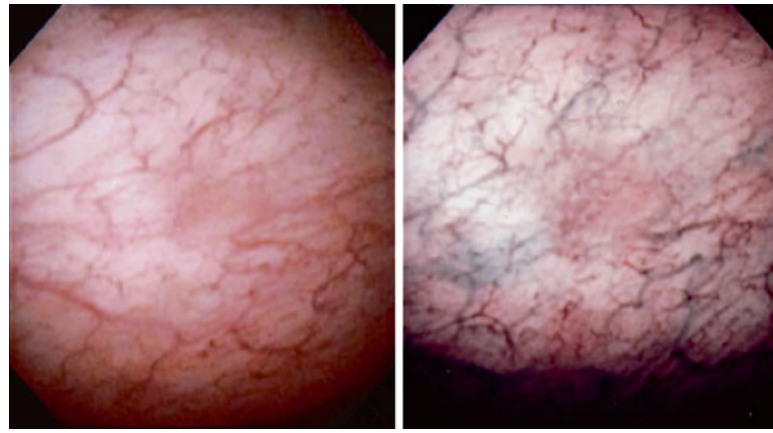

**Fig. 2.4** Small papillary tumor missed on WLI cystoscopy (*left*) is clearly seen on NBI cystoscopy (*right*) (From Herr [27], with permission)

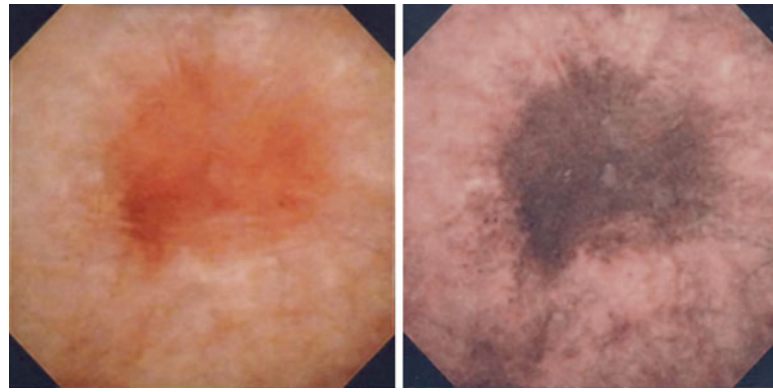

**Fig. 2.5** Carcinoma in situ of bladder visualized on WLI cystoscopy (*left*) and NBI cystoscopy (*right*) (From Herr [27], with permission)

two morphologic types of bladder cancer is best illustrated in mixed lesions (Fig. 2.6), composed of visible papillary tumors with surrounding ill-defined carcinoma in situ. The urologist can switch back and forth between white-light and narrow band mode by simply pushing a button on a digital flexible cystoscope or camera head attached to a resectoscope, to change the optical filter. There is no need for an intravesical dye, time constraints owing to photo-bleaching, or postoperative monitoring required as occurs with fluorescence cystoscopy.

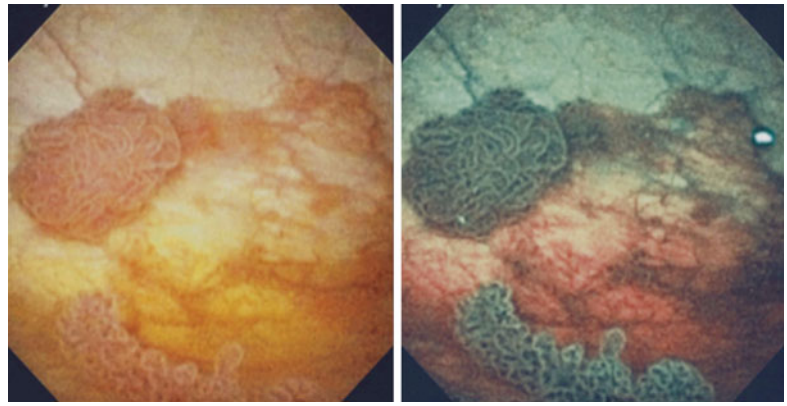

**Fig. 2.6** Papillary tumors on WLI cystoscopy (*left*) appear *dark green* on NBI cystoscopy (*right*), but surrounding *brown* lesions indicate associated carcinoma in situ (From Herr [27], with permission)

**Table 2.1** Detection of bladder tumors by white-light imaging (*WLI*) and narrow band imaging (*NBI*) cystoscopy

| Series | No. of cases | Cystoscopy | Sensitivity (%) | Specificity (%) | PPV (%) | NPV (%) |
|---|---|---|---|---|---|---|
| Bryan et al. [4] | 29 | WLI | 82 | 79 | 70 | 81 |
| | | NBI | 96 | 85 | 61 | 92 |
| Herr and Donat [5] | 427 | WLI | 87 | 85 | 66 | 96 |
| | | NBI | 100 | 82 | 63 | 100 |
| Cauberg et al. [6] | 95 | WLI | 79 | 75 | – | – |
| | | NBI | 95 | 69 | – | – |
| Tatsugami et al. [7] | 104 | WLI | 57 | 86 | 69 | 79 |
| | | NBI | 93 | 71 | 63 | 95 |
| Shen et al. [8] | 78 | WLI | 77 | 82 | – | 79 |
| | | NBI | 92 | 73 | – | 87 |
| Xiaodong et al. [9] | 64 | WLI | 79 | 76 | – | – |
| | | NBI | 97 | 68 | | |
| Geavlete et al. [10] | 95 | WLI | 84 | – | – | – |
| | | NBI | 95 | – | – | – |
| Zhu et al. [11] | 12 | WLI | 50 | 91 | – | – |
| | | NBI | 78 | 80 | – | – |
| Chen et al. [12] | 179 | WLI | 97 | 81 | – | – |
| | | NBI | 79 | 79 | – | – |

*PPV* positive predictive value, *NPV* negative predictive value

## NBI Detection of Bladder Tumors

Bryan et al. [4] were the first to describe the results of flexible NBI cystoscopy in 29 patients with recurrent bladder tumors. They found 15 additional tumors in 12 patients compared with WLI cystoscopy. Table 2.1 lists results from nine series, all showing enhanced detection of tumors using NBI diagnostic cystoscopy [4–12]. Although the series by Zhu et al. [11] included only 12 patients, they were evaluated by NBI for positive urine cytology and negative WLI cystoscopy. NBI found evidence of carcinoma in situ in 5 (42 %) patients. Collectively, the studies show superior sensitivity and negative predictive value (>90 %) for NBI over WLI cystoscopy, making it useful for identifying abnormal lesions and for excluding a diagnosis of bladder tumor. Although more negative biopsies of false-positive lesions (lower specificity) occurred with NBI, this is not believed to be significant or detrimental, since many patients have denuded mucosa and positive

**Table 2.2** Detection of carcinoma in situ by WLI and NBI cystoscopic biopsy

| Series | No. of cases | Cystoscopy | Sensitivity (%) | Specificity (%) | PPV | NPV |
|---|---|---|---|---|---|---|
| Herr and Donat [5] | 67 | WLI/NBI | 83; 100 | 72; 76 | 36;36 | 97;100 |
| Tatsugami et al. [7] | 30 | WLI/NBI | 50;90 | 83;75 | 76;78 | 61;87 |
| Cauberg et al. [6] | 14 | WLI/NBI | 55;69 | – | – | – |
| Shen et al. [8] | 11 | WLI/NBI | 68;77 | 82;77 | – | 75;83 |

*PPV* positive predictive value, *NPV* negative predictive value

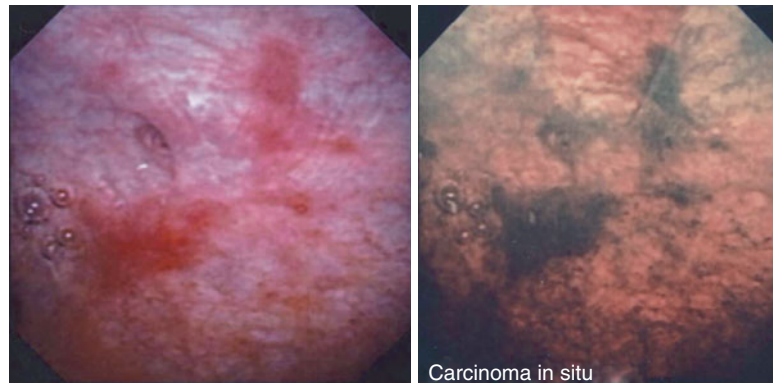


**Fig. 2.7** Carcinoma in situ visualized on WLI (*left*) appears more extensive by NBI (*brown-black* lesions) cystoscopy (*right*). Wide transurethral resection around visible lesions confirmed extensive carcinoma in situ (From Herr [27], with permission)

urine cytology, indicating carcinoma in situ (CIS), and additional biopsies have not led to increased toxicity. Negative tumor margins of suspicious lesions indicated by NBI also confirm a complete resection. Table 2.2 shows NBI enhances detection of biopsy-proved carcinoma in situ.

We recently updated our results in 538 patients undergoing surveillance cystoscopy for recurrent bladder tumors. Of 151 patients (28 %) with recurrences, 89 % were found with both WLI and NBI. In 11 % of patients, recurrent tumors were detected only by NBI. In 58 patients (38 %), additional tumors were discovered by NBI cystoscopy. Other series have also reported more tumors found on NBI over WLI cystoscopy in 27–41 % of cases. For example, Chen et al. recently found that NBI detected a total of 59 additional tumors in 44 of 143 patients [12]. Zheng et al. performed a meta-analysis of eight studies including 1,022 patients and found NBI cystoscopy consistently improved detection of bladder tumors, including carcinoma in situ, compared with WLI cystoscopy [13]. Li et al. also conducted a meta-analysis in 1,040 patients having 1,476 tumors detected by biopsy [14]. An additional 17 % of patients had tumors detected only by NBI and 24 % of patients had more tumors found by NBI than WLI ($p=0.03$). NBI provides a clearer view of papillary lesions, better defines the extent and margins of CIS lesions from surrounding normal-appearing epithelium, and facilitates wider resection or fulguration of diseased mucosa (Fig. 2.7).

NBI is usually used as an add-on procedure to WLI cystoscopy, raising a question of whether observer bias favors enhanced tumor detection after a "first-look" cystoscopy, because the same urologist usually performs NBI after first observation with WLI cystoscopy. Cauberg et al. studied 45 patients in which NBI cystoscopy was performed by a second surgeon who was blinded to the results of the initial WLI cystoscopy; additional tumors were found in 24 %, including one patient with CIS detected only by NBI [15]. On the other hand, we have seen subtle tumors recognized first with NBI cystoscopy become visible when the image was switched back to white light [5]. The issue is not whether one modality is better than the other but that NBI plus WLI cystoscopy detected more tumors, at no increased risk or cost to patients.

## NBI Evaluation of BCG Response

Intravesical BCG is used to treat residual CIS after complete resection of visible papillary tumors. The response to BCG is determined after 3 months by cystoscopy, biopsy, or TUR as necessary. BCG causes an intense inflammatory reaction, which resembles CIS on WLI cystoscopy. The mucosa often appears diffusely red, friable, and edematous, individual lesions are poorly defined, and vision is sometimes poor. Sixty-one patients were evaluated 3 months after BCG by NBI cystoscopy [16]. All had red lesions suggesting BCG inflammation or CIS on white-light imaging cystoscopy. Of 22 patients having residual tumor, NBI correctly identified CIS present in 21 (Fig. 2.8). Ten patients had a negative biopsy despite abnormal NBI findings (false-positive rate of 32 %). Only 1 of 30 patients who had negative NBI cystoscopy had persistent disease. Figure 2.9 shows a red lesion at cystoscopy to evaluate early response to BCG. The NBI appearance is consistent with inflammation, which was confirmed by biopsy. We now defer the 3-month biopsy in BCG-treated patients who have negative urine cytology and benign-appearing lesions visualized on NBI cystoscopy. Inflammatory lesions present a challenge for both WLI and NBI cystoscopy, and more study is needed in differentiating benign from malignant disease, especially in patients at risk following BCG therapy or radiation therapy or with interstitial cystitis.

## Therapeutic Impact of NBI

Therapeutic impact of NBI has not been proved; however, it seems logical that better visualization of tumors would translate in improved tumor staging, better local control, and fewer tumor recurrences. Naselli et al. found that NBI biopsies detected more tumors in 13 % of 47 patients

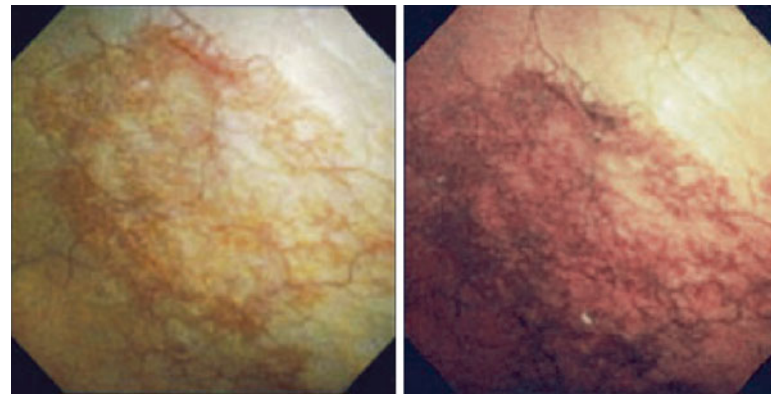

**Fig. 2.8** WLI cystoscopy (*left*) shows *faint red* mucosa after BCG. NBI (*right*) shows capillary-dense *brown* lesions typical of carcinoma in situ (From Herr [27], with permission)

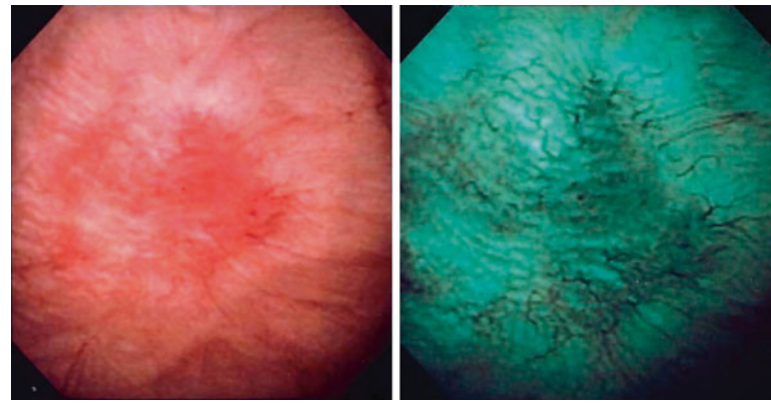

**Fig. 2.9** WLI cystoscopy (*left*) shows *red*, granular lesions after BCG. NBI (*right*) shows prominent mucosal vessels, but absence of brownish capillary density, consistent with inflammation (From Herr [27], with permission)

missed during a WLI-assisted second TUR [17], suggesting that NBI facilitates complete tumor resections. The same authors also proved the feasibility and safety of performing TUR entirely by means of narrow band imaging [18]. Cauberg and colleagues reported that among 158 patients, tumors recurred in 30 % after WLI-assisted TUR compared to 15 % with NBI-assisted TUR [19], and we found fewer tumor recurrences over 3 years in 126 patients who had recurrent low-grade papillary tumors treated by outpatient fulguration using flexible NBI versus WLI cystoscopy [20]. A prospective cohort study involving 92 patients who were treated sequentially by either WLI- or NBI-assisted TUR reported that residual tumor was found in 33 % after NBI TUR versus 43 % in the WLI group and the 1-year recurrence rate was reduced by 15 % (35 % vs. 50 %) in the NBI group [21]. In early results from an ongoing randomized study, we find NBI-assisted second TUR results in fewer tumor recurrences than restaging TUR using WLI (Herr HW. Randomized trial of narrow band versus white light imaging transurethral resection of bladder tumors (unpublished data)). Figure 2.10 shows in 238 patients, NBI-assisted TUR prolonged the 2-year recurrence-free survival time over WLI-facilitated TUR. A multicenter, randomized international study has been launched to compare the impact of NBI to WLI transurethral resection on recurrence of bladder tumors [22]. Prospective studies are required to determine whether visual advantages of NBI can translate into real therapeutic benefit for individual patients.

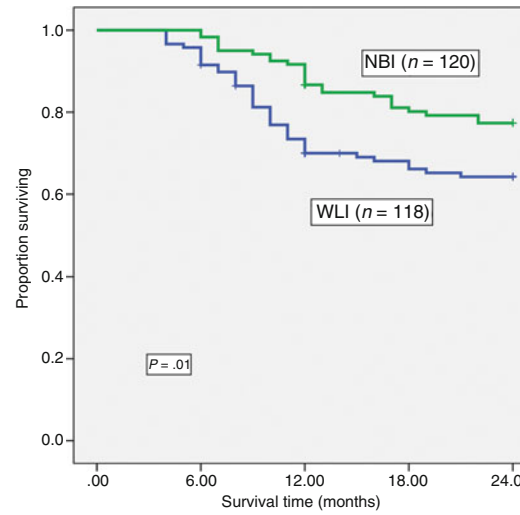


**Fig. 2.10** Two-year tumor recurrence-free survival after restaging TUR by narrow band imaging (*NBI*) or white-light imaging (*WLI*) cystoscopy

## NBI Cystoscopy Learning Curve

Two papers have addressed new user's experience with NBI cystoscopy. We evaluated 50 patients subjected to WLI and NBI cystoscopy for recurrent bladder tumors. Each patient was independently viewed by three experienced urologists, and one novice (fellow in training), assessing the presence or absence of tumor. We found no significant differences among urologists adapting to NBI cystoscopy to visualize lesions or in determining final pathology [23]. Bryan et al. also found no difference between a new user and an experienced user in detecting more tumors using NBI technology over WLI cystoscopy [24].

## NBI Ureteroscopy

NBI visualization of the upper collecting system is truly in its infancy. However, current ureteroscopes are available adapted to NBI technology, and NBI ureteroscopy has been applied to evaluate upper tract tumors. The first and only report shows in 27 patients that NBI ureteroscopy improved tumor detection rate involving the upper tracts by 23 % over WLI ureteroscopy [25]. Further, five additional tumors were found in four patients (14 %). We have used NBI ureteroscopy to detect and verify complete TUR and fulguration of upper tract urothelial tumors in over 20 cases. Further investigations are needed before NBI ureteroscopy can be advocated in daily clinical practice.

### Conclusions

NBI cystoscopy has become integrated into clinical practice to evaluate and manage bladder tumors. Many questions remain, however, such as does NBI cystoscopy detect more significant tumors and result in better outcomes?

Can NBI predict histopathologic diagnosis? Are false positives a problem that may pose risks to patients because of unnecessary biopsies, especially after intravesical therapy?

Is observer bias significantly distorting results in favor of NBI over WLI cystoscopy? Is NBI cost effective? And lastly, since imaging is inherently subjective, the quality of the surgeon must be considered when interpreting results. For example, quantifiable factors of surgeon quality, such as the time the urologist takes to complete a cystoscopy, may be as or more important than a second look with another light source.

Like other new optical methods, such as fluorescence cystoscopy, optical coherence tomography, and confocal endomicroscopy, NBI will likely be used mostly as a supplement to standard WLI cystoscopy [26]. More prospective clinical research is prescribed to define how NBI and other imaging modalities can best be implemented in the management of noninvasive bladder cancer.

## References


1. Herr HW. Max Nitze, the cystoscope and urology. J Urol. 2006;176:1313–6.
2. Herr HW, Al-Hamadi H, Dalbagni G, et al. Bladder cancer in cystoscopically normal-appearing mucosa. Br J Urol Int. 2010;106:1499–501.
3. Goh AC. Application of new technology in bladder cancer diagnosis. World J Urol. 2009;27:301–7.
4. Bryan RT, Billingham LI, Wallace DMA. Narrow-band imaging flexible cystoscopy in the detection of recurrent urothelial cancer of the bladder. Br J Urol Int. 2007;101:702–6.
5. Herr HW, Donat SM. A comparison of white-light cystoscopy and narrow-band imaging cystoscopy to detect bladder tumor recurrences. Br J Urol Int. 2008;102:1111–4.
6. Cauberg EC, Kloen S, Visser M, et al. Narrow band imaging cystoscopy improves detection of non-muscle-invasive bladder cancer. Urology. 2010;76:658–63.
7. Tatsugami K, Kuroiwa K, Kamoto T, et al. Evaluation of narrow-band imaging as a complementary method for the detection of bladder cancer. J Endourol. 2010;24:1807–11.
8. Shen YL, Zhu YP, Ye DW, et al. Narrow-band imaging flexible cystoscopy in the detection of primary non-muscle invasive bladder cancer: a 'second look' matters. Int Urol Nephrol. 2012;44:451–7.
9. Xiaodong S, Zhangqun Y, Shixin B, et al. Application of narrow band imaging in the early diagnosis and recurrent monitoring of bladder cancer. J Contemp Urol Reprod Oncol. 2009;6:325–7.
10. Geavlete B, Jecu M, Multescu R, et al. Narrow-band imaging cystoscopy in non-muscle-invasive bladder cancer: a prospective comparison to the standard approach. Ther Adv Urol. 2012;4:211–7.
11. Zhu YP, Shen YJ, Ye DW, et al. Narrow-band imaging flexible cystoscopy in the detection of clinically unconfirmed positive urine cytology. Urol Int. 2012;88:84–7.
12. Chen G, Wang B, Hongzhao L, et al. Applying narrow-band imaging in complement with white-light imaging cystoscopy in the detection of urothelial carcinoma of the bladder. Urol Oncol. 2013;31:475–9.
13. Zheng C, Lv Y, Zhong Q, et al. Narrow band imaging diagnosis of bladder cancer: systematic review and meta-analysis. Br J Urol Int. 2012;110:E680–7.
14. Li K, Lin T, Fan X, et al. Diagnosis of narrow-band imaging in non-muscle-invasive bladder cancer: a systematic review and meta-analysis. Int J Urol. 2013;20:602–9.
15. Cauberg ECC, de la Rosette J, de Reijke TM. How to improve the effectiveness of transurethral resection in nonmuscle invasive bladder cancer? Curr Opin Urol. 2009;19:504–10.
16. Herr HW. Narrow-band imaging cystoscopy to evaluate the response to BCG therapy: preliminary results. Br J Urol Int. 2010;105:314–6.
17. Naselli A, Introini C, Bertolotto F, et al. Narrow band imaging for detecting residual/recurrent cancerous tissue during second transurethral resection of newly diagnosed non-muscle-invasive high-grade bladder cancer. Br J Urol Int. 2009;105:208–11.
18. Naselli A, Introini C, Bertolotto F, et al. Feasibility of transurethral resection of bladder lesion performed entirely by means of narrow-band imaging. J Endourol. 2010;24:1131–4.
19. Cauberg EC, Mamoulakis C, de la Rosette J, et al. Narrow band imaging-assisted transurethral resection for non-muscle invasive bladder cancer significantly reduces residual tumor rate. World J Urol. 2011;29(4):503–9.
20. Herr HW, Donat SM. Reduced bladder tumor recurrence rate associated with narrow-band imaging surveillance cystoscopy. Br J Urol Int. 2011;107:396–8.
21. Montanari E, de la Rosette J, Longo F, et al. Narrow-band imaging (NBI) and white light (WLI) transurethral resection of the bladder in the treatment of non-muscle-invasive bladder cancer. Arch Ital Urol Androl. 2012;84:179–83.
22. de la Rosette J, Gravas S. A multi-center, randomized international study to compare the impact of narrow band imaging versus white light cystoscopy in the recurrence of bladder cancer. J Endourol. 2010;24:660–1.

23. Herr H, Donat M, Dalbagni G, Taylor J. Narrow-band imaging cystoscopy to evaluate bladder tumors-individual surgeon variability. Br J Urol Int. 2010;106:53–5.
24. Bryan RT, Shat ZH, Collins SI, et al. Narrow-band imaging flexible cystoscopy: a new user's experience. J Endourol. 2010;24:1339–43.
25. Traxer O, Geavlete B, de Medina SG, et al. Narrow-band imaging flexible digital flexible ureteroscopy in detection of upper urinary tract transitional-cell carcinoma: initial experience. J Endourol. 2011;25:19–23.
26. Cauberg EC, de Bruin DM, Faber DJ, et al. A new generation of optical diagnostics for bladder cancer: technology, diagnostic accuracy, and future applications. Eur Urol. 2009;56:287–96.
27. Herr HH. Narrow band imaging cystoscopy. Urol Oncol. 2011;29(4):353–7.

# Optical Coherence Tomography in Bladder Cancer

3

M.T.J. Bus, D.M. de Bruin, Th.M. de Reijke, and J.J.M.C.H. de la Rosette

## OCT Technology

### OCT System Design

OCT is based on depth-resolved detection of elastic light scattering. The OCT system (Fig. 3.1) consists of an interferometer, generally constructed from fibre-optic components, illuminated by a broad wavelength-range light source operating in the near infrared (typically 1,250–1,350 nm for non-ophthalmic applications). When light is directed at a tissue sample, it will be partially backscattered. This backscattered light is measured at different depths at a particular location on the tissue using low-coherence interferometry resulting in a reflection profile in the depth ($z$-)direction. The magnitude of the OCT signal at each depth is determined by the different cellular structures in the imaged volume (typically in the order of $10^3$ μm$^3$ or 1 pL), and as a result it differs per tissue type. Several adjacent depth profiles can be acquired in the lateral (x-) direction and displayed as a greyscale image in real time which is known as an OCT B-scan. Subsequently, the OCT beam can be scanned across a tissue sample in the other lateral (y-) direction, resulting in a 3-dimensional image representation with acquisition speeds reported up to several volumes per second.

### Endoscopic OCT

The development of optical fibres for light transport in telecommunication made fibre-based OCT systems possible. This has led to the development of ultrathin fibre-based sample arm devices that allowed endoscopic integration. Small OCT probes were first and mainly developed for cardiovascular applications, allowing visualisation of cardiovascular plaque, thrombi or stent placement. More recently, this resulted in the commercial development of disposable in vivo OCT probes with a diameter less than 1 mm which are already used in several medical settings, i.e. to be used in endoscopes or in combination with 16G/18G needles to access internal tissue. However, these probes are mainly developed for circumferential (lighthouse-like) scanning and are therefore excellent for imaging tubular tissue. This makes them less usable for imaging the bladder where forward scanning, covering the same field of view as a regular cystoscope, is more preferable. Forward scanning

M.T.J. Bus, MD, MSc (✉) • T.M. de Reijke, MD, PhD • J.J.M.C.H. de la Rosette, MD, PhD
Department of Urology, Academic Medical Center Amsterdam, Amsterdam, The Netherlands
e-mail: m.t.bus@amc.uva.nl

D.M. de Bruin, PhD
Department of Urology, Academic Medical Center Amsterdam, Amsterdam, The Netherlands

Department of Biomedical Engineering & Physics, Academic Medical Center Amsterdam, Amsterdam, The Netherlands

J.C. Liao, L.-M. Su (eds.), *Advances in Image-Guided Urologic Surgery*,
DOI 10.1007/978-1-4939-1450-0_3, 

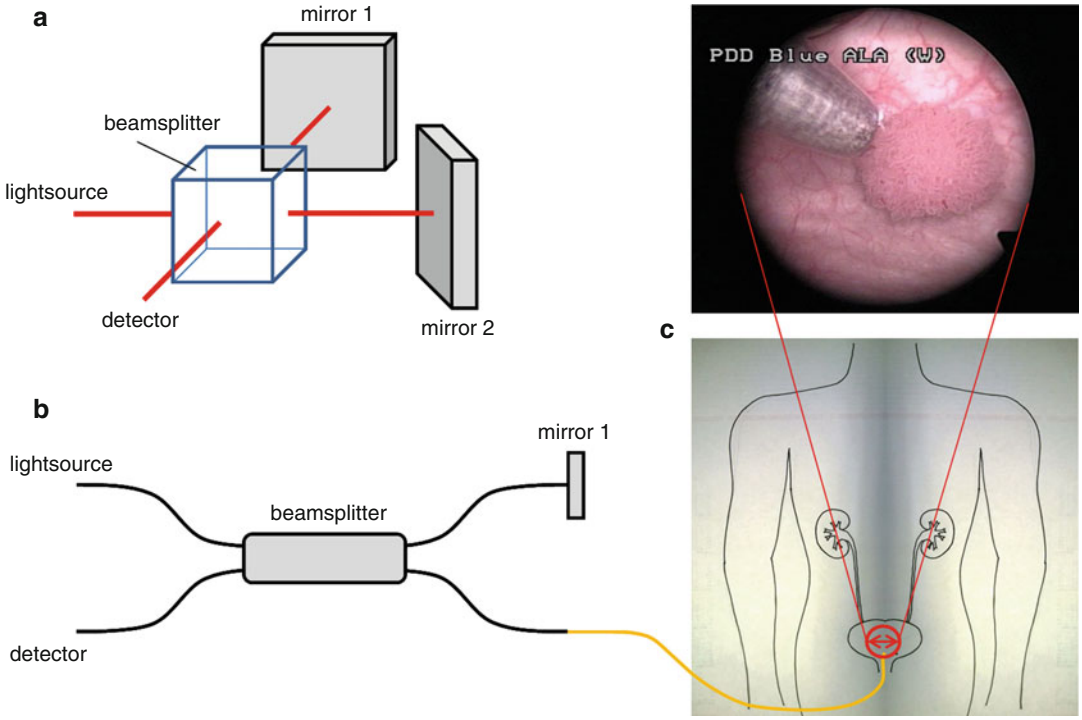


**Fig. 3.1** Schematic overview displaying time-domain, low-coherence interferometry which can measure echo time delays of light. (**a**) A Michelson-type interferometer is equipped with a sample and reference arm. Light which is back-reflected from *mirror 1* interferes with light travelling a known reference path length (*mirror 2*). The reference arm is mechanically translated in order to produce a time-varying path length difference between both arms. Using a low-coherence light source, interference will only be observed when light from the tissue arrives nearly at the same time as light from the reference arm. Axial (depth) scan information is obtained by detecting the interference signal. An image is formed by colour-mapping the amplitude of adjacent axial scans in a 2D or 3D representation. (**b**) Clinical usable OCT systems are equipped with fibre optics which are, in the case of bladder OCT, interfaced with a fibre optical scanning probe (**c**) that fits through the working channel of a cystoscope (*black inset*, Courtesy of Dr. Jörg Schmidbauer)

has been developed using small moving mirrors on the tip of a fibre. A clinical applicable OCT system employing forward-looking OCT technology has been developed by Imalux known as the Niris® Imaging System. This system employs a 2.7 mm-diameter imaging probe (Niris® Optical Imaging Probe). The Imalux Niris system has been used in most bladder cancer studies. However, novel designs are researched to reduce the size, which is currently the limiting factor for scope integration.

## Functional OCT

Clinical usability of OCT images depends on obvious factors such as high resolution, high imaging speed and adequate contrast to discriminate between benign and malignant tissues. Contrast in OCT is caused by spatial differences in refractive index of different tissue constituents, e.g. contrast originates from reflection of different structures. It is known that the refractive index is proportional to the density of the cells and cell structure. Because malignant cells display an increased number, larger and more irregularly shaped nuclei with a higher refractive index and more active mitochondria, OCT images are expected to be different in malignant tissue compared to normal and benign tissue [1]. These differences can be elucidated from the light scattering properties [2] that are measured from the signal decrease with depth from OCT images,

which is quantified by the attenuation coefficient $\mu_{oct}$. Studies have shown that quantitative measurement of $\mu_{oct}$ allows in vivo differentiation between different tissue types. An animal study by Xie et al. [3] showed differences in scattering properties between normal and cancerous urothelium. Similar studies on lesions in the kidney [4], vulva [5], oral tissue [6] and lymph node metastasis [7] confirmed the ability of OCT to distinguish tissue types based on $\mu_{oct}$. However, initial studies on ex vivo human bladder urothelial biopsies showed that factors typical for ex vivo settings (e.g. cauterisation of bladder tissue specimens) on $\mu_{oct}$-based grading of human bladder cancer were inconclusive but indicative of the need for in vivo evaluation [8].

## OCT in Bladder Cancer: State of the Art

### Literature Survey on Animal Studies

The feasibility of OCT on urothelium has been investigated in a variety of animal models. The potential of OCT as a diagnostic tool was demonstrated in rabbit [3] and porcine bladders [9]. OCT in the porcine bladder, a close homolog to the human bladder, showed the ability to image the anatomical layers of the porcine bladder including the urothelium, lamina propria and muscularis propria. The first systematic study of OCT in urological tumours was performed on bladders of Fischer rats that were exposed to methyl-nitroso-urea, a standard rat model for bladder cancer studies. In this rat bladder cancer model, edema, inflammatory infiltrates, submucosal blood congestions and abnormal growth of urothelium were seen [9].

Although the first animal studies of OCT in urology showed the high potential of OCT as a diagnostic tool in urothelial carcinoma, they also showed the major technical limitations of the OCT systems that had to be overcome before introducing the technique in a clinical setting. An in vivo setting in the rabbit bladder using transverse OCT imaging probe indicated two problems using this probe. First, since the bladder is a relatively large and irregularly shaped organ and the catheter used was designed to have a fixed working distance, the bladder wall was predominantly displaced from the focal plane during imaging, which resulted in relatively low transverse resolutions, as the distance from the imaging probe to the wall did not remain constant. Second, since the number of transverse pixels is constant, over a larger circumference, the lateral imaging resolution decreased as the size of the pixel increased. These two results emphasised that redesign of the imaging probe was mandatory [3].

### Literature Survey on Humans *Ex Vivo*

After the feasibility of OCT was demonstrated in cardiology and ophthalmology, OCT was applied for the first time on human urological tissue in 1997 [10]. OCT measurements were performed on normal bladder tissue obtained from autopsy. Ex vivo was seen that OCT is able to delineate the microstructure of the normal human bladder wall. Anatomical layers in the human bladder, including the urothelium, lamina propria and muscularis propria, can be identified (Figs. 3.2 and 3.3) [3, 10, 11].

The capability of OCT in distinguishing between different anatomical layers is based on the different back-reflection characteristics of each layer [11]. The urothelium is slightly lower scattering, and therefore higher and more regular back-reflection intensity is seen. This gives the urothelium a darker appearance on OCT images compared to the underlying lamina propria. Secondly, OCT is capable to identify capillaries within the submucosa in normal human bladder tissue and vessels in the bladder wall [3]. Unlike animal carcinogenesis models, the first preliminary human studies showed that bladder cancers in humans are more complicated in terms of urothelial backscattering. Tumorigenesis induces complex surface condition changes resulting in enhanced backscattering in some lesions and reduced backscattering in others. Nevertheless, promising results can be provided when incorporating other diagnostic parameters such as urothelial heterogeneity, visibility of anatomical layers and vascularisation changes [12]. The anatomical microstructure of the bladder could no longer

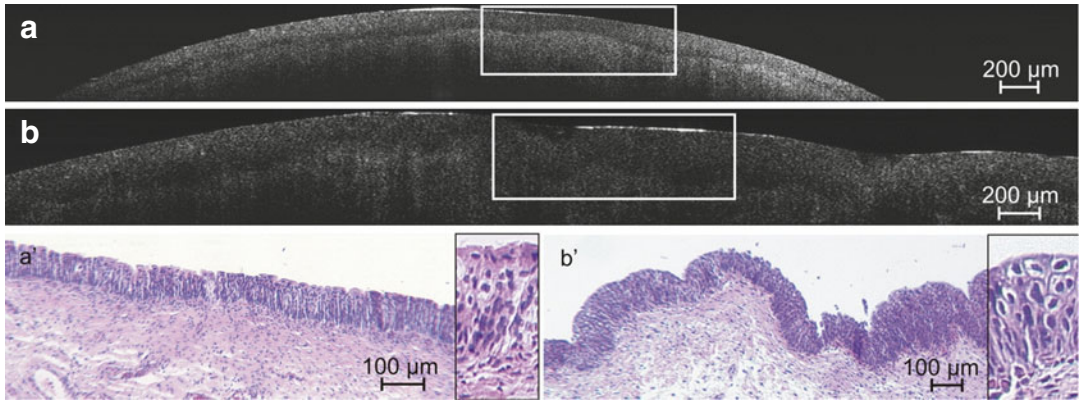


**Fig. 3.2** OCT bladder pathology correlated with pathohistology (Courtesy of Prof. R. Knüchel). Correlation of ultrahigh-resolution OCT B-scans of healthy tissue (**a**) and carcinoma in situ (*CIS*) (**b**) with histological findings (**a**′ and **b**′). Histological sections (haematoxylin-eosin staining) represent the marked areas within the corresponding OCT images. The insets in (**a**′ and **b**′) represent magnified views of the urothelial layer of the tissue. OCT representation of healthy tissue (**a**) and CIS (**b**) both demonstrate a continuous dark layer in between the higher scattering urothelium and stroma representing the basement membrane zone. The urothelium illustrated is very homogeneous for healthy tissue (**a**), which is not the case for CIS (**b**) in which the tissue appears coarse grained and inhomogeneous

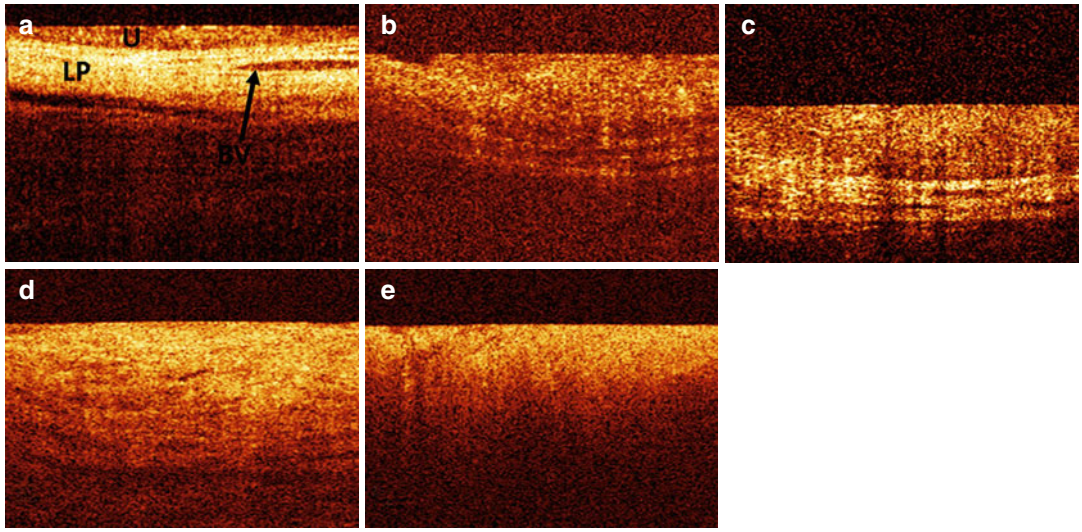


**Fig. 3.3** OCT bladder pathology. (**a**) Normal bladder lining which is characterised by high contrast and a stratified structure. The urothelial (*U*) layer is visible as an upper dark layer, while the second bright layer is the lamina propria (*LP*). Blood vessels (*BV*) are visible as dark structures in the lamina propria. (**b**) Carcinoma in situ (*CIS*) is recognised by its low contrast compared to normal-appearing OCT bladder images. The urothelial and lamina propria layer appears to be more bright. The horizontal structures of the anatomical layers are still recognisable. (**c**) Ta carcinoma of the bladder is recognised on OCT image as thickened upper urothelial layer, clearly distinguishable from the second bright lamina propria layer, showing no signs of invasion. (**d**) T1 carcinoma of the bladder. Horizontal structures are losing contrast resulting in indistinguishable urothelial and lamina propria layer. The muscularis is still visible. (**e**) T2 carcinoma of the bladder. OCT image of a T2 tumour showed tumour extending into the muscle indicated by the total loss of horizontal structures (Courtesy of Dr. Jörg Schmidbauer)

be visualised in *ex vivo* bladders of patients suffering muscle-invasive bladder cancer (Fig. 3.3) [3]. However, due to the limited axial resolutions to about 10 μm of the standard OCT systems, a valid decision of invasion and the assessment of urothelial dysplasia are not possible.

The standard OCT systems are very well able to visualise the urothelium, lamina propria and muscularis propria, and the integrity of the basement membrane cannot be reproduced because of restricted resolution power of such systems [11]. Ultrahigh resolution OCT, however, is able to visualise the basement membrane zone in healthy and diseased bladder wall tissue by providing high-resolution OCT images [11]. The basement membrane zone is visualised as a thin layer showing a minimum of signal intensity between the moderately scattering urothelium and the higher scattering lamina propria. In tissue samples of invasive bladder tumours, the basement membrane appears no longer as a continuous signal-free layer but shows interruption in ultrahigh resolution OCT images [11]. This latest advantage gives OCT the potential to give real-time information on tumour stage.

An initial study on $\mu_{oct}$-based grading of bladder cancer in bladder tissue specimens collected during transurethral tumour resection (TURT) was inconclusive due to typical factors for ex vivo settings [8]. Cauterisation of bladder tissue specimens after transurethral resection, orientation of the biopsies and the effect of tissue relaxation of the biopsies are all factors that reflect limitations due to *ex vivo* circumstances. This outcome indicates the need for in vivo evaluation of OCT as a diagnostic tool for both grading and staging in bladder cancer.

## Literature Survey on Humans In Vivo

Since the bladder is a relatively large and irregularly shaped hollow organ, OCT measurements are hampered as was seen in vivo animal studies. The first step in implementation of OCT in hollow organs was endoscopic implementation to provide a reliable and convenient access of probing OCT to the surface of the urinary bladder. However, this first step included several optical, engineering and biomedical aspects such as creation of an OCT interferometer with a flexible arm, development of miniaturised lateral scanning probe with a remote control and acquisition of OCT data in parallel with common endoscopic imaging. In 1997 the first OCT imaging probe was successfully developed with endoscopes by integrating the sampling arm of an all-optical-fibre interferometer into standard endoscopy using their biopsy channel to transmit low-coherence radiation to the tissue, providing direct access of OCT to the bladder wall possible in vivo [13]. To probe the surface of the urinary bladder, a miniaturised electromechanical unit was developed, controlling the lateral scanning process by terminating the sampling arm of the fibre interferometer [13]. Polarisation fading due to polarisation distortions occurring by bending the endoscopes arm was avoided by using polarisation maintaining fibres to transport the light. This first endoscopic integration resulted in an endoscopic OCT system with a central wavelength of 830 nm, an image depth of 3 mm and a scanning rate of 30 cm/s and finally in an OCT picture of 200×200 pixel size in approximately 1 s.

Results on application of this new OCT device were compatible with *ex vivo* results; due to the different backscattering intensity of each different anatomical layer, they could be identified. Like in *ex vivo* settings, the urothelial layer was seen as a weakly scattering layer, while the lamina propria was seen as a bright layer with the highest scattering intensity. In the lamina propria, vessels could be identified. The muscularis propria was identified as a less scattering layer beneath the lamina propria [1, 13, 14]. Benign conditions of the bladder such as cystitis were seen as edematous thickened urothelial layer and thickness of the lamina propria. In case of prolonged chronic cystitis, sclerosis and fibrosis was seen as increased backscattering from these structures, combined with increased vascularisation of the bladder wall [1]. In chronic cystitis in children, typical accumulation of fluid under the urothelial layer was seen on tomograms [1, 14]. Also bladder wall inflammation and von Brunn's nests were correctly diagnosed using OCT [15].

**Table 3.1** Diagnostic accuracy of OCT on the bladder urothelium

| Author | Stage of Research | Sensitivity | Specificity |
|---|---|---|---|
| Hermes et al. [11] | 142 *ex vivo* human bladder biopsy specimens | 83.8 % | 78.1 % |
| Manyak et al. [15] | OCT cystoscopically | 100 % | 89 % |
| Goh et al. [16] | OCT cystoscopically | Ta 90 %, T1 75 %, T2 100 % | Ta 89 %, T1 97 %, T2 90 % |
| Sengottayan et al. [18] | OCT cystoscopically | Ta 90 %, T1 75 %, T2 100 % | Ta 89 %, T1 97 %, T2 90 % |
| Ren et al. [17] | OCT cystoscopically | 94.40 % | 81.3 % |
| Karl et al. [19] | OCT cystoscopically | 100 % | 65 % |

In cancerous tissue, anatomical layers of the urinary bladder are completely lost [1, 13, 14].

Secondly, a higher homogeneity and typically higher urothelium backscattering characterised the OCT images. The latter resulted in a decreased depth of optical imaging, because of the strong scattering in malignant cells. Finally, a higher vascularisation degree was found in tomograms of cancerous tissue [13].

Studies on sensitivity and specificity of OCT on real time classifying bladder lesions as benign or malignant show high overall sensitivity of 100 %, overall specificity of 89 %, positive predictive value of 75 %, negative predictive value of 100 % and an accuracy of 92 % [15]. Positive predictive value for invasion into the lamina propria was 90 % [15]. Other in vivo studies showed similar results on sensitivity, specificity, positive predictive value, negative predictive value and accuracy in staging urothelial cancer of the bladder [11, 15–18] (Table 3.1) but also suggest that disruptions of the bladder wall from erosion, scarring or granuloma could result in false-positive results [15, 16]. In addition, for large tumours with extensive broadened urothelium, tumour depth will transcend OCT imaging depth and compromise the staging ability of OCT. This problem may be overcome by applying OCT to the tumour base [14].

One study showed a limited specificity of 65 %, probably due to a learning curve [19]. However, these results are very promising; a small study population limits them. Despite these limitations, emerging OCT with WLC increases the positive predictive value and negative predictive value of WLC dramatically [17], and a combination of these two techniques could possibly be helpful in the discrimination between cancer and benign lesions of the bladder wall.

The diagnostic value of OCT to determine tumour stage correlated to regular diagnostics like cytology, histology and white-light cystoscopy has yet to be elucidated in large controlled studies. Secondly, also the role for OCT in diagnosing CIS is not yet known [20].

## Future Perspectives on Clinical Applications

The combination of a high-resolution imaging technique (higher than any other clinical imaging technology) and modern endo-urological approaches seems promising to improve both diagnosis and therapy of bladder tumours [21]. Several features of OCT make it well suited for intraluminal diagnostics. OCT can be constructed with common optical fibre components and integrated within conventional endoscopes. Finally, the OCT system is compact and portable. All of these features make OCT an ideal tool for these purposes in the urinary bladder. Unfortunately, OCT still needs comprehensive investigation before implemented in clinical practice. In order to know the real value of OCT, extended in vivo studies should provide insight in the ability of OCT to differentiate between low-grade, high-grade and CIS lesions. Secondly, extended studies should provide the diagnostic accuracy including sensitivity, specificity, positive predictive value and negative predictive value [22]. Finally by comparing OCT with established preoperative and intraoperative methods like CT scan, (selective) cytology and biopsies, the added

value of OCT in clinical practice can be determined. Despite this lack of knowledge, there are several clinical applications conceivable, which are outlined below.

First of all, OCT might be of value in improving the quality of resection of urothelial tumours in the bladder. By evaluating the resection margins with OCT, one might be able to know if the resection is complete at the time of the operation. Besides evaluating the lateral borders of the resection area, these techniques could also be of benefit in determining the depth of the resection. If OCT measurements of the base of a resection plane confirm urothelial carcinoma, one can complete the resection in depth, if technically possible. However, an initial study performed on ex vivo human bladder urothelial biopsies showed that factors typical for ex vivo settings (e.g. cauterisation of bladder tissue specimens) on $\mu_{oct}$-based grading of human bladder cancer were inconclusive but indicative of the need for in vivo evaluation [8]. More knowledge on the appearance of cauterised urothelium in OCT images is necessary and should be obtained in an in vivo setting, as cauterisation at resection margins might lead to problematic artefacts [23].

In patients with low-grade, low-stage disease and a recurrence shown by OCT to be again low grade, endoscopic laser fulguration and/or coagulation may be applied. One of the drawbacks of laser treatment is the fact that no specimen for pathology is obtained for definite diagnosis. The risk exists that progression has occurred without being noticed. OCT measurements of these tumours might provide this diagnosis, so that laser fulguration becomes a safer treatment modality [23].

One of the most promising future perspectives is the merging of OCT with other optical diagnostic techniques, photodynamic diagnosis (PDD) and narrow band imaging (NBI). Both PDD and NBI aim at better visualisation of urothelial tumours by enhancing contrast between normal urothelium and malignant lesions. Unfortunately, both techniques have a relative high false-positive rate. Merging these techniques with OCT could increase the diagnostic accuracy by combining the high sensitivity of fluorescence for detecting cancer-specific biochemical changes and the high resolution of OCT for diagnosing tumorigenesis-induced morphological changes. In other words, OCT as an adjunct tool to PDD enhances the specificity of PDD significantly [24]. Consequently, OCT can be used to confirm urothelial cancer in lesions detected by NBI and PDD [22]. Studies performed on ex vivo rat bladders showed that both PDD and OCT were able to identify urothelial cancers, and when combined both techniques enhanced the efficiency and sensitivity of early bladder cancer diagnosis dramatically [25, 26]. In vivo human studies confirmed the earlier results in animal studies, by increasing significantly per-lesion sensitivity and specificity of fluorescence-targeted OCT [27, 28]. Emerging techniques that enhance tumour visualisation with OCT can therefore potentially reduce unnecessary biopsies, without extra morbidity. However not investigated yet, this scenario can also be imagined for NBI combined with OCT. This scenario is especially interesting for the case of cytology suspicious of high-grade malignancy and negative cystoscopy findings; so-called at-random biopsies are taken to exclude or confirm carcinoma in situ (CIS). OCT measurements via the working channel of a cystoscope could be of value in the diagnosis of CIS, i.e. guiding the biopsy procedure by visualising CIS lesions. Nowadays, CIS detection knows several challenges and OCT confirmation is limited by reliance on white-light cystoscopy to identify the suspicious lesions. Combining fluorescence cystoscopy with OCT can potentially overcome this limitation. Secondly, as CIS often presents with bladder urothelium denudation, precise pathological correlations with in vivo imaging (co-registration) may be challenging [29]. Hypothetical OCT is less suitable for follow-up of CIS, as OCT is known for false positives in inflammatory states, e.g. after BCG, and CIS and high-grade lesions are often treated with BCG instillations. A follow-up study should provide more insight in this specific state of inflammation and the effect of intravesical installations in general on OCT outcome. In addition, the effect of radiation on OCT images is not known.

If the effect of intravesical installations and radiation on OCT is known, OCT might be a very useful tool for follow-up purposes. For recurrent small bladder tumours in patients previously diagnosed

with low-grade, low-stage disease, office-based fulguration can be applied instead of TURBT. One of the disadvantages of this technique is that no specimen for pathology is obtained, which makes that the urologist has to predict tumour stage and grade. Since estimation is not reliable, a pathological confirmation of low-grade, low-stage disease is desirable. OCT measurement of lesion grade and stage can provide this confirmation and make office-based fulguration a more safe and reliable mode of treatment. Secondly, it is a less invasive determination of disease grade and stage than office-based biopsies. A final possible implementation of OCT in a clinical setting could be OCT-guided marker placement in the bladder wall in radiation therapy. Using OCT can help to precisely determine the tumour margin. This gives the urologist information to place markers close to the tumour margin, making precise external beam radiation therapy possible.

## Future Perspectives on OCT Technology Integration

### Imaging, NBI

Combining OCT with white-light imaging or NBI is a challenge pursued by several research groups, and whether NBI could play a part in the scenario has to be established in future research. However, the increasingly smaller camera CCD chips, combined with improved illumination, have shown promising results, especially in case of NBI. NBI could therefore be used to visualise or target a suspected lesion. Additionally, OCT could assist in epithelial lesion differentiation by addressing grade and stage as shown by several studies [5, 30]. Moreover, in case of mucosal red spots at first cystoscopy or at follow-up cystoscopy, office-based OCT measurements via the working channel of a cystoscope could be of use in differentiating between CIS and inflammation or post-instillation effects.

### Fluorescence Imaging, PDD

As with NBI, fluorescence imaging, also known as photodynamic detection (PDD), aims at improving visualisation of bladder tumours. Because relatively straightforward illumination and imaging methods are used, several groups have looked into combining these two technologies. For example, it would be helpful to target the biopsies by improving the visual detection of CIS. In this scenario, PDD could be the answer since it has been shown that it significantly improves the detection of CIS. OCT would have the same added value as in the combination with NBI. Again, OCT could allow for quantitative and qualitative differentiation of a lesion found with PDD [26–28].

### Raman

Raman spectroscopy and OCT are two relatively new optical diagnostic techniques both aiming at providing an objective histopathological diagnosis real time and in a minimal invasive way. While Raman spectroscopy can estimate the molecular composition of the tissue, OCT can produce cross-sectional images with high resolutions comparable to histopathology. Both methods show promising preliminary results, but extensive research still has to be done before any of the techniques can be implemented in the management of upper urinary tract urothelial carcinoma (UTUC). Technologically, integration of these two techniques seems feasible [31] because they share a large part of the technology platform. However, Raman measurements are still very time consuming and therefore sensitive to tissue movement. Tissue background fluorescence is an additional challenge that needs to be addressed by technological advancements.

## Novel Analysis Methods: Relating Optical Properties to Functional Information

OCT is in essential an imaging method, providing images that resemble the tissue structure on a microscopic level. However, these images allow for quantification by studying the physics of light and tissue interaction. This research area investigates the origin of the OCT signal, covering the physics of scattering [28, 29] and absorption

[30], phase sensitivity including polarisation sensitivity [31], Doppler shift [32] and speckle [33] which is a coherent noise source in OCT imaging. Understanding and quantification of these principles based on known optical and electrical properties of the used OCT system and the optical and mechanical properties of the material under study could result in a powerful tool in medical diagnostics. Physical properties such as wavelength, refractive index, Brownian motion, orientation, size and phase function of tissue scatters are parameters that play a major role in scattering of tissue and might be related to biological conditions of tissue or cells. Hence, the development of algorithms that are based on these physical properties and underlying principles is paramount.

## Attenuation Coefficient

Light scattering causes a decrease of OCT signal magnitude with depth and limits the imaging range to approximately 2 mm. This rate of OCT signal decrease is quantified by the attenuation coefficient $\mu_{oct}$ that allows in vivo differentiation between different tissue types (Fig. 3.4) [4, 5]. During carcinogenesis, changes occur in cellular architecture resulting in an increased nuclear-cytoplasm ratio and increased amount of mitochondria. Physically, this subcellular organisation of tissue determines light scattering properties [32]. We therefore hypothesise that lesion stage can be obtained from image-based assessment of the presence of a visible basement membrane and that lesion grade correlates with $\mu_{oct}$.

An animal study by Xie et al. [3] predicted and showed differences in scattering properties between normal and cancerous urothelium. Similar studies on lesions in the ureter [30], kidney [4, 33], vulva [5], oral tissue [6] and lymph node metastasis [7] confirmed the ability of OCT to distinguish tissue types based on $\mu_{oct}$. However, an initial study by Cauberg et al. on ex vivo human bladder urothelial biopsies showed that factors typical for ex vivo settings (e.g. cauterisation of bladder tissue specimens) on $\mu_{oct}$-based grading of human bladder cancer were inconclusive but indicative of the need for in vivo evaluation [8].

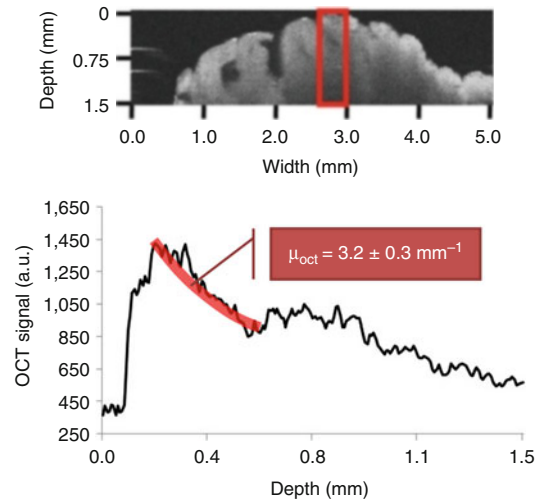


**Fig. 3.4** Attenuation coefficient mapping of OCT data. A region of interest (ROI) is selected within an OCT image (indicated by the *red square*). From the ROI, the average OCT signal vs. depth can be plotted as shown in the graph below. From this graph, the attenuation of the OCT signal by means of the attenuation coefficient ($\mu_{oct}$, $mm^{-1}$) is calculated using Beer's law

## Layer Thickness

In case of a bladder cancer lesion, cells grow and change and the urothelial layer thickens [26]. This layer thickness can be measured from OCT images [23], though it does not provide information about the architectural and cellular changes that occur in the layer itself during carcinogenesis. When visible, this layer thickness can be determined with 10 μm uncertainty (corresponding to the OCT depth resolution of most systems).

An animal study by Pan et al. [25] showed increased thickening of the urothelium after induction of tumorigenesis. At onset of the hyperplasia, the urothelial thickness ranged from less than 60–70 to 600 μm or higher.

## Flow and Diffusion

Similar as in ultrasound (US) imaging, blood flow profiles can be extracted based on either Doppler analysis or speckle correlation of the OCT signal. However, since OCT improves significantly on resolution compared with US, it

enables the visualisation of small capillaries and arterioles [34]. Application of superficial blood flow detection in bladder cancer lesions has been demonstrated in a pilot study by Liu et al. showing the potential application of this technology to study bladder cancer lesion-related blood flow properties which could contribute in understanding angiogenesis [29].

## Polarisation

By detecting not only the intensity but also the polarisation state of light back-reflected from a sample, polarisation-sensitive OCT (PS-OCT) yields depth-resolved information on any light polarisation changing properties of the sample. Birefringence, the main polarisation property of interest for biological tissues, is caused by a difference in index of refraction that results in phase retardation between orthogonal polarisation states. This technique has been applied to a wide variety of clinical situations, including ophthalmology for possible early diagnosis of glaucoma [17] and in dermatology for the detection of burn wounds [ [18] and basal cell carcinoma (BCC) [19]. A typical cell that exhibits polarisation-sensitive behaviour is collagen. This has been shown for an epithelial lesion such as basal cell carcinoma (BCC), which contains a certain polarisation state.

The combined use of fluorescence cystoscopy and cross-polarisation optical coherence tomography (CP OCT) was assessed in 92 bladder zones of 26 patients and combined with quantitative estimation of the OCT signal. The diagnostic accuracy in detecting superficial bladder cancer was 93.6 %, sensitivity 96.4 %, specificity 92.1 %, positive predictive value 87 % and negative predictive value 97.9 % [27].

## Statistical Analysis: Image Texture and Speckle

During the development of carcinogenesis, the epithelial tissue structure is believed to change from a nicely layered architecture towards a more heterogeneous tissue structure. This has been studied in a transgenic CIS mouse model by Ren et al. [35]. This change of structure takes place on an intracellular level and on an extracellular, more architectural tissue level. These structural changes can be quantified by statistical analysis of the OCT signal. First, small changes in the OCT signal are called speckle and can be measured as a function of time or place. This is achieved by measuring the standard deviation of OCT signal of adjacent pixels. The distribution of all these standard deviations is called a speckle histogram. During carcinogenesis, a cell contains more and irregular organelles. This results in a change of the speckle distribution. The larger or more structural tissue variations can be analysed by plotting the distribution of all intensities within an OCT image. The resulting intensity histogram will also change if there are more irregularities in the tissue associated with, i.e. increase of lesion grade.

Ren et al. study both the speckle and intensity distribution where they found an increase of speckle distribution and a decrease of intensity distribution with increase of CIS. However, this behaviour needs to be validated in a larger population study [36].

**Acknowledgements** The authors like to thank Dr. Jörg Schmidbauer from the Medical University of Vienna and professor Ruth Knüchel from the University Hospital of Aachen for generously providing the OCT figures used in this paper.

## References

1. Feldchtein F, Gelikonov G, Gelikonov V, Kuranov R, Sergeev A, Gladkova N, Shakhov A, Shakhova N, Snopova L, Terent'eva A, Zagainova E, Chumakov Y, Kuznetzova I. Endoscopic applications of optical coherence tomography. Opt Express. 1998;3:257–70.
2. Faber DJ, van der Meer FJ, Aalders MCG, van Leeuwen TG. Quantative measurement of attenuation coefficients of weakly scattering media using optical coherence tomography. Optics Express 2004;12:19:4353–65.
3. Jesser CA, Boppart SA, Pitris C, Stamper DL, Nielsen GP, Brezinski ME, Fujimoto JG. High resolution imaging of transitional cell carcinoma with optical coherence tomography: feasibility for the evaluation of bladder pathology. Br J Radiol. 1999;72:1170–6.
4. Barwari K, de Bruin DM, Faber DJ, van Leeuwen TG, de la Rosette JJ, Laguna MP. Differentiation between normal renal tissue and renal tumours using functional

optical coherence tomography: a phase I in vivo human study. BJU Int. 2012;110:E415–20.
5. Wessels R, de Bruin DM, Faber DJ, van Boven HH, Vincent AD, van Leeuwen TG, van Beurden M, Ruersa TJ. Optical coherence tomography in vulvar intraepithelial neoplasia. J Biomed Opt. 2012;17: 116022.
6. Tomlins PH, Adegun O, Hagi-Pavli E, Piper K, Bader D, Fortune F. Scattering attenuation microscopy of oral epithelial dysplasia. J Biomed Opt. 2010;15: 066003.
7. McLaughlin RA, Scolaro L, Robbins P, Saunders C, Jacques SL, Sampson DD. Mapping tissue optical attenuation to identify cancer using optical coherence tomography. Med Image Comput Comput Assist Interv. 2009;12:657–64.
8. Cauberg EC, de Bruin DM, Faber DJ, de Reijke TM, Visser M, de la Rosette JJ, van Leeuwen TG. Quantitative measurement of attenuation coefficients of bladder biopsies using optical coherence tomography for grading urothelial carcinoma of the bladder. J Biomed Opt. 2010;15:066013.
9. Pan Y, Lavelle JP, Bastacky SI, Meyers S, Pirtskhalaishvili G, Zeidel ML, Farkas DL. Detection of tumorigenesis in rat bladders with optical coherence tomography. Med Phys. 2001;28:2432–40.
10. Tearney GJ, Brezinski ME, Southern JF, Bouma BE, Boppart SA, Fujimoto JG. Optical biopsy in human urologic tissue using optical coherence tomography. J Urol. 1997;157:1915–9.
11. Hermes B, Spoler F, Naami A, Bornemann J, Forst M, Grosse J, Jakse G, Knuchel R. Visualization of the basement membrane zone of the bladder by optical coherence tomography: feasibility of noninvasive evaluation of tumor invasion. Urology. 2008;72: 677–81.
12. Wang ZG, Lee C, Waltzer W, Yuan ZJ, Wu ZL, Xie HK, Pan YT. Optical coherence tomography for noninvasive diagnosis of epithelial cancers. Conf Proc IEEE Eng Med Biol Soc. 2006;1:129–32.
13. Sergeev A, Gelikonov V, Gelikonov G, Feldchtein F, Kuranov R, Gladkova N, Shakhova N, Snopova L, Shakhov A, Kuznetzova I, Denisenko A, Pochinko V, Chumakov Y, Streltzova O. In vivo endoscopic OCT imaging of precancer and cancer states of human mucosa. Opt Express. 1997;1:432–40.
14. Zagaynova EV, Streltsova OS, Gladkova ND, Snopova LB, Gelikonov GV, Feldchtein FI, Morozov A. In vivo optical coherence tomography feasibility for bladder disease. J Urol. 2002;167:1492–6.
15. Manyak MJ, Gladkova ND, Makari JH, Schwartz AM, Zagaynova EV, Zolfaghari L, Zara JM, Iksanov R, Feldchtein FI. Evaluation of superficial bladder transitional-cell carcinoma by optical coherence tomography. J Endourol. 2005;19:570–4.
16. Goh AC, Tresser NJ, Shen SS, Lerner SP. Optical coherence tomography as an adjunct to white light cystoscopy for intravesical real-time imaging and staging of bladder cancer. Urology. 2008;72:133–7.
17. Ren H, Waltzer WC, Bhalla R, Liu J, Yuan Z, Lee CS, Darras F, Schulsinger D, Adler HL, Kim J, Mishail A, Pan Y. Diagnosis of bladder cancer with microelectromechanical systems-based cystoscopic optical coherence tomography. Urology. 2009;74:1351–7.
18. Sengottayan VK, Vasudeva P, Dalela D. Intravesical real-time imaging and staging of bladder cancer: use of optical coherence tomography. Indian J Urol. 2008;24:592–3.
19. Karl A, Stepp H, Willmann E, Buchner A, Hocaoglu Y, Stief C, Tritschler S. Optical coherence tomography for bladder cancer – ready as a surrogate for optical biopsy? Results of a prospective mono-centre study. Eur J Med Res. 2010;15:131–4.
20. Goh AC, Lerner SP. Application of new technology in bladder cancer diagnosis and treatment. World J Urol. 2009;27:301–7.
21. Ku JH, Lerner SP. Strategies to prevent progression of high-risk bladder cancer at initial diagnosis. Curr Opin Urol. 2012;22:405–14.
22. Cauberg EC, de Bruin DM, Faber DJ, van Leeuwen TG, de la Rosette JJ, de Reijke TM. A new generation of optical diagnostics for bladder cancer: technology, diagnostic accuracy, and future applications. Eur Urol. 2009;56:287–96.
23. Cauberg EC, de la Rosette JJ, de Reijke TM. How to improve the effectiveness of transurethral resection in nonmuscle invasive bladder cancer? Curr Opin Urol. 2009;19:504–10.
24. Jichlinski P, Lovisa B. High magnification cystoscopy in the primary diagnosis of bladder tumors. Curr Opin Urol. 2011;21:398–402.
25. Pan YT, Xie TQ, Du CW, Bastacky S, Meyers S, Zeidel ML. Enhancing early bladder cancer detection with fluorescence-guided endoscopic optical coherence tomography. Opt Lett. 2003;28:2485–7.
26. Wang ZG, Durand DB, Schoenberg M, Pan YT. Fluorescence guided optical coherence tomography for the diagnosis of early bladder cancer in a rat model. J Urol. 2005;174:2376–81.
27. Schmidbauer J, Remzi M, Klatte T, Waldert M, Mauermann J, Susani M, Marberger M. Fluorescence cystoscopy with high-resolution optical coherence tomography imaging as an adjunct reduces false-positive findings in the diagnosis of urothelial carcinoma of the bladder. Eur Urol. 2009;56:914–9.
28. Gladkova N, Kiseleva E, Streltsova O, Prodanets N, Snopova L, Karabut M, Gubarkova E, Zagaynova E. Combined use of fluorescence cystoscopy and cross-polarization OCT for diagnosis of bladder cancer and correlation with immunohistochemical markers. J Biophotonics. 2013;6(9):687–98.
29. Liu JJ, Droller MJ, Liao JC. New optical imaging technologies for bladder cancer: considerations and perspectives. J Urol. 2012;188:361–8.
30. Bus MT, Muller BG, de Bruin DM, Faber DJ, Kamphuis GM, van Leeuwen TG, de Reijke TM, de la Rosette JJ. Volumetric in vivo visualization of upper urinary tract tumors using optical coherence tomography: a pilot study. J Urol. 2013;190:2236–42.

31. van Leeuwen TG, Faber DJ, Aalders MC. Measurement of the axial point spread function in scattering media using single-mode fiber-based optical coherence tomography. Sel Top Quantum Electron IEEE J. 2003;9:227–33.
32. Xie T, Zeidel M, Pan Y. Detection of tumorigenesis in urinary bladder with optical coherence tomography: optical characterization of morphological changes. Opt Express. 2002;10:1431–43.
33. Barwari K, de Bruin DM, Cauberg EC, Faber DJ, van Leeuwen TG, Wijkstra H, de la Rosette J, Laguna MP. Advanced diagnostics in renal mass using optical coherence tomography: a preliminary report. J Endourol. 2011;25:311–5.
34. Vakoc BJ, Lanning RM, Tyrrell JA, Padera TP, Bartlett LA, Stylianopoulos T, Munn LL, Tearney GJ, Fukumura D, Jain RK, Bouma BE. Three-dimensional microscopy of the tumor microenvironment in vivo using optical frequency domain imaging. Nat Med. 2009;15:1219–23.
35. Ren H, Yuan Z, Waltzer W, Shroyer K, Pan Y. Enhancing detection of bladder carcinoma in situ by 3-dimensional optical coherence tomography. J Urol. 2010;184:1499–506.
36. Ren H, Park KC, Pan R, Waltzer WC, Shroyer KR, Pan Y. Early detection of carcinoma in situ of the bladder: a comparative study of white light cystoscopy, narrow band imaging, 5-ALA fluorescence cystoscopy and 3-dimensional optical coherence tomography. J Urol. 2012;187:1063–70.

# Optical Coherence Tomography for Prostate Cancer and Beyond

4

Mohit Gupta and Li-Ming Su

## Optical Coherence Tomography

Optical Coherence Tomography (OCT) is an emerging optical imaging modality that provides high-resolution, real-time, cross-sectional imaging of tissue structures and substructures. Analogous to B-mode ultrasound, OCT relies on information gathered by reflected energy. In comparison, however, OCT utilizes near-infrared light rather than acoustical waves and, unlike ultrasound, does not require direct contact with tissue or a transducing medium. Backscattered light is combined with a reference signal to produce a high-resolution, two-dimensional map of tissue microstructure [1]. Because OCT does not require a conducting medium, it can image through both air and water with far greater resolution than ultrasound. OCT provides images with a depth of penetration of 2 mm and spatial resolutions of 1–15 μm, over one order of magnitude higher than conventional ultrasound [2, 3] (Table 4.1).

M. Gupta, MD
Department of Urology, University of Florida College of Medicine, Gainesville, FL, USA
e-mail: GuptaM23@gmail.com

L.-M. Su, MD (✉)
Division of Robotic and Minimally Invasive Urologic Surgery, Department of Urology, University of Florida College of Medicine, Gainesville, FL, USA
e-mail: Li-Ming.Su@urology.ufl.edu

Given its ability to provide real-time, high-resolution images, OCT has emerged as a promising imaging modality because of its ability to function as a type of "optical biopsy," yielding information on tissue pathology in situ and in real time, without the need for excision of specimens and processing as in conventional biopsy and histopathology [4, 5]. In addition, OCT can easily be integrated into existing surgical instruments, such as laparoscopes, endoscopes, catheters, hand-held probes, or needles [6–8]. As a result, OCT can potentially guide surgical intervention or help image tissue microstructure in situations where conventional excisional biopsy would be hazardous or impossible [5]. While initially used in the field of ophthalmology to image the retina and macula in vivo, OCT has been investigated for its roles in imaging the gastrointestinal, cardiovascular, gynecologic, skin, and nervous systems [9–14].

OCT imaging in the genitourinary system was first demonstrated in 1997, and since then, multiple studies have emerged examining its use as a tool to guide clinical decisions. Early ex vivo studies noted significant levels of correlation between OCT images and histologic architecture of urologic tissues sampled. They noted that OCT was also able to differentiate early changes in mucosal surfaces of urologic tissues such as hyperplasia, dysplasia, and frank carcinoma and thus could serve as a near surrogate for histology [15, 16]. OCT has been best studied in the realm of bladder cancer, which will be covered in a separate chapter. In this chapter, we review and

J.C. Liao, L.-M. Su (eds.), *Advances in Image-Guided Urologic Surgery*,
DOI 10.1007/978-1-4939-1450-0_4, 

**Table 4.1** Imaging modalities commonly used in the field of urology and their relative scale and resolution as compared to OCT

| Imaging modality | Objects visualized, scale and resolution | Detail of objects visualized | Energy source |
|---|---|---|---|
| CT and MRI | Whole organs | Bone, organs, fat, air (gross level) | X-ray (for CT) or radiofrequency EM waves (for MRI) |
| Ultrasound | Whole organs<br>Penetration (cm)<br>Resolution (150 μm) | Soft tissue, fat, fluid (macroscopic level) | Sound waves (2–30 MHz) |
| OCT | Tissues<br>Penetration (2 mm)<br>Resolution (10–15 μm) | Tissue layers, architecture and structural organization (mesoscopic level) | Near-infrared light (1,300 nm) |

discuss preclinical and clinical studies of OCT in other urologic organs such as the prostate, kidney, and testis.

## Prostate OCT

Prostate cancer has remained the leading soft tissue cancer diagnosed in men in the USA. The use of OCT has been explored as a modality to help image the architecture of the prostate gland and periprostatic tissues in animal and human studies.

Regarding the imaging of periprostatic tissues, the cavernous nerve (CN) was an obvious choice of tissue to try to image using OCT owing to its close proximity to the prostate surface and importance in preservation during prostatectomy to improve postoperative sexual function. Radical prostatectomy inherently carries significant quality-of-life risks including incontinence and erectile dysfunction due to injuries to the cavernous nerves (CN). Although nerve-sparing radical prostatectomy can positively impact postoperative outcomes, there is currently no established visual modality available to conclusively identify the microscopic fibers within the neurovascular bundle (NVB) during radical prostatectomy. Improvements in real-time imaging and identification of the CNs intraoperatively via OCT could potentially aid in preventing injuries to the nerves and thus improve potentially postoperative potency and continence.

Initial studies demonstrated significant correlation of OCT findings with the histologic findings in differentiating cavernous nerves from the underlying prostate glandular architecture in small animal models (Fig. 4.1). CNs and ganglions could be differentiated using OCT from periprostatic structures such as the bladder, prostate gland, seminal vesicles, and periprostatic fat, with a unique imaging signature for each of these structures (Fig. 4.2) [3, 17, 18] (Figs. 4.1 and 4.2). In a study by Fried et al., simultaneous cavernous nerve stimulation was performed following identification of the neurovascular structures in rats to provide confirmation of the actual neurovascular bundle (NVB) imaged by OCT with promising results [3].

OCT has also been studied in vivo for intraoperative use in identifying neurovascular bundles in patients undergoing nerve-sparing radical prostatectomy. In a preliminary experience by Aron et al. on 24 patients undergoing either laparoscopic or robot-assisted radical prostatectomy, OCT was applied intraoperatively in an attempt to preserve NVBs using real-time data acquisition [1]. In an attempt to evaluate the feasibility of nerve-sparing prostatectomy, specimens were examined both in vivo and in vitro for the presence or absence of the neurovascular bundles. The OCT images were found to correlate independently of the surgeon's subjective impression of the tissue being imaged. Moreover, in four patients who underwent a wide excision of the neurovascular bundle, bench examination of the specimen proved a 100 % correlation between the OCT image and the histological examination of the prostate (Fig. 4.3). Aron and colleagues also found that identification of the NVBs required an experienced operator to

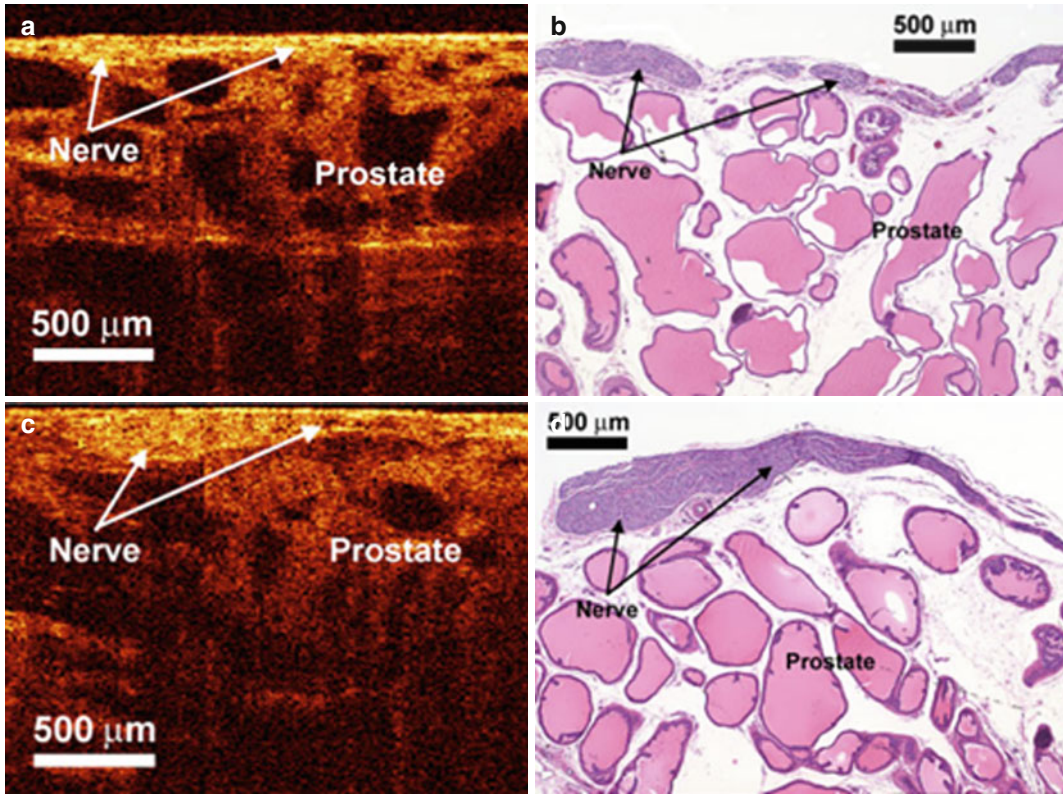


**Fig. 4.1** OCT and histologic images of the rat cavernous nerve: (**a**, **b**) longitudinal section; (**c**, **d**) in each section, the cavernous nerve lies superficial to the prostatic stroma and glands and has a relatively hyperintense signal as compared to the underlying hypointense prostate glands (From Fried et al. [3], with permission)

distinguish them from adipose tissue, small vessels, and lymphatics [1].

Other studies noted that identification of the NVB proved to be difficult because of the presence of more periprostatic blood vessels and fat resulting in a degradation of the OCT resolution [18]. Furthermore, the limitations of OCT's field of view make intraoperative mapping of the NVB for nerve-sparing radical prostatectomy challenging if not impractical. Thus, the ability to apply OCT technology for the purposes of directing cavernous nerve preservation remains to be determined.

The use of OCT has also been applied to prostate cancer treatment. Historically, approximately 85 % of patients with American Joint Commission on Cancer (AJCC) staging pathologic Stage T2 disease remain without clinical evidence of disease 15 years after radical prostatectomy [19–21]. The reported estimate of 10-year prostate-specific antigen (PSA) failure-free survival, however, declines to 82, 42–54, 43, and 0 % for those surgically treated patients found to have focal or established extracapsular extension, established extracapsular extension, seminal vesicle invasion, and positive pelvic lymph nodes, respectively [22]. Oncological outcomes following prostatectomies have also been linked to positive surgical margins. Despite advances in diagnostic imaging, however, it is still not possible to visualize the extent of microscopic disease reliably before or during definitive local therapy [21].

OCT has consequently been evaluated for potential use in evaluating positive surgical margins and extracapsular extension. Dangle et al. correlated OCT images of post-prostatectomy ex vivo specimens to detect positive margins and found a sensitivity, specificity, and negative predictive value of 70, 84, and 96 %, respectively

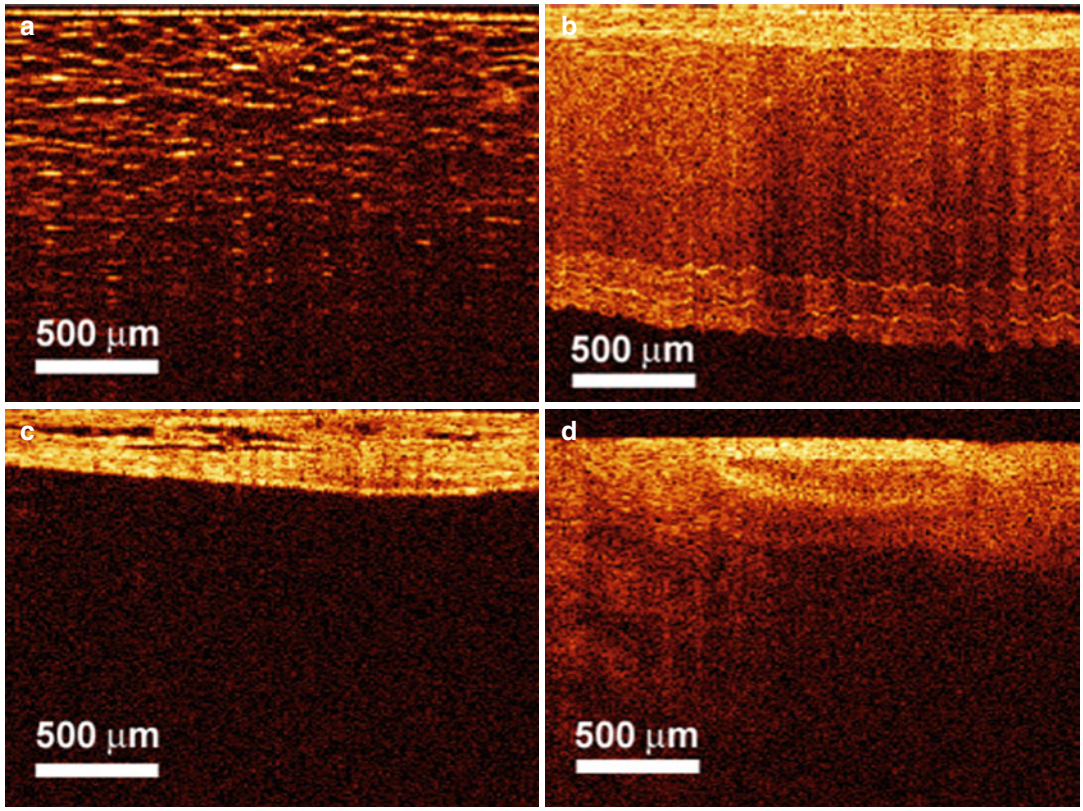


**Fig. 4.2** OCT images of rat (**a**) periprostatic fat, (**b**) seminal vesicles, (**c**) bladder wall, and (**d**) periprostatic blood vessels (From Fried et al. [3] with permission)

[23]. They noted the low positive predictive value for detecting positive margins could be due to the heterogeneous appearance of the tumor and the low depth of penetration (2–3 mm) with OCT. Based on the high negative predictive value, however, they concluded that OCT could be useful to rule out positive surgical margin, extraprostatic extension, and seminal vesicle invasion.

OCT has also been applied to help differentiate benign from malignant microscopic structures in the prostate gland. In their study, D'Amico and colleagues obtained three to six samples from radical prostatectomy specimens of seven men with localized prostate cancer [21]. These specimens were first imaged with OCT and then sent for histopathologic examination. The investigators found that structural architecture on the order of 50–150 μm within benign glandular epithelium, fibroadipose tissue, and malignant glandular epithelium could be resolved to a depth of 0.5 mm using OCT. Thus, as in other urologic organ systems, OCT functioned as a type of "optical biopsy" to provide ultra-high-resolution images of tissue architectural morphology without the need to excise and process a specimen as in conventional biopsy and histopathologic analysis. Regions within the prostate identified as suspicious for prostate cancer based on OCT could then be preferentially sampled. The major technical limitation noted in this study, however, was that the 10-μm order of resolution that was achieved was limited to a depth of just 0.5 mm.

## Kidney OCT

OCT has been applied in evaluating kidney morphology and renal masses incidentally discovered by CT or MRI. OCT was initially investigated in kidneys of rats both ex vivo and in vivo. Initial studies demonstrated that OCT was able to correctly visualize structures including the renal capsule, the renal parenchyma, and surrounding tissues (Fig. 4.4).

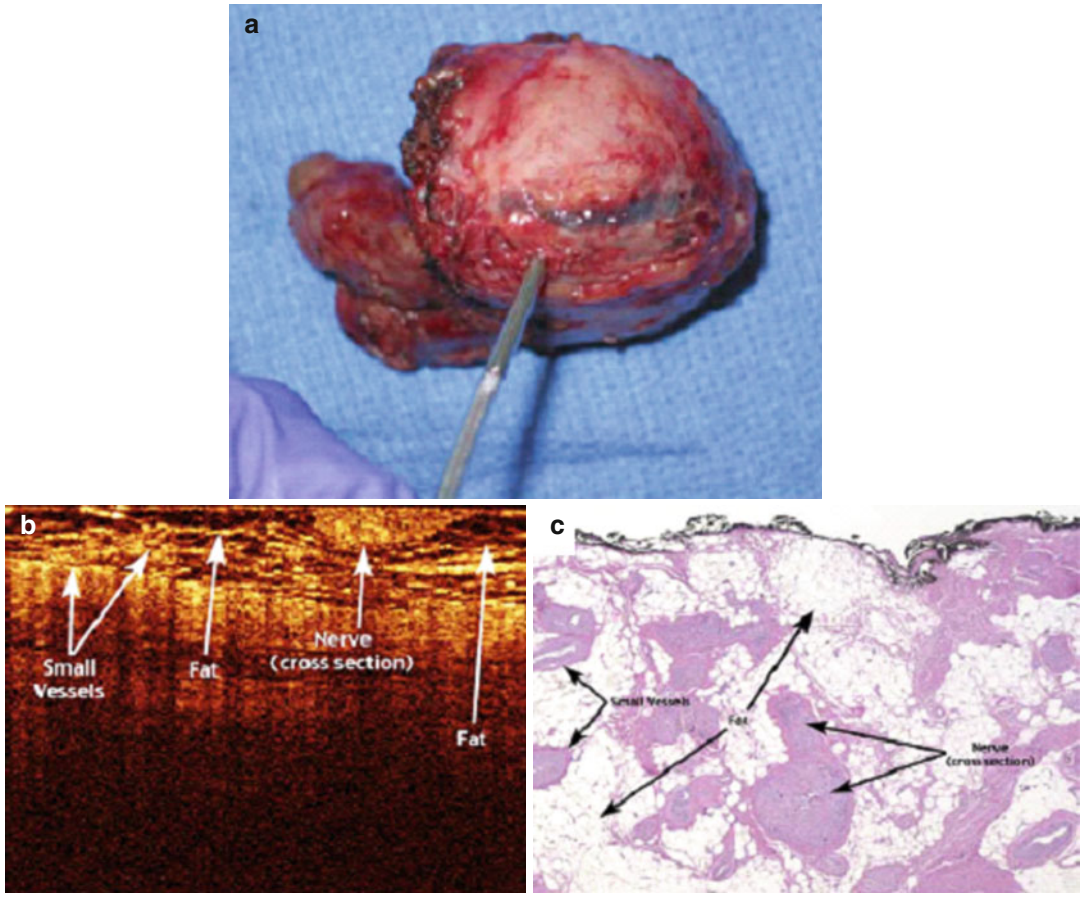


**Fig. 4.3** Images of (**a**) human robotic-assisted radical prostatectomy specimen with NVB resected, (**b**) OCT imaging, and (**c**) histologic (hematoxylin-eosin) correlation of ex vivo human prostatectomy specimens revealing intact overlying neurovascular bundle (From Rais-Bahrami et al. [18], with permission)

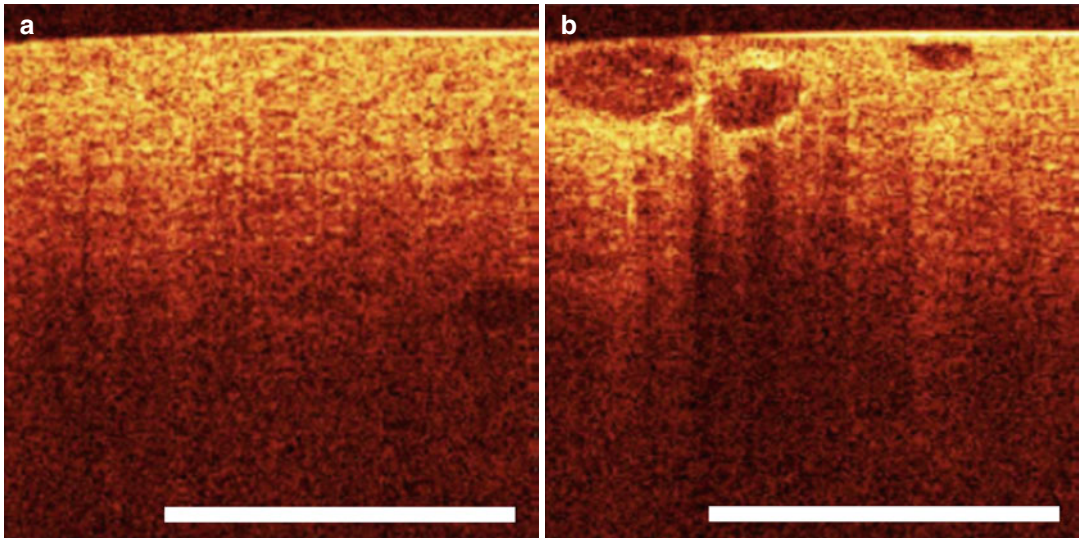


**Fig. 4.4** (**a**) OCT of normal renal parenchyma. (**b**) Optical coherence tomography image of heterogeneous well-defined structures of renal parenchyma histologically proven to be renal cell carcinoma (From Goel and Kaouk [40], with permission)

In addition, OCT was able to show histopathologic alterations to renal morphology in samples that had been subjected to ischemic or nephrotoxic insults [24–26]. When renal ischemia was induced, for example, OCT revealed dramatic shrinkage of tubular lumens, diminished flow of filtrate through nephrons, and deterioration of the microvillus brush-border lining the proximal tubules [25]. As a result, groups like Li et al. examined how OCT could be applied in areas such as transplant surgery to image donor kidney structures and to evaluate organ viability following physiologic insult and acute kidney injuries [27].

Subsequent studies on OCT were also applied in renal oncology: OCT could be used not only to delineate anatomical structures such as the blood vessels, renal tubules, and glomeruli but also to evaluate renal masses. Given the significant rise of incidentally discovered renal masses detected through advances in CT and MR, OCT is being evaluated as a promising tool in the diagnostic evaluation of renal tumors.

A disadvantage to CT and MR imaging techniques is that often benign renal masses cannot be distinguished from those that are malignant, and therefore up to 20–30 % of extirpated renal masses smaller than 4 cm are benign on histopathological examination [28]. Though limited in number, preliminary studies have begun to investigate OCT's ability to distinguish benign from malignant renal tumors and appear promising [29, 30]. Barwari et al. concluded that ex vivo OCT attenuation coefficients were different between normal renal parenchyma and renal cell carcinoma (RCC) tissue. RCC tissue showed a significant higher attenuation coefficient than normal parenchyma [29]. If these results are confirmed in vivo, OCT may be applied to evaluate surgical margins after partial nephrectomy or combined with percutaneous diagnostic biopsy to provide a functional optical biopsy, allowing cross-sectional images to be immediately correlated to histopathology data.

Another group found OCT of renal neoplasms was most successful in distinguishing angiomyolipomas (AML) and transitional cell carcinoma (TCC) from normal parenchyma [31]. AML, for example, showed a unique identifiable signature because of its fat content and could therefore be readily distinguished.

Limitations in these studies, however, include small sample sizes, ex vivo study designs, and the need for numerous images to evaluate the relatively large surface area of a kidney. As with bladder cancer, OCT's limited penetration depth into tissue can also preclude visualization deeper structures, thus limiting information on invasion or stage especially for tumors that are endophytic in location. Lastly, resolution of OCT at its current stage falls short of providing information on histologic subtype.

## Testicular and Infertility OCT

Nonobstructive azoospermia (NOA) affects nearly 1 % of all men and 10–15 % of all infertile men [32]. Advances in sperm retrieval techniques such as microdissection testicular sperm extraction (micro-TSE) have made it possible for affected men to father their own children. Micro-TSE, however, is very technically demanding, and an important challenge in the procedure has been the inability to definitively identify seminiferous tubules that contain sperm without removing testicular tissue for histopathologic analysis. Currently, after the tunica albuginea is surgically opened to expose testicular tissue, tubules are examined histologically, subjectively evaluated for the presence of sperm and are then removed to assess if sperm are indeed present. Studies have shown that sperm is retrieved in only 40–60 % of men using this technique [33–35]. Consequently, the concept of OCT-assisted TESE has been investigated to improve retrieval rates while minimizing testicular trauma [36, 37]. By providing high-resolution images of scrotal structures, OCT may in the future help improve sperm retrieval rates by better identifying specific seminiferous tubules with isolated foci of spermatogenesis in men with NOA.

OCT still has limitations, however, that need to be further examined prior to regular clinical use. Although OCT can image individual seminiferous tubules, for example, the tunica albuginea was

found to have a high reflective index which limits the depth to which OCT images can be acquired. As a result, a tunical incision may still be required to visualize all seminiferous tubules. As with other areas in urology, the depth of penetration of OCT is 2 mm, which limits its ability to image deeply within tissues. This also restricts its use for transcutaneous imaging, which is commonplace with ultrasound. Thus, additional studies are needed before OCT can be readily applied to image and target-specific tubules in the treatment of NOA [37].

### Conclusion

Since it was first used to evaluate human genitourinary tissue in 1997, OCT has emerged as a promising modality to provide real-time, high-resolution imaging of urologic organs. Several small, ex vivo studies have shown promising results in the ability of OCT to demonstrate histopathologic alterations to renal morphology such as in renal ischemia and malignancy. It may also in the future improve sperm retrieval rates by better identifying tubules with isolated foci of spermatogenesis in these men with nonobstructive azoospermia. Finally, multiple studies have begun to demonstrate OCT's ability to differentiate between the periprostatic anatomy and aid in the visualization of the neurovascular bundle and surgical margins.

Despite the promising results of these initial studies, several limitations remain. In almost all studies, depth of penetration was recognized as a common limiting factor. At a maximum of 2 mm depth, OCT cannot provide imaging of deep tissue. In bladder cancer, for example, OCT cannot always provide sufficient imaging to judge the invasion depth of a tumor if the diameter of the tumor is already greater than 2 mm [38, 39]. In addition, most OCT studies have taken place in ex vivo. Larger clinical, in vivo trials are required to determine its ability to provide information to guide clinical decisions and if its use positively affects outcomes. Theoretically, future improvements of OCT delivery could allow for such technology to be placed at the end of robotic and laparoscopic instruments, thus providing "smart instruments" that could provide immediate and real-time assessment of tissue structure and architecture.

## References


1. Aron M, Kaouk J, Hegarty N, et al. Preliminary experience with NIRIS optical coherence tomography system during laparoscopic and robotic prostatectomy. J Endourol. 2007;21(8):814–8.
2. Manyak MJ, Javitt M, Kang PS, Kreuger WR. The evolution of imaging in advanced prostate cancer. Urol Clin N Am. 2006;33:133–46.
3. Fried N, Rais-Bahrami S, Lagoda G, Chuang Y, Burnett A, Su L-M. Imaging the cavernous nerves in the rat prostate using optical coherence tomography. Lasers Surg Med. 2007;39:36–41.
4. Fujimoto JG. Optical and acoustical imaging of biological media. C. R. Acad. Sci. Paris, t. 2, Série Physique appliquée/*Applied physics* 2001;IV:1099–1111.
5. Fujimoto J, Pitris C, Boppart S. Optical coherence tomography: an emerging technology for biomedical imaging and optical biopsy. Neoplasm. 2000;2(2):9–25.
6. Tearney G, Boppart S, Bouma B, Brezinksi M, Weissman N, Southern J, Fujimoto J. Scanning single-mode fiber optic catheter-endoscope for optical coherence tomography. Opt Lett. 1996;21:543–5.
7. Boppart S, Bouma B, Pitris C, Tearney G, Fujimoto J. Forward-imaging instruments for optical coherence tomography. Opt Lett. 1997;22:1618–20.
8. Li X, Chudoba C, Ko T, Pitris C, Fujimoto J. Imaging needle for optical coherence tomography. Opt Lett. 2000;25:1520–2.
9. Hee MR, Izatt JA, Swanson EA. Optical coherence tomography of the human retina. Arch Ophthalmol. 1995;113:325–32.
10. Puliafto CA, Hee M, Lin C. Imaging of macular diseases with optical coherence tomography. Opthalmology. 1995; 102:217–29.
11. Pitris C, Goodman A, Boppart S. High-resolution imaging of gynecologic neoplasms using optical coherence tomography. Obstet Gynecol. 1999;93:135–9.
12. Tearney G, Brezinski M, Southern J. Optical biopsy in human gastrointestinal tissue using optical coherence tomography. Am J Gastroenterol. 1997;93:1800–4.
13. Sun C, Wang Y, Lu L, Lu C, Hsu I, Tsai M. Myocardial tissue characterization based on polarization-sensitive optical coherence tomography system with an ultrashort pulsed laser. J Biomed Opt. 2006;11(5):054016.
14. Gambichler T, Regeniter P, Bechara F, Orlikov A. Characterization of benign and malignant melanocytic skin lesions using optical coherence tomography in vivo. J Am Acad Dermatol. 2007;57(4):629–37.
15. Tearney G, Brezinski M, Southern J, Boppart S, Fujimoto J. Optical biopsy in human urologic tissue

using optical coherence tomography. J Urol. 1997; 157(5):1915–9.
16. Parekattil S, Yeung LL, Su L-M. Intraoperative tissue characterization and imaging. Urol Clin N Am. 2009;36:213–21.
17. Fried N, Rais-Bahrami S, Lagoda G, Chuang A-Y, Su L-M, Burnett III A. Identification and imaging of the nerves responsible for erectile function in rat prostate, in vivo, using optical nerve stimulation and optical coherence tomography. IEEE J Sel Top Quantum Electron. 2007;13(6):1641–5.
18. Rais-Bahrami S, Levinson A, Fried N, Lagoda G, Hristov A, Chuang Y, Burnett A, Su L-M. Optical coherence tomography of cavernous nerves: a step toward real-time intraoperative imaging during nerve-sparing radical prostatectomy. Urology. 2008;72:198–204.
19. Culp O. Radical perineal prostatectomy: its past, present, and possible future. J Urol. 1968;98:625–32.
20. Blute M, Nativ O, Zincke H. Pattern of failure after radical retropubic prostatectomy for clinically and pathologically localized adenocarcinoma of the prostate: influence of tumor deoxyribonucleic acid ploidy. J Urol. 1989;142:1262–6.
21. D'amico A, Weinstein M, Li X, Richie J, Fujimoto J. Optical coherence tomography as a method for identifying benign and malignant microscopic structures in the prostate gland. Urology. 2000;55(5):783.
22. Walsh P, Partin A, Epstein J. Cancer control and quality of life following anatomical radical retropubic prostatectomy: results at 10 years. J Urol. 1994;152:1831–5.
23. Dangle PP, Shah KK, Kaffenberger B, Patel VR. The use of high resolution optical coherence tomography to evaluate robotic radical prostatectomy specimens. Int Braz J Urol. 2009;35(3):344.
24. Chen Y, Andrews P, Aguirre A, Schmitt J, Fujimoto J. High-resolution three-dimensional optical coherence tomography imaging of kidney microanatomy ex vivo. J Biomed Opt. 2007;12:034008.
25. Andrews P, Chen Y, Onozato M. High-resolution optical coherence tomography imaging of the living kidney. Lab Invest. 2008;88:441–9.
26. Li Q, Onozato M, Andrews P. Automated quantification of microstructural dimensions of the human kidney using optical coherence tomography. Opt Express. 2009;17:16000–16.
27. Li Q, Mristel O, Andrews P, Chen C-W, Paek A, Naphas R, Yuan S, Jiang J, Cable A, Chen Y. Automated quantification of microstructural dimensions of the human kidney using optical coherence tomography (OCT). Opt Soc Am. 2009;17(18):16000.
28. Volpe A, Jewett M. Current role, techniques and outcomes of percutaneous biopsy of renal tumors. Expert Rev Anticancer Ther. 2009;9:773–83.
29. Barwari K, de Bruin DM, Cauberg EC, Faber DJ, van Leeuwen TG, Wijkstra H, de la Rosette J, Laguna MP. Advanced diagnostics in renal mass using optical coherence tomography: a preliminary report. J Endourol. 2011;25(2):311–5.
30. Lee H-C, Zhou C, Cohen D, Mondelblatt A, Wang Y, Aguirre A, Shen D, Sheikine Y, Fujimoto J, Connolly J. Integrated optical coherence tomography and optical coherence microscopy imaging of ex vivo human renal tissues. J Urol. 2012;187:691–9.
31. Linehan J, Bracamonte E, Hariri L, Sokoloff M, Rice P, Barton J, Nguyen M. Feasibility of optical coherence tomography imaging to characterize renal neoplasms: limitations in resolution and depth of penetration. Br J Urol Int. 2011;108:1820–4.
32. Thonneau P, Marchand S, Tallec A, Ferial M. Incidence and main causes of infertility in a resident population (1,850,000) of three French regions (1988–1989). Hum Reprod. 1991;6:811–6.
33. Ramasamy R, Yagan N, Schlegel P. Structural and functional changes to the testis after conventional versus microdissection for nonobstructive azoospermia. Urology. 2002;65:1190–4.
34. Okada H, Dobashi M, Yamazaki T, Hara I, Fujisawa M, Arakawa S. Conventional versus microdissection testicular sperm extraction for nonobstructive azoospermia. J Urol. 2002;168:1063–167.
35. Schlegl P. Testicular sperm extraction: microdissection improves sperm yield with minimal tissue excision. Hum Reprod. 1999;14:131–5.
36. Ramasamy R, Sterling J, Manzoor M, Salamoon B, Jain M, Fisher E. Full field optical coherence tomography can identify spermatogenesis in a rodent sertoli-cell only model. J Pathol Inform. 2012;3:4.
37. Davis C, Kuang W. Optical coherence tomography: a novel modality for scrotal imaging. Can Urol Assoc J. 2009;3(4):319–22.
38. Zagayanova E, Streltzova O, Gladkova N, Shakhova N, Feldchtein F. Kamensky V. Optical coherence tomography in diagnostics of precancer and cancer of human bladder, In: Laser in surgery: advanced characterization, therapeutics, and systems; 2004.
39. Zagaynova E, Streltzova O, Gladkova N, Shakhova N, Feldchtein F, Kamensky V, Gelikonov G, Donchenko E. Optical coherence tomography in diagnostics and guided surgery of bladder cancer. In: Coherence domain optical methods and optical coherence tomography in biomedicine VIII Proc of SPIE; 2004.
40. Goel RK, Kaouk JH. Optical coherence tomography: the past, present and future. J Robotic Surg. 2007; 1:179–84.

# Fluorescence Image-Guided Robotic Surgery

5

Guan Wu

Fluorescence image-guided surgery (FIGS) is a surgical modality that employs a fluorescence optical detection and tracking system to identify fluorescence-labeled tissue structures in real time to guide a surgical procedure [1, 2]. FIGS relies on imaging devices that provide real-time simultaneous information from color reflectance images and fluorescence emission signals. The fluorescence emission signals are collected using optical filters that match the emission spectrum of the fluorophore [1, 3, 4]. Live images or videos are generated through a combination of optical filters, lenses, digital imaging sensors, and designated computer graphic processors and imaging software. Fluorescence images are digitally enhanced and can be pseudo-colored to improve signal-to-background ratio and image clarity [3, 4]. The fluorescence images and white-light images of a surgical field can be toggled back and forth or combined together in real time. Fluorescence-labeled tissue structures can help surgeons to identify tissue structures that are not easily recognizable under white light in the bright field during surgery [3, 4]. While radiographic imaging modalities, such as X-ray, CT, MRI, and ultrasound images, provide critical information for diagnosis and preoperative surgical planning, intraoperative fluorescence imaging not only offers superior resolution and sensitivity for tissue structure recognition but also provides means for functional evaluation of tissue perfusion and viability in real time during surgery [1, 4].

Research and development has been very active in the field of FIGS, and numerous preclinical and clinical studies have demonstrated the potential benefits of FIGS [2, 3, 5]. FIGS has already been used for intraoperative angiography, intraoperative cholangiogram, sentinel lymph node mapping, tumor-specific labeling, tissue perfusion, and reconstructive microsurgery, just to name a few [3–5]. Although different fluorescence dyes have been utilized in preclinical and clinical studies, near-infrared fluorescence (NIRF) contrast indocyanine green (ICG) is the most widely used fluorescence dye in FIGS due to its safety profile and its excitation and emission wavelength. ICG was approved by the FDA for human clinical use in the 1950s [6].

The first use of FIGS was in open surgery. During open surgery, a fluorescence imaging device is turned on and off in the surgical field to identify the structure of tissues of interest. The main issue that arises with the use of FIGS in open surgery is that the operating theater lights must be dimmed or switched off during fluorescence image acquisition [1, 4, 7]. Otherwise, the white lights of the operating theater will interfere with the fluorescence emission signals. Therefore, surgeons have to alternate between looking at the

G. Wu, MD, PhD
Departments of Urology, Pathology, and Oncology,
University of Rochester Medical Center,
Rochester, NY, USA
e-mail: gwu@urmc.rochester.edu

J.C. Liao, L.-M. Su (eds.), *Advances in Image-Guided Urologic Surgery*,
DOI 10.1007/978-1-4939-1450-0_5, © Springer Science+Business Media New York 2015

surgical field and looking at the imaging display monitor, which may not be convenient during surgery [7]. FIGS has also been used in minimally invasive surgery with fluorescence imaging laparoscopes [8]. Unlike open surgery, the external lights do not interfere with the fluorescence emission detection, and laparoscopic surgeons can operate based on real-time images or videos displayed on the monitors [9]. Incorporating FIGS into a robotic surgery platform is a natural evolution in this field and provides advanced integration of multimodal imaging systems with enhanced minimally invasive surgical instrumentation [10, 11].

The robotic surgery platform (da Vinci Surgical System) developed by Intuitive Surgical Inc. (Sunnyvale, California, USA) has revolutionized minimally invasive surgical procedures in many surgical specialties. Essentially all transabdominal urologic surgeries can be performed with the da Vinci Surgical System [12]. This robotic surgery platform provides advanced 3D vision and unparalleled instrument controls with enhanced precision and dexterity. This system allows minimally invasive surgeries to be performed in complex surgical scenarios [12]. The da Vinci Surgical System is a computerized information machine with capabilities to incorporate imaging information from other sources into a real-time operation. Through the TilePro™ function, multiple images or videos, such as real-time intraoperative ultrasound images, endoscopy images, and preoperatively acquired CT and MRI images, can be displayed in the surgeon's console simultaneously. Although the da Vinci Surgical System provides superb 3D color images for surgeons, under white light, human eyes still cannot discern certain tissue structures well enough and cannot provide objective assessment of tissue functional status [10]. With the recently added NIRF imaging function, the da Vinci Surgical System now provides surgeons with an advanced intraoperative NIRF tool with ease of use. In this chapter, we will review NIRF imaging; the commonly used NIRF contrast, indocyanine green (ICG); and the current applications for intraoperative NIRF imaging in urologic robotic surgery.

## Near-Infrared Fluorescence Imaging and Indocyanine Green

### Near-Infrared Fluorescence Imaging

During the past decades, various near-infrared fluorescence (NIRF) imaging systems have been developed for open, microscopic, and minimally invasive surgeries [2, 4, 8, 13, 14]. An NIRF imaging system consists of a near-infrared (NIR) excitation light, collection optics, NIR filters, and an NIR video camera as well as a white-light illumination and video system for the surgical field. NIRF and white-light images can be displayed separately or merged with NIRF signals shown in a pseudo color [4]. Figure 5.1 is a schematic illustration of an NIRF imaging system. NIRF imaging does not rely on ionizing radiation, making it a very safe imaging modality used in the operating room. Near-infrared (NIR) light (700–900 nm) is invisible to the human eye and can only be visualized on the display monitor of the system [3, 4]. NIRF does not alter the appearance of the surgical field, making the incorporation of white-light visions and computer-processed pseudo-color images possible in real time. Unlike visible light, which can only travel through tissues on the micrometer scale, NIR light can penetrate several millimeters of tissue (5–8 mm) depending on the tissue properties [3]. This allows detection of fluorescence signals underneath the surface. However, like visible light, NIR light is attenuated in tissues exponentially as a function of depth by absorption and scatter. Correction for attenuation of excitation light through computer adjustment can improve target detection, but overcompensation can produce false-positive signals [3]. The quantitative measurement of fluorescence signals for intraoperative NIRF imaging is still in the research phase [3].

During the surgery, an NIRF contrast is administered intravenously, topically, intraparenchymally, or intraluminally depending upon the application. There are several NIRF contrasts that have been used in experimental, preclinical, and clinical investigations, including methylene blue, 5-aminolevulinic acid (5-ALA), indocyanine green (ICG), and 800CW [3, 6]. For FIGS,

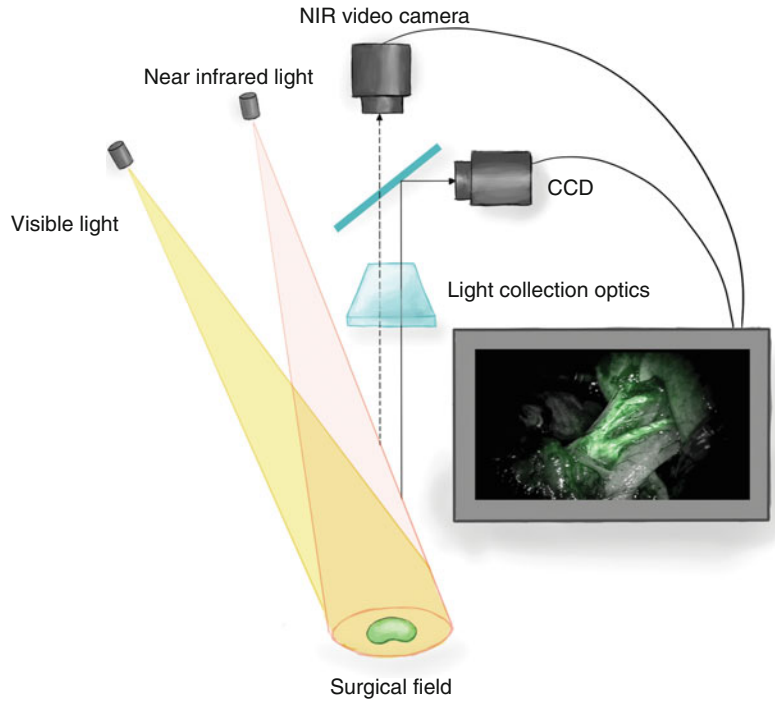


**Fig. 5.1** Schematic illustration of an NIRF imaging system. Essential components of an NIRF imaging system include an NIR excitation light, collection optics, NIR filters, an NIRF video camera, a white-light illumination source, a CCD video camera, and a computer and imaging display system

NIRF contrasts with excitation >750 nm and red-shifted emission are the preferred fluorescent molecules due to the significant tissue penetration of excitation light and emission light as well as the lack of tissue autofluorescence at that wavelength [3, 4]. Methylene blue, while widely used as a blue dye for non-NIRF imaging purposes in medicine, can act as an NIRF imaging contrast at very low concentrations, emitting fluorescence at 700-nm wavelength [15]. It has also been used extensively as a blue dye for sentinel lymph node mapping without NIRF imaging [16]. 5-ALA is the major substrate for protoporphyrin synthesis [17]. After given to patients, it induces synthesis and accumulation of the fluorescent molecule protoporphyrin IX in epithelial and neoplastic tissues and generates fluorescence signals at 700 nm [17, 18]. 5-ALA is also known as a photodynamic therapy agent [17]. ICG, first approved by the FDA in 1958 as a contrast agent for retinal angiography [6], has since been widely used in preclinical and clinical investigations for NIRF imaging [3, 4]. ICG is an ideal NIRF imaging contrast for FIGS based on the abovementioned criteria [3, 4]. However, the major drawback of ICG is its lack of a reactive chemical group for labeling selected biomolecules [6]. ICG cannot be conjugated to targeting biomolecules, such as antibodies, with the purpose of creating cell-type-specific fluorescent contrasts [6]. Further information on ICG will be detailed in the following section of this chapter. Lastly, 800CW, which is 50 times brighter than ICG, is a newer NIRF agent currently in the preclinical development [6, 19, 20]. 800CW can be conjugated to a number of biomolecules including antibodies and peptide ligands for targeted fluorescence imaging [6, 19]. 800CW has a similar excitation and emission profile to ICG; thus, NIRF imaging systems used for ICG fluorophore can be used for 800CW [6].

Fluorescein, a non-NIRF imaging contrast with excitation and emission wavelengths of 494 and 518 nm, respectively, was approved by the FDA as a contrast agent for angiography and has been used extensively by ophthalmologists in the diagnosis of corneal abrasions, corneal ulcers, and retinal disease [3]. However, fluorescein is

not ideal for FIGS secondary to its excitation and emission wavelengths within a spectrum with significant tissue autofluorescence, reducing its sensitivity [3]. Nonetheless, two landmark studies using antibodies labeled with fluorescein as intraoperative imaging contrasts have provided proof-of-principle demonstrations that FIGS has a potential to improve cancer surgery by "painting" cancer cells with a bright color [21, 22].

## Indocyanine Green

Indocyanine green (ICG) is a water-soluble, tricarbocyanine dye with a molecular weight of 774.98 Da and peak spectral absorption at 800 nm. Autofluorescence of tissues and blood is very low in the 800-nm wavelength range, making the signal-to-noise ratio very high in the ICG-NIRF imaging. The chemical name for ICG is 1H-benz[e]indolium, 2-[7-[1,3-dihydro-1,1-dimethyl-3-(4-sulfobutyl)-2H-benz[e]indo-2-ylidene]-1,3,5-heptatrienyl]-1,1-dimethyl-3-(4-sulfobutyl)-, hydroxide, inner salt, sodium (Fig. 5.2). It was originally developed in the Kodak Research Laboratories in the early 1950s and was used as a cyan-forming layer of Technicolor film [4]. ICG was first used medically for cardiac output evaluation in 1956, and it later received FDA approval for clinical use [4, 23]. Soon thereafter, it was found that ICG was excreted exclusively by the liver into the bile, leading to its application for measuring hepatic function and blood flow [23]. In 1969, Kogure et al. demonstrated ICG infrared absorption angiography of the canine brain vasculature [24]. In the 1970s, Flower et al. studied retinal and choroidal blood flow using ICG angiography with a modified fundus camera and Kodak high-speed infrared black and white film [25]. ICG angiography eventually became widely accepted as a diagnostic modality for various eye diseases in ophthalmology.

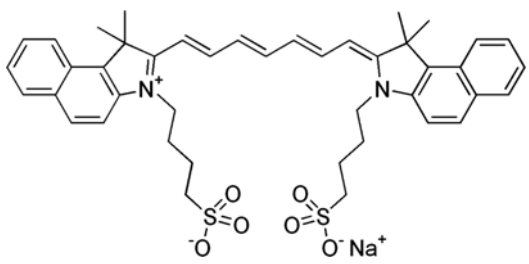


**Fig. 5.2** Chemical structure of indocyanine green (ICG)

ICG is an FDA-approved NIRF dye for clinical use for cardiovascular function testing, hepatic clearance, and retinal angiography [4]. ICG's safety profile has allowed its clinical applications and research to be expanded to other fields. Off-label uses of ICG for clinical studies are very common in many medical disciplines [3, 4]. ICG for injection is a sterile, lyophilized dark green powder containing 25 mg of ICG with no more than 5 % sodium iodide. ICG dye for clinical use can be obtained from Akorn, Inc. (Lake Forest, IL, USA) and Novadaq Technologies Inc. (Ontario, Canada). Since ICG contains sodium iodide, it should be used with caution in patients who have a history of an allergy to iodides. Anaphylactic or urticarial reactions have been reported in patients with and without history of allergy to iodides. Anaphylactic deaths have also been reported following ICG administration during cardiac catheterization [4]. Other more common side effects of ICG administration include nausea, headache, discoloration of feces, and diaphoresis [4]. No research reports have been published regarding ICG's carcinogenicity, mutagenicity, and impairment of fertility. It is also unknown whether ICG can cause fetal harm when administered to a pregnant woman. ICG should be given to a pregnant woman only if clearly indicated and under caution.

The ICG solution must be prepared fresh. Freshly prepared ICG solutions are considered to be extremely safe; however, ICG becomes unstable once in solution and must be used within 6 h. Aged ICG solution should never be used. The concern is the potential link between aged ICG preparation and cardiac arrhythmia [26]. There is no clear explanation for this phenomenon. It has been known that based on high-performance liquid chromatography analyses, freshly prepared ICG contains two fractions, the genuine ICG (95–99 %) and a degradation product of ICG. The degradation product of ICG is likely dimerized

ICGs based on its molecular weight [27]. Ott et al. reported that ICG solutions aged after 7 and 30 days of daylight exposure containing only the degraded ICG could trigger severe cardiac arrhythmias within 10 s after being injected in pigs and could result in death [26]. For this reason, one should always prepare the ICG solution right before injection. If additional injections are needed 6 h after the first injection, a new vial of ICG should be used.

After intravenous injection, ICG binds to plasma proteins, mainly to albumin and lipoproteins [4]. Its half-life in the bloodstream is only 2½–3 min. ICG is rapidly taken up by hepatocytes and is excreted via the hepatobiliary system, resulting in intense fluorescence in the liver and the bile duct. ICG is not metabolized in the liver and does not undergo enterohepatic recirculation [3, 4]. After intravenous injection, short-term tissue retention of ICG is only observed in the liver and kidneys, presumably because one of the possible ICG membrane carrier molecules, bilitranslocase, is only expressed in these two organs [4, 7]. ICG is known to be retained in liver cancer cells longer than normal hepatocytes after intravenous injection, making it ideal for intraoperative liver cancer detection [28, 29]. ICG is generally not excreted through the nephron, and therefore, there are no fluorescence signals in the urinary collecting system after intravenous injection of ICG [20]. Since ICG is not retained in tissues besides the liver after intravenous injection, it is ideal for angiography of small vessels [4]. While ICG binds to plasma proteins nonspecifically, ICG conjugated to nanoparticles could potentially be retained in specific tissue types or cancer cells [6].

## Near-Infrared Fluorescence Imaging in Robotic Surgery

Many seminal preclinical and clinical research works leading to the current clinical applications of ICG-NIRF imaging in robotic urologic surgery were carried out in the Department of Urology at the University of Rochester Medical Center [7, 9]. Those research activities were supported by the Department of Urology and Novadaq Technologies Inc. Early research efforts explored ICG-NIRF imaging in intraoperative angiography, tissue perfusion, lymphatic drainage, cholangiography, and nerve labeling with animal models. Retention of ICG in the renal parenchyma was noticed, albeit in a shorter period than ICG retention in the liver. Since it was known that hepatocyte carcinoma cells retain ICG longer than normal hepatocytes, we hypothesized that it was possible that kidney cancer cells might exhibit similar ICG retention as the liver cancer does, allowing us to "paint" renal cancer in bright color with the ICG-NIRF imaging. Initial studies, led by Dr. Dragan Golijanin, were launched to investigate clinical applications of intraoperative ICG-NIRF imaging in renal cancer surgery, including open, laparoscopic, and robotic partial and radical nephrectomies. To our surprise, initial findings showed that malignant renal tumors were hypofluorescent or afluorescent in contrast to bright normal parenchyma. This led us to focus on "reverse painting" renal tumors for partial nephrectomy, i.e., painting the normal parenchyma with bright color, thus leaving the renal tumor as black under the ICG-NIRF imaging. These pilot studies with open, laparoscopic, and robotic partial nephrectomies using the Novadaq NIRF laparoscope (SPY imaging system) were later published [7, 9]. In January 2009, Novadaq announced an alliance with Intuitive Surgical Inc. to develop a SPY imaging system to be integrated with the da Vinci Surgical Robotic System. Novadaq provided specific hardware components for Intuitive Surgical Inc. to develop the current NIRF imaging platform (named Firefly system) integrated into the da Vinci Si model. A clinical trial with robotic partial nephrectomy with the Firefly system was done at the University of Rochester Medical Center in 2010 [10], which led to FDA approval of the system. Intuitive Surgical Inc. initiated commercialization of the Firefly system in February 2011 and full launch of the system began in July 2011.

The Firefly system is well integrated into the da Vinci Surgical Robot and user friendly, without impeding the surgeon's workflow. The system has a 1080i 3D high-definition stereoscopic

fluorescence-capable camera and a laser generator emitting near-infrared wavelength light at 806 nm. The normal white light view and NIRF view can be quickly toggled back and forth using a foot paddle and hand controllers. After switching to the NIRF mode, the surgical field is illuminated in shades of black and gray, and ICG fluorescence signals are displayed in a bright green color with the 3D view unaffected. The video can be viewed in real time on all video monitors connected to the system in the operating room. The white-light system has been reengineered with a LED illuminator, providing even better imaging quality than a non-Firefly system. For unclear reasons, unlike the Novadaq NIRF laparoscope, Intuitive Surgical Inc. did not incorporate the capability of combining fluorescence images with white-light views in the current system; therefore, surgeons can only view the fluorescence images with black and white backgrounds. The current Intuitive Surgical da Vinci Surgical Platform with NIRF imaging capability is depicted in Fig. 5.3.

After robotic surgery platforms with NIRF imaging capability became available, robotic surgeons in many centers quickly embraced this technology. Feasibility and pilot studies from different surgical specialties continue to emerge. A recent animal study in cardiac surgery has shown that the use of the ICG-NIRF imaging is feasible and beneficial in off-pump robot-assisted coronary artery bypass procedure [30]. The system easily facilitated the identification of the internal mammary artery, delineation of the coronary anatomy, and assessment of anastomotic patency [30]. For robotic single-site cholecystectomy, intraoperative ICG-NIRF cholangiography appeared to be effective to prevent common bile duct injury. This new technology was shown to be superior to the conventional intraoperative cholangiography [31, 32]. In another recent study evaluating the influence of the ICG-NIRF imaging on the location of bowel transection during robotic left-sided colorectal surgery, Hellan et al. reported that the ICG-NIRF imaging provided important additional information and resulted in a change of the proximal transection location in 40 % (16/40) of patients [33]. The ICG-NIRF imaging has also been explored by gynecologists for SLN mapping during uterine and cervical

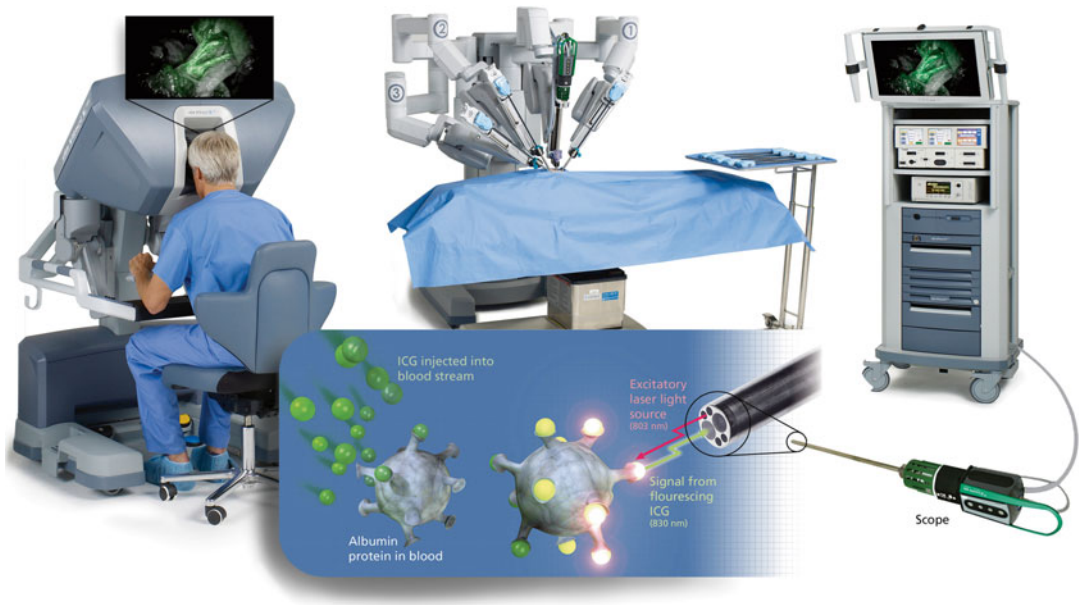


**Fig. 5.3** The Intuitive Surgical da Vinci Surgical Platform with NIRF imaging capability (© 2014 Intuitive Surgical, Inc.)

cancer surgery [16]. In urology, the ICG-NIRF imaging has been used in many different robotic procedures, including partial nephrectomy, radical prostatectomy, and upper urinary tract reconstructive procedures [10, 34–37]. These clinical reports, though considered preliminary pilot studies, have spurred significant interests in FIGS and paved the way for future advancements in this field.

## Applications of Near-Infrared Fluorescence Imaging in Robotic Urologic Surgery

### Partial Nephrectomy

Nephron-sparing surgery is currently a gold standard for surgical management of small renal masses and should be performed whenever technically feasible [38–40]. Even for renal tumors equal to or larger than 7 cm, partial nephrectomy may provide similar oncologic outcomes compared with radical nephrectomy in select patients [41]. Several retrospective studies have demonstrated the benefits of partial nephrectomy with improved long-term survival [42–45]. The robot-assisted laparoscopic partial nephrectomy approach has facilitated the increasing use of minimally invasive nephron-sparing surgery. When the NIRF imaging system became integrated into the da Vinci Si Surgical System, Tobis et al. carried out a pilot study on the first 11 patients who underwent a robotic partial nephrectomy with this system at the University of Rochester Medical Center in 2010 [10]. After renal hilar dissection was completed and the renal tumor was exposed, a bolus dose of ICG was given intravenously by the anesthesiologist. Different dosages were tested ranging from 0.75 to 7.5 mg. Since the half-life of ICG is only 2–5 min, repeated injections with different dosages were performed to achieve the optimal level of fluorescence. During the study, renal vascular structures could be clearly visualized [10]. Most RCCs appeared to be nonfluorescent or hypofluorescent, similar to the findings observed during open and laparoscopic surgery [7, 9, 10]. Clear macroscopic tumor margins were displayed with strong fluorescence signals [10]. This pilot study demonstrated that the ICG-NIRF imaging incorporated into the da Vinci System was a safe and effective addition to the robotic surgery platform for a robotic partial nephrectomy. This technology may provide additional advantages for intraoperative studies on the renal vasculature, renal perfusion assessments, and tumor margin identification, which may further improve the robotic partial nephrectomy [10]. Figure 5.4 demonstrates ICG-NIRF

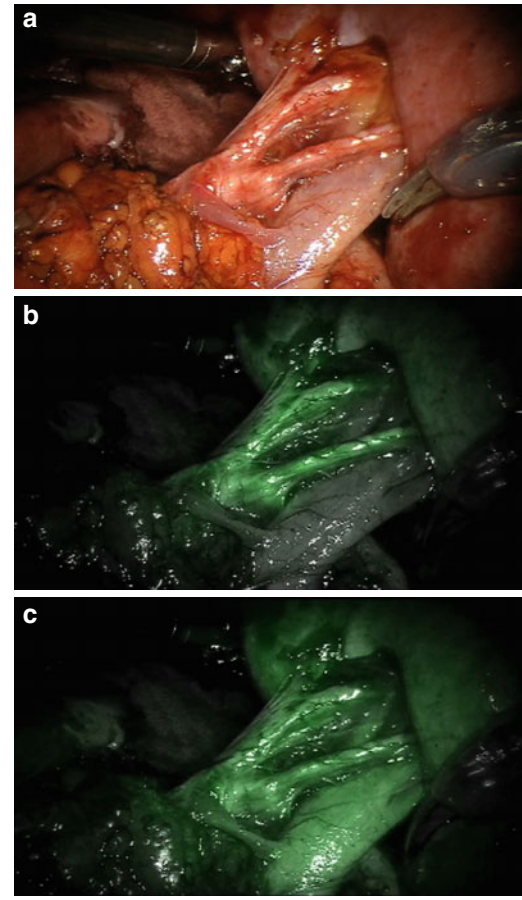


**Fig. 5.4** ICG-NIRF imaging of renal vasculature at the renal hilum. (**a**) A white-light image of a renal hilum with the main renal artery, secondary and tertiary branches, and the renal vein exposed. (**b**) The arterial phase of ICG-NIRF imaging after ICG was given intravenously. The renal arterial structure turned fluorescent. (**c**) Renal vein turned fluorescent a few seconds later after renal artery became fluorescent

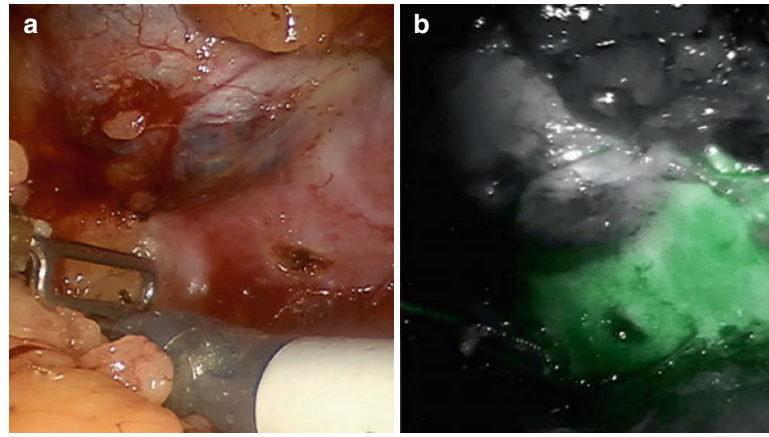


**Fig. 5.5** A fluorescent renal tumor under ICG-NIRF imaging. (**a**) A white-light image of a renal tumor. (**b**) Corresponding NIRF image of the same renal tumor. Note that the normal renal parenchyma exhibited fluorescent green color while the renal tumor (renal cell carcinoma) showed no fluorescent signals

images of renal vasculature, and Fig. 5.5 shows a typical afluorescent renal tumor.

Krane et al. reported a comparative study of 94 patients who underwent a robotic partial nephrectomy with or without the ICG-NIRF imaging and found that ICG-NIRF imaging was associated with decreased warm ischemia time and subjectively enhanced visualization of renal vasculature and the mass-parenchymal interface [34]. A subsequent analysis by the same group, to evaluate the relationship of fluorescence patterns and pathologic diagnosis, showed that ICG-NIRF imaging could not differentiate renal malignancies from benign lesions [46]. All 23 benign lesions were either hypofluorescent or afluorescent, while 74 out of 77 (96 %) malignant renal tumors were also either hypofluorescent or afluorescent [46]. However, this study did highlight the usefulness of ICG-NIRF imaging in verifying macroscopic negative margins during a robotic partial nephrectomy. Since this technology is still in its infancy, there is currently a lack of standardization for the use of ICG-NIRF imaging. While the optimal dose of ICG injection during a robotic partial nephrectomy has not been established, it is clear that underdosing of ICG prevents adequate fluorescence of the peritumor renal parenchyma, while overdosing results in tumor fluorescent and loses the purpose of fluorescence differentiation between the normal renal parenchyma and the tumor tissues. Angell et al. described a dosing strategy to optimize ICG dosing for NIRF imaging during robotic partial nephrectomy [37]. In their study, a minimum of two doses of ICG were given intravenously, with an initial testing dose followed by a calibrated second dose before the renal artery was clamped for tumor resection. The test dose was given as soon as the tumor was identified. If the test dose was too high, causing renal parenchyma and tumor fluorescence, then the surgeon could wait until fluorescent signals were washed out from the kidney and the tumor in order to give another lower dose of ICG while at the same time continuing with additional dissection and preparation for the tumor resection [37]. During the 18-month study period, a total of 79 cases underwent a robotic partial nephrectomy using the NIRF imaging. The initial ICG testing doses ranged from 0.625 to 2.5 mg, and the calibrated second doses ranged from 0.625 to 5 mg. Overall, 65 of 76 tumors exhibited fluorescent patterns consistent with expectations based on pathologic findings. Of the 60 RCC patients, 55 (92 %) showed no fluorescence corresponding to the original impressions reported by Tobis et al. [10, 37]. Angell et al. recommended a starting dose of 1.25 mg based on their experience [37]. In our current practice, we start initial dosing at 2.5 mg of ICG. After the normal kidney parenchyma turns a green fluorescent color and the fluorescent intensity is optimal, the renal artery is clamped with laparoscopic bulldogs. If the intensity is not optimal, additional time is allowed for

the ICG signals to be washed out and the dose is readjusted. While the arterial blood flow stopped, ICG is retained in the kidney and will last until the renal artery is unclamped. After renorrhaphy is completed, another dose of ICG may be given to reevaluate kidney perfusion as needed. The clinical value of this immediate post-partial nephrectomy perfusion assessment is unknown.

Patel et al. described their experience of a robotic partial nephrectomy for a rare renal epithelioid angiomyolipoma using NIRF imaging with ICG [47]. The tumor, a 6.5-cm right lower pole renal mass, appeared to be nonfluorescent under NIRF imaging using an intravenous injection of 5 mg of ICG. Thus, intraoperative NIRF imaging provided a real-time visual differentiation between the mass and the normal renal parenchyma. Additional experiences using the ICG-NIRF imaging system in managing uncommon types of renal tumors are needed.

While select small exophytic renal tumors could be excised without using renal hilar vessel control, the majority of endophytic and relatively large tumors require vascular control. An early unclamping technique has helped decrease the warm ischemic time during laparoscopic partial nephrectomy [48]. Gill et al. reported a strategy to further minimize the ischemic injury in robotic and laparoscopic partial nephrectomies by fine dissection of the renal vessels into the renal hilum and parenchyma to control the immediate tumor-feeding vessels and avoid the global ischemia [49]. NIRF with ICG has further facilitated the development of selective clamping and super-selective clamping in the robot-assisted laparoscopic partial nephrectomy [36, 50, 51]. NIRF with ICG renal angiography and perfusion assessment is easy to perform and allows surgeons to see the demarcation of the affected area clearly and with greater confidence.

Preoperative CT angiogram with 3D reconstruction based on 0.5–1 mm cuts is helpful for planning of super-selective clamping. Intraoperatively, the entire renal hilum is exposed in case the global arterial and/or venous control becomes necessary during the procedure. The renal vessels are mobilized to the tertiary and quaternary branches as necessary. A dose of 5 mg of ICG given intravenously is sufficient for optimal renal angiography and perfusion assessment. When the administration of ICG begins, vascular bulldogs are placed on selected arteries and the light is switched to NIRF. In complex cases, intraoperative ultrasound may be used for additional confirmation of tumor location and tumor blood flow, as tumors may be completely nonfluorescent and additional large vessels may be feeding the area. These tumor-feeding vessels may be ligated with Hem-o-lok clips (Teleflex Medical, Research Triangle Park, NC, USA). If satisfactory arterial control is achieved, the tumor can be excised under normal white-light view. The normal and NIRF view can be quickly toggled back and forth to check tumor margins. Once the tumor is excised, the tumor bed is sutured to control small bleeding vessels and repair the renal collecting system if warranted. The vascular bulldogs are removed and additional bleeding points are controlled with precise suturing. Renorrhaphy with the sliding clip technique is then employed to close the renal defect. Figure 5.6 demonstrates ICG-NIRF imaging to facilitate super-selective clamping of quaternary renal arterial branch during a robotic partial nephrectomy. Three reports have been published recently describing the experience with ICG-NIRF imaging for super-selective arterial clamping during robotic partial nephrectomy [36, 50, 51]. These authors concluded that NIRF with ICG renal angiography simplified the robotic partial nephrectomy with selective renal arterial clamping and will have an impact on functional outcome in terms of preservation of renal function by decreasing warm ischemia time.

## Sentinel Node Identification

The potential prognostic and therapeutic value of sentinel lymph node (SLN) mapping in solid cancer management was recognized over 50 years ago [52]. This has been extensively studied in many different types of cancer [53]. SLN mapping has been integrated into the clinical management of breast cancer and melanoma [53–55]. ICG-NIRF imaging has been used in clinical studies of SLN mapping in solid tumors

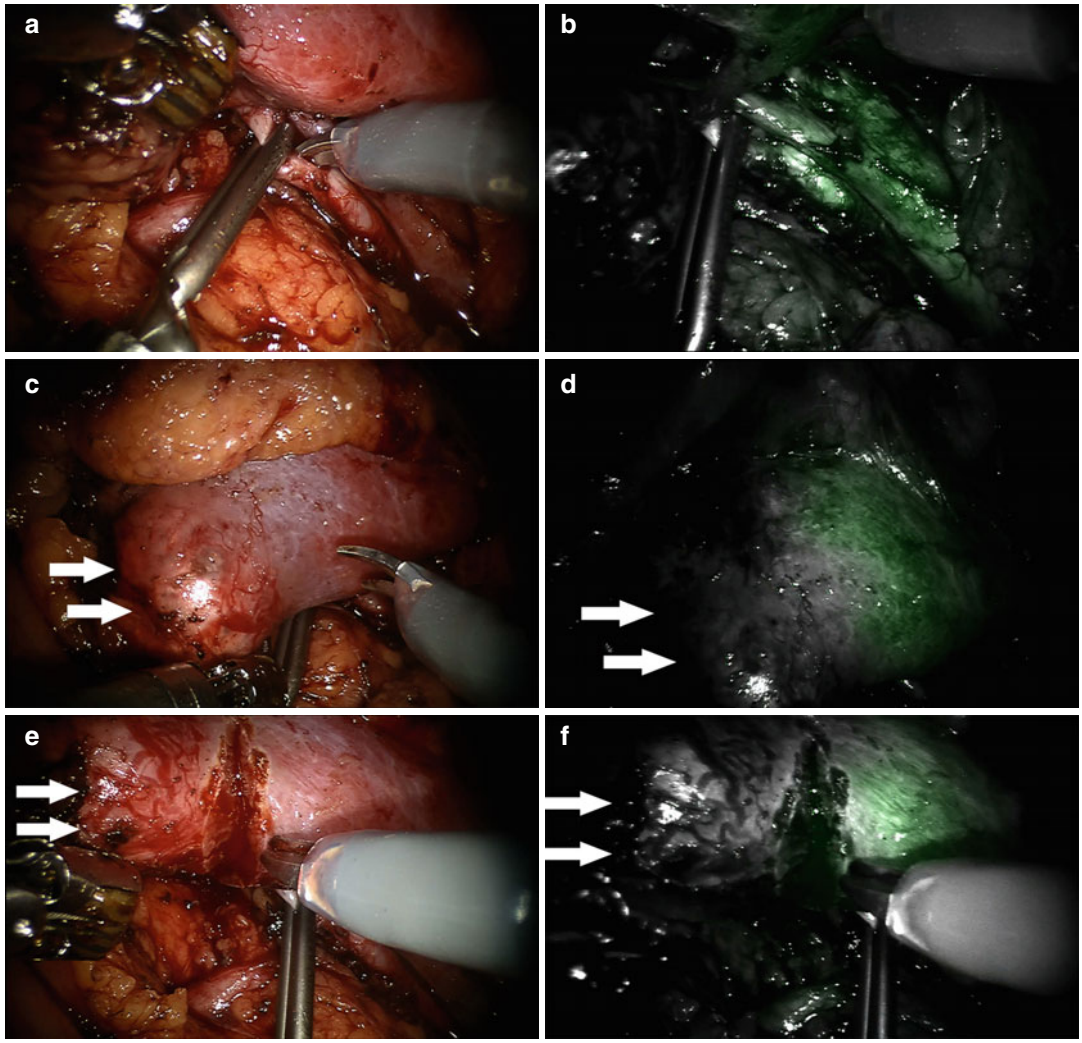


**Fig. 5.6** ICG-NIRF imaging during a robotic partial nephrectomy with super-selective renal arterial clamping. (**a** and **b**) White-light and NIRF views of a renal arterial quaternary branch feeding to the lower pole of the kidney clamped with a small laparoscopic bulldog. Note that under the NIRF view (**b**) the distal portion of the renal arterial segment was not fluorescent, indicating no blood flow through the arterial brunch. (**c**, **d**) White-light and NIRF views of the demarcation of the renal parenchyma after the renal arterial quaternary branch was clamped. Note that the NIRF image (**d**) shows a clear demarcation line. (**e**, **f**) White-light and NIRF views of excision of the renal tumor after super-selective clamping. No significant bleeding was encountered. *Arrows* in the figure indicate the renal tumor

[3, 4, 51]. In the past, various combinations of blue dye and radioactive tracers with different injection methods have been described in endometrial and cervical cancers with SLN detection rates ranging from 84 to 97 % [16]. Recently, Jewell et al. reported a study of SLN detection in 227 cases during robotic hysterectomies for endometrial and cervical cancers using robotic platform with ICG-NIRF imaging system [16]. In this study, the overall SLN detection rate was 95 and 10 % of patients had an SLN beyond the standard lymphadenectomy template [16]. Three other smaller studies in gynecologic cancers also demonstrated the ease of use of the robotic platform with ICG-NIRF imaging in SLN mapping [56–58]. These authors also concluded that the ICG-NIRF imaging method was superior to blue dye injection.

ICG-NIRF imaging has also been used in prostate cancer SLN mapping. In a pioneering study, van der Poel et al. injected an ICG-$^{99m}$Tc-NanoColl (NIRF and radioactive hybrid imaging tracer) via transrectal ultrasound (TRUS) guidance 3 h prior to a prostatectomy with subsequent lymphoscintigraphy and single-photon emission computed tomography/computed tomography (SPECT/CT) imaging to map the radiotracer signals [59]. Intraoperatively, an NIRF laparoscope was used to visualize the lymph nodes identified on SPECT/CT. Another study published by Jeschke et al. described injection of $^{99m}$Tc-labeled human serum albumin colloid into the prostate 18 h preoperatively under TRUS guidance [60]. Static planar scintigraphy images were obtained 1 h preoperatively and ICG injected into the prostate under TRUS guidance just prior to the surgery. A laparoscopic γ-detection probe and an NIRF laparoscope were used to detect the SLNs [60]. Obviously, these strategies are cumbersome, time-consuming, and expensive and involve radioactive hazardous materials. Two pilot reports by Manny et al. took the advantage of the robotic platform equipped with NIRF imaging capability to investigate real-time lymphangiography and tissue marking during robotic radical prostatectomies and cystectomies [35, 61]. A total of 50 cases were included in their radical prostatectomy study. Three intraprostatic injection techniques were tested, including percutaneous robot guided, TRUS guided, and cystoscopy guided. They found that the percutaneous robot-guided injection of 1 mg of ICG into each lobe provided the most efficient and successful method with less extraprostatic spillage and avoided additional setups for transrectal ultrasound and cystoscopy. After ICG intraprostatic injection, the prostate tissue was marked with uniform fluorescence in contrast to the relatively dark seminal vesicles, vas deferens, and neurovascular pedicles after a mean time of 10 min, and SLNs were seen at a mean time of 30 min [35]. This pilot study demonstrates the feasibility and usefulness of ICG-NIRF imaging in studying prostate cancer SLNs.

SLN mapping using ICG-NIRF imaging has the potential added benefit of assessing lymph nodes and lymphatic drainage patterns from the pelvic organs, such as prostate, bladder, and uterus [16, 35, 61]. The robotic surgery platform with the ICG-NIRF imaging may help further investigate and define SLNs and lymphatic mapping in pelvic organ cancers and other intra-abdominal malignancies improving oncologic outcomes of those surgeries. One potential application is, instead of performing super extended lymph node dissection on every moderate- to high-risk patient, performing targeted lymphadenectomy to remove additional sentinel nodes that are identified beyond the originally planned template as demonstrated by SLN mapping.

## Tissue Perfusion and Viability

The ICG-NIRF imaging technology has also provided a simple method to confirm tissue perfusion during robotic surgery. Bjurlin et al. described their experience of ICG-NIRF imaging in tissue perfusion assessment during robotic upper urinary tract reconstruction procedures, including pyeloplasty, ureteral reimplantation, ureterolysis, and ureteroureterostomy [36]. ICG (in 5–10 mg doses) was given intravenously to evaluate perfusion of the tissue planned for reconstruction. For robotic pyeloplasties, Bjurlin et al. focused on tissue viability of the renal pelvis and ureter at the planned anastomotic regions. Poorly perfused fibrotic scar tissues were evident as nonfluorescent dark regions. When poorly perfused tissues were identified, additional trimming was performed to ensure healthy tissue margins at the anastomotic site. A total of 20 pyeloplasty procedures were performed with intraoperative NIRF imaging [36]. Since the successful rate of robotic pyeloplasty is 96 %, NIRF imaging might not provide further benefit for routine pyeloplasty; however, NIRF imaging with ICG might be valuable for secondary pyeloplasty patients who have failed previous open or robotic pyeloplasties, as these patients may have significant tissue fibrosis and devascularization secondary to their history of previous surgery [36]. For robotic ureterolysis or ureteroureterostomy, ICG was administered prior to excising the strictured segment to show the

location and length of the stricture [36]. For these patients, NIRF imaging can demonstrate perfusion pattern and help to identify poorly perfused tissues and strictured areas to ensure that diseased tissues are removed adequately and healthy tissues are approximated for anastomoses [36]. This ICG-NIRF imaging strategy could be applied to vesicovaginal fistula and vesicorectal fistula repairs.

Another important application of intraoperative tissue viability assessment is during robotic intracorporeal urinary diversions [61]. Two types of urinary diversions are commonly performed during robotic cystectomy, ileal conduit urinary diversion and ileal neobladder. With increasing experience using robotic cystectomy, intracorporeal urinary diversions have become popular and become the first choice of many experienced robotic surgeons. In our current practice, ICG-NIRF imaging is performed for selected patients during robotic intracorporeal urinary diversion. Before the side-to-side small bowel anastomosis, the two ileal limbs are approximated together. ICG (5 mg) is injected intravenously to assess the viability of the small bowel segments. The segment of bowel in question of devascularization should be removed. Small bowel segments do sometimes exhibit lighter color due to peristalsis and spasm. However, when the peristalsis passes through and the spasm segment relaxes, normal ICG fluorescent signals should return to that segment of tissue. When in doubt, a second dose of ICG could be given after the initial ICG signals have been washed out. After the anastomosis is completed, another dose of ICG may be given to further demonstrate good perfusion. Figure 5.7 shows ICG-NIRF imaging performed after reestablishing the continuity of the small bowel. Intraoperative ICG-NIRF imaging provides surgeons with another visual confirmation of the quality of small bowel anastomosis and small bowel segment harvested for urinary diversion.

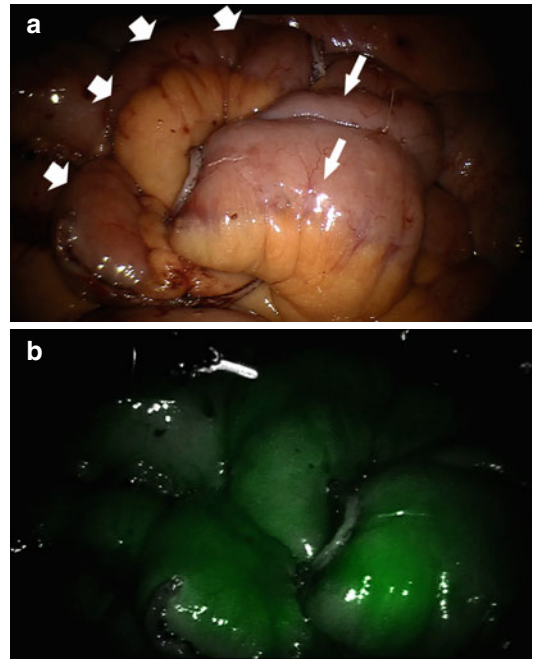


**Fig. 5.7** ICG-NIRF imaging performed after reestablishing the continuity of the small bowel during a robotic intracorporeal ileal conduit diversion. (**a**) A white-light image of the side-to-side anastomosis of the small bowel (*long arrows*) and the ileal conduit segment (*short arrows*). (**b**) Corresponding NIRF image of the small bowel anastomotic area and the ileal conduit segment in uniform *green*, indicating good perfusion

## Ureteral Visualization

The intraoperative visualization of the ureters in the surgical field is important, not only for urologists during upper urinary tract reconstruction or repair surgeries but also for general surgeons and gynecologists alike, to avoid iatrogenic ureteral injury. Identification of ureters embedded in surrounding tissue, especially in dense scar tissues, can be very challenging. In an animal study, Tanaka et al. demonstrated that retrograde injection of ICG solution into pig ureters could illuminate the ureter under NIRF imaging [20]. Tanaka et al. also showed that intravenous injection of CW800-CA (LI-COR, Lincoln, Nebraska), a NIRF dye excreted through the kidneys without chemical modification, could make ureters fluorescent under NIRF imaging [20]. However, CW800-CA is still under development and not approved for human use at this time [6].

Lee et al. recently reported that intraureteral ICG injection and visualization under NIRF facilitated identification and delineation of ureteral strictures during robot-assisted laparoscopic ureteral stricture repair [62]. A total of seven patients

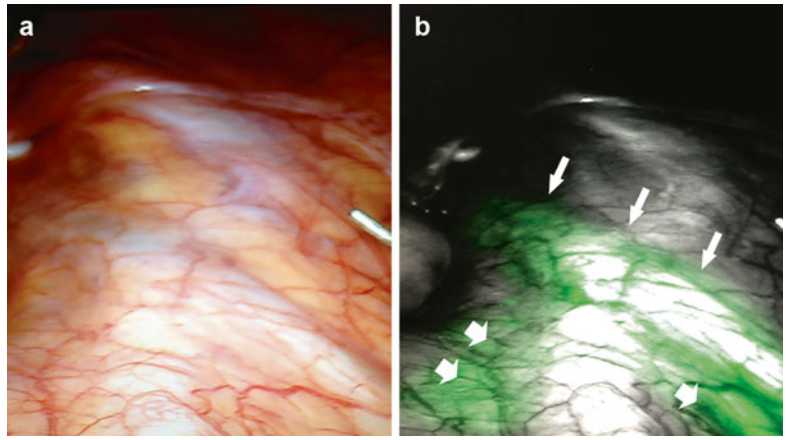


**Fig. 5.8** Illuminating the ureter using ICG-NIRF imaging. (**a**) White-light view of a healthy mid ureter. (**b**) NIRF view of the ureter with aqueous ICG solution injected into the ureter (*long arrows*). Note that fluorescent signals are evident at the para-ureteral tissues (*short arrows*), likely caused by absorption of ICG into the ureteral wall (Courtesy of Dr. Daniel Eun, Department of Urology, Temple University School of Medicine, Philadelphia, PA, USA)

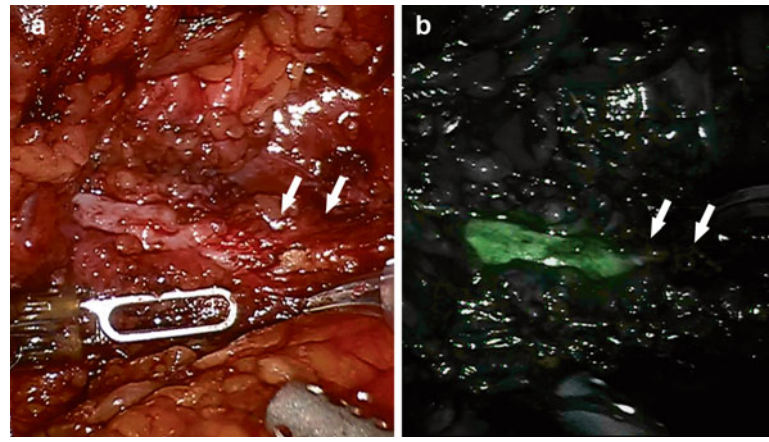


**Fig. 5.9** Identification of ureteral stricture area with ICG intraluminal injection. (**a**) Ureteral stricture area under white light. (**b**) ICG was injected through a nephrostomy tube. Note that the healthy ureteral segment is green under NIRF imaging while the strictured area is dark. The ureteral stricture area is indicated by the *arrows*

underwent the procedure. Intraoperative localization of the ureteral stricture was performed with ICG solution (25 mg in 10 cc of sterile water) injected both above and below the level of stenosis through a ureteral catheter, a percutaneous nephrostomy tube, or both. Intense fluorescence was observed in the healthy segments of the ureter, and the diseased areas were clearly delineated by NIRF imaging [62]. Densely scarred ureteral segments showed no fluorescence signals. Since ICG requires binding to plasma protein to be fluorescent, the exact mechanism of fluorescence generated by intraureteral lumen injection of aqueous ICG solution is unclear. It is possible that pressure generated by the intraureteral injection of aqueous ICG may result in the absorption of ICG into the ureteral wall. As demonstrated in Fig. 5.8, a segment of fluorescent normal ureter is seen after intraureteral injection of aqueous ICG solution. Note that capillary drainage of ICG around the para-ureteral soft tissues is evident, indicating absorption or leakage of ICG through the ureteral wall.

In our own experience, intraureteral injection of aqueous ICG solution has been helpful to identify the strictured ureteral area. Figure 5.9 shows

a robotic ureteral stricture repair with ICG intraureteral injection through a nephrostomy tube with NIRF imaging. The fibrotic area showed no fluorescence, indicating a poorly perfused area. Bjurlin et al. also reported on the potential benefit of using intravenous injection of ICG to identify poorly perfused ureteral segments during ureteral stricture repair [36]. In their study, NIRF imaging with ICG provided an additional visual evidence of the boundary between the healthy and diseased tissue, thereby, minimizing unnecessary removal of healthy tissue.

For general surgeons and gynecologists, who may not be as familiar with the anatomy of the ureter as urologists, a simple way of visualizing the ureters is ideal during colorectal and gynecologic surgeries, especially in challenging cases. Commonly, ureteral catheters are placed preoperatively in the ureters to aid in identification during colon or gynecologic surgeries with high-risk of ureteral injuries. However, with the increased use of laparoscopic and robotic surgery in colorectal and gynecologic surgeries, the loss of tissue palpation may not allow for such ease with ureteral identification even with catheters in place. Here, direct visualization is desirable. An ICG-coated ureteral catheter would be ideal with NIRF imaging. To prove this concept, we placed an ICG-coated ureteral stent with NIRF imaging during a robotic surgery to help identify and protect a deviated ureter. Figure 5.10 shows the fluorescence signals along the ureter. Further development in this field is anticipated.

## Other Applications

Manny et al. recently published their preliminary clinical experience with robot-assisted partial adrenalectomy with ICG-NIRF imaging [63]. Only three cases were reported including one pheochromocytoma, one lipoadenoma, and one follicular lymphoid hyperplasia. Interestingly, compared to normal adrenal gland tissue, all three adrenal tumors were hypofluorescent after 5 mg of ICG was given intravenously. The authors concluded that the addition of ICG-NIRF may help with mass identification and excision and promote the use of partial adrenalectomy [63]. This pilot observation is the first of many that will lead the way for further investigation to evaluate the potential benefits ICG-NIRF imaging may provide during robotic partial adrenalectomy.

## Future Advancement

Recent advances in ICG fluorescence image-guided robotic surgery have opened up a new frontier in robotic surgery. The surgical robot with NIRF imaging functionality (da Vinci Surgical Robot with the Firefly system) can create real-time 3D hybrid images that exhibit excellent tissue resolution and vascular details. Future developments in ICG fluorescence image-guided robotic surgery will likely broaden its applications in urology and other surgical specialties. Real-time small vessel imaging, sentinel lymph node identification, intraoperative lymphangiography, tumor painting or reverse painting, and tissue viability assessment are currently active research fields. Surgeons as end-user innovators, will not only apply this technology to clinical practice but also conduct clinical research to advance the FIGS field. Next-generation surgical robots with multispectral fluorescence imaging systems able to detect fluorescent tracers in different spectrums simultaneously are desirable. Fluorescent contrasts with different excitation and emission wavelengths could be displayed with different pseudo colors in real time overlaying with white-light images to achieve color-coded tissue recognition during robotic surgery.

NIRF contrasts brighter than ICG will improve the sensitivity of intraoperative NIRF imaging. However, due to the intrinsic limitation of the depth of penetrance, further improvements in intraoperative NIRF imaging will likely need to combine other imaging modalities, such as preoperatively obtained tomography imaging, intraoperative ultrasound, real-time confocal microscopy, tissue autofluorescence imaging, and virtual reality. Targeted antibodies for clinical therapeutic applications are already available for various tumors and tumor markers,

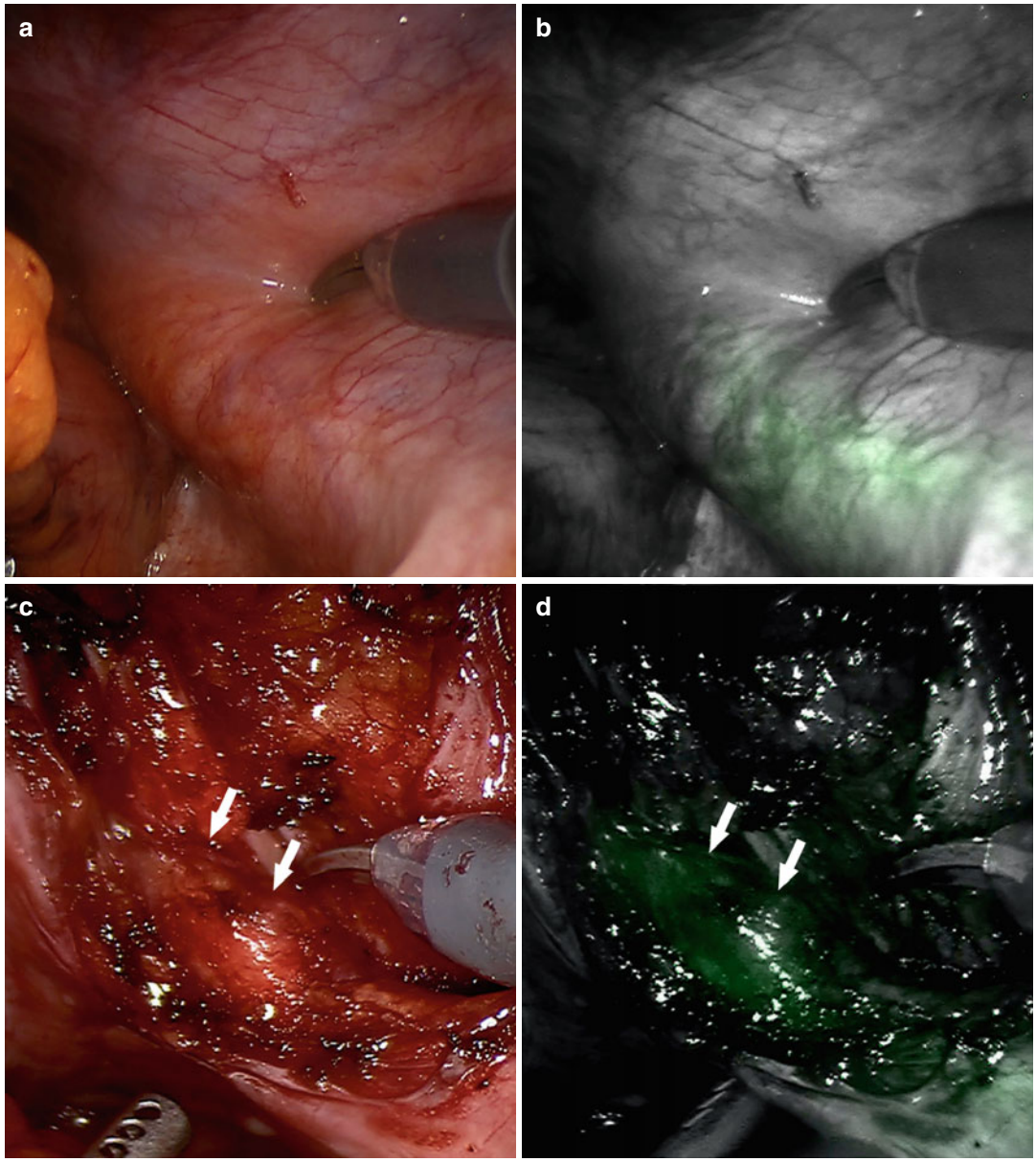


**Fig. 5.10** Visualization of the ureter facilitated by inserting an ICG-coated ureteral stent during pelvic area surgery. (**a**) A white-light image of the pelvic area on the right side. Note that the ureter is not noticeable. (**b**) Under NIRF imaging, the fluorescent signals from the ureter underneath are shown in *green*. (**c** and **d**) Corresponding views of the right distal ureter under white light and NIRF imaging. The peritoneal layer was incised and the right distal ureter was exposed. Note that the ureter is indicated by the *arrows* and the fluorescent ureter is in *green*

including bevacizumab against VEGF, cetuximab against EGFR, and trastuzumab against HER2. Conjugating these antibodies with an NIRF fluorophore will create target-specific NIRF imaging contrasts for intraoperative real-time tumor visualization [2, 3]. Tissue- or cell-type-specific binding biomolecules, such as peptide ligands and antigen binding fragments, will help to expand the repertoire of target-specific NIRF contrasts for intraoperative NIRF imaging [2, 3].

Future efforts to quantify the effectiveness, either in terms of improved patient outcomes or cost savings with these advanced surgical robots using NIRF imaging, are still needed to justify the future expenditure in research and development in this field and deployment of newer-generation surgical robots [3]. This will only be achieved through well-designed and well-executed clinical trials.

## Conclusion

Fluorescence image-guided robotic surgery is exciting and only in its infancy. The current surgical robot with NIRF imaging function has provided surgeons with an advanced surgical platform with real-time fluorescence image-guided capabilities. Surgeons as end-user innovators will be able to expand the applications of fluorescence image-guided surgeries in the future. Urologists have been in the forefront of exploring the potential of fluorescence-guided robotic surgery in urinary tract cancer surgeries and reconstructive procedures. Early experiences obtained from different academic urologic surgeons have demonstrated that ICG-NIRF image-guided robotic surgeries are feasible and safe and have the potential to improve the qualities and outcomes of certain major urologic procedures. Convincing data demonstrating the effectiveness in terms of improving the quality and outcome of surgery with reasonable costs or with decreased costs of overall care are still needed. The key advancement in image-guided robotic surgery will rely on future engineering of robotic surgery imaging systems and developing tissue- or cell-type-specific fluorescent contrasts suitable for clinical use. With future robotic surgical platforms incorporating advanced imaging technologies, we will be able to perform surgery with unprecedented precision not only beyond human hands but also beyond human eyes.

**Acknowledgments** The author wishes to thank the Department of Urology, University of Rochester Medical Center, for continual research support and to thank many colleagues who have played leading roles or participated in ICG-NIRF imaging research in our medical center. Special thanks to Drs. Dragan Golijanin, Ron Wood, Scott Tobis, Hani Rashid, and Edward Messing. The author also wishes to thank Dr. Helen Levey for preparing the manuscript and Catherine Wu for preparing photographs and illustrations for this chapter.

## References

1. Frangioni JV. New technologies for human cancer imaging. J Clin Oncol. 2008;26(24):4012–21.
2. Nguyen QT, Tsien RY. Fluorescence-guided surgery with live molecular navigation – a new cutting edge. Nat Rev Cancer. 2013;13(9):653–62.
3. Vahrmeijer AL, Hutteman M, van der Vorst JR, van de Velde CJ, Frangioni JV. Image-guided cancer surgery using near-infrared fluorescence. Nat Rev Clin Oncol. 2013;10(9):507–18.
4. Marshall MV, Rasmussen JC, Tan IC, Aldrich MB, Adams KE, Wang X, et al. Near-infrared fluorescence imaging in humans with indocyanine green: a review and update. Open Surg Oncol J. 2010;2(2):12–25.
5. Verbeek FP, Troyan SL, Mieog JS, Liefers GJ, Moffitt LA, Rosenberg M, et al. Near-infrared fluorescence sentinel lymph node mapping in breast cancer: a multicenter experience. Breast Cancer Res Treat. 2014; 143(2):333–42.
6. Marshall MV, Draney D, Sevick-Muraca EM, Olive DM. Single-dose intravenous toxicity study of IRDye 800CW in Sprague-Dawley rats. Mol Imaging Biol. 2010;12(6):583–94.
7. Tobis S, Knopf JK, Silvers CR, Marshall J, Cardin A, Wood RW, et al. Near infrared fluorescence imaging after intravenous indocyanine green: initial clinical experience with open partial nephrectomy for renal cortical tumors. Urology. 2012;79(4):958–64.
8. Verbeek FP, Schaafsma BE, Tummers QR, van der Vorst JR, van der Made WJ, Baeten CI, et al. Optimization of near-infrared fluorescence cholangiography for open and laparoscopic surgery. Surg Endosc. 2014;28(4):1076–82.
9. Tobis S, Knopf JK, Silvers C, Messing E, Yao J, Rashid H, et al. Robot-assisted and laparoscopic partial nephrectomy with near infrared fluorescence imaging. J Endourol. 2012;26(7):797–802.
10. Tobis S, Knopf J, Silvers C, Yao J, Rashid H, Wu G, et al. Near infrared fluorescence imaging with robotic assisted laparoscopic partial nephrectomy: initial clinical experience for renal cortical tumors. J Urol. 2011;186(1):47–52.
11. Calatayud D, Milone L, Elli EF, Giulianotti PC. ICG-fluorescence identification of a small aberrant biliary canaliculus during robotic cholecystectomy. Liver Int. 2012;32(4):602.
12. Singh I. Robotics in urological surgery: review of current status and maneuverability, and comparison of robot-assisted and traditional laparoscopy. Comput Aided Surg. 2011;16(1):38–45.

13. Yamamoto T, Yamamoto N, Azuma S, Yoshimatsu H, Seki Y, Narushima M, et al. Near-infrared illumination system-integrated microscope for supermicrosurgical lymphaticovenular anastomosis. Microsurgery. 2014;34(1):23–7.
14. Alander JT, Kaartinen I, Laakso A, Patila T, Spillmann T, Tuchin VV, et al. A review of indocyanine green fluorescent imaging in surgery. Int J Biomed Imaging. 2012;2012:940585.
15. Verbeek FP, van der Vorst JR, Schaafsma BE, Swijnenburg RJ, Gaarenstroom KN, Elzevier HW, et al. Intraoperative near infrared fluorescence guided identification of the ureters using low dose methylene blue: a first in human experience. J Urol. 2013;190(2): 574–9.
16. Jewell EL, Huang JJ, Abu-Rustum NR, Gardner GJ, Brown CL, Sonoda Y, et al. Detection of sentinel lymph nodes in minimally invasive surgery using indocyanine green and near-infrared fluorescence imaging for uterine and cervical malignancies. Gynecol Oncol. 2014;133(2):274–7.
17. Colditz MJ, Leyen K, Jeffree RL. Aminolevulinic acid (ALA)-protoporphyrin IX fluorescence guided tumour resection. Part 2: theoretical, biochemical and practical aspects. J Clin Neurosci. 2012;19(12): 1611–6.
18. Colditz MJ, Jeffree RL. Aminolevulinic acid (ALA)-protoporphyrin IX fluorescence guided tumour resection. Part 1: clinical, radiological and pathological studies. J Clin Neurosci. 2012;19(11):1471–4.
19. Heuveling DA, Visser GW, de Groot M, de Boer JF, Baclayon M, Roos WH, et al. Nanocolloidal albumin-IRDye 800CW: a near-infrared fluorescent tracer with optimal retention in the sentinel lymph node. Eur J Nucl Med Mol Imaging. 2012;39(7):1161–8.
20. Tanaka E, Ohnishi S, Laurence RG, Choi HS, Humblet V, Frangioni JV. Real-time intraoperative ureteral guidance using invisible near-infrared fluorescence. J Urol. 2007;178(5):2197–202.
21. Folli S, Wagnieres G, Pelegrin A, Calmes JM, Braichotte D, Buchegger F, et al. Immunophotodiagnosis of colon carcinomas in patients injected with fluoresceinated chimeric antibodies against carcinoembryonic antigen. Proc Natl Acad Sci U S A. 1992;89(17):7973–7.
22. van Dam GM, Themelis G, Crane LM, Harlaar NJ, Pleijhuis RG, Kelder W, et al. Intraoperative tumor-specific fluorescence imaging in ovarian cancer by folate receptor-alpha targeting: first in-human results. Nat Med. 2011;17(10):1315–9.
23. Cherrick GR, Stein SW, Leevy CM, Davidson CS. Indocyanine green: observations on its physical properties, plasma decay, and hepatic extraction. J Clin Invest. 1960;39:592–600.
24. Kogure K, Choromokos E. Infrared absorption angiography. J Appl Physiol. 1969;26(1):154–7.
25. Flower RW. Infrared absorption angiography of the choroid and some observations on the effects of high intraocular pressures. Am J Ophthalmol. 1972;74(4): 600–14.
26. Ott P, Keiding S, Johnsen AH, Bass L. Hepatic removal of two fractions of indocyanine green after bolus injection in anesthetized pigs. Am J Physiol. 1994;266(6 Pt 1):G1108–22.
27. Ott P, Keiding S, Bass L. Intrinsic hepatic clearance of indocyanine green in the pig: dependence on plasma protein concentration. Eur J Clin Invest. 1992;22(5): 347–57.
28. Gotoh K, Yamada T, Ishikawa O, Takahashi H, Eguchi H, Yano M, et al. A novel image-guided surgery of hepatocellular carcinoma by indocyanine green fluorescence imaging navigation. J Surg Oncol. 2009; 100(1):75–9.
29. Lim C, Vibert E, Azoulay D, Salloum C, Ishizawa T, Yoshioka R, et al. Indocyanine green fluorescence imaging in the surgical management of liver cancers: current facts and future implications. J Visc Surg. 2014;151(2):117–24.
30. Hassan M, Kerdok A, Engel A, Gersch K, Smith JM. Near infrared fluorescence imaging with ICG in TECAB surgery using the da Vinci Si surgical system in a canine model. J Card Surg. 2012;27(2):158–62.
31. Spinoglio G, Priora F, Bianchi PP, Lucido FS, Licciardello A, Maglione V, et al. Real-time near-infrared (NIR) fluorescent cholangiography in single-site robotic cholecystectomy (SSRC): a single-institutional prospective study. Surg Endosc. 2013;27(6):2156–62.
32. Buchs NC, Pugin F, Azagury DE, Jung M, Volonte F, Hagen ME, et al. Real-time near-infrared fluorescent cholangiography could shorten operative time during robotic single-site cholecystectomy. Surg Endosc. 2013;27(10):3897–901.
33. Hellan M, Spinoglio G, Pigazzi A, Lagares-Garcia JA. The influence of fluorescence imaging on the location of bowel transection during robotic left-sided colorectal surgery. Surg Endosc. 2014;28(5):1695–702.
34. Krane LS, Manny TB, Hemal AK. Is near infrared fluorescence imaging using indocyanine green dye useful in robotic partial nephrectomy: a prospective comparative study of 94 patients. Urology. 2012; 80(1):110–6.
35. Manny TB, Patel M, Hemal AK. Fluorescence-enhanced robotic radical prostatectomy using real-time lymphangiography and tissue marking with percutaneous injection of unconjugated indocyanine green: the initial clinical experience in 50 patients. Eur Urol. 2014;65(6):1162–8.
36. Bjurlin MA, Gan M, McClintock TR, Volpe A, Borofsky MS, Mottrie A, et al. Near-infrared fluorescence imaging: emerging applications in robotic upper urinary tract surgery. Eur Urol. 2014;65(4): 793–801.
37. Angell JE, Khemees TA, Abaza R. Optimization of near infrared fluorescence tumor localization during robotic partial nephrectomy. J Urol. 2013;190(5): 1668–73.
38. Gill IS, Aron M, Gervais DA, Jewett MA. Clinical practice. Small renal mass. N Engl J Med. 2010; 362(7):624–34.

39. Campbell SC, Novick AC, Belldegrun A, Blute ML, Chow GK, Derweesh IH, et al. Guideline for management of the clinical T1 renal mass. J Urol. 2009; 182(4):1271–9.
40. Ljungberg B, Cowan NC, Hanbury DC, Hora M, Kuczyk MA, Merseburger AS, et al. EAU guidelines on renal cell carcinoma: the 2010 update. Eur Urol. 2010;58(3):398–406.
41. Becker F, Roos FC, Janssen M, Brenner W, Hampel C, Siemer S, et al. Short-term functional and oncologic outcomes of nephron-sparing surgery for renal tumours >/=7 cm. Eur Urol. 2011;59(6):931–7.
42. Huang WC, Elkin EB, Levey AS, Jang TL, Russo P. Partial nephrectomy versus radical nephrectomy in patients with small renal tumors–is there a difference in mortality and cardiovascular outcomes? J Urol. 2009;181(1):55–61; discussion -2.
43. Lane BR, Fergany AF, Weight CJ, Campbell SC. Renal functional outcomes after partial nephrectomy with extended ischemic intervals are better than after radical nephrectomy. J Urol. 2010;184(4):1286–90.
44. Weight CJ, Lieser G, Larson BT, Gao T, Lane BR, Campbell SC, et al. Partial nephrectomy is associated with improved overall survival compared to radical nephrectomy in patients with unanticipated benign renal tumours. Eur Urol. 2010;58(2):293–8.
45. Weight CJ, Larson BT, Gao T, Campbell SC, Lane BR, Kaouk JH, et al. Elective partial nephrectomy in patients with clinical T1b renal tumors is associated with improved overall survival. Urology. 2010;76(3):631–7.
46. Manny TB, Krane LS, Hemal AK. Indocyanine green cannot predict malignancy in partial nephrectomy: histopathologic correlation with fluorescence pattern in 100 patients. J Endourol. 2013;27(7):918–21.
47. Patel TH, Sirintrapun SJ, Hemal AK. Surgeon-controlled robotic partial nephrectomy for a rare renal epithelioid angiomyolipoma using near-infrared fluorescence imaging using indocyanine green dye: a case report and literature review. Can Urol Assoc J. 2012; 6(2):E91–4.
48. Gill IS, Kamoi K, Aron M, Desai MM. 800 Laparoscopic partial nephrectomies: a single surgeon series. J Urol. 2010;183(1):34–41.
49. Gill IS, Eisenberg MS, Aron M, Berger A, Ukimura O, Patil MB, et al. "Zero ischemia" partial nephrectomy: novel laparoscopic and robotic technique. Eur Urol. 2011;59(1):128–34.
50. Borofsky MS, Gill IS, Hemal AK, Marien TP, Jayaratna I, Krane LS, et al. Near-infrared fluorescence imaging to facilitate super-selective arterial clamping during zero-ischaemia robotic partial nephrectomy. BJU Int. 2013;111(4):604–10.
51. Harke N, Schoen G, Schiefelbein F, Heinrich E. Selective clamping under the usage of near-infrared fluorescence imaging with indocyanine green in robot-assisted partial nephrectomy: a single-surgeon matched-pair study. World J Urol. 2014;32(5): 1259–65.
52. Tanis PJ, Nieweg OE, Valdes Olmos RA, Th Rutgers EJ, Kroon BB. History of sentinel node and validation of the technique. Breast Cancer Res. 2001;3(2): 109–12.
53. Chen SL, Iddings DM, Scheri RP, Bilchik AJ. Lymphatic mapping and sentinel node analysis: current concepts and applications. CA Cancer J Clin. 2006;56(5):292–309; quiz 316–7.
54. Kim T, Giuliano AE, Lyman GH. Lymphatic mapping and sentinel lymph node biopsy in early-stage breast carcinoma: a metaanalysis. Cancer. 2006; 106(1):4–16.
55. Morton DL, Wen DR, Wong JH, Economou JS, Cagle LA, Storm FK, et al. Technical details of intraoperative lymphatic mapping for early stage melanoma. Arch Surg. 1992;127(4):392–9.
56. Rossi EC, Jackson A, Ivanova A, Boggess JF. Detection of sentinel nodes for endometrial cancer with robotic assisted fluorescence imaging: cervical versus hysteroscopic injection. Int J Gynecol Cancer. 2013;23(9):1704–11.
57. Rossi EC, Ivanova A, Boggess JF. Robotically assisted fluorescence-guided lymph node mapping with ICG for gynecologic malignancies: a feasibility study. Gynecol Oncol. 2012;124(1):78–82.
58. Holloway RW, Bravo RA, Rakowski JA, James JA, Jeppson CN, Ingersoll SB, et al. Detection of sentinel lymph nodes in patients with endometrial cancer undergoing robotic-assisted staging: a comparison of colorimetric and fluorescence imaging. Gynecol Oncol. 2012;126(1):25–9.
59. van der Poel HG, Buckle T, Brouwer OR, Valdes Olmos RA, van Leeuwen FW. Intraoperative laparoscopic fluorescence guidance to the sentinel lymph node in prostate cancer patients: clinical proof of concept of an integrated functional imaging approach using a multimodal tracer. Eur Urol. 2011;60(4): 826–33.
60. Jeschke S, Lusuardi L, Myatt A, Hruby S, Pirich C, Janetschek G. Visualisation of the lymph node pathway in real time by laparoscopic radioisotope- and fluorescence-guided sentinel lymph node dissection in prostate cancer staging. Urology. 2012;80(5): 1080–6.
61. Manny TB, Hemal AK. Fluorescence-enhanced robotic radical cystectomy using unconjugated indocyanine green for pelvic lymphangiography, tumor marking, and mesenteric angiography: the initial clinical experience. Urology. 2014;83(4):824–30.
62. Lee Z, Simhan J, Parker DC, Reilly C, Llukani E, Lee DI, et al. Novel use of indocyanine green for intraoperative, real-time localization of ureteral stenosis during robot-assisted ureteroureterostomy. Urology. 2013;82(3):729–33.
63. Manny TB, Pompeo AS, Hemal AK. Robotic partial adrenalectomy using indocyanine green dye with near-infrared imaging: the initial clinical experience. Urology. 2013;82(3):738–42.

# Multiphoton Microscopy in Urologic Surgery

6

Sushmita Mukherjee, Manu Jain, and Douglas S. Scherr

In this chapter, we describe the current status of research in multiphoton microscopy (MPM), as it pertains to its applications in urologic surgery. Specifically, we discuss how MPM fits in the general area of "optical biopsy," which constitutes a set of imaging techniques that utilize visible or near-infrared light to allow the visualization of fresh tissue at high resolution, without the need to process it in any way. We start this chapter with an overview of specific surgical contexts where such optical biopsies might be particularly useful. We then provide a summary of the optical biopsy techniques currently available for clinical use, along with their utilities and limitations. Next, we provide a brief introduction to the basic principles of MPM and how it might overcome some of the limitations of current optical biopsy techniques. Based on the narrative summarized above, we posit that MPM may be the next step in optical biopsy during urologic surgeries, providing solutions to some of the current unmet challenges. We then provide specific examples from published and unpublished studies from our group that demonstrates the power of MPM to make accurate diagnoses in fresh (unfixed, unsectioned, unstained) human surgical tissue from urological organs (bladder, prostate, kidney, testis, and the spermatic cord). We end this chapter with a discussion of what is on the horizon in terms of in vivo imaging, device miniaturization, and the hurdles that must be overcome before MPM can be used in the operating room.

## The Surgical Context

There are many situations in routine urologic surgery practice, where access to real-time histologic information would be highly valuable for improving precision, reducing surgical time, and minimizing unnecessary resections and their associated risks of complications. This is especially true in urologic oncology, such as cystoscopic surveillance of the bladder mucosa and the ureters for urothelial carcinoma; needle core biopsies to identify prostatic, renal, and testicular carcinoma; as well as margin assessments during robotic or open surgical procedures for the resection of various urological carcinomas. In addition to oncology applications, direct visualization of healthy sperms in the seminiferous tubules might significantly shorten surgical times during microdissection testicular sperm extraction (micro-TESE) for in vitro fertilizations. Also, the ability

S. Mukherjee, PhD, MS (✉)
Department of Biochemistry, Weill Medical College of Cornell University, New York, NY, USA
e-mail: smukherj@med.cornell.edu

M. Jain, MD
Department of Pathology and Laboratory Medicine, Weill Medical College of Cornell University, New York, NY, USA

D.S. Scherr, MD
Department of Urology, Weill Medical College of Cornell University, New York, NY, USA

J.C. Liao, L.-M. Su (eds.), *Advances in Image-Guided Urologic Surgery*,
DOI 10.1007/978-1-4939-1450-0_6, 

to simultaneously visualize and ablate nerves might improve outcomes for microsurgical denervation of the spermatic cord as a treatment for chronic orchialgia.

In current clinical practice, in all these situations, a urologist is obligated to resect or biopsy tissue, which is then formalin fixed, sectioned, and stained to render a histopathologic diagnosis. For intra-surgical frozen section or cytology consults, this prolongs the surgical time spent to await tissue preparation, analysis, and interpretation by a pathologist. For small tissues (e.g., cystoscopic or needle core biopsies), the risk of tissue damage or loss is too high for intra-procedural consult. Consequently, both the urologist and the patient must wait up to a week to receive diagnosis following the preparation, analysis, and interpretation of permanent histopathology specimens.

## High-Resolution "Optical Biopsy" Techniques May Substantially Facilitate Many of These Procedures

A growing array of optical biopsy techniques are being investigated and, in certain cases, applied clinically to assess histologic characteristics of tissue in situ, before any surgical intervention. Two major techniques already in clinical use, albeit in limited types of procedures, are optical coherence tomography (OCT) and confocal laser endomicroscopy (CLE) [1]. OCT, the most mature of these technologies, is an interference-based optical imaging technique, very similar in principle to ultrasound imaging [2–5]. Current commercial OCT systems have lateral resolutions of 10–15 μm, with a depth of imaging of approximately 1 mm. Thus, while this technique is very good at rapidly generating three-dimensional image volumes reflecting different layers of tissue components (e.g., epithelial cells, connective tissue, muscle), the image resolution is similar to a 4× objective of a histology microscope. It is thus typically not sufficient for differential histopathologic diagnoses, especially in situations where the major determinant in a differential diagnosis is cytological rather than architectural (e.g., determining the degree of dysplasia or grade of carcinoma). Confocal laser endomicroscopy [6], on the other hand, has higher spatial resolution (current commercial systems have spatial resolutions of ~3.5 μm, which is comparable to a 10× objective of a histology microscope) but much lower depth of imaging (≤50 μm). The images generated from these systems are en face, and their resolution approaches those used by pathologists for diagnostic purposes. However, very few tissue components are intrinsically fluorescent in the excitation wavelengths used in these systems (elastin and lipofuscin in macrophages). Thus, visualization of any other tissue components (including all cells other than macrophages) using fluorescence requires administration of exogenous contrast agents, with accompanying concerns of patient preparation pre-procedure and possibility of allergic responses. Confocal microscopy can also be used in reflectance (non-fluorescence) mode, which removes the need for exogenous contrast agents but also significantly reduces imaging depth, making the technique essentially a surface scanning technique not unlike regular white light intra-surgical or endoscopic imaging, albeit at a much higher lateral resolution. Furthermore, none of the commercial confocal endoscopes to date generate three-dimensional image sets; thus, the diagnostic potential of images generated from these systems is very much dependent on operator skill.

## Multiphoton Microscopy (MPM): The Next Frontier for Optical Biopsy?

MPM is a next-generation nonlinear optical microscopy technique that overcomes several of the significant limitations of OCT and confocal microscopy described above. MPM relies on the simultaneous absorption of two (or three) low-energy (near-infrared) photons to cause a nonlinear excitation equivalent to that created by a single photon of bluer light (Fig. 6.1a). Excitation only occurs where there is sufficient photon density (i.e., at the point of laser focus), providing intrinsic optical sectioning with resolution equivalent to traditional confocal microscopy. Tissue penetration is greater than with standard confocal microscopy because absorption and scattering of the laser excitation are reduced at near-infrared

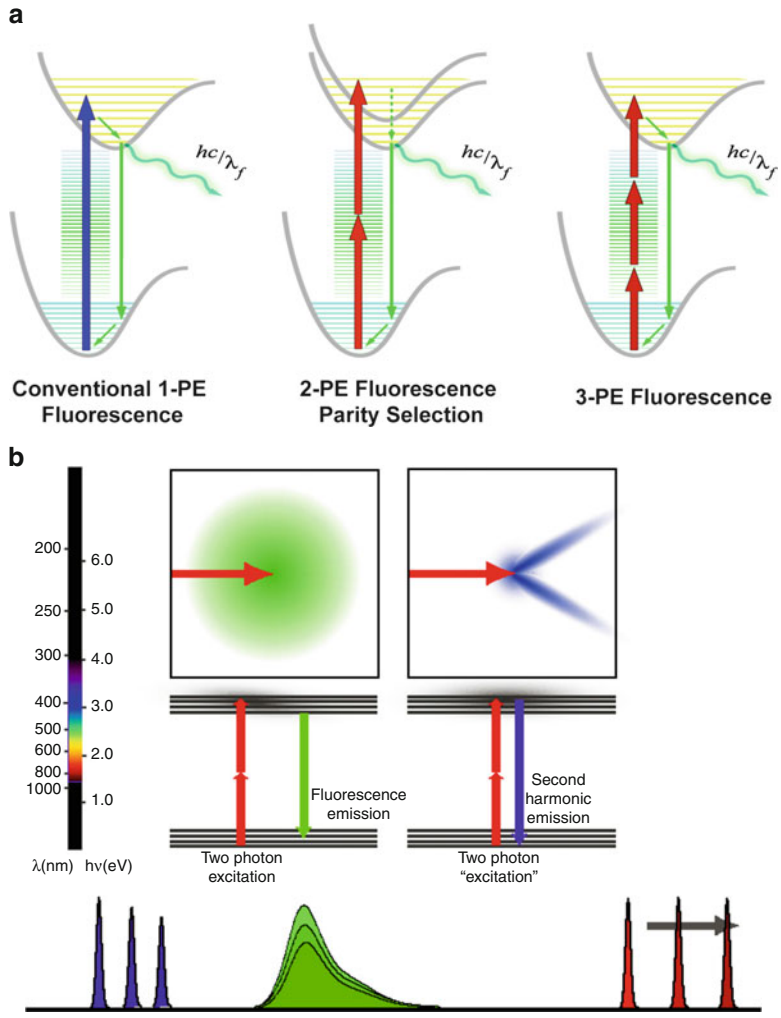


**Fig. 6.1** Basic principles of multiphoton microscopy (MPM). (**a**) The Jablonski diagram showing how MPM fluorescence emission is caused by the simultaneous absorption of two or three low-energy (near-infrared) photons, which cause a nonlinear excitation equivalent to that created by a single photon of bluer light. (**b**) Two types of signals are generated by MPM: fluorescence and second harmonic generation (SHG). While fluorescence signal is broad and isotropic, SHG signal is narrow and occurs at precisely half the exciting wavelength

wavelengths compared to the visible or ultraviolet region of the spectrum [7, 8].

Most importantly, by utilizing two-photon excitation in the 700–800 nm range, MPM enables both in vivo and ex vivo imaging of fresh, unprocessed, and unstained tissue via intrinsic tissue emissions (ITEs). The ITE signal is composed of two components: (1) tissue autofluorescence, in part from reduced nicotinamide adenine dinucleotide (NADH) and flavin adenine dinucleotide (FAD) in cells (both benign and malignant), elastin in the connective tissue, and lipofuscin in fat and other cells, and (2) second harmonic generation (SHG), a nonlinear scattering signal which arises from non-centrosymmetric structures such as tissue collagen (see Fig. 6.1b) [7–9]. It has been shown that MPM/ITE imaging is capable of generating distinctive optical signals that enable imaging of animal [8, 10–14] and human [15–22] tissues at submicron resolution in three dimensions to a depth of up to 0.5 mm below the specimen surface, at acquisition rates of ~1 image/s. These imaging parameters enable detailed visualization of cellular and subcellular structures.

## Potential Applications of MPM in Urologic Practice

Below, we have summarized some recent applications of MPM in the identification and diagnosis of several urological tissues. We present MPM

imaging results in two types of specimens. For detailed diagnostics, we present results on ex vivo human surgical samples – either taken during cystoscopic procedures or taken after partial or radical organ resections. All these specimens were imaged without further processing, i.e., there was no fixation, sectioning, or staining of the tissue. Fresh tissue was placed on a slide or a tissue culture dish, hydrated with buffered saline, and placed directly on the microscope stage under the objective of an upright microscope.

Olympus FluoView FV1000MPE imaging system (Olympus America, Center Valley, PA) in an upright configuration was used for all MPM imaging reported here. Briefly, fresh (unprocessed and unstained) specimens were excited using 780 nm light from a tunable Ti-sapphire laser (Mai Tai DeepSee, Spectra-Physics, Newport Corporation, Irvine, CA). Three distinct ITE signals were collected using photomultiplier tubes and then color coded by using MetaMorph v7.0r4 (Molecular Devices, Sunnyvale, CA) as follows: (1) SHG (360–400 nm, color-coded red), a nonlinear scattering signal originating from tissue collagen; (2) short-wavelength autofluorescence (420–490 nm, color-coded green), originating in part from reduced nicotinamide adenine dinucleotide (NADH) and flavin adenine dinucleotide (FAD) and from elastin; and (3) long-wavelength autofluorescence (550–650 nm, color-coded blue), originating in part from lipofuscin.

Images were acquired at both low (4×/0.28NA dry objective) and high magnification (25×/1.05 NA water immersion objective) in order to assess architectural and cytological details of the tissue, respectively. The 4× objective allowed imaging up to ~0.5 mm into the tissue (imaged area in a single frame: 3.2 $mm^2$). The 25× objective allowed imaging up to ~0.25 mm depth (imaged area in a single frame: 0.51 $mm^2$). Scanner zooms and automated tiling functions were used to achieve a higher magnification and larger area, respectively, if needed. Typically, the collection of each image frame shown in the figures took 1–3 s, and acquisition of an entire image stack (20–40 images) took 1–1.5 min. Minor post-processing was done using Adobe Photoshop CS4 (San Jose, CA), which primarily included adjustment of intensity and color balance and occasional removal of single-photon shot noise by Gaussian blurring. However, we would like to point out that a research pathologist who was present during the imaging session was able to make correct diagnoses in most cases by just looking at the real-time images as they were being acquired (i.e., without any post-processing). Thus, while post-processing improves the quality of the images for presentation, it is not strictly necessary for rendering real-time diagnosis.

In addition to the imaging of ex vivo tissue described above, we also report MPM imaging of urological tissues (prostate and spermatic cord) in live rats under anesthesia, to document the feasibility of its use in intra-surgical contexts.

## Applications for the Management of Bladder Diseases

Approximately 70 % of all newly diagnosed urothelial carcinoma present as early-stage superficial (i.e., non-muscle-invasive) disease [23, 24]. Of these superficial cancers, carcinoma in situ (CIS) is the most aggressive intraepithelial neoplasm. It is a high-grade lesion, which when left untreated will progress to muscle-invasive disease in 80–100 % of cases and cause of mortality in 39 % of cases [25–27]. White light cystoscopy (WLC) and urine cytology are current diagnostic tools for detection of CIS. Although urine cytology is positive in over 90 % of patients with CIS, it cannot determine the extent and location of the disease [28]. White light cystoscopy accompanied by histopathologic diagnosis of the TURBT (transurethral resection of bladder tumor) from the suspicious lesions is the standard of management for bladder cancer patients. However, approximately 50 % of CIS lesions are missed on WLC alone [28]. This is mainly due to flat architecture of these lesions and the lack of cellular resolution of WLC. Thus, patients with positive urine cytology but no obvious tumor during cystoscopic exam may be subjected to repeat cystoscopy and numerous repeat biopsies in order to rule out carcinoma. In fact, an unpublished analysis of all cystoscopic submissions to surgical pathology over a 2-month period at our institution revealed that ~70 % of the biopsies and ~32 % of the TURBT

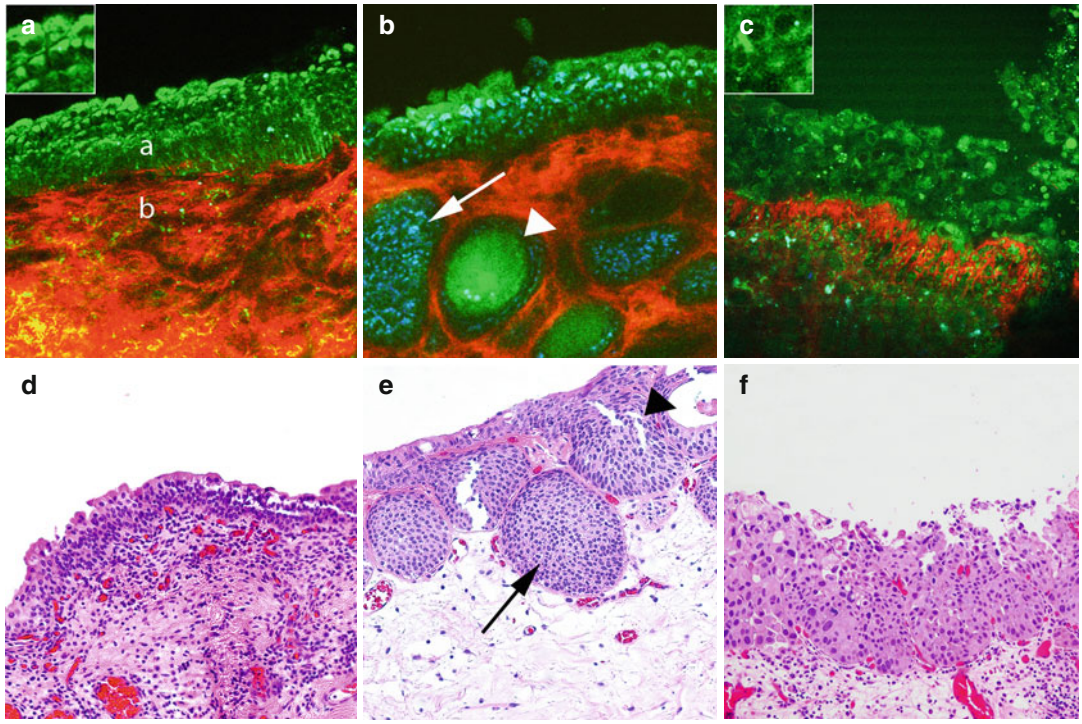


**Fig. 6.2** MPM assessment of flat lesions of the bladder. MPM image (**a**) and corresponding H&E image (**d**) show a multilayered urothelium (**a**) with superficial umbrella cells (*inset*) and lamina propria (**b**). Lamina propria is composed of collagen bundles (*red*) and elastin fibers (*green*). The MPM image (**b**) and the corresponding H&E image (**e**) of cystitis showing von Brunn's nests (*arrows*) and some with cystic dilatation (cystitis cystica; *arrowhead*). The MPM image (**c**) and corresponding H&E image (**f**) at high magnification show disorganized urothelium with cells having high-grade cytologic features of CIS (marked pleomorphism and increased nuclear-to-cytoplasmic ratio; *arrows*). Original magnifications: MPM: **a**–**c** = 300. Insets = 600×. H&E: **d**–**f** = 200×

resections were found to be benign upon histopathologic diagnosis (Robinson et al., unpublished). Additionally, although TURBT resections and bladder biopsies are standard procedures, they are not without associated complications, such as bleeding, infection, and, for a small proportion, bladder perforation. Thus, they are currently performed in a hospital setting. Also, patients require a Foley catheter for a mean period of 1.7 days post-procedure.

MPM-assisted cystoscopy, if successful, would reduce unnecessary biopsies, thus minimizing the above discomforts and complications. Moreover, a better cystoscopy procedure that does not miss any malignant lesions and especially any flat lesions of CIS [29] means a better surveillance for the patients who have a high chance of recurrence [30]. Additionally, accurate assessment of surgical margins during radical or partial cystectomies in situ would obviate the extra time and statistical uncertainties of frozen section analysis.

Here, we show that MPM is able to identify all flat lesions of the bladder mucosa, including cystitis and CIS (Fig. 6.2), low- and high-grade papillary carcinoma (Fig. 6.3), and invasive urothelial carcinoma (Fig. 6.3), as confirmed by gold standard H&E histopathology. Some of these results have been previously published [15, 19]. One of these studies [19] reported an accuracy of 88 % in diagnosing benign and malignant lesions with overall sensitivity and specificity of 90 and 77 %, respectively. A positive (neoplastic) diagnosis on MPM had a high predictive value (94 %), and negative (benign) diagnoses were sustained on histopathology in two-thirds of cases. Cytological grade, however, was accurate only in 38 of 56 (68 %) of cases in this study [19]. However, this study included both flat and papillary bladder

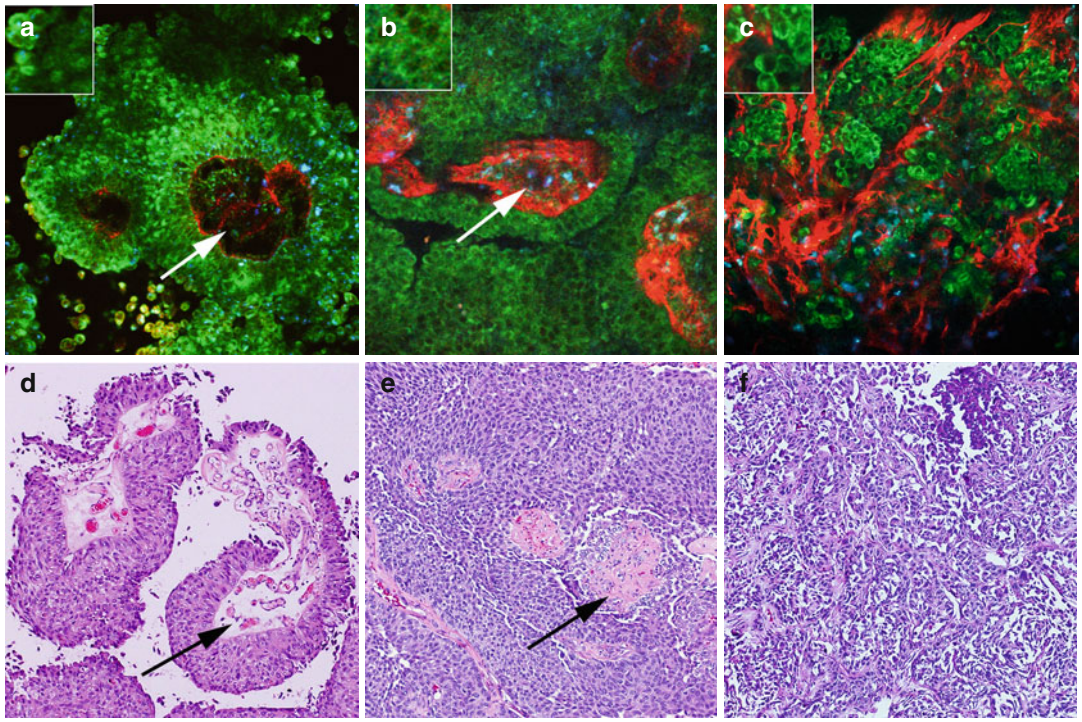


**Fig. 6.3** MPM assessment of urothelial carcinoma of bladder. MPM image (**a**) and corresponding H&E image (**d**) of low-grade papillary urothelial carcinoma show papillae with fibrovascular core (*arrows*). Papillae are lined by urothelial cells having low N:C ratio (*inset*). MPM image (**b**) and corresponding H&E image (**e**) of high-grade papillary urothelial carcinoma show papillae with fibrovascular core (*arrows*). Papillae are lined by urothelial cells having high N:C ratio (*inset*). MPM image (**c**) and corresponding H&E image (**f**) of invasive urothelial carcinoma with tumor cells (color coded; *green*) invading stroma of lamina propria (color coded; *red*). Original magnifications: MPM: **a**–**c** = 300. *Insets* = 600×. H&E: **d**–**f** = 200×

lesions, and the sample size of CIS lesions was small. In a recent follow-up study assessing flat lesions alone, we were able to obtain sensitivity and specificity of MPM diagnosis of 98 % and 94 %, respectively. A positive (neoplastic) diagnosis on MPM had a high predictive value (96 %), and negative (benign) diagnoses had a predictive value of 97 % (Jain et al., unpublished).

## Applications for the Management of Prostate Cancer

Prostate cancer is the most common male cancer. When confined to the gland, it can be successfully treated by radical prostatectomy. However, the success of this surgery is judged by three measures: (1) complete removal of the cancer-harboring glands, (2) preservation of nerves that control sexual function, and (3) preservation of sphincteric structures, which maintain urinary control. Anatomically, the prostate gland is surrounded by a fibrous capsule, with a thickness that varies significantly in different parts of the gland. This incomplete capsule, in turn, is surrounded by a multilayered, anatomically complex fascia that contains fat cells intermingled with loose areolar tissue, autonomic ganglia, neural plexus, nerve trunks, arteries, and veins. This fascia adheres to the capsule and is pierced by vessels and nerves. Both the erectile nerve, which has a variable branching pattern, and the sphincteric sling are intermingled with the fascial fat, connective tissue, and blood vessels.

Cancer cells sometimes migrate beyond the gland and either involve the surrounding nerves or grow into the sphincter – a phenomenon termed extra-prostatic extension (EPE). Since these nerves and any clusters of cancer cells are too small to be visualized by eye or using the 10–12× magnification of the stereoscope of a surgical robot, the competing goals of cancer extirpation versus preservation of potency and continence have to be balanced during surgery [31]. Surgeons make judgments based on information that includes presurgical PSA levels, MRI results, digital rectal examination results, and intra-surgical subjective cues such as color changes, fibrosis, and the ease of separating the different fascial layers. One option for more detailed feedback, intraoperative frozen sections, takes time, may damage the delicate structures one is trying to save, and suffers from sampling errors. As a result, the current methods for discriminating between EPE and the tissues that need to be preserved during surgery are imprecise and impact the outcomes of this surgery.

Indeed, this inability to identify cancerous cells and their association with nerves can result in incomplete removal of cancer, resulting in positive surgical margins (10–40 % occurrence) [32– 35], postoperative impotence due to the damage to or excision of these nerves (25–70 %) [36–40], or both positive margins and an impotent patient. It has been estimated that half the patients who undergo radical prostatectomy require postoperative treatment for erectile dysfunction. In addition to causing psychological and quality-of-life compromises, these complications exact a staggering financial cost on the US healthcare system. In addition, certain patients are excluded as candidates for nerve-sparing surgery based on the less-than-optimal preoperative assessments and thus may be denied a chance for a better postoperative quality of life.

In summary, access to high-resolution, high-contrast live imaging of the prostatic capsule, apex, sphincter, and the surrounding nerves and tissues would improve surgical decision-making and patient outcomes and reduce the emotional and financial impact of postsurgical complications.

Here, we show that MPM is able to correctly identify all surgically relevant components of the periprostatic tissue (Fig. 6.4) and the prostate gland (Fig. 6.5), including the ability to distinguish between benign and malignant glands (Fig. 6.5). Some of these results have been previously published [17, 41]. Additionally, in a recent study, we utilized MPM imaging in live anesthetized Sprague-Dawley rats with minilaparotomies to expose one lobe of the prostate (Durand et al., unpublished). Images of periprostatic nerve, connective tissue, prostatic glands, seminal vesicle, and vas deference were comparable to their corresponding histology. Motion artifacts could be sufficiently controlled to obtain high-resolution MPM images. At the end of the imaging session, the animals were closed and recovered from anesthesia. They were followed for 15 days after which they were re-laparotimized and reimaged. Neither the second look MPM imaging nor subsequent histopathology of the imaged tissue showed any identifiable damage (Durand et al., unpublished).

## Applications for the Management of Kidney Cancers

Over the past two decades or so, there has been an exponential increase in incidentally detected small and localized renal masses due to a substantial increase in noninvasive imaging for a variety of indications [42, 43]. Unfortunately, these noninvasive imaging techniques, such as CT or MRI, are not efficient at distinguishing benign from indolent from aggressively malignant renal carcinomas. Consequently, there is significant overtreatment of renal carcinoma, with imaging-detected masses often turning out to be benign or indolent after radical or partial nephrectomy [42]. Such overtreatment not only has deleterious effects on long-term renal function [44] but has also been shown to have negative effects on cardiovascular disease [45].

There is thus a real need to diagnose renal tumors more accurately before a surgical intervention. However, traditional excisional renal biopsies under ultrasound guidance are less than optimal at the current time. In a recent single-center retrospective study of pediatric

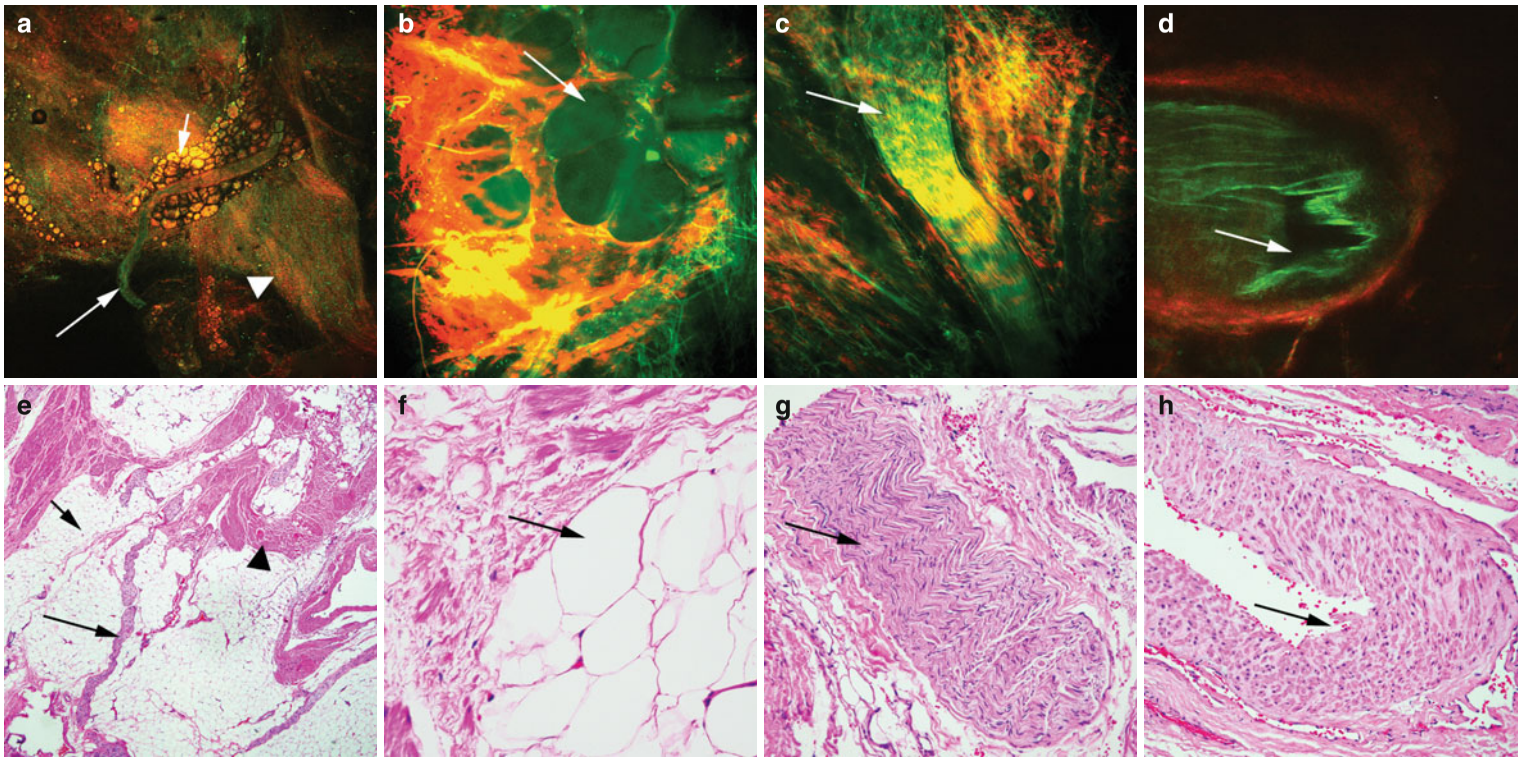


**Fig. 6.4** MPM assessment of periprostatic tissue. MPM and corresponding H&E images of periprostatic tissue showing (**a**–**e**) a nerve (*arrows*) embedded in adipocytes (*small arrows*) and connective tissue (*arrowheads*) at low magnification. (**b**–**f**) Adipocytes (*arrows*). (**c**–**g**) A nerve bundle with fluorescence that derives from the axoplasm or the cytoplasm of the Schwann cells and (**d**–**h**) a medium-sized blood vessel with lumen (*arrows*) at high magnification. Original magnifications: MPM: **a** = 48×, **b**–**d** = 300×. H&E: **e** = 40×, **f**–**h** = 200×

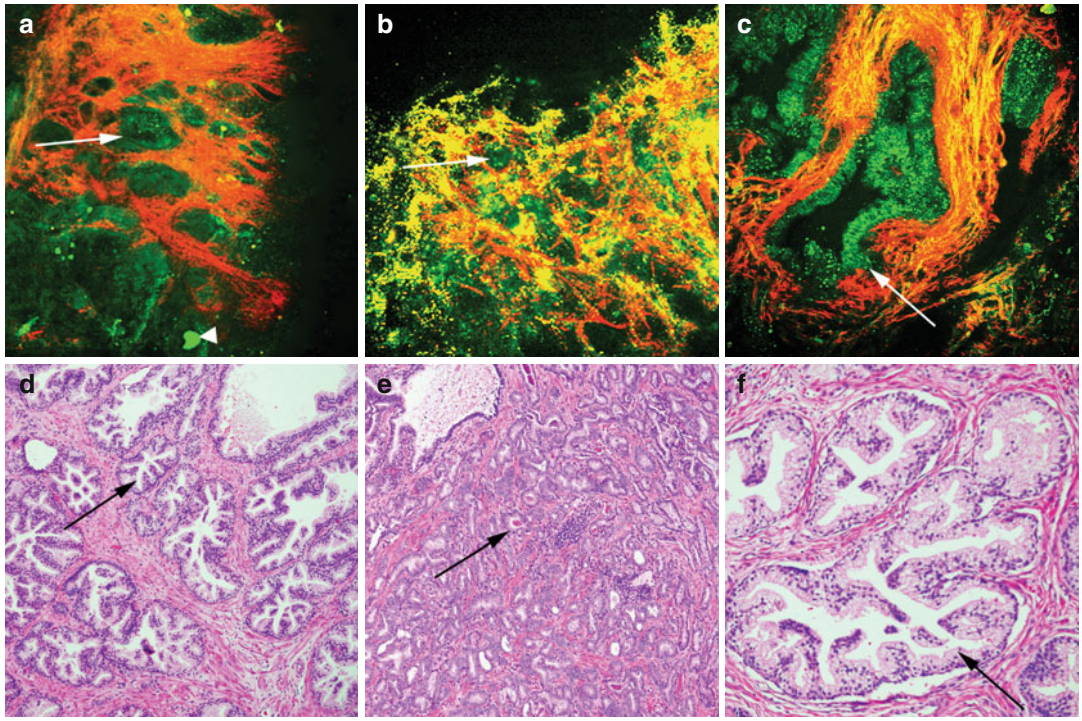


**Fig. 6.5** MPM assessment of the prostate gland. MPM and corresponding H&E images of prostate gland showing (**a**–**d**) benign glands (*arrows*) with surrounding connective tissue (collagen; color-coded *red*). Concretion is shown with an *arrowhead* in one of the begin glands. (**b**–**e**) Adenocarcinoma of prostate with clusters of small tightly packed glands (*arrows*) and (**c**–**f**) benign glands at high magnification with infolded luminal epithelium. Original magnifications: MPM: **a** = 48×, **b** = 120×, **c** = 300×. H&E: **d** = 40×, **e** = 100×, **f** = 200×

renal patients, it was found that ~12 % of the biopsies did not shed light on the diagnosis and were unhelpful in patient management, another ~11 % were nondiagnostic, and an additional 1.5 % failed to yield enough tissue for examination [46]. Thus, MPM-assisted optical biopsy may serve to overcome some of the current bottlenecks in renal carcinoma management. Furthermore, during open or robotic nephrectomies, MPM could help accurately assess surgical margins in situ and thus prevent any unnecessary loss of renal tissue that may negatively impact patient prognosis.

Here, we show evidence that MPM can accurately identify all important histological components of normal kidney (Fig. 6.6), as well as correctly diagnose non-papillary (Fig. 6.7) and papillary (Fig. 6.8) kidney tumors of various histological subtypes.

## Applications in Testes

Sperm retrieval from testicular sperm extraction (TESE) coupled with intracytoplasmic sperm injection into isolated oocytes in vitro has made it possible for men with severely impaired sperm production, including those with nonobstructive azoospermia (NOA), to father their own children [47]. NOA is the lack of sperm in ejaculate, affecting 1 % of all men and 10–15 % of all men with infertility [48]. Microdissection testicular sperm extraction (micro-TESE) uses an operating light microscope to direct testis biopsies [49] and has become the first-line procedure for sperm retrieval in men with NOA. Micro-TESE can be a technically demanding procedure requiring a significant learning curve and long operative times [47]. A significant limitation of micro-TESE has been the inability to identify seminiferous tubules

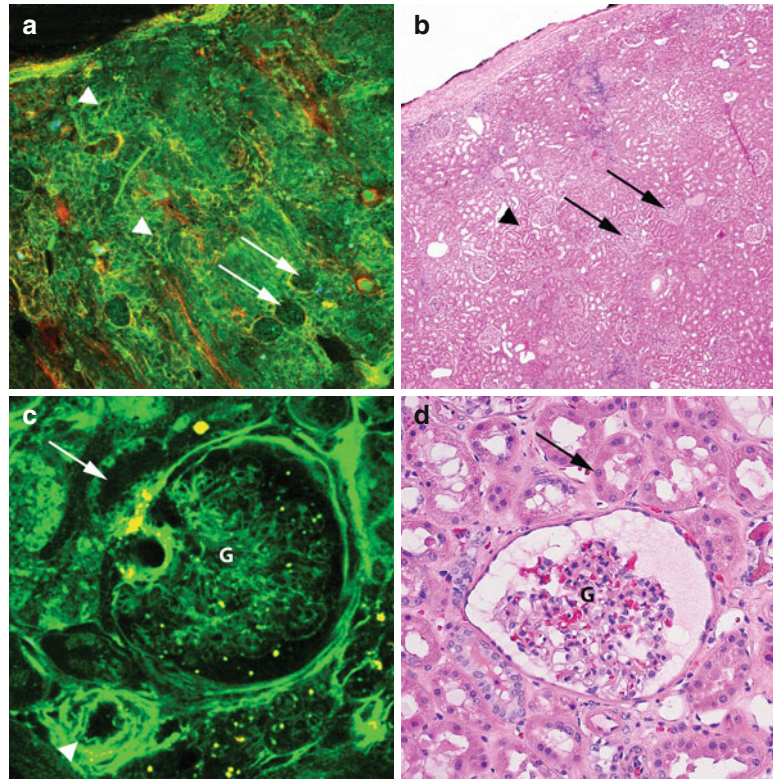


**Fig. 6.6** MPM assessment of normal histology of kidney. MPM image (**a**) and corresponding H&E image (**b**) show a low-magnification image of normal kidney with glomeruli (*arrows*) and surrounding tubules (*arrowheads*). The MPM image (**c**) and the corresponding H&E image (**d**) show a glomerulus (**g**), tubule (*arrow*), and an arteriole (*arrowhead*) at high magnification. Original magnifications: MPM: **a** = 48×, **c** = 300×. H&E: **b** = 40×, **d** = 200×

that contain spermatozoa. Sperm-containing tubules are evaluated using a subjective assessment of tubular size and color. With this technique, sperm have been retrieved in 40–60 % of men depending on the underlying cause of low sperm production [50, 51].

Infertile men show significantly lower serum testosterone levels at baseline due to impaired Leydig cell function [52]. With removal of testicular tissue in biopsy, there inevitably is loss of Leydig cells, which can further reduce serum testosterone levels resulting in serious long-term consequences such as osteoporosis, increased insulin resistance, and depression [53]. Some of these biopsies can unfortunately result in a permanent decrease in serum testosterone levels [54, 55], requiring long-term testosterone replacement therapy. With such potential risks, optimizing the ability to identify sperm during testis biopsy and thus removing less testicular tissue (preferably only sperm-containing tubules) could increase the benefit/risk ratio for men attempting fatherhood by this method.

Multiphoton microscopy (MPM) provides an opportunity for real-time visualization of seminiferous tubules at high resolution in living tissue. Utilizing MPM to directly visualize tubules has the potential to improve success in micro-TESE procedures. Additionally, MPM-guided testis biopsy can prevent loss of Leydig cells in interstitial testicular tissue, thereby decreasing the risk of iatrogenic male hypogonadism.

Here, we show that MPM is able to correctly assess the status of spermatogenesis in human testicular seminiferous tubules (Fig. 6.9). Our previous published study reported an overall concordance rate of 86 % between MPM imaging and H&E-stained slides prepared from the same specimens [22].

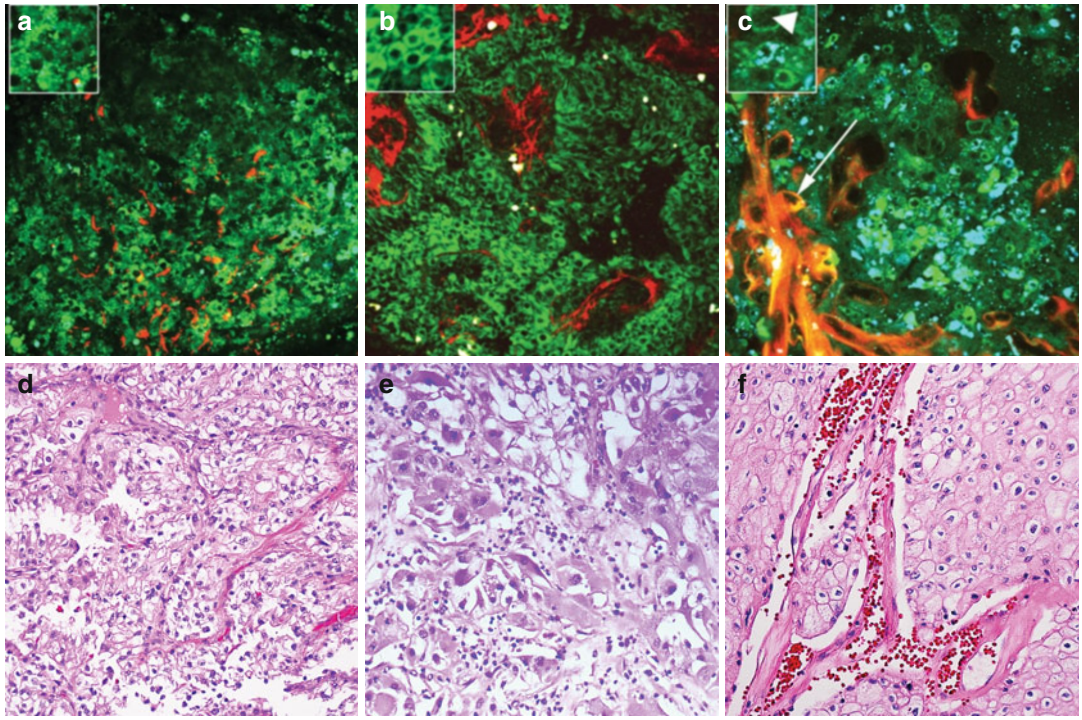


**Fig. 6.7** MPM assessment of non-papillary kidney tumors. MPM image (**a**) and corresponding H&E image (**d**) of low-grade clear cell renal cell carcinoma, showing sheets of cells with intervening collagen fibers (*red*). *Inset* shows tumor cells with lipidic droplets in the cytoplasm and low N:C ratio. MPM image (**b**) and corresponding H&E image (**e**) of high-grade clear cell renal cell carcinoma showing tumor cells and stroma (*red*). *Inset* shows cells with homogeneous cytoplasm lacking lipid droplets and high N:C ratio. MPM image (**c**) and corresponding H&E image (**f**) of chromophobe renal cell carcinoma, showing sheets of tumor cells (*green*) and thickened blood vessels (*arrow*). *Inset* shows prominent intracytoplasmic granules (*blue*, hypothesized to correspond to cytoplasmic vesicles) and a cell with irregular enlarged nuclei (*arrowhead*). Original magnifications: MPM: **a**–**c** = 300×. H&E: **d**–**f** = 200×

## Applications in Spermatic Cord Denervation

Chronic orchialgia, defined as intermittent or constant, unilateral or bilateral testicular pain lasting for more than 3 months, significantly interferes with daily activities and is often a challenging management dilemma for urologists [56]. Microsurgical denervation of spermatic cord is currently the most effective surgical treatment for chronic orchialgia (testicular pain) [57]. However, this procedure is effective only in 70 % of men [58]. Additionally, it is associated with risks due to extensive dissection of the spermatic cord that is necessary to ligate the nerves. There is a possibility of serious complications (~1 %) due to accidental injury to testicular artery [58] and lymphatics leading to testicular atrophy and hydrocele, respectively. The problem is that with the current technology, the nerves cannot be visualized due to their small diameters. Therefore, a noninvasive real-time imaging modality that can specifically identify and selectively ablate the nerves, while preserving all vasculature and lymphatics, will be highly desirable to improve outcomes and reduce operative time and complications.

We have reported successful identification and denervation of spermatic cords in vivo in the Sprague-Dawley rat model [12, 14]. There was a

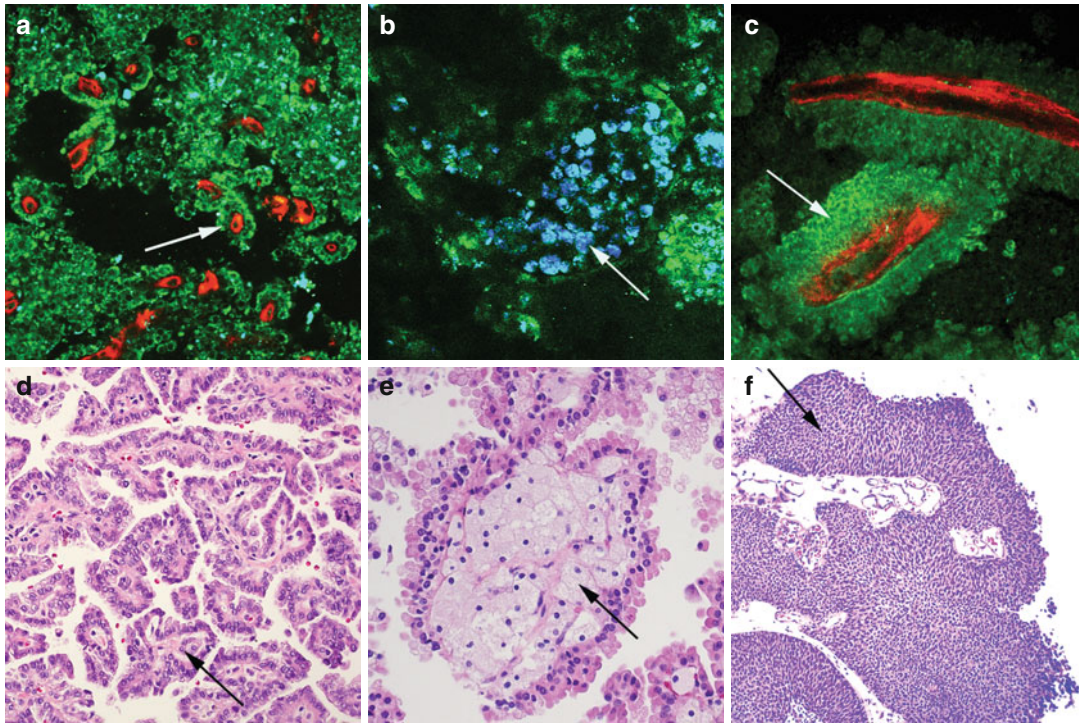


**Fig. 6.8** MPM assessment of papillary kidney tumors. MPM image (**a**) and corresponding H&E image (**d**) of papillary renal cell carcinoma showing small papillae (*arrow*) with fibrovascular core (*red*). Papillae are lined by cuboidal cells. MPM image (**b**) and corresponding H&E image (**e**) of papillary renal cell carcinoma showing a papilla filled with histiocytes (*blue*; *arrows*). MPM image (**c**) and corresponding H&E image (**f**) of urothelial carcinoma showing broad papillae (*arrow*) with fibrovascular core. Papillae are lined by multilayered urothelium. Original magnifications: MPM: **a**–**c** = 300×. H&E: **d**–**f** = 200×

significant decrease in median number of nerves remaining around the vas deferens with microsurgical denervation alone (3.5 nerves) or microsurgical denervation with MPM (1.5 nerves) compared to sham (15.5 nerves), $p = 0.003$ [12]. No deleterious effects on spermatogenesis or vas patency were observed in the MPM-imaged group when compared to sham rats, after a post-imaging follow-up period of 2 months [12].

## Future Directions

In the discussion above, we have provided several examples in ex vivo human urological tissue and in vivo rat models that strongly support the potential real-time clinical applications for MPM technology as an intra-surgical visualization and diagnostic tool.

Several groups are currently developing endoscopic and laparoscopic MPM devices [59–63]. One class of these devices is small and rigid [made using gradient index (GRIN) lenses] and has proven to be relatively robust when used for imaging several types of tissues in live, anesthetized rodents [59]. The GRIN lenses are commercially available with a variety of diameters (0.5–2 mm) and lengths (24–183 mm), and longer and thinner lenses can be custom manufactured. These devices can potentially be used during robotic or open urologic surgeries, e.g., to assess surgical margins in situ, as well as for needle core biopsies of organs such as the prostate and kidney.

Several flexible endoscope prototypes have also been developed and tested in live, anesthetized rodents [20, 60]. Several further improvements have been made on this basic design,

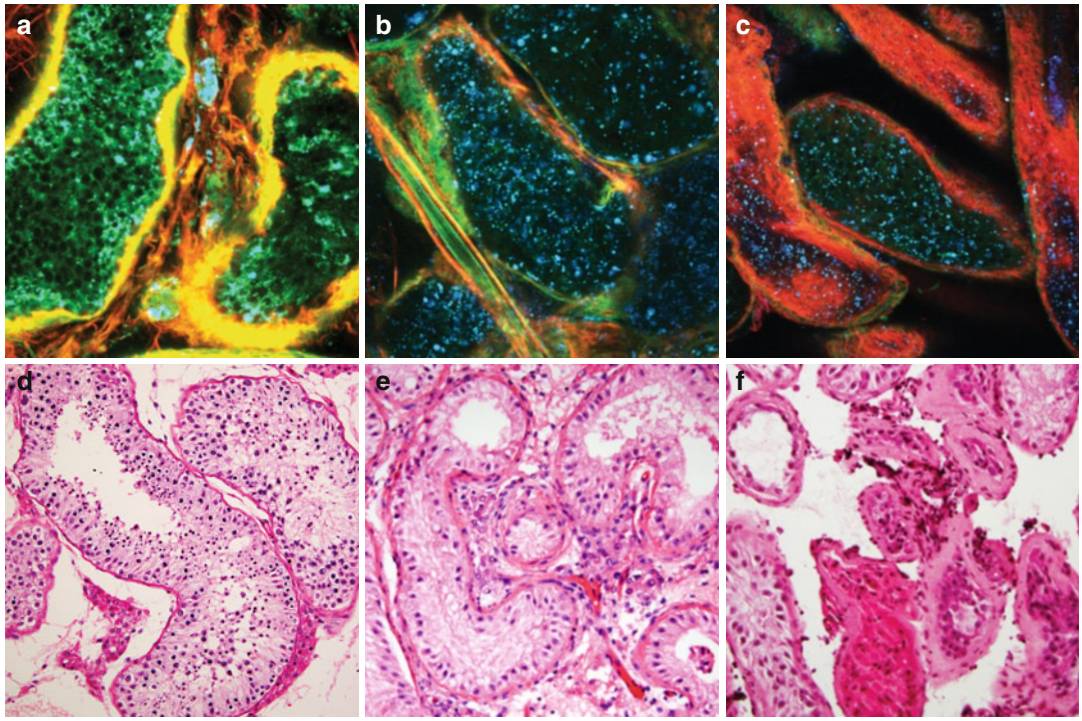


**Fig. 6.9** MPM assessment of spermatogenesis status in seminiferous tubules of the testes. MPM and corresponding H&E images of seminiferous tubules. (**a**, **b**) Normal spermatogenesis: spermatogenic cells autofluorescence in shorter wavelength channel (420–490 nm; color-coded *green*). (**c**, **d**) Sertoli cell-only pathology: Sertoli cells autofluorescence is in the longer wavelength range (550–650 nm; color-coded *blue*). And (**e**, **f**) Sertoli cell-only pathology with peritubular fibrosis: fibrosis characterized by SHG (360–400 nm; color-coded *red*). Total magnification **a**, **c**, **e** = 300× and **b**, **d**, **f** = 200×

including larger field of view while maintaining high spatial resolution [63] and the use of multifocal lens design to obtain images simultaneously from three (or more) depths in the tissue [62]. Various designs with dual-zoom capabilities are also being investigated [61]. It is foreseeable that such a flexible MPM device can be integrated into a cystoscope and be used to differentiate between inflammatory and neoplastic lesions, thus guiding the urologist about which lesions to biopsy and/or resect.

At this time, it is difficult to predict the relative roles of the clinicians (surgeons and endoscopists) versus pathologists in the use of miniaturized devices meant for use in the operating or endoscopy rooms. Currently, most OCT probes and confocal microendoscopes are used by clinicians trained in their use and interpreted for the most part in the procedure room with the help of reference images (sometimes assisted by trained technicians from the device companies). The role of pathologists in these interventional contexts appears to be limited in the institutions that we are aware of. However, even if interventional MPM images are mostly interpreted by a clinician, expert pathology consult can be easily sought at any time since the images are digital and can be streamed in real time to a consulting pathologist with training and experience in interpreting these types of images.

In summary, in this chapter, we present evidence supporting the potential of MPM to serve as a valuable tool in the diagnosis of neoplastic and other clinically important benign lesions in a variety of urological organ systems. It is likely that using this technology will eventually save time and reduce both patient morbidity and cost.

## References


1. Hsu M, Gupta M, Su LM, et al. Intraoperative optical imaging and tissue interrogation during urologic surgery. Curr Opin Urol. 2014;24:66.
2. Ikeda M, Matsumoto K, Choi D, et al. The impact of real-time 3D imaging by ultra-high speed optical coherence tomography in urothelial carcinoma. BMC Urol. 2013;13:65.
3. Skolarikos A. Differentiation between normal renal tissue and renal tumours using functional optical coherence tomography: a phase I in vivo human study. BJU Int. 2012;110:E421.
4. Wessels R, De Bruin DM, Faber DJ, et al. Optical biopsy of epithelial cancers by optical coherence tomography (OCT). Lasers Med Sci. 2014;29(3): 1297–305.
5. Linehan JA, Bracamonte ER, Hariri LP, et al. Feasibility of optical coherence tomography imaging to characterize renal neoplasms: limitations in resolution and depth of penetration. BJU Int. 2011;108:1820.
6. Chang TC, Liu JJ, Hsiao ST, et al. Interobserver agreement of confocal laser endomicroscopy for bladder cancer. J Endourol. 2013;27:598.
7. Denk W, Strickler J, Webb W. Two-photon laser scanning fluorescence microscopy. Science. 1990;248:73.
8. Zipfel W, Williams R, Christie R, et al. Live tissue intrinsic emission microscopy using multiphoton-excited native fluorescence and second harmonic generation. Proc Natl Acad Sci U S A. 2003;100:7075.
9. Zipfel W, Williams R, Webb W. Nonlinear magic: multiphoton microscopy in the biosciences. Nat Biotechnol. 2003;21:1369.
10. Pavlova I, Hume KR, Yazinski SA, et al. Multiphoton microscopy as a diagnostic imaging modality for lung cancer. Proc Soc Photo Opt Instrumen Eng. 2010;24:756918.
11. Pavlova I, Hume KR, Yazinski SA, et al. Multiphoton microscopy and microspectroscopy for diagnostics of inflammatory and neoplastic lung. J Biomed Opt. 2012;17:036014.
12. Laudano MA, Osterberg EC, Sheth S, et al. Microsurgical denervation of rat spermatic cord: safety and efficacy data. BJU Int. 2014;113(5): 795–800.
13. Ramasamy R, Sterling J, Fisher ES, et al. Identification of spermatogenesis with multiphoton microscopy: an evaluation in a rodent model. J Urol. 2011;186:2487.
14. Ramasamy R, Sterling J, Li PS, et al. Multiphoton imaging and laser ablation of rodent spermatic cord nerves: potential treatment for patients with chronic orchialgia. J Urol. 2012;187:733.
15. Mukherjee S, Wysock J, Ng C, et al. Human bladder cancer diagnosis using multiphoton microscopy. Proc Soc Photo Opt Instrumen Eng. 2009;7161:nihpa96839.
16. Rogart J, Nagata J, Loeser C, et al. Multiphoton imaging can be used for microscopic examination of intact human gastrointestinal mucosa ex vivo. Clin Gastroenterol Hepatol. 2008;6:95.
17. Yadav R, Mukherjee S, Hermen M, et al. Multiphoton microscopy of prostate and periprostatic neural tissue: a promising imaging technique for improving nerve-sparing prostatectomy. J Endourol. 2009;23:861.
18. Aggarwal A, Jain M, Frykman PK, et al. Multiphoton microscopy to identify and characterize the transition zone in a mouse model of Hirschsprung's disease. In: American Academy of Pediatrics National Conference and Exhibition, New Orleans; 2012.
19. Jain M, Robinson BD, Scherr DS, et al. Multiphoton microscopy in the evaluation of human bladder biopsies. Arch Pathol Lab Med. 2012;136:517.
20. Makino T, Jain M, Montrose DC, et al. Multiphoton tomographic imaging: a potential optical biopsy tool for detecting gastrointestinal inflammation and neoplasia. Cancer Prev Res (Phila). 2012;5:1280.
21. Jain M, Narula N, Aggarwal A, et al. Multiphoton microscopy: a potential "optical biopsy" tool for real-time evaluation of lung tumors without the need for exogenous contrast agents. Arch Pathol Lab Med. 2014; 138(8):1037–47. doi: 10.5858/arpa.2013-0122-OA.
22. Najari BB, Ramasamy R, Sterling J, et al. Pilot study of the correlation of multiphoton tomography of ex vivo human testis with histology. J Urol. 2012;188:538.
23. Jones S, Campbell S. Non–muscle-invasive bladder cancer (Ta, T1, and CIS). 9th ed. PA: Saunders Elsevier; 2007.
24. Messing E. Urothelial tumors of the bladder. In: Wein AJ, editor. Wein: Campbell-Walsh urology, vol. 3. 9th ed. PA: Saunders Elsevier; 2007.
25. Utz DC, Hanash KA, Farrow GM. The plight of the patient with carcinoma in situ of the bladder. J Urol. 1970;103:160.
26. Wolf H, Melsen F, Pedersen SE, et al. Natural history of carcinoma in situ of the urinary bladder. Scand J Urol Nephrol Suppl. 1994;157:147.
27. Cheng L, Cheville JC, Neumann RM, et al. Survival of patients with carcinoma in situ of the urinary bladder. Cancer. 1999;85:2469.
28. Lerner SP, Liu H, Wu MF, et al. Fluorescence and white light cystoscopy for detection of carcinoma in situ of the urinary bladder. Urol Oncol. 2012;30(3):285–9.
29. Sylvester RJ, van der Meijden AP, Oosterlinck W, et al. Predicting recurrence and progression in individual patients with stage Ta T1 bladder cancer using EORTC risk tables: a combined analysis of 2596 patients from seven EORTC trials. Eur Urol. 2006;49:466.
30. Lee CSD, Yoon CY, Witjes JA. The past, present and future of cystoscopy: the fusion of cystoscopy and novel imaging technology. BJU Int. 2008;102:1228.
31. Tewari A, Rao S, Martinez-Salamanca JI, et al. Cancer control and the preservation of neurovascular tissue: how to meet competing goals during robotic radical prostatectomy. BJU Int. 2008;101:1013.
32. Smith RC, Partin AW, Epstein JI, et al. Extended followup of the influence of wide excision of the neurovascular bundle(s) on prognosis in men with clinically localized prostate cancer and extensive capsular perforation. J Urol. 1996;156:454.

33. Wieder JA, Soloway MS. Incidence, etiology, location, prevention and treatment of positive surgical margins after radical prostatectomy for prostate cancer. J Urol. 1998;160:299.
34. Watson RB, Civantos F, Soloway MS. Positive surgical margins with radical prostatectomy: detailed pathological analysis and prognosis. Urology. 1996;48:80.
35. Sofer M, Hamilton-Nelson KL, Schlesselman JJ, et al. Risk of positive margins and biochemical recurrence in relation to nerve-sparing radical prostatectomy. J Clin Oncol. 2002;20:1853.
36. Bentas W, Wolfram M, Jones J, et al. Robotic technology and the translation of open radical prostatectomy to laparoscopy: the early Frankfurt experience with robotic radical prostatectomy and one year follow-up. Eur Urol. 2003;44:175.
37. Ahlering TE, Skarecky D, Lee D, et al. Successful transfer of open surgical skills to a laparoscopic environment using a robotic interface: initial experience with laparoscopic radical prostatectomy. J Urol. 2003;170:1738.
38. Eden CG, Cahill D, Vass JA, et al. Laparoscopic radical prostatectomy: the initial UK series. BJU Int. 2002;90:876.
39. Rassweiler J, Marrero R, Hammady A, et al. Transperitoneal laparoscopic radical prostatectomy: ascending technique. J Endourol. 2004;18:593.
40. Saranchuk JW, Kattan MW, Elkin E, et al. Achieving optimal outcomes after radical prostatectomy. J Clin Oncol. 2005;23:4146.
41. Tewari AK, Shevchuk MM, Sterling J, et al. Multiphoton microscopy for structure identification in human prostate and periprostatic tissue: implications in prostate cancer surgery. BJU Int. 2011;108:1421.
42. Corcoran AT, Russo P, Lowrance WT, et al. A review of contemporary data on surgically resected renal masses–benign or malignant? Urology. 2013;81:707.
43. Hollingsworth JM, Miller DC, Daignault S, et al. Rising incidence of small renal masses: a need to reassess treatment effect. J Natl Cancer Inst. 2006;98:1331.
44. McKiernan J, Simmons R, Katz J, et al. Natural history of chronic renal insufficiency after partial and radical nephrectomy. Urology. 2002;59:816.
45. Miller DC, Schonlau M, Litwin MS, et al. Renal and cardiovascular morbidity after partial or radical nephrectomy. Cancer. 2008;112:511.
46. Scheckner B, Peyser A, Rube J, et al. Diagnostic yield of renal biopsies: a retrospective single center review. BMC Nephrol. 2009;10:11.
47. Tsujimura A, Matsumiya K, Miyagawa Y, et al. Conventional multiple or microdissection testicular sperm extraction: a comparative study. Hum Reprod. 2002;17:2924.
48. Thonneau P, Marchand S, Tallec A, et al. Incidence and main causes of infertility in a resident population (1,850,000) of three French regions (1988–1989). Hum Reprod. 1991;6:811.
49. Schlegel PN. Testicular sperm extraction: microdissection improves sperm yield with minimal tissue excision. Hum Reprod. 1999;14:131.
50. Ramasamy R, Yagan N, Schlegel PN. Structural and functional changes to the testis after conventional versus microdissection testicular sperm extraction. Urology. 2005;65:1190.
51. Okada H, Dobashi M, Yamazaki T, et al. Conventional versus microdissection testicular sperm extraction for nonobstructive azoospermia. J Urol. 2002;168:1063.
52. Johansson JE, Andren O, Andersson SO, et al. Natural history of early, localized prostate cancer. JAMA. 2004;291:2713.
53. MacIndoe JH. The challenges of testosterone deficiency. Uncovering the problem, evaluating the role of therapy. Postgrad Med. 2003;114(51).
54. Ishikawa T, Yamaguchi K, Chiba K, et al. Serum hormones in patients with nonobstructive azoospermia after microdissection testicular sperm extraction. J Urol. 2009;182:1495.
55. Takada S, Tsujimura A, Ueda T, et al. Androgen decline in patients with nonobstructive azoospermia after microdissection testicular sperm extraction. Urology. 2008;72:114.
56. Davis BE, Noble MJ, Weigel JW, et al. Analysis and management of chronic testicular pain. J Urol. 1990; 143:936.
57. Levine LA, Matkov TG. Microsurgical denervation of the spermatic cord as primary surgical treatment of chronic orchialgia. J Urol. 2001;165:1927.
58. Strom KH, Levine LA. Microsurgical denervation of the spermatic cord for chronic orchialgia: long-term results from a single center. J Urol. 2008;180:949.
59. Huland DM, Brown CM, Howard SS, et al. In vivo imaging of unstained tissues using long gradient index lens multiphoton endoscopic systems. Biomed Opt Express. 2012;3:1077.
60. Brown CM, Rivera DR, Ouzounov DG, et al. In vivo multiphoton endoscopy. J Biomed Opt. 2012;17:040505.
61. Ouzounov DG, Rivera DR, Brown CM, et al. Dual modality microendoscope with optical zoom capability. In: Presented at the Conference on Lasers and Electro-Optics (CLEO) 2012, postdeadline paper ATh5A.2, San Jose; 2012.
62. Rivera DR, Brown CM, Ouzounov DR, et al. Multifocal multiphoton endoscope. Opt Lett. 2012;37:1349.
63. Rivera DR, Brown CM, Ouzounov DG, et al. Use of a lensed fiber for a large-field-of-view, high-resolution, fiber-scanning microendoscope. Opt Lett. 2012;37:881.

# 7 Hyperspectral Imaging of Renal Oxygenation (Near-Infrared Tissue Oximetry for Renal Ischemia)

Janet Laura Colli and Benjamin R. Lee

## Renal Ischemia

It is recognized that after recovery from acute renal injury, the postischemic kidney is not fully restored to its preinjury state and some exhibit progressive deterioration in renal function [1]. Researchers have attempted to elucidate the mechanisms by which renal ischemia and reperfusion injury lead to the development of chronic kidney disease [2, 3]. Histologically, kidney ischemia/reperfusion injury is characterized by tubular damage [4]. Furthermore, when animal kidneys are microscopically examined in the postischemic recovery period, they demonstrate diminished renal microvasculature, interstitial fibrosis, tubular atrophy, and persistent inflammation [5]. Microarray analyses have shed light on the role genes contribute to the long-term consequences of ischemic acute kidney injury [6].

Partial nephrectomy involves temporary occlusion of the renal artery, during tumor resection. While decreasing hemorrhage, this exposes the kidney to ischemia and reperfusion injury via free oxygen radicals. Experimental studies with human subjects demonstrated that irreversible ischemic damage to the kidney and cellular degeneration of the nephron begins after 30 min of hilar clamping [7, 8]. Warm ischemia time remains the principal factor determining renal recovery after renal clamping. In cases which warm ischemia is expected to exceed 30 min, experts recommend providing reno-protection with cold ischemia [9]. However, many times during laparoscopic and robotic-assisted partial nephrectomies, a limited period of warm ischemia is sometimes unavoidable. Researchers have evaluated a variety of therapeutic agents to prevent renal injury induced by renal ischemia and reperfusion injury [10–12].

## Hyperspectral Imaging

Hyperspectral imaging assesses tissue oxygenation by mapping real-time hemoglobin saturation levels. The ViOptix Tissue Oximeter (T. Ox™) indirectly measures tissue oxygen saturation by quantifying the oxygen content of hemoglobin in tissue. The device has a noninvasive fiber optic sensor with dual light sources which measures near-infrared light (wavelength 700–900 nm) which is emitted from biologic tissue. Detectors in the sensor head measure returned infrared light from a mixture of arterial, capillary, and venous blood (Fig. 7.1). All hemoglobin molecules in the light pathway (to a depth of 10 mm) contribute to the overall hemoglobin

J.L. Colli, MD
Department of Urology,
University of Tennessee, Memphis, TN, USA
e-mail: jcolli.tulane@gmail.com

B.R. Lee, MD (✉)
Departments of Urology and Oncology,
Tulane University School of Medicine,
New Orleans, LA, USA
e-mail: brlee@tulane.edu

J.C. Liao, L.-M. Su (eds.), *Advances in Image-Guided Urologic Surgery*,
DOI 10.1007/978-1-4939-1450-0_7, 

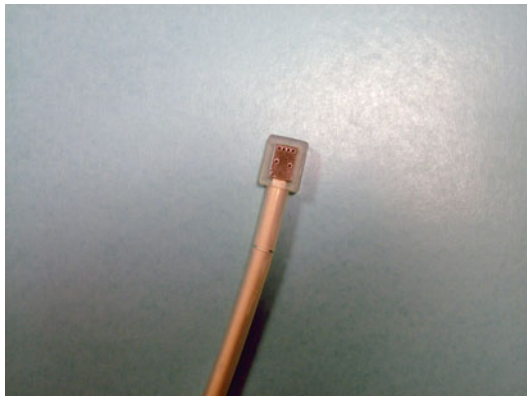

**Fig. 7.1** The ViOptix (tissue oximetry) silicone surround sensor


**Fig. 7.2** Digital display of the ViOptix sensor

oxygen reading. The returned optics and calculated absorption coefficients are recorded every 4 s, and a computer displays "real-time" measurement of the local tissue oxygen saturation (Fig. 7.2). In comparison to tissue oximetry, pulse oximetry detects reflected light from *pulsating* blood and not tissue and also requires penetration of the signal through the entire tissue with a detector array on the posterior aspect of the tissue.

The ViOptix Tissue Oximeter (T.Ox™) [(ViOptix Inc., Fremont, CA)] utilizes near-infrared spectroscopy to measure local tissue oxygen saturation ($StO_2$). Near-infrared spectroscopy has been assessed as a noninvasive technique for tissue investigation in various animal models [13–15]. Furthermore, various investigators have analyzed the clinical applications of near-infrared tissue oximetry [8, 16–20]. Keller was able to evaluate the role of $StO_2$ as an indicator of tissue hypoxia by measuring the $StO_2$ drop rate (change in $StO_2$/change time) [16]. Oximetry technology has also been utilized in breast cancer during free-flap reconstruction [15, 16] and applied in post-occlusive reactive hyperemia to evaluate extremities of patients with peripheral vascular disease [17]. It has also been employed in men with erectile dysfunction to quantify penile oxygen saturation [18]. Furthermore, tissue oximetry has been applied in measuring renal ischemia during hilar clamping in a porcine model [19].

Partial nephrectomy for renal carcinoma involves temporarily occluding the renal artery, rendering the kidney ischemic during tumor resection. Warm ischemia time is the strongest modifiable surgical risk factor for postoperative chronic kidney disease [8]. Prior studies evaluating renal parenchymal oxygen saturation levels in response to hilar occlusion during partial nephrectomy are scarce. The first study evaluating hyperspectral imaging as a noninvasive method to assess renal oxyhemoglobin saturation during renal hilar occlusion was by Holzer et al. [21]. In a porcine model, he showed that renal oxygenation decreases rapidly after clamping, and nadir oxyhemoglobin is attained within 10 min of hilar occlusion and returns to baseline 30 min after reperfusion [21].

Cadeddu et al. [22] described the initial intraoperative hyperspectral imaging experience during open partial nephrectomy in 2011 on a porcine model. This was executed by illuminating the kidney with light arrays specific for hemoglobin (520–645 nm). Reflectance images were captured at each pixel and digitally processed to determine the percent of oxyhemoglobin [22].

Hyperspectral imaging has also been used to characterize renal oxygenation during laparoscopic partial nephrectomies [23–25]. In 2011, Cadeddu and colleagues [23] used this real-time technology to monitor renal perfusion/ oxygenation during hilar occlusion and kidney recovery. They found a baseline percent hyperspectral oxyhemoglobin in the kidney to be 74.6 %. After 10 min of hilar occlusion, there was a median 20.0 % decrease

from pre-occlusion baseline, where it remained for the duration of kidney ischemia. Upon reperfusion, the percent of oxyhemoglobin returned to baseline at a median of 5 min [24].

In 2011, Olweny, et al. [25] investigated the association between tissue oxygen saturation %HbO(2) and estimated glomerular filtration rate (eGFR). They customized the hyperspectral digital light imaging (DLP(®)-HSI) for use during laparoscopic partial nephrectomy by combining a hyperspectral illumination source with a conventional laparoscopic light and merging it with a digital data device [25]. They found the median %HbO(2) dropped after hilar clamping and recovered to baseline levels shortly after unclamping. Furthermore, baseline %HbO(2) was inversely associated with preoperative eGFR ($\tau = -0.38$; $P = 0.036$) and eGFR at postoperative follow-up ($\tau = -0.38$; $P = 0.036$). Baseline and ischemic tissue oxygen saturation levels exhibited no correlation with hypertension, diabetes, and age and/or tobacco history. Overall, the laparoscopic hyperspectral imaging device successfully characterized dynamic changes in renal oxygenation during partial nephrectomy and may potentially to predict postoperative individual kidney function [25].

A study by Lee et al. [19] compared tissue oximeter to a digital imaging software which was programmed to track ischemia by detecting color change in renal parenchyma during renal hilar clamping. The digital imaging detected "red" when the computer was directed at renal tissue in which oxygen was bound to hemoglobin. And during warm ischemia, loss of bound oxygen to hemoglobin resulted in the development of a cyanotic or "blue" kidney. Tissue oximetry levels decreased during hilar clamping then returned to baseline after unclamping. Digital image software produced a histogram which demonstrated red and blue differences that correlated with non-ischemic and ischemic levels in the respective tissues. Tissue oximetry and digital image analysis were both able to calculate a drop in tissue oxygen saturation during periods of acute renal ischemia.

Using tissue oximetry, Lee et al. [26] also demonstrated clamping artery alone resulted in less ischemic damage compared to clamping artery and vein together. Yorkshire swines were subjected to hilar clamping (either artery versus artery and vein together), and near-infrared renal oximetry measurements were obtained at baseline, during warm ischemia (15- and 30-min trials), and after unclamping. Tissue oximetry analysis during renal arterial clamping alone demonstrated larger drops in tissue oxygen saturation and faster recovery of tissue ischemia compared to combined renal artery/vein clamping together, indicating reduced ischemic changes when clamping artery alone. These findings suggest that clamping artery alone may protect against renal reperfusion injury during renal hilar clamping [26].

In summary, hyperspectral imaging is a real-time noninvasive method to assess renal oxyhemoglobin saturation intraoperatively throughout the kidney. In addition, tissue oximetry has been used to evaluate kidney perfusion during ischemia caused by renal hilar clamping during partial nephrectomy. This technology may allow us to assess future surgical or pharmacological interventions ability to minimize ischemic injury during renal hilar clamping.

## References

1. Pagtalunan ME, Olson JL, Tilney NL, Meyer TW. Late consequences of acute ischemic injury to a solitary kidney. J Am Soc Nephrol. 1999;10:366–73.
2. Pagtalunan ME, Olson JL, Meyer TW. Contribution of angiotensin II to late renal injury after acute ischemia. J Am Soc Nephrol. 2000;11:1278–86.
3. Sikorski EM, Hock T, Hill-Kapturczak N, Agarwal A. The story so far: molecular regulation of the heme oxygenase-1 gene in renal injury. Am J Physiol Renal Physiol. 2004;286:F425–41.
4. Basile DP, Donohoe D, Roethe K, Osborn JL. Renal ischemic injury results in permanent damage to peritubular capillaries and influences long-term function. Am J Physiol Renal Physiol. 2001;281:F887–99.
5. Forbes JM, Hewitson TD, Becker GJ, Jones CL. Ischemic acute renal failure: long-term histology of cell and matrix changes in the rat. Kidney Int. 2000;57:2375–85.
6. Basile DP, Fredrich K, Alausa M, Vio CP, Liang M, Rieder MR, Greene AS, Cowley Jr AW. Identification of persistently altered gene expression in the kidney after functional recovery from ischemic acute renal failure. Am J Physiol Renal Physiol. 2005;288:F953–63.

7. Novick AC. Renal hypothermia: in vivo and ex vivo. Urol Clin N Am. 1983;10:637–44.
8. Thompson RH, Frank I, Lohse CM, et al. The impact of ischemia time during open nephron sparing surgery on solitary kidneys: a multi-institutional study. J Urol. 2007;177:471–6.
9. Gill IS, Abreu SC, Desai MM, et al. Laparoscopic ice slush renal hypothermia for partial nephrectomy: the initial experience. J Urol. 2003;170:52–6.
10. Sadis C, Teske G, Geurt G. Nicotine protects kidney from renal ischemia/reperfusion injury though the cholinergic ant-inflammatory pathway. PLoS ONE. 2007;2(5):e469. doi:10.1371/journal.pone.0000469.
11. Mejía-Vilet JM, Ramírez V, Cruz C, et al. Renal ischemia-reperfusion injury is prevented by the mineralocorticoid receptor blocker spironolactone. Am J Physiol Renal Physiol. 2007;293(1):F78–86. Epub 2007 Mar 20.
12. Park KM, Kim JI, Ahn Y, Bonventre AJ, Bonventre JV. Testosterone is responsible for enhanced susceptibility of males to ischemic renal injury. J Biol Chem. 2004;279(50):52282–92.
13. Cheng X, Mao JM, Bush R, et al. Breast cancer detection by mapping hemoglobin concentration and oxygen saturation. Appl Opt. 2003;42(31):6412–21.
14. Srinivasan S, Pogue BW, Carpenter C, et al. Developments in quantitative oxygen-saturation imaging of breast tissue in vivo using multispectral near-infrared tomography. Antioxid Redox Signal. 2007;9:1143.
15. Keller A. A new diagnostic algorithm for early prediction of vascular compromise in 208 microsurgical flaps using tissue oxygen saturation measurements. Ann Plast Surg. 2009;62:538.
16. Keller A. Noninvasive tissue oximetry for flap monitoring: an initial study. J Reconstr Microsurg. 2007;23:189.
17. Cheng X, Mao JM, Xu X, et al. Post-occlusive reactive hyperemia in patients with peripheral vascular disease. Clin Hemorheol Microcirc. 2004;31:11.
18. Padmanabhan P, McCullough AR. Penile oxygen saturation in the flaccid and erect penis in men with and without erectile dysfunction. J Androl. 2007;28:223.
19. Caire AA, Alvarez X, Conley S, Lee BR, et al. Near-infrared tissue oximetry and digital image analysis: quantification of renal ischaemia in real time during partial nephrectomy. BJU Int. 2012;109(2):311–5.
20. Thompson RH, Lane BR, Lohse CM, et al. Every minute counts when the renal hilum is clamped during partial nephrectomy. Eur Urol. 2010;58(3):340–5.
21. Holzer MS, Best SL, Jackson N, et al. Assessment of renal oxygenation during partial nephrectomy using hyperspectral imaging. J Urol. 2011;186(2):400–4.
22. Best SL, Thapa A, Holzer MJ, Cadeddu JA. Minimal arterial in-flow protects renal oxygenation and function during porcine partial nephrectomy: confirmation by hyperspectral imaging. Urology. 2011;78(4):961–6.
23. Best S, Thapa A, Jackson N, Cadeddu J. Renal oxygenation measurement during partial nephrectomy using hyperspectral imaging may predict acute post-operative renal function. J Endourol. 2013;27(8):1037–40. doi:10.1089/end.2012.0683.
24. Tracy CR, Terrell JD, Francis RP, Wehner EF, Cadeddu JA. Characterization of renal ischemia using DLP hyperspectral imaging: a comparison of artery-only occlusion (AO) versus artery and vein occlusion (AV). J Endourol. 2010;24:321.
25. Olweny EO, Faddegon S, Best SL. Renal oxygenation during robot-assisted laparoscopic partial nephrectomy: characterization using laparoscopic digital light processing hyperspectral imaging. J Endourol. 2013;27(3):265–9.
26. Colli JL, Wang Z, Johnsen N, Grossman L, Lee BR. Clamping renal artery alone produces less ischemic damage compared to clamping renal artery and vein together in two animal models: near-infrared tissue oximetry and quantitation of 8-isoprostane levels. Int Urol Nephrol. 2013;45:421–8.

# Light Reflectance Spectroscopy and Autofluorescence (Kidney and Prostate)

8

Ephrem O. Olweny and Jeffrey A. Cadeddu

Spectroscopy involves the study of the interaction of light and other radiation with matter, and its capabilities for diagnostic and therapeutic medical applications have been extensively investigated in recent years. As light travels through a substance, it is reflected, absorbed, transmitted, and/or scattered in a very specific pattern that is dependent on the wavelength of the incident light as well as the molecular and structural composition of the illuminated target; the study of this interaction can be exploited for the noninvasive identification and quantification of specific molecules within a sample. A plethora of spectroscopy types have been applied in medicine, including but not limited to absorption, fluorescence, visible reflectance, ultraviolet, infrared, near-infrared (NIR), Raman, and nuclear magnetic resonance.

Light reflectance spectroscopy measures the intensity of diffusely reflected light after interaction with tissue. The intensity of reflected light as a function of the wavelength defines the reflectance spectrum, which is measured for each wavelength of light produced by a broadband light source [1]. Light reflectance spectroscopy is generally applied in the study of substances located at or near the surface of samples. Light interaction with tissue also includes absorption and scatter. Tissue absorption is characterized spectroscopically by the absorption coefficient, which is directly related to the concentration of the molecule absorbing the incident light. Concentrations of molecules such as beta-carotene and hemoglobin are measurable in the visible light range, while water, adipose tissue, and collagen are measurable in the NIR range [2]. Light scattering by tissue is dependent upon the underlying cellular structure and contains information about cellular morphology as well as about processes such as cellular death and proliferation [2].

Tissue autofluorescence refers to the natural emission of fluorescent light by endogenous fluorophores when excited by light of a suitable wavelength [3]. It is an intrinsic property of cells and tissue. Within cells, endogenous fluorophores include aromatic amino acids, lipo-pigments, and flavin coenzymes that are largely contained within mitochondria and lysosomes. Within tissues, endogenous fluorophores consist primarily of collagen and elastin that compose the extracellular matrix [3]. Changes in the amount and distribution of endogenous fluorophores and/or their microenvironments due to various biological processes can be monitored by autofluorescence spectroscopy.

Light reflectance spectroscopy and fluorescence spectroscopy have been investigated for

E.O. Olweny, MD
Department of Urology, University of Texas Southwestern Medical Center, Dallas, TX, USA
e-mail: eolweny@gmail.com

J.A. Cadeddu, MD (✉)
Department of Urology, UT Southwestern Medical Center, Dallas, TX, USA
e-mail: Jeffrey.Cadeddu@utsouthwestern.edu

J.C. Liao, L.-M. Su (eds.), *Advances in Image-Guided Urologic Surgery*,
DOI 10.1007/978-1-4939-1450-0_8, © Springer Science+Business Media New York 2015

potential use in a wide variety of clinical applications, including but not limited to differentiation between benign and malignant skin lesions, early detection of premalignant lesions in the oral cavity, differentiation between benign and malignant breast lesions, differentiation between benign and malignant endobronchial lesions, early detection of cervical abnormalities, and detection of esophageal dysplasia [4–10]. In urology, these techniques have been investigated in studies involving bladder, kidney, and prostate tissue. In this chapter, we review the research to date on application of light reflectance and autofluorescence spectroscopy in the kidney and prostate.

## Light Reflectance Spectroscopy in Kidneys

### Conventional Reflectance Spectroscopy

Fitzgerald et al. reported the earliest uses of optical spectroscopy in kidney tissue diagnosis [11]. They described autofluorescence and NIR-reflectance spectra in ischemic kidneys and non-ischemic controls in a rat model of warm and cold ischemia in pre-transplanted kidneys. Several intervals of ischemia from 0 to 120 min were studied. NIR-reflectance spectroscopy was found to achieve the best differentiation between normal and ischemic kidneys when backscattered light was captured through an 800 nm filter. The intensity ratio of injured/normal was found to consistently decrease with increasing warm ischemia time, providing a possible framework for future quantification of the duration of warm ischemia time in pretransplant allografts, an important outcome that is often "guessed" by the transplant surgeon [11].

Parekh et al. reported on the first use of optical spectroscopy for differentiating malignant from benign renal tissue [12]. Similar to Fitzgerald and colleagues, they used fluorescence and NIR reflectance spectroscopy, alone and in combination. Spectra were measured ex vivo in human kidneys removed during radical nephrectomy. The authors found that the intensity of reflectance spectra for renal cell carcinoma (RCC) increased with increasing wavelength in the 600 and 800 nm (NIR) range [12]. This was true for both clear cell and papillary RCC. One patient in the series had a benign diagnosis (cystic nephroma) and was found to have an opposite spectral trend, whereby reflectance intensity decreased with increasing wavelength in the 400–850 nm range. These findings were distinct from those observed for normal kidneys, which showed no change in reflectance intensity with increasing wavelength [12]. Hemoglobin spectra were prominent between 400 and 600 nm. When combined with fluorescence spectroscopy parameters, algorithms were developed which distinguished cancerous from noncancerous kidneys with high sensitivity and specificity [12].

Similarly, Bensaleh et al. investigated the use of reflectance spectroscopy in the NIR and visible light ranges in the differentiation of tumor-bearing from normal renal tissue in patients undergoing radical or partial nephrectomy [13]. A goal of their study was to evaluate the potential usefulness of optical spectroscopy in assessment of positive margins in partial nephrectomy specimens. To minimize the influence of hemoglobin on their data, NIR spectra were analyzed between 630 and 880 nm, while visible light spectra were analyzed between 550 and 620 nm. Hemoglobin has strong absorption peaks at 400–410 nm and secondary peaks at 550–600 nm, depending on its state of reduction/oxidation. Spectra were measured at multiple locations within the tumor as well as within normal regions of the kidney including at the resection margin in partial nephrectomy specimens. Twenty-one specimens were analyzed, 15 with malignant histology (14 clear cell and 1 papillary RCC) and 6 with benign histology (oncocytoma). There was one positive margin in the series in a patient with oncocytoma. The authors found that in the NIR region (630–880 nm), slopes for the reflectance curves were significantly different between tumor-bearing and normal renal tissue ($p = 0.03$). In the visible range, there were strong correlations within individual spectral measurements obtained intratumor and those obtained within normal kidney but poor correlations between tumor and normal [13]. In the patient with a positive margin, there was a poor correlation between measurements at

the presumed positive margin site and adjacent parenchymal margin but a strong correlation between positive margin site and tumor. The authors concluded that in conjunction with NIR spectroscopy, quantifying correlations in spectra between tumor and normal kidney could be a useful technique to assess for positive margins during partial nephrectomy [13].

In a follow-up study within the same patient cohort, Bensaleh et al. used similar methodology to determine the usefulness of optical reflectance spectroscopy in differentiating between malignant and benign renal tissue [14]. Twenty-eight spectra obtained from malignant tissue were compared with 12 spectra obtained from benign tissue. The slope of the mean reflectance curve for malignant tissue significantly differed from that for benign tissue in both the visible light ($p=0.02$) and NIR ($p=0.005$) regions. Correlations within malignant tumor and within benign tumor were strong ($r>0.95$ for each) but were poor for malignant vs. benign tumor (r−0.49) [14].

Recently, Couapel et al. investigated the ability of light reflectance spectroscopy and Raman spectroscopy to differentiate benign from malignant renal tissue as well as to differentiate between histological subtypes of RCC [15]. Spectra were collected prospectively in a cohort of 60 patients who underwent radical or partial nephrectomy for suspicion of cancer. Support vector machine (SVM) analysis was used for comparison of benign vs. malignant and also for comparison among histologic subtypes. A subset analysis was performed for small renal masses (<4 cm in size). A random integer number function was used in conjunction with the SVM where a discrepancy between the sample numbers of spectra existed. Light reflectance spectroscopy was performed using similar methodology as previously reported by Bensaleh et al. [13, 14]. The SVM for light reflectance spectroscopy was found to differentiate malignant from benign renal tissue with 88 % accuracy (sensitivity 96 % and specificity 80 %). For small renal masses, accuracy improved to 95 % (sensitivity 98 % and specificity 92 %). Accuracy for distinguishing between histological subtypes was 88–90 % overall and 89–95 % for small renal masses. Accuracy for distinguishing between chromophobe RCC and benign histology was 98–100 % [15]. To date, these findings have not been investigated in vivo and technology that would enable this is pending.

## Hyperspectral Imaging

Hyperspectral imaging (HSI) is a unique imaging system developed in the early to mid-1980s that combines high-resolution remote imaging with reflectance spectroscopy, such that each image pixel carries spectroscopic information about the illuminated target [16]. It has been used in a wide variety of settings, such as in the military for identifying ground targets from airborne and satellite platforms, in identifying oil fields, in mapping of earth's minerals, and many others. Its use in the clinical setting was first described in 2001 [17], when Zuzak et al. developed the first portable HSI system. This early prototype used a liquid crystal tunable filter (LCTF) system for recording of high-resolution spectra and a large array detector for the detection and rendering of a spectrally resolved macroscopic image of the target. The authors demonstrated the usefulness of this system in monitoring skin perfusion in real time in an experimental model of vascular dysfunction [17, 18]. Digital light processing technology (DLP®; Texas Instruments, Dallas, TX), which employs a digital micro-mirror array device to produce complex spectral illumination at extremely fast switching rates, was subsequently incorporated with HSI. This greatly reduced imaging processing times from approximately 30–40 s per image with conventional LCTF systems, to 3–4 frames per second in the "3-shot" mode [19]. The current DLP®-HSI system is calibrated for measurement of hemoglobin spectra. In this setting, the DLP® chip is incorporated with a broadband white light source, and by digitally programming the micro-mirror array of the DLP® chip, an illumination spectrum spanning the reflectance range for oxy- and deoxyhemoglobin (520–645 nm) is delivered by the light source. Reflected light from the illuminated target is captured by a focal plane array detector, digitized, and transferred to a computer

for processing. A customized computer algorithm synchronizes the selective output from the light source with that from the image detector and deconvolutes the sample reflectance spectra by performing a least squared fit to determine the best linear combination of oxy- and deoxyhemoglobin at each detector pixel. The relative hemoglobin saturation at each detector pixel is calculated, and these data are color-coded using a combination of colors between blue (deoxyhemoglobin) and red (oxyhemoglobin). The color-coded image is displayed on the computer monitor as an "oxygenation map" of the kidney. Changes in relative hemoglobin saturation (%$HbO_2$) can qualitatively and quantitatively be tracked in real time using this system.

The DLP®-HSI system has successfully been used in several preclinical studies of renal ischemia during partial nephrectomy. In a porcine model, Tracy et al. demonstrated a difference in kidney oxygenation with artery only vs. artery+vein occlusion during partial nephrectomy, with significantly higher oxygenation levels for artery only occlusion between 16 and 24 min of ischemia [20]. The authors hypothesized that the DLP®-HSI system may be useful in identifying an "ischemic window" in which artery only occlusion may provide benefit over artery+vein occlusion. Best et al. demonstrated that the DLP®-HSI system was sufficiently sensitive to detect subtle differences in renal oxygenation during partial nephrectomy when comparing 0 % vs. 10 % vs. 25 % arterial inflow during parenchymal resection [21]. In their solitary kidney model, they further demonstrated that 25 % inflow resulted in significantly less change from baseline serum creatinine postoperatively [21].

DLP®-HSI has also been used in several studies of open and minimally invasive partial nephrectomy in humans. In a cohort of 21 patients undergoing open partial nephrectomy, Holzer et al. demonstrated that relative hemoglobin saturation (%$HbO_2$) decreased to nadir levels (20 % below baseline levels), within 10 min of hilar occlusion, with baseline levels restored within 6 min of reperfusion [22]. Best et al. demonstrated significant baseline variation in baseline %$HbO_2$ in 26 patients undergoing open partial nephrectomy, with preservation of early postoperative estimated glomerular filtration rate (eGFR) only in patients with baseline %$HbO_2$ >75 % [23]. Subsequently, Liu et al. investigated artery only vs. artery+vein occlusion in 37 patients undergoing open partial nephrectomy, demonstrating that in the artery+vein group, a lower mean ischemic %$HbO_2$ was associated with significantly lower eGFR at most recent follow-up on both univariate and multivariate analysis [24]. Most recently, Olweny et al. used a novel laparoscopic DLP®-HSI system to study renal oxygenation in patients undergoing robotic-assisted laparoscopic partial nephrectomy [25]. They demonstrated a significant inverse association between baseline %$HbO_2$ and baseline eGFR as well as between baseline %$HbO_2$ and eGFR at most recent follow-up ($p<0.05$). Furthermore, younger patients had a lower median baseline %$HbO_2$ and a significantly higher median preoperative eGFR, perhaps reflective of age-related decline in renal oxygen consumption. No significant associations between %$HbO_2$ and diabetes, hypertension, and smoking history were observed [25].

The promising findings of these initial studies with DLP®-HSI experimentally and in humans suggest that pending further device enhancements and output parameterization, it has the potential for development as an optimal device for the intraoperative assessment of specific aspects of renal metabolism in real time. Furthermore, calibration of the device for measurement of spectra other than those for hemoglobin can potentially expand versatility and therefore capabilities for use in a wide variety of tissue types.

Blanco et al. evaluated the use NIR-hyperspectral imaging in characterizing ex vivo kidney stones [26]. Artificial neural networks were used to analyze the unique spectra generated for each different stone type, and an algorithm that achieved a greater than 90 % probability for the correct classification of the stones was created. This may aid future rapid identification of renal stone composition, reducing latent errors in stone classification characteristic of present-day techniques [26].

## Autofluorescence Spectroscopy in Kidneys

The initial study of use of optical spectroscopy kidney tissue diagnosis by Fitzgerald et al. [11] was notable for the evaluation of both light reflectance and autofluorescence spectra. Data for NIR-reflectance spectroscopy were presented above. With regard to autofluorescence, the authors similarly found that the intensity ratio of injured/normal kidney consistently decreased with increasing warm ischemia time. The best differentiation between normal and ischemic kidneys with autofluorescence was achieved with a 450 nm emission filter, following excitation with a 335 nm laser [11]. NADH, produced during oxidative metabolism, is known to have peak fluorescence at 470 nm when excited at <380 nm [27]. Although NADH could have accounted for some of the fluorescence observed, the authors postulated that a compound other than NADH was also likely, given the decrease in autofluorescence intensity ratio with increasing warm ischemia time. Alternatively, changes in pH could have altered the emission efficiency of the endogenous fluorophores [11]. In follow-up studies, the same group demonstrated the feasibility of using autofluorescence spectroscopy to monitor real-time kidney tissue changes during ischemia and reperfusion in an in vivo rat model [28–30]. A limitation of the above studies was the absence of correlation of autofluorescence spectroscopic findings with tissue histology. Tirapelli et al. addressed this limitation in studies in which grades of ischemic renal tissue injury at several intervals of ischemia were correlated with autofluorescence at 520 nm (excitation 442 nm) and 622 nm (excitation 532 nm). A strong association between tissue damage and autofluorescence intensity was demonstrated, more pronounced with excitation at 442 nm [31, 32].

Renal autofluorescence spectra were also characterized by Parekh et al. in their study investigating the use of optical spectroscopy for the differentiation malignant from benign renal tissue [12]. Renal tissue was demonstrated to produce two primary emission peaks at 340 nm (peak A) and 460 nm (peak B), with excitation at 285 and 340 nm, respectively. Tryptophan and nicotinamide adenine dinucleotide phosphate (NADP) were believed to be the fluorophores for peak A and peak B, respectively. When comparing malignant with benign renal tissue, intensity of peak B from benign renal tissue was found to be greater than for malignant tissue. Additionally, multiple low-intensity emission peaks were observed between 400 and 700 nm for both clear cell and papillary RCC, with no additional peaks for normal renal tissue in this region. Excitation wavelength for Peak A was found to be shorter for benign renal tissue than for malignant tissue [12]. By combining selective spectral features from both fluorescence and diffuse reflectance spectroscopy, algorithms were developed that distinguished malignant from benign renal tissue with high sensitivity and specificity [12].

Bellini et al. described the autofluorescence spectra of protoporphyrin IX, a porphyrin derivative known to accumulate in cancerous tissue [33]. Murine renal cell carcinoma (Renca) cells were implanted into five groups of Balb/c mice that were sacrificed at different intervals after tumor inoculation. A control group was also incorporated. Tissue autofluorescence was measured after excitation at 405 nm. Histological evidence of tumor progression with time was confirmed. Significant differences in autofluorescence spectra between normal and cancer-bearing kidney tissue was demonstrated at emission wavelengths between 600 and 700 nm, with peak intensity at 635 nm. There was an increase in fluorescence intensity in correspondence with increase in tumor size [33].

## Light Reflectance Spectroscopy in Prostates

### Conventional Reflectance Spectroscopy

Optical properties of prostate tissue were characterized as early as the 1990s in the context of defining optical dosimetry parameters for planning of photodynamic therapy [34]. Nearly 15 years later, these techniques were subsequently applied in vivo [35]. During

photodynamic therapy, an oxygen-sensitive photosensitizing drug is delivered into tissue and is activated by light in the presence of oxygen [36]. Accurate monitoring of tissue oxygenation is therefore an important component of photodynamic therapy and has been a major subject of research in prostate optical spectroscopy [37]. An additional and perhaps more practical goal for prostate spectroscopy is the differentiation of malignant from benign prostate tissue. Real-time spectroscopic identification of prostate cancer in vivo could potentially aid future intraoperative positive margin assessment during radical prostatectomy and improved tumor targeting during prostate biopsy. Salomon et al. reported some of the premier work in this context, using a triple spectroscopy approach that incorporated light reflectance spectroscopy, autofluorescence spectroscopy, and high-frequency impedance spectroscopy [38]. The authors measured spectra in ex vivo prostate specimens obtained during radical prostatectomy. Spectra were measured in peripheral zones of the prostate specimens where cancer was thought to exist based on the preoperative biopsy, and histological confirmation was later obtained. Spectra confirmed to have been measured over malignant tissue ($n=16$) were compared with those measured over benign tissue ($n=79$). Normalized autofluorescence, reflectance, and impedance spectral measurements were combined in a principal component analysis, and statistically significant principal components were then used in a linear discriminant analysis to achieve the most accurate differentiation between cancerous and benign tissue. An algorithm was developed that achieved sensitivity and specificity of 87.5 and 87.3 %, respectively, for light reflectance + autofluorescence spectra alone, with improvement to 93.8 and 92.4 %, respectively, when impedance spectral data were added to the model. The cross-validated algorithm had a sensitivity of 75 % and a specificity of 87.3 % for differentiation of malignant and benign prostate tissue [38].

Sharma et al. [39] described specific properties of prostate light reflectance spectra that achieved excellent discrimination between benign and malignant prostate tissue. In their study, specific parameters ($k_1$, $k_2$, $\mu_a$, and $\mu_s$') of light reflectance spectra were first obtained from tissue-simulating phantoms made of animal blood and intralipid solutions. $k_1$ and $k_2$ are determined by the geometrical characteristics of the spectral measurement system, $\mu_a$ is the light absorption coefficient, and $\mu_s$' is the light scattering coefficient. These parameters were incorporated into an algorithm that predicted the concentrations of dissolved oxyhemoglobin ([HbO]) and deoxyhemoglobin ([Hb]) in the tissue phantoms with high accuracy. Reflectance spectra were then measured in ex vivo human prostates obtained from patients undergoing radical prostatectomy using identical methodology. Tissue spectra were separately measured over cancer-bearing and benign sections of the prostate glands as confirmed by subsequent histology. The prostate spectra were then fitted using the novel algorithm, and significant differences in [HbO] and [Hb] between cancerous and benign prostate tissue were demonstrated [39].

Sharma et al. subsequently used the above methodology in the detection of prostate cancer in vivo in a rat model [40]. Dunning R 3327 AT3.1, rat prostate carcinoma cells were injected into the backs of Copenhagen rats, and tumor growth was monitored until a volume of at least 1.5 cc was achieved. The rats were then anesthetized and optical spectra were measured over the tumor as well as over normal tissue. Light reflectance spectral parameters analyzed were [HbO], [Hb], total hemoglobin concentration ([HbT]), and $\mu_s$'. Significant differences between tumor and normal tissue were found for [HbO] ($p=0.03$), [HbT] ($p=0.03$), and $\mu_s$' ($p=0.01$), but not [Hb] ($p=0.22$) [40].

## Hyperspectral Imaging

Akbari et al. demonstrated that hyperspectral imaging could differentiate cancerous from benign prostate tissue in experiments in a murine model of prostate cancer as well as in histological slides of human prostate tissue [41]. In their study, CWR22 prostate cancer cells were inoculated into athymic nude mice that had received

preimplantation testosterone injection. After prostate cancer growth, hyperspectral imaging was performed over tumor and normal areas at a wavelength range of 450–950 nm. Hyperspectral imaging was also performed over histology slides prepared from prostate specimens of four men who had undergone radical prostatectomy. A least-squares support vector machine (LS-SVM) was used to classify the hyperspectral data. The trained LS-SVM was then used in the classification of malignant from benign prostate tissue. Within the mouse model, the LS-SVM was demonstrated to be able to automatically differentiate normal from cancerous prostate tissue on the hyperspectral image with a mean sensitivity and specificity of 92.8 and 96.9 %, respectively. In the in vitro study of pathology slides, the mean reflectance for cancer tissue was found to have a lower intensity than for normal tissue between 560 and 770 nm, while in the in vivo experiment, the mean reflectance for cancer tissue had a lower intensity than for normal tissue over the entire wavelength span of 450–950 nm [41].

## Autofluorescence Spectroscopy in Prostates

Sharma et al. provided the first identification of specific parameters of prostate autofluorescence spectra that differentiated malignant from benign prostate tissue with high accuracy [42]. This was based on measurement of intensity-weighted autofluorescence decay half-life ($\tau_m$), which avoids some of the pitfalls associated with measurement of fluorescence intensity. Autofluorescence lifetime decay is measured in the nanosecond range and is highly sensitive to the biochemical environment of the sample tissue. Autofluorescence lifetime measurement spectroscopy (AFLS) was measured in 23 human prostates removed during radical prostatectomy. Fluorescence was excited at 447 nm and emission was filtered through four wavelengths (532, 562, 632, and 684 nm). $\tau_m$ was determined for each emission wavelength. The decay curve for each emission wavelength was normalized and then fitted to an intensity-weighted two exponent model. This resulted in five unique spectral parameters for each emission wavelength, resulting in a total of 20 spectral parameters. These parameters were incorporated in a mixed model, and multinomial logistic regression was used to identify the optimal combination of parameters that best differentiated prostate cancer from BPH or normal prostate tissue. The ability of the model to differentiate individual grades of prostate cancer from benign tissue was also investigated. Sensitivity, specificity, accuracy, and area under curve (AUC) for discrimination between these tissue types were determined. For overall discrimination between cancerous vs. noncancerous tissue, these values were 64.2, 69.2, 67.1, and 73 %, respectively. Sensitivity, specificity, and accuracy for prediction of Gleason 8 and 9 tumors were higher than for Gleason 7 tumors [42]. In a subsequent analysis, the authors used identical methodology to reanalyze prostate spectra from the same patient cohort using a combination of AFLS and diffuse light reflectance spectroscopy. Overall sensitivity, specificity, accuracy, and AUC for cancerous vs. noncancerous tissue improved to 79.0, 85.2, 82.7, and 90.8 %, respectively, for the combined modalities (unpublished data).

## Summary

Optical spectroscopy has undergone extensive evaluation in recent years across a wide range of clinical settings. In evaluation within kidneys and prostates, promising initial findings with regard to differentiating malignant from benign tissue, characterizing tissue response to ischemia, and identifying kidney stone composition rapidly and accurately have been demonstrated. At the present time, several limitations need to be overcome before optical spectroscopy techniques can be applied in routine clinical practice. These include but are not limited to bulk of most of the spectroscopic equipment, long spectral acquisition and processing times, and limited capability of individual spectroscopy probes in processing a variety of different metabolic processes that occur simultaneously within tissues. Additionally,

many of these techniques have not been evaluated in vivo in humans, where factors such as blood flow, exposure to air or carbon dioxide during surgery, intraoperative lighting, and a host of other factors are likely to impact accuracy of spectral measurements. Given these and other considerations, it seems apparent that combining a variety of spectroscopy techniques will likely be required during clinical use. Development of computer algorithms capable of rapidly processing large amounts of spectral data in real time would greatly facilitate future clinical implementation. Further development of these techniques in the preclinical setting is required.

## References


1. Richards-Kortum R, Sevick-Muraca E. Quantitative optical spectroscopy for tissue diagnosis. Annu Rev Phys Chem. 1996;47:555–606.
2. Evers D, Hendriks B, Lucassen G, Ruers T. Optical spectroscopy: current advances and future applications in cancer diagnostics and therapy. Future Oncol. 2012;8(3):307–20.
3. Monici M. Cell and tissue autofluorescence research and diagnostic applications. Biotechnol Annu Rev. 2005;11:227–56.
4. Rajaram N, Aramil TJ, Lee K, Reichenberg JS, Nguyen TH, Tunnell JW. Design and validation of a clinical instrument for spectral diagnosis of cutaneous malignancy. Appl Opt. 2010;49(2):142–52.
5. de Veld DC, Skurichina M, Witjes MJ, Duin RP, Sterenborg HJ, Roodenburg JL. Autofluorescence and diffuse reflectance spectroscopy for oral oncology. Lasers Surg Med. 2005;36(5):356–64.
6. Bigio IJ, Bown SG, Briggs G, Kelley C, Lakhani S, Pickard D, et al. Diagnosis of breast cancer using elastic-scattering spectroscopy: preliminary clinical results. J Biomed Opt. 2000;5(2):221–8.
7. Fawzy Y, Zeng H. Intrinsic fluorescence spectroscopy for endoscopic detection and localization of the endobronchial cancerous lesions. J Biomed Opt. 2008;13(6):064022.
8. Fawzy YS, Petek M, Tercelj M, Zeng H. In vivo assessment and evaluation of lung tissue morphologic and physiological changes from non-contact endoscopic reflectance spectroscopy for improving lung cancer detection. J Biomed Opt. 2006;11(4):044003.
9. Cardenas-Turanzas M, Freeberg JA, Benedet JL, Atkinson EN, Cox DD, Richards-Kortum R, et al. The clinical effectiveness of optical spectroscopy for the in vivo diagnosis of cervical intraepithelial neoplasia: where are we? Gynecol Oncol. 2007;107(1 Suppl 1):S138–46.
10. Georgakoudi I, Jacobson BC, Van Dam J, Backman V, Wallace MB, Muller MG, et al. Fluorescence, reflectance, and light-scattering spectroscopy for evaluating dysplasia in patients with Barrett's esophagus. Gastroenterology. 2001;120(7):1620–9.
11. Fitzgerald JT, Demos S, Michalopoulou A, Pierce JL, Troppmann C. Assessment of renal ischemia by optical spectroscopy. J Surg Res. 2004;122(1):21–8.
12. Parekh DJ, Lin WC, Herrell SD. Optical spectroscopy characteristics can differentiate benign and malignant renal tissues: a potentially useful modality. J Urol. 2005;174(5):1754–8.
13. Bensalah K, Tuncel A, Peshwani D, Zeltser I, Liu H, Cadeddu J. Optical reflectance spectroscopy to differentiate renal tumor from normal parenchyma. J Urol. 2008;179(5):2010–3.
14. Bensalah K, Peswani D, Tuncel A, Raman JD, Zeltser I, Liu H, et al. Optical reflectance spectroscopy to differentiate benign from malignant renal tumors at surgery. Urology. 2009;73(1):178–81.
15. Couapel JP, Senhadji L, Rioux-Leclercq N, Verhoest G, Lavastre O, de Crevoisier R, et al. Optical spectroscopy techniques can accurately distinguish benign and malignant renal tumours. BJU Int. 2013;111(6):865–71.
16. Goetz AF, Vane G, Solomon JE, Rock BN. Imaging spectrometry for Earth remote sensing. Science. 1985;228(4704):1147–53.
17. Zuzak KJ, Schaeberle MD, Gladwin MT, Cannon 3rd RO, Levin IW. Noninvasive determination of spatially resolved and time-resolved tissue perfusion in humans during nitric oxide inhibition and inhalation by use of a visible-reflectance hyperspectral imaging technique. Circulation. 2001;104(24):2905–10.
18. Zuzak KJ, Schaeberle MD, Lewis EN, Levin IW. Visible reflectance hyperspectral imaging: characterization of a noninvasive, in vivo system for determining tissue perfusion. Anal Chem. 2002;74(9):2021–8.
19. Zuzak KJ, Francis RP, Wehner EF, Litorja M, Cadeddu JA, Livingston EH. Active DLP hyperspectral illumination: a noninvasive, in vivo, system characterization visualizing tissue oxygenation at near video rates. Anal Chem. 2011;83(19):7424–30.
20. Tracy CR, Terrell JD, Francis RP, Wehner EF, Smith J, Litorja M, et al. Characterization of renal ischemia using DLP hyperspectral imaging: a pilot study comparing artery-only occlusion versus artery and vein occlusion. J Endourol. 2010;24(3):321–5.
21. Best SL, Thapa A, Holzer MJ, Jackson N, Mir SA, Cadeddu JA, et al. Minimal arterial in-flow protects renal oxygenation and function during porcine partial nephrectomy: confirmation by hyperspectral imaging. Urology. 2011;78(4):961–6.
22. Holzer MS, Best SL, Jackson N, Thapa A, Raj GV, Cadeddu JA, et al. Assessment of renal oxygenation during partial nephrectomy using hyperspectral imaging. J Urol. 2011;186(2):400–4.
23. Best SL, Thapa A, Jackson N, Olweny EO, Holzer MJ, Park SK, et al. Renal oxygenation measurement

during partial nephrectomy using hyperspectral imaging may predict acute post-operative renal function. J Endourol. 2013;27(8):1037–40.
24. Liu ZW, Faddegon S, Olweny EO, Best SL, Jackson N, Raj GV, et al. Renal oxygenation during partial nephrectomy: a comparison between artery-only occlusion versus artery and vein occlusion. J Endourol. 2013;27(4):470–4.
25. Olweny EO, Faddegon S, Best SL, Jackson N, Wehner EF, Tan YK, et al. Renal oxygenation during robot-assisted laparoscopic partial nephrectomy: characterization using laparoscopic digital light processing hyperspectral imaging. J Endourol. 2013;27(3):265–9.
26. Blanco F, Lopez-Mesas M, Serranti S, Bonifazi G, Havel J, Valiente M. Hyperspectral imaging based method for fast characterization of kidney stone types. J Biomed Opt. 2012;17(7):076027.
27. Wagnieres GA, Star WM, Wilson BC. In vivo fluorescence spectroscopy and imaging for oncological applications. Photochem Photobiol. 1998;68(5):603–32.
28. Fitzgerald JT, Michalopoulou A, Pivetti CD, Raman RN, Troppmann C, Demos SG. Real-time assessment of in vivo renal ischemia using laser autofluorescence imaging. J Biomed Opt. 2005;10(4):44018.
29. Michalopoulou AP, Fitzgerald JT, Troppmann C, Demos SG. Spectroscopic imaging for detection of ischemic injury in rat kidneys by use of changes in intrinsic optical properties. Appl Opt. 2005;44(11):2024–32.
30. Raman RN, Pivetti CD, Matthews DL, Troppmann C, Demos SG. A non-contact method and instrumentation to monitor renal ischemia and reperfusion with optical spectroscopy. Opt Express. 2009;17(2):894–905.
31. Tirapelli LF, Bagnato VS, Tirapelli DP, Kurachi C, Barione DF, Tucci Jr S, et al. Renal ischemia in rats: mitochondria function and laser autofluorescence. Transplant Proc. 2008;40(5):1679–84.
32. Tirapelli LF, Trazzi BF, Bagnato VS, Tirapelli DP, Kurachi C, da Costa MM, et al. Histopathology and laser autofluorescence of ischemic kidneys of rats. Lasers Med Sci. 2009;24(3):397–404.
33. Bellini MH, Coutinho EL, Courrol LC, Rodrigues de Oliveira Silva F, Vieira Junior ND, Schor N. Correlation between autofluorescence intensity and tumor area in mice bearing renal cell carcinoma. J Fluoresc. 2008;18(6):1163–8.
34. Arnfield MR, Chapman JD, Tulip J, Fenning MC, McPhee MS. Optical properties of experimental prostate tumors in vivo. Photochem Photobiol. 1993;57(2):306–11.
35. Svensson T, Alerstam E, Einarsdottir M, Svanberg K, Andersson-Engels S. Towards accurate in vivo spectroscopy of the human prostate. J Biophotonics. 2008;1(3):200–3.
36. Dougherty TJ, Gomer CJ, Henderson BW, Jori G, Kessel D, Korbelik M, et al. Photodynamic therapy. J Natl Cancer Inst. 1998;90(12):889–905.
37. Yu G, Durduran T, Zhou C, Zhu TC, Finlay JC, Busch TM, et al. Real-time in situ monitoring of human prostate photodynamic therapy with diffuse light. Photochem Photobiol. 2006;82(5):1279–84.
38. Salomon G, Hess T, Erbersdobler A, Eichelberg C, Greschner S, Sobchuk AN, et al. The feasibility of prostate cancer detection by triple spectroscopy. Eur Urol. 2009;55(2):376–83.
39. Sharma V, Kashyap D, Mathker A, Narvenkar S, Bensalah K, Kabbani W, et al. Optical reflectance spectroscopy for detection of human prostate cancer. Conf Proc IEEE Eng Med Biol Soc. 2009;2009:118–21.
40. Sharma V, Patel N, Shen J, Tang L, Alexandrakis G, Liu H. A dual-modality optical biopsy approach for in vivo detection of prostate cancer in a rat model. J Innov Opt Health Sci. 2011;4(3):269–77.
41. Akbari H, Halig LV, Schuster DM, Osunkoya A, Master V, Nieh PT, et al. Hyperspectral imaging and quantitative analysis for prostate cancer detection. J Biomed Opt. 2012;17(7):076005.
42. Sharma V, Olweny EO, Kapur P, Cadeddu JA, Roehrborn CG, Liu H. Prostate cancer detection using combinded auto-flourescence and light reflectance spectroscopy: ex vivo study of a dual-modal optical technique. Biomedical Optical Express 5(5): doi: 10.1364/BOE.5.001512, May 2014.

# Part II

# Ultrasound-Guided Interventions

# Intraoperative Doppler Ultrasound During Robotic Surgery

9

Ahmet Gudeloglu, Jamin V. Brahmbhatt, Annika Mulaney, and Sijo Parekattil

Currently, many open surgical approaches in urology have almost completely been replaced by minimally invasive techniques [1]. Minimally invasive surgery in urology began with first report of a laparoscopic nephrectomy by Clayman et al. [2] in 1991. Approximately 10 years later, a report of robotic-assisted laparoscopic prostatectomy pioneered another era of minimally invasive urological surgery. This novel robotic-assisted laparoscopic minimally invasive approach allowed surgeons to perform technically challenging laparoscopic cases with greater ease [3]. The use of robotic assistance for minimally invasive laparoscopy has continued to expand, and it is estimated that more than 80 % of all radical prostatectomies in the United States will be performed using robotic assistance [4]. Currently, the da Vinci robotic system (Intuitive Surgical Inc., Sunnyvale, CA) is the primary FDA-approved robotic system utilized in urology. More than 2,500 robotic systems are used worldwide. This system provides surgeons with digital magnification, high-definition 3-D visualization, elimination of physiologic tremor, and motion scaling. Robotic assistance also allows for easier laparoscopic dissection [5].

A. Gudeloglu, MD (✉) • J.V. Brahmbhatt, MD
A. Mulaney • S. Parekattil, MD (✉)
Department of Urology, The PUR Clinic,
South Lake Hospital in Partnership with Orlando Health, Clermont, FL, USA
e-mail: a_gudeloglu@yahoo.com; jaminbrahmbhatt@gmail.com; amulaney@gmail.com; sijo_p@hotmail.com

Despite all the advantages, there are some limitations. Initially, with laparoscopy compared to open surgery, surgeons lost 3-D visualization capability and the ability to have tactile or palpation ability. Direct palpation is one of the key advantages of open surgery. A previous study has shown that direct palpation has significant advantages to both conventional instruments and laparoscopic instruments in the accuracy of shape identification in randomly ordered objects ($p<0.001$) [6]. Although surgeons regained 3-D visualization with the da Vinci robotic system, tactile feedback is still lacking. The sense of touch and pulse palpation is very helpful for surgeons in identifying specific anatomical structures such as arteries, veins, and tumor masses. Lack of tactile force feedback can cause inadvertent tissue laceration or suture breaks during knot tying in robotic-assisted procedures [7]. Tactile feedback is especially important in robotic renal procedures where vascular anomalies are often present with an increased risk of hemorrhage [8].

The lack of tactile feedback has created a demand for adjunctive tools for intraoperative imaging or sensing to aid in the detection of certain anatomic structures such as blood vessels. Intraoperative laparoscopic ultrasound is one such tool that has gained increasing use due to its real-time sensing/imaging capability, non-invasiveness, low cost, and easy handling [9]. Intraoperative ultrasound has been used since the late 1980s even in open procedures to identify non-palpable tumors or deep parenchymal lesions

J.C. Liao, L.-M. Su (eds.), *Advances in Image-Guided Urologic Surgery*,
DOI 10.1007/978-1-4939-1450-0_9, © Springer Science+Business Media New York 2015

[10]. This chapter will cover the basic technology in both ultrasound and Doppler ultrasound systems and then focus on uses of intraoperative Doppler ultrasound (IODU) during robotic surgical procedures in urology.

## Fundamentals of Ultrasound Imaging

The frequency of sound waves is measured in Hertz (Hz) or number of the cycles per second. Normal human adults can perceive auditory sound waves between 20 and 20,000 Hz. Ultrasound technology utilizes sound waves between 2 and 15 MHz (million cycles per second). Currently, ultrasound imaging is usually implemented using a pulse-echo approach with a brightness-mode (B-Mode) display. This approach involves transmitting small pulses of ultrasound waves into the body structures, detecting reflected echo signals from them, and finally processing the echo signals to obtain an image [11].

Laparoscopic ultrasound (LUS) devices have been developed for minimal invasive surgery. LUS devices have small linear-array transducers mounted on 6–10 mm diameter probes allowing intraoperative ultrasonic evaluation through standard laparoscopic trocars. The transducer generates ultrasonic waves and then receives the reflected echo from body structures. For LUS imaging/sensing, the linear-array transducer is set between 5.0 and 10.0 MHz (usually 7.5 MHz) for optimal resolution and depth of penetration [9, 12]. Lower frequencies would allow for better tissue penetration, but this leads to lower image resolution [11].

Although different types of LUS probes are available, the most common type is a longitudinal rod-type configuration, which can be either rigid or flexible (Fig. 9.1) [12]. The flexibility is crucial when maintaining contact with curved organs such as the kidney [9]. Although the flexible LUS probes provide better contact maintenance during robotic procedures, the surgeon has to direct or guide the surgical assistant in positioning the probe correctly to optimize visualization.

Recently, a robotic transducer, the ProART (BK Medical Herlev, Denmark), with Doppler capability was developed. It has a unique fin over the array, which can be grasped by robotic instruments. Yakoubi et al. demonstrated the feasibility of this novel probe in an animal model [13]. Similarly, another novel fully articulated transducer has been developed to reach complex angles that are difficult with traditional flexible LUS probes (Hitachi-Aloka, Tokyo, Japan) [14]. This novel drop-in transducer probe has a 33-mm width linear array with a frequency rate of 4–13 MHz. Robotic instruments can also easily handle it, and the surgeon can remotely control its movement with greater precision and dexterity (Fig. 9.2). Additionally, micro-ultrasound probes have been made for better handling with robotic instruments (Fig. 9.3). The da Vinci surgeon console has a software imaging program called TilePro (Intuitive Surgical, Sunnyvale, CA) that

**Fig. 9.1** Flexible laparoscopic ultrasound probe (From Hitachi-Aloka, Wallingford, CT)


**Fig. 9.2** Robotic flexible ultrasound probe (Courtesy of Hitachi-Aloka, Wallingford, CT)

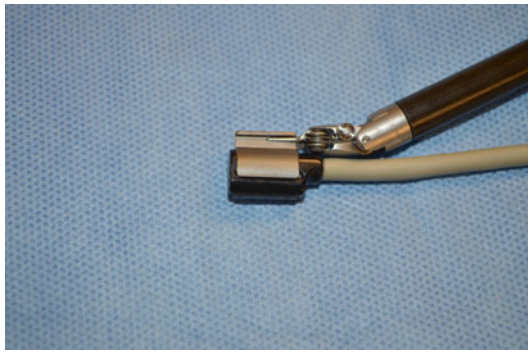

**Fig. 9.3** Robotic micro-ultrasound probe (From Hitachi-Aloka)

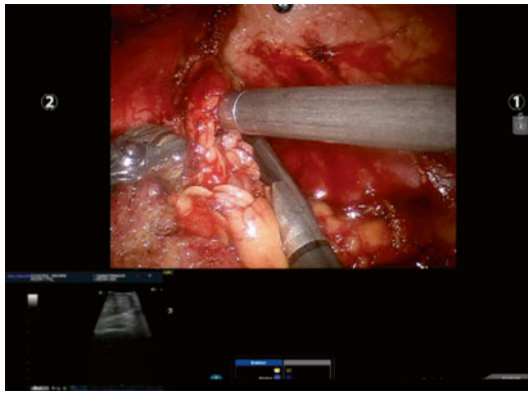

**Fig. 9.4** Real-time ultrasound visualization in the surgeon console. A renal mass is being identified

allows up to two adjunctive imaging inputs to be viewed by the surgeon simultaneously with the regular 3D camera field view. Figure 9.4 shows real-time ultrasound visualization in the surgeon console during robotic nephron sparing surgery. While the image from the robotic camera is seen on the main screen, the ultrasound image is visible simultaneously in the lower left-hand corner.

## Fundamentals of Ultrasound Doppler Imaging/Sensing

The basis of Doppler ultrasound sensing is that as an object emitting sound moves, the wavelength of the perceived sound is compressed and its frequency is increased in the forward direction. In the receding direction, the perceived wavelength would be expanded and frequency decreased. Doppler

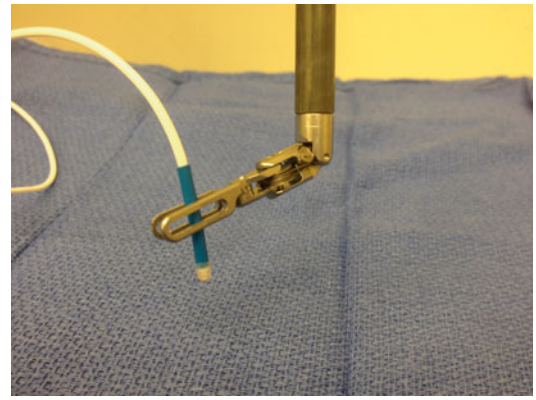

**Fig. 9.5** Disposable audible micro-Doppler probe (Courtesy of Vascular Technology Inc., Nashua, NH)

ultrasound probes have the ability to detect velocity or flow of material based on this measured increase or decrease of sound frequency. The delay in wave sensing between the primary and secondary reflected waves depends on the depth and the speed of the sound waves in various tissues [15]. Several LUS probes today have Doppler ultrasound capability, which allows for differentiation of blood vessels or highly vascularized masses compared to normal parenchymal tissue.

Recently, a sterile, disposable laparoscopic drop-in Doppler ultrasound (LDU) probe has been introduced for robotic procedures (Fig. 9.5) (VTI Vascular Technology Inc., Nashua, NH). The system includes a Doppler transceiver (8 or 20 MHz) with flexible disposable probes that emit ultrasound waves and sense reflected echo from blood flow. The 8 MHz is used to detect larger vessels such as the renal artery and vein. The 20 MHz probe is used to detect smaller vessels (1 mm or less) for microsurgical procedures (such as the testicular artery). This system provides an auditory pulse signal to identify blood flow allowing clear differentiation of arteries and veins [16].

## Intraoperative Doppler Ultrasound During Ablative and Reconstructive Robotic Renal Surgeries

Both extirpative and reconstructive robotic renal procedures are performed routinely with the da Vinci robotic platform such as radical

and partial nephrectomy, nephroureterectomy, living-donor nephrectomy, pyeloplasty, and renovascular surgery [17]. Surgical maneuvers with robotic instruments around the renal hilum can in some cases be intimidating because of the lack of tactile feedback, scarring from prior surgeries and due to variations in renal vascular anatomy. A preoperative imaging study using helical CT angiography looked at 102 living donors. It revealed the presence of multiple renal arteries (31 % on the left, 20 % on the right) and multiple renal veins (5 % on the left, 20 % on the right) [18]. Although advanced preoperative imaging techniques such as multidetector helical CT or MR-angiography are reasonably accurate in showing renal vascular anatomy, accessory vessels can be missed by imaging techniques [19, 20]. Even though this occurs in a small number patients, it can lead to surgical complexity and result in open conversion due to bleeding from unexpected vessel trauma [21]. Additionally, patient positioning, pneumoperitoneum, and intraoperative mobilization during robotic renal surgery can change the anatomical relationship between the renal hilum and other landmarks compared to preoperative imaging studies [22]. Recently, an analysis of 886 robotic partial nephrectomy procedures revealed that perioperative hemorrhage occurred in 0.5 % of the patients (two due to renal vein injury and two due to a missed unclamped renal artery) [23]. Lee et al. also described iatrogenic injury of the posterior segmental branch of renal artery during robot-assisted partial nephrectomy [8]. Unfortunately, these injuries can result in renal parenchymal loss, excessive blood loss, and longer operative times. Robotic pyeloplasty procedures can become a challenge due to obesity, a large floppy liver, redundant colon, crossing vessels, large calculi, and previous surgery [24].

For all the reasons mentioned above, IODU provides surgeons with an adjunctive tool to assist in identifying vessels and tissue perfusion during complex and challenging robotic renal procedures.

## Intraoperative Audible Doppler and Ultrasound Imaging During Robotic Partial Nephrectomy

The incidence of kidney cancer has globally increased possibly due to increased prevalence of risk factors and common utilization of imaging techniques [25]. There has also been a shift to increased detection of smaller and Stage 1 tumors from more advanced tumors [26]. These smaller, earlier stage kidney tumors are better suited for minimally invasive approaches such as partial nephrectomy [27]. Today, with the advantages of the robotic platform, the number of robotic partial nephrectomy (RPN) procedures is progressively increasing [28].

The flexible laparoscopic ultrasound probe is very helpful in RPN and is used to demarcate tumor margins after Gerota's fascia is opened [29]. It is particularly helpful for tumors that have more of an intraparenchymal component. A previous study illustrated that surgeons were more likely to use IODU when the tumor was more intraparenchymal [30].

Kaczmarek et al. reported preliminary outcomes of the drop-in robotic ultrasound probe (Hitachi-Aloka, Tokyo, Japan) for tumor identification in RPN [14]. Ninety-six percent of the tumors were endophytic with a mean size of 2.7 cm. They successfully completed 22 RPN with negative surgical margins using the robotic ultrasound probe without any intraoperative complications. They also reported that the robotic ultrasound probe could be articulated by the robotic surgeon to maintain perpendicular contact between the probe and kidney surface even in difficult angles [14].

The same drop-in probe was also compared with a four-directional flexible laparoscopic ultrasound probe during 150 RPN procedures [31]. There was no statistically significant difference in perioperative parameters and functional and oncologic outcomes. However, the authors found that the robotic drop-in probe could provide surgeon autonomy when an experienced surgical assistant is not available [31].

Hyams et al. reported the use of a simple 5 mm rigid disposable Doppler probe that produced audible signals for renal hilar vessel identification [22]. This probe was able to identify aberrant or accessory vessels that were not seen in preoperative imaging studies. The probe also confirmed ischemia or no flow in the main renal vessels during clamping and restoration of flow after unclamping during RPN [22]. The study demonstrated that the mean Doppler scanning duration for the renal hilum was 1.5 min and the mean renal hilar dissection duration was 7.9 min (26 RPN cases). They also reported that surgical management was altered with the Doppler evaluation in five patients (19 %) either by repositioning of the hilar clamp or additional selective arterial clamping [32]. Sethi et al. evaluated the disposable Doppler ultrasound in 20 laparoscopic partial nephrectomy patients. And they concluded that the system was easy to use without any formal training [33]. They also reported that the assessment of the renal hilum with the disposable Doppler probe provided a "road map" in patients who have anatomic distortion due to infection and previous surgery. It was also been pointed out that standard laparoscopic ultrasound probes are side firing and required careful interpretation; however, the small end firing tip of the audible Doppler probe provided very precise vascular localization and was easier to interpret. The study suggested that the identification of renal hilar vascular anatomy was easier and faster with the disposable audible Doppler probe compared to standard laparoscopic ultrasound imaging probes [33].

Standard Doppler ultrasound appears to be more sensitive in confirming no flow or ischemia in the renal hilar vessels during clamping (100 % vs. 85 %) when compared to the disposable audible Doppler ultrasound during 20 laparoscopic partial nephrectomy cases [16]. This study also showed that the disposable audible Doppler probe was faster and easier to use: The mean duration for hilar blood flow assessment was 68.6 s with the standard laparoscopic Doppler ultrasound and 44.5 s with the disposable audible Doppler probe. The disposable audible probe was able to provide adequate renal vascular and parenchymal sensing from a range of different angles [16].

Hyams et al. compared the hilar dissection operative duration with and without the disposable Doppler probe in 27 and 26 RPN procedures, respectively [34]. They found that hilar dissection time was significantly less with the use of the disposable Doppler probe (7.2 min vs. 11 min, $P<0.05$). This study also further illustrated that the use of the probe led to a change in the surgical management of seven patients (26 %) during 27 RPN procedures: either by detecting accessory vessels or identifying incomplete clamping.

The key value of using such adjunctive technology in RPN is if it really makes a difference in surgical management. Table 9.1 summarizes a review of recent studies that have shown an advantage in the use of intraoperative Doppler and ultrasound imaging in terms of altering surgical management during partial nephrectomy procedures. The use of this technology has impacted surgical management in these cases from 10 to 38 % of the time (Table 9.1). The audible Doppler probe cannot evaluate tumor morphology, margins, and depth, and therefore in some cases, the standard Doppler ultrasound probe may provide more functionality [22].

**Table 9.1** Listing of studies showing the impact of adjunctive intraoperative Doppler ultrasound in altering surgical management in partial nephrectomy

| Study | Surgical technique | Number of partial nephrectomy cases | Number of cases in which intraoperative Doppler altered surgical technique |
|---|---|---|---|
| Hyams et al. [22] | Laparoscopic | 8 | 3 (38 %) |
| Mues et al. [16] | Laparoscopic | 20 | 2 (10 %) |
| Perlmutter et al. [32] | Laparoscopic | 26 | 5 (19 %) |
| Hyams et al. [34] | Robotic | 27 | 7 (26 %) |

## Intraoperative Audible Doppler and Ultrasound Imaging During Robotic Radical Nephrectomy and Nephroureterectomy

A recent study on 855 patients who underwent angiographic evaluation to assess renal artery anatomy and its variations illustrated that accessory renal arteries were present in 16 % of cases on the right side and 13 % of cases on the left side. This variation in renal arterial anatomy may allow adjunctive intraoperative arterial mapping tools helpful for surgeons. Hyams et al. have illustrated that the audible Doppler probe can precisely identify renal arterial anatomy or any variations and help surgeons during real surgery [22]. The disposable audible Doppler probe can also be used to confirm the absence of aberrant arterial flow before ligating the renal vein in nephrectomy cases. The use of Doppler mapping did not seem to add much time to the total operative time and was relatively easy to use. Perlmutter et al. found that the mean Doppler imaging time was 1.8 min and the mean hilar dissection time was 10.4 min during 16 laparoscopic renal cases (11 radical nephrectomy and 5 nephroureterectomy cases) [32]. The utility of such mapping may also have benefits when training surgeons to perform such procedures and to build their confidence in understanding renal arterial anatomy and its possible variations.

Intraoperative ultrasound can be employed during robotic radical nephrectomy (RRN) procedures especially for tumors that extend into the vena cava. Abaza et al. described the utilization of the flexible laparoscopic ultrasound probe to identify the extent of the thrombus within vena cava [35]. A similar technique is reported by Lee et al. to visualize the tumor thrombus during RRN and vena caval tumor thrombectomy [36].

## Intraoperative Audible Doppler and Ultrasound Imaging During Robotic Living-Donor Nephrectomy

The safety and efficacy of robotic donor nephrectomy (RDN) has been demonstrated even in living donors who have multiple renal arteries [37]. Laparoscopic donor nephrectomy can be performed either by hand-assisted or robotic-assisted techniques [38, 39].

Sethi et al. have reported the feasibility of the use of a disposable audible Doppler ultrasound probe during eight pure laparoscopic donor nephrectomy procedures [33]. In their study, they demonstrated that audible Doppler mapping was able to accurately detect all renal units that had two renal arteries at the time of donor nephrectomy. Thus, it was suggested that intraoperative Doppler mapping be used to accurately characterize the hilar renal anatomy and improve future graft function [33].

Van der Meijden et al. have shown that tactile feedback, especially in cases where palpation of aberrant vessels may help, may reduce surgical errors and potentially increase patient safety [40]. RDN is such a case where the use of intraoperative Doppler mapping may have a direct impact in reducing both donor and recipient morbidity by providing surgeons an accurate anatomical assessment of renal hilar vasculature.

## Intraoperative Audible Doppler and Ultrasound Imaging During Robotic Assisted Pyeloplasty

Robotic-assisted pyeloplasty (RAP) is a viable and increasingly utilized alternative to conventional laparoscopic pyeloplasty [41, 42]. Previous imaging studies have shown that approximately 45 % of patients who have ureteropelvic junction (UPJ) obstruction had a crossing vessel as the cause of the obstruction [43, 44]. Intraoperative surgical complication rates during RAP are low [45–48]. However, unrecognized crossing vessels can be injured during the dissection of the UPJ and lead to intraoperative bleeding [24]. The use of intraoperative Doppler mapping may reduce this potential risk of inadvertent vascular injury.

Hyams et al. illustrated that the utilization of intraoperative Doppler mapping during RAP altered the surgical course of treatment in one out of three cases (33 %) since a crossing vessel was identified using the Doppler that had been missed on the preoperative imaging studies [22]. This study also found that use of the Doppler helped to

reduce operative duration by aiding the surgeon in clearly identifying the renal vascular anatomy during UPJ dissection. Perlmutter et al. have also demonstrated that the mean Doppler mapping duration to identify crossing vessels during eight RAP cases was only 2.6 min and that this led to an approximately 15 min reduction in overall operative duration by allowing for an easier dissection of the UPJ [32].

## Intraoperative Audible Doppler and Ultrasound Imaging During Robotic-Assisted Radical Prostatectomy

Over the past decade, robotic-assisted laparoscopic radical prostatectomy (RRP) has become the most common surgical method for the treatment of localized prostate cancer. A recent study estimated that every two out of three radical prostatectomy cases were being performed with the assistance of a robot in 2010 [49]. Although robotic assistance provides some advantages over open or laparoscopic techniques such as magnification, improved surgeon dexterity, and precise surgical dissection, postoperative erectile dysfunction still remains a challenge and its incidence ranges from 6 to 81 % [5, 50].

The preservation of the periprostatic neurovascular bundles is postulated as the key surgical component in protecting potency regardless of the technique used: open, laparoscopic, or robotic-assisted laparoscopic prostatectomy. This has led to the use of various real-time intraoperative ultrasound and Doppler mapping systems to try to aid in the visualization or mapping of these bundles to minimize injury during these procedures.

Han et al. and Long et al. have described real-time robotic transrectal ultrasound imaging methods to identify the neurovascular bundle during robotic radical prostatectomy [51, 52]. These methods use robotic transrectal Doppler ultrasound imaging to monitor arterial blood flow during the dissection of the neurovascular bundle and ensure minimal injury. These preliminary studies show the feasibility and safety of such systems [51, 52].

Badani et al. published the first study reporting the utilization of the audible Doppler probe during RRP [53]. They used the Doppler probe in nine RRP cases (patients with low- or intermediate-risk localized prostate cancer and had normal baseline erectile function). The use of Doppler mapping during the case added a mean of 8.2 min to the operative duration. Utilization of the Doppler probe altered the nerve sparing technique in 44 % of the cases on the right and 56 % of the cases on the left side. Preoperative and postoperative neurovascular bundle evaluation across all cases with the audible Doppler probe revealed that there was an 80 % maintenance in arterial flow, 16 % decrease in flow, and 4 % increase in arterial flow. On long-term follow-up (8 months postoperative), 78 % of the patients had regained erectile function [53]. Thus, it appears that the Doppler mapping at the end of the case seemed to correlate with the long-term erectile function recovery of these patients.

The use of such imaging and guidance technology in RRP is still in its infancy, but these preliminary studies do seem to provide some promise of its utility in improving patient outcomes.

## Intraoperative Audible Doppler and Ultrasound Imaging During Robotic Microsurgical Procedures

Robotic-assisted microsurgery has been slowly evolving in urology over the last 10 years [54–56] and is still in its infancy. Robotic-assisted microsurgical (RAM) procedures include subinguinal varicocelectomy, vasectomy reversal, and targeted denervation of the spermatic cord [57]. Our group has the largest robotic-assisted microsurgery case series so far (972 cases). We have performed 238 RAM varicocelectomies, 180 RAM vasectomy reversals, and 554 RAM targeted denervation of the spermatic cord.

During subinguinal microsurgery of the spermatic cord, for example, in varicocelectomy cases or targeted denervation of the spermatic cord, identification of the testicular artery or arteries is of prime importance to preserve the vascular supply to the testicle. The use of Doppler mapping for testicular artery identification for such microsurgical cases has thus become fairly common. Greenberg et al. recommended the use

of intraoperative Doppler to identify testicular arteries in the 1980s [58]. Cocuzza et al. reported a study comparing 213 microsurgical subinguinal varicocelectomies with and without (90 with vs. 123 without) intraoperative Doppler mapping [59]. They found that the number of ligated veins and the number of preserved arteries were significantly higher in Doppler group than in the non-Doppler group. There were no arterial injuries in the Doppler group. However, two arterial injuries (1.1 %) occurred in the non-Doppler group [59].

At the subinguinal location of the spermatic cord, it has been demonstrated that 75 % of patients have multiple arteries (two or more). Variation in testicular arterial anatomy may explain inadvertent testicular artery injuries which occur in approximately 1 % of microsurgical varicocelectomy procedures [60]. Injury of these testicular arteries may lead to less unfavorable outcomes for patients [60]. Thus, we utilize intraoperative Doppler mapping during RAM procedures for both subinguinal varicocelectomy and targeted denervation of the spermatic cord.

We utilize either the audible micro-Doppler probe (Vascular Technology Inc., Nashua, NH) or a new reusable micro-ultrasound probe (Hitachi-Aloka, Wallingford, CT) in our RAM varicocelectomy and denervation procedures [57]. The audible micro-Doppler probe has advantages in that it is easy to maneuver using the robotic micro-instruments and provides in line direct detection of the artery making localization of the artery simple (Fig. 9.6). The micro-ultrasound probe has advantages in that it is reusable, allows for full depth (up to 6 cm) ultrasound and Doppler flow visualization of all structures (tissue planes, arteries and veins), and is relatively easy to grasp using one of the larger robotic grasping instruments (Fig. 9.7).

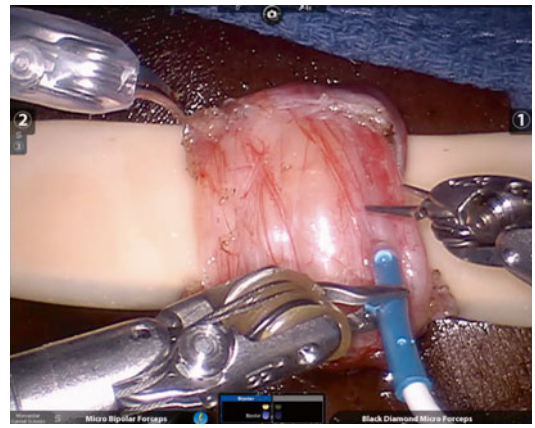


**Fig. 9.6** Micro-ultrasound probe from Hitachi-Aloka being used to identify spermatic cord vessels

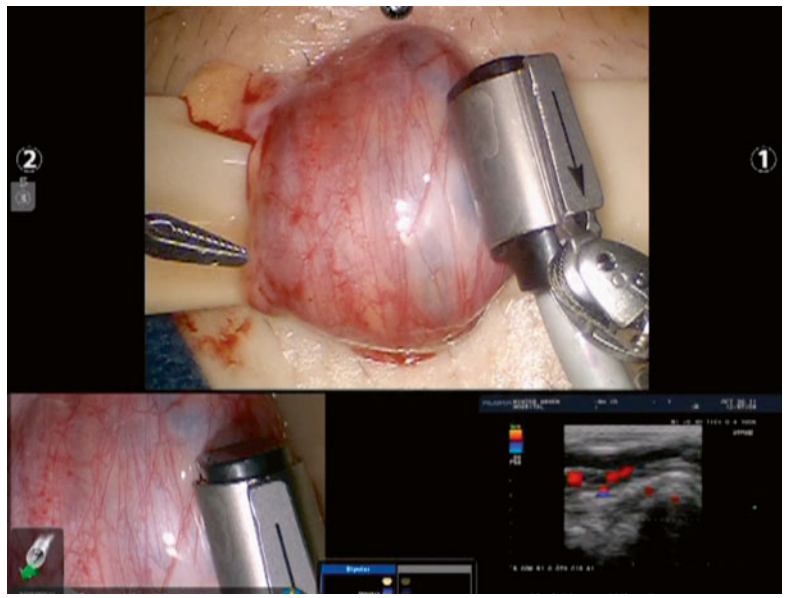


**Fig. 9.7** Disposable audible micro-Doppler probe is being used to identify spermatic cord vessels (Courtesy of Vascular Technology Inc., Nashua, NH)

**Conclusion**

Intraoperative Doppler ultrasound imaging and mapping provides a very useful adjunctive tool during robotic urological procedures. Doppler evaluation may prevent potential inadvertent vascular injury. It also provides helpful information about the perfusion status of the kidney during robotic partial nephrectomy procedures. It is just one of many adjunctive technologies that help surgeons with overcoming the shortcomings of lack of tactile feedback in robotic-assisted procedures.

## References


1. Rassweiler J, Rassweiler MC, Kenngott H, Frede T, Michel MS, Alken P, Clayman R. The past, present and future of minimally invasive therapy in urology: a review and speculative outlook. Minim Invasive Ther Allied Technol. 2013;22(4):200–9.
2. Clayman RV, Kavoussi LR, Soper NJ, Dierks SM, Merety KS, Darcy MD, Long SR, Roemer FD, Pingleton ED, Thomson PG. Laparoscopic nephrectomy. N Engl J Med. 1991;324(19):1370–1. [Case Reports Letter].
3. Abbou CC, Hoznek A, Salomon L, Lobontiu A, Saint F, Cicco A, Antiphon P, Chopin D. Remote laparoscopic radical prostatectomy carried out with a robot. Report of a case. Prog Urol. 2000;10(4):520–3. [Case Reports].
4. Skarecky DW. Robotic-assisted radical prostatectomy after the first decade: surgical evolution or new paradigm. ISRN Urol. 2013;2013:157379.
5. Finkelstein J, Eckersberger E, Sadri H, Taneja SS, Lepor H, Djavan B. Open versus laparoscopic versus robot-assisted laparoscopic prostatectomy: the European and US experience. Rev Urol. 2010;12(1):35–43.
6. Bholat OS, Haluck RS, Murray WB, Gorman PJ, Krummel TM. Tactile feedback is present during minimally invasive surgery. J Am Coll Surg. 1999;189(4):349–55. [Clinical Trial Randomized Controlled Trial Research Support, Non-U.S. Gov't].
7. De Wilde RL, Herrmann A. Robotic surgery – advance or gimmick? Best Pract Res Clin Obstet Gynaecol. 2013;27(3):457–69.
8. Lee JW, Yoon YE, Kim DK, Park SY, Moon HS, Lee TY. Renal artery injury during robot-assisted renal surgery. J Endourol. 2010;24(7):1101–4. [Case Reports].
9. Ukimura O, Okihara K, Kamoi K, Naya Y, Ochiai A, Miki T. Intraoperative ultrasonography in an era of minimally invasive urology. Int J Urol. 2008;15(8):673–80. [Review].
10. Gilbert BR, Russo P, Zirinsky K, Kazam E, Fair WR, Vaughan Jr ED. Intraoperative sonography: application in renal cell carcinoma. J Urol. 1988;139(3):582–4. [Case Reports].
11. Hangiandreou NJ. AAPM/RSNA physics tutorial for residents: topics in US B-mode US: basic concepts and new technology. Radiographics. 2003;23(4):1019–33.
12. Kolecki R, Schirmer B. Intraoperative and laparoscopic ultrasound. Surg Clin N Am. 1998;78(2):251–71. [Review].
13. Yakoubi R, Autorino R, Laydner H, Guillotreau J, White MA, Hillyer S, Spana G, Khanna R, Isaac W, Haber GP, Stein RJ, Kaouk JH. Initial laboratory experience with a novel ultrasound probe for standard and single-port robotic kidney surgery: increasing console surgeon autonomy and minimizing instrument clashing. Int J Med Robot. 2012;8(2):201–5. [Research Support, Non-U.S. Gov't].
14. Kaczmarek BF, Sukumar S, Petros F, Trinh QD, Mander N, Chen R, Menon M, Rogers CG. Robotic ultrasound probe for tumor identification in robotic partial nephrectomy: initial series and outcomes. Int J Urol. 2013;20(2):172–6.
15. Boote EJ. AAPM/RSNA physics tutorial for residents: topics in US Doppler US techniques: concepts of blood flow detection and flow dynamics. Radiographics. 2003;23(5):1315–27.
16. Mues AC, Okhunov Z, Badani K, Gupta M, Landman J. Intraoperative evaluation of renal blood flow during laparoscopic partial nephrectomy with a novel Doppler system. J Endourol. 2010;24(12):1953–6. [Clinical Trial].
17. Warren J, da Silva V, Caumartin Y, Luke PP. Robotic renal surgery: the future or a passing curiosity? Can Urol Assoc J. 2009;3(3):231–40.
18. Patil UD, Ragavan A, Nadaraj, Murthy K, Shankar R, Bastani B, Ballal SH. Helical CT angiography in evaluation of live kidney donors. Nephrol Dial Transplant. 2001;16(9):1900–4. [Comparative Study].
19. Tombul ST, Aki FT, Gunay M, Inci K, Hazirolan T, Karcaaltincaba M, Erkan I, Bakkaloglu A, Yasavul U, Bakkaloglu M. Preoperative evaluation of hilar vessel anatomy with 3-D computerized tomography in living kidney donors. Transplant Proc. 2008;40(1):47–9.
20. Hodgson DJ, Jan W, Rankin S, Koffman G, Khan MS. Magnetic resonance renal angiography and venography: an analysis of 111 consecutive scans before donor nephrectomy. BJU Int. 2006;97(3):584–6. [Evaluation Studies].
21. Holden A, Smith A, Dukes P, Pilmore H, Yasutomi M. Assessment of 100 live potential renal donors for laparoscopic nephrectomy with multi-detector row helical CT. Radiology. 2005;237(3):973–80.
22. Hyams ES, Kanofsky JA, Stifelman MD. Laparoscopic Doppler technology: applications in laparoscopic pyeloplasty and radical and partial nephrectomy. Urology. 2008;71(5):952–6.
23. Tanagho YS, Kaouk JH, Allaf ME, Rogers CG, Stifelman MD, Kaczmarek BF, Hillyer SP, Mullins JK, Chiu Y, Bhayani SB. Perioperative complications

of robot-assisted partial nephrectomy: analysis of 886 patients at 5 United States centers. Urology. 2013; 81(3):573–9. [Multicenter Study].
24. Thiel DD. Navigating the difficult robotic assisted pyeloplasty. ISRN Urol. 2012;2012:291235.
25. Mathew A, Devesa SS, Fraumeni Jr JF, Chow WH. Global increases in kidney cancer incidence, 1973–1992. Eur J Cancer Prev. 2002;11(2):171–8.
26. Kane CJ, Mallin K, Ritchey J, Cooperberg MR, Carroll PR. Renal cell cancer stage migration: analysis of the National Cancer Data Base. Cancer. 2008; 113(1):78–83.
27. Gill IS, Kavoussi LR, Lane BR, Blute ML, Babineau D, Colombo Jr JR, Frank I, Permpongkosol S, Weight CJ, Kaouk JH, Kattan MW, Novick AC. Comparison of 1,800 laparoscopic and open partial nephrectomies for single renal tumors. J Urol. 2007;178(1):41–6. [Comparative Study Multicenter Study].
28. Patel HD, Mullins JK, Pierorazio PM, Jayram G, Cohen JE, Matlaga BR, Allaf ME. Trends in renal surgery: robotic technology is associated with increased use of partial nephrectomy. J Urol. 2013; 189(4):1229–35.
29. Patel MN, Bhandari M, Menon M, Rogers CG. Robotic-assisted partial nephrectomy. BJU Int. 2009; 103(9):1296–311.
30. Sun MR, Wagner AA, San Francisco IF, Brook A, Kavoussi L, Russo P, Steele G, Viterbo R, Pedrosa I. Need for intraoperative ultrasound and surgical recommendation for partial nephrectomy: correlation with tumor imaging features and urologist practice patterns. Ultrasound Q. 2012;28(1):21–7. [Comparative Study].
31. Kaczmarek BF, Sukumar S, Kumar RK, Desa N, Jost K, Diaz M, Menon M, Rogers CG. Comparison of robotic and laparoscopic ultrasound probes for robotic partial nephrectomy. J Endourol. 2013;27(9): 1137–40.
32. Perlmutter MA, Hyams ES, Stifelman MD. Laparoscopic Doppler technology in laparoscopic renal surgery. JSLS. 2009;13(3):406–10.
33. Sethi AS, Regan SM, Sundaram CP. The use of a Doppler ultrasound probe during vascular dissection in laparoscopic renal surgery. J Endourol. 2009; 23(9):1377–82. [Clinical Trial].
34. Hyams ES, Perlmutter M, Stifelman MD. A prospective evaluation of the utility of laparoscopic Doppler technology during minimally invasive partial nephrectomy. Urology. 2011;77(3):617–20. [Evaluation Studies].
35. Abaza R. Initial series of robotic radical nephrectomy with vena caval tumor thrombectomy. Eur Urol. 2011;59(4):652–6. [Case Reports].
36. Lee JY, Mucksavage P. Robotic radical nephrectomy with vena caval tumor thrombectomy: experience of novice robotic surgeons. Korean J Urol. 2012;53(12): 879–82.
37. Gorodner V, Horgan S, Galvani C, Manzelli A, Oberholzer J, Sankary H, Testa G, Benedetti E. Routine left robotic-assisted laparoscopic donor nephrectomy is safe and effective regardless of the presence of vascular anomalies. Transpl Int. 2006; 19(8):636–40.
38. Horgan S, Galvani C, Gorodner MV, Jacobsen GR, Moser F, Manzelli A, Oberholzer J, Fisichella MP, Bogetti D, Testa G, Sankary HN, Benedetti E. Effect of robotic assistance on the "learning curve" for laparoscopic hand-assisted donor nephrectomy. Surg Endosc. 2007;21(9):1512–7.
39. Hubert J, Renoult E, Mourey E, Frimat L, Cormier L, Kessler M. Complete robotic-assistance during laparoscopic living donor nephrectomies: an evaluation of 38 procedures at a single site. Int J Urol. 2007; 14(11):986–9.
40. van der Meijden OA, Schijven MP. The value of haptic feedback in conventional and robot-assisted minimal invasive surgery and virtual reality training: a current review. Surg Endosc. 2009;23(6):1180–90. [Review].
41. Peters CA. Pediatric robot-assisted pyeloplasty. J Endourol. 2011;25(2):179–85. [Review].
42. Autorino R, Eden C, El-Ghoneimi A, Guazzoni G, Buffi N, Peters CA, Stein RJ, Gettman M. Robot-assisted and laparoscopic repair of ureteropelvic junction obstruction: a systematic review and meta-analysis. Eur Urol. 2014;65(2):430–52. pii: S0302-2838(13)00668-4.
43. Quillin SP, Brink JA, Heiken JP, Siegel CL, McClennan BL, Clayman RV. Helical (spiral) CT angiography for identification of crossing vessels at the ureteropelvic junction. AJR Am J Roentgenol. 1996;166(5):1125–30.
44. Braun P, Guilabert JP, Kazmi F. Multidetector computed tomography arteriography in the preoperative assessment of patients with ureteropelvic junction obstruction. Eur J Radiol. 2007;61(1):170–5. [Clinical Trial].
45. Braga LH, Pace K, DeMaria J, Lorenzo AJ. Systematic review and meta-analysis of robotic-assisted versus conventional laparoscopic pyeloplasty for patients with ureteropelvic junction obstruction: effect on operative time, length of hospital stay, postoperative complications, and success rate. Eur Urol. 2009; 56(5):848–57. [Meta-Analysis Review].
46. Bird VG, Leveillee RJ, Eldefrawy A, Bracho J, Aziz MS. Comparison of robot-assisted versus conventional laparoscopic transperitoneal pyeloplasty for patients with ureteropelvic junction obstruction: a single-center study. Urology. 2011;77(3):730–4. [Comparative Study].
47. Etafy M, Pick D, Said S, Hsueh T, Kerbl D, Mucksavage P, Louie M, McDougall E, Clayman R. Robotic pyeloplasty: the University of California-Irvine experience. J Urol. 2011;185(6):2196–200.
48. Tobis S, Venigalla S, Balakumaran K, Scosyrev E, Lloyd GL, Golijanin DJ, Joseph JV, Rashid H, Wu G. Analysis of a large single-center experience with robot-assisted pyeloplasty. Int J Urol. 2013;20(2):230–4. [Comparative Study Evaluation Studies].
49. Lowrance WT, Eastham JA, Savage C, Maschino AC, Laudone VP, Dechet CB, Stephenson RA, Scardino PT, Sandhu JS. Contemporary open and robotic

radical prostatectomy practice patterns among urologists in the United States. J Urol. 2012;187(6): 2087–92. [Research Support, N.I.H., Extramural Research Support, Non-U.S. Gov't].
50. Ficarra V, Novara G, Ahlering TE, Costello A, Eastham JA, Graefen M, Guazzoni G, Menon M, Mottrie A, Patel VR, Van der Poel H, Rosen RC, Tewari AK, Wilson TG, Zattoni F, Montorsi F. Systematic review and meta-analysis of studies reporting potency rates after robot-assisted radical prostatectomy. Eur Urol. 2012;62(3):418–30. [Meta-Analysis Review].
51. Han M, Kim C, Mozer P, Schafer F, Badaan S, Vigaru B, Tseng K, Petrisor D, Trock B, Stoianovici D. Tandem-robot assisted laparoscopic radical prostatectomy to improve the neurovascular bundle visualization: a feasibility study. Urology. 2011;77(2):502–6. [Research Support, N.I.H., Extramural Research Support, Non-U.S. Gov't].
52. Long JA, Lee BH, Guillotreau J, Autorino R, Laydner H, Yakoubi R, Rizkala E, Stein RJ, Kaouk JH, Haber GP. Real-time robotic transrectal ultrasound navigation during robotic radical prostatectomy: initial clinical experience. Urology. 2012;80(3):608–13. [Research Support, Non-U.S. Gov't].
53. Badani KK, Shapiro EY, Berg WT, Kaufman S, Bergman A, Wambi C, Roychoudhury A, Patel T. A pilot study of laparoscopic Doppler ultrasound probe to map arterial vascular flow within the neurovascular bundle during robot-assisted radical prostatectomy. Prostate Cancer. 2013;2013:810715.
54. Kuang W, Shin PR, Matin S, Thomas Jr AJ. Initial evaluation of robotic technology for microsurgical vasovasostomy. J Urol. 2004;171(1):300–3. [Comparative Study In Vitro].
55. Schiff J, Li PS, Goldstein M. Robotic microsurgical vasovasostomy and vasoepididymostomy: a prospective randomized study in a rat model. J Urol. 2004;171(4):1720–5.
56. Fleming C. Robot-assisted vasovasostomy. Urol Clin N Am. 2004;31(4):769–72. [Review].
57. Parekattil SJ, Gudeloglu A. Robotic assisted andrological surgery. Asian J Androl. 2013;15(1):67–74.
58. Greenberg SH. Doppler ultrasound for localization of testicular artery during varicocelectomy. Urology. 1981;17(5):480.
59. Cocuzza M, Pagani R, Coelho R, Srougi M, Hallak J. The systematic use of intraoperative vascular Doppler ultrasound during microsurgical subinguinal varicocelectomy improves precise identification and preservation of testicular blood supply. Fertil Steril. 2010;93(7):2396–9. [Clinical Trial].
60. Chan PT, Wright EJ, Goldstein M. Incidence and postoperative outcomes of accidental ligation of the testicular artery during microsurgical varicocelectomy. J Urol. 2005;173(2):482–4.

# TRUS of the Prostate: State of the Art

10

Osamu Ukimura, Toru Matsugasumi, and Sunao Shoji

## Background

Historically, most prostate cancers were initially detected by systematic random biopsy, either through elevated PSA or abnormal DRE. This diagnostic process used in prostate cancer was unlikely for most cancers in other organs, which are initially detected by an imaging technique. In most other cancers, detailed imaging information such as localization, contour and volume of the cancer, and its staging plays a critical role in the choice of treatment which includes organ preservation therapy. On the other hand, since the whole grand prostate has conventionally been the therapeutic target, clinicians demanded only knowledge of the presence of cancer anywhere in the prostate, and detailed visualization of the prostate cancer was not required.

However, the role of real-time transrectal ultrasonography (TRUS) has already changed. Its role is not simple guidance to sample biopsy tissue from the rough sextant portion of the prostate to determine whether cancer exists or not in the prostate. Today, the location and characteristics of the cancer are required. According to the increasing interest in avoiding treatment-related side effects with conventional radical whole grand treatment, future options in the management of clinically localized prostate cancer likely require more detailed anatomical and functional imaging to determine the most adequate management from the various options, including functional preservation whole grand therapy, active surveillance, or focal therapy to potentially control or cure the cancer while preserving function. What patients and clinicians need would be imaging to accurately visualize and stage the cancer and also to adequately guide the targeted sampling in order to distinguish aggressive from indolent cancer.

Ideal imaging may provide a detailed three-dimensional (3D) model of clinically significant cancer in the 3D space of the prostate, to provide detailed tissue characteristics (aggressiveness), and spatial location in relation to the important functional anatomy such as the prostate capsule, neurovascular bundle, or external sphincter in order to assist reliable surgical intervention. Nowadays, intraoperative image guidance is becoming an essential part of the surgical techniques for reliable image-guided surgery. Recently, TRUS guidance during radical prostatectomy has been increasingly reported [1–3].

O. Ukimura, MD, PhD (✉)
Department of Urology, Norris Cancer Center, Keck School of Medicine, University of Southern California, Los Angeles, CA, USA
e-mail: ukimura@med.usc.edu

T. Matsugasumi, MD
Department of Urology, Norris Cancer Center, University of Southern California, Los Angeles, CA, USA

S. Shoji, MD, PhD
Department of Urology, Tokai University Hachioji Hospital, Hachioji, Japan

J.C. Liao, L.-M. Su (eds.), *Advances in Image-Guided Urologic Surgery*,
DOI 10.1007/978-1-4939-1450-0_10, 

Among potential alternatives of focal therapy, cryoablation, HIFU, photodynamic therapy, and brachytherapy are all guided by real-time TRUS. Again, the role of real-time TRUS has already changed from being a simple diagnostic tool to becoming a comprehensive image guidance system, including the entire process of the management of prostate cancer from diagnosis to therapeutics and then the follow-up. This chapter focuses on the contemporary role of TRUS for image-guided urological surgery.

## Evolving Technology to Enhance Real-Time TRUS Guidance

In principle, the prostate is a mobile and deformable organ. The prostate can move due to movement in the bowel, bladder filling, or postural change [4, 5], and also it can swell by multiple needle insertions or ablative energy [6]. While external radiation therapy (EBRT) is an image-guided standard therapy for localized prostate cancer, a study demonstrated that in over half of the patients undergoing EBRT, 5 mm or greater realignment errors in the required daily realignment of the beams had occurred, to cause potential missing cancer cells and serious damage to adjacent healthy tissues [7, 8]. Also, during a 20-min EBRT session, the prostate was found to move as much as 3 mm [9]. For image-guided surgery, the real-time feedback of the real spatial location of the target organ or cancer lesion is essential. Real-time TRUS has several advantages for intraoperative use, especially to visualize the reality of the target or any intraoperative change and motion of the organ.

Recent evolving digitalized technology has significantly improved the TRUS system (Table 10.1). Firstly, a 3D image can be constructed for preoperative planning and intraoperative monitoring, and importantly, real-time 3D TRUS is now routinely available in the urological field. Secondly, not only improvement toward a higher resolutional grayscale image but also multi-parametric ultrasound functions are now available. Multi-parametric TRUS includes Doppler, elastography, contrast-enhanced imaging, and image fusion technology with other imaging modalities such as MRI (magnetic resonance imaging). Thirdly, robotic manipulation of the TRUS probe enhances accuracy in

**Table 10.1** Key points in the use of TRUS

| |
|---|
| Key point 1: role of real-time TRUS has changed |
| Role of real-time TRUS has already changed from being a simple diagnostic tool to becoming a comprehensive image guidance system, including the entire process of the management of prostate cancer from diagnosis to therapeutics and then the follow-up |
| In principle, the prostate is a mobile and deformable organ. The prostate can move due to movement in the bowel, bladder filling, or postural change, and also it can swell by multiple needle insertions or ablative energy |
| For image-guided surgery, the real-time feedback of the real spatial location of the target organ or cancer lesion is essential. Real-time TRUS has several advantages for intraoperative use, especially to visualize the reality of the target or any intraoperative change and motion of the organ |
| Key point 2: evolving technology for TRUS guidance |
| 1st, a 3D image can be constructed for preoperative planning and intraoperative monitoring, and importantly, real-time 3D TRUS probe and real-time biplane TRUS probe is now routinely available |
| 2nd, multi-parametric ultrasound functions are now available, including image fusion techniques and contrast enhancement |
| 3rd, robotic manipulation of the TRUS probe enhances accuracy with minimizing operator dependency |
| 4th, computer-assisted automated interpretation of an image potentially enhances the accuracy of tissue characterization |
| Key point 3: essential image guidance for focal therapy |
| TRUS is the most popular image guidance for urologist |
| Intraoperative feedback or navigation using real-time TRUS monitoring is the key for safety and efficacy for focal therapy of prostate cancer |
| Image fusion, contrast enhancement, and multi- parametric TRUS is a promising technology to support focal therapy strategy |

visualization, targeting, revisiting, and reconstruction of 3D images by a 2D image, resulting in the potential decrease on operator dependency. Fourthly, computer-assisted automated interpretation of an image (tissue characterization) potentially enhances the accuracy of the visualization of prostate cancer, again resulting in a potential decrease on operator dependency.

A 3D image of the prostate could be reconstructed from continuous scanning of 2D TRUS images to visualize the entire prostate by use of a magnetic tracker or mechanical robotic arm attached to the 2D (end-fire or side-fire) TRUS probe. The magnetic sensor or mechanical sensor can digitally track the spatial motion of the manipulated 2D TRUS probe. A 3D ultrasound image is more accurate, with lower variability and higher reliability, than using 2D imagery in the measurement of the prostate volume and increased sensitivity in the detection of prostate cancer [10, 11]. Biopsy and surgical planning can be enhanced by an understanding of the 3D anatomy of the prostate (including the median lobe or protrusion to the bladder) as well as the suspicious or biopsy-proven lesion, in relation to the adjacent vital anatomies such as the sphincter muscle and neurovascular bundle. A 3D image enables us to interpret the prostate anatomy in every desired direction and to confirm it using multi-planar display of the sagittal, transverse, and coronal planes simultaneously. However, the prostate motion and deformations may also be induced by the use of endorectal instruments such as the TRUS probe itself. As such, the intraoperative image of the prostate can be already different from the previously acquired reconstructed 3D image of the prostate. It should be noted that continuous intraoperative feedback using real-time imagery to recognize the reality in the therapeutic target is essential in order to improve accuracy.

A real-time 3D TRUS image can be obtained using a specific end-fire 3D TRUS probe to scan the entire prostate automatically in only 3 s by freehand without any tracking system. This unique real-time 3D TRUS probe can enhance the accuracy of 3D registration of the biopsy trajectories in the digitalized volume data of the prostate [12]. The real-time 3D TRUS imaging to acquire a hyperechoic image of the metallic biopsy needle indwelling in the real 3D prostate could precisely register the spatial location of each biopsy in the prostate as a reality. Such information would be critical to develop reliable revisiting confirmatory biopsy in the active surveillance protocol, as well as to establish a clinically successful focal therapy protocol by precise 3D localization of the biopsy-proven cancer [13].

Recently, updated utility of Doppler and elastography have been increasingly reported. An important shortcoming of current systematic prostate biopsies is that they are most often image-blind procedures; in other words, they are unlikely to target any TRUS-visible lesions. However, when comparing TRUS-visible with image-invisible index lesions, the cancer-involved core lengths were 6.1 versus 1.5 mm ($P<0.001$), respectively. Image visibility of prostate cancer allows the precise targeting of cancer and leads to a better characterization of tumor extent. Furthermore, targeted biopsies may enhance the appropriate selection of patients for active surveillance as well as focal therapy, augment the precision of targeted treatment, and provide an image-integrated monitoring protocol [14].

Contrast TRUS has shown promising results in cancer detection with improved accuracy of targeted biopsy. It may be useful for monitoring therapeutic effect for tissue preservation therapy as well as surveillance of local recurrence after treatment. This technology is based on the development of contrast enhancers and the computerized analysis of the pharmacokinetics of the contrast enhancement pattern. A major limitation of the widespread use of contrast TRUS was the difficulty in scanning and analyzing the entire prostate at the best timing of contrast enhancement, if using 2D TRUS; however, the introduction of a real-time 3D TRUS probe would provide a novel opportunity for simultaneous analysis of the entire prostate at the best timing of contrast enhancement. Nowadays, multi-sectional documentation of the early, middle, and late phase of contrast enhancement as well as pharmacokinetic analysis is available for contrast TRUS techniques, making them similar to contrast CT or MRI [15].

Image fusion technology has proved to enhance the image-targeted biopsy and potentially improve intraoperative targeting [13]. Multimodal MRI is emerging as a more reliable modality to detect clinically significant prostate cancer [16]. TRUS/MRI fusion image guidance could potentially increase the spatial accuracy of targeted biopsy or targeted focal intervention. However, this requires multiple steps including image acquisition, segmentation, image fusion, biopsy, and confirmation of biopsy trajectory. There are potential errors in each of these steps. It should be noted that since the MR-fused lesion is only a virtual image, the fundamental question is whether the virtual lesion biopsied was even in fact the real MR lesion. A recent study showed that when an MR lesion is TRUS visible, MR/US-targeted biopsy enhances the detection of clinically significant cancer [16]. This suggests that TRUS is important because the TRUS image is real, not virtual. When using TRUS/MR fusion for real-time guidance, it is important for the operator not to look at the virtual MR image but to look at the real-time TRUS image which is likely to have an ultrasound sign (such as hypoechoic lesion) corresponding with the MR suspicious lesion. The fused MR image should be used as a reference, not the real target. The reality of the target is always shown in the real-time image of TRUS.

Image fusion techniques also open the new opportunity to use augmented reality navigation for surgical guidance [17]. The surgical planning generally starts with the surgeon's consideration of the preoperative image together with the pathology of the biopsy. For intraoperative guidance, a 3D surgical model can be developed from the preoperative image as well as intraoperatively acquired images. In the operating room, this information is registered and overlaid onto the real-time endoscopic surgical view, to display the superimposed images of the 3D model on the display of the surgical view, using an intraoperative position sensor system which typically consists of ultrasound, CT, MRI, and 3D localization (laser, magnetic, or optical) system [17]. If necessary when the target organ moves or deforms, the surgical plan can be updated using the intraoperative real-time image.

Robotic control of the TRUS probe enhances the digitalized documentation of the trajectory of the positive biopsy, to achieve precise revisiting therapeutic delivery toward the biopsy-proven cancer [18]. Once the spatial location of the biopsy-proven cancer has been determined as a digitalized product of coordinates from (x1, y1, z1) to (x2, y2, z2), targets and needle paths are defined based on both real-time image and coordinates according to planning algorithms, and the robot can align the angle and depth and can direct the needle toward the specific point. The determination of the specific point with coordinates of (x1, y1, z1) in the 3D space needs to be determined using at least two crossing planes of real-time TRUS images. Therefore, a simultaneous biplane TRUS probe is also promising. As such, intraoperative guidance using real-time 3D or biplane TRUS probe would enhance the precision of the TRUS intervention.

The shortcoming of conventional grayscale ultrasound imagery for diagnosis of prostate cancer is the interobserver variability or operator dependency. Although a highly experienced expert can detect the majority of clinically significant cancers, a novice using conventional grayscale TRUS may have difficulty in discriminating between benign versus malignant nodules. A computerized analysis of tissue characterization can automate the contouring process of suspicious lesions according to algorithms based on the classification system of the signals. Since the computerized tissue characterization can include the invisible signs such as radiofrequency signals in addition to visible ultrasound signals, it may also be helpful to the expert.

## Role of Real-Time TRUS Guidance for Ablative Intervention of the Prostate

TRUS-guided brachytherapy is an established procedure, with further recent advancements from evolved technologies (Table 10.1). In recent years, many advances have been made in

3D-reconstructed TRUS imagery [19]. They include boundary segmentation [20], pubic arch detection [21], needle segmentation, and seed segmentation [22]. These advances in brachytherapy have greatly enhanced the role of TRUS in image-guided surgery. In the same time period, initial robot-assisted TRUS intervention has been developed [23]. Since a robot can achieve precise position, orientation, and manipulation of surgical tools along the various trajectories in the 3D space, the medical robotic system is increasingly gaining interest in image-guided intervention. Such precision of the robotic delivery is supported digitally, dynamically programmed by computer workstation, and effectively integrated with the real-time TRUS navigation system to allow reconstruction of the 3D prostate.

Photodynamic therapy is another promising transperineal surgical approach that could be suitable for TRUS image-guided surgery of organ-confined prostate cancer [24–26]. A recent study in 85 patients using TOOKAD® soluble vascular targeted photodynamic therapy demonstrated it was a well-tolerated and effective therapy and followed by a phase III multicenter study in the form of hemi-ablation [26].

The initial medical use of ultrasonic waves was investigated in the 1950s [27], and the use of HIFU in the treatment of prostate cancer began in the 1990s with a pulsed ultrasound beam to generate heat sufficient to cause necrosis [28]. The ultrasound waves penetrate through the rectal wall with only minimum absorption of energy and reflection of the beam in it, but are centered on the focus point in the prostate. Current commercially available endorectal HIFU machines provide simultaneous TRUS imaging and therapeutics. The step-sectional transverse TRUS images are used to plan a treatment, including identifying the prostate boundary, neurovascular bundle, sphincter, urethra, bladder neck, and rectal wall for maximizing safety and efficacy. HIFU treatment automatically follows the predetermined computerized program which fits the individual anatomy of the prostate. During the procedure, according to potential movement in the bowels or positional change, it may be required to adjust the thickness of the water-filled balloon of the TRUS probe or readjustment of the location of the TRUS probe itself. The HIFU procedures can all be documented with each treated focus registered and overlaid on each step-sectional TRUS image, which can be reviewed for future reference in order to determine the potential requirement of additional therapeutics in addition to the initial plan. Since the prostate swells intraoperatively due to edema or inflammation, the shift of the prostate or targeted lesion needs to be taken into account to enhance efficacy [6]. Again, intraoperative feedback or navigation using real-time TRUS monitoring as well as following a specifically programmed safety system is the key for safety and efficacy.

Real-time biplane TRUS guidance is essential for performing modern cryosurgery for prostate cancer. Accurate TRUS measurement of the dimension of the prostate and identification of the anatomical relation to the adjacent organs are important initial steps for surgical planning of where and how big to create the ice ball. Real-time image guidance using both transverse and sagittal views is needed for precise cryoprobe and thermocouple placement and also essential for monitoring the freezing extension to achieve efficient ablation as well as prevent complications such as rectal injury. For reliable tissue destruction of cancers, freezing temperatures must reach certain critical limits (such as –40 °C or lower), which are monitored in real time by the thermocouples placed in the critical points, such as in the targeted tumor, sphincter, neurovascular bundle, and Denonvilliers space.

With the recent advent of the focal therapy of prostate cancer, TRUS image guidance for localizing biopsy-proven cancer and precise therapeutic targeting have become extremely important in patient care [24, 29]. Since the inadequate limited space between the prostate and the rectal wall involves the risk of rectal injury, the surgeon may hesitate to achieve adequate extension of freezing beyond the posterior margin of the prostate to result in inadequate cancer control if the cancer is located close to the posterior margin of the prostate.

The search to establish a reliable technique to protect the rectal wall from any thermal energy

continues in order to establish safety in ablative therapy for prostate cancer in contact with the posterior prostatic surface. Using hydrogel (polyethylene glycol, named a "spacer") was investigated for developing a technique of expansion of the Denonvilliers space during focal cryoablation and also temperature mapping to secure protection of the rectal wall [30–32]. The application seems promising, when delivered precisely in the Denonvilliers space by TRUS guidance.

## Role of TRUS in the Era of Endoscopic Surgery and Robotic Surgery

Intraoperative TRUS guidance during open radical prostatectomy (RP) was first reported by Zisman et al. in 1997. Since RP is associated with difficulty in determining the division site of the urethra adjacent to the apical region of the prostate, Zisman et al. demonstrated the utility of intraoperative TRUS guidance that assisted to identify the apex contour and a detailed view of the urethral stump and also to identify the residual apical tissue to perform complete excision of the prostate [33]. During minilaparotomy RP, Okihara et al. reported that application of TRUS resulted in a lower rate of positive margins and a longer postoperative membranous urethral length to be associated with an earlier return to urinary continence [2].

Intraoperative TRUS guidance during laparoscopic RP has been increasingly reported since 2004 [1, 3, 34–37]. The eventual goal of TRUS image guidance is to enhance the oncological and functional outcome of the laparoscopic approach even under limited tactile feedback in comparison to the open approach. TRUS guidance during laparoscopic RP appeared to be helpful for various technical aspects including (a) defining prostate apex contour, (b) identifying the bladder neck which was blind in the surgical view, (c) evaluating location and extent of the hypoechoic biopsy-proven cancer nodule, (d) identifying the neurovascular bundles in relation to the posterior laterally located cancer nodule. When identifying the higher risks of microscopic extra-prostate extension of the cancer, it may offer the surgeon the possibility of performing calibrated wider dissection at the site of the extra-prostate extension of the cancer nodule in order to achieve a negative margin, while maximizing preservation of the neurovascular bundle during lateral pedicle transection. According to the individual contour of the apex in relation to the sphincter, TRUS guidance may offer tailored apical dissection, to maximize the preservation of the membranous urethra and sphincter muscle. Comparing without versus with TRUS guidance, positive surgical margins significantly decreased in patients with pT3 disease (57 % versus 18 %, $p=0.002$) [1].

Since robotic-assisted laparoscopic RP has a complete loss of tactile feedback, a more image-guided approach would be beneficial [38]. There is increasing interest in applying image guidance including the use of TRUS, the laparoscopic ultrasound probe, and the miniature drop-type ultrasound probe.

In the da Vinci S System (intuitive Surgical, Sunnyvale, CA), tile-pro system enables the display of two extra images referenced simultaneously with the 3D surgical endoscopic view. In 2008 van der Poel et al. reported real-time TRUS image-guided bladder neck dissection for facilitating the learning of robotic-assisted RP during its initial experience, to result in improved oncological outcomes [38]. The basal surgical margins (bladder neck and basal areas of both prostate lobes) were positive for cancer in 9.1 % versus 2.3 % of patients treated without versus with real-time TRUS guidance ($p=0.001$).

Furthermore, recent researchers have developed various new robotic arms for automated manipulation of the TRUS probe to enable robotic control of TRUS image navigation during robotic-assisted RP [39–41]. The previous approach required an assistant to manipulate or reposition the TRUS probe inserted in the rectum, and also there is only limited space between the patient's legs in the lithotomy position for the assistant to access for manipulating the TRUS probe after the robot has been docked. However, the novel robotic arm for holding the TRUS probe provides a new opportunity to allow self-control image guidance by the console surgeon himself. When applying robotic control of the

TRUS probe, automatic registration of the kinematic frames of the da Vinci surgical system and the robotic TRUS probe manipulator is critical in order to register real-time TRUS images to the da Vinci system. Mohareri et al. recently reported an automatic registration technique based on automatic 3D TRUS localization of the robot instrument tips pressed against the air–tissue boundary anterior to the prostate [42].

Instead of using a TRUS probe, another approach for intraoperative ultrasound monitoring during robotic-assisted RP uses a laparoscopic ultrasound probe [43] or dropped mini US probe [44]. Using a laparoscopic ultrasound probe, elastography guidance may have higher accuracy and specificity in tumor detection, localization, and measuring of diameters and depths of the tumor [43]. A drop-type mini US probe is available for the surgeon to manipulate the US probe directly by a robotic arm [44]. The console surgeon's direct manipulation of the drop-type US probe may facilitate the recognition of the bladder neck as well as localization of the biopsy-proven hypoechoic cancer.

These new approaches for real-time ultrasound guidance could enhance the precision of image-guided robotic-assisted surgery by providing an understanding of the blinded anatomy or pathology beyond the endoscopic surgical view.

## References


1. Ukimura O, Magi-Galluzzi C, Gill IS. Real-time transrectal ultrasound guidance during laparoscopic radical prostatectomy: impact on surgical margins. J Urol. 2006;175(4):1304–10.
2. Okihara K, Kamoi K, Kanazawa M, et al. Transrectal ultrasound navigation during minilaparotomy retropubic radical prostatectomy: impact on positive margin rates and prediction of earlier return to urinary continence. Int J Urol. 2009;10:820–5.
3. Azuma H, Ibuki N, Inamoto T, et al. Utility of transrectal ultrasonography guidance and seven key elements of operative skill for early recovery of urinary continence after laparoscopic radical prostatectomy. Int J Oncol. 2011;38(2):293–304.
4. Melian E, Mageras GS, Fuks Z, et al. Variation in prostate motion: quantification and implications for three-dimensional conformal radiation therapy. Int J Radiat Oncol Biol Phys. 1997;38(1):73–81.
5. Schild S, Casale HE, Bellefontaine L. Movements of the prostate due to rectal and bladder distension: implication for radiotherapy. Med Dosim. 1993;18(1):13–5.
6. Shoji S, Uchida T, Nakamoto M, et al. Prostate swelling and shift during high intensity focused ultrasound: implication for targeted focal therapy. J Urol. 2013;190(4):1224–32.
7. Lattanzi J, McNeeley S, Pinover W, et al. A comparison of daily CT localization to a daily ultrasound-based system in prostate cancer. Int J Radiat Oncol Biol Phys. 1999;43(4):719–25.
8. Lattanzi J, McNeeley S, Donnelly S, et al. Ultrasound-based stereotactic guidance in prostate cancer–quantification of organ motion and set-up errors in external beam radiation therapy. Comput Aided Surg. 2000;5(4):289–95.
9. Artignan X, Rastkhah M, Balosso J, et al. Quantification of prostate movements during radiotherapy. Cancer Radiother. 2006;10(6–7):381–7.
10. Tong S, Cardinal HN, McLoughlin RF, et al. Intra- and inter-observer variability and reliability of prostate volume measurement via two-dimensional and three-dimensional ultrasound imaging. Ultrasound Med Biol. 1998;24(5):673–81.
11. Sedelaar JP, van Roermund JG, van Leenders GL, et al. Three-dimensional grayscale ultrasound: evaluation of prostate cancer compared with benign prostatic hyperplasia. Urology. 2001;57(5):914–20.
12. Ukimura O, Desai M, Palmer S, et al. Three-dimensional elastic registration system of prostate biopsy location by real-time 3-dimensional transrectal ultrasound guidance with magnetic resonance/transrectal ultrasound image fusion. J Urol. 2012;187:1080–6.
13. Ukimura O, Faber K, Gill IS. Intraprostatic targeting. Curr Opin Urol. 2012;22(2):97–103.
14. Ukimura O, de Castro Abreu AL, Gill IS, et al. Image visibility of cancer to enhance targeting precision and spatial mapping biopsy for focal therapy of prostate cancer. BJU Int. 2013;111(8):354–64.
15. Kuenen MP, Saidov TA, Wijkstra H, et al. Contrast-ultrasound dispersion imaging for prostate cancer localization by improved spatiotemporal similarity analysis. Ultrasound Med Biol. 2013;39(9):1631–41.
16. Ukimura O, Coleman JA, de la Taille A, Emberton M, Epstein JI, Freedland SJ, Giannarini G, Kibel AS, Montironi R, Ploussard G, Roobol MJ, Scattoni V, Jones JS. Contemporary role of systematic prostate biopsies: indications, techniques, and implications for patient care. Eur Urol. 2013;63(2):214–30.
17. Ukimura O, Gill IS. Image-fusion, augmented reality, and predictive surgical navigation. Urol Clin North Am. 2009;36(2):115–23.
18. Ukimura O, Hung AJ, Gill IS. Innovations in prostate biopsy strategies for active surveillance and focal therapy. Curr Opin Urol. 2011;21(2):115–20.
19. Fenster A, Downey DB, Cardinal HN. Three-dimensional ultrasound imaging. Phys Med Biol. 2001;46(5):R67–99.

20. Shen D, Zhan Y, Davatzikos C. Segmentation of prostate boundaries from ultrasound images using statistical shape model. IEEE Trans Med Imaging. 2003;22(4):539–51.
21. Haberman K, Pathak SD, Kim Y. Effects of video digitization in pubic arch interference assessment for prostate brachytherapy. IEEE Trans Inf Technol Biomed. 2003;7(1):8–15.
22. Ding M, Wei Z, Gardi L, et al. Needle and seed segmentation in intra-operative 3D ultrasound-guided prostate brachytherapy. Ultrasonics. 2006;22(44 Suppl 1):e331–6.
23. Wei Z, Ding M, Downey D, et al. 3D TRUS guided robot assisted prostate brachytherapy. Med Image Comput Comput Assist Interv. 2005;8(Pt 2):17–24.
24. Windahl T, Andersson SO, Lofgren L. Photodynamic therapy of localised prostatic cancer. Lancet. 1990;336(8723):1139.
25. Nathan TR, Whitelaw DE, Chang SC, et al. Photodynamic therapy for prostate cancer recurrence after radiotherapy: a phase I study. J Urol. 2002;168(4 Pt 1):1427–32.
26. Azzouzi AR, Barret E, Moore CM, et al. TOOKAD® Soluble Vascular Targeted Photodynamic (VTP) therapy: determination of optimal treatment conditions and assessment of effects in patients with localised prostate cancer. BJU Int. 2013;112(6):766–74.
27. Fry WJ, Barnard JW, Fry EJ, et al. Ultrasonic lesions in the mammalian central nervous system. Science. 1955;122(3168):517–8.
28. Gelet A, Chapelon JY, Bouvier R, et al. Treatment of prostate cancer with transrectal focused ultrasound: early clinical experience. Eur Urol. 1996;29(2): 174–83.
29. Bahn D, de Castro Abreu AL, Gill IS, et al. Focal cryotherapy for clinically unilateral, low-intermediate risk prostate cancer in 73 men with a median follow-up of 3.7 years. Eur Urol. 2012;62(1):55–63.
30. Hatiboglu G, Pinkawa M, Vallée JP, et al. Application technique: placement of a prostate-rectum spacer in men undergoing prostate radiation therapy. BJU Int. 2012;110(11 Pt B):E647–52.
31. Eckert F, Alloussi S, Paulsen F, et al. Prospective evaluation of a hydrogel spacer for rectal separation in dose-escalated intensity-modulated radiotherapy for clinically localized prostate cancer. BMC Cancer. 2013;13:27.
32. de Castro Abreu AL, Ma Y, Shoji S, et al. Denonvilliers' space expansion by transperineal injection of hydrogel: implications for focal therapy of prostate cancer. Int J Urol. 2014;21(4):416–8. doi:10.1111/iju.12290.
33. Zisman A, Strauss S, Siegel YI, et al. Transrectal ultrasonographically assisted radical retropubic prostatectomy. J Ultrasound Med. 1997;16(12):777–82.
34. Ukimura O, Gill IS, Desai MM, et al. Real-time transrectal ultrasonography during laparoscopic radical prostatectomy. J Urol. 2004;172(1):112–8.
35. Ukimura O, Gill IS. Real-time transrectal ultrasound guidance during nerve sparing laparoscopic radical prostatectomy: pictorial essay. J Urol. 2006;175(4): 1311–9.
36. Haber GP, Aron M, Ukimura O, et al. Energy-free nerve-sparing laparoscopic radical prostatectomy: the bulldog technique. BJU Int. 2008;102(11):1766–9.
37. Mizutani Y, Uehara H, Fujisue Y, et al. Urinary continence following laparoscopic radical prostatectomy: association with postoperative membranous urethral length measured using real-time intraoperative transrectal ultrasonography. Oncol Lett. 2012; 3(1):181–4.
38. van der Poel HG, de Blok W, Bex A, et al. Peroperative transrectal ultrasonography-guided bladder neck dissection eases the learning of robot-assisted laparoscopic prostatectomy. BJU Int. 2008;102(7):849–52.
39. Han M, Kim C, Mozer P, et al. Tandem-robot assisted laparoscopic radical prostatectomy to improve the neurovascular bundle visualization: a feasibility study. Urology. 2011;77(2):502–6.
40. Long JA, Lee BH, Guillotreau J, et al. Real-time robotic transrectal ultrasound navigation during robotic radical prostatectomy: initial clinical experience. Urology. 2012;80(3):608–13.
41. Hung AJ, Abreu AL, Shoji S, et al. Robotic transrectal ultrasonography during robot-assisted radical prostatectomy. Eur Urol. 2012;62(2):341–8.
42. Mohareri O, Ramezani M, Adebar TK, et al. Automatic localization of the da Vinci surgical instrument tips in 3-D transrectal ultrasound. IEEE Trans Biomed Eng. 2013;60(9):2663–72.
43. Fleming IN, Kut C, Macura KJ, et al. Ultrasound elastography as a tool for imaging guidance during prostatectomy: initial experience. Med Sci Monit. 2012;18(11):CR635–42.
44. Shoji S, Abreu AL, Leslie S, et al. Intraoperative ultrasonography with a surgeon manipulated micro transducer during robotic radical prostatectomy. In J Urol. 2014;21:736–9.

# Ultrasound-Guided Prostate Cryotherapy

11

Kathleen F. McGinley, Bryce W. Polascik, and Thomas J. Polascik

The technologies and applications of cryotherapy in the management of prostate cancer continue to evolve. From humble beginnings in the 1960s with Dr. Gonder, who developed a vacuum-insulated probe inserted transurethrally to treat the prostate and used the surgeon's finger within the rectal vault to afford protection against rectal freezing, to third-generation modern cryotherapy probes with transrectal ultrasound imaging and thermocouples, the safety, efficacy, and role of cryotherapy has developed [1]. Per the American Urologic Association's Best Practice Statement on Cryosurgery, primary prostate cryosurgery is a therapeutic option for the management of clinically organ-confined disease of any grade with a negative metastatic evaluation; salvage cryosurgery can be considered as a treatment option for curative intent in men who have failed radiation therapy for primary management of their disease [2]. Following appropriate patient selection, delivery of effective cryotherapy is predicated upon a thorough understanding of normal prostate anatomy on ultrasound and recognition of the essential visual cues that arise during the procedure to further direct therapy.

K.F. McGinley, DO • B.W. Polascik • T.J. Polascik, MD, FACS (✉)
Division of Urology, Department of Surgery, Duke University Medical Center, Durham, NC, USA
e-mail: kathleen.mcginley@dm.duke.edu; thomas.polascik@duke.edu

## Using Transrectal Ultrasound to Define Pelvic Anatomy Prior to Treatment

After the transrectal ultrasound probe is placed, the first step is to survey the pelvic structures. This serves several useful functions. First, it provides an opportunity for the operator to study the ultrasonographic appearance of the pelvic structures and their relationship to one another. It is amazing how each patient's particular anatomy can be unique, and the surgeon has the chance to appreciate these subtleties. For example, it is important to understand the spatial relationship of the seminal vesicles to the prostate. In some men, the seminal vesicles remain superior to the prostate, while in others they are located posterior to the prostate and can insert quite distally. Another area to appreciate is the relationship of the apex of the prostate to the rectal wall and urinary sphincter.

Second, recognizing the spatial relationship among these critical structures will provide the surgeon with an anatomical map to avoid or minimize inadvertent injury to surrounding tissue. Third, normal versus aberrant anatomy can often be identified with transrectal ultrasonography. For example, the course of the urethra can vary between patients and needs to be appreciated in order to avoid placing the cryoprobes too close to this structure. Finally, real-time ultrasound using Doppler allows the surgeon to identify and locate the neurovascular bundles prior to treatment.

J.C. Liao, L.-M. Su (eds.), *Advances in Image-Guided Urologic Surgery*,
DOI 10.1007/978-1-4939-1450-0_11, 

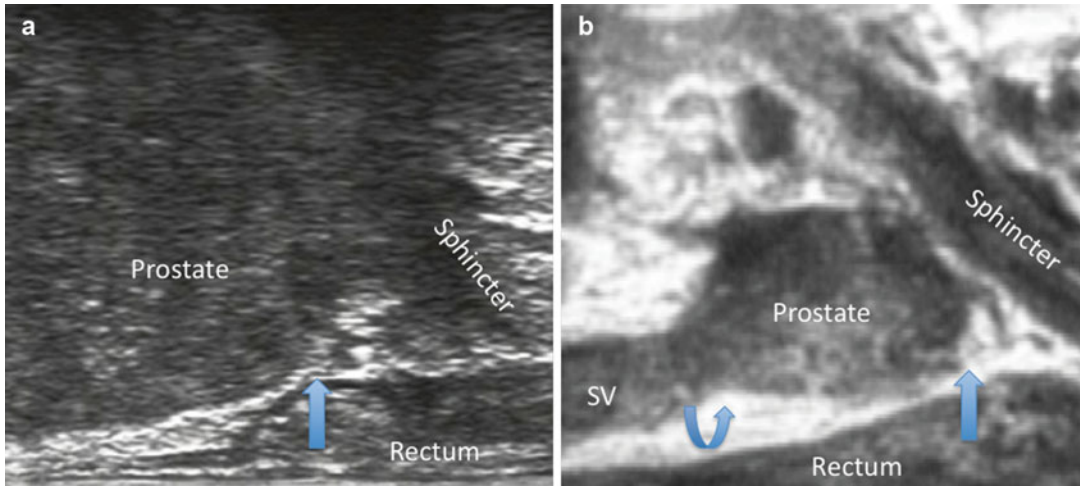


**Fig. 11.1** (**a**) Sagittal view of the prostatic apex. In this view near the midline of the prostate, the structures can be challenging to distinguish. (**b**) Sagittal view of the lateral aspect of the prostate. When one rolls the ultrasound laterally away from the midline, often these three structures [prostatic apex, rectum, and sphincter] are more readily distinguishable

## Defining the Prostatic Apex

Figure 11.1a shows three important structures and their relationship to one another: the prostatic apex, the rectal wall, and the urinary sphincter. Upon first view, the location of the apex might not be clear to the novice as there could be some temptation to confuse the sphincter as the distal-most aspect of the prostate. However, note that Denonvilliers fascia is bright (hyperechoic) as it is comprised largely of adipose tissue, and this provides contrast between the other isoechoic structures. When viewing the image from the bottom left, one sees that the hyperechoic fat of Denonvilliers fascia angles anteriorly, thereby denoting the true prostatic apex (blue arrow). The urinary sphincter can be seen merging with the rectal wall.

When one wishes to better define the apex of the prostate, the urinary sphincter, and the rectal wall, it is best to angle the transducer slightly away from the midline toward the lateral aspect (Fig. 11.1b). In this case, the anatomy is well delineated as the patient has an abundance of hyperechoic fat surrounding these structures. The prostatic apex is denoted by the arrow. Also note the junction between the prostate and seminal vesicle (curved arrow).

## Defining the Course of the Urethra

It is interesting to note the variations in the course of the urethra among men. In general, the urethra tends to be located within the middle of the prostate from a horizontal or transverse perspective; however, in the anterior-posterior view, there is much variation. The urethra is apt to have an "S-shaped" curve that can deviate to various degrees along the *Y*-axis (Fig. 11.2a). For this reason, it is better to keep all cryoprobes sufficiently away from the urethra in order to avoid inadvertent injury (Fig. 11.2b). Many cryosurgeons avoid a segment of tissue both anterior and posterior to the urethra referred to as the "urethral zone." Probes should rarely be placed in this area; rather, it is better to move the probes laterally outside the urethral zone to avoid inadvertent injury or a subsequent prostatic urethral slough.

Figure 11.3a displays a sagittal view of the prostate, with the posterior urethra at the base of the prostate in its normal expected position. However, toward the prostatic apex, the urethra courses anteriorly significantly. This observation is important as treatment probes need to stay away from the course of the urethra. Similarly, on the transverse view, note how anteriorly displaced the urethra is in the mid-prostate (Fig. 11.3b).

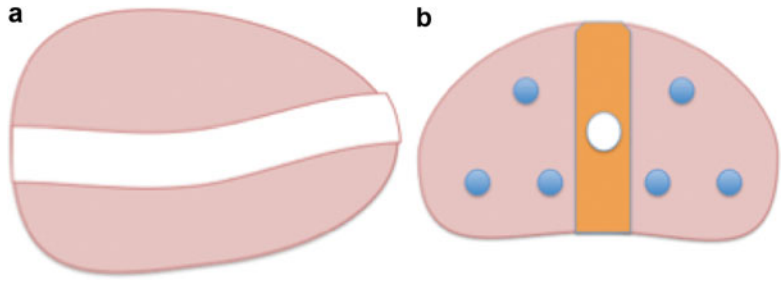


**Fig. 11.2** (**a**) Drawing depicting the natural "S-shaped" curve of the urethra when viewed sagittally. There is much variation in the course of the urethra among men. (**b**) Transverse view of the prostate depicting the "urethral zone" as highlighted in orange. It is best to keep the cryotherapy probes outside of the urethral zone to avoid injury. In this figure, the cryoprobes (*blue circles*) are placed around, but not within, the urethral zone

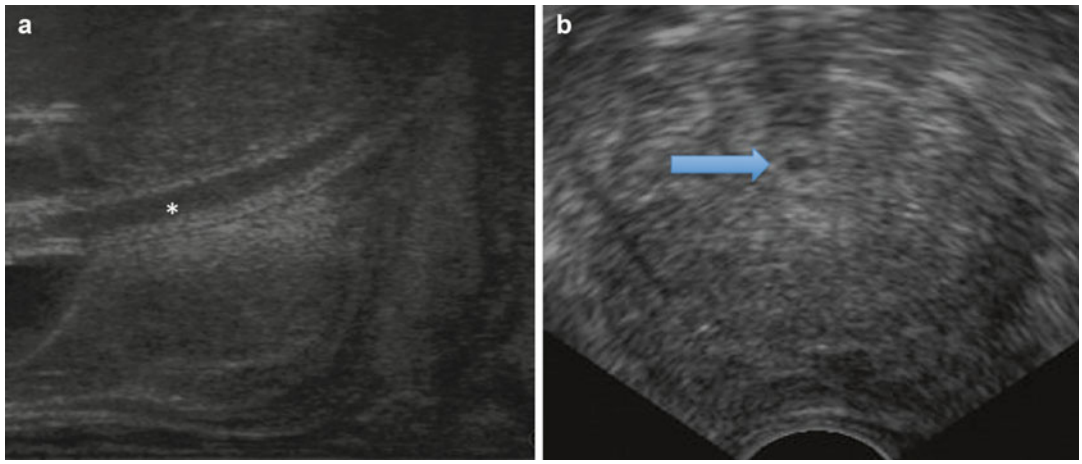


**Fig. 11.3** (**a**) Sagittal, midline view of the prostate with an indwelling Foley catheter (*white asterisk*) within the urethra. (**b**) Transverse view of the mid-prostate with the urethra displaced anteriorly (*blue arrow*)

## Setting the Amount of Compression by the Transrectal Ultrasound Probe

Before one begins to apply energy to treat the prostate, one needs to ensure that Denonvilliers space is sufficiently wide and that there is not undue compression of the prostate by the ultrasound probe. Figure 11.4a shows a transverse view of the prostate. Note that there is too much compression by the transrectal ultrasound probe on the posterior capsule of the prostate causing the lateral wings to appear to deviate further posteriorly (the "Mickey Mouse ears" sign). Actually, the exaggerated compression in the midline (large arrow) is causing the left and right segments of the prostate (small arrows) to move offscreen. Also note that the Foley catheter (white asterisk) is marked by two hyperechoic lines in addition to some reverberations and shadowing seen anteriorly. The urethra has a slight deviation to the patient's right (left of the screen). Finally, the separation between the transition zone and the peripheral zone is readily apparent (curved arrow).

In Fig. 11.4b, the transrectal ultrasound probe has been dropped further posteriorly so that there is not problematic compression of the transrectal ultrasound on the posterior prostate as evidenced by a very thick, non-compressed isoechoic rectal wall and a generous fat-laden (hyperechoic) Denonvilliers space (black asterisk). Also note that the seminal vesicle (SV) is inserting midway along the sagittal length of the prostate.

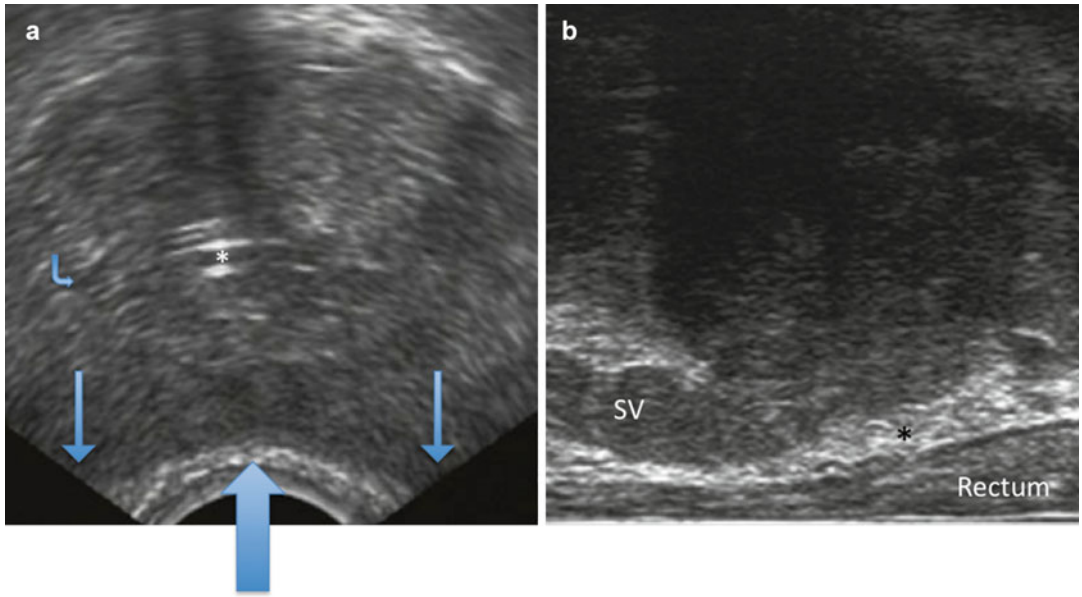


**Fig. 11.4** (**a**) Transverse view of the mid-prostate. (**b**) Sagittal view of the prostate

## Ultrasound Identification of the Seminal Vesicles

The insertion of the seminal vesicles and associated ducts along the sagittal length of the prostate can vary between patients. In Fig. 11.4b, note that this patient's seminal vesicle is easily identified as it is surrounded by hyperechoic fat within Denonvilliers fascia and also between the anterior seminal vesicle and the posterior wall of the prostate. This seminal vesicle inserts quite distally toward the apex. It is important to appreciate this on a sagittal view as when one is treating the prostate with cryotherapy and the ice is approaching the rectum as viewed sagittally, one needs to know where the edge of the prostate capsule is compared to the seminal vesicle. In this particular patient, cryotherapy would freeze a significant portion of the seminal vesicle length that is anterior to the rectal wall.

Figure 11.5a shows a transverse view of the prostate and the seminal vesicles taken between the mid-prostate and the base. The seminal vesicles are relatively hypoechoic as these are fluid-filled structures, which contrast the isoechoic nature of the dense parenchyma comprising the prostate. The posterior prostate and seminal vesicles are separated by a hyperechoic rim of adipose tissue within Denonvilliers fascia. Note the characteristic ultrasound appearance of the Foley within the urethra represented as two hyperechoic horizontal lines and the resultant shadowing in the far field. Again, it is important to appreciate these subtleties as when one is dropping the ice front posteriorly toward the rectal wall, one needs to be able to distinguish where the prostate ends and any tissue that might represent the seminal vesicles.

Figure 11.5b shows a transverse ultrasound section of the prostate taken further toward the apex in the same patient. In this transverse view of the mid-prostate, one may initially think that they see the posterior capsule; however, the hypoechoic structures (arrow) sitting just anterior to the rectum are remnants of the seminal vesicles and associated ducts. Note also in this patient that the urethra is perfectly midline.

## Localizing the Neurovascular Bundles

For some patients who are interested in attempting to preserve erectile function, localizing the neurovascular bundles before treatment is necessary. The neurovascular bundles can usually be found at 5 and 7 o'clock on the posterolateral surfaces of the prostate bilaterally. Color Doppler, or

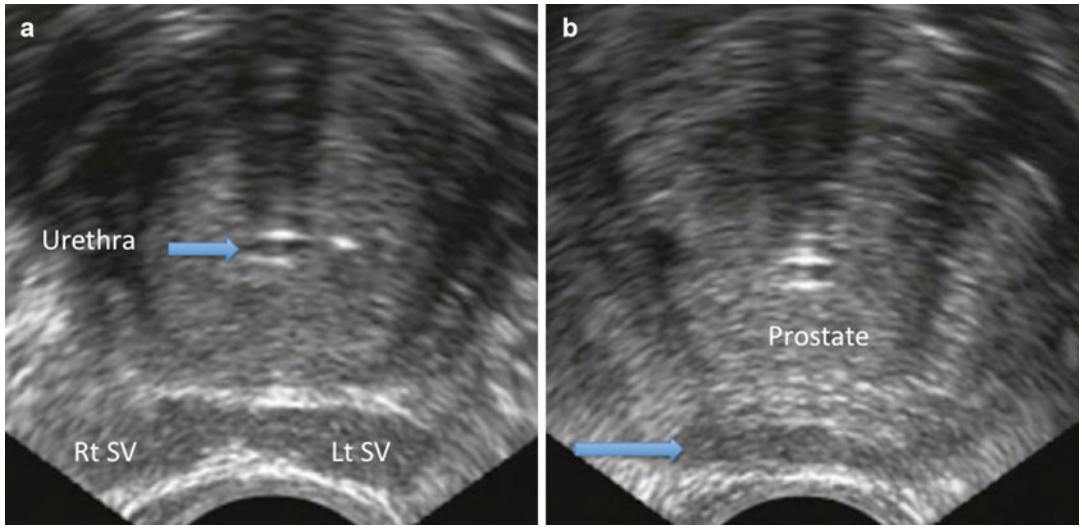


**Fig. 11.5** (**a**) Transverse view of the prostate showing relationship to left and right seminal vesicles and the catheterized urethra. (**b**) Transverse view of the prostate still shows a segment of the seminal vesicles and associated ducts posteriorly, as indicated at the level of the *blue arrow*

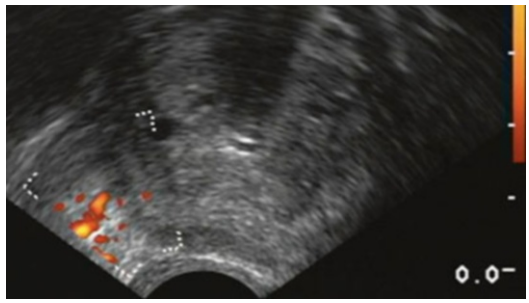

**Fig. 11.6** Transverse view of the prostate and the right neurovascular bundle using power Doppler. Note the characteristic appearance of the urethra containing a catheter and the acoustical shadowing seen beyond it

alternatively power Doppler, can be utilized to pinpoint these important structures.

Figure 11.6 demonstrates the right neurovascular bundle as highlighted with power Doppler. Also note that the hypoechoic area just anterior to the rectal wall represents the most distal aspects of the seminal vesicles and associated ducts, not the prostate.

## Incomplete Ablation of the Prostate

The premise of prostate cryoablation is that all parenchymal tissue will be effectively treated within the intended zone of ablation. A number of reasons for incomplete ablation, often inadvertent, of segments of the prostate are possible. Clinically, inadequate ablation can be identified by persistent prostate-specific antigen (PSA) after treatment (biochemical persistence) or by a positive post-treatment biopsy demonstrating malignancy. Since prostate cryotherapy is not intended to ablate the entire gland, some degree of PSA elevation after therapy is expected. For example, the urethral warming catheter is utilized in an attempt to preserve the urethra, thereby preventing urethral slough. Prostate tissue circumferentially located a few millimeters beyond the caliber of the urethra is likely not frozen to the required temperature that causes cell death. It is rare for primary prostate cancers to grow in areas exquisitely close to the urethra, but on occasion, these tumors can be identified by surgical pathology following a salvage radical prostatectomy after radiation failure. However, in the primary setting, preserving a small rim of periurethral tissue is likely clinically insignificant. The first step to understanding the concept of incomplete ablation of segments of the prostate revolves around understanding the particular cryotherapy technology that one is using. The ice ball grows radially from the probe outward. The isotherms, or temperature gradients within the ice region, are not uniform (Fig. 11.7). For example, the outer edge of the ice typically measures 0 °C and is not thought to be

lethal. Lethal temperatures beginning with the minus 20 °C isotherm are encountered approximately 3–4 mm within the edge of the ice ball. As one proceeds deeper within the ice ball, temperatures within the minus 40° Celsius isotherm are encountered. These temperatures are usually cold enough to kill most cancers [3].

In order to eradicate the target parenchyma, the probes need to be placed in such a manner that the ice fields overlap without pockets of tissue that are warmer than minus 20 °C. Thus the operator must be familiar with the particular manufacturer's cryotherapy products and their associated isotherms. Figure 11.8a shows a schematic of a transverse view of the prostate with good probe placement allowing for sufficient overlap of ice fields. However, as is demonstrated in Fig. 11.8b, there is a variable free zone (warm pocket) between the proximal and distal ice fields posteriorly when viewed in the sagittal dimension. Therefore, one must be vigilant when evaluating proper probe placement in both the transverse and sagittal views.

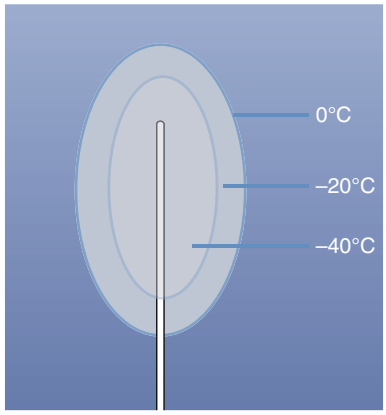


**Fig. 11.7** Schematic depicting the cryoprobe and corresponding isotherms. The ice generated exists within a temperature gradient based on distance from the source. The shaded colors depict temperature approximations within that particular isotherm

Another potential cause for an untreated area of parenchyma is due to skewed probe placement (Fig. 11.9a). All cryoprobes should be placed in proper horizontal position through the stepper. As is illustrated in Fig. 11.9a, the anterior-most probe is placed in a non-horizontal fashion. One can see that as the probe gets farther away from the other probes from the apex of the prostate, the angle itself widens (Fig. 11.9a. b).

Men having a median lobe may account for persistent PSA elevation following cryoablation. In general, it is unusual for cancer to occupy the median lobe, but it is quite common for the median lobe not to be completely treated, depending upon its size. Freezing the median lobe, although it would reduce the PSA further, may be risky due to the proximity of the median lobe to the ureteral orifices. Finally, one needs to be sure that the posterior-most segment of the prostate, including the capsule, is sufficiently treated with lethal temperatures. As previously stated, the ice ball needs to run 3–4 mm beyond the posterior capsule to achieve this. In order to prevent inadvertent injury to the rectum, the rectal wall needs to be dropped further posteriorly away from the ice field. This can be accomplished either by reducing the anterior pressure on the transrectal ultrasound itself or, alternatively, by injecting

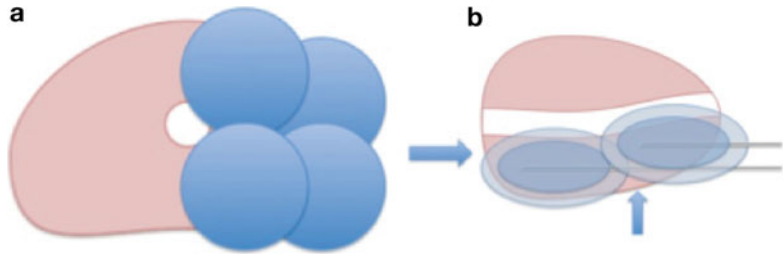


**Fig. 11.8** (**a**) Transverse schematic showing correct cryoprobe placement. Each *blue round circle* represents an ice ball. Each of these ice balls overlaps to some degree, thereby obviating any warm areas of incompletely treated tissue. (**b**) Sagittal view of nonoverlapping ice fields. In this case, there are two areas indicated by the *arrows* that have incompletely treated tissue

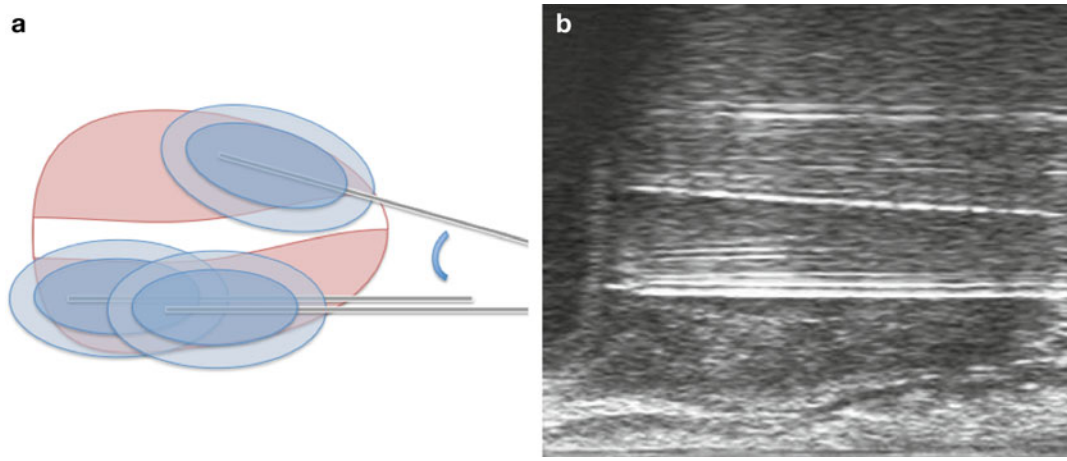


**Fig. 11.9** (**a**) Schematic of skewed probe placement. Note that the initial takeoff angle between the first and second row probes is great, but as the probe moves from apex to base of the prostate, the distance between consecutive probes increases. (**b**) Sagittal ultrasound view demonstrating the middle probe has an angulation anteriorly. All probes should be placed horizontally and in parallel with adjacent probes

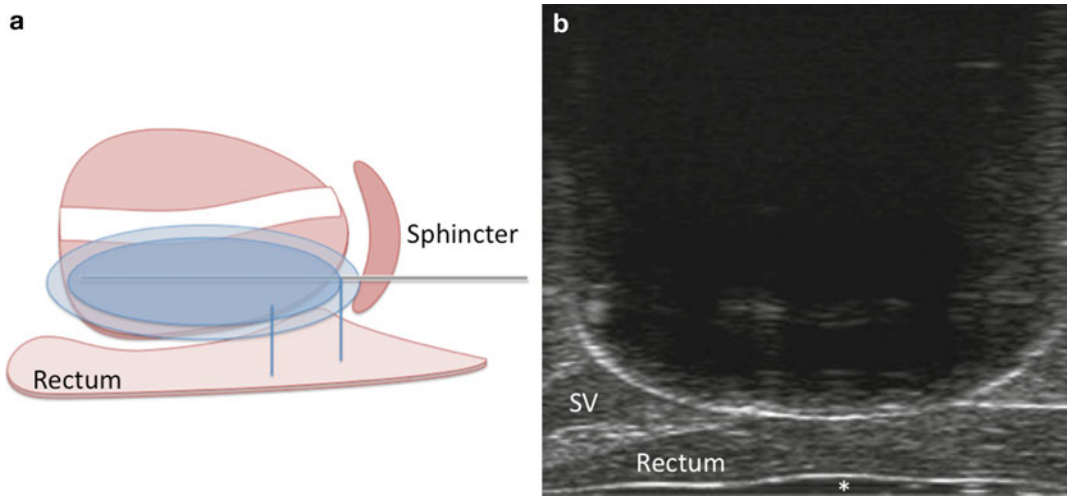


**Fig. 11.10** (**a**) Schematic sagittal view of ice ball covering the apex of the prostate. Despite the proximity of the rectum and the urinary sphincter, it is feasible to achieve sufficiently cold and lethal temperatures at the apex while avoiding collateral damage to the sphincter and rectum. (**b**) Sagittal view of the ice ball upon completion of freezing. The hyperechoic rim of the ice ball can be easily seen resting upon the rectal wall. Note that (*1*) the entire prostate is covered in ice, (*2*) there is minimal compression of the rectal wall and it remains quite thick, and (*3*) a portion of the seminal vesicle (*SV*) base often is incorporated in the ice field. The *asterisk* (*) denotes the ultrasound jelly within the condom sheath [the white hyperechoic line] surrounding the transrectal ultrasound probe

saline into Denonvilliers space. Either of these maneuvers will help to widen Denonvilliers space and reduce compression on the rectal wall.

Another possible area of incompletely treated tissue is the prostatic apex. This may be due to the physician's reluctance to aggressively freeze this region due to the surrounding rectal wall and urinary sphincter. Figure 11.10a depicts a schematic of the ice ball covering the posterior apex of the prostate and avoiding the urinary sphincter. Note that the "rectal hump" toward the apex of the prostate has a gentle curve upward that

matches the natural anterior curve of the ice ball (Fig. 11.10b). Some physicians believe that by utilizing a minimum of two thermocouples placed at the urinary sphincter and Denonvilliers fascia allows safe monitoring of the temperature while freezing. In addition, paying attention to proper probe placement, ice field coverage, and adjacent structures will lead to better oncologic and functional results.

## Primary Prostate Cryoablation

When positioning the patient for cryotherapy, it is important that he be placed in a true lithotomy position. In this respect, the lower legs should be parallel to the floor and be approximately at a right angle to the upper legs. This position should minimize the chance of pubic arch interference, sometimes encountered when treating a larger gland. If pubic arch interference still occurs, the lithotomy can be slightly exaggerated to better open the perineum for access.

After the perineum is shaved, prepped, and draped, we use an Ioban dressing to elevate the scrotum off the perineum. A Foley catheter is sterilely placed into the bladder and clamped, allowing the bladder to be filled with urine or fluid to provide an acoustic window against which to better view the prostate. The transrectal ultrasound probe is placed per rectum. The cryotherapy grid is placed against the perineal surface, and the patient's anatomy is viewed [see section "Using transrectal ultrasound to define pelvic anatomy prior to treatment" above for more detail].

Developing an appreciation of the ultrasonic appearance of a patient's anatomy should not be understated. One needs to definitively know the location of the urinary sphincter, the rectal wall, and where the seminal vesicles/ducts insert into the prostate. Often, one has to rotate the stage of the ultrasound transducer away from the midline to better appreciate these structures. The relationship of the seminal vesicles to the prostate is interesting and almost unique to each patient. Some seminal vesicles insert very close to the base, while others can be seen posterior to the prostate extending to the apex or mid-region. Appreciating the sonographic characteristics of the seminal vesicles compared to the prostate is important before commencing the application of cryotherapy.

It is sometimes challenging to appreciate the location of the urinary sphincter when viewing sagittally along the midline prostate. A better means to view the location/junction of the urinary sphincter to the prostatic apex is to begin viewing laterally in the sagittal plane where the levator and sphincteric musculature is more readily appreciated. Once one finds the levators laterally, one can then rotate the probe medially in the sagittal plane to determine where these muscles become confluent with the urinary sphincter. It is important to note whether or not a patient has a median lobe. Many cryotherapists do not treat the median lobe as it would pose potential risk of injury to the ureteral orifices in select cases. In addition, the majority of median lobes are not malignant.

Measurements of height and width of the prostate (Fig. 11.11a) are then taken at the widest transaxial dimension followed by prostate length (base to apex) in the sagittal direction (Fig. 11.11b). The prostate volume is calculated, and the surgeon then decides on the number and types of cryoprobes to utilize. For example, one particular technology allows the surgeon to preset the length of lethal ice, while other technologies will grow a fixed length of ice. If the surgeon is planning to use variable ice length settings, we typically advise taking three measurements along the sagittal axis of the prostate: one measurement at the anterior region, one in the midsagittal plane, and one in the posterior region. The cryoprobes that are then subsequently placed into these locations can have the precise ice measurements set for their lethal kill zones.

In general, the manufacturer provides recommendations regarding a particular product's ability to deliver spherical ice of various lengths and diameters attaining approximate temperatures in the 0 °C, −20 °C, and −40 °C zones [isotherms]. However, the operator needs to be sure that when these cryotherapy probes are placed, there is sufficient overlap of the ice balls, obviating any

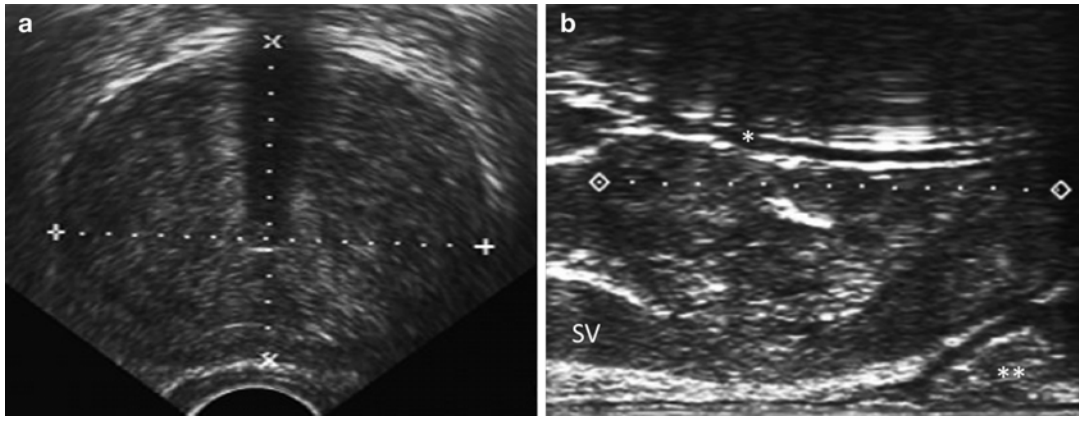


**Fig. 11.11** (**a**) Transverse view of the mid-prostate. Volumetric measurements are being taken in both the anterior-posterior dimension ("height") and the width. Note that the urethra is near the exact middle of the prostate in this case, and the acoustic shadowing cast by the indwelling catheter is seen in the far field. (**b**) Sagittal view of the prostate with a Foley catheter (*) running through the urethra. The sagittal length is measured from apex to base. Note that the prostate is measured at the widest part in the sagittal view, which typically is the midline segment. Note that in this particular patient, the urethra runs anterior to the widest length of the prostate. The seminal vesicle (*SV*) is identified, layered between the hyperechoic fat of Denonvilliers fascia and the posterior wall of the prostate. The posterior capsule of the prostate gently sweeps anteriorly toward the apex. In the uncompressed rectal wall, a wider section of the rectum (**) is usually identified toward the prostatic apex. In layman's terms, this is often referred to as the "rectal wall hump"

"warm pockets" or "variable freeze zones" that suggest untreated, potentially viable parenchyma (Fig. 11.8b). Alternatively, computer-generated cryoprobe placement schemes are commonly available on the manufacturer's cryotherapy generators. Computerized models can be a means to help guide probe placement, but ultimately this responsibility rests with the cryosurgeon. Finally, the operator has the ability to measure distances between the probe and the urethra, the probe and the capsule, and between probes. One should consult the manufacturer's recommendations for guidelines regarding these measurements.

We typically place the two anterior probes first. Each probe is localized and then placed using the transverse ultrasound view. The depth of the probes into the parenchyma is determined in sagittal view with each needle tip positioned at the base of the prostate. It is important to realize that there is little lethal ice generated beyond the tip of the cryoprobe, and for this reason the probes are placed right to the prostatic base/bladder wall junction. Typically, two probes are placed in the second or mid-transverse row and anywhere from two to four probes are placed in the posterior row. Again, the depths of all probes should be confirmed using the sagittal ultrasound view. It is important to also note that when viewing probe placement from a sagittal dimension, each individual probe should be placed horizontally (Fig. 11.12a). If there is any torque placed on the cryoprobe during placement, one may end up with skewed, or a non-horizontal probe placement, increasing the likelihood of treatment failure (Fig. 11.9a, b).

The cryoablation kits include a number of thermocouples that can be utilized at the discretion of the treating surgeon. Many cryotherapists will place one thermocouple at the urinary sphincter and another at Denonvilliers fascia to monitor temperature in these critical regions. Other areas that surgeons may place thermocouples include the neurovascular bundle or areas of known cancer where one wants to make sure the temperature achieved is sufficiently lethal.

Following placement of the probes, the Foley catheter is removed and cystoscopy is performed. It is important to ensure that there is no violation of the urethral mucosa or bladder wall with a cryoprobe. If this is recognized, there is the opportunity to reposition the probe(s) and still proceed with the intended procedure. A super

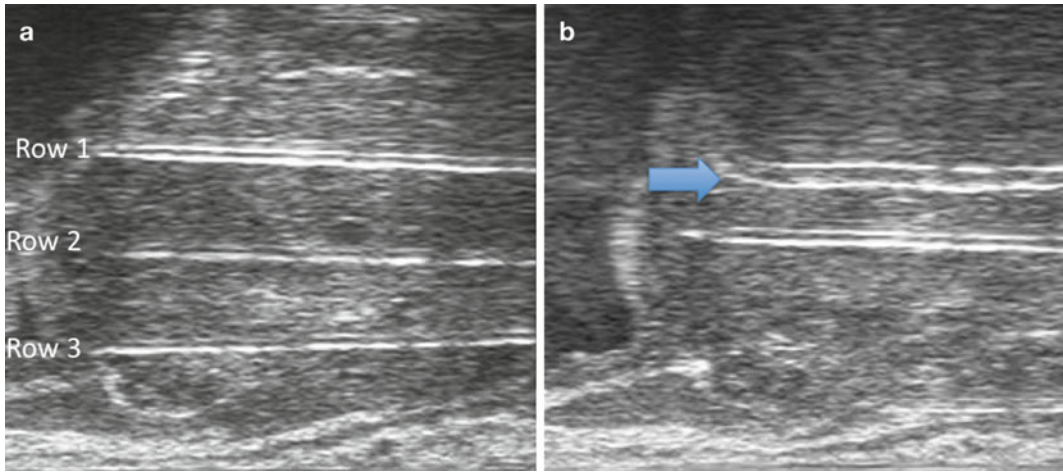


**Fig. 11.12** (**a**) Sagittal view of the prostate with three rows of cryotherapy probes that have been positioned. It is common for these three rows of probes to be in different planes and not be seen simultaneously as is viewed in this image. (**b**) Sagittal view of the prostate. Note that row 1 (the anterior row) has been activated, and the hyperechoic rim of ice (*arrow*) can be seen slightly posterior to the cryoprobe. When the probe is first activated, one does not see much hypoechoic shadowing beyond the probe as the ice front has not had sufficient time to become dense. The second row probe (still not activated) can be seen posterior to the first row

stiff guidewire is then passed as the cystoscope is withdrawn. A lubricated urethral warming catheter is then placed and secured to the drape. We recommend performing a final ultrasound verification of probe placement before beginning cryoablation. It is often helpful to visually inspect the insulated hubs of the needles externally to ensure that they are all aligned within a few millimeters of each other.

Two freeze-thaw cycles then ensue. Freezing is begun anteriorly. It is important to verify that the entire intended length of the cryo-active probe generates ice, and this can be visualized under sagittal ultrasound guidance (Fig. 11.12b). Following the first few minutes of freezing of the anterior rows, freezing of the second row typically commences. The entire freezing process should be monitored under the sagittal axis of ultrasonography. On the sagittal view, the entire length of ice may be monitored as compared to only viewing a "slice" of the field in the transverse plane. Many cryotherapists initially run the bottom or most posterior row of cryoprobes on a slower setting. For example, the posterior row can be run on approximately 60 % to allow the tissues in the posterior zone to become sufficiently cold before the ice front reaches the rectal wall. Most devices allow the operator to set the rate of cryotherapy between 10 and 100 % in increments of 10 %.

Cryotherapy can be monitored by both temperature thermocouples and ultrasonographic visualization of the ice. As the ice front advances, one sees the hyperechoic edge of the ice ball and an anechoic area of thick ice beyond it as the sound waves are unable to penetrate the dense ice structure (Fig. 11.13a, b). It is important when viewing the completion of the posterior row freeze to ensure that the ice is coming down evenly and that one side does not get ahead of the other (Fig. 11.13a). Denonvilliers fascia should be widened to allow sufficient space to run the lethal isotherm of the ice ball beyond the prostatic capsule. This can be achieved by decreasing the pressure placed by the transrectal ultrasound probe off the prostate by dropping the stage of the stepper posteriorly. Alternatively, saline can be injected into Denonvilliers space to widen the area. Cryotherapy is judged to be complete based upon the sagittal view of the ultrasound demonstrating the ice edge at the rectal wall (Fig. 11.10b). Ideally, temperatures of at least minus 20 °C should be attained at the posterior capsule of the prostate.

The prostate is then thawed. The surgeon has the option of using an active or a passive thaw;

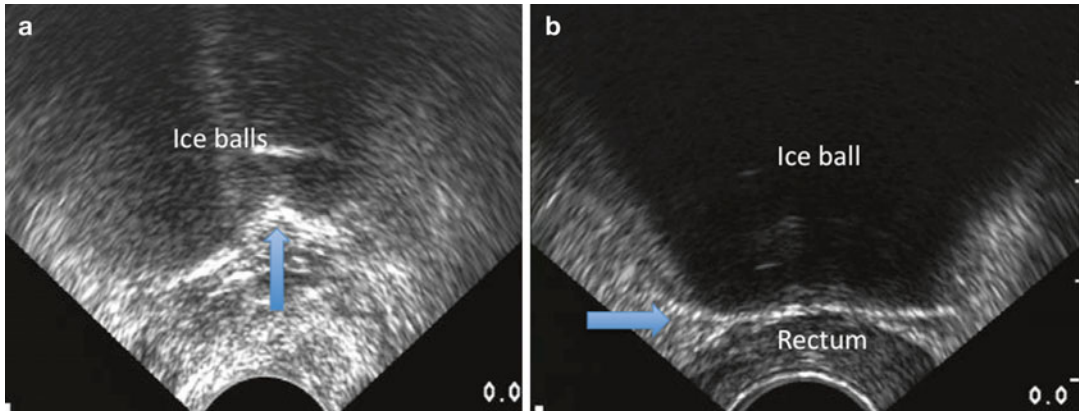


**Fig. 11.13** (**a**) Transverse view of evolving ice front with its hyperechoic rim. Note that the ice front on the patient's right (left side of figure) is slightly ahead of the contralateral ice field. In the transverse view, the last segment of ice to freeze is usually located at the apex. It is here that the ice fields need to coalesce, which has not yet occurred as evident by the "bird's wing sign" (*arrow*). (**b**) Transverse view of the ice ball. Note how the "bird's wing" has flattened out at the apex and the entire parenchyma is engulfed in ice. The ice balls have coalesced over time, and now one has a single sheet of ice that is anechoic, as the sound waves are not capable of penetrating it. Note also how the hyperechoic ice front (*arrow*) was brought to rest completely horizontal on the rectal surface. There is little compression of the ultrasound probe on the rectum as the rectal wall is quite thick

most will use an active thaw after the first freeze. The operator wants to observe that all the ice has melted and the prostate has returned to its original echotexture. After the ice has thawed, the second freeze cycle is begun. This usually takes a shorter time compared to the first freeze as the prostate is already cold. Following the second freeze, the ice is thawed again, most commonly by passive means.

The warming catheter remains in place for an additional 5–15 minutes following completion of the second freeze cycle. During this time, the stepper, transrectal ultrasound probe, cryoprobes, and thermocouples are removed, and pressure is held on the needle ablation sites in the perineum to prevent ecchymosis. Following this, the urethral warmer can be sterilely exchanged for a urinary catheter.

## Oncologic Outcomes of Primary Prostate Cryoablation

Similar to surgical and radiation therapy, the oncologic outcomes of cryotherapy are strongly dependent upon the pathology and risk stratification of the treated prostate cancer. Patients with low-risk disease most commonly have good oncologic outcomes, while those with high-risk or more advanced disease oftentimes require multimodality therapy. However, unlike surgical and radiation therapy, the definition of biochemical failure post-cryotherapy is not well-defined. PSA-producing periurethral tissue is intentionally preserved during cryotherapy (Fig. 11.2b); accordingly, application of the definition of surgical biochemical failure does not directly apply. Similarly, the ASTRO and Phoenix definitions of biochemical failure following radiation therapy, while commonly employed in the cryotherapy literature, are not directly translatable. The introduction of new technology, including third-generation systems employing smaller probes and an insertion template with stepping device, has enabled more effective control of the freezing process. Long-term oncologic outcomes data often hybridizes second- and third-generation systems, as the third-generation systems were initially introduced in the late 1990s. However, despite the lack of consensus regarding interpretation of biochemical failure and the evolution of technology with time, an assessment of oncologic outcomes following cryotherapy is essential to understand the appropriate application of this intervention (Table 11.1) [4–14].

**Table 11.1** Oncologic outcomes of primary cryoablation

| Reference | Definition of failure | # of patients | Biochemical disease-free survival |
|---|---|---|---|
| Cohen et al.[a] [4] | Phoenix | 370 | 56.0 % at 10 years |
| Chin et al.[b] [5] | Phoenix | 62 | 17.4 % at 8 years |
| Bahn et al.[a] [6] | ASTRO | 590 | 89.5 % at 7 years |
| Dhar et al. [7] | ASTRO | 860 | 79 % at 5 years |
| Jones et al. [8] | ASTRO | 1,198 | 77.1 % at 5 years |
| DiBlasio et al. [9] | ASTRO | 78 | 71.1 % at 5 years<br>95.7 % at 3 years<br>97.9 % at 1 year |
| Donnelly et al. [10] | Phoenix | 117 | 75 % at 5 years<br>82.9 % at 3 years |
| Ellis et al. [11] | ASTRO | 291 | 79.6 % at 4 years |
| Han et al. [12] | PSA ≥ 0.4 ng/mL | 106 | 75 % at 1 year |
| Hubosky et al. [13] | ASTRO | 89 | 94 % at 1 year |
| Cresswell et al. [14] | PSA ≥ 0.5 ng/mL | 31 | 60 % at 1 year |

Phoenix definition of biochemical failure = a rise by 2 ng/mL or more above the nadir PSA ASTRO definition of biochemical failure = three consecutive PSA rises after a nadir with the date of failure as the point halfway between the nadir date and the first rise, or any rise great enough to provoke initiation of therapy
[a]Data includes a proportion of patients treated with earlier generation technology
[b]High-risk patients

Despite the previously reviewed caveats of interpretation of cryotherapy oncologic outcomes, available data reveals that biochemical disease-free survival at 1 year varies from 60 [14] to 97.9 % [9]. Applying radiation oncology definitions of biochemical failure (ASTRO and Phoenix), disease-free survival at 5 years following cryotherapy ranges from 70 to 80 % [7–10]. In a review of the longest follow-up data available, Cohen et al. revealed a 56.0 % biochemical disease-free survival rate in 370 patients at 10 years posttreatment [4]. Of note, patients were treated with second-generation technology; long-term follow-up with third-generation technology is not yet available.

A significant deviation from other published biochemical disease-free survival rates was noted by Chin et al. [5], who cited a 17.4 % biochemical disease-free survival rate at 8 years. In contrast to other studies, the patient population treated with primary cryotherapy in this group was exclusively high risk.

From available data, the oncologic outcomes of primary cryotherapy appear to be acceptable. However, long-term studies with third-generation technology remain outstanding. With further study, the importance of adopting a common definition of biochemical failure post-cryotherapy is critical.

## Salvage Prostate Cryoablation for Recurrent Disease

Although the basic procedure for performing salvage cryoablation is quite similar to that in the primary setting, there are a few important differences. Much of this centers on trying to minimize injury to surrounding tissue. The complication rate of cryoablation in the salvage setting is higher than that in the primary setting. For patients who have received primary radiotherapy, one must keep in mind that the two sphincteric mechanisms, that of the bladder neck and the external urinary rhabdosphincter, have often received exposure to radiation. This predisposes the patient to urinary incontinence identified in approximately 5–10 % of patients following salvage prostate cryoablation [15–18]. In addition, the rectal wall has also received exposure to irradiation and therefore the potential blood supply and ability of the rectum to tolerate a cryothermic injury is much reduced. For these reasons, it is important to be even more judicious

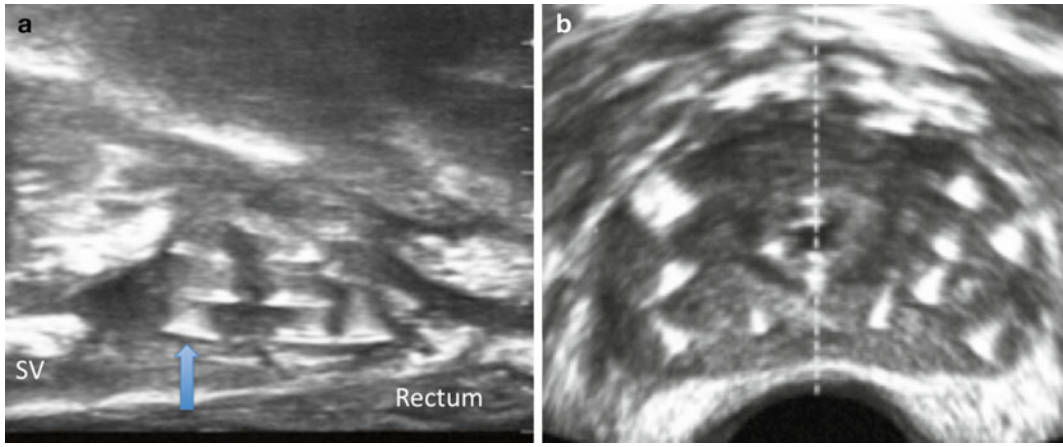


**Fig. 11.14** (**a**) Sagittal view of a prostate previously treated with brachytherapy, with the rectum and seminal vesicle (*SV*) identified. Shown are multiple brachytherapy seeds placed within the prostate. A representative seed is identified by the *blue arrow*. Some degree of acoustic shadowing can also be noted. However, in the sagittal view, the reverberations are minimal compared to the transverse view. (**b**) Transverse view of the prostate with multiple brachytherapy seeds. Note that the urethra is perfectly aligned in the midline plane

with salvage cryosurgery and cognizant of potential pitfalls that may lead to a complication.

In a majority of patients, the prostate volume contracts following radiotherapy. Likewise, the prostatic length is also proportionally shorter. Since there is a smaller volume of tissue to freeze, the treatment time is often reduced. Some cryosurgeons will run the posterior channels on a lower output level to have more effective control over the ice front before it reaches the anterior rectal wall. One of the principles of prostate cryotherapy in the salvage setting is to avoid freezing too deeply into the anterior rectal wall, as this structure is not tolerant to injury following irradiation. Similarly, because the external urinary sphincter has likely been exposed to radiotherapy, one should not freeze beyond the prostatic apex. In clinical practice, this translates into making sure that one has an accurate sagittal length of the prostate and the length of desired ice is limited to that sagittal measurement so as to avoid freezing into the urinary sphincter.

Prior exposure to brachytherapy presents a challenging case in that the brachytherapy seeds interfere with the operator's ability to visualize the cryoprobe. Therefore, when treating brachytherapy patients with salvage prostate cryoablation, it is optimal to work in the sagittal view to distinguish between the cryoprobes and brachy seeds (Fig. 11.14a). One of the main difficulties in treating prostates previously exposed to brachytherapy is that in the transverse mode it is difficult to distinguish where the cryoprobe is being placed and real-time movement of nearby brachytherapy seeds (Fig. 11.14b). Because both the cryoprobes and the brachy seeds are metallic, there are reverberations to contend with as well. This problem can be overcome by becoming familiar with working in the sagittal view. Therefore, it is important for the operator to develop the ability to distinguish whether the cryo needle is at the midline of the prostate (the widest area), the far lateral area (the narrowest segment), or the mid section when viewing sagittal images.

It has also been shown in prior studies that radio-recurrent or persistent cancer can be located closer to the urethra compared to the primary setting. In a study by Dr. Huang et al. [19] investigating the distribution of tumor lesions on whole-mount salvage radical prostatectomy specimens following failed primary radiation therapy, periurethral tumors were identified in 67 % of cases, with 17.4 % of tumors located within 2 mm of the urethra. In the primary setting, it is unusual for prostate cancer to be located so close to the urethra, but recurrent or resistant cancer has been more commonly observed in that

location. The urethral warming catheter is used as a means to protect the urethra from slough, yet it may, at least theoretically, interfere with achieving sufficiently cold temperatures to kill resistant cancers if located in close proximity to the urethra. This could potentially represent a cause for failure to cure with prostate cryoablation in the salvage setting.

Also, as reviewed by Drs. Gage and Baust [20], the nadir freezing temperature to achieve cell death in vivo is markedly variable, from −2 °C in dog osteocytes to −60 °C in mouse sarcoma specimens. More recently, Drs. Klossner, Baust, Gage, and VanBuskirk [21] discovered that the molecular changes that arise with the development of androgen insensitivity in prostate cancer cells also enable a shift to freeze resistance with cryotherapy. In vitro freezing of androgen-sensitive prostate cancer cells demonstrated an inability to recover after exposure to temperatures less than or equal to minus 25 °C, whereas androgen-insensitive prostate cancer cells required exposure to temperatures of minus 40 °C to result in cell death. Therefore, radio-resistant cancers often require colder nadir temperatures in the salvage setting compared to primary cryoablation. Again, given the confines of the prostate surrounded by normal tissues that one desires to preserve, it may be difficult to achieve sufficiently cold temperatures within the prostate to kill radio-resistant cancers.

As the ice ball approaches the posterior capsule of the prostate and the rectal wall, it is important to ensure that there is sufficient space to run the ice a few millimeters beyond the capsule yet not into the anterior rectal wall. There are some experts in cryoablation who feel that the rectum becomes more adherent to the prostate following radiotherapy, while others feel that there is not much difference as compared to the primary setting. However, it is nonetheless essential to drop the rectal wall away from the ablation field whether it is by decreasing the pressure of the ultrasound transducer against the prostate or by infusing saline into Denonvilliers space.

When a patient presents for consideration of salvage cryoablation after primary therapy failure, it is important to restage the patient's disease. The best means to radiologically evaluate the pelvis is with a multiparametric MRI. It is valuable to see if the cancer has breached the capsule and involves the seminal vesicles or the lymph nodes. In addition to cross-sectional imaging, the status of the lymph nodes can be ascertained by a pelvic lymphadenectomy. It is highly recommended to do a seminal vesicle biopsy along with a prostate biopsy when considering the patient as a potential candidate for salvage prostate cryoablation. Seminal vesicle invasion is quite common after radiation therapy, having been demonstrated in approximately 25–30 % of patients based on salvage prostatectomy series [19]. Knowing the status of the seminal vesicles is important before performing salvage cryoablation to minimize the chance of failure. We recommend performing biopsies of each seminal vesicle along its length and labeling these as "seminal vesicle base" or "seminal vesicle tip." For example, if the base of a seminal vesicle were involved with prostate cancer, it is still conceivable to perform salvage cryoablation. The base of the seminal vesicle is attached to the prostate in the midline, and one simply needs to place the cryotherapy probe deeper into the affected seminal vesicle to treat this area. In contrast, the tip of the seminal vesicle is located much farther laterally and is not aligned with the sagittal axis of the prostate. Therefore, to attempt to ablate prostate cancer involving the seminal vesicle tip would potentially be associated with a higher complication rate. Furthermore, if disease is identified at the tip of the seminal vesicle, cancer is likely located in the tissues surrounding the area that cannot be cured by salvage prostate cryoablation alone. It is not uncommon for an experienced cryosurgeon to perform salvage cryoablation of the prostate along with freezing of the base of the seminal vesicle(s) if it is believed that disease is confined to that area.

Traditionally, salvage cryoablation has been utilized to treat patients failing prior radiotherapy. However, with newer ablative devices used in clinical practice, we have seen a number of patients present requesting salvage cryotherapy after primary failure. This includes patients previously treated with high-intensity focused ultrasound

**Table 11.2** Oncologic outcomes of salvage cryoablation

| Reference | Definition of failure | # of patients | Biochemical disease-free survival |
|---|---|---|---|
| Williams et al. [22] | Phoenix | 187 | 39 % at 10 years |
| Wenske et al.[a] [15] | Phoenix | 328 | 35 % at 10 years<br>63 % at 5 years |
| Bahn et al.[a] [16] | PSA ≥ 0.5 ng/mL | 59 | 59 % at 7 years |
| Pisters et al.[a] [17] | ASTRO | 279 | 59 % at 5 years |
| Ng et al. [23] | Phoenix | 187 | 56 % at 5 years |
| Spiess et al. [24] | PSA ≥ 0.5 ng/mL | 450 | 39.6 % at 3.4 years |
| Ghafar et al. [18] | Nadir + 0.3 | 38 | 74 % at 3 years<br>86 % at 1 year |
| Ismail et al. [25] | ASTRO | 100 | 59 % at 3 years<br>83 % at 1 year |
| Cresswell et al. [14] | PSA ≥ 0.5 ng/mL | 20 | 66.7 % at 1 year |
| Gowardhan et al. [26] | PSA ≥ 0.5 ng/mL | 42 | 61 % at 1 year |

Phoenix definition of biochemical failure = a rise by 2 ng/mL or more above the nadir PSA ASTRO definition of biochemical failure = three consecutive PSA rises after a nadir with the date of failure as the point halfway between the nadir date and the first rise, or any rise great enough to provoke initiation of therapy
[a]Data includes a proportion of patients treated with earlier generation technology

(HIFU), laser therapy, prior cryoablation, and photodynamic therapy, among others. Cryoablation is a feasible procedure that can be utilized to salvage men with recurrent prostate cancer previously treated using these devices as well. However, if the patient has had the prostatic urethra treated by prior transurethral resection of the prostate, transurethral incision of the prostate, or other types of ablation, one must be certain that there is sufficient prostatic urethra present to coapt to the warming catheter. It is the coaptation between the warming catheter and the mucosa that protects the urethra. If there is a gap present between the warming device and the urethra, it is possible to develop a prostatic slough.

## Oncologic Outcomes of Salvage Prostate Cryoablation for Recurrent Disease

Reviews of oncologic efficacy for salvage cryotherapy conducted after failure of primary radiotherapy for management of prostate cancer are beset by the same difficulties in interpretation as previously detailed in primary therapy, principally the lack of a common definition of biochemical failure and the utilization of different generations of cryotherapy equipment. Nonetheless, an assessment of oncologic outcomes following salvage cryotherapy is essential to understand the appropriate application of this intervention (Table 11.2).

Applying the Phoenix definition of biochemical recurrence, the 10-year biochemical disease-free survival rate following salvage cryotherapy is 35–39 % [15, 22]. Applying the ASTRO and Phoenix definitions of biochemical recurrence, 5-year biochemical disease-free survival is 56–63 % in various studies [15, 17, 23]. At 1 year, biochemical disease-free survival, again applying various definitions of failure, varies from 61–86 % [14, 18, 24–26].

Similar to outcomes assessment with primary cryotherapy, oncologic outcomes following salvage cryotherapy require further study. A consensus definition on biochemical failure following salvage cryotherapy is needed, as well as more detailed study evaluating the results of third-generation cryotherapy systems.

## Focal Therapy: Targeted Cryoablation with Parenchyma Preservation

The concept of focal therapy for prostate cancer has evolved over time in several respects. Initially, it was utilized to perform ultrasound-guided

hemi-ablation when prostate cancer was determined to be unilateral based on prostate biopsy. In this fashion, the probes would be placed into the side of the prostate containing the known malignancy following the same pattern that would be used for whole gland cryoablation, although only one side (left or right) would be treated. Additionally, the surgeon would likely position the thermocouples near the neurovascular bundles to verify that these important structures were not being inadvertently frozen. Prostate hemi-ablation was initially described for the low-risk patient, most commonly with Gleason 6 or limited Gleason 3+4=7 disease.

However, several changes have occurred since the initial description of prostate hemi-ablation that have prompted the further development of parenchymal-preserving approaches initiated parenchymal-preserving approaches to further develop. First, for men with limited, low-volume Gleason 6 disease, often the best initial approach is active surveillance. Therefore, several investigators and surgeons involved with focal therapy are now focusing on intermediate risk prostate cancer. Second, there have been a number of different regional treatment templates described by Dr. John Ward, who evaluated the application of targeted prostate ablation on radical prostatectomy specimens of men with unilateral prostate cancer on preoperative biopsy. Dr. Ward concluded that regionally targeted prostate ablation is capable of eradicating all dominant tumors and the vast majority of clinically significant tumors in men with unilateral disease by biopsy [27]. Suggested treatment templates include image-guided index lesion ablation, quadrant ablation, hemi-ablation, and three-quarter ablation sparing the uninvolved neurovascular bundle. Third, multiparametric MRI (mpMRI) has been adopted by several centers, enabling tumors to be radiographically identified, targeted for confirmatory biopsy, and then subsequently treated. Image-guided targeted treatment of the index lesion would fit the truest definition of focal therapy. Fourth, it is recognized that the majority of prostate cancers are multifocal and that small Gleason 6 tumors may not grow within a decade to threaten a man's life expectancy. Therefore, several investigators now are attempting to identify the index lesion. Or the lesion most characteristic of the biologic potential of the cancer, using various modalities. The index lesion can be identified either with biopsy techniques and/or by multiparametric MRI (mpMRI). In order to consider image-guided focal lesion ablation, the index lesion needs to be correctly identified either by using a combination of mpMRI along with a confirmatory biopsy or, alternatively, multi-core saturation biopsies.

A three-dimensional transperineal mapping biopsy (3D-TMB) is a technique to obtain representative tissue samples of the prostate at 5 mm increments throughout the volume of the gland. 3D-TMB can be utilized for a number of reasons. One indication is the patient with a high clinical suspicion of prostate cancer who has undergone prior negative routine office-based TRUS biopsies and wishes to know if he has cancer. A second clinical scenario is the gentleman who is considering active surveillance but desires a more comprehensive evaluation to understand with greater confidence if he is truly a candidate, as it is recognized that the traditional 12-core biopsy has limitations, including a 30–40 % rate of understaging by conventional office biopsy. The third indication is the man considering focal therapy for which the locations of the clinically significant tumor(s) need to be precisely mapped in the three-dimensional volume of the prostate. If a patient is considering focal therapy, it is imperative that each of the needle biopsies remains within the intended target zone. This ensures that the surgeon can map where the cancer is located, and those same zones can subsequently be ablated.

Although there are a number of variations of the mapping biopsy technique, the first description was by Onik and Barzell [28]. A Foley catheter is placed similar to cryotherapy, whereby a liquid-filled bladder provides an acoustic window to the prostate. After placing the patient in dorsal lithotomy position, the TRUS probe is introduced per rectum. The cryotherapy grid is attached to the stepper and placed flush against the perineum. It is imperative to align the urethra with the cryotherapy grid so that biopsies taken will remain within the intended sampled sectors (Fig. 11.15a, b). Proximal and distal biopsies are first taken beginning in the suburethral zone. The right hemi-prostate is subdivided into three

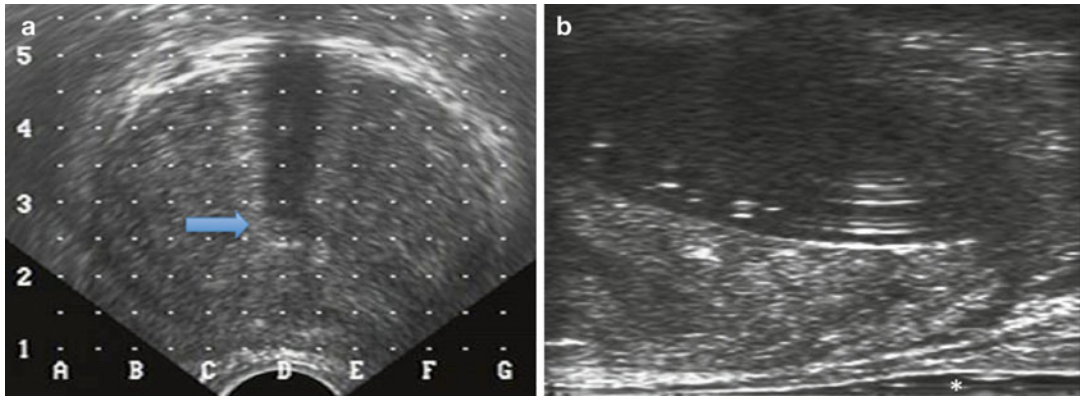


**Fig. 11.15** (**a**) The figure displays the widest surface area of the prostate in transaxial view with grid overlay. Note that each grid hole is 5 mm from the adjacent hole in each direction. The urethra (*arrow*) is perfectly aligned in the middle of the grid (row D). (**b**) In this sagittal view of the midline of the prostate, note that the catheter within the entire urethra can be readily seen on the image. This assures that the prostate is centered and ready for mapping prostate biopsies. The *asterisk* (*) denotes the ultrasound jelly within the condom sheath (*fine white line*) surrounding the ultrasound transducer

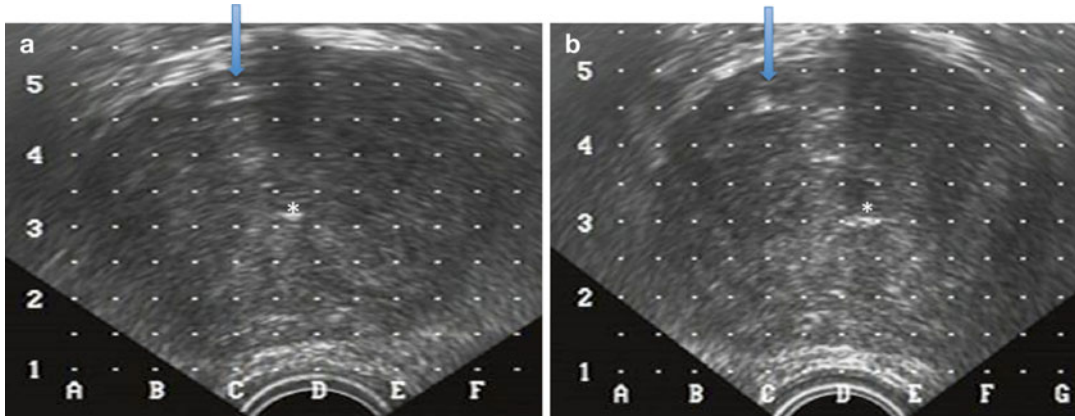


**Fig. 11.16** (**a**) Transaxial view of the mid-prostate. To commence 3D-TMB on the patient's right hemi-prostate, the biopsy needle (seen at C4.75, *arrow*) is initially positioned in transaxial view. Biopsies begin anteriorly in Zone I (corresponding to column C), the medial segment. Biopsies will subsequently be taken every hole along the C axis until C1.5. The urethra (*) is located at approximately C3.5. (**b**) Transaxial view of the biopsy needle placed at C4.5 (*arrow*). Biopsies taken further posteriorly down column C in this case will result in Zone II (intermediate region) sampling. Note that in order to align the mid-region of the right hemi-prostate with the grid holes, the stage was moved further laterally (urethra is now at D3.5) as can be seen by movement of the urethra (*) between images (**a**, **b**). Sampling of Zone III will be down column B

regions with Zone I being most medial, Zone II being intermediate, and Zone III most lateral. Within each of these zones, biopsies are taken from the proximal, distal, anterior, and posterior segments. Therefore, within the right hemi-prostate, there are 12 pathology cups that may contain anywhere from one to multiple biopsies per specimen cup, depending on the volume of the prostate. A similar procedure is performed on the left side of the prostate. Altogether, 26 specimen containers are submitted to surgical pathology for histological interpretation.

Transrectal ultrasound is used to verify biopsy needle placement, first in the transverse dimension to confirm the specific zone that is being biopsied (e.g., Zone I, II, or III, Fig. 11.16a, b).

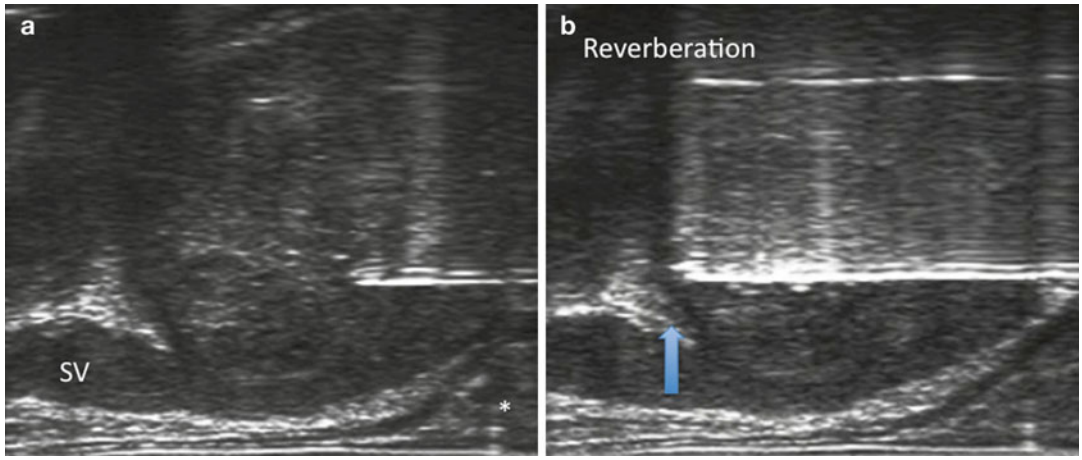


**Fig. 11.17** (**a**) Sagittal view of the prostate. To take a proximal biopsy of the prostate, one places the needle at the vertical halfway point of the prostate. One must account for the throw length of the needle when determining where to begin the biopsy. Also note that the needle is quite horizontal which prevents it from entering different biopsy sectors. (*SV* seminal vesicle, * rectal hump). (**b**) Sagittal view showing completion of the proximal posterior biopsy. Again, note that the needle is perfectly horizontal. Also note that when the needle biopsy was fired, the tip did not penetrate the base of the prostate (*arrow*), which prevents bleeding and/or hematuria, depending on the location of the needle. Reverberations can be seen anterior to the biopsy needle

Once the particular zone is localized, the biopsies are performed under sagittal view, as the operator needs to determine the depth of needle penetration into the prostatic parenchyma (e.g., for a proximal vs. a distal biopsy, Fig. 11.17a, b). When performing these saturation biopsies, it is important to ensure that the needle does not penetrate either the urethra or the bladder so as not to trigger problematic hematuria thereafter. One must also be careful not to inadvertently biopsy the neurovascular bundles.

When a patient is considered a candidate for focal therapy, usually there is a targeted region of the prostate that requires ablation. This can be either based upon 3D-TMB or a biopsy-verified suspicious mpMRI lesion. Prior to image-guided therapy, the surgeon will bring up representative mpMRI images, or perhaps a pathology-based map of the cancer location(s), in the three-dimensional volume of the prostate. Cryoprobes are then placed into those regions using the same cryotherapy technique, ensuring that there is sufficient overlap of ice balls within the target zone. It is important to confirm that there is a margin of normal tissue that is ablated to increase the likelihood that all cancer has been treated. The remainder of the cryoablation procedure follows the standard protocol utilizing two freeze-thaw cycles.

## Oncologic Outcomes of Focal Therapy

Though conceptually attractive, application of focal therapy in the management of prostate cancer is limited. Focal therapy remains in its infancy in regard to evaluation of oncologic efficacy; available follow-up is summarized in Table 11.3.

Similar to outcomes in primary and salvage cryotherapy, consensus definitions for biochemical disease-free survival in focal cryotherapy are needed. Early follow-up studies of oncologic efficacy are promising, with biochemical disease-free survival rates of 75–94 % cited [29, 30], applying the ASTRO definition of biochemical failure.

**Acknowledgment** The authors would like to thank Trina Orgain for her assistance with manuscript preparation.

**Table 11.3** Oncologic outcomes of focal cryoablation

| Reference | Definition of failure | # of patients | Biochemical disease-free survival |
|---|---|---|---|
| Onik et al. [29] | ASTRO | 48 | 94 % at mean follow-up of 4.5 years |
| Bahn et al. [30] | ASTRO | 73 | 75 % at mean follow-up of 3.7 years |
| Ward et al. [31] | ASTRO | 1,160 | 75.7 % at 3 years |
| Lambert et al. [32] | <50 % reduction of PSA nadir | 25 | 85 % at mean follow-up of 2.3 years |
| Ellis et al. [33] | ASTRO | 60 | 80 % at mean follow-up of 1.3 years |

ASTRO definition of biochemical failure = three consecutive PSA rises after a nadir with the date of failure as the point halfway between the nadir date and the first rise, or any rise great enough to provoke initiation of therapy

## References


1. Gage AA. History of cryosurgery. Semin Surg Oncol. 1998;14:99–109.
2. Babaian RJ, Donnelly B, Bahn D, Baust JG, Dineen M, Ellis D, et al. Best practice policy statement on cryosurgery for the treatment of localized prostate cancer. AUA clinical guidelines. J Urol. 2008;180(5):1993–2004.
3. Gage AA, Huben RP. Cryosurgical ablation of the prostate. Urol Oncol. 2000;5:11–9.
4. Cohen JK, Miller RR, Ahmed S, Lotz MJ, Baustaff J. Ten-year biochemical disease control for patients with prostate cancer treated with cryosurgery as primary therapy. Urology. 2008;71(3):515–8.
5. Chin JL, Al-Zahrani AA, Autran-Gomez AM, Williams AK, Bauman G. Extended followup oncologic outcome of randomized trial between cryoablation and external beam therapy for locally advanced prostate cancer (T2c-T3b). J Urol. 2012;188(4):1170–5.
6. Bahn DK, Lee F, Badalament R, Kumar A, Greski J, Chernick M. Targeted cryoablation of the prostate: 7-year outcomes in the primary treatment of prostate cancer. Urology. 2002;60:3–11.
7. Dhar N, Ward JF, Cher ML, Jones JS. Primary full-gland prostate cryoablation in older men (>age of 75 years): results from 860 patients tracked with the COLD registry. Br J Urol Int. 2011;108:508–12.
8. Jones JS, Rewcastle JC, Donnelly BJ, Lugnani FM, Pisters LL, Katz AE. Whole gland primary prostate cryoablation: initial results from the cryo on-line data registry. J Urol. 2008;180:554–8.
9. DiBlasio CJ, Derweesh IH, Malcolm JB, Maddox MM, Aleman MA, Wake RW. Contemporary analysis of erectile, voiding, and oncologic outcomes following primary targeted cryoablation of the prostate for clinically localized prostate cancer. Int Braz J Urol. 2008;34:443–50.
10. Donnelly BJ, Saliken JC, Brasher PM, Ernst SD, Rewcastle JC, Lau H, et al. A randomized trial of external beam radiotherapy versus cryoablation in patients with localized prostate cancer. Cancer. 2010;116:323–30.
11. Ellis DS, Manny TB, Rewcastle JC. Cryoablation as primary treatment for localized prostate cancer followed by penile rehabilitation. Urology. 2007;69(2):306–10.
12. Han KR, Cohen JK, Miller RJ, Pantuck AJ, Freitas DG, Cuevas CA, et al. Treatment of organ confined prostate cancer with third generation cryosurgery: preliminary multicenter experience. J Urol. 2003;170(4):1126–30.
13. Hubosky SG, Fabrizio MD, Schellhammer PF, Barone BB, Tepera CM, Given RW. Single center experience with third-generation cryosurgery for management of organ-confined prostate cancer: critical evaluation of short-term outcomes, complications, and patient quality of life. J Endourol. 2007;21:1521–31.
14. Cresswell J, Asterling S, Chaudhary M, Sheikh N, Greene D. Third-generation cryotherapy for prostate cancer in the UK: a prospective study of the early outcomes in primary and recurrent disease. Br J Urol Int. 2006;97:969–74.
15. Wenske S, Quarrier S, Katz AE. Salvage cryosurgery of the prostate for failure after primary radiotherapy or cryosurgery: long-term clinical, functional, and oncologic outcomes in a large cohort at a tertiary referral centre. Eur Urol. 2013;64:1–7.
16. Bahn DK, Lee F, Silverman P, Bahn E, Badalament R, Kumar A, et al. Salvage cryosurgery for recurrent prostate cancer after radiation therapy: a seven-year follow-up. Clin Prostate Cancer. 2003;2:111–4.
17. Pisters LL, Rewcastle JC, Donnelly BJ, Lugnani FM, Katz AE, Jones JS. Salvage prostate cryoablation: initial results from the cryo on-line data registry. J Urol. 2008;180:559–63.
18. Ghafar MA, Johnson CW, De La Taille A, Benson MC, Bagiella E, Fatal M, et al. Salvage cryotherapy using an argon based system for locally recurrent prostate cancer after radiation therapy: the Columbia experience. J Urol. 2001;166:1333–7; discussion 1337–8.
19. Huang WC, Lee CL, Eastham JA. Locally ablative therapies for primary radiation failures: a review and critical assessment of the efficacy. Curr Urol Rep. 2007;8:217–23.
20. Gage AA, Baust JM, Baust JG. Experimental cryosurgery investigations *in vivo*. Cryobiology. 2009;59:229–43.
21. Klossner DP, Baust JM, VanBuskirk RG, Gage AA, Baust JG. Cryoablative response of prostate cancer

cells is influenced by androgen receptor expression. Br J Urol Int. 2008;101(10):1310–6.
22. Williams AK, Martinez CH, Lu C, Ng CK, Pautler SE, Chin JL. Disease free survival following salvage cryotherapy for biopsy-proven radio-recurrent prostate cancer. Eur Urol. 2011;60:405–10.
23. Ng CK, Moussa M, Downey DB, Chin JL. Salvage cryoablation of the prostate: followup and analysis of predictive factors for outcome. J Urol. 2007;178: 1253–7; discussion 1257.
24. Spiess PE, Katz AE, Chin JL, et al. A pretreatment nomogram predicting biochemical failure after salvage cryotherapy for locally recurrent prostate cancer. Br J Urol Int. 2010;106:194–8.
25. Ismail M, Ahmed S, Kastner C, Davies J. Salvage cryotherapy for recurrent prostate cancer after radiation failure: a prospective case series of the first 100 patients. Br J Urol Int. 2007;100:760–4.
26. Gowardhan B, Thomas B, Asterling S, Sheikh N, Greene DR. Cryosurgery for prostate cancer – experience with third-generation cryosurgery and novel developments in the field. Eur Urol Suppl. 2007;6: 516–20.
27. Ward JF, Nakanishi H, Pisters L, et al. Cancer ablation with regional templates applied to prostatectomy specimens from men who were eligible for focal therapy. Br J Urol Int. 2009;104:490–7.
28. Onik G, Barzell W. Transperineal 3D mapping biopsy of the prostate: an essential tool in selecting patients for focal prostate cancer therapy. Urol Oncol. 2008;26(5):506–10.
29. Onik G, Vaughan D, Lotenfoe R, et al. The "male lumpectomy": focal therapy for prostate cancer using cryoablation results in 48 patients with at least 2-year follow-up. Urol Oncol. 2008;26(5):500–5.
30. Bahn D, de Castro Abreu AL, Gill IS, et al. Focal cryotherapy for clinically unilateral, low-intermediate risk prostate cancer in 73 men with a median follow-up of 3.7 years. Eur Urol. 2012;62(1):55–63.
31. Ward JF, Jones JS. Focal cryotherapy for localized prostate cancer: a report from the national Cryo On-Line Database (COLD) Registry. BJU Int. 2012;109(11):1648–54.
32. Lambert EH, Bolte K, Masson P, et al. Focal cryosurgery: encouraging health outcomes for unifocal prostate cancer. Urology. 2007;69(6):1117–20.
33. Ellis DS, Manny Jr TB, Rewcastle JC. Focal cryosurgery followed by penile rehabilitation as primary treatment for localized prostate cancer: initial results. Urology. 2007;70(6 Suppl):9–15.

# Endoluminal Ultrasonography

# 12

Sima Porten, Raghu Vikram, and Surena F. Matin

The use of endoluminal ultrasonography (ELUS) to image the urinary tract was introduced more than two decades ago. This imaging technique is extensively used to evaluate vascular, gastrointestinal, and pulmonary organs, particularly for cancer [1–4]. But despite the fact that the tubular system of the lower and upper urinary tracts lends itself easily to ELUS, little information exists on the use of this method for evaluating the urinary tract, and the utility of this approach has not yet been fully proven for this organ. In this chapter, we discuss the technology of and the uses for ELUS throughout the urinary tract, from the urethra to the renal pelvis.

## The Physics of ELUS

Sonography relies on the use of crystals with a unique property called the piezoelectric effect. These crystals vibrate on electrical stimulation and produce sound waves, and they convert the vibrations from reflected sound waves back to electrical energy. Thus, these crystals are both producers and receivers of sound waves. The time a reflected sound wave takes to return and the known speed of sound through different types of tissue are used to calculate the distance of the reflecting object. This return signal is processed and displayed on a map. Regions that emit a stronger signal appear brighter on the map. This is the principle behind sonographic imaging.

A single piezoelectric crystal produces a single beam of sound; the frequency of the sound wave depends on the crystal. Crystals are arranged in arrays to image a wider region of tissue. Higher frequencies offer higher resolution images but at the cost of lower depth of imaging (also called depth of penetration). ELUS probes use a higher frequency than external probes (12–40 MHz versus 3–12 MHz).

## ELUS Equipment

Two types of probes are used with ELUS, catheter and sidesaddle. The catheter probe has a round tip and is stiff enough to be inserted directly through the cystoscope into the ureter. The more flexible sidesaddle probe, which is inserted over a guidewire, is useful in negotiating tight strictures when the guidewire can be passed through them. Both catheter and sidesaddle probes come in various sizes but the smallest is about 5 French in diameter.

Due to the features of these probes and the small diameter of the human ureter, the usefulness

S. Porten, MD, MPH • S.F. Matin, MD (✉)
Department of Urology, The University of Texas MD Anderson Cancer Center, Houston, TX, USA
e-mail: surmatin@mdanderson.org

R. Vikram, MD
Department of Diagnostic Radiology, The University of Texas MD Anderson Cancer Center, Houston, TX, USA
e-mail: rvikram@mdanderson.org

J.C. Liao, L.-M. Su (eds.), *Advances in Image-Guided Urologic Surgery*,
DOI 10.1007/978-1-4939-1450-0_12, 


**Fig. 12.1** ELUS probe and system. (**a**) Photograph of a 5.4 French (1.8 mm) ELUS probe. This probe can be passed over a guidewire, and it has a shielded transducer, which continuously rotates to provide radial images with adjustable scanning depths of 1–6 cm. (**b**) Photograph of the ELUS system setup at our institution. The actual system generator is hidden underneath the keyboard; a cable that houses the cable drive and electronics connects the generator to the probe, which is carefully placed in a holder and kept sterile with surrounding plastic drape. The monitor, recording capability, and cart are not part of the standard system but were put together by operating room personnel. (**c**) Photograph of system keyboard (All images copyright S.F. Matin 2013)

of ELUS in imaging the urinary tract is limited. For example, a 5-French probe is too large to pass through a ureteroscope. Thinner probes (3.5 French [1 mm]) are being developed that may fit through some ureteroscopes, allowing ultrasound to be used under direct vision [5]. Another limitation is that the presence of a probe disallows artificial distension of the ureter (particularly the distal ureter) with saline or the attachment of a balloon coupler at the tip of the ultrasound probe. Moreover, the inability to steer probes limits visualization of mid and lower pole calyces.

For the ureter and renal pelvis, we use a UM-S20-17S sidesaddle probe that is 5.4 French (1.8 mm) in diameter (Olympus America, Inc., Orangeburg, NY) placed over a guidewire (Fig. 12.1). This probe has a 20-MHz resolution and provides adequate resolution for up to 2 cm from the probe, which is generally sufficient for periureteric pathologic assessment. The detector element at the tip of this probe is attached to a motor that continually rotates the tip during scanning, thereby providing a 360-degree image (Fig. 12.2) approximately 10° from the true perpendicular to the catheter.

For ELUS imaging of the ureter and renal pelvis, retrograde pyelography is initially performed to evaluate the tissue for multifocality and to confirm the location of the index tumor. A guidewire is passed through the ureter, and the ELUS probe is placed over this and under fluoroscopy is passed to the site of the index tumor. The ultrasonographic image gain and contrast are adjusted to produce an anechoic signal for the surrounding fluid in the ureteral and renal pelvic lumen for optimal image acquisition. The imaging depth is

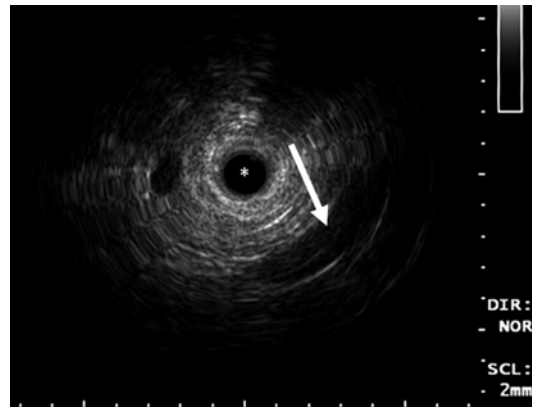


**Fig. 12.2** Typical ELUS images of the left mid-distal ureter. The catheter (*asterisk*) occupies the distal ureter, which is not distended. The iliac vessels are seen posterior and lateral to the ureter in the 5 o'clock position (*arrow*). An ultrasonographic shadow is generated by the guidewire (*tail of arrow*) (Copyright S.F. Matin 2013)

then adjusted to obtain optimal viewing and resolution (usually at 2–3 cm). The probe is passed methodically from below to above the tumor, and any abnormalities suggestive of invasion are noted (discussed below). A combination of intermittent fluoroscopy to view the position of the probe and recognition of anatomic landmarks is necessary for real-time interpretation of endoscopic ultrasonographic images. Once adequate imaging and documentation are completed, the probe is withdrawn, and ureteroscopic evaluation with biopsy and any other adjunctive procedures, such as stent placement, is performed.

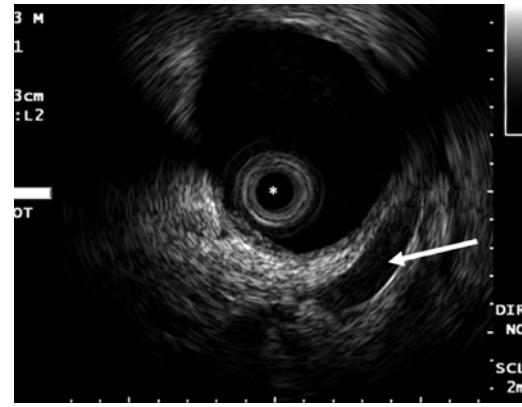


**Fig. 12.3** Typical ELUS image of the right renal pelvis. The renal pelvis is distended and filled with fluid. The mucosal layer is poorly visible; the muscularis layer itself is hypoechoic compared with the surrounding parenchyma and sinus fat. Reverberation artifact can be seen around the transducer (*asterisk*). The renal vein (*arrow*) is anterior to the pelvis and can be used to identify the anterior and posterior walls of the pelvis (Copyright S.F. Matin 2013)

## Interpretation of ELUS Images

While normal urologic anatomy is easily recognizable with ELUS, some familiarity with axial ultrasound images is helpful. The ureters traverse anterior to the iliac vessels at the level of the lumbar-sacral joint (Fig. 12.2). The segment inferior to the iliac vessels is the distal or pelvic ureter, and the segment superior to the iliac vessels to the pelvi-ureteric junction is the abdominal ureter. The capacious renal pelvis is usually filled with fluid and lacks the cylindrical contour of the ureters. The renal vein, which is anterior to the pelvis, is a useful landmark for identifying the anterior and posterior pelvic walls (Fig. 12.3).

Ureteral vessels, which are branches of renal, internal gonadal, hypogastric, or inferior vesicles, are seen as hypoechoic tubular structures running parallel to the ureteral lumen (Fig. 12.4). Three distinct layers of the ureters can be appreciated on high-frequency ultrasonography: an inner hyperechoic mucosa (the transitional epithelium), a middle hypoechoic layer comprised of circular and longitudinal muscles, and an outer hyperechoic layer which merges with the hyperechoic periureteric fat (which is composed of loose fibrous tissue) (Fig. 12.5). Renal parenchyma and pyramids are visible adjacent to the outer layer in the calyces.

Inflammatory and neoplastic lesions are difficult to differentiate on ELUS. Most lesions

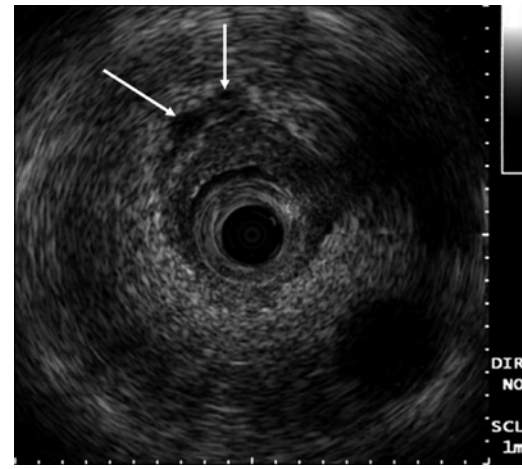


**Fig. 12.4** Typical ELUS image of the distal ureter. Ureteral vessels (*arrows*) run parallel to the ureter. These can be identified on real-time imaging and appear as hypoechoic tubular structures compared with periureteric fat (Copyright S.F. Matin 2013)

are isoechoic to the intermediate muscle layer or exhibit slightly low echogenicity. In a non-distended ureter, these lesions are seen as eccentric masses surrounding the ultrasound probe (Fig. 12.6). Visualization of the three sonographically distinct layers in the ureter

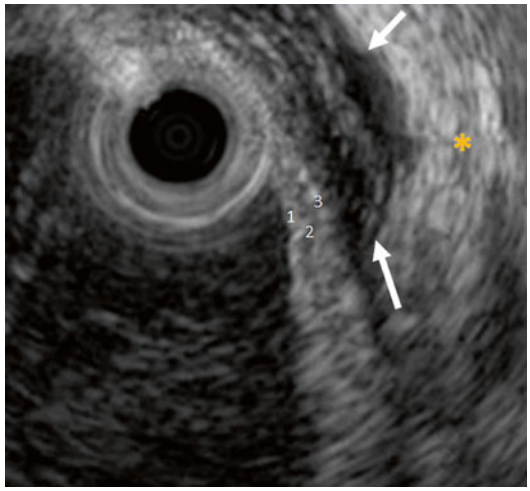


**Fig. 12.5** Three subtle but distinguishable layers of the ureter appear as alternating hyperechoic and hypoechoic bands. The inner hyperechoic mucosa (*1*), the middle hypoechoic muscularis (*2*), and the outer hyperechoic adventitious layer (*3*). The outer layer is difficult to appreciate in most examinations because it merges with the hyperechoic periureteric fat (*yellow asterisk*) unless separated by periureteric fluid (*arrows*) (Copyright S.F. Matin 2013)

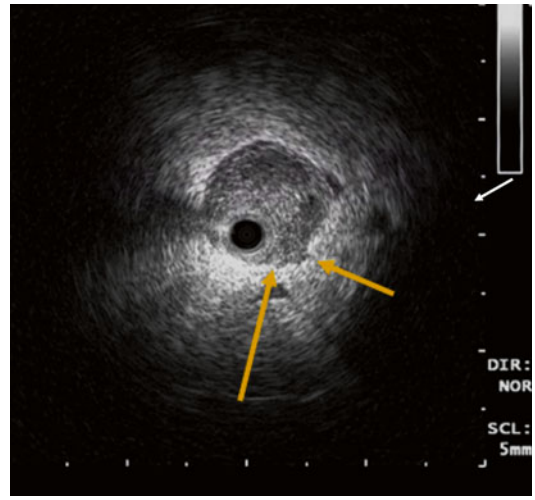


**Fig. 12.7** ELUS image of a mass in the right ureter of an UTUC at the level of the ureteropelvic junction. Loss of the smooth contour of the outer surface of the ureter (*arrows*) suggests periureteric spread. Periureteric vessels are indicated by the *white arrow* (Copyright S.F. Matin 2013)

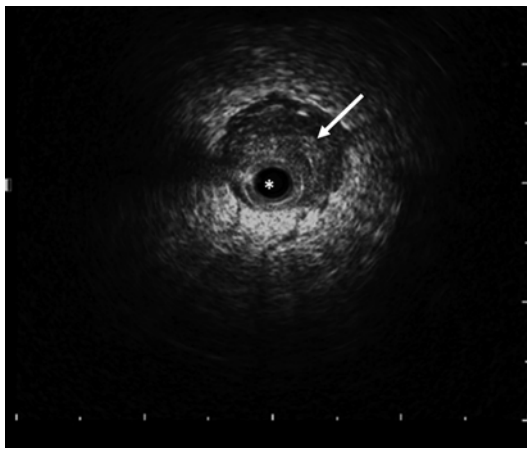

**Fig. 12.6** ELUS image of the right ureter of an UTUC. The catheter (*asterisk*) occupies the non-distended ureter, which shows eccentric thickening (*arrow*) compatible with urothelial tumor. The wire shadow is visible at the 9–10 o'clock position (Copyright S.F. Matin 2013)

should allow accurate assessment of the depth of invasion of tumor, similar to the experience of ELUS with assessing various gastrointestinal malignancies [6, 7]. Invasive tumors can be seen extending into the middle hypoechoic layer comprising the muscularis. Extension into the periureteric fat can be challenging to diagnose because the outer adventitious layer often has an echogenicity similar to that of the surrounding periureteric fat [8]. Lobularity (distortion of the smooth round or ovoid contours) of the outer surface of the ureter indicates periureteric spread of a lesion (Fig. 12.7).

If the ureter is not distended, the differentiation of sessile and polypoidal lesions can be challenging. The concomitant use of ureteroscopy makes this limitation less critical. In a well-distended system and in the renal pelvis, it is often possible to make this differentiation without ureteroscopy (Fig. 12.8). Pedunculated tumors can be diagnosed from sonographic imaging results in a distended system when a stalk and its attachment can be seen. The presence of a fluid interface between the mass and the ureteric wall suggests a pedunculated mass (Fig. 12.9).

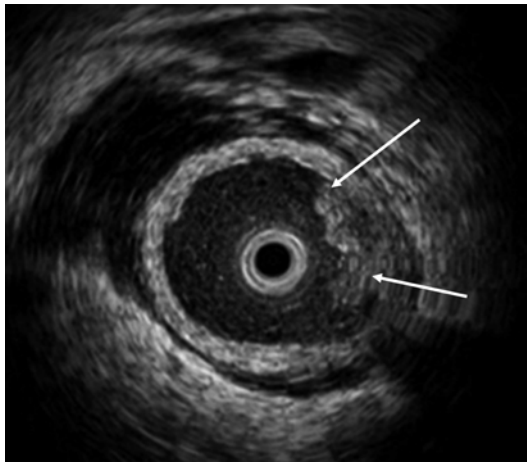

**Fig. 12.8** ELUS image of a mass in the left ureter of a 70-year-old male with UTUC. The ureter is distended and exhibits minimal periureteric fluid. There is a sessile mass between the 1 and 4 o'clock positions (*arrows*) (Copyright S.F. Matin 2013)

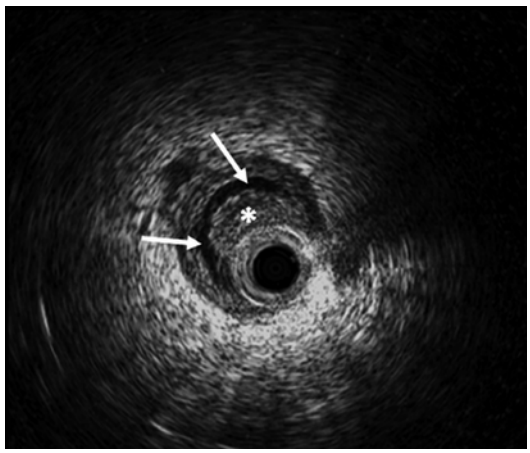

**Fig. 12.9** ELUS image of a mass in the left ureter of a 73-year-old female with UTUC. The mass (*asterisk*) is applied against the ultrasound catheter. A column of fluid (*arrows*) separates the mass from the ureteric wall (Copyright S.F. Matin 2013)

## Use of ELUS in Urologic Surgery

### Urethra

Very few studies have evaluated the use of ELUS in imaging the urethra. Chancellor et al. [9] assessed the usefulness of intraurethral sonography in a small case series of patients with urethral diverticula. Because a physical examination and clinical history are usually sufficient for a preoperative diagnosis, the role of ELUS in making this diagnosis is unclear. However, intraoperative ELUS improved the ability to perform complete dissection, ensured complete resection, helped to prevent injury, and helped in characterizing the diverticula [9].

Another potential application of ELUS is in the evaluation of the urethral rhabdosphincter [10, 11]. The capability of dynamic imaging using ELUS is advantageous and allows for real-time visualization. Klauser et al. [11] demonstrated that ELUS can distinguish morphologic changes in the sphincter mechanism; these changes translated to functional changes as measured by degree of urinary incontinence. In addition, ELUS was used by Rivas et al. [12] to evaluate and study the placement of periurethral collagen in a porcine system. The ability to use ELUS in relatively noninvasive fashion to evaluate the depth of collagen injection and to perform serial evaluations to assess durability of the collagen led the authors to conclude that submucosal injection was in optimal place. This animal model demonstrated the usefulness of ELUS for research purposes and scientific observation [12].

### Bladder

In 2000, Horiuchi and colleagues [13] reported on the use of ELUS for the assessment of invasion of bladder cancer in patients. They found that they were able to distinguish superficial muscle invasive tumors, but could distinguish Ta from T1 tumors due to lack of resolution, or evaluate the depth of invasion for tumors greater than 2 cm due to lack of penetration of the sonographic beam. In a follow-up animal study of porcine bladders, they used a 30-MHz probe to correlate the ultrasonographic imaging findings to the histologic findings of the bladder wall [14]. The bladder wall was depicted as five layers by ELUS, the first hyperechoic layer being a margin echo of

the urothelium and upper part of the lamina propria. The second hypoechoic layer corresponded to the lamina propria, and the third hyperechoic layer was a margin echo of the upper muscle layer. The fourth hypoechoic layer corresponded to the muscle layer, and the fifth hyperechoic layer was a margin echo of the upper adventitia. Saga et al. [13] reported that ELUS had a diagnostic accuracy of 84 % for tumor stage in a small group of 19 patients. However, an important limitation of this technique in that study was its inability to accurately evaluate the depth of invasion of large tumors. Additionally, tumors at the bladder neck were difficult to image. Determination of the dimensions of the tumor base, which is paramount to proper staging, was particularly difficult with ELUS [13]. Due primarily to limitations in assessing deeper structures, utility of ELUS in bladder imaging remains to be determined.

## Renal Pelvis and Ureter

The first clinical application of ELUS in urologic imaging, in 1995 [15], was for evaluating crossing vessels and ureteropelvic junction obstruction, and this is still the main use for this technique [16]. The use of ELUS has also been reported as an adjunctive tool in assessing the location of these strictures and crossing vessels in order to make endopyelotomy safer and more effective (at the time of its advent, in the early 1990s endopyelotomy represented a somewhat "blind" approach to treating ureteropelvic junction obstruction) [15]. However, with improvements in cross-sectional imaging, the need for ELUS in this setting has somewhat diminished.

The greatest potential for ELUS lies in the preoperative staging of ureteral and renal pelvic tumors or upper tract urothelial carcinomas (UTUCs). Although ureteroscopic biopsy analysis and architecture evaluation have prognostic value [17, 18], a significant proportion of patients with UTUC are misclassified preoperatively. Cross-sectional imaging of UTUC has notable limitations and is particularly prone to understaging the disease [8]. The problem of understaging is magnified by the limited tools available for ureteroscopy and the human anatomy, which does not allow for resection of the full thickness of the ureteral or renal pelvic wall. More accurate preoperative risk stratification has gained in importance as neoadjuvant chemotherapy is increasingly being considered for patients whose treated cancers are at high risk for relapse [19, 20]. Patients who undergo nephroureterectomy are at significant risk of worsening chronic kidney disease (or developing it), limiting the effective administration of *cis*-platinum-based cytotoxic therapy [17, 19, 21].

Because staging tumors with radiographic images has limitations, such as inability to assess muscular invasion or beyond, several attempts have been made to assess whether ELUS imaging can be used to more accurately stage UTUCs preoperatively. To date, very few patients have undergone sonographic-pathologic correlation of imaging findings to evaluate the utility of this imaging technology [3, 4, 22]. In 1997, Liu and colleagues [23] evaluated two patients with UTUC who then underwent surgical excision. For both patients, postoperative pathologic analysis of the tumors confirmed invasive disease. In 2008, Ingram and colleagues [24] published a set of findings using ELUS (termed as transureteric ultrasound, TUU, in that report), noting that UTUC typically appeared as a focal eccentric irregular hypoechoic wall thickening with bulging into the lumen, which may or may not demonstrate invasion into the surrounding tissues, and that nonmalignant causes of ureteric wall thickening and demonstrated a more concentric and symmetrical appearance. However, considerable overlap was found, and aside from one set of figures, no patient data or sonographic-pathologic correlation was provided. More than a decade later, a pilot evaluation of ELUS was performed to assess its utility as an UTUC staging tool [22]. Of 15 patients evaluated, 7 subsequently underwent initial surgery, allowing for correlation between sonographic images and pathologic findings. Six of those seven patients were found to have had accurately staged tumors with ELUS; the seventh patient had been diagnosed with T2 disease, but on final pathologic analysis this tumor was determined to be noninvasive. Thus, the positive and negative predictive values for invasion on ELUS

images were 66.7 and 100 %, respectively, in this limited population [22]. Additional studies are being performed to confirm these initial results, with currently over 60 patients having undergone evaluation at our institution.

One limitation of using ELUS for evaluating UTUCs is the inability to "steer" the probe, which is relevant to tumors in the lower or mid calyces, where the guidewire usually does not migrate. A water column around the probe can improve the sonographic image, but the column is difficult to maintain, particularly at the mid and distal ureters [25].

### Conclusion

Although the first feasibility study of the use of ELUS in the upper urinary tract was reported in 1995, just a few further small studies have studied the utility of this technique in this region. In addition, most patients with urologic cancer receive chemotherapy to downstage tumors prior to surgical excision, which does not permit accurate radiopathological correlation. There is a need for large well-designed studies to validate the use of ELUS in routine practice. Despite the lack of these studies, ELUS of the urinary tract has been shown to be feasible and has the potential to improve the diagnosis, staging, and treatment of many benign and malignant urologic conditions. Currently, its greatest utility is imaging of the upper urinary tract because it overcomes some limitations of cross-sectional imaging and traditional ureteroscopy. The ability of ELUS to capture dynamic images also makes it an attractive tool for evaluation of urethral disease. Further research is needed to determine its true diagnostic capability, the benefit it provides to patients, and its dissemination and acceptance into general practice.

## References


1. Liu JB, Goldberg BB. 2-D and 3-D endoluminal ultrasound: vascular and nonvascular applications. Ultrasound Med Biol. 1999;25(2):159–73.
2. Liu J-B, Miller LS, Bagley DH, Goldberg BB. Endoluminal sonography of the genitourinary and gastrointestinal tracts. J Ultrasound Med. 2002;21(3):323–37.
3. Grotas A, Grasso M. Endoluminal sonographic imaging of upper urinary tract: three-dimensional reconstruction. J Endourol. 2001;15(5):485–8.
4. Kondabolu S, Khan SA, Whyard J, Diblasio C, Ayyala M, Pentyala S. The role of endoluminal ultrasonography in urology: current perspectives. Int Braz J Urol. 2004;30(2):96–101.
5. Lee DI, Bagley DH, Liu JB. Experience with endoluminal ultrasonography in the urinary tract. J Endourol. 2001;15(1):67–74.
6. Gravante G, Giordano P. The role of three-dimensional endoluminal ultrasound imaging in the evaluation of anorectal diseases: a review. Surg Endosc. 2008;22(7):1570–8.
7. Reid AW, Reid DB, Roditi GH. Imaging in endovascular therapy: our future. J Endovasc Ther. 2009;16 Suppl 1:I22–41.
8. Browne RFJ, Meehan CP, Colville J, Power R, Torreggiani WC. Transitional cell carcinoma of the upper urinary tract: spectrum of imaging findings. Radiographics. 2005;25(6):1609–27.
9. Chancellor MB, Liu JB, Rivas DA, Karasick S, Bagley DH, Goldberg BB. Intraoperative endoluminal ultrasound evaluation of urethral diverticula. J Urol. 1995;153(1):72–5.
10. Strasser H, Frauscher F, Helweg G, Colleselli K, Reissigl A, Bartsch G. Transurethral ultrasound: evaluation of anatomy and function of the rhabdosphincter of the male urethra. J Urol. 1998;159(1):100–4; discussion 104–5.
11. Klauser A, Frauscher F, Strasser H, Helweg G, Kolle D, Strohmeyer D, et al. Age-related rhabdosphincter function in female urinary stress incontinence: assessment of intraurethral sonography. J Ultrasound Med. 2004;23(5):631–7; quiz 638–9.
12. Rivas DA, Chancellor MB, Liu JB, Hanau C, Bagley DH, Goldberg B. Endoluminal ultrasonographic and histologic evaluation of periurethral collagen injection. J Endourol. 1996;10(1):61–6.
13. Horiuchi K, Tsuboi N, Shimizu H, Matsuzawa I, Kimura G, Yoshida K, et al. High-frequency endoluminal ultrasonography for staging transitional cell carcinoma of the bladder. Urology. 2000;56(3):404–7.
14. Horiuchi K, Shimizu H, Yoshida K, Nishimura T. Identification of the layers of the bladder wall on high-frequency endoluminal ultrasonography by a needle puncture experiment. Ultrasound Med Biol. 2005;31(3):307–9.
15. Bagley DH, Liu JB, Goldberg BB, Grasso M. Endopyelotomy: importance of crossing vessels demonstrated by endoluminal ultrasonography. J Endourol. 1995;9(6):465–7.
16. Keeley Jr FX, Moussa SA, Miller J, Tolley DA. A prospective study of endoluminal ultrasound versus computerized tomography angiography for detecting crossing vessels at the ureteropelvic junction. J Urol. 1999;162(6):1938–41.

17. Brown GA, Matin SF, Busby JE, Dinney CPN, Grossman HB, Pettaway CA, et al. Ability of clinical grade to predict final pathologic stage in upper urinary tract transitional cell carcinoma: implications for therapy. Urology. 2007;70:252–6.
18. Margulis V, Shariat SF, Matin SF, Kamat AM, Zigeuner R, Kikuchi E, et al. Outcomes of radical nephroureterectomy: a series from the upper tract urothelial carcinoma collaboration. Cancer. 2009;115(6):1224–33.
19. Igawa M, Urakami S, Shiina H, Kishi H, Himeno Y, Ishibe T, et al. Neoadjuvant chemotherapy for locally advanced urothelial cancer of the upper urinary tract. Urol Int. 1995;55(2):74–7.
20. Matin SF, Margulis V, Kamat A, Wood CG, Grossman HB, Brown GA, et al. Incidence of downstaging and complete remission after neoadjuvant chemotherapy for high-risk upper tract transitional cell carcinoma. Cancer. 2010;116(13):3127–34.
21. Hall MC, Womack S, Sagalowsky AI, Carmody T, Erickstad MD, Roehrborn CG. Prognostic factors, recurrence, and survival in transitional cell carcinoma of the upper urinary tract: a 30-year experience in 252 patients. Urology. 1998;52(4):594–601.
22. Matin SF, Kamat AM, Grossman HB. High-frequency endoluminal ultrasonography as an aid to the staging of upper tract urothelial carcinoma: imaging findings and pathologic correlation. J Ultrasound Med. 2010;29(9):1277–84.
23. Liu JB, Bagley DH, Conlin MJ, Merton DA, Alexander AA, Goldberg BB. Endoluminal sonographic evaluation of ureteral and renal pelvic neoplasms. J Ultrasound Med. 1997;16(8):515–21; quiz 523–4.
24. Ingram MD, Sooriakumaran P, Palfrey E, Montgomery B, Massouh H. Evaluation of the upper urinary tract using transureteric ultrasound–a review of the technique and typical imaging appearances [review]. Clin Radiol. 2008;63(9):1026–34.

# Part III

# Cross-Sectional Image-Guided Interventions

# 13 Multiparametric Magnetic Resonance Imaging for Prostate Cancer

Geoffrey A. Sonn, Daniel J.A. Margolis, and Katherine J. To'o

Since the advent of PSA screening in the 1980s [1, 2], a clinical paradigm has existed whereby an abnormal PSA level in the blood prompts a biopsy to evaluate for prostate cancer. A biopsy showing cancer most often leads to definitive treatment. This approach has coincided with a decline in prostate cancer-specific mortality over the last 20 years [3].

Despite the decline in mortality, PSA screening has received wide criticism. In 2012, the US Preventive Services Task Force (USPSTF) concluded that the harms of screening outweigh its benefits and therefore recommended against PSA screening. The report highlighted the good prognosis of most cases of untreated prostate cancer while criticizing the substantial rate of prostate cancer overdiagnosis (17–50 %) and overtreatment [4–6]. The problem of overtreatment stems from an inability to distinguish indolent from aggressive cancer. This is critically important because low-grade, indolent cancers are slow growing and rarely harmful, while high-grade, aggressive cancers pose a substantial risk of prostate cancer-related morbidity and death. Yet, all treatments for prostate cancer, whether the cancer is indolent or aggressive, are associated with substantial rates of morbidity.

The USPSTF report states that "the inevitability of overdiagnosis and overtreatment of prostate cancer as a result of screening means that many men will experience the adverse effects of diagnosis and treatment of a disease that would have remained asymptomatic throughout their lives." This provides a clear mandate to change the current paradigm of prostate cancer diagnosis and management.

Fortunately, the problems associated with management of prostate cancer noted in the USPSTF statement have a variety of potential solutions. These include reducing the number of men who undergo prostate biopsy, reducing detection of insignificant cancers by changing from systematic prostate biopsy to an image-targeted approach, reducing the number of men who pursue definitive treatment by increasing the appeal of active surveillance via improved detection of aggressive cancers, and reducing the treatment-related morbidity.

Unlike all other solid organ malignancies, imaging has until now played an extremely

G.A. Sonn, MD (✉)
Department of Urology,
Stanford University School of Medicine,
Stanford, CA, USA
e-mail: gsonn@stanford.edu

D.J.A. Margolis, MD
Department of Radiological Sciences,
UCLA Geffen School of Medicine,
Los Angeles, CA, USA
e-mail: daniel.margolis@ucla.edu

K.J. To'o, MD
Department of Radiology,
VA Palo Alto Health Care System,
Palo Alto, CA, USA

Department of Radiology,
Stanford University School of Medicine,
Stanford, CA, USA

J.C. Liao, L.-M. Su (eds.), *Advances in Image-Guided Urologic Surgery*,
DOI 10.1007/978-1-4939-1450-0_13, 

limited role in prostate cancer diagnosis. Improvements in imaging of localized prostate cancer have the potential to achieve the solutions noted above. Improved imaging could aid cancer detection and staging, improve risk stratification by differentiating indolent from aggressive cancer, guide biopsy, personalize treatment selection, and monitor treatment response. Of currently available imaging modalities, only magnetic resonance imaging (MRI) has both the spatial-resolution and soft-tissue contrast necessary to accurately image localized prostate cancer [7]. This chapter describes the fundamentals of prostate cancer multiparametric MRI (mpMRI) by summarizing the individual MR imaging techniques that together comprise state-of-the-art mpMRI, addresses interpretation and reporting, and discusses the role of MRI in clinical practice.

## Primer on Prostate MRI

The intense interest in prostate MRI over the past 5 years belies the fact that prostate MRI is not new. Rather, it was initially described over 30 years ago using a magnet operating at 0.35 T [8, 9]. Until recently, prostate MRI relied on morphologic and signal changes on T1- and T2-weighted images and suffered from relatively poor sensitivity and specificity [7]. As a result of its poor performance, prostate MRI developed the widespread reputation as a technique of limited clinical utility.

The advent of stronger magnets and multiparametric protocols has transformed prostate MRI into a technique with a variety of clinical applications. Unlike the MRI systems of the early 1980s, most current scanners operate at 1.5 or 3.0 Tesla (T). Stronger magnetic fields provide a greater signal-to-noise ratio (SNR). This allows for either better resolution or shorter image acquisition time.

To obtain MR images, patients are placed on a gantry that passes through the bore of the magnet. When exposed to the strong magnetic field present in a clinical MRI scanner, the free water protons in the patient orient themselves along the head-to-toe axis ($z$-axis) of the magnetic field. A radiofrequency (RF) coil transmits RF pulses through the patient. When the RF pulse stops, protons release their energy. Detecting and processing this energy release generates the MR image (Fig. 13.1). MR sequences make use of the unique transverse and longitudinal energy absorption and release of different body tissues. This allows MRI to resolve the many tissue types in the body.

To receive signal, prostate MRI requires a pelvic phased-array coil laid directly across the patient's pelvis. This can be supplemented with an optional endorectal coil (ERC) (Fig. 13.2). The ERC is particularly useful for 1.5-T MRI but is less necessary for 3.0 T. The ERC is placed transrectally. Due to its close proximity to the prostate, it can augment the amount of signal available to generate the image. While it is clear that the highest quality MRI results from the combination of a pelvic phased-array coil and an ERC at 3.0 T (Fig. 13.3), a measurable clinical benefit of adding the ERC to the pelvic coil has yet to be proven [10]. Literature comparing cancer staging with T2-weighted imaging at 3.0 T with and without an ERC is conflicting [11, 12]. In addition to the unproven clinical benefit, use of an ERC is more time consuming, expensive, uncomfortable for the patient; requires trained staff to place it; and can introduce magnetic susceptibility and motion-related artifacts. As a result, use of an ERC varies across institutions and study protocols. For 3.0-T prostate MRI at UCLA, an ERC is used for staging purposes prior to prostatectomy but omitted when using MRI for cancer detection prior to targeted biopsy.

MR images are typically described as being T1 or T2 weighted. Weighting depends on how energy is imparted through the physics of the pulse sequence. T1-weighted images are generated by the time to return to equilibrium in the $z$-axis, while T2-weighted images are produced by the time to return to equilibrium in the $xy$-axis. Practically speaking, on T1-weighted images fluid is low signal and appears dark. On T2-weighted MR images, fluid is high signal and appears bright.

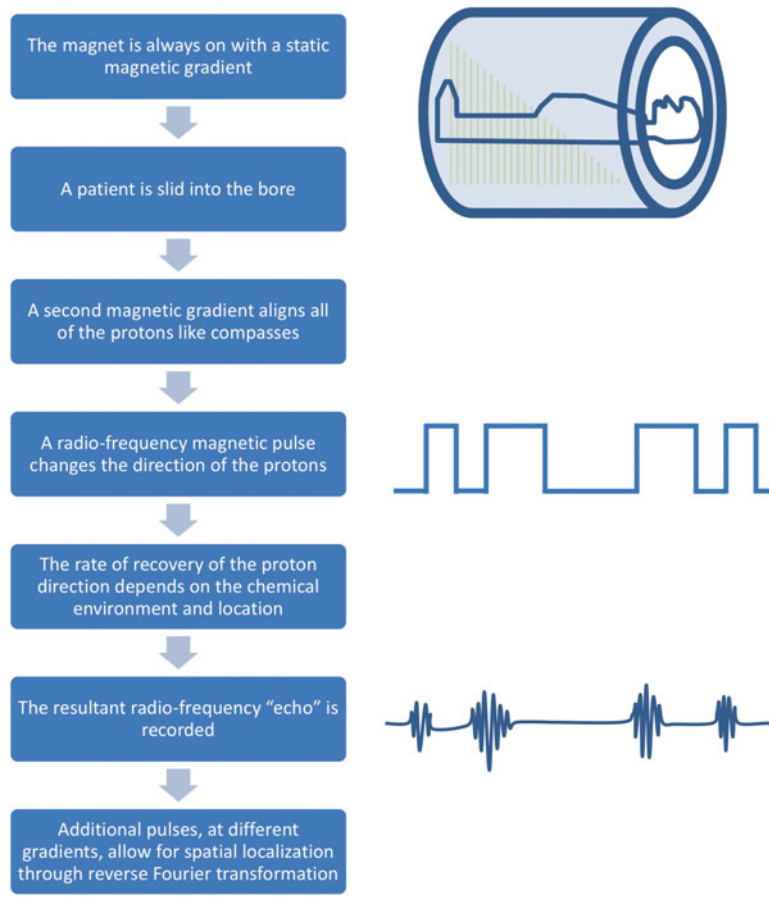


**Fig. 13.1** Schematic describing the physics underlying magnetic resonance imaging

## Multiparametric MR Imaging Techniques

### T2-Weighted Imaging

T2-weighted imaging provides information on prostate morphology, internal structure (zonal anatomy), and cancer margins. It is typically acquired in multiple planes at high resolution using a narrow image thickness (3–4 mm) [7]. The peripheral zone (PZ) can be clearly differentiated from the central gland (CG), which includes the transition zone (TZ) and the central zone. The PZ classically has homogenous high signal intensity. In contrast, the CG has lower signal intensity and is often markedly heterogeneous in appearance. The urethra, seminal vesicles, and verumontanum can also be visualized on T2-weighted MRI (Fig. 13.4).

Seventy percent of all prostate cancers originate in the peripheral zone. These cancers classically appear on T2-weighted MRI as round or ill-defined, low-signal-intensity (dark) foci [13]. This appearance is not always present as some cancers are isointense. In addition, specificity is limited. Prostatic atrophy, prior prostatitis, hemorrhage after biopsy, or posttreatment changes can have variable signal intensity in the PZ and mimic cancer (Figs. 13.5 and 13.6) [10]. Noncontrast T1-weighted images are useful to rule out biopsy-related hemorrhage as the cause of low signal intensity in the PZ [10]. As the appearance of post-biopsy changes could mask the presence prostate cancer on T2-weighted imaging, it is customary to delay MRI for at least 4–6 weeks after biopsy [14]. Others recommend a longer interval of >8 weeks [15].


**Fig. 13.2** Photographs of sample MRI scanner (**a**) and external phased-array coil (**b**) used for all prostate MRI examinations. An optional endorectal coil (**c**) can be inserted into the rectum and inflated with perfluorocarbon to achieve improved signal to noise (© Siemens Healthcare 2014. Used with permission)

The high resolution achieved with T2-weighted imaging proves useful for cancer staging (Fig. 13.7). Extracapsular extension (ECE) can manifest itself as direct tumor extension into the periprostatic fat, an interruption of the thin black line representing the prostate capsule, asymmetric capsular bulge with irregular margins, obliteration of the rectoprostatic angle, or asymmetry of the neurovascular bundle (NVB). Seminal vesicle invasion (SVI) appears as low-signal foci that directly extend from the tumor at the prostatic base into the seminal vesicles. This differs markedly from the uniform high signal of normal seminal vesicles.

Cancers in the central gland are more difficult to detect because of the heterogenous appearance of the normal central gland on MRI. Benign prostatic hyperplasia (BPH), a ubiquitous finding in aging men, often mimics cancer on MRI. When cancers are visible in the central gland, they typically appear as a homogenous low-signal-intensity lesion with indistinct, irregular margins that often invades the pseudocapsule [16].

A recent meta-analysis of 19 articles found T2-weighted imaging alone to have a sensitivity of 60 %, specificity of 76 %, and area under the ROC curve of 0.75 for cancer detection [17]. This compilation of the data obscures the great variability in performance of T2-weighted imaging across different studies. In a 2009 review article, Turkbey et al. concluded that wide ranges in sensitivity (22–85 %) and specificity (50–99 %)

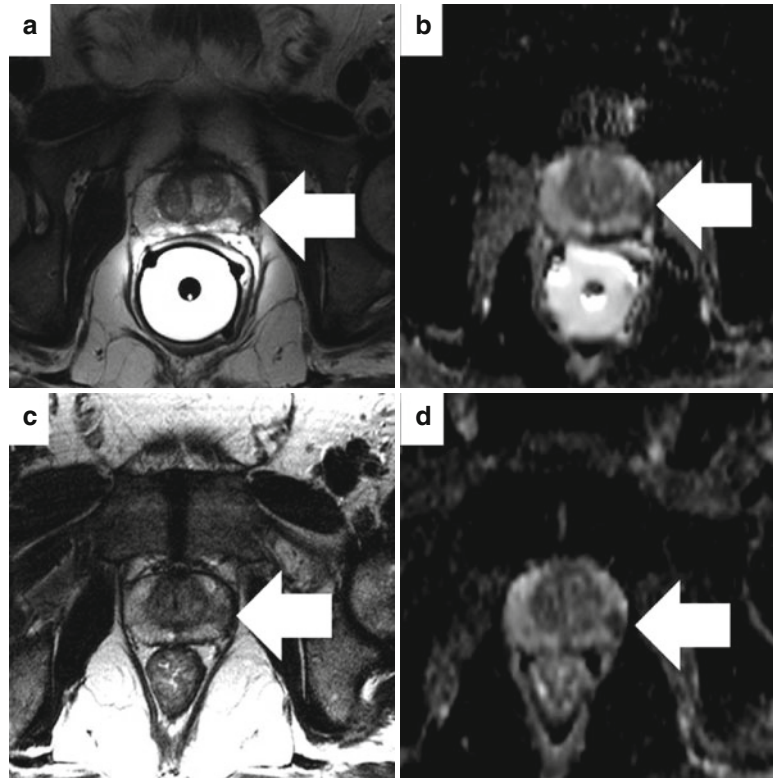


**Fig. 13.3** Comparison of imaging with (**a**, **b**) and without (**c**, **d**) an endorectal coil at 3 T. An axial T2-weighted image (**a**) and ADC map (**b**) show a discrete focus of low signal in the left peripheral prostate with a broad base of contact with the capsule (*arrow*) but preservation of the *dark line* representing the capsule itself. This is characteristic of cancer confined within the prostate. The same axial T2-weighted image (**c**) and ADC map (**d**) without the endorectal coil show the low-signal area, but the capsule is less well resolved. Focally restricted diffusion is evident on both acquisitions

stem from differences in equipment, patient selection, experience, and methodology for pathologic correlation [10]. The authors concisely summarized the difficulty of performing correlation studies of MRI and histopathology due to differences in alignment of MRI and histologic sections. As a result, excessively strict interpretation of MRI and pathology correlation without considering the effect of misregistration can lead to sensitivity/specificity outcomes that are too low, while overly lenient interpretation can overestimate the ability of MRI to detect prostate cancers [10]. This issue is pertinent to all studies evaluating the performance of mpMRI.

Given the limitations of T2-weighted imaging, it became clear that additional sequences were needed to more accurately identify and characterize localized prostate cancer. This realization led to the development of functional parameters (diffusion-weighted imaging, dynamic contrast-enhanced imaging, and MR spectroscopy) that have enabled substantial improvement in the utility of mpMRI.

## Diffusion-Weighted Imaging

In diffusion-weighted imaging (DWI), image contrast is generated by differences in the Brownian motion of water molecules within different tissues. While water molecules in a container outside the body are in constant, uninhibited motion, the movement of water molecules in biologic tissues is restricted because of interactions with cell membranes and macromolecules [18]. The motion of water molecules is more restricted in tissues with high cellular density and intact cell membranes. The high cellular density and more complex intracellular microstructure of tumors restrict water diffusion in the tissue, a phenomenon that is detectible as a bright signal on DWI.

Diffusion-weighted gradients are applied to water protons, and the resultant signal is related to the ability of water protons to move freely in space. The "*b*-value" (in s/mm$^2$) of DWI is a function of the strength of the diffusion gradient. Low *b*-values measure water movement over a

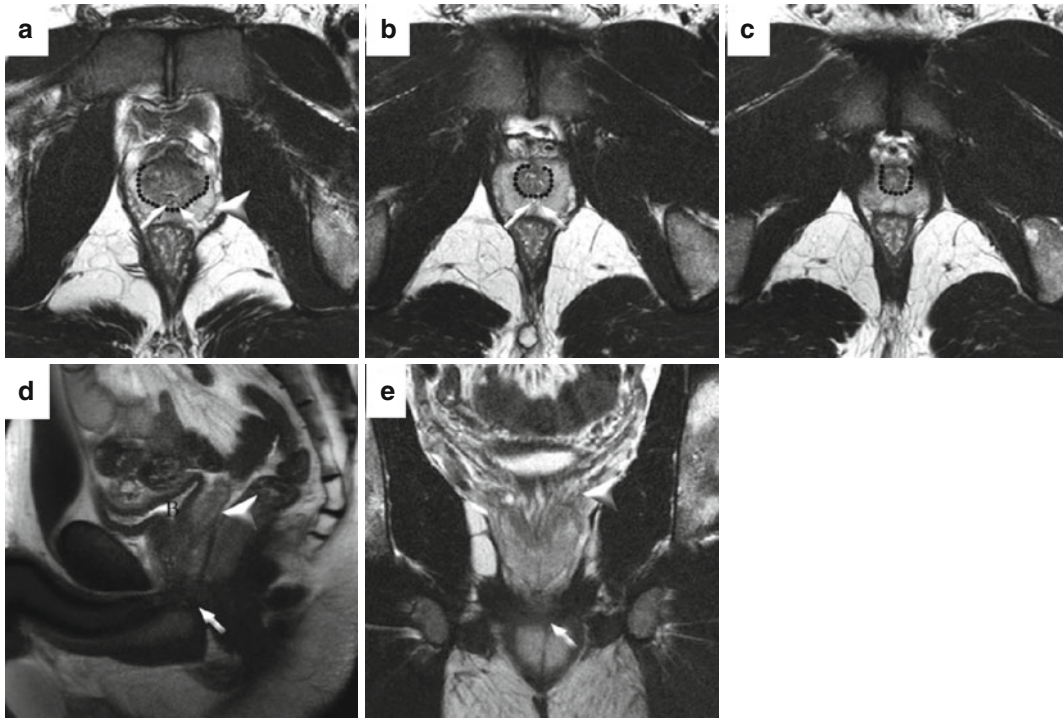


**Fig. 13.4** Normal prostate anatomy on T2-weighted sequences in a healthy 31-year-old. Transaxial images at the base (**a**), midgland (**b**), and apex (**c**). The *dotted line* outlines the "pseudocapsule" which is the T2 hypointense boundary between the heterogeneous central gland (composed of both central and transitional zones) and T2 hyperintense peripheral zone. The capsule (*arrowhead*) is a low T2 signal-intensity rim at the junction of the prostate and periprostatic fat. The ejaculatory ducts are denoted by *oblique arrows*. Sagittal (**d**) and coronal (**e**) T2W images show the hyperintense seminal vesicles (*arrowheads*) and low-signal urogenital diaphragm (*oblique arrows*). The bladder (*B*) is empty

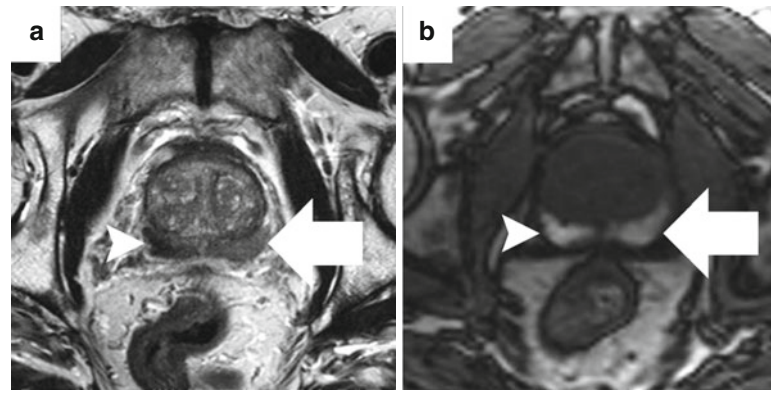


**Fig. 13.5** Abnormal T2 signal from hemorrhage artifact. Low T2 signal intensity within bilateral peripheral zones (**a**), right (*arrowhead*) greater than left (*arrow*), corresponds to regions of T1 shortening, consistent with post-biopsy hemorrhage (**b**)

large length (i.e., capillary perfusion). High *b*-values measure water movement over a small length (i.e., within cells). The use of higher *b-values* (1,000–2,000 s/mm$^2$) has been shown to improve prostate cancer detection [19, 20]. When at least two *b*-values are acquired, an apparent diffusion coefficient (ADC) map can be generated which displays the ADC value of each voxel. According to Barentsz, minimal requirements for generating ADC maps are *b*-values of 0, 100, and

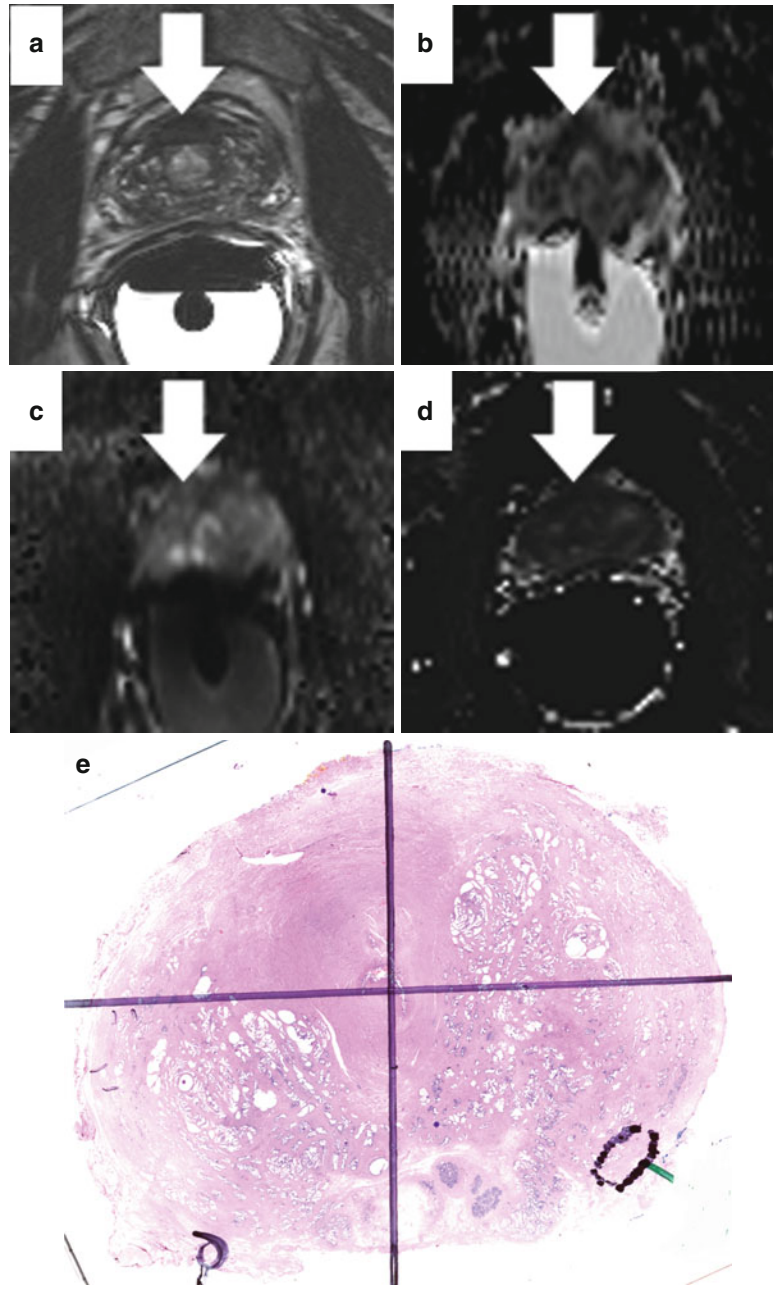


**Fig. 13.6** T2-weighted images (**a**) show an asymmetric hypointense "mass" in the anterior fibromuscular stroma with bulges into the transitional zone (*arrow*). Low signal on the ADC map (**b**) suggests abnormal cellularity. However, the DWI (**c**) shows low signal, signifying that the low signal on the ADC map is from lack of water protons rather than truly restricted diffusion. The perfusion map (**d**) confirms relative hypoperfusion, consistent with hypertrophic anterior fibromuscular stroma, confirmed on whole-mount histology (**e**)

800–1,000 and optimally a *b*-value of 500 would also be included [13]. The ADC map is especially useful for prostate cancer identification. Prostate cancer typically has a high signal intensity (bright) on DWI at high *b*-value and low signal intensity (dark) on ADC maps (Fig. 13.8).

DWI is exquisitely sensitive to motion artifact and is intrinsically a low SNR sequence that is affected by magnetic susceptibility effects which result in spatial distortion and signal loss [13]. This results in relatively low-resolution, "noisy" images. In spite of this, DWI is an essential part of mpMRI because of improved specificity, information about tumor aggressiveness, and correlation with the volume of the index lesion [13]. DWI is relatively easy to implement as

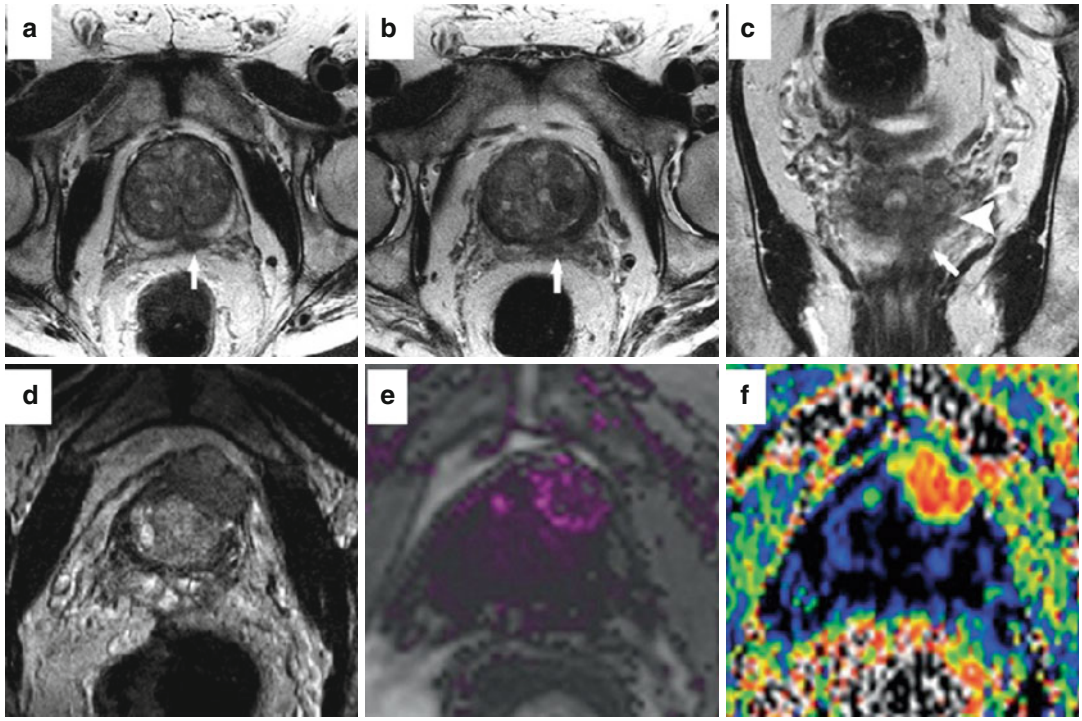


**Fig. 13.7** Sample cases of staging with multiparametric MRI at 3 T. In patient #1, an ill-defined low-signal mass on the *left* shows irregularity of the prostate capsule on axial images and extends from the midgland (**a**) to the base (**b**) where it abuts the seminal vesicles. The mass (*arrow*) also extends to the seminal vesicles (*arrowhead*) on coronal images (**b**). This was confirmed as a pT3b Gleason 4+5 adenocarcinoma with ECE at prostatectomy. In patient #2, (**d**) axial T2-weighted image shows a large mass with marked extraprostatic extension arising from the *left*, anterior prostate. Corresponding abnormalities were seen on dynamic contrast-enhanced imaging (**e**) and the ADC map (**f**)

acquisition time is short, and no exogenous contrast is required. It yields qualitative and quantitative information reflecting changes at a cellular level. As a result of its simplicity and added value, DWI should be included in all prostate MRI protocols.

Numerous publications have documented the value of DWI for prostate cancer imaging [17, 21–25]. A recent meta-analysis including data from 627 patients showed a sensitivity of 76 % and specificity of 82 % for the combination of DWI and T2-weighted imaging [25]. A separate meta-analysis further corroborated the value of adding DWI to T2-weighted imaging. The addition of DWI increased sensitivity from 60 to 70 % and specificity from 76 to 83 %. Notably, the area under the ROC curve was better for DWI alone than DWI+T2 (0.85 vs. 0.73), while sensitivity and specificity were comparable [17].

In addition to improving cancer detection, DWI also provides information about cancer aggressiveness. ADC values have been shown in multiple studies to be inversely correlated with Gleason score, the pathologic criteria that serves as the gold standard for predicting biologic behavior of prostate cancer [26–30]. Unfortunately, defining numerical ADC values to differentiate benign from malignant tissue that apply across institutions is difficult due to considerable inter-patient variability, overlap between ADC values for cancer and normal prostate, differences in scanner software and hardware, and a strong dependence between ADC and specific *b*-values used [7, 13, 31]. Standardization of protocols for image acquisition and data analysis is important to facilitate widespread adoption of DWI and enable accurate comparison of results from different institutions.

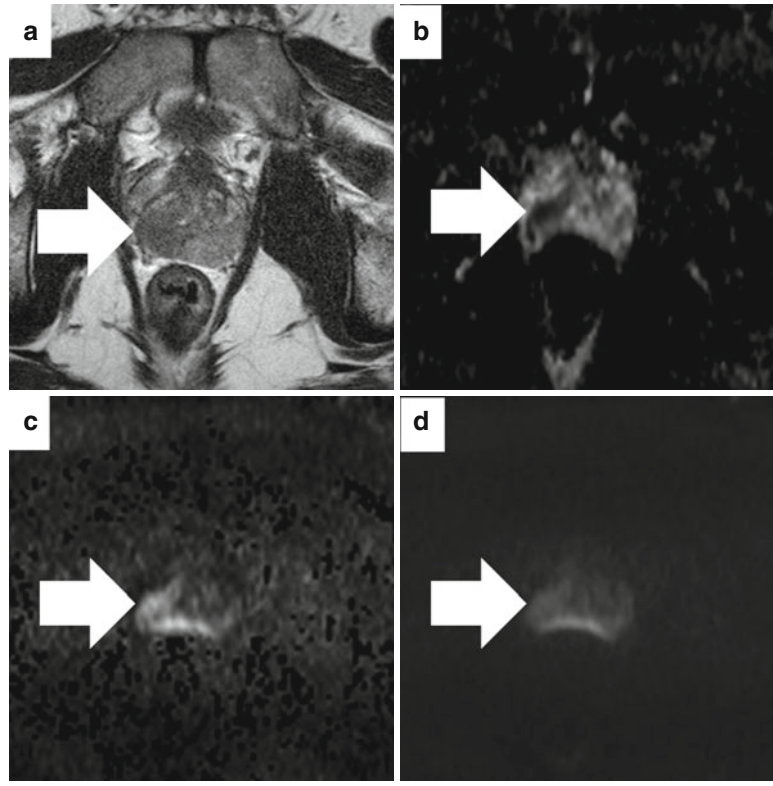


**Fig. 13.8** Diffusion-weighted imaging (*DWI*) and apparent diffusion coefficient map on 3T magnet without endorectal coil in a patient with Gleason 5+4 pT3b adenocarcinoma at subsequent prostatectomy. On the axial T2-weighted image (**a**), a low-signal region (*arrow*) bulges the capsule. The corresponding apparent diffusion coefficient (*ADC*) map (**b**) shows low signal ($0.938 \times 10^{-3}$ mm$^2$/s). The axial high *b*-value DWI ($b = 1{,}400$ s/mm$^2$) image (**c**) shows asymmetric high signal (*arrow*) concordant with the ADC map. However, this lesion is less obvious on the lower *b*-value DWI ($b = 800$ s/mm$^2$ image) (**d**)

Adoption of the imaging protocols proposed in the recently issued ESUR prostate MRI guidelines should help this effort [13].

## Dynamic Contrast-Enhanced MRI

Dynamic contrast-enhanced (DCE) MRI is another functional sequence that contributes to diagnostic accuracy through improved sensitivity. DCE detects angiogenesis by measuring differences in blood flow between cancer and normal tissue. Classically, prostate cancer demonstrates rapid and intense contrast enhancement and rapid washout [32, 33].

DCE MRI most often consists of a series of fast T1-weighted sequences performed before and after rapid infusion of gadolinium contrast material [7, 13]. Interpretation can be qualitative, semiquantitative, or quantitative. Qualitative analysis includes either visual inspection of the images for areas that rapidly and intensely enhance or plotting kinetic curves of signal intensity vs. time. This method is simple, quick, and unlike other analytic methods does not require dedicated hardware or software [34]. Kinetic curve analysis is recommended in the recent ESUR guidelines [13]. However, simple comparison of pre- and post-contrast images is usually insufficient to detect prostate cancer because of the highly vascularized nature of the normal prostate [35]. Semiquantitative analysis involves calculation of kinetic parameters (time to peak enhancement, wash-in rate, wash-out rate) for each voxel. These parameters are then constructed into colorized maps overlaid on T2-weighted images (Fig. 13.9). Quantitative analysis uses pharmacokinetic models to determine the rate of exchange of contrast between blood and the extracellular space [36]. The quantitative vascular parameters $K^{trans}$ (transfer constant for contrast moving between blood plasma and extravascular space) and $K_{ep}$ (rate constant between extravascular space and blood plasma) have been shown to be elevated in tumors. Quantitative analysis is considered to be more resistant to variation in injection-related factors

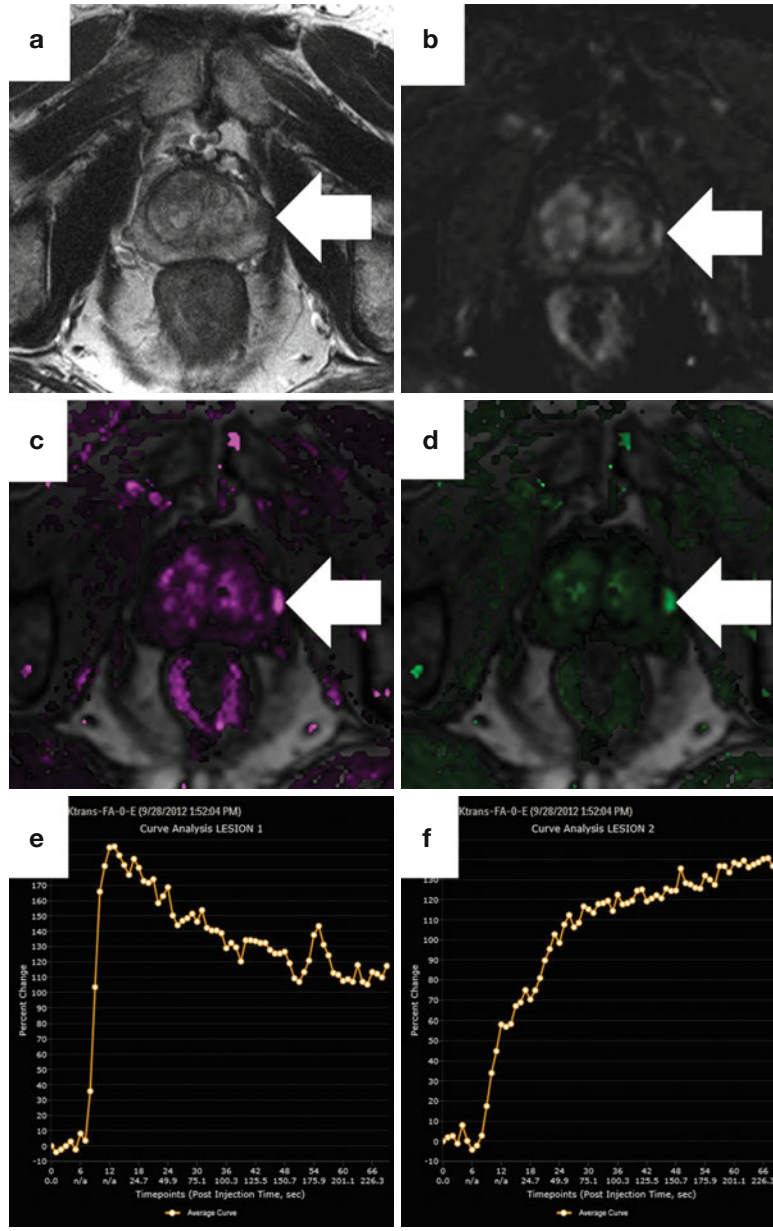


**Fig. 13.9** Dynamic contrast-enhanced perfusion imaging obtained at 3 T with pharmacokinetic map and time-intensity curves in a patient with Gleason 3 + 4 cancer on MRI-US fusion targeted biopsy. On the axial T2-weighted image (**a**), a round focus of low signal (*arrow*) is suspicious. The corresponding dynamic subtraction image at 15 s after the arrival of contrast (**b**) shows early arrival of contrast, but this is more conspicuous on both the $K^{trans}$ (**c**) and $K_{ep}$ (**d**). Maps were generated using the iCAD VersaVue engine. A representative time-intensity curve of the tumor (**e**) shows a type III washout curve (rapid uptake and washout), whereas the normal peripheral gland (**f**) shows a type I progressive curve

[36] and potentially more reproducible for indications such as monitoring response to therapy [37]. A preliminary study correlating DCE MRI and prostatectomy specimens in 45 men showed that quantitative and semiquantitative DCE parameters have the potential to discriminate low-grade from intermediate-grade and high-grade prostate cancer [38].

Still, DCE MRI is not used alone because it cannot reliably discriminate between cancer, prostatitis, and BPH [34]. Nonetheless, it should be included in mpMRI protocols because of the sensitivity that it can add [39–41].

## MR Spectroscopic Imaging

Protons in different metabolites have unique resonant frequencies. MR-spectroscopic imaging (MRSI) makes use of these intrinsic differences

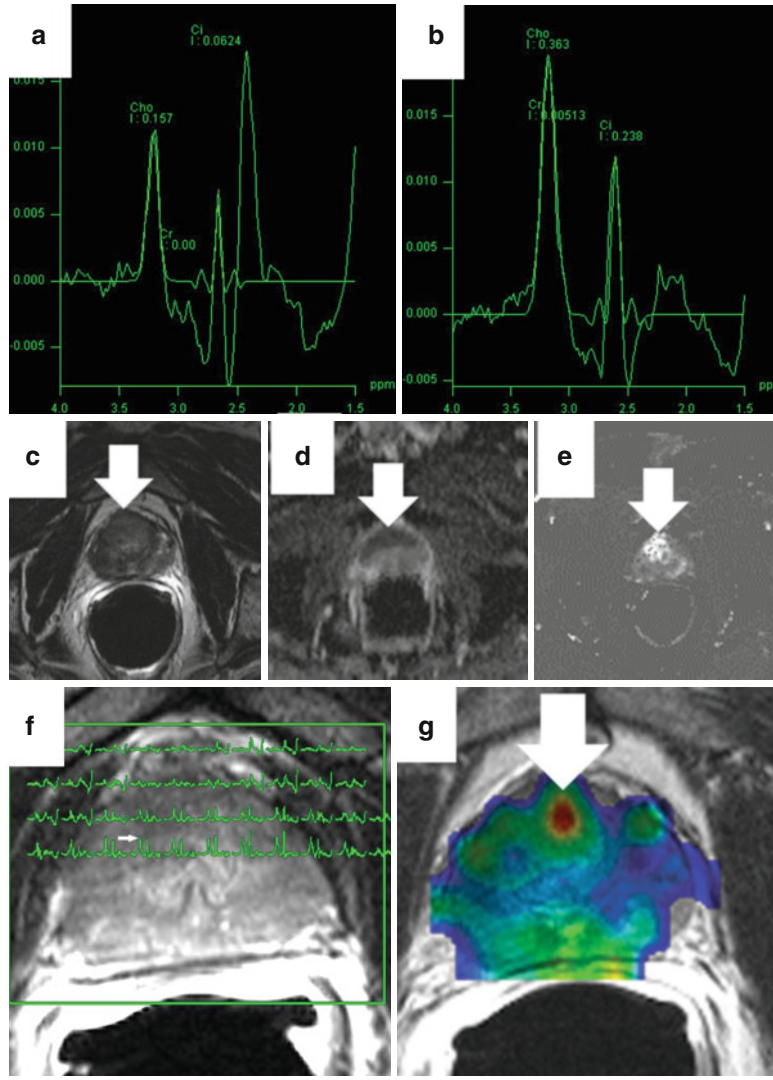


**Fig. 13.10** Magnetic resonance spectroscopic imaging (*MRSI*). Panel (**a**) shows a sample normal spectra (citrate peak higher than choline) while (**b**) shows a spectra characteristic of cancer (choline peak higher than citrate). In a representative case, an axial T2-weighted image (**c**) is equivocal with abnormal signal throughout. The corresponding ADC (**d**) and $K^{trans}$ (**e**) maps are abnormal in the anterior prostate. The spectral overlay (**f**) shows elevation of the choline peak to the left of the citrate peak for voxels corresponding to the low-signal area (*arrow*). The creatine + choline/citrate ratio color map (**g**) is also focally abnormal

to provide information about the relative concentration of various metabolites in tissues. In the case of prostate cancer, the metabolites of interest are citrate, choline, and creatine. Citrate, whose levels are higher in normal prostate tissue, serves as a marker of benign tissue. Choline, a key player in cell membrane synthesis, is elevated in malignant tissue [42]. The spectral profile of creatine overlaps that of choline so the two are measured together. This issue is insignificant given the relatively constant levels of tissue creatine [13]. After post-processing with commercially available software, the spectral tracings measuring the metabolite concentrations are overlaid on the T2-weighted images (Fig. 13.10). Analysis is either qualitative (compare peak heights visually) or quantitative. For quantitative analysis, a choline + creatine to citrate ((Cho + Cr)/Cit) ratio is calculated. The ratio is higher in cancer and the elevation of the ratio is used to determine the likelihood of cancer. Furthermore, higher (Cho + Cr)/Cit ratios are associated with more aggressive tumors.

In prostate MRSI exams, imaging is performed in a volume that covers the whole prostate. The prostate is divided into a three-dimensional grid of multiple voxels. To perform MRSI an ERC is mandatory at 1.5 T and strongly recommended at 3 T [7]. The ERC makes it possible to perform MRSI spectra of

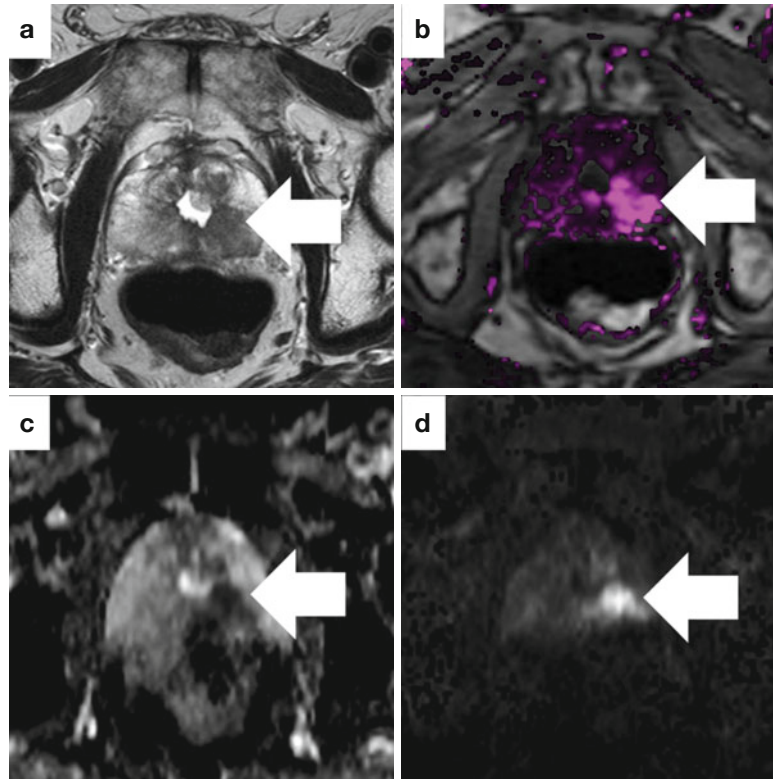


**Fig. 13.11** Sample case where all MRI parameters are abnormal in an 81-year-old man with high-grade prostate cancer and a prior TURP. The axial T2-weighted image (**a**), dynamic contrast-enhanced image (**b**), ADC map (**c**), and high *b*-value DWI (**d**) all show a suspicious area in the *left*, posterior prostate

voxels <1 $cm^3$. The (Cho + Cr)/Cit ratio is calculated for each voxel.

MRSI can add information about both the presence of cancer and its aggressiveness [43–48]. It is limited by poor spatial resolution which precludes its usefulness for staging. A prospective, multicenter study done by the American College of Radiology (ACR) imaging network enrolled 100 men undergoing prostate mpMRI with MRSI at 1.5 T. This study showed equivalent accuracy for T2WI with and without MRSI [49]. MRSI is also time consuming (imaging time and placement of ERC) and technically challenging so many centers do not include it in mpMRI protocols. In the recent ESUR guidelines, MRSI is listed as optional [13].

## Interpretation and Reporting of Prostate MRI

Convincing evidence exists that adding functional sequences to T2-weighted imaging improves the performance of MRI in detecting localized prostate cancer. Specifically, DWI and MRSI add to specificity, while DCE can improve sensitivity [13]. The best way to summarize and concisely report the results of mpMRI is not always clear. Large, aggressive cancers often cause all parameters to appear abnormal (Fig. 13.11). In these cases, reporting the result is not difficult. However, in the era of PSA screening, the majority of patients in the United States present with smaller, lower-grade lesions. In these cases, mpMRI parameters often conflict (Fig. 13.12). In this situation, interpretation is more difficult. As a result, efforts have been made to standardize interpretation and reporting of prostate MRI.

The European Society of Urogenital Radiologists (ESUR) recently met and released a report "to promulgate high-quality MRI in acquisition and evaluation" [13]. They initially addressed MRI acquisition and recommended three different protocols: detection, staging, and bones/nodes. The *detection protocol* includes T2WI, DWI, and DCE of the prostate only +/– MRSI. This protocol takes <30 min and uses no ERC unless MRSI is included. The *staging*

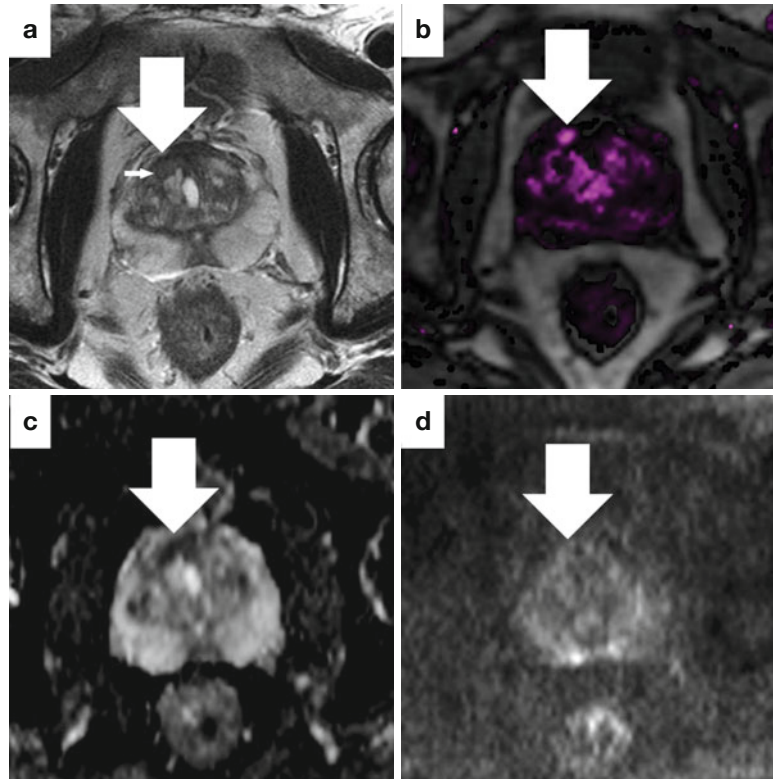


**Fig. 13.12** Sample case with conflicting findings on mpMRI in a 58-year-old man with a PSA of 2.8 ng/ml and a strong family history. The axial T2-weighted image (**a**) shows a focus of low signal (*large arrow*) with a sharp, low-signal border (*small arrow*), typical of a benign prostatic hyperplasia (*BPH*) nodule. Perfusion at this site is focally increased (**b**), but the ADC map (**c**) and DWI (**d**) are only moderately abnormal and also consistent with BPH. This was graded as moderately suspicious overall. Targeted biopsies subsequently revealed low-volume Gleason 3 + 4 prostate cancer

*protocol* is optimized to evaluate for minimal extracapsular extension. It includes the same sequences as the detection protocol. In this case an ERC is considered preferable, and the exam takes approximately 45 min. The *bones/nodes protocol* is designed to detect regional metastasis in men with high-risk disease. It is done separately from the other two protocols because it is unnecessary in most men. It includes T1WI, T2WI, and DWI and takes approximately 30 min. Traditionally, staging of the bones and nodes is performed with a pelvic CT and bone scan rather than MRI. The clinical indication for the detection and staging protocols has not been clearly defined, and the two different protocols have yet to be widely adopted. Most centers in the United States choose to perform MRI similar to the ESUR detection protocol (no ERC) or similar to the staging protocol (with ERC) in all patients.

In interpreting the MRI, the authors of the ESUR report proposed a system termed "prostate imaging reporting and data systems" or "PI-RADS"; this is analogous to the BI-RADS system used in breast imaging interpretation. Following PI-RADS, each parameter is assigned a score from 1 to 5 that reflects the degree of abnormality. The prostate is divided into anatomic regions (minimum of 16, but 27 is considered optimal), and lesions are assigned to these regions. The report includes a score relaying the probability of cancer and its aggression, the cancer location, and the probability of extracapsular extension for all identified lesions. The overall score for each lesion is a simple compilation of the component scores from each mpMRI parameter. A targeted biopsy study validating the ESUR scoring system was recently published [50]. However, compilation of component scores may be overly simplistic as it is widely recognized that some parameters of mpMRI impart more valuable information than others. In the view of many experts, diffusion-weighted imaging is the most powerful single parameter in determining the confidence that a lesion is cancer and the degree to which it is clinically significant. The best method to weigh the individual scores to make an overall score that accurately reflects the cancer's actual histopathology has yet to be defined.

## Capabilities of Multiparametric Prostate MRI

### Lesion Localization and Size

In a frequently quoted study correlating MRI with prostatectomy histopathology in 45 men with known prostate cancer who underwent mpMRI (T2WI, DWI, DCE, and MRSI) at 3 T with an ERC prior to prostatectomy, Turkbey et al. found a 98 % positive predictive value for prostate cancer detection [40]. In the study, the sensitivity was higher for tumors larger than 5 mm in diameter and for those with a Gleason score >7. In order to overcome the problem described previously with studies correlating MRI and whole-mount prostatectomy specimens, the prostates were cut in customized molds designed to align the slices from MRI with those from the surgical specimen.

Most publications that include a comparison of MRI performance in the peripheral zone to that in the central gland conclude that outcomes are superior in the peripheral zone. However, results from specialized centers with expertise in prostate MRI have also been excellent in the central gland [22, 40]. It is unknown if centers with less expertise can replicate these results in the central gland. MRI has also been demonstrated to perform better for imaging large, high-grade lesions when compared to smaller lesions or those with intermixed normal and malignant tissue [40, 51].

Despite the ongoing improvements in MRI, some cancers are missed. One recent study evaluated the histopathologic differences between cancers seen on MRI and those that were missed [52]. On DWI, Gleason score and a solid tumor growth pattern were independent predictors of tumor identification on multivariate analysis. For T2WI, tumor size and Gleason score impacted identification, but this finding was no longer significant on multivariable analysis. For DCE, identification of cancer was associated with intermixed benign epithelium, loose stroma, and high malignant epithelium-to-stroma ratio. Whether the ability to visualize tumors on MRI is an independent predictor of clinical outcome has yet to be determined.

In the authors' experience, the ability of MRI to accurately predict tumor size at the time of prostatectomy is limited. This is likely due to the infiltrative nature of many prostate cancers in which fingerlike projections are sent out from the main tumor that are difficult to identify on MRI. Still, one recent report comparing MRI with prostatectomy specimens showed a positive correlation between MRI tumor volume and histopathology tumor volume [53]. Continued improvement in the ability to accurately determine cancer size on MRI is necessary to improve the clinical usefulness of MRI for applications such as focal therapy and patient selection for active surveillance.

### Assessment of Cancer Aggressiveness

More important than the identification of all prostate cancers is the ability to assess cancer aggressiveness and to selectively diagnose the most clinically significant cancers. Accurate assessment of Gleason score on biopsy is the most important factor in determining cancer aggressiveness. Using current methods incorporating transrectal ultrasound (TRUS) to guide systematic biopsy, accurate risk stratification is lacking. Rates of Gleason score upgrading from biopsy to prostatectomy range from 25 to 40 % [54]. This uncertainty plays a major role in underutilization of active surveillance. A noninvasive imaging modality that can more accurately assess cancer risk is highly desirable.

Among all parameters of mpMRI, DWI performs the best in assessing disease aggressiveness. Higher-grade cancers tend to have higher cellular density and therefore display more restricted diffusion. Numerous recent publications have reported the inverse correlation between Gleason score and ADC value [26, 27, 29, 55–57]. However, developing ADC value cutoffs to differentiate low- and high-grade cancer that can be applied across institutions has not been possible due to variability in ADC values

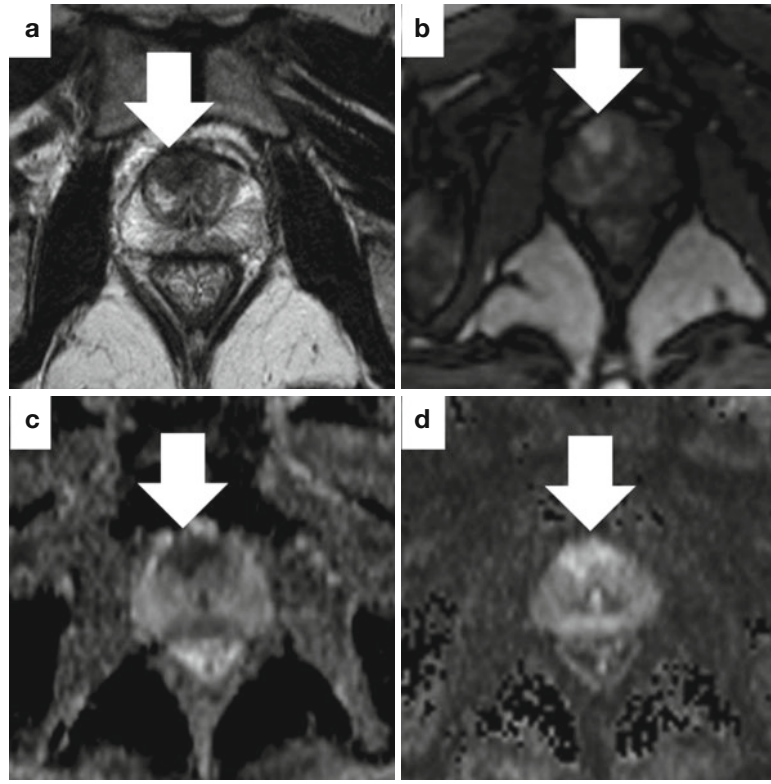


**Fig. 13.13** Sample case where a highly suspicious MRI was more informative than biopsy. This 65-year-old man with a rapidly rising PSA underwent MRI following negative systematic biopsies. The axial T2-weighted image (**a**) shows a low-signal focus with irregular borders in the anterior central gland (*arrow*). The lesion shows early enhancement with contrast on DCE (**b**). ADC (**c**) and DWI (**d**) maps show increased perfusion and highly restricted diffusion. Targeted biopsy showed high-volume, low-grade cancer (Gleason 3 + 3). Repeat targeted biopsy 6 months later showed Gleason 3 + 5 cancer. Pathology at prostatectomy was Gleason 4 + 3 with tertiary pattern 5

between patients and differences in the way scans are performed.

In some cases, the ability of MRI alone to determine cancer aggressiveness exceeds that of biopsy results (Fig. 13.13). At the same time, MRI can miss some clinically significant cancers, overestimate disease severity for others, and classify lesions as high-risk cancer that are actually benign on prostatectomy pathology. Because of these limitations, a well-performed biopsy remains necessary to confirm the MRI.

## Cancer Staging

Accurate local staging requires information about cancer volume, laterality, extraprostatic extension (EPE), and presence of bony or nodal metastases. Prior to MRI, staging of localized prostate cancer was limited to a digital rectal exam, a test that proves unreliable in determining the extent of cancer in the prostate. Nomograms were developed incorporating PSA, DRE, and biopsy result to predict the presence of cancer spread outside the prostate. Such extraprostatic extension of cancer results in increased rates of cancer recurrence. Knowledge of this prior to prostatectomy enables the surgeon to modify the surgical technique to remove more tissue in that area and reduce the change of leaving prostate cancer.

In a small study involving 27 subjects with radical prostatectomy pathology as the gold standard, MRI was shown to perform better than a commonly used nomogram (Partin tables) in discriminating the 21 men with organ-confined disease from the 6 with extracapsular extension [58]. The most recent study of mpMRI for evaluation of EPE involved 183 men divided into low-, intermediate-, and high-risk groups based on the preoperative d'Amico criteria [59] and compared the MRI result (3 T with ERC using T2WI, DWI, and DCE) to the prostatectomy specimen for each group. The staging accuracy of mpMRI was 73.8 % (PPV 84.1 %, NPV 68.3 %). The PPV

was best in the high-risk group (88.8 %), while the NPV was best in the low-risk group (87.7 %). Overall, when including clinical stage, PSA, biopsy Gleason score, and risk classification in a multivariate model, mpMRI (OR 10.3, 95 % CI 4.4–24.2) was the best preoperative predictor of extraprostatic extension [60]. Whether this result can be reproduced in a center with less prostate MRI experience remains to be seen.

The accuracy of staging is highly dependent on the skill and experience of the radiologist. Renard-Penna et al. compared the 1.5-T mpMRI result (T2, DCE, no DWI, no ERC) to the prostatectomy specimen in a prospective study of 101 patients. Two different radiologists with different levels of experience (Reader 1: 7 years in prostate imaging, Reader 2: <1 year) independently interpreted the studies. They found an AUC for Reader 1 of 0.895 (PPV 72 %, NPV 96 %) and an AUC of 0.687 (PPV 50 %, NPV 89 %) for Reader 2. The K-index of interobserver agreement was just 0.56. This difference highlights the importance of a skilled reader [61].

While T-staging is assessed in all mpMRI exams, the need to check for extraprostatic spread to the bone and lymph nodes is limited. According to the National Comprehensive Cancer Network (NCCN), a CT or MRI should be done for cT3–T4 cancers or if the probability of lymph node involvement is >20 % using validated nomograms. The same holds true for the bones/nodes MRI protocol. It has been conclusively shown that in light of the rarity of gross lymphatic spread in low-risk prostate cancer, imaging to evaluate the bone and lymph nodes is clearly overused [62–64].

## Clinical Applications of Prostate MRI

### Targeted Biopsy

Conventional TRUS-guided biopsy is used to diagnose >240,000 cases of prostate cancer in the United States each year [65]. This method, largely unchanged over the last 30 years, involves removal of 10–12 biopsy cores evenly spaced throughout the prostate. It is limited by over-detection of low-grade (Gleason 6), micro-focal "cancers" of little clinical significance and underdetection of large, aggressive cancers (Gleason >7) [66]. While simply taking more systematic cores has been proposed as a way to compensate for the limited diagnostic ability of this largely image-blind technique, a more rational approach is to improve the quality of each biopsy using real-time targeting [67]. Because MRI performs much better than US in detecting prostate cancer, it has the potential to transform the conventional biopsy process into an image-guided one by targeting biopsy needles to abnormal areas.

Targeted biopsy can be performed either "in bore" under direct MR guidance [68] or using MR-US fusion [69, 70], a method that aligns a pre-procedure MRI with real-time US to enable targeted biopsy in an office-based procedure. Moore et al. recently published a comprehensive review of MR-guided biopsy that included studies of direct MR-guided and fusion-guided biopsy. Overall, 62 % of 599 biopsy-naïve men had an MRI abnormality and 66 % of those had cancer on biopsy. The combination of targeted and systematic biopsy found significant cancer in 43 % (236 of 555). When comparing targeted to systematic biopsy, targeted biopsy found clinically significant cancer in an equivalent number of men, but this was achieved with fewer cores and with a reduction in the diagnosis of clinically insignificant cancer [71].

In gantry biopsy under direct MR guidance has the advantage of direct registration. Unlike MR-US fusion, it does not require registration of one imaging modality to another—a process that inherently introduces some degree of error. In a large, single-center review of MR-guided biopsy in 265 men with a PSA >4 and ≥1 negative TRUS biopsy who had a lesion on MRI, cancer was found in 108 (41 %). Of these, 87 % were deemed clinically significant [72]. While this method has been used with success it is expensive, is time consuming, requires MRI-compatible equipment, and is not available in most hospitals. For these reasons, it is unlikely that in-bore biopsy will replace conventional prostate biopsy.

MR-US fusion biopsy uses the information provided by the pre-procedure MRI to direct biopsy needles under real-time ultrasound guidance. Like conventional biopsy, this method can be performed in a urologist's office under local anesthesia in a procedure lasting approximately 20 min. MR-US fusion targeted biopsy can be performed using either cognitive fusion [73] or a fusion device [69, 70, 74]. Both methods have been used successfully.

When employing cognitive fusion, the operator first identifies a suspicious lesion on MRI, imagines its location within the prostate, and then attempts to biopsy that location using real-time US. This method is quick, requires no additional equipment, and has had good results in expert centers. The review by Moore et al. details results of more than 20 studies employing cognitive fusion [71]. However, mentally fusing the MRI with TRUS to aim for cancers that are often <1 cm in diameter introduces the possibility of human error. While experts have achieved excellent results, the extent to which these results are reproducible by less experienced operators has not been evaluated.

Fusion devices superimpose (coregister) the stored MRI and real-time US using computer software. Real-time US is acquired in 2D. The tracking system of fusion devices enables computer-assisted construction of a three-dimensional (3D) representation of the prostate using individual US images. At biopsy, the device generates a 3D model of the prostate incorporating both MRI and US, thereby enabling targeted biopsy and tracking of each biopsy location. Biopsy accuracy is heavily dependent upon the fidelity of registration of the 3D models from MRI and US. Registration, complicated by changes in gland location and deformation, can be rigid or elastic. Rigid registration involves alignment of MRI and US by simple rotation and/or magnification. The variation between the shape of the prostate at MRI and that at biopsy makes this method suboptimal [67]. Elastic fusion is more sophisticated; it attempts to compensate for changes in prostate shape or position between MRI and biopsy [75]. This allows for "elastic" deformation of the 3D model from preoperative MRI to mirror changes in TRUS imaging in real time.

MR-US fusion has been performed using several different technologies including a robotic arm with encoders (Artemis, Eigen), electromagnetic sensors (UroNav, Invivo), optical sensors, and 3D TRUS (Urostation, Koelis) (Fig. 13.14). Each method attempts to accurately match MRI to US. The use of a fusion device may reduce the learning curve, making the results reported by experts achievable by all urologists. This will require validation in studies of new users of these technologies. A brief description of several MR-US fusion devices follows.

### Robotic Tracking

The Artemis device tracks the location of a TRUS probe in space by direct attachment to a robotic arm. This enables creation of a 3D model of the prostate based on US which is then elastically fused to the MRI model. The device enables office-based targeted biopsy and tracks the location of all biopsy cores (Fig. 13.15). Robotic tracking provides superior accuracy, but the bulkiness of the device makes the procedure somewhat more cumbersome and time consuming when compared to free-hand methods. The UCLA group reported the first clinical use of this 3D biopsy tracking and targeting device in men with prior negative biopsies and those on active surveillance [70, 76]. Cancer was detected in 55 % of subjects overall and in 94 % of those with the highest level of suspicion on MRI [70]. In men with prior negative biopsies who had a suspicious MRI, cancer yield was 50 %. Targeted biopsy identified more significant cancers and fewer insignificant cancers than systematic biopsy [77]. Preferential detection of significant cancers is an exciting feature of targeted biopsy that should diminish the risk of aggressive cancers missed on conventional biopsy and reduce overtreatment of low-risk disease through a reduction in overdiagnosis.

### Electromagnetic Tracking

The UroNav device electromagnetically tracks the location of the TRUS probe in space using a sensor attached to the probe and assessing its location within a small electromagnetic field

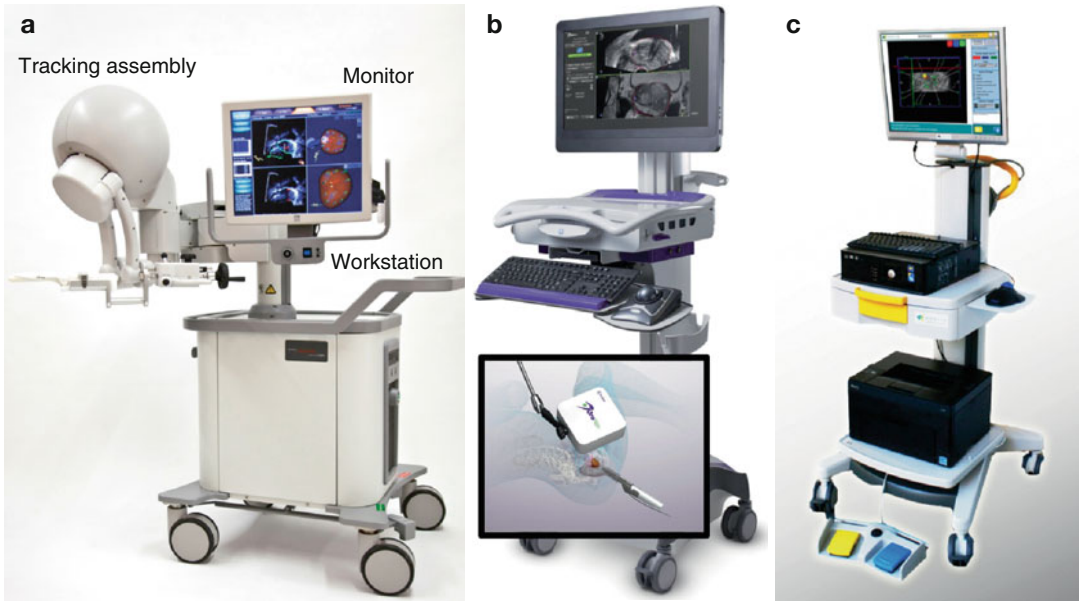


**Fig. 13.14** Images of three FDA-approved MR-US fusion targeted biopsy devices. Each enables targeted biopsy of lesions identified on MRI by tracking the location of the ultrasound probe in space and fusing real-time US to MRI performed previously. The Artemis device (**a**) uses a robotic arm with encoders, UroNav (**b**) transmits an electromagnetic field from a small field generator (*inset*) and attaches a sensor to the ultrasound probe, and Urostation (**c**) uses 3D ultrasound to track the probe location ((**a**) Courtesy of Eigen, Grass Valley, CA, USA; (**b**) Courtesy of UroNav, Invivo, Gainesville, FL; (**c**) Courtesy of UroStation, KOELIS, La Tronche, France)

around the patient's pelvis. The free-hand nature of this technique is more familiar to urologists, but the electromagnetic method is somewhat less accurate than robotic tracking. A group at the National Institutes of Health performed the preclinical and early clinical development of this device [78]. They reported cancer detection rates of 28, 67, and 89 % in men with MRIs demonstrating low-risk, moderate-risk, and high-risk features, respectively [69]. In a separate study of men with prior negative biopsies, cancer was found in 37 % overall and in 11 % of those with high-risk, Gleason ≥8 cancer [79].

### Image-Based Tracking

The Urostation device uses real-time 3D TRUS to track the location of each biopsy core. In a validation study for the ESUR scoring system, cancer was detected in 62 of 129 (48 %) men with ≥1 prior negative biopsy [50].

### Active Surveillance

Active surveillance is a management strategy that calls for close follow-up of men with untreated, low-risk prostate cancer with the intent to treat the cancer only if it shows signs of growth or progression. A variety of different criteria have been used to determine optimal candidates for active surveillance. Published series consistently demonstrate that approximately 30 % of men on active surveillance progress to higher-volume or higher-grade cancer over time [80]. It has also been shown that 20–30 % of candidates for active surveillance who instead choose radical prostatectomy have adverse pathologic features including higher-grade cancer than that seen on biopsy or extracapsular extension [81–83]. When taken together, these findings suggest that in the short term, most "progression" is actually misclassification on initial biopsy. Therefore, patients considering active surveillance are typically told that they harbor an approximately 30 % risk of having significant cancer now or in the near future. This uncertainty contributes to the vast underutilization of active surveillance [84]. The extent to which MRI can reduce uncertainty and help with patient selection is addressed by several studies.

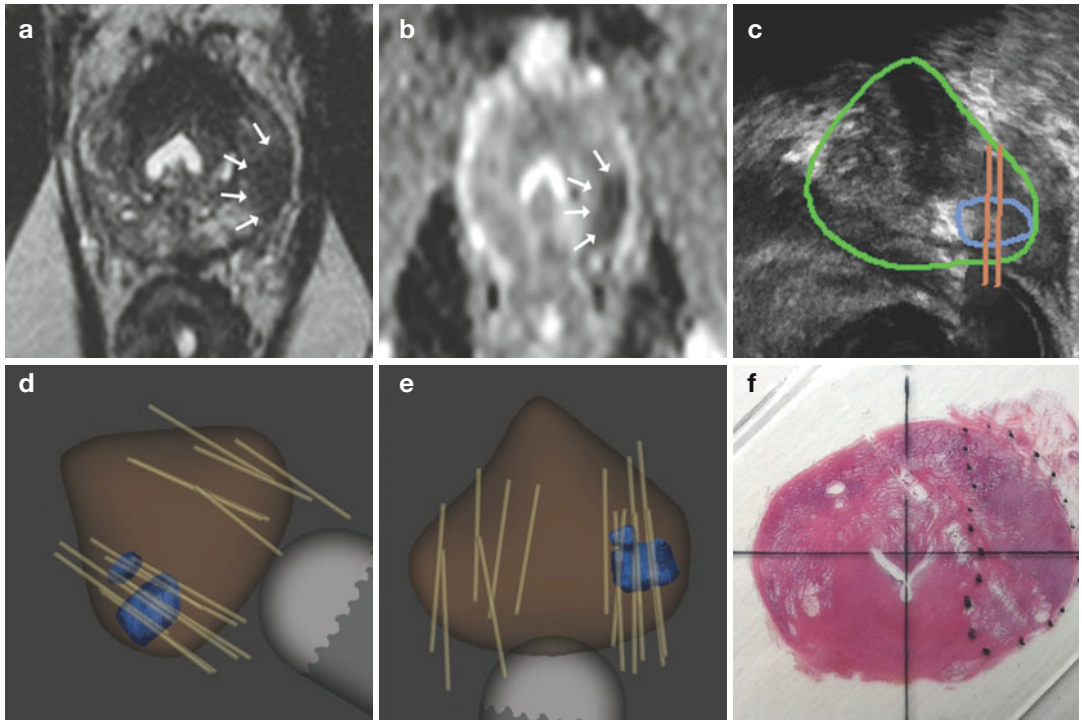


**Fig. 13.15** Sample case of MR-US fusion targeted biopsy in a 59-year-old man with a PSA of 7.4 and 1 prior negative biopsy. (**a**) T2-weighted axial MR image demonstrating a lesion in the left peripheral prostate with focal low signal (*arrows*). (**b**) Diffusion-weighted axial MR image with restricted diffusion in the corresponding area. The radiologist outlined the lesion in each axial image. Open-source imaging software then produced a 3D model of the prostate including the 3D target. (**c**) Real-time ultrasound image of the area of interest (*outlined in blue*). Note the absence of ultrasound abnormality. A 3D model is generated based on ultrasound. The two models were then dynamically fused, generating the composite *virtual* 3D model seen in the panels (**d**, **e**). The prostate is mapped in *brown*, and the target identified in *blue*. Systematic and targeted biopsies were obtained, generating the final 3D model demonstrating the location of all biopsy cores (*light-brown cylinders*). Targeted biopsies in this patient revealed Gleason 7 cancer. (**f**) Radical prostatectomy whole-mount pathology confirmed the presence of a 2 cm Gleason 7 cancer in the left peripheral zone (From Sonn et al. [70], with permission)

Vargas et al. at Memorial Sloan-Kettering conducted a retrospective evaluation of 388 men with low-risk prostate cancer (Gleason $\leq$6, PSA <10, clinical stage $\leq$ T2a) who underwent T2-weighted MRI prior to active surveillance confirmatory biopsy. MRIs were scored on a 5-point scale. An MRI score $\leq$2 had a 96–100 % NPV for upgrading on confirmatory biopsy, while an MRI score of 5 had an 87–98 % sensitivity for upgrading [85]. This study suggests that even T2-weighted MRI alone may help selecting patients for active surveillance. Specifically, those men with normal MRIs are highly likely to have low-risk cancer, while those with highly suspicious MRIs are much more likely to have clinically significant prostate cancer.

Borofsky et al. retrospectively analyzed 1.5-T mpMRIs (T2WI and DWI) performed prior to radical prostatectomy in 55 men who were eligible for active surveillance based on biopsy criteria and correlated the MRI result with the prostatectomy pathology. Men whose MRI was equivocal or strongly suspicious ($n$=42) had a much greater chance of adverse pathology (Gleason $\geq$7 or pT3) than those with a normal MRI ($n$=13) (47.6 % vs. 7.7 %, $p$=0.01) [86]. While small and retrospective, this study indicates the ability of MRI to further predict disease risk beyond that achievable by current risk assessment nomograms.

Turkbey et al. retrospectively compared patient selection using current clinical parameters

(Epstein, D'Amico, CAPRA) [59, 87, 88] to that using mpMRI alone in 133 men who underwent subsequent prostatectomy. Prostatectomy pathology served as the gold standard, and eligibility criteria for surveillance was defined as Gleason 6 only, <0.5 $cm^3$ of cancer, and absence of extracapsular extension and seminal vesicle invasion. When applying this definition, 14 of 133 men were eligible for active surveillance. MRI performed better than clinical parameters ($p<0.005$). Sensitivity, PPV, and overall accuracy were 93, 57, and 92 % for MRI; 93, 25, and 70 % for D'Amico; 64, 45, and 88 % for Epstein; and 93, 20, and 59 % for CAPRA [89]. While this single-center study is limited by the small number of men eligible for surveillance ($n=13$), it does suggest that mpMRI may be the best way to select patients for active surveillance.

It appears that the ADC value is particularly useful as a predictive biomarker of progression in men on active surveillance. Giles et al. found a significant difference in the mean ADC value of 14 men upgraded on repeat biopsy (1,070 ± 110) compared to 41 men who were stable on repeat biopsy (1,356 ± 357, $p<0.001$) [90]. However, this study does not evaluate the proportion of men in whom mpMRI is helpful or provide information about the PPV and NPV of mpMRI in men undergoing active surveillance. Lee et al. retrospectively analyzed 188 candidates for active surveillance who underwent diffusion-weighted MRI before radical prostatectomy. They divided the cohort into two groups (group 1, normal MRI or suspicious tumor <1 cm, and group 2, suspicious tumor lesion >1 cm). At prostatectomy, 49 % of those in group 1 had insignificant cancer vs. 25 % of those in group 2 ($p=0.001$). The diameter of suspicious tumor lesions was a predictor of insignificant cancer on multivariate logistic regression analysis (OR 0.32, $p=0.014$) [91].

In conclusion, early evidence exists to support the role of mpMRI in selecting patients for active surveillance. It is hoped that the use of imaging will result in more men choosing active surveillance. Still, the optimal MRI protocol and criteria for patient selection has yet to be conclusively defined.

## Surgical Planning

Sparing of the nerve bundles that run alongside the prostate during prostatectomy offers the best chance of return of erections after surgery. However, this is not always possible due to concern about cancer spread out of the prostate at the site of the nerves. Accurate staging and, in particular, precise evaluation for extracapsular extension near the neurovascular bundle are critical to surgical planning prior to radical prostatectomy. Nomograms have been developed to estimate the chance of extracapsular extension that integrate the results of biopsy and digital rectal exam. However, inaccuracy is common making personalized decisions about nerve sparing during surgery difficult. Improved staging with MRI has the potential to aid decision making about nerve sparing and thereby reduce rates of positive surgical margins and increase postoperative quality of life.

McClure et al. prospectively evaluated 104 consecutive men with prostate cancer who underwent preoperative mpMRI with an endorectal coil before robotic prostatectomy. Prior to surgery a surgeon determined a plan for or against nerve sparing based on clinical information alone. The plan was reevaluated after MRI and the differences between the two plans compared to the final surgical pathology. The initial surgical plan was changed in 28 men (27 %), including 11 to non-nerve sparing (39 %) and 17 to nerve sparing (61 %). Overall, 7 (6.7 %) had positive margins, none of which occurred on a side where the MRI changed the plan from non-nerve sparing to nerve sparing [92].

## Focal Therapy

The realization that radical prostatectomy constitutes overtreatment in a large proportion of men with prostate cancer, coupled with the emerging ability to image cancers within the prostate using MRI, has spawned great interest in focal ablative therapy for localized prostate cancer. This method involves the targeted destruction of the cancerous portion of the prostate while attempting to leave

the remainder of the prostate intact. To date, focal therapy remains in its infancy, yet it is hoped that it may offer similar rates of cancer control and reduced rates of morbidity.

To make focal therapy efficacious, imaging must be sufficiently accurate to identify the most aggressive cancer ("index lesion") [93], assess its size and location, and evaluate for additional cancers in the prostate. As the best modality available for prostate cancer imaging, MRI is expected to play a major role. Applications may include patient selection, targeting during the ablation procedure, and post-ablation follow-up [94]. MRI has been used extensively for tumor localization, targeting, and treatment follow-up in the most rigorously performed studies of focal therapy [95, 96].

## Treatment Follow-Up

Biochemical recurrence after prostatectomy presents a frequent diagnostic dilemma because an elevated PSA cannot definitively differentiate local recurrence from distant metastasis. In these situations it is critical to determine if the PSA arises from local or distant recurrence. Historically, lacking the ability to image the site of recurrence, an educated guess is made about the site of recurrence. Patients thought to have local recurrence are treated with salvage radiation. Seeking to change this paradigm using imaging, Sella et al. found that endorectal MRI correctly identified 39 of 41 (95 %) men thought to have locally recurrent disease [97]. More recently, Panebianco et al. retrospectively analyzed 242 men thought to have local recurrence after radical prostatectomy with mpMRI at 3 T. Accuracy ranged from 86 to 93 %. They found DCE-MRI to be the most reliable indicator of local cancer recurrence. DWI also proved beneficial [98]. Further study is necessary to substantiate these findings and to determine what proportion of men with biochemical recurrence after prostatectomy benefit from MRI.

Cancer recurrence after radiation therapy is also common, occurring in 10–60 % of cases [99]. MRI has been used to detect these recurrences. In a small study of 16 men, Tamada et al. found a 77 % sensitivity and 92 % specificity for mpMRI in men with biochemical recurrence after high-dose-rate brachytherapy [100]. The sensitivity using DWI was better than that with T2-weighted imaging. In a separate study, Westphalen et al. found MRSI (accuracy 87 %) to improve upon T2 and DWI in 26 men with suspected biochemical recurrence after external beam radiation therapy [101]. In another small study, Morgan et al. performed MRI on 24 men with a rising PSA after radiation. Of these, 16 had a positive biopsy. The overall sensitivity, specificity, PPV, and NPV for MRI in detecting tumor were 94, 75, 88, and 86 %, respectively [102].

## Areas of Future Research

Despite the great promise shown by prostate MRI, ample areas exist for future research. To date, most published literature on prostate MRI has been single-center studies from a handful of centers of excellence. The extent to which the results achieved at these centers can be replicated by less experienced radiologists remains to be seen. This is especially pertinent for prostate MRI, a technique that requires substantial expertise.

With data emerging about the risks of prostate biopsy [103], many have questioned whether men with a normal MRI can safely avoid biopsy. This requires accurate data about the negative predictive value of MRI that does not yet exist. This important question will be answered by the ongoing PROMIS trial in the United Kingdom in which all men who have been recommended to undergo prostate biopsy receive an mpMRI followed by an extensive biopsy procedure. In the meantime, most experts recommend that MRI cannot yet replace biopsy given the fact that some significant prostate cancers are not seen on MRI.

Finally, research continues by physicists and biomedical researchers to further develop and refine MRI sequences and molecular tracers to expand the ability of MRI to accurately image prostate cancer.

## Conclusion

When compared to the early experience with prostate MRI using T2WI alone, the use of stronger magnets and multiparametric protocols has added tremendously to the ability to detect and characterize prostate cancer. Useful parameters include T2-weighted imaging, DWI, DCE, and MRSI. mpMRI has been shown to aid in cancer staging, biopsy targeting, and selecting patients for active surveillance. Still, mpMRI remains a difficult modality to interpret and requires substantial radiologic expertise. Standardization of performing, interpreting, and reporting mpMRI is essential to ensuring reproducibility and clinical utility [104]. Moving forward, efforts are needed to bring more radiologists to the level of those at specialty centers. Given its ability to identify many cancers, assess aggressiveness, and guide biopsy, as well as its applications for active surveillance and focal therapy, the future of prostate MRI appears bright.

## References


1. Hudson MA, Bahnson RR, Catalona WJ. Clinical use of prostate specific antigen in patients with prostate cancer. J Urol. 1989;142:1011–7.
2. Catalona WJ, Smith DS, Ratliff TL. Measurement of prostate-specific antigen in serum as a screening test for prostate cancer. N Engl J Med. 1991;324(17):1156–61.
3. National Center for Health Statistics, Division of Vital Statistics. US mortality volumes 1930-1959, US mortality data 1960–1968. Hyattsville: Centers for Disease Control and Prevention; 2011.
4. Miller AB. New data on prostate-cancer mortality after PSA screening. N Engl J Med. 2012;366(11):1047–8.
5. Andriole GL, Crawford ED, Grubb III RL, Buys SS, Chia D, Church TR, et al. Mortality results from a randomized prostate-cancer screening trial. N Engl J Med. 2009;360:1310–9.
6. Schroder FH, Hugosson J, Roobol MJ, Tammela TL, Ciatto S, Nelen V, et al. Screening and prostate-cancer mortality in a randomized European study. N Engl J Med. 2009;360:1320–8.
7. Gupta RT, Kauffman CR, Polascik TJ, Taneja SS. The state of prostate MRI in 2013. Oncology (Williston Park). 2013;27(4):262–70.
8. Hricak H, Williams RD, Spring DB, Moon Jr KL, Hedgcock MW, Watson RA, et al. Anatomy and pathology of the male pelvis by magnetic resonance imaging. AJR Am J Roentgenol. 1983;141(6):1101–10. http://www.ncbi.nlm.nih.gov/pubmed/6196961.
9. Steyn JH, Smith FW. Nuclear magnetic resonance imaging of the prostate. Br J Urol. 1982;54:726–8.
10. Turkbey B, Albert PS, Kurdziel K, Choyke PL. Imaging localized prostate cancer: current approaches and new developments. AJR Am J Roentgenol. 2009;192:1471–80.
11. Heijmink SW, Futterer JJ, Hambrock T, Takahashi S, Scheenen TW, Huisman HJ, et al. Prostate cancer: body-array versus endorectal coil MR imaging at 3 T—comparison of image quality, localization, and staging performance. Radiology. 2007;244:184–95.
12. Kim BS, Kim T-H, Kwon TG, Yoo ES. Comparison of pelvic phased-array versus endorectal coil magnetic resonance imaging at 3 Tesla for local staging of prostate cancer. Yonsei Med J. 2012;53:550–6.
13. Barentsz JO, Richenberg J, Clements R, Choyke P, Verma S, Villeirs G, et al. ESUR prostate MR guidelines 2012. Eur Radiol. 2012;22(4):746–57.
14. Wang L, Mazaheri Y, Zhang J, Ishill NM, Kuroiwa K, Hricak H. Assessment of biologic aggressiveness of prostate cancer: correlation of MR signal intensity with Gleason grade after radical prostatectomy. Radiology. 2008;246:168–76.
15. Qayyum A, Coakley FV, Lu Y, Olpin JD, Wu L, Yeh BM, et al. Organ-Confined confined Prostate prostate Cancercancer: Effect effect of Prior prior Transrectal transrectal Biopsy biopsy on Eendorectal MRI and MR Spectroscopic spectroscopic Imagingimaging. AJR Am J Roentgenol. 2004;183(4):1079–83. http://www.ncbi.nlm.nih.gov/pubmed/15385308.
16. Akin O, Sala E, Moskowitz CS, Kuroiwa K, Ishill NM, Pucar D, et al. Transition zone prostate cancers: features, detection, localization, and staging at endorectal MR imaging. Radiology. 2006;239:784–92.
17. Tan CH, Wei W, Johnson V, Kundra V. Diffusion-weighted MRI in the detection of prostate cancer: meta-analysis. AJR Am J Roentgenol. 2012;199:822–9.
18. Koh D-M, Collins DJ. Diffusion-weighted MRI in the body: applications and challenges in oncology. AJR Am J Roentgenol. 2007;188:1622–35.
19. Kim CK, Park BK, Kim B. High-b-value diffusion-weighted imaging at 3 T to detect prostate cancer: comparisons between b values of 1,000 and 2,000 s/mm2. AJR Am J Roentgenol. 2010;194(1):W33–7.
20. Katahira K, Takahara T, Kwee TC, Oda S, Suzuki Y. Ultra-high-b-value diffusion-weighted MR imaging for the detection of prostate cancer: evaluation in 201 cases with histopathological correlation. Eur Radiol. 2011;21(1):188–96.
21. Delongchamps NB, Rouanne M, Flam T, et al. Multiparametric magnetic resonance imaging for the detection and localization of prostate cancer: combination of T2-weighted, dynamic contrast-enhanced and diffusion-weighted imaging. BJU Int. 2011;107:1411–8.
22. Delongchamps NB, Beuvon F, Eiss D, Flam T, Muradyan N, Zerbib M, et al. Multiparametric MRI is helpful to predict tumor focality, stage, and size in patients diagnosed with unilateral low-risk prostate cancer. Prostate Cancer Prostatic Dis. 2011;14:232–7.
23. Tamada T, Sone T, Higashi H, Jo Y, Yamamoto A, Kanki A, et al. Prostate cancer detection in patients

with total serum prostate-specific antigen levels of 4–10 ng/mL: diagnostic efficacy of diffusion-weighted imaging, dynamic contrast-enhanced MRI, and T2-weighted imaging. AJR Am J Roentgenol. 2011;197(3):664–70.
24. Isebaert S, Van den Bergh L, Haustermans K, Joniau S, Lerut E, De Wever L, et al. Multiparametric MRI for prostate cancer localization in correlation to whole-mount histopathology. J Magn Reson Imaging. 2013; 37:1392–401.
25. Wu L-M, Xu J-R, Ye Y-Q, Lu Q, Hu J-N. The clinical value of diffusion-weighted imaging in combination with T2-weighted imaging in diagnosing prostate carcinoma: a systematic review and meta-analysis. AJR Am J Roentgenol. 2012;199:103–10.
26. Woodfield CA, Tung GA, Grand DJ, Pezzullo JA, Machan JT, Renzulli JF. Diffusion-weighted MRI of peripheral zone prostate cancer: comparison of tumor apparent diffusion coefficient with Gleason score and percentage of tumor on core biopsy. AJR Am J Roentgenol. 2010;194:W316–22.
27. Verma S, Rajesh A, Morales H, Lemen L, Bills G, Delworth M, et al. Assessment of aggressiveness of prostate cancer: correlation of apparent diffusion coefficient with histologic grade after radical prostatectomy. AJR Am J Roentgenol. 2011;196(2):374–81.
28. Hambrock T, Somford DM, Huisman HJ, van Oort IM, Witjes JA, Hulsbergen-Van de Kaa CA, et al. Relationship between apparent diffusion coefficients at 3.0-T MR imaging and Gleason grade in peripheral zone prostate cancer. Radiology. 2011;259:453–61.
29. Turkbey B, Shah VP, Pang Y, Bernardo M, Xu S, Kruecker J, et al. Is apparent diffusion coefficient associated with clinical risk scores for prostate cancers that are visible on 3-T MR images? Radiology. 2010;258:488–95.
30. Tamada T, Sone T, Jo Y, Toshimitsu S, Yamashita T, Yamamoto A, et al. Apparent diffusion coefficient values in peripheral and transition zones of the prostate: comparison between normal and malignant prostatic tissues and correlation with histologic grade. J Magn Reson Imaging. 2008;28:720–6.
31. Thörmer G, Otto J, Reiss-Zimmermann M, Seiwerts M, Moche M, Garnov N, et al. Diagnostic value of ADC in patients with prostate cancer: influence of the choice of b values. Eur Radiol. 2012;22:1820–8.
32. Barentsz JO, Engelbrecht M, Jager GJ, Witjes JA, de LaRosette J, van der Sanden BPJ, et al. Fast dynamic gadolinium-enhanced MR imaging of urinary bladder and prostate cancer. J Magn Reson Imaging. 1999;10: 295–304.
33. Franiel T, Lüdemann L, Rudolph B, Rehbein H, Staack A, Taupitz M, et al. Evaluation of normal prostate tissue, chronic prostatitis, and prostate cancer by quantitative perfusion analysis using a dynamic contrast-enhanced inversion-prepared dual-contrast gradient echo sequence. Invest Radiol. 2008;43:481–7.
34. Hoeks CMA, Barentsz JO, Hambrock T, Yakar D, Somford DM, Heijmink SWTPJ, et al. Prostate cancer: multiparametric MR imaging for detection, localization, and staging. Radiology. 2011;261:46–66.
35. Huisman HJ, Engelbrecht MR, Barentsz JO. Accurate estimation of pharmacokinetic contrast-enhanced dynamic MRI parameters of the prostate—Huisman—2001—Journal of Magnetic Resonance Imaging—Wiley Online Library. J Magn Reson Imaging. 2001;13:607–14.
36. Verma S, Turkbey B, Muradyan N, Rajesh A, Cornud F, Haider MA, et al. Overview of dynamic contrast-enhanced MRI in prostate cancer diagnosis and management. AJR Am J Roentgenol. 2012;198(6):1277–88. http://www.ncbi.nlm.nih.gov/pubmed/22623539.
37. Low RN, Fuller DB, Muradyan N. Dynamic gadolinium-enhanced perfusion MRI of prostate cancer: assessment of response to hypofractionated robotic stereotactic body radiation therapy. AJR Am J Roentgenol. 2011;197:907–15.
38. Vos EK, Litjens GJS, Kobus T, Hambrock T, de Kaa CAH-V, Barentsz JO, et al. Assessment of prostate cancer aggressiveness using dynamic contrast-enhanced magnetic resonance imaging at 3 T. Eur Urol. 2013;64(3):448–55.
39. Turkbey B, Pinto PA, Mani H, Bernardo M, Pang Y, McKinney YL, et al. Prostate cancer: value of multiparametric MR imaging at 3 T for detection–histopathologic correlation. Radiology. 2010;255:89–99.
40. Turkbey B, Mani H, Shah V, Rastinehad AR, Bernardo M, Pohida T, et al. Multiparametric 3T prostate magnetic resonance imaging to detect cancer: histopathological correlation using prostatectomy specimens processed in customized magnetic resonance imaging based molds. J Urol. 2011;186:1818–24.
41. Ocak I, Bernardo M, Metzger G, Barrett T, Pinto P, Albert PS, et al. Dynamic contrast-enhanced MRI of prostate cancer at 3 T: a study of pharmacokinetic parameters. AJR Am J Roentgenol. 2007;189:849.
42. Awwad HM, Geisel J, Obeid R. The role of choline in prostate cancer. Clin Biochem. 2012;45:1548–53.
43. Coakley FV, Kurhanewicz J, Lu Y, Jones KD, Swanson MG, Chang SD, et al. Prostate cancer tumor volume: measurement with endorectal MR and MR spectroscopic imaging. Radiology. 2002;223:91–7.
44. Wetter A, Engl TA, Nadjmabadi D, Fliessbach K, Lehnert T, Gurung J, et al. Combined MRI and MR spectroscopy of the prostate before radical prostatectomy. AJR Am J Roentgenol. 2006;187:724–30.
45. Weis J, Ahlström H, Hlavcak P, Häggman M, Ortiz-Nieto F, Bergman A. Two-dimensional spectroscopic imaging for pretreatment evaluation of prostate cancer: comparison with the step-section histology after radical prostatectomy. Magn Reson Imaging. 2009;27: 87–93.
46. Kobus T, Vos PC, Hambrock T, De Rooij M, Hulsbergen-van de Kaa CA, Barentsz JO, et al. Prostate cancer aggressiveness: in vivo assessment of MR spectroscopy and diffusion-weighted imaging at 3 T. Radiology. 2012;265:457–67.
47. Kobus T, Hambrock T, Hulsbergen-van de Kaa CA, Wright AJ, Barentsz JO, Heerschap A, et al. In vivo assessment of prostate cancer aggressiveness using magnetic resonance spectroscopic imaging at 3 T with an endorectal coil. Eur Urol. 2011;60:1074–80.

48. Nagarajan R, Margolis D, Raman S, Sarma MK, Sheng K, King CR, et al. MR spectroscopic imaging and diffusion-weighted imaging of prostate cancer with Gleason scores. J Magn Reson Imaging. 2012;36:697–703.
49. Weinreb JC, Blume JD, Coakley FV, Wheeler TM, Cormack JB, Sotto CK, et al. Prostate cancer: sextant localization at MR imaging and MR spectroscopic imaging before prostatectomy – results of ACRIN prospective multi-institutional clinicopathologic study. Radiology. 2009;251:122–33.
50. Portalez D, Mozer P, Cornud F, Renard-Penna R, Misrai V, Thoulouzan M, et al. Validation of the European Society of Urogenital Radiology Scoring System for prostate cancer diagnosis on multiparametric magnetic resonance imaging in a cohort of repeat biopsy patients. Eur Urol. 2012;62(6):986–96.
51. Langer DL, van der Kwast TH, Evans AJ, Sun L, Yaffe MJ, Trachtenberg J, et al. Intermixed normal tissue within prostate cancer: effect on MR imaging measurements of apparent diffusion coefficient and T2–sparse versus dense cancers. Radiology. 2008;249:900–8.
52. Rosenkrantz AB, Mendrinos S, Babb JS, Taneja SS. Prostate cancer foci detected on multiparametric magnetic resonance imaging are histologically distinct from those not detected. J Urol. 2012;187(6):2032–8.
53. Turkbey B, Mani H, Aras O, Rastinehad AR, Shah V, Bernardo M, et al. Correlation of magnetic resonance imaging tumor volume with histopathology. J Urol. 2012;188:1157–63.
54. Isariyawongse BK, Sun L, Banez LL, Robertson C, Polascik TJ, Maloney K, et al. Significant discrepancies between diagnostic and pathologic Gleason sums in prostate cancer: the predictive role of age and prostate-specific antigen. Urology. 2008;72:882–6.
55. Vargas HA, Akin O, Franiel T, Mazaheri Y, Zheng J, Moskowitz C, et al. Diffusion-weighted endorectal MR imaging at 3 T for prostate cancer: tumor detection and assessment of aggressiveness. Radiology. 2011;259:775–84.
56. Hambrock T, Hoeks C, Hulsbergen-van de Kaa C, Scheenen T, Bouwense S, et al. Prospective assessment of prostate cancer aggressiveness using 3-T diffusion-weighted magnetic resonance imaging-guided biopsies versus a systematic 10-core transrectal ultrasound prostate biopsy cohort. Eur Urol. 2011;61:177–84.
57. Oto A, Yang C, Kayhan A, Tretiakova M, Antic T, Schmid-Tannwald C, et al. Diffusion-weighted and dynamic contrast-enhanced MRI of prostate cancer: correlation of quantitative MR parameters with Gleason score and tumor angiogenesis. AJR Am J Roentgenol. 2011;197:1382–90.
58. Augustin H, Fritz GA, Ehammer T, Auprich M, Pummer K. Accuracy of 3-Tesla magnetic resonance imaging for the staging of prostate cancer in comparison to the Partin tables. Acta Radiol. 2009;50:562–9.
59. D'Amico AV, Whittington R, Malkowicz SB. Biochemical outcome after radical prostatectomy, external beam radiation therapy, or interstitial radiation therapy for clinically localized prostate cancer. JAMA. 1998;280(11):969–74.
60. Somford DM, Hamoen EH, Futterer JJ, van Basten JP, van de Kaa CAH, Vreuls W, et al. The predictive value of endorectal 3-Tesla multiparametric MRI for extraprostatic extension in low-, intermediate and high-risk prostate cancer patients. J Urol. 2013;190(5):1728–34.
61. Renard-Penna R, Rouprêt M, Comperat E, Ayed A, Coudert M, Mozer P, et al. Accuracy of high resolution (1.5 tesla) pelvic phased array magnetic resonance imaging (MRI) in staging prostate cancer in candidates for radical prostatectomy: results from a prospective study. Urol Oncol. 2013;31:448–54.
62. Choi WW, Williams SB, Gu X, Lipsitz SR, Nguyen PL, Hu JC. Overuse of imaging for staging low risk prostate cancer. J Urol. 2011;185:1645–9.
63. Lavery HJ, Brajtbord JS, Levinson AW, Nabizada-Pace F, Pollard ME, Samadi DB. Unnecessary imaging for the staging of low-risk prostate cancer is common. Urology. 2011;77:274–8.
64. Cooperberg MR, Lubeck DP, Grossfeld GD, Mehta SS, Carroll PR. Contemporary trends in imaging test utilization for prostate cancer staging: data from the cancer of the prostate strategic urologic research endeavor. J Urol. 2002;168:491–5.
65. Siegel R, Naishadham D, Jemal A. Cancer statistics, 2012. CA Cancer J Clin. 2012;62:10–29.
66. Taira AV, Merrick GS, Galbreath RW, Andreini H, Taubenslag W, Curtis R, et al. Performance of transperineal template-guided mapping biopsy in detecting prostate cancer in the initial and repeat biopsy setting. Prostate Cancer Prostatic Dis. 2010;13:71–7.
67. Ukimura O, Hung AJ, Gill IS. Innovations in prostate biopsy strategies for active surveillance and focal therapy. Curr Opin Urol. 2011;21:115–20.
68. Hambrock T, Somford DM, Hoeks C, Bouwense SA, Huisman H, Yakar D, et al. Magnetic resonance imaging guided prostate biopsy in men with repeat negative biopsies and increased prostate specific antigen. J Urol. 2010;183:520–7.
69. Pinto PA, Chung PH, Rastinehad AR, Baccala AAJ, Kruecker J, Benjamin CJ, et al. Magnetic resonance imaging/ultrasound fusion guided prostate biopsy improves cancer detection following transrectal ultrasound biopsy and correlates with multiparametric magnetic resonance imaging. J Urol. 2011;186:1281–5.
70. Sonn GA, Natarajan S, Margolis DJA, Macairan M, Lieu P, Huang J, et al. Targeted biopsy in the detection of prostate cancer using an office based magnetic resonance ultrasound fusion device. J Urol. 2012;189(1):86–91.
71. Moore CM, Robertson NL, Arsanious N, Middleton T, Villers A, Klotz L, et al. Image-guided prostate biopsy using magnetic resonance imaging-derived targets: a systematic review. Eur Urol. 2012;63(1):125–40.
72. Hoeks CM, Schouten MG, Bomers JG, Hoogendoorn SP, Hulsbergen-Van de Kaa CA, T T, et al. Three-tesla magnetic resonance-guided prostate biopsy in men with increased prostate-specific antigen and repeated, negative, random, systematic, transrectal ultrasound biopsies: detection of clinically significant prostate cancers. Eur Urol. 2012;62(5):902–9.

73. Kasivisvanathan V, Dufour R, Moore CM, Ahmed HU, Abd-Alazeez M, Charman SC, et al. Transperineal magnetic resonance image targeted prostate biopsy versus transperineal template prostate biopsy in the detection of clinically significant prostate cancer. J Urol. 2013;189:860–6.
74. Hadaschik BA, Kuru TH, Tulea C, Rieker P, Popeneciu IV, Simpfendorfer T, et al. A novel stereotactic prostate biopsy system integrating pre-interventional magnetic resonance imaging and live ultrasound fusion. J Urol. 2011;186:2214–20.
75. Baumann M, Mozer P, Daanen V, Troccaz J. Prostate biopsy tracking with deformation estimation. Med Image Anal. 2012;16:562–76.
76. Natarajan S, Marks LS, Margolis DJ, Huang J, Macairan ML, Lieu P, et al. Clinical application of a 3D ultrasound-guided prostate biopsy system. Urol Oncol. 2011;29:334–42.
77. Sonn GA, Chang E, Natarajan S, Margolis DJ, Macairan M, Lieu P, et al. Value of targeted prostate biopsy using magnetic resonance-ultrasound fusion in men with prior negative biopsy and elevated prostate-specific antigen. Eur Urol. 2014;65(4):809–15.
78. Xu S, Kruecker J, Turkbey B, Glossop N, Singh AK, Choyke P, et al. Real-time MRI-TRUS fusion for guidance of targeted prostate biopsies. Comput Aided Surg. 2008;13:255–64.
79. Vourganti S, Rastinehad A, Yerram NK, Nix J, Volkin D, Hoang A, et al. Multiparametric magnetic resonance imaging and ultrasound fusion biopsy detect prostate cancer in patients with prior negative transrectal ultrasound biopsies. J Urol. 2012;188(6):2152–7.
80. Dall'era MA, Albertsen PC, Bangma C, Carroll PR, Carter HB, Cooperberg MR, et al. Active surveillance for prostate cancer: a systematic review of the literature. Eur Urol. 2012;62(6):976–83.
81. Tosoian JJ, Johnbull E, Trock BJ, Landis P, Epstein JI, Partin AW, et al. Pathological outcomes in men with low risk and very low risk prostate cancer: implications on the practice of active surveillance. J Urol. 2013;190(4):1218–22.
82. Conti SL, Dall'era M, Fradet V, Cowan JE, Simko J, Carroll PR. Pathological outcomes of candidates for active surveillance of prostate cancer. J Urol. 2009; 181:1628–33; discussion 1633–4.
83. Smaldone MC, Cowan JE, Carroll PR, Davies BJ. Eligibility for active surveillance and pathological outcomes for men undergoing radical prostatectomy in a large, community based cohort. J Urol. 2010;183: 138–43.
84. Cooperberg MR, Broering JM, Carroll PR. Time trends and local variation in primary treatment of localized prostate cancer. J Clin Oncol. 2010;28:1117–23.
85. Vargas HA, Akin O, Afaq A, Goldman D, Zheng J, Moskowitz CS, et al. Magnetic resonance imaging for predicting prostate biopsy findings in patients considered for active surveillance of clinically low risk prostate cancer. J Urol. 2012;188(5):1732–8.
86. Borofsky MS, Rosenkrantz AB, Abraham N, Jain R, Taneja SS. Does suspicion of prostate cancer on integrated T2 and diffusion-weighted MRI predict more adverse pathology on radical prostatectomy? Urology. 2013;81(6):1279–83.
87. Epstein JI, Walsh PC, Carmichael M, Brendler CB. Pathologic and clinical findings to predict tumor extent of nonpalpable (stage T1c) prostate cancer. JAMA. 1994;271:368–74.
88. Cooperberg MR, Pasta DJ, Elkin EP, Litwin MS, Latini DM, Du Chane J, et al. The University of California, San Francisco Cancer of the Prostate Risk Assessment score: a straightforward and reliable preoperative predictor of disease recurrence after radical prostatectomy. J Urol. 2005;173:1938–42.
89. Turkbey B, Mani H, Aras O, Ho J, Hoang A, Rastinehad AR, et al. Prostate cancer: can multiparametric MR imaging help identify patients who are candidates for active surveillance? Radiology. 2013;268(1):144–52.
90. Giles SL, Morgan VA, Riches SF. Apparent diffusion coefficient as a predictive biomarker of prostate cancer progression: value of fast and slow diffusion components. AJR Am J Roentgenol. 2011;196(3):586–91.
91. Lee DH, Koo KC, Lee SH, Rha KH, Choi YD, Hong SJ, et al. Tumor lesion diameter on diffusion weighted magnetic resonance imaging could help predict insignificant prostate cancer in patients eligible for active surveillance: preliminary analysis. J Urol. 2013;190(4):1213–7.
92. McClure TD, Margolis DJA, Reiter RE, Sayre JW, Thomas MA, Nagarajan R, et al. Use of MR imaging to determine preservation of the neurovascular bundles at robotic-assisted laparoscopic prostatectomy. Radiology. 2012;262:874–83.
93. Rosenkrantz AB, Deng F-M, Kim S, Lim RP, Hindman N, Mussi TC, et al. Prostate cancer: multiparametric MRI for index lesion localization—a multiple-reader study. AJR Am J Roentgenol. 2012;199:830–7.
94. Rosenkrantz AB, Scionti SM, Mendrinos S, Taneja SS. Role of MRI in minimally invasive focal ablative therapy for prostate cancer. AJR Am J Roentgenol. 2011;197:W90–6.
95. Ahmed HU, Freeman A, Kirkham A, Sahu M, Scott R, Allen C, et al. Focal therapy for localized prostate cancer: a phase I/II trial. J Urol. 2011;185:1246–54.
96. Ahmed HU, Hindley RG, Dickinson L, Freeman A. Focal therapy for localised unifocal and multifocal prostate cancer: a prospective development study. Lancet Oncol. 2012;13(6):622–32.
97. Sella T, Schwartz LH, Swindle PW, Onyebuchi CN, Scardino PT, Scher HI, et al. Suspected local recurrence after radical prostatectomy: endorectal coil MR imaging. Radiology. 2004;231:379–85.
98. Panebianco V, Barchetti F, Sciarra A, Musio D, Forte V, Gentile V, et al. Prostate cancer recurrence after radical prostatectomy: the role of 3-T diffusion imaging in multi-parametric magnetic resonance imaging. Eur Radiol. 2013;23:1745–52.
99. Allen GW, Howard AR, Jarrard DF, Ritter MA. Management of prostate cancer recurrences after radiation therapy-brachytherapy as a salvage option. Cancer. 2007;110:1405–16.

100. Tamada T, Sone T, Jo Y, Hiratsuka J, Higaki A, Higashi H, et al. Locally recurrent prostate cancer after high-dose-rate brachytherapy: the value of diffusion-weighted imaging, dynamic contrast-enhanced MRI, and T2-weighted imaging in localizing tumors. AJR Am J Roentgenol. 2011;197:408–14.
101. Westphalen AC, Reed GD, Vinh PP, Sotto C, Vigneron DB, Kurhanewicz J. Multiparametric 3T endorectal mri after external beam radiation therapy for prostate cancer. J Magn Reson Imaging. 2012;36:430–7.
102. Morgan VA, Riches SF, Giles S, Dearnaley D, deSouza NM. Diffusion-weighted MRI for locally recurrent prostate cancer after external beam radiotherapy. AJR Am J Roentgenol. 2012;198: 596–602.
103. Loeb S, Carter HB, Berndt SI, Ricker W, Schaeffer EM. Complications after prostate biopsy: data from SEER-Medicare. J Urol. 2011;186:1830–4.
104. Dickinson L, Ahmed HU, Allen C, Barentsz JO, Carey B, Fütterer JJ, et al. Magnetic resonance imaging for the detection, localisation, and characterisation of prostate cancer: recommendations from a European consensus meeting. Eur Urol. 2011;59: 477–94.

# MR-Guided Prostate Interventions

# 14

Ashley E. Ross, Dan Stoianovici,
and Mohamad E. Allaf

Prostate cancer represents the most common visceral malignancy in man, with roughly 240,000 patients diagnosed in the United States last year and 1 in every 36 men dying of the disease [1]. Widespread use of PSA screening has resulted in the earlier detection of prostate cancer and has contributed to the nearly 40 % decrease in prostate cancer mortality since its peak in 1991 [2]. Associated with this has been a greater likelihood of diagnosis of prostate cancer at a clinically localized stage, with a nearly tenfold reduction in the amount of men diagnosed with metastatic disease since the start of the PSA era and thus the vast majority of men currently being diagnosed with localized prostate cancer. Despite these advances, due to the lead time associated with PSA-based screening, and its relative inability to distinguish patients with indolent and life-threatening cancers, there is a growing concern for overdiagnosis and overtreatment in screened populations [3–5]. Indeed, the majority of patients currently diagnosed with prostate cancer have low-grade (Gleason pattern 3 or less), favorable-risk disease and, if not upgraded at the time of surgery, might have low cancer-specific mortality even without intervention [6, 7]. Regardless, there is a rationale for the use of definitive local therapy, as up to 30 % of men with low-risk disease will be upgraded at prostatectomy [8]. Indeed, trepidation regarding the undertreatment of a known but possibly undersampled malignancy has led to an underuse of active surveillance of low-risk disease [9]. Unfortunately, current whole-gland treatment of prostate cancer is associated with the risk of long-term urinary and sexual side effects and decreased quality of life [10]. For these reasons, there has been a growing emphasis on the development of focal therapies which may treat prostate cancer or the index prostatic lesion while limiting damage to the urethral sphincter and neurovascular bundles. However, while the "male lumpectomy" for prostate cancer was originally proposed by Onik and colleagues two decades ago, adoption of focal ablation for prostate cancer treatment has been slow, in part due to the inability of imaging modalities to adequately identify localized prostate cancer [11, 12].

Relatively recent advances in multiparametric MRI imaging now allow for the localization of larger (≥0.5 cm) prostate cancer lesions with relatively high sensitivity and specificity and

A.E. Ross, MD, PhD
Departments of Urology, Oncology, Pathology,
Johns Hopkins Brady Urological Institute,
Baltimore, MD, USA
e-mail: aross2@jhmi.edu

D. Stoianovici, PhD (✉)
Departments of Urology, Mechanical Engineering,
and Neurosurgery, Johns Hopkins Brady
Urological Institute, Baltimore, MD, USA
e-mail: dss@jhu.edu

M.E. Allaf, MD
Departments of Urology, Oncology,
and Biomedical Engineering, Johns Hopkins Brady
Urological Institute, Baltimore, MD, USA

J.C. Liao, L.-M. Su (eds.), *Advances in Image-Guided Urologic Surgery*,
DOI 10.1007/978-1-4939-1450-0_14, 

have become the gold standard for imaging disease within the prostate. This thus allows for improved patient selection for subtotal and focal therapies. In addition, use of specialized MRI sequences allows not only for patient selection and treatment planning but also for true focal therapy with treatment guidance, real-time treatment monitoring, and posttreatment evaluation. Below we review the features of prostate MRI and discuss MRI-guided interventions to treat prostate cancer, focusing on the modalities of high-intensity-focused ultrasound (HIFU), laser thermoablation, and cryoablation.

## Magnetic Resonance Imaging of the Prostate

MRI of the prostate was first reported in the mid-1980s and has since evolved to provide both anatomical and also functional information [13]. Anatomic information is provided primarily via T2-weighted imaging, which allows for high spatial resolution and very clearly identifies the distinct zones of the prostate. On T2-weighted imaging, prostate cancer can appear as an area of low signal within the normally high-signal peripheral zone. Historically, MRI was performed using a 1.5 Tesla (T) scanner and an endorectal coil. The introduction of higher strength (3 T) magnets allowed for higher spatial resolution. This prompted many radiologists to perform 3 T scans in the absence of endorectal coil, making MRI more tolerable by patients [14]. T2-weighted imaging is limited in that areas of low signal can also represent prostatitis, biopsy tracts, and other benign abnormalities. Because of this, a recent consensus panel for the use of focal therapy in prostate cancer recommends that staging MRI be performed with a 3 T magnet and in a multiparametric fashion using T1-, T2-, and diffusion-weighted imaging (DWI) and dynamic contrast-enhanced imaging (DCE) [14]. The use of these combinations allows for high specificity, positive and negative predictive value (all over 90 %) albeit with lower sensitivities (~60 %) [14, 15].

DWI examines proton diffusion properties of water within prostate tissue to determine an apparent diffusion coefficient (ADC). In cases of prostate cancer, where cellular density is increased thus restricting the movements of water, ADCs are lower than in benign tissue. DWI can be determined without the use of contrast and can be obtained rapidly. The ADC also changes with treatment, and DWI can be used to actively monitor the development of ablated tissue during treatment [16]. While very practical, the use of DWI is limited by its susceptibility to motion artifact.

As its name implies, DCE involves the use of contrast and its monitoring by T1-weighted sequences. Contrast-enhanced imaging can identify neovascularization of tumors by looking at the time to peak enhancement, level of peak enhancement, and washout. As ablation of the prostate alters these characteristics by causing necrosis, fibrosis, inflammation, and devascularization, DCE can be performed following treatment to gauge the extent of ablation with hypo-vascular tissue generally appearing hypointense on T1 [17].

In addition to DWI and DCE, magnetic resonance spectroscopic imaging has also been explored as part of mpMRI. Spectroscopic imaging can demonstrate relative concentrations of citrate, creatine, and choline of which prostate cancer tends to have lower and higher levels, respectively, compared to normal tissue [17]. While multiple studies demonstrate an added value of spectroscopic imaging to T2-weighted imaging alone, it is technically demanding and has low reproducibility, limiting its routine use [14].

Beyond providing cancer detection and 3D imaging information, MRI can also be used for temperature monitoring during thermal ablation. This is most commonly performed by temperature monitoring via proton-resonant frequency shift thermometry [18, 19]. This technique takes advantage of the temperature dependence for the water proton chemical shift and allows for highly reproducible, accurate, and rapid measurements of temperature change. This technique is employed for increases in temperature and cannot be readily used to study freezing due to artifacts produced at the leading edge of freezing tissue [20].

## MRI-Targeted Therapies for Prostate Cancer

A recently convened expert panel of urologists, radiologists, and basic researchers from Europe and North America concluded that mpMRI is an important component of patient selection for focal therapy [14]. While these conclusions were based on considerations for primary prostate cancer treatment, MRI can additionally play a valuable role in targeting salvage therapies both after radiation and surgical treatment. Below we focus on three emerging modalities for targeted therapy based on their ability to be integrated with MRI and their acceptance as ablative modalities. Additionally, it is important to highlight that all of the MRI-guided interventions discussed below have only been examined in relatively small safety and feasibility studies and further that the concept of focal therapy itself, despite mounting evidence, has not been accepted by the AUA and should still be considered experimental in nature.

## MRI-Guided High-Intensity-Focused Ultrasound (HIFU) Therapy for Prostate Cancer

HIFU is a form of thermoablation whereby piezoelectric transducers are used to generate a focused ultrasound field. This allows the temperature to rise quickly in the focal zone of treatment, while the surrounding tissue, which is exposed to unfocused low acoustic energy, is unaffected [21]. Heating of tissue to over 55 °C causes cytotoxic effects and results in coagulative necrosis [22]. HIFU can be performed either transrectally or transurethrally and, as it requires no incision or puncture, represents the most externally noninvasive treatment modality available for prostate cancer. In addition, HIFU, as another ablative therapy, can be performed within the MRI ("in bore") with real-time MR imaging or by fusing a previously obtained MR image onto an ultrasound. The advantage of in-bore techniques is that real-time image acquisition and therapeutic guidance can be employed. In addition, in-bore techniques allow for the use of thermal monitoring and adjustment of treatment. A disadvantage to in-bore techniques is that they are costly and can be resource and time intensive. Fusion techniques offer a less costly alternative but can be inaccurate and real-time monitoring of ablation is not possible.

Recently, Dickinson and colleagues reported on 26 men undergoing focal HIFU using the Sonablate 500 system and nonrigid registration software to couple US and mpMRI imaging [23]. This represented a pilot study, nested within the INDEX trial, a multicentered investigator-driven trial in the United Kingdom to observe the 3-year outcomes following HIFU. Here they demonstrated feasibility of using HIFU and fusion software for MR and ultrasound imaging with no technical difficulties experienced while using the fusion software during HIFU. Mean overall operative time was 141 min. Postoperative histologic and oncologic outcomes were not reported; however, the decision to ablate additional tissue outside of the initial treatment plan was made in half the cases. This highlights the uncertainly inherent in fusion imaging and lack of real-time ablation visualization.

In order to facilitate real-time temperature feedback and ablation localization and monitoring, transurethral HIFU therapies have been developed that are coupled to MRI. The feasibility of such a technique was shown first in canines and then extended to a pilot phase 0 study in humans [24, 25]. In this study, Chopra et al. treated eight men with localized prostate cancer immediately prior to prostatectomy by transurethral HIFU. In their system, the transurethral ultrasound heating applicator was coupled to a MRI-compatible rotational positioning system which additionally had circulating deionized water in a flowing circuit to allow cooling and coupling across the urethra. The transducer emits linear beams with rotation allowing selection of the ablated volume. By design in this feasibility study, the peripheral zone was not treated, and accordingly no rectal cooling was used. Following treatment men were taken immediately to prostatectomy, and prostates were step sectioned as whole mounts to compare to MRI ablation images. The average treatment time was 3 h, and

the accuracy of the treatment zone was concordant to roughly 2.5 mm. Histologic analysis showed a contiguous treatment area with a transition zone from ablated to normal tissue of less than 4 mm. In a subsequent canine study using a similar prototype MRI-guided US therapy system developed by Philips, treatments were extended to all of the zones of the prostate including the peripheral zone [16]. This study demonstrated ablation of the peripheral zone and high correlation of ablation with posttreatment MRI imaging, as measured by DWI or DCE compared to histology ($r^2$ of 0.91 and 0.89, respectively).

Recently, a small MR-coupled transrectal HIFU study prior to prostatectomy was also reported [26]. In this study, HIFU was used with a 3 T MRI and temperature monitoring by proton frequency shift. Of the five patients treated that underwent immediate prostatectomy, all had untreated prostate cancer in their specimen with two having clinically significant tumors outside the treatment zone.

While the above studies demonstrate the technical feasibility of real-time MRI-targeted focal therapy of the prostate, the actual clinical utility of this method remains a matter for further study. A clear case can be made for the benefit of mpMRI in appropriately selecting men for subtotal gland ablation; however, the argument for a need of true focal therapy (as oppose to hemi-ablation or other subtotal ablation) is more debatable. In part, this is due to the anatomy of the prostate. The prostate gland itself serves minimal function but is situated in an important area, surrounded distally and anteriorly by the striated urethral sphincter and posterolaterally by the neurovascular bundles of Walsh. Ablation of prostate tissue per say is of no or minimal consequence, and partial ablation of the urethral sphincter or one of two redundant neurovascular bundles may have only marginal effects. Indeed, in 2011, Ahmed et al. reported results of a phase I/II trial of 20 men with low- to intermediate-risk prostate cancer who underwent hemi-ablation of the prostate by HIFU after having mpMRI and template trans-perineal prostate biopsies to confirm unilateral disease [27]. In this small series, 95 % of men preserved potency, 95 % were continent, and 89 % had no histological evidence of cancer after 1 year of follow-up. Currently, larger studies with longer follow-up comparing focal therapy to hemi-ablation therapy are needed in order to determine whether focal therapy can improve outcomes over subtotal or hemi-gland ablation while preserving oncologic efficacy.

## MRI-Guided Focal Laser Ablation of Prostate Cancer

Laser ablation represents another form of predictable and accurate, light-based energy thermal ablation. In this method, a laser fiber is positioned within the tumor (usually via a trans-perineal introducer), and then light is delivered through the laser fiber. Advantages of laser therapy are that treatment times are short and sharply demarcated boundaries can be visualized. Like HIFU therapy, real-time MRI thermal monitoring can be used as well as live monitoring of the ablation zone.

Initial reports of laser ablation in humans involved fusion imaging of MRI with ultrasound to guide treatment [28]. In a phase I trial of 12 patients, Lindner et al. used a 3D ultrasound to guide the treatment laser to an MRI-defined lesion. Ablation was monitored using contrast-enhanced ultrasound as a thermal sensor. As with HIFU, this study suggested limitations in fusion imaging with only 67 % of patients having ablation in the target area and of the patients that failed ablation, 75 % showing poor overlap between pre- and posttreatment MRI. In a follow-up study of focal laser treatment of four patients followed by MRI and prostatectomy, the authors found good correlation between MRI and whole-mount histology and concluded that MRI "might prove to be the sole imaging modality for targeting the index PCa lesion, facilitating laser fiber placement for ablation and monitoring the ablation in real time using thermometry" [29].

Oto and colleagues recently reported a phase I trial of nine men undergoing in-bore MRI-guided and MRI-monitored laser ablation of the prostate [30]. Here, freehand trans-perineal insertion of a

titanium obturator which would house the laser fiber was performed under real-time MRI guidance. Treatment times were 2.5–4 h with laser durations of approximately 4 min. At 6 months of follow-up, there were no grade 3 or 4 complications, and no men had significant changes in their urinary or sexual function. Cancer control was evaluated by MRI-guided biopsy and demonstrated no cancer in seven of the nine patients and Gleason 6 disease in the remaining two.

## MRI-Guided Cryoablation of Prostate Cancer

Cryoablation of the prostate is an FDA-approved minimally invasive outpatient procedure by which subfreezing temperatures (less than 40 °C) can be used to induce tumor cell death. Freezing is accomplished by use of the Joule-Thompson effect with argon gas to cause freezing of a percutaneously inserted needle. Thawing can be passive, or active, with use of helium gas. MRI-compatible probes are currently available (Galil Medical). The urethra is protected by a urethral warming catheter, and when performed with in-bore MRI guidance, the rectum can be protected by a rectal warming balloon. After treatment, coagulative necrosis of the tissue results, and within 24 h there is an associated intense inflammatory infiltrate [31].

Traditionally, cryoablation of the prostate has been performed under transrectal ultrasound guidance. This imaging modality however only allows for visualization of the proximal ice edge, due to the acoustic shadowing effect of the ice ball. When performed with MRI however, near real-time three-dimensional monitoring can be undertaken by T1-weighted imaging which depicts a hypointense ice ball with a hyperintense border [20]. As stated above, artifacts at the ice-tissue transition limit the use of thermal monitoring.

In 2012, Gangi and colleagues reported real-time, in-bore percutaneous whole-gland MRI-monitored cryoablation in eight primary and three radiation-salvage patients [32]. They confirmed sharp visualization of ice ball formation and, with rectal thermal protection, had no fistula and no cancer recurrences at 15 months, as defined by the Phoenix criteria. Bomers et al. recently reported on MRI-guided and MRI-monitored focal cryoablation of ten radio-recurrent prostate cancer patients. Treatment times had a median of 210.5 min but decreased throughout their study. Of the ten patients treated, no patient experienced incontinence [20].

As with HIFU, in the setting of localized prostate cancer, the clinical advantage to direct 3D visualization of ice ball formation and the use of true focal therapy remain unclear. Again, this is due to the favorable functional and oncologic results for transrectal ultrasound-guided hemi-ablation or subtotal ablation of the prostate. Ward and Jones provided a recent review of the results of 1,160 patients treated with targeted cryoablation of primary prostate cancer as reported in the COLD registry [33]. With the caveat that these results are self-reported and unstandardized, results were favorable with incontinence rates of 1.6 % and rectourethral fistula rates of 0.1 %. Results of hemigland cryoablation in a smaller but more modern cohort were reported recently by Bahn et al. [34]. Here, 73 patients with low- or intermediate-risk prostate cancer were treated with hemi-ablative cryotherapy from 2002 to 2011 after localization of unilateral prostate cancer aided by preoperative mpMRI. Continence rates were 100 %, and potency rates were 74 and 86 % at 1 and 2 years, respectively, in men who were previously potent. No rectourethral fistulas were reported. In addition, of the men who underwent posttreatment biopsy (48 of the 73 men), only one had disease on the treated side. Similar to hemi-ablation via HIFU, the results above, utilizing preoperative mpMRI for patient selection but not intraoperative MRI for true focal therapy, set a high bar for improvement by MRI-coupled techniques.

In addition to targeting the intact prostate, MRI may play a crucial role in the targeting ablative therapies for recurrent disease after surgery. Woodrum et al. recently performed a study involving 18 patients with biochemical recurrence following radical prostatectomy and nodules in the prostatic bed detected on mpMRI

which were biopsy positive for prostate cancer [35]. Under MRI guidance, cryoablation probes were placed freehand trans-perineally into the recurrent lesion, and cryoablation with multiplanar ice ball imaging was performed under MRI guidance. Of patients with more dense probe placement (nine men), 89 % had undetectable PSAs 6 months following treatment.

### Conclusions

mpMRI has emerged as the gold standard for imaging localized prostate cancer within the prostate. As such, mpMRI currently plays an important role in patient selection for subtotal prostate gland therapies (such as HIFU, laser ablation, and cryoablation). The development of MRI-compatible equipment allows for in-bore, real-time MRI-guided procedures. This permits the use of MRI in direct lesion targeting as well as for the use of real-time temperature monitoring and evaluation of lesion formation. While the accuracy of focal ablation appears augmented by in-bore coupling to MRI, it is unclear whether true MR-guided focal therapies will be able to treat patients with less morbidity and better oncologic outcomes than less elegant ultrasound-guided gland hemi-ablation and subtotal ablation and this will have to be determined by larger head-to-head studies with longer follow-up. In a similar circumstance, while DCE and DWI imaging correlate well with lesion ablation, it is unclear whether MRI can replace biopsy in the follow-up after targeted treatment and this will also need to be examined experimentally. A unique niche for MR-guided treatments may be in the treatment of localized recurrences and oligo-metastatic disease, where precise localization and monitoring of treatment may be crucial for acceptable outcomes.

## References


1. Siegel R, Naishadham D, Jemal A. Cancer statistics, 2012. CA Cancer J Clin. 2012;62(1):10–29.
2. ACS. ACS: cancer facts & figures. Atlanta: American Cancer Society; 2012.
3. Andriole GL, Crawford ED, Grubb 3rd RL, Buys SS, Chia D, Church TR, et al. Mortality results from a randomized prostate-cancer screening trial. N Engl J Med. 2009;360(13):1310–9.
4. Schroder FH, Hugosson J, Roobol MJ, Tammela TL, Ciatto S, Nelen V, et al. Screening and prostate-cancer mortality in a randomized European study. N Engl J Med. 2009;360(13):1320–8.
5. Draisma G, Boer R, Otto SJ, van der Cruijsen IW, Damhuis RA, Schroder FH, et al. Lead times and overdetection due to prostate-specific antigen screening: estimates from the European Randomized Study of Screening for Prostate Cancer. J Natl Cancer Inst. 2003;95(12):868–78.
6. Bill-Axelson A, Holmberg L, Filen F, Ruutu M, Garmo H, Busch C, et al. Radical prostatectomy versus watchful waiting in localized prostate cancer: the Scandinavian prostate cancer group-4 randomized trial. J Natl Cancer Inst. 2008;100(16):1144–54.
7. Stephenson AJ, Kattan MW, Eastham JA, Bianco Jr FJ, Yossepowitch O, Vickers AJ, et al. Prostate cancer-specific mortality after radical prostatectomy for patients treated in the prostate-specific antigen era. J Clin Oncol. 2009;27(26):4300–5.
8. Cohen MS, Hanley RS, Kurteva T, Ruthazer R, Silverman ML, Sorcini A, et al. Comparing the Gleason prostate biopsy and Gleason prostatectomy grading system: the Lahey Clinic Medical Center experience and an international meta-analysis. Eur Urol. 2008;54(2):371–81.
9. Cooperberg MR, Broering JM, Carroll PR. Time trends and local variation in primary treatment of localized prostate cancer. J Clin Oncol. 2010;28(7):1117–23.
10. Sanda MG, Dunn RL, Michalski J, Sandler HM, Northouse L, Hembroff L, et al. Quality of life and satisfaction with outcome among prostate-cancer survivors. N Engl J Med. 2008;358(12):1250–61.
11. Onik GM, Cohen JK, Reyes GD, Rubinsky B, Chang Z, Baust J. Transrectal ultrasound-guided percutaneous radical cryosurgical ablation of the prostate. Cancer. 1993;72(4):1291–9.
12. Hoang AN, Volkin D, Yerram NK, Vourganti S, Nix J, Linehan WM, et al. Image guidance in the focal treatment of prostate cancer. Curr Opin Urol. 2012;22(4):328–35.
13. Hoeks CM, Barentsz JO, Hambrock T, Yakar D, Somford DM, Heijmink SW, et al. Prostate cancer: multiparametric MR imaging for detection, localization, and staging. Radiology. 2011;261(1):46–66.
14. Muller BG, Futterer JJ, Gupta RT, Katz A, Kirkham A, Kurhanewicz J, et al. The role of magnetic resonance imaging in focal therapy for prostate cancer: recommendations from a consensus panel. BJU Int. 2014;113:218.
15. Turkbey B, Mani H, Shah V, Rastinehad AR, Bernardo M, Pohida T, et al. Multiparametric 3T prostate magnetic resonance imaging to detect cancer: histopathological correlation using prostatectomy specimens

processed in customized magnetic resonance imaging based molds. J Urol. 2011;186(5):1818–24.
16. Partanen A, Yerram NK, Trivedi H, Dreher MR, Oila J, Hoang AN, et al. Magnetic resonance imaging (MRI)-guided transurethral ultrasound therapy of the prostate: a preclinical study with radiological and pathological correlation using customised MRI-based moulds. BJU Int. 2013;112(4):508–16.
17. Sciarra A, Barentsz J, Bjartell A, Eastham J, Hricak H, Panebianco V, et al. Advances in magnetic resonance imaging: how they are changing the management of prostate cancer. Eur Urol. 2013;59(6):962–77.
18. Rieke V, Butts PK. Echo combination to reduce proton resonance frequency (PRF) thermometry errors from fat. J Magn Reson Imaging. 2008;27(3):673–7.
19. Ishihara Y, Calderon A, Watanabe H, Okamoto K, Suzuki Y, Kuroda K. A precise and fast temperature mapping using water proton chemical shift. Magn Reson Med. 1995;34(6):814–23.
20. Bomers JG, Yakar D, Overduin CG, Sedelaar JP, Vergunst H, Barentsz JO, et al. MR imaging-guided focal cryoablation in patients with recurrent prostate cancer. Radiology. 2013;268(2):451–60.
21. Jenne JW, Preusser T, Gunther M. High-intensity focused ultrasound: principles, therapy guidance, simulations and applications. Z Med Phys. 2012;22(4):311–22.
22. Chopra R, Tang K, Burtnyk M, Boyes A, Sugar L, Appu S, et al. Analysis of the spatial and temporal accuracy of heating in the prostate gland using transurethral ultrasound therapy and active MR temperature feedback. Phys Med Biol. 2009;54(9):2615–33.
23. Dickinson L, Hu Y, Ahmed HU, Allen C, Kirkham AP, Emberton M, et al. Image-directed, tissue-preserving focal therapy of prostate cancer: a feasibility study of a novel deformable magnetic resonance-ultrasound (MR-US) registration system. BJU Int. 2013;112(5):594–601.
24. Siddiqui K, Chopra R, Vedula S, Sugar L, Haider M, Boyes A, et al. MRI-guided transurethral ultrasound therapy of the prostate gland using real-time thermal mapping: initial studies. Urology. 2010;76(6):1506–11.
25. Chopra R, Colquhoun A, Burtnyk M, N'Djin WA, Kobelevskiy I, Boyes A, et al. MR imaging-controlled transurethral ultrasound therapy for conformal treatment of prostate tissue: initial feasibility in humans. Radiology. 2012;265(1):303–13.
26. Napoli A, Anzidei M, De Nunzio C, Cartocci G, Panebianco V, De Dominicis C, et al. Real-time magnetic resonance-guided high-intensity focused ultrasound focal therapy for localised prostate cancer: preliminary experience. Eur Urol. 2013;63(2):395–8.
27. Ahmed HU, Freeman A, Kirkham A, Sahu M, Scott R, Allen C, et al. Focal therapy for localized prostate cancer: a phase I/II trial. J Urol. 2011;185(4):1246–54.
28. Lindner U, Weersink RA, Haider MA, Gertner MR, Davidson SR, Atri M, et al. Image guided photothermal focal therapy for localized prostate cancer: phase I trial. J Urol. 2009;182(4):1371–7.
29. Lindner U, Lawrentschuk N, Weersink RA, Davidson SR, Raz O, Hlasny E, et al. Focal laser ablation for prostate cancer followed by radical prostatectomy: validation of focal therapy and imaging accuracy. Eur Urol. 2010;57(6):1111–4.
30. Oto A, Sethi I, Karczmar G, McNichols R, Ivancevic MK, Stadler WM, et al. MR imaging-guided focal laser ablation for prostate cancer: phase I trial. Radiology. 2013;267(3):932–40.
31. Finley DS, Pouliot F, Miller DC, Belldegrun AS. Primary and salvage cryotherapy for prostate cancer. Urol Clin North Am. 2010;37(1):67–82. Table of Contents.
32. Gangi A, Tsoumakidou G, Abdelli O, Buy X, de Mathelin M, Jacqmin D, et al. Percutaneous MR-guided cryoablation of prostate cancer: initial experience. Eur Radiol. 2012;22(8):1829–35.
33. Ward JF, Jones JS. Focal cryotherapy for localized prostate cancer: a report from the national Cryo On-Line Database (COLD) registry. BJU Int. 2011;109(11):1648–54.
34. Bahn D, de Castro Abreu AL, Gill IS, Hung AJ, Silverman P, Gross ME, et al. Focal cryotherapy for clinically unilateral, low-intermediate risk prostate cancer in 73 men with a median follow-up of 3.7 years. Eur Urol. 2012;62(1):55–63.
35. Woodrum DA, Kawashima A, Karnes RJ, Davis BJ, Frank I, Engen DE, et al. Magnetic resonance imaging-guided cryoablation of recurrent prostate cancer after radical prostatectomy: initial single institution experience. Urology. 2013;82(4):870–5.

# CT-Guided Renal Ablation

# 15

Michael J. Glamore, Raymond J. Leveillee, and Thomas Scagnelli

The past decade has witnessed a significant evolution in the management of small renal masses. As the incidence of renal cancer and incidental findings has increased, so have our options for assessing and treating them. Options currently available for solid enhancing renal tumors include initial biopsy (Bx), Active surveillance (AS), and surgical extirpation (SE) – such as radical nephrectomy (RN) or partial nephrectomy (PN) and probe-based thermal ablation (TA). Nonthermal ablative technologies such as focused high-intensity beam radiotherapy (Cyberknife) and high-voltage bipolar electrical current also known as irreversible electroporation (NanoKnife) have limited applications to support their usage at this time. High-Intensity Focused Ultrasound (HiFU), another form of thermal ablation, has yet to find a place in renal TA.

Among the most commonly utilized modalities are freezing (CRY) and heating with radiofrequency wavelength energy (RFA). This chapter will focus on needle-based thermal ablation as it pertains to percutaneous renal biopsy and RFA, although the principles can be applied to any needle-based therapy. It will include discussions on patient selection, commercially available probes, timing of renal biopsy, technique (step-by-step approach), and results. Newer imaging modalities such as multislice computerized tomography (CT), three-dimensional renderings, flat panel detector fluoroscopic imaging, image fusion techniques, robotic needle placement, and CT/US fusion are being investigated. Results of both short-term and long-term series will conclude this chapter.

## Indications

The incidence and detection of small renal masses (SRMs) has been increasing. It is believed that widespread use of abdominal cross-sectional imaging has been instrumental in the discovery of incidental renal neoplasms. Most of these SRMs are classified as renal cell carcinomas (RCCs) [1, 2]. TA management has become more widely accepted, especially for patients with clinical stage T1a (<4 cm) solid renal masses. Although initially only offered for patients who were not surgically fit to undergo more extensive extirpative treatment (RN or PN), long-term data make

M.J. Glamore, MD (✉)
Herbert Wertheim College of Medicine,
Florida International University,
University Park, FL, USA
e-mail: m.glamore@gmail.com

R.J. Leveillee, MD, FRCS-G (✉)
Department of Urology, University of Miami
Miller School of Medicine, Miami, FL, USA
e-mail: rleveill@med.miami.edu;
patsfan37@gmail.com

T. Scagnelli, MD, FSIR
Department of Interventional Radiology,
Baptist Cardiac and Vascular Institute,
Doctor's Hospital, Miami, FL, USA

J.C. Liao, L.-M. Su (eds.), *Advances in Image-Guided Urologic Surgery*,
DOI 10.1007/978-1-4939-1450-0_15, 

it attractive as an alternative option for select, compliant patients. Several papers have recently reported mid- to long-term oncologic results after TA suggesting improved oncologic outcomes. Olweny et al. reported comparative 5-year oncologic outcomes for RFA versus PN in patients with clinical T1a RCC [3]. They found comparable cancer-specific survival (97.2 % versus 100 % [$p=0.31$]) overall survival (97.2 % versus 100 % [$p=0.31$]), and local recurrence-free survival (91.7 % versus 94.6 % [$p=0.96$]) between the two groups. Psutka et al. reported on long-term oncologic outcomes for 185 patients with T1 RCC with a median follow-up of 6.43 years [4]. While 13 % were retreated for recurrent disease, overall disease-free survival (DFS) was 88.6 % (92.3 % for T1a and 76.2 for T1b). DFS was impacted primarily by tumor stage on multivariate analysis. Zagoria et al. published nearly identical results in a much smaller series of only 24 patients with a median follow-up of 5.0 years [5]. Retreatment rates were greater for tumors larger than 4 cm thus leading to the suggestion that tumors greater than 4 cm should be approached cautiously. One of the limitations of performing RFA under CT guidance has been the determination of end of treatment. Since heat is responsible for cellular death, and we know that time at hyperthermia (over body temperature of 37 °C) will determine minimal temperature to be achieved, it has been our contention that real-time temperature monitoring is essential to successful treatment. For that reason we have been utilizing peripherally placed, needle-guided, fiber-optic temperature probes at 5 mm from the edge of the renal tumor at the time of the ablation to determine when the "edge" of the tumor reaches >60 °C [6]. With the addition of this "extra step," we feel that RFA can be more effective and can be used for deep and central tumors as well as during salvage procedures to ensure a measurable quantifiable end point [7, 8].

## RFA Principles and Equipment

The majority of cases thus far have been performed with monopolar expandable needle probes (Starburst, Angiodynamics, Latham, NY; LeVeen, Boston Scientific, Natick, MA) or internally perfused single needles (Cool-Tip, Covidien, Boulder, CO). Radio waves (in the vicinity of 400 MHz) are delivered via the needle probe(s) to the target tissue. The electrical current causes ions in the tissues to move, thus leading to frictional heating. It is the heat thus generated that effectively destroys cells by several mechanisms – protein denaturation, DNA/RNA unraveling, vascular congestion, and ischemic damage. Heating >60 °C causes irreversible cell damage, whereas heating >70 °C will lead to cell death and tissue coagulation. Hemostasis, therefore, is easily achievable utilizing RFA. When target temperature exceeds 100 °C, then vaporization occurs and limits further spread of heat by passive conduction due to the insulating effects of carbonized ("charcoaled") tissue. A more detailed description is beyond the scope of this chapter but is available [9].

## Step by Step

One of the most important aspects of urointerventional oncology is precise positioning of needle probes, sensors, and/or biopsy needles. Device placement may be performed either with ultrasound, CT guidance, or both using fusion modalities. A renal biopsy can comfortably and safely be performed with a minimal amount of analgesia. This can be achieved utilizing local anesthetic alone or in combination with moderate intravenous sedation. Needle access is dependent upon location of the mass within the kidney and the position of surrounding structures. Many interventionists prefer a posterior approach with the patient placed in the lateral decubitus position with the lesion side dependent. This position may have some stabilizing effect on the kidney within the retroperitoneal space and aids in limiting the effect of breathing motion on the kidney and can limit bowel and lung interposition.

When performing a TA, however, it may be preferable to utilize a general endotracheal anesthetic. This will allow for optimal airway control and patient safety when prone and assist with targeting by utilizing controlled breathing which can eliminate organ movement [10].

Once under general anesthesia patients are typically placed in the prone position, on chest rolls, to assist with ventilation and both arms tucked by the side (Fig. 15.1). Occasionally the

arms may need to be raised above the head if the body habitus will not pass easily through the aperture of the CT gantry. One must be careful, however, to avoid brachial plexus nerve injuries should shoulder hyperextension be needed. It is helpful to place an indwelling Foley catheter.

The classic approach involves the interventional radiologist using a hand-guided needle placement based upon his/her understanding of the local target anatomy after creating a mental picture of the optimal placement. This requires a great deal of skill and experience. The best analogy is one of a gunnery sergeant trying to hit a faraway target by firing mortars and making fine adjustments to hit the target.

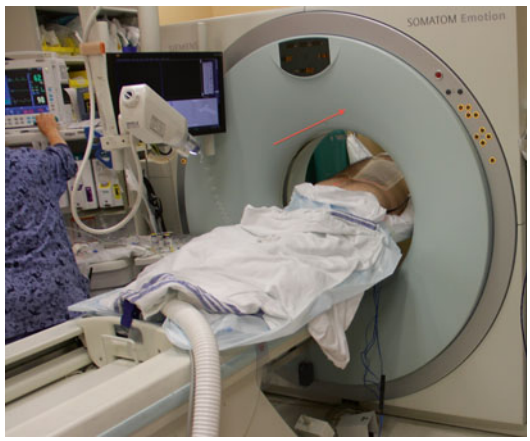


**Fig. 15.1** Patient on standard CT gantry, under general anesthesia lying prone on chest rolls with arms tucked. Note limited working space even in thin patients such as this (*Arrow* points towards head of patient)

Initially one marks the entrance site on the patient's skin surface with use of the CT software grid or a skin surface grid with embedded wires. Then, under maximal sterile barrier, an anesthesia needle is inserted at the site into the subcutaneous tissue and repeat CT imaging is performed confirming the position of the selected access site. A skin incision is made and the subcutaneous tissue may be dissected with a hemostat probe. We typically incrementally advance a 16 g blunt cannula and intermittently perform CT imaging to the periphery of the lesion. Intravenous contrast is sometimes administered to better localize the mass.

Once the position of the blunt cannula is confirmed with CT imaging, the blunt stylet is withdrawn from the cannula, and a combination of fine needle aspiration of the lesion with a 22 g Chiba needle and core needle sampling with an 18 gauge spring-loaded biopsy needle is performed. FNA (20–25 gauge needles) or core biopsy (16–18 gauge needles) may be used, but many interventionalists prefer use of a coaxial needle system allowing both FNA and core samples to be obtained at the same setting. This combination may result in a higher diagnostic yield although many physicians have abandoned the FNA. While leaving the blunt cannula in position as a guide, the thermal probe is inserted in tandem alongside the cannula and repeat CT imaging is obtained confirming adequate position of the probe. Ablation parameters and end points of treatment are device specific. Further discussion is beyond the scope of this chapter. See reference for additional information [9] (Fig. 15.2).

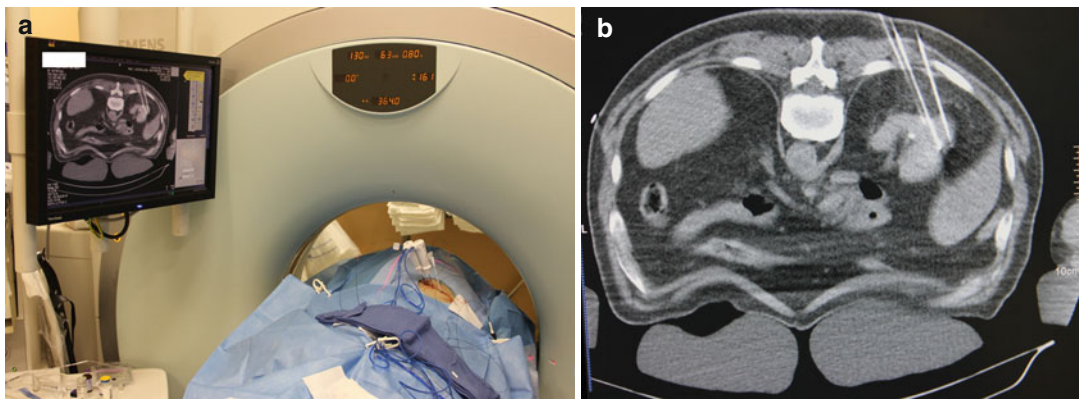


**Fig. 15.2** (**a**) Image demonstrates 2 RF ablation probes in place with peripheral fiber-optic temperature probes along side. Video monitor displays right kidney with needle probes into the tumor mass and the temperature probe. Close-up shot of the monitor (**b**)

**Table 15.1** CT-based imaging and guidance modalities for renal ablation

| System | Tip-target distance mean ± SD (if available) | Method of determining error |
|---|---|---|
| Cone beam CT | 1.2 ± 0.4 mm [Tovar-Arriaga] | Phantom device |
| PercuNav | 5.85 ± 4.48 [Venkatesan]<br>3.4 ± 2.1 [Krucker] | Patient biopsies liver/patient biopsies kidney |
| MAXIO robotic assistant platform | 6.5 ± 2.5 mm [Koethe] | Phantom |
| PAKY-RCM | 1.66 mm [Solomon] | Phantom |
| Veran | 2.2 ± 2.1 mm [Holzknecht] | Patient |
| Ultrasound-guided motion-adapted instrument | 1.7 mm [Hong] | Moving phantom |
| Ultrasound with integrated GPS | 1.8 mm [Hung] | In vivo canine |
| Augmented reality system | 2 mm/5 mm [Nicolau] | Phantom/patients |

## Advancements to Augment CT-Based Imaging and Guidance

Several CT-based imaging and guidance modalities have been developed and are commercially available but not widely utilized in clinical practice to date. These include conventional CT, CT fluoroscopy, and cone beam CT which can then be fused with other modalities such as positron emission tomography (PET) or real-time imaging modalities like electromagnetic navigation or ultrasound (Table 15.1).

All of the techniques focus on visualizing a safe linear trajectory from a selected entry point on the skin surface to the target. From there, either manually or robotically, the needle is placed on the selected entry point on the skin, oriented to the correct angle, and inserted along the trajectory until the target is reached [11, 12].

Few centers have embraced these new technologies. Possible barriers include a high cost of entry as the equipment can be expensive to obtain, the need for additional training, and the lack of long-term data on the efficacy of such procedures. Additionally, operator comfort with present techniques is most likely a factor. However, it has been shown these initial entry costs may be recouped through long-term cost savings of CT-guided procedures which are estimated at saving between $3,625 and $5,155 per procedure [13–15].

Additionally, the large variety of available systems and a lack of understanding on how they compare to one another makes it difficult to choose a particular modality. The following review of many of the available technologies may prove helpful.

### Cone Beam CT

Digital fluoroscopy systems can provide high-quality 3D reconstruction of cannulated structures but is unable to image soft tissues well [16]. Cone beam CT utilizes a rotating C arm with a large flat panel detector to capture over 200 X-ray images from varying angles in a process known as rotational angiography. This scan takes only 6 s and allows easy access to the patient. These images are then combined in what is termed cone beam reconstruction to create 3D CT-like volumes (Fig. 15.3). The resulting images can then be scrolled through similar to CT in order to plan appropriate needle pathways for interventional procedures. Three commercially available systems applying this technique are the DynaCT (Artis Zeego, Siemens Medical Solutions, Erlangen, Germany), Innovact (GE Healthcare, Schenectady, New York), and XperCT (Phillips Healthcare, Amsterdam, Netherlands). The images can be coupled with Artis Zeego iGuide technology (Siemens Medical Solutions, Erlangen, Germany) which assists in planning and mapping the trajectory. The tumor is first marked on coronal, axial, and sagittal planes. The skin entry point and trajectory are then chosen

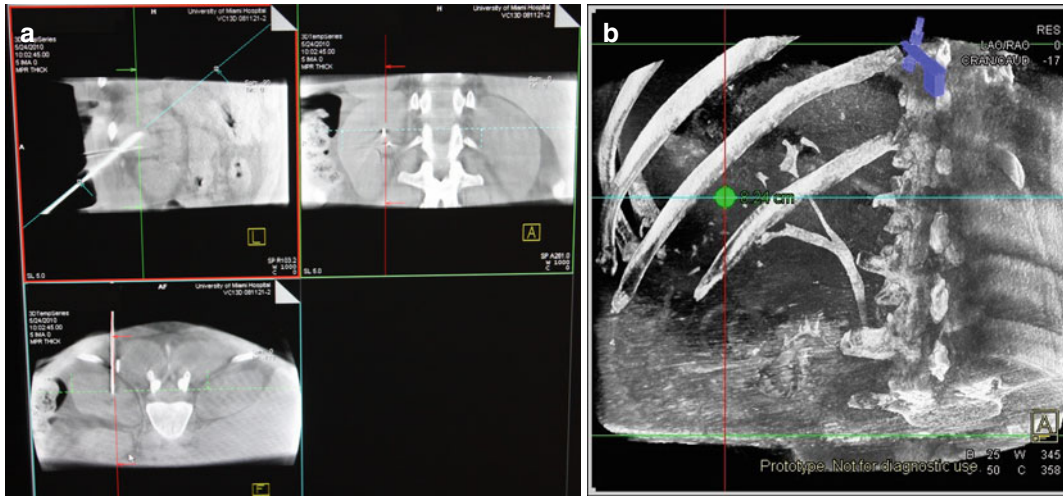


**Fig. 15.3** (**a**) Sagittal, coronal, and axial views obtained with the cone beam CT. The angles of view can be altered on the computer to coordinate with "in-line" viewing "down the barrel" of the needle. These images are also utilized for 3D reconstructions (**b**)

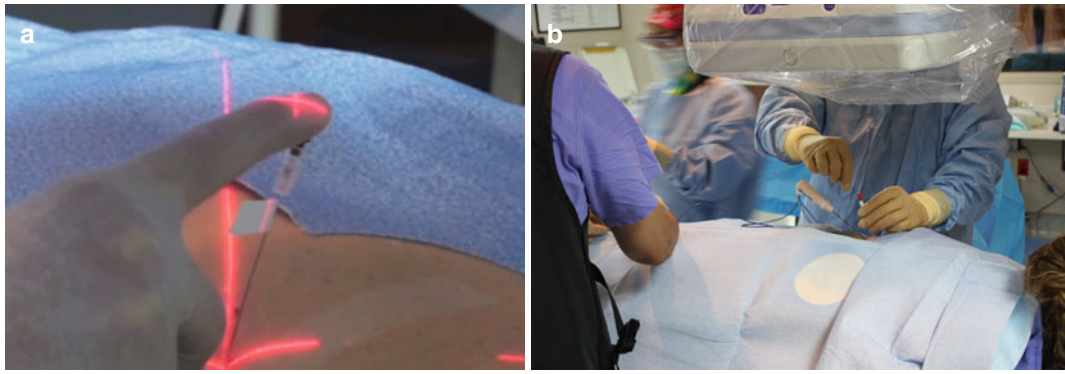


**Fig. 15.4** (**a**) Demonstration of fingertip control of needle placement using laser crosshairs (Artis Zeego, Siemens). (**b**) Note the open space in which to work utilizing cone beam Fluoroscopic technique

and the software displays the desired needle path which is then projected live on the patient with laser crosshairs (Fig. 15.4). Laser navigation systems like these have been shown to greatly improve target point accuracy. For instance, Moser et al. were able to decrease their target point error from a mean 3.5 mm freehand to 2.0 mm using a laser navigation system in spinal injection procedures [17]. Real-time fluoroscopy can then be used to compare the needle path with the planned trajectory. Manual needle placements allow for tactile feedback for the surgeon.

Tovar-Arriaga et al. additionally incorporated the DLR/KUKA Light Weight Robot III with the cone beam CT system. This robotic arm integrates the imaging and guidance technology and orients the needle itself while still utilizing manual insertion [12]. They measured their accuracy in a phantom model utilizing an Artis Zeego imaging system for error visualization. They determined the compilation of errors from the robot calibration, camera, and image construction to result in an average of $1.2 \pm 0.4$ mm from tip of the needle to the target distances [12].

This technique has been used by several centers in the ablation of small renal tumors with results showing recurrence-free rates >90 % [18, 19]. Additionally, it has successfully been implemented as a biopsy technique with accuracies as high as 95 % [20].

While allowing for fast and accurate soft tissue imaging, the cone beam CT imaging systems are still hindered by respiratory-dependent organ motion. To minimize the error, both the imaging and the procedure must be done at identical points in respiration which is usually held at end expiration. Additionally, while some real-time information of needle placement can be gathered through fluoroscopy, the majority of the imaging is performed intermittently.

## Electromagnetic Navigation

Electromagnetic navigation (EMN) has been shown in phantom models to increase accuracy and reduce procedure time when combined with CT fluoroscopy guidance [21]. These systems consist of a field generator producing an alternating electromagnetic field which induces a voltage in small coils which have been placed into the needles. The resulting voltage is measured and used to calculate the current position and the orientation of the coil. Passive fiducial markers placed on the patient's skin allow for fusion of prior CT imaging with real-time electromagnetic navigation. Holzknecht et al. implemented the Ultraguide (Tirat Hacarmel, Israel) electromagnetic tracking system for 50 image-guided biopsies and found the deviation between tip and target to be 2.2 ± 2.1 mm [22]. However, these results do not necessarily translate to improved outcomes for patients. In comparing CT-guided percutaneous lung biopsy alone to that with an electromagnetic navigation system in 60 patients, Grand et al. using the ig4 EMN system (Veran Medical Inc., St Louis, MO) found that adding electromagnetic navigation gave no statistical improvement in operative time, radiation dose, number of needle repositions, or diagnostic yield [23]. Additionally, the necessary hardware for these systems, including instruments with the appropriate coils, can be expensive.

## Ultrasound CT Fusion

Several systems have been developed allowing for real-time imaging and feedback during percutaneous procedures [24]. One such system described by Venkatesan et al. combines electromagnetic device tracking and computed tomography (CT) with ultrasound (US) and FDG positron emission tomography (PET) imaging fusion [25]. This system fuses a prior PET/CT done on average 2 weeks before admission, with a navigation CT scan done with the patient in position and a sequence of tracked intraoperative US images using the PercuNav (Philips, Eindhoven, Netherlands) software. Utilizing the information from PET, a physician can better localize the target. Passive fiducial markers are placed near the entry site and are coregistered to the markers and radiopaque grid in the preprocedural CT. Intraoperatively, an electromagnetic field generator is placed about 30 cm from the sterile field. The electromagnetic tracking space is then registered to the navigational images by pointing the tracked needle to each fiducial at the interrupted point in ventilation and averaging the signal observed. During needle insertion they could then display PET/CT images, the fused real-time US images, and the electromagnetic-tracked needle location and trajectory. On 14 patients in which the system was used by Venkatesan et al., a verification CT scan showed a basic tracking error of 5.85 ± 4.48 mm. In performing this technique for 36 biopsies, 31 (86 %) of them were diagnostic. Additionally, one patient received hepatic RFA without complication of short-term recurrence at 56 days [25]. Krucher et al. used a similar system on 12 patients undergoing kidney tumor RFA ablation with an average tip to target error of 3.4 ± 2.1 mm [26].

Another US-based system was explored by Hung et al. It exclusively used real-time 2D US with a multiplanar Global Positioning System (MyLab, 70XVGm Biosound Esaote, Indianapolis, IN) which can track the magnetic sensors mounted on the ultrasound and treatment probes. First 2D US images are compiled into a 3D volume which is used as a planning image then overlaid as axial, sagittal, and coronal views onto real-times US images. The location of the

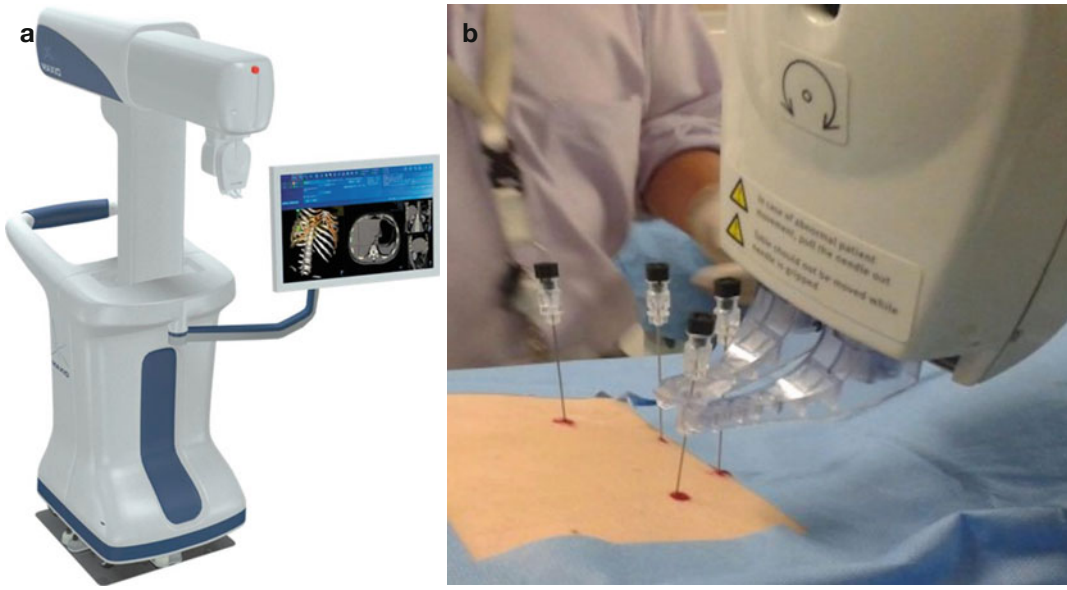


**Fig. 15.5** (**a**) Maxio robotic platform (Courtesy of Perfint Healthcare Corp., Redmond, WA, USA) (**b**) Close-up of the actual needle holder

probe based on GPS data is then overlaid onto the fused real-time and planning US images. Using this system Hung at al. was able to ablate 32 virtual tumors marked by gold fiducial markers in the renal parenchyma in 16 canine kidneys with a target to tip distance averaging 1.8 mm. They found the learning curve for the system to be quite steep with their initial experiences having much larger errors (6.3 mm) [27].

Other systems have been developed that utilize real-time ultrasound in order to track a moving target. Hong et al. describe a CT/US fusion system in which they use image feedback from visual sensors to control a robotic needle holder (termed servoing) [28]. In this case, their robot automated alignment of a needle using a rigidly placed ultrasound fixed to the base of a 7° of freedom manipulator. By putting the ultrasound in the same plane as the needle, they could ensure direct visualization of the location of the needle tip. Then, by extracting the image based on the change in density at the tumor edge, the instrument will move to compensate for the motion of organs secondary to respiration. In a phantom study, they were able to follow an oscillating moving target at 10 Hz feedback rate with an error of 1.7 mm with most of this error arising from soft tissue needle deflection [28].

## Robotic Arm Assistant Platforms

Other robotic assistant platforms have been developed that do not track moving objects but instead work to improve the accuracy of needle insertions. One such system described by Koethe et al. uses the MAXIO robotic assistance platform (Perfint Healthcare, Chennai, India) with 5° of freedom that will place the needle into position. The platform is placed next to the patient and registers with the CT table by a mechanical docking mechanism, optical registration, and tilt sensing (Fig. 15.5). Physicians can plan the target and needle pathway on coronal, axial, and sagittal views which is then displayed as a 3D reconstruction. The software then instructs the operator to move the CT table to a particular z-axis location. The robotic guide arm receives the CT images along with the planned needle pathway, moves to the appropriate position, and the physician manually inserts the needle through the needle guide. Koethe et al. tested this system using a custom-made opaque phantom which showed a shorter mean needle tip to target distance using the robotic assistant platform compared with the freehand technique (6.5 ± 2.5 mm vs. 15.8 ± 9.2 mm) [29].

Another system named iSYS – 1 (Medizintechnik GmbH, Kitzbühel Austria) uses joystick controls to maneuver a needle held by a robotic arm into position and to the correct angle. Physicians can then manually insert the needle towards the target.

These can be compared to the PAKY-RCM (Percutaneous Access of the Kidney and Remote Center of Motion) (Johns Hopkins, Baltimore, MD) developed by Solomon et al. and Patriciu et al. which is a robotic system with 11° of freedom which is mounted to a large frame and attached to the CT table. The robot takes advantage of the laser light that is in every CT scanner in order to achieve section selection to achieve patient registration. The mechanical arm is placed so the tip of the needle is in the skin dermotomy site which is planned by spiral CT imaging. The robot itself will then move the needle to the correct trajectory and under CT fluoroscopy advance the needle using a rolling dowel mechanism to the target location. In phantom studies, they showed a mean tip to target error of 1.66 mm. In 21 percutaneous procedures performed on patients, the robot was able to meet the target adequately 17 (81 %) times with the remaining four requiring joystick fine tuning [30, 31]. This allows for minimal radiation exposure to the clinician but eliminates any tactile feedback by the physician on needle insertion.

## Camera Feedback

Camera-based augmented reality systems can also be used to provide real-time feedback during procedures. Nicolau et al. developed a system using passive markers placed on the patient's abdomen and two calibrated cameras to register 3D CT images to the patient. These cameras provide real-time feedback about patient motion, including respiratory motion. This information allows them to complete a respiratory gating technique, in which guiding information is provided regularly at the point in the respiratory cycle at which they performed preoperative CT images. Using this technique they were able to reduce their errors to 2 mm in an abdominal phantom and below 5 mm in patients [32].

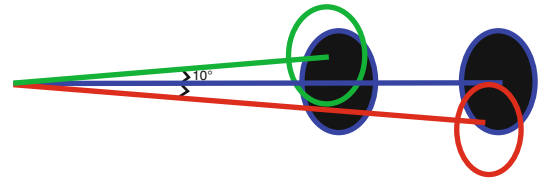


**Fig. 15.6** Small errors in the initial angle at the skin entry can lead to large differences in the attempted and actual ablation zones. As the needle goes deeper into tissues and continues to veer off course, the effect will be exaggerated over these larger distances

## Challenges

There are several challenges faced by all guidance systems. One of the biggest is that of patient motion, particularly respiratory-dependent motion which is difficult to control. Many systems work to image and act at the same points in the respiratory cycle and rely on the target in being in the same location with varying results. Additionally, tissue deformation caused by needle insertion can often change target position. Algorithms have been developed to try to account for this deformation and guide a needle appropriately [33]. Lastly, the accumulation of error from each step of the process from imaging, registration of the patient, equipment positions, and to robotic motion error needs to be minimized to ensure properly reaching the target. Even small errors in the initial targeting angle are compounded over the distance traveled by the needle and can result in large errors in the ablation zone (Fig. 15.6).

## References

1. Campbell SC, Novick AC, Belldegrun A, et al. Guideline for management of the clinical T1 renal mass. J Urol. 2009;182:1271–9.
2. Ljungberg B, Cowan NC, Hanbury DC, et al. EAU guidelines on renal cell carcinoma: the 2010 update. Eur Urol. 2010;58:398–406.

3. Olweny EO, Park SK, Tan YK, et al. Radiofrequency ablation versus partial nephrectomy in patients with solitary clinical T1a renal cell carcinoma: comparable oncologic outcomes at a minimum of 5 years of follow-up. Eur Urol. 2012;61:1156–61.
4. Psutka SP, Feldman AS, McDougall WS, et al. Long-term oncologic outcomes after radiofrequency ablation for T1 renal cell carcinoma. Eur Urol. 2013;63(3):486–92.
5. Zagoria RJ, Pettus JA, Rogers M, et al. Long-term outcomes after radiofrequency ablation for renal cell carcinoma. Urology. 2011;77:1393–9.
6. Leveillee RJ, Castle SM, Gorbatiy V, et al. Oncologic outcomes using real-time peripheral thermometry-guided radiofrequency ablation of small renal masses. J Endourol. 2013;27(4):480–9.
7. Wingo MS, Leveillee RJ. Central and deep renal tumors can be effectively ablated: radiofrequency ablation outcomes with fiberoptic peripheral temperature monitoring. J Endourol. 2008;22:1261–7.
8. Castle SM, Salas N, Leveillee RJ. Radio-frequency ablation helps preserve nephrons in salvage of failed microwave ablation for a renal cancer in a solitary kidney. Urol Ann. 2013;5(1):42–4.
9. Sterrett SP, Nakada SY, Wingo MS, et al. Renal thermal ablative therapy. Urol Clin North Am. 2008;35(3):397–414.
10. Gupta A, Raman JD, Leveillee RJ, et al. General anesthesia and contrast-enhanced computed tomography to optimize renal percutaneous radiofrequency ablation: multi-institutional intermediate-term results. J Endourol. 2009;23(7):1099–105.
11. Masamune K, Fichtinger G, Patriciu A, et al. System for robotically assisted percutaneous procedures with computed tomography guidance. Comput Aided Surg. 2001;6(6):370–83.
12. Tovar-Arriaga S, Tita R, Pedraza-Ortega JC, Gorrostieta E, Kalender WA. Development of a robotic FD-CT-guided navigation system for needle placement-preliminary accuracy tests. Int J Med Robot. 2011;7(2):225–36.
13. Badwan K, Maxwell K, Venkatesh R, et al. Comparison of laparoscopic and percutaneous cryoablation of renal tumors: a cost analysis. J Endourol. 2008;22(6):1275–7.
14. Link RE, Permpongkosol S, Gupta A, Jarrett TW, Solomon SB, Kavoussi LR. Cost analysis of open, laparoscopic, and percutaneous treatment options for nephron-sparing surgery. J Endourol. 2006;20(10):782–9.
15. Castle SM, Gorbatiy V, Avallone MA, Eldefrawy A, Caulton DE, Leveillee RJ. Cost comparison of nephron-sparing treatments for cT1a renal masses. Urol Oncol Sem Original Inv. 2013;31(7):1327–32.
16. Soria F, Delgado MI, Sánchez FM, et al. Effectiveness of three-dimensional fluoroscopy in percutaneous nephrostomy: an animal model study. Urology. 2009;73(3):649–52.
17. Moser C, Becker J, Deli M, Busch M, Boehme M, Groenemeyer DH. A novel laser navigation system reduces radiation exposure and improves accuracy and workflow of CT-guided spinal interventions: a prospective, randomized, controlled, clinical trial in comparison to conventional freehand puncture. Eur J Radiol. 2013;82(4):627–32.
18. Leveillee RJ, Ramanathan R. Optimization of image-guided targeting in renal focal therapy. J Endourol. 2010;24(5):729–44.
19. Leveillee RJ, Castle SM, Salas N, et al. Improved targeting of radio-frequency ablation probes and thermal sensors: a preliminary investigation of flat-panel CT guided ablation of renal tumors in the cardiac catheterization lab. J Endourol. 2011;25(7):1119–23.
20. Braak SJ, van Melick HH, Onaca MG, van Heesewijk JP, van Strijen MJ. 3D cone-beam CT guidance, a novel technique in renal biopsy–results in 41 patients with suspected renal masses. Eur Radiol. 2012;22(11):2547–52.
21. Banovac F, Wilson E, Zhang H, Cleary K. Needle biopsy of anatomically unfavorable liver lesions with an electromagnetic navigation assist device in a computed tomography environment. J Vasc Interv Radiol. 2006;17(10):1671–5.
22. Holzknecht N, Helmberger T, Schoepf UJ, et al. Evaluation of an electromagnetic virtual target system (CT-guide) for CT-guided interventions. Rofo. 2001;173(7):612–8.
23. Grand DJ, Atalay MA, Cronan JJ, Mayo-Smith WW, Dupuy DE. CT-guided percutaneous lung biopsy: comparison of conventional CT fluoroscopy to CT fluoroscopy with electromagnetic navigation system in 60 consecutive patients. Eur J Radiol. 2011;79(2):e133–6.
24. Najmaei N, Mostafavi K, Shahbazi S, Azizian M. Image-guided techniques in renal and hepatic interventions. Int J Med Robot. 2013;9(4):379–95.
25. Venkatesan AM, Kadoury S, Abi-Jaoudeh N, et al. Real-time FDG PET guidance during biopsies and radiofrequency ablation using multimodality fusion with electromagnetic navigation. Radiology. 2011;260(3):848–56.
26. Krucker J, Xu S, Venkatesan A, et al. Clinical utility of real-time fusion guidance for biopsy and ablation. J Vasc Interv Radiol. 2011;22(4):515–24.
27. Hung AJ, Ma Y, Zehnder P, Nakamoto M, Gill IS, Ukimura O. Percutaneous radiofrequency ablation of virtual tumours in canine kidney using global positioning system-like technology. BJU Int. 2012;109(9):1398–403.
28. Hong J, Dohi T, Hasizume M, Konishi K, Hata N. Ultrasound guided motion adaptive instrument for percutaneous needle insertion therapy. In: 6TH international conference on biomedical engineering and rehabilitation engineering. China: Guilin; 2002. p. 225–7.

29. Koethe Y, Xu S, Velusamy G, Wood BJ, Venkatesan AM. Accuracy and efficacy of percutaneous biopsy and ablation using robotic assistance under computed tomography guidance: a phantom study. Eur Radiol. 2014;24(3):723–30.
30. Solomon SB, Patriciu A, Bohlman ME, Kavoussi LR, Stoianovici D. Robotically driven interventions: a method of using CT fluoroscopy without radiation exposure to the physician. Radiology. 2002;225(1):277–82.
31. Patriciu A, Awad M, Solomon SB, et al. Robotic assisted radio-frequency ablation of liver tumors–randomized patient study. Med Image Comput Comput Assist Interv. 2005;8(Pt 2):526–33.
32. Nicolau SA, Pennec X, Soler L, et al. An augmented reality system for liver thermal ablation: design and evaluation on clinical cases. Med Image Anal. 2009;13(3):494–506.
33. Asadian A, Kermani MR, Patel RV. A novel force modeling scheme for needle insertion using multiple Kalman filters. IEEE Trans Instrum Meas. 2012;61(2):429–38.

# MR-Guided Renal Ablation

# 16

Michael Ordon, Laura Findeiss, and Jaime Landman

It is estimated that over 64,000 new cases of renal cortical neoplasms (RCN) will be detected in the United States in 2012 [1]. The incidence of renal cell carcinoma (RCC) has increased by an average of 3 % per year for whites and 4 % per year for African-Americans, since the 1970s [2]. This has largely been a result of the more prevalent use of ultrasonography (US) and computed tomography (CT) for the evaluation of a variety of abdominal complaints [3–6]. In fact, up to 66 % of RCCs are now detected incidentally [7].

Radical nephrectomy represented the standard of care for the surgical treatment of RCC until recent evidence revealed the potential long-term sequelae of non-nephron-sparing surgery [8–10]. Specifically, studies have shown an increased risk for chronic kidney disease (CKD) with radical nephrectomy, as well as an association between CKD and cardiovascular morbidity and mortality that has led to the desire to preserve as much normal renal parenchyma as possible [8–11]. These findings in combination with the evidence showing excellent oncologic outcomes with partial nephrectomy [12] support the importance of preserving nephrons when possible to improve patients' long-term outcomes. Accordingly, the American Urologic Association guidelines for the management of RCN released in 2009 reflected this shift in treatment paradigm. Partial nephrectomy is now recommended for the management of all clinical T1 ($\leq$7 cm) renal masses, provided adequate oncologic control can be achieved [12].

In addition, the increased discovery of small, organ-confined tumors has stimulated advances in minimally invasive nephron-sparing treatment options, with ablative therapies such as cryoablation (CA) and radiofrequency ablation (RFA) gaining traction as nephron-sparing alternatives to partial nephrectomy. Percutaneous ablation in particular offers several advantages over partial nephrectomy. Percutaneous ablation is associated with fewer complications and faster convalescence [13]. Percutaneous ablations may be applied repeatedly with greater ease in patients with syndromic renal cancers, who are destined to develop multiple tumors over their lifetime. Finally, percutaneous ablation is the only local treatment option in patients who are unable to undergo surgical procedures that require general anesthesia.

A number of different of modalities exist for performing percutaneous ablation; however, the

M. Ordon, MD, MSc, FRCSC (✉)
Division of Urology, Department of Surgery,
University of California, Irvine, CA, USA
e-mail: michael.ordon@utoronto.ca

L. Findeiss, MD, FSIR, FAHA
Department of Radiology, University of Tennessee
Graduate School of Medicine, Nashville, TN, USA
e-mail: djarvis@utmck.edu

J. Landman, MD
Department of Urology,
University of California Irvine, Orange, CA, USA
e-mail: landmanj@uci.edu

J.C. Liao, L.-M. Su (eds.), *Advances in Image-Guided Urologic Surgery*,
DOI 10.1007/978-1-4939-1450-0_16, 

largest experience to date is with two forms of thermal ablation – RFA and CA. At present, short- and intermediate-term results exist in the literature, showing local recurrence-free survival rates around 90 % [12, 14]. Other ablative therapies such as microwave therapy, irreversible electroporation, interstitial laser therapy, and high-intensity focused ultrasound are currently considered experimental. Ultimately, large-scale, long-term studies are needed to confirm the oncologic efficacy of thermal ablation.

Image-guided percutaneous therapy can be performed with CT or magnetic resonance imaging (MRI) guidance. In this chapter we will focus on MRI-guided renal ablation, including a discussion of the advantages of MRI, treatment techniques, necessary equipment, safety issues, and complications.

## Role of MRI

The idea of using MRI for image-guided interventional procedures emerged shortly after the clinical implementation of MRI as an imaging modality and the realization of the unparalleled soft-tissue details obtainable on MRI scans. Before interventional procedures could be performed under MRI guidance, initial studies focused on the development of MRI-compatible needle prototypes [15] and the feasibility of needle insertion under MRI guidance [16, 17]. Following this came testing the effects of various magnetic resonance (MR) parameters on needle visualization [18]. Subsequently, with the introduction of open-configuration scanners and improved gradients and receiver chains that allowed rapid acquisition of high signal-to-noise images, the clinical applications of interventional MRI have begun to expand [19].

Image-guided renal ablation can be performed using US, CT, or MRI guidance, as each will allow the accurate placement of treatment probes into the tumor. However, the rationale for using MRI to guide interventions, over the other modalities, includes excellent soft-tissue contrast, high spatial resolution, multiplanar and near-real-time imaging capabilities, lack of ionizing radiation, and ability to detect temperature and blood flow [19, 20].

The excellent soft-tissue contrast, high spatial resolution, and multiplanar and near-real-time imaging capabilities are features specific to MRI that allow for a greater suitability to target and treat difficult-to-access tumors with respect to visibility, proximity to vital structures, and trajectory limitations. For example, upper pole tumors situated near the diaphragm can be challenging to treat and require mastery of triangulation techniques, if CT guidance is utilized. Even with mastery, excessive triangulation will be associated with significant risk for pneumothorax in such cases. Alternatively, if US is employed to target such lesions, it can be greatly hampered by air artifacts from the lung bases, increasing the risks for inadvertent injuries to important structures [19].

The lack of ionizing radiation associated with MRI guidance is another obvious attractive feature. This has become particularly important in light of recent reports that have raised the awareness of both the public and medical communities about the risk of excessive radiation exposures associated with current CT scan use [21–23].

The major advantage of MRI is in fact not with aiding targeting, but in guiding the thermal ablation. MRI allows for monitoring of the zone of thermal tissue destruction during the procedure as a result of its ability to show changes in tissue temperature. Subsequently, the size and configuration of the thermal ablation zone can be adjusted during the procedure to account for deviations from the preoperative prediction, based on probe placement. Importantly, the sensitivity of MRI to the immediate changes occurring at the ablation zone and to the surrounding reactive tissue changes is universal to all methods of thermal ablation. As such unlike CT, the effects of both RFA [24–27] and CA can be shown with MRI during the procedure. However, this sensitivity for thermal changes is best exploited during laser ablation or CA compared to RFA. This is because MRI can be easily performed during laser ablation and CA but is complicated by interference with the scanner during RFA. Performing intermittent MR scanning between the ablation cycles typically circumvents this limitation.

As mentioned, CT is insensitive to the immediate temperature-mediated tissue changes except

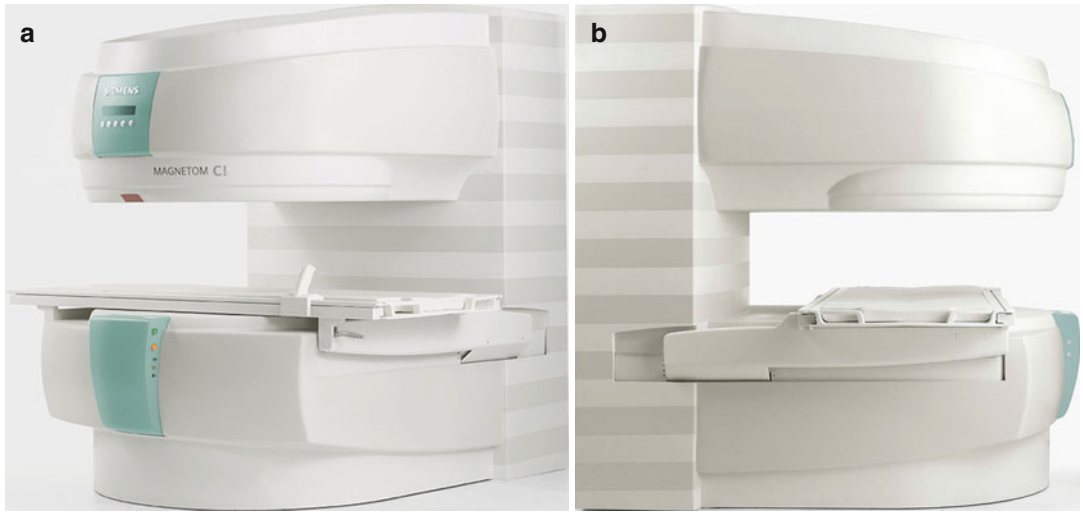


**Fig. 16.1** (**a**, **b**) Siemens Magnetom MRI (low-field (0.2-T) biplanar magnet design) (Courtesy of Siemens Healthcare 2014)

in the case of CA, where the ice ball can be temporarily detected as a hypoattenuating lesion before thawing is performed. However, MRI is superior at displaying the entire ice ball, as the ice can also be viewed well in the perinephric fat [28], unlike on CT. Iodinated contrast material can be administered intravenously after RFA and a nonenhanced area appears at the site of ablation on CT that is typically interpreted as the extent of the ablation zone, although direct correlation with the exact extent of cell death has not been investigated.

There are also several limitations with MRI guidance, which must be considered, including: generally long procedure times, high cost of MRI units and limited availability of interventional MRI units, narrower gantry size compared with CT, and limitations of ECG monitoring of patients with ischemic heart disease [28].

## Interventional MRI Setup for Ablation

Although an interventional MRI suite is not yet a standard component of modern radiology departments, an increasing number of institutions are becoming equipped with capabilities to perform MR-guided interventions as the field of interventional MRI continues to evolve and expand.

Performing MR-guided renal ablation requires an open-magnet scanner, so the patient can be accessed during treatment. Both low-field (0.2-T) biplanar magnet design (Fig. 16.1a, b) and high-field (1.5-T) short-bore magnet design (Fig. 16.2a, b) interventional MRI scanners have been successfully used for renal ablations. The open MRI system of the low-field biplanar magnet design facilitates proper access to the patient during the procedure and thereby allows ample room for RFA or CA probe placement and manipulation. More recent trends in interventional MRI have favored a shift to the high-field short-bore magnet design to exploit the higher spatial and temporal resolutions offered by these high-field MRI systems. This, however, does come at the expense of a relatively tighter room within the wide-bore, open-configuration 1.5-T interventional scanners. Despite the more restricted access compared with the biplanar design, the bore is still significantly shorter and wider than in regular diagnostic scanners, allowing reasonable access to average-sized patients with the advantage of higher spatial and temporal resolution scans.

MR-guided ablation also requires the ability to operate the scanner and review images at the patient's bedside. Most systems will come equipped with an in-room monitor with mouse or built-in trackball and foot pedal to allow for control of MR

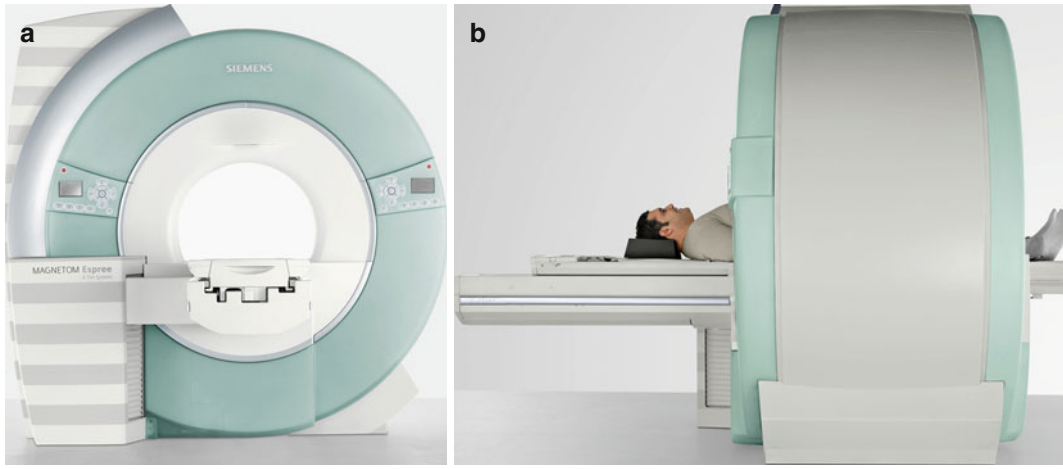


**Fig. 16.2** (**a**, **b**). Siemens Magnetom Espree MRI (high-field (1.5-T) short-bore magnet design) (Courtesy of Siemens Healthcare 2014)

**Fig. 16.3** Philips Medical Systems Open Configuration interventional MRI unit with in-room monitor, in-room workstation with imaging capability, and a foot pedal for the operator which controlled sequence start

sequences from the scanner side, facilitating interactive near-real-time navigation of the ablation probes into the targeted tumor (Fig. 16.3).

An MRI-compatible ablation system is also necessary. Meaning MRI-compatible electrodes for RFA and cryoprobes for CA need to be utilized. MRI-compatible systems are available for both RFA and CA and are discussed in more detail below.

In addition, MRI-compatible anesthesia equipment and monitoring devices are integral parts of the MRI-guided renal ablation and are typically already available in most diagnostic MRI suites.

## Patient Selection

It is important to emphasize that the recommended treatment and standard of care for the management of clinical T1a renal cell carcinoma is nephron-sparing surgical extirpation [12]. However, partial nephrectomy remains associated with significant morbidity and is not always feasible or suitable. Alternatively, image-guided percutaneous ablation represents a less invasive treatment option with reduced morbidity ideally suited for patients of advanced age or with major comorbidities and increased surgical risk who prefer a proactive approach but are not optimal candidates for conventional surgery. Thermal ablation also represents a good treatment option in patients with solitary kidney, renal insufficiency, bilateral tumors, local recurrence after previous nephron-sparing surgery, and patients with a genetic predisposition for developing multiple tumors (e.g., VHL syndrome) [29]. The American Urological Association guidelines on the management of small renal masses recommend thermal ablation as a treatment option for patients with major comorbidities or increased surgical risk who want active treatment [12]. The European Association of Urology guidelines on RCC recommend thermal ablation for patients with small tumors and/or significant comorbidity who are unfit for surgery [30].

Tumor size also represents an important factor in patient selection. Current technology does not allow for reliable treatment of lesions larger than 4.0 cm in diameter [31]. The evidence in the literature suggests that smaller tumors are more effectively ablated than larger ones. In one retrospective series using RFA in 100 renal tumors, complete ablation was achieved in 100 % of tumors smaller than 3 cm, 92 % of tumors between 3 and 5 cm, and 25 % of tumors larger than 5 cm [32]. Similarly, another study showed that with each 1-cm increase in tumor diameter over 3.6 cm, the likelihood of recurrence-free survival decreased by a factor of 2.19 [33]. In our experience, the optimal tumor size for percutaneous thermal ablation is ≤3 cm as higher local recurrence rates and complication rates occur with tumors larger than this.

Contraindications to percutaneous ablative therapy include poor life expectancy of <1 year, multiple metastases, low possibility of successful treatment due to size or location of tumor, irreversible coagulopathy, inability to lie supine or prone for prolonged periods because of pulmonary compromise, or other medical comorbidities [20, 30].

## Patient Position

Patients are placed in a position that allows the shortest and least complicated access to the tumor. The *prone* or *lateral decubitus* positions are most commonly used. Unfortunately, there are no studies comparing the efficacy of these different positions.

### Prone

The prone position is advantageous because it is a stable position that is usually comfortable for the patient and it also typically allows a short targeting distance, especially to lower pole renal masses. If the prone position is used, it is helpful to place a pillow under the abdomen of the patient to separate the costal margin and iliac crest, to provide a larger window for probe placement.

Of note, most patients' pre-procedure imaging is performed in the supine position, and a recent study performed at our institution revealed some clinically important anatomic alternations associated with change from the supine to the prone position [34]. Specifically, in the prone position, the kidneys are more anterior and more cranially located, with an associated significantly shorter skin to tumor distance. In addition, the colon is closer to the kidney and more posteriorly located on both sides. Lastly, on the right side, more of the kidney is covered posteriorly by the lung. Accordingly, the prone position may limit access, particularly for right upper pole tumors.

### Lateral Decubitus

Conversely, the lateral decubitus position also provides some distinct advantages. Either the ipsilateral or contralateral side may be placed on the downside depending on the situation. When the ipsilateral side is placed down, the kidney moves less with respiration, and there is less chance of a pneumothorax because the ipsilateral lung is deflated relative to the other side. This position is particularly helpful when targeting upper pole tumors that require an intercostal approach [20]. When the contralateral side is placed down, the bowels fall medially and away from the kidney making it useful for treating anterior lesions close to the bowel [20]. Additionally, this position provides a greater working area, which can allow for easier access to the lesion.

## Safety Issues

When performing MRI-guided ablation, one has to be acutely aware of the magnetic field. Although risks and safety issues are less prominent with low and medium field-strength (0.2–0.5-T) magnets, which are typically used for MR-guided renal ablation, hazardous consequences can result nonetheless when ferromagnetic instruments become accelerated in the fringe field of the scanner. To avoid serious or even fatal injuries, no ferromagnetic materials

should be brought within the 5-G line of any scanner. Additionally, all scalpels, needles, RF electrodes or cryoprobes, and anesthesia equipment should be made of MRI-compatible materials. Similarly, physiologic monitors should be non-ferromagnetic or should be kept outside the fringe field of the magnet.

Electric burns can also be a concern and typically result from direct electromagnetic induction in a conductive loop, induction in a resonant conducting loop, or electric field resonant coupling with a wire [35–37]. Limiting conductive loops, wire–patient contact, and cable lengths can minimize the risk of electric burns [20].

## Ablation Modality

As mentioned previously, a number of ablation modalities exist; however, the most widely clinically applied and most thoroughly investigated are RFA [32, 38–41] and CA [42–45]. The choice of ablative modality is based on numerous factors but is largely dependent on equipment availability and the experience and preference of the urologist/interventional radiologist. Also of key importance with MR-guided ablation is an MRI-compatible ablation system.

### Radiofrequency Ablation

RFA works by delivering radiofrequency current (375–500 kHz) into target tissue through an electrode connected to a radiofrequency generator. Tissue impedance from the radiofrequency current causes ionic agitation of intracellular molecules, resulting in frictional heating [19, 46]. At 60 °C there is denaturation of structural proteins and near instantaneous coagulative necrosis of tissue [20].

MR-compatible electrodes have been made available by at least two manufacturers. These are the titanium electrodes of the Cool-tip™ RF system (Covidien, Boulder, CO, USA) and the nitinol electrodes of the StarBurst Semi-Flex™ from the AngioDynamics system (AngioDynamics, Queensbury, NY, USA).

The Cool-tip™ RF system provides electrodes that can be continuously cooled with circulating iced water inside the electrode shaft that is meant to reduce charring at the electrode–tissue interface, thereby maximizing the ablation size.

The StarBurst Semi-Flex™ RF electrode provides electrodes with multiple active tines that can be deployed in the target tissue to produce larger ablation zones, in addition to a flexible shaft that can be bent to improve the capability for electrode navigation in the rather tight space usually available during interventional MRI procedures.

A number of reports of successful treatment of RCN with CT-guided percutaneous RFA have been published. However, CT guidance does not allow for real-time monitoring of RFA, as the thermal ablation zone is not visible. Conversely, RFA can be monitored in real time with MRI [24, 25] but is limited by the need to interrupt the radiofrequency energy during MR imaging due to significant interference it causes otherwise.

The first report of MR-guided renal RFA was an in vivo study in a porcine model, which demonstrated the suitability and benefits of MR guidance. Subsequently a couple of clinical studies have shown the safety and efficacy of MR-guided RFA for RCN <4 cm in diameter [25, 27].

### Cryoablation

CA works by freezing tissue to below −30° to −40 °C, which subsequently results in direct cellular damage and cell death due to cellular dehydration and cell membrane rupture [47]. Additionally, there is indirect reperfusion injury during the thawing phase that results in microcirculatory failure and small vessel thrombosis.

Currently, only one MR-compatible CA system is available. The MRI SeedNet® System (Galil Medical, Yokneam, Israel) is a stand-alone CA system, compatible with all MRI systems (closed or open bore) up to 1.5 T (Fig. 16.4a). The


**Fig. 16.4** (**a**) MRI-compatible Galil SeedNet® Cryoablation System. (**b**) Galil MRI-compatible IceSeed® 1.5 MRI Cryoablation Needle and IceRod® 1.5 MRI Cryoablation Needle (Used with permission. ©2013 Galil Medical)

SeedNet® MRI mobile unit is placed within the MRI room, allowing the treating physician access to both the patient and the needles during the CA treatment. A full range of small-diameter MRI-compatible CA needles are available (Fig. 16.4b).

Several reports have been published demonstrating the safety and efficacy of CT-guided percutaneous CA of RCN [44, 48, 49]. Although the ice ball is readily apparent as hypoattenuating lesion in the renal parenchyma on CT guidance, there are a couple of limitations to monitoring the zone of CA with CT. First, the portion of the ice ball in the perinephric fat is not clearly demarcated, which limits its use for real-time monitoring of the effect of ablation on adjacent critical structures such as bowel, ureter, pancreas, and adrenal gland [50–52]. Second, the streak artifact created by the cryoprobes with CT imaging can interfere with ice ball visibility [28].

Conversely, MRI depicts the ice ball with sharp edge definition in multiple planes in all surrounding tissue and with minimal applicator artifact. In addition, ice ball volume on intra-procedural MRI has been shown to correlate well with volume of cryonecrosis on post-procedural MRI. Furthermore, the ice ball is well depicted on all pulse sequences, so the ablation can be monitored using pulse sequences that best display tumor or adjacent critical structures [53].

## Procedure Guidance and Treatment Monitoring

Once the patient is appropriately positioned and sedation or general anesthesia is administered, axial fast spin-echo images are obtained to localize the kidneys and target the mass. These images are also used to plan probe entry site and trajectory. The skin entry point may be located using a fingertip, syringe filled with water for T2-weighted image guidance, or with dilute gadolinium for a T1-weighted approach [54].

Next, the skin site is marked and prepared and draped in sterile fashion. After anesthetizing the skin with 1 % lidocaine with epinephrine, a 2–3 mm incision is made, through which the ablation probe is to be placed. The ablation probe (RF electrode or cryoprobe) is placed percutaneously and advanced into the targeted tumor under MR continuous monitored guidance, usually using fast spin-echo images [42], short repetition time/short echo time gradient echo sequences, or mirrored fast imaging with steady-state precession [19].

## Probe Guidance

The guidance phase consists of continuous imaging with automated sequential acquisition, reconstruction, and in-room display. Two methods of real-time MRI guidance can be employed. In the first method, multiple sets of three contiguous, parallel, thin, 5-mm slices centered on the ablation probe shaft are obtained to detect and correct slight trajectory deviations during probe navigation [25]. With this three-slice method, the presence and direction of deviation are readily detected if the needle tip begins to leave the middle slice and moves into one of the adjacent slices [51]. Additionally, sets of orthogonal scans are performed intermittently to guide and confirm probe trajectory with respect to the three dimensional geometry of the tumor.

The second, more recently described method, utilizes triorthogonal image plane MRI guidance [55, 56]. In this technique continuously updated sets of adjustable sagittal, coronal, and axial scans are used to interactively guide ablation probe placement in three planes. The adjustable sagittal, coronal, and axial (triorthogonal) scans can be acquired relative to the electrode axis, relative to the target tumor itself, or in any three arbitrary planes relative to each other and to the patient's body [55]. In this technique, the reconstruction and display program is modified to simultaneously project the three planes immediately as they are acquired [55]. The ideal trajectory is first determined and then the localizing planes are positioned along this trajectory. The ablation probe is then introduced and advanced under interactive three-plane imaging guidance. Most often, the probe is initially seen on only one or two of the three planes. The in-room monitor and controller are then utilized to localize the ablation probe in the missing plane or planes using the plane(s) where the probe is already visualized.

## Probe Confirmation

It is recommended that once the ablation probes have been positioned within the targeted lesion, the probe tip position be confirmed in various planes using higher spatial resolution scans than the scan used for MRI real-time guidance. This is to confirm that the probes are positioned to achieve adequate ablation, as well as to ensure the tip of the probes are not in close proximity to adjacent structures (i.e., duodenum, colon, renal vein) that are not be included in the ablation zone (Fig. 16.5a–c).

Ideally the tip of the ablation probe in CA should be positioned 5 mm beyond the deepest margin of the tumor, when possible, to prevent inadequate ablation, as CA probes do not ablate beyond the tip of the probe. The ice ball and subsequently the ablation zone extend laterally. In the case of RFA, ideal placement of the electrode tip is at the deepest or distal border of the tumor. For RFA electrodes with deployable tines, multiplanar imaging confirmation of the tine positions after deployment is important to identify and correct if the tumor has been pushed away rather than penetrated by the deployed tines, if the tines are clustered together or unevenly deployed, or most importantly if one of the tines has extended into an undesirable location, such as into the collecting system or through the diaphragm [19].

## Ablation Monitoring

The ablation zone can be monitored in a continuous interactive manner with MRI similar to probe placement. This provides the advantage of direct observation of the size and configuration of the developing thermal ablation zone and permits the identification of any foci of residual viable tumor. The RFA ablation zone appears hypointense on T2-weighted and short tau inversion recovery (STIR) images [19], whereas the ice ball that develops with CA is represented by a signal void on both T1-weighted images (Fig. 16.6a, b) and T2-weighted images (Fig. 16.7a–c).

A post-ablation gadolinium-enhanced T1-weighted series is performed after the ablation probes are removed as confirmatory imaging to ensure complete treatment of the targeted tumor and exclude complications. The presence of any remaining enhancing tissue within the zone of the targeted tumor suggests residual tumor with incomplete ablation.

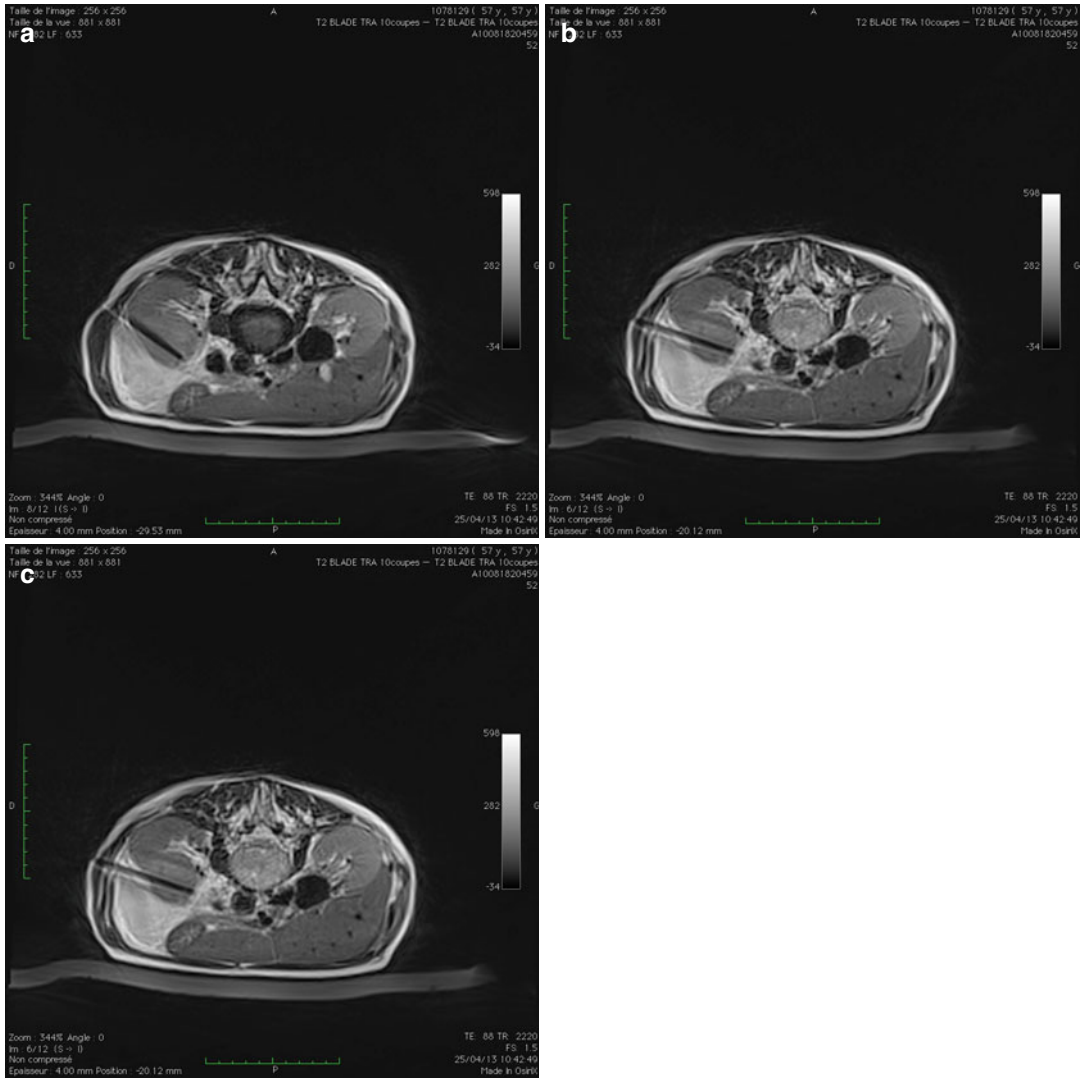


**Fig. 16.5** Axial T2-weighted MRI images confirming position of cryoablation probe (*1*) (**a**), (*2*) (**b**), and (*3*) (**c**) in a left anterior renal tumor

## Follow-Up and Post-ablation Surveillance

Although either CT with intravenous contrast or MRI with gadolinium can be used for patient follow-up, ideally the same technique used to guide the ablation will be used for follow-up. This can allow for the intra-procedure images to be matched to the post-procedure images potentially helping to detect recurrences. In the case of MR-guided ablation, a further advantage to continuing with MRI as the imaging modality is the avoidance of ionizing radiation with the follow-up imaging. This can be substantial when considering the cumulative dose that would be received from serial imaging exams over time in post-ablation surveillance period, based on current recommendations. Although the optimal radiographic follow-up regimen has yet to be defined, it is generally recommended that patients be imaged at 3 and 6 months post-ablation and then yearly thereafter [57]. At our institution patients are imaged at 3 and 12 months post-ablation and then yearly thereafter.

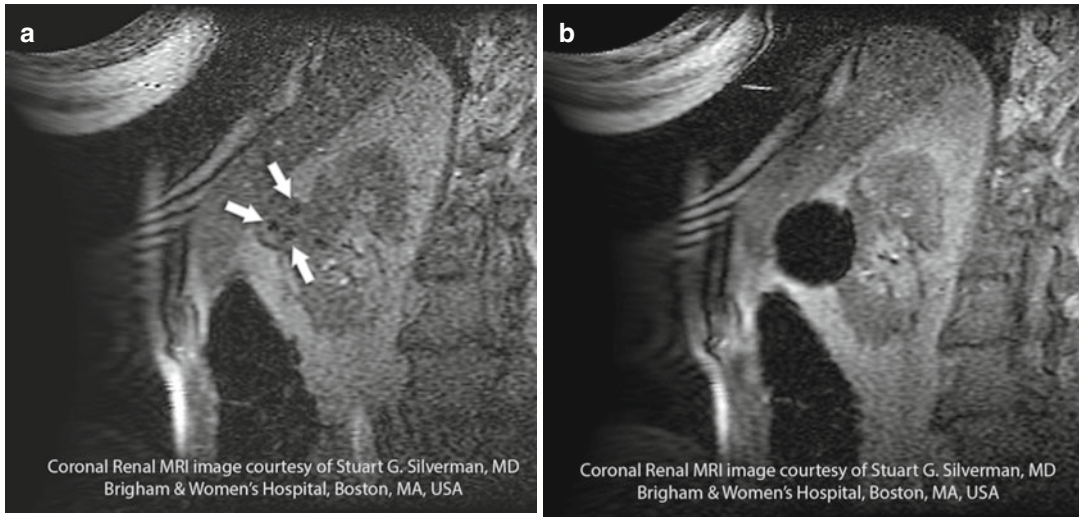


**Fig. 16.6** (**a**) Coronal MRI image of renal tumor prior to cryoablation. (**b**) Coronal T2-weighted MRI images of renal tumor post-cryoablation (Courtesy of Stuart Silverman, MD, Brigham and Women's Hospital, Boston, MA, USA)

MRI imaging after renal ablation typically includes three-plane localizer images and axial T2-weighted, axial T2-weighted fat-saturated, axial dual-echo, coronal dual-echo, axial dynamic 3D gradient-recalled echo before and after gadolinium injection (20-, 70-, and 180-s delayed), and 5-min delayed spoiled gradient-recalled echo imaging [20]. Additionally subtracted MRI images can be obtained [20]. The ablation zone typically appears hypointense on T2-weighted images and STIR images and hyperintense on T1-weighted images [20].

The MRI findings that are suggestive of residual or recurrent tumor on follow-up imaging include an enlarging ablated lesion on serial post-ablation imaging or nodular enhancement post-gadolinium on T1-weighted and subtraction images [20]. In addition, any marginal irregularity should be interpreted with suspicion, particularly if it is associated with focal loss of the uniform hypointense signal expected on T2-weighted images [19].

However, there are some factors that may render the assessment of residual or recurrent tumor more complex. Specifically, the development of post-ablation infection, hematoma, or urinoma adjacent to the site of ablation can complicate the interpretation of follow-up MRI scans. Review of the intra-procedural post-ablation scan can help to monitor interval development of new isointense or hyperintense areas within the area of the hypointense ablation zone on T2-weighted images or the development of a new focal enhancement along a uniform margin. In addition, post-contrast enhancement may also be secondary to inflammation in the early post-ablation period [58].

Nevertheless, MRI is a well-suited modality to evaluate for residual tumor or early tumor recurrence because it allows assessment of the margins in multiple planes and with different tissue contrast weightings, as well as the information afforded on the gadolinium-enhanced scans [19].

## Complications

In general, complications with percutaneous ablation are less common compared to laparoscopic ablation and to extirpative nephron-sparing modalities.

### Hemorrhage

Although uncommon, the most frequent complication during or after percutaneous renal ablation is bleeding. Development of a perinephric hema-

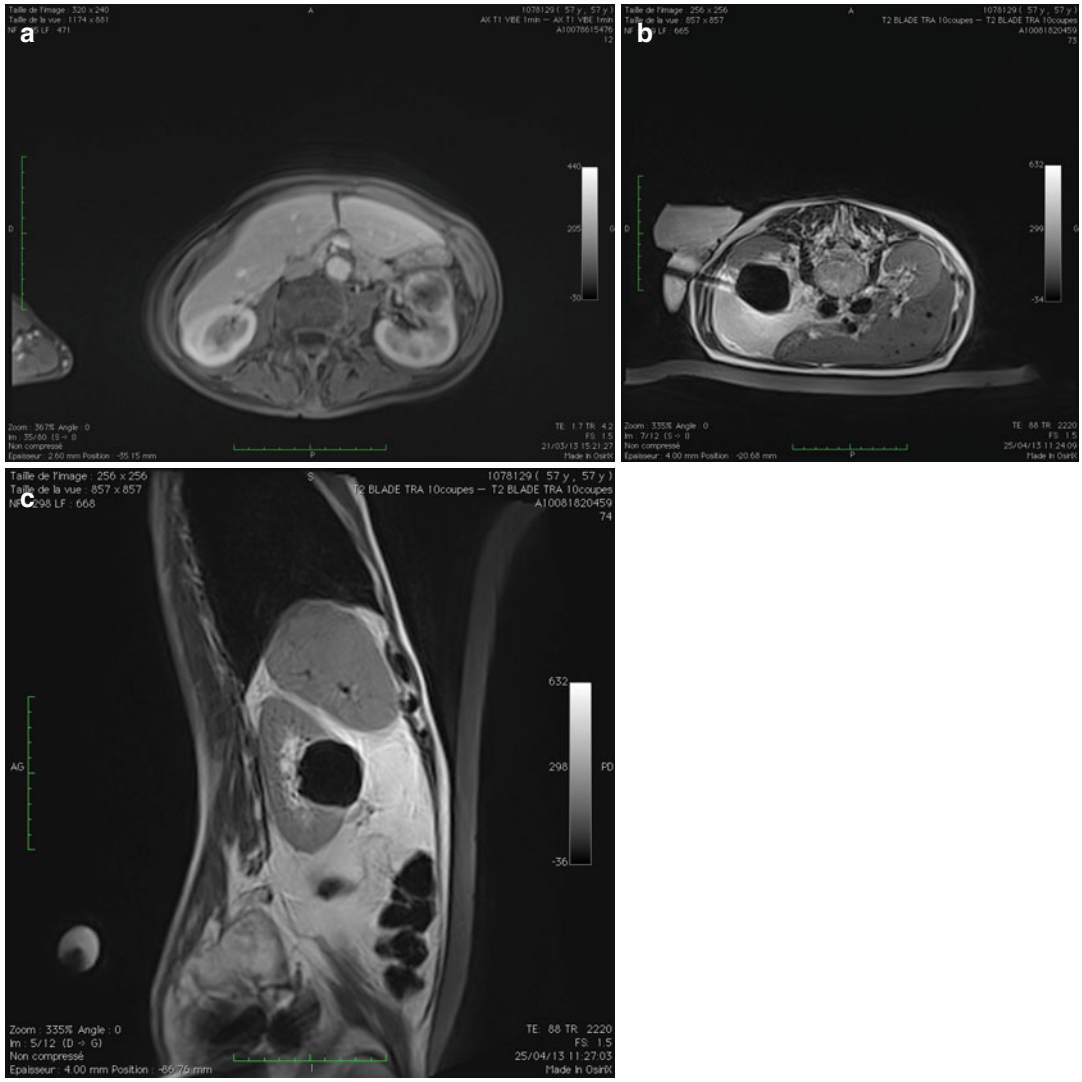


**Fig. 16.7** (**a**) Axial T1-weighted MRI image of left anterior renal tumor prior to cryoablation. (**b**) Axial T2-weighted MRI image of ice ball encompassing left anterior renal tumor post-cryoablation. (**c**) Sagittal T2-weighted MRI image of ice ball encompassing left anterior renal tumor post-cryoablation

toma is not uncommon; however, larger hemorrhage may require hospital admission, close patient monitoring, serial hematocrit measures, and rarely a blood transfusion. In the case of persistent bleeding, selective embolization is typically the first technique employed to control the bleeding. Open or laparoscopic exploration would be considered only if embolization were to fail. The incidence of hemorrhage is higher in patients treated with CA compared with RFA, likely due to the protective coagulative properties of RFA on small vessels and desiccation of the treated area [20].

## Ureteral or Renal Pelvic Injury

An extremely rare complication of percutaneous ablation is urine leakage secondary to ablation of the collecting system. The intrarenal collecting system is resilient to CA, with previous studies showing that the urothelium normalizes after CA

within just a few days [59]. Unfortunately, the renal pelvis and ureter do not respond like the intrarenal collecting system to CA and will scar and stenose if ablated. Unlike CA, RFA does not spare the collecting system acutely [59]. As such, it is imperative to avoid ablation of the renal pelvis and ureter to avoid serious potential complication.

Ureteral injury typically presents as a urinoma or hydronephrosis secondary to a stricture. Ureteral injury can be managed with placement of a nephrostomy tube +/– percutaneous drainage tube into the urinoma.

## Bowel Injury

Injury to the colon and duodenum may occur during percutaneous ablation, either as a result of inadvertent puncture with a thermal probe or by extending the ablation zone too close to the bowel.

In the case of CA, the periphery of the ice ball may be extended up to a critical structure without harming it, as the outer portion of the ice ball (5 mm from the edge) is not lethal. However, if the ice ball is extended too far into the bowel, necrosis may occur.

## Pneumothorax

A pneumothorax can occur as the result of treating upper pole or interpolar lesions where the probes pass through the pleural space. Small pneumothoraces may be observed with serial chest radiographs performed 2 and 4 h after the procedure [20]. If the patient is symptomatic or the pneumothorax is greater than 25 % or enlarging, then intervention is indicated with either aspiration of the pneumothorax or placement of a chest tube.

## Track Seeding

Tumor seeding of the needle track is very rare. Only seven cases of track seeding following renal biopsy have been reported in the literature and the overall estimated risk is less than 0.01 % [60]. Of note, after percutaneous, ablation inflammatory nodules can mimic tumor seeding along the applicator track [61], as such all post-ablation nodules along the applicator track should be biopsied and not presumed to be tumor seeding.

## Nerve Injury

The genitofemoral nerve, because of its proximity to the kidney, has been reported to have sustained thermal injury during RFA [62]. The genitofemoral nerve arises from the first and second lumbar nerve, passes through the psoas muscle, and then runs along its anterior margin. Damage to the genitofemoral nerve can cause chronic pain and tenderness and diminished sensitivity of the skin in the ipsilateral groin.

### Conclusion

Image-guided percutaneous ablation has emerged as a promising, minimally invasive, nephron-sparing alternative for the treatment of renal tumors. In particular, MRI guidance for ablation offers excellent soft-tissue contrast, high spatial resolution, and multiplanar, near-real-time imaging capabilities that allow for more accurate targeting of tumors and identification of adjacent vital structures. In addition, the absence of ionizing radiation and the ability to monitor the zone of thermal tissue destruction during the procedure regardless of the ablation modality, represent distinct advantages of MRI over other imaging modalities.

**Acknowledgment** Special thanks to Dr. Afshin Gangi, Professor of Diagnostic and Interventional Radiology at the University Hospital of Strasbourg, France and Dr. Stuart G. Silverman, Professor of Radiology, Harvard Medical School, Brigham and Women's Hospital, Boston, MA, USA for their contribution of MRI renal ablation images.

## References

1. Siegel R, Naishadham D, Jemal A. Cancer statistics, 2012. CA Cancer J Clin. 2012;62(1):10–29.
2. Mathew A, Devesa SS, Fraumeni Jr JF, Chow WH. Global increases in kidney cancer incidence, 1973–1992. Eur J Cancer Prev. 2002;11(2):171–8.

3. Chow WH, Devesa SS, Warren JL, Fraumeni Jr JF. Rising incidence of renal cell cancer in the United States. JAMA. 1999;281(17):1628–31.
4. Luciani LG, Cestari R, Tallarigo C. Incidental renal cell carcinoma-age and stage characterization and clinical implications: study of 1092 patients (1982–1997). Urology. 2000;56(1):58–62.
5. Hollingsworth JM, Miller DC, Daignault S, Hollenbeck BK. Rising incidence of small renal masses: a need to reassess treatment effect. J Natl Cancer Inst. 2006;98(18):1331–4.
6. Parsons JK, Schoenberg MS, Carter HB. Incidental renal tumors: casting doubt on the efficacy of early intervention. Urology. 2001;57(6):1013–5.
7. Volpe A, Panzarella T, Rendon RA, Haider MA, Kondylis FI, Jewett MA. The natural history of incidentally detected small renal masses. Cancer. 2004;100(4):738–45.
8. Huang WC, Levey AS, Serio AM, Snyder M, Vickers AJ, Raj GV, et al. Chronic kidney disease after nephrectomy in patients with renal cortical tumours: a retrospective cohort study. Lancet Oncol. 2006;7(9):735–40.
9. McKiernan J, Simmons R, Katz J, Russo P. Natural history of chronic renal insufficiency after partial and radical nephrectomy. Urology. 2002;59(6):816–20.
10. Thompson RH, Boorjian SA, Lohse CM, Leibovich BC, Kwon ED, Cheville JC, et al. Radical nephrectomy for pT1a renal masses may be associated with decreased overall survival compared with partial nephrectomy. J Urol. 2008;179(2):468–71; discussion 472–3.
11. Go AS, Chertow GM, Fan D, McCulloch CE, Hsu CY. Chronic kidney disease and the risks of death, cardiovascular events, and hospitalization. N Engl J Med. 2004;351(13):1296–305.
12. Campbell SC, Novick AC, Belldegrun A, Blute ML, Chow GK, Derweesh IH, et al. Guideline for management of the clinical T1 renal mass. J Urol. 2009;182(4):1271–9.
13. Hui GC, Tuncali K, Tatli S, Morrison PR, Silverman SG. Comparison of percutaneous and surgical approaches to renal tumor ablation: meta-analysis of effectiveness and complication rates. J Vasc Interv Radiol. 2008;19(9):1311–20.
14. El Dib R, Touma NJ, Kapoor A. Cryoablation vs radiofrequency ablation for the treatment of renal cell carcinoma: a meta-analysis of case series studies. BJU Int. 2012;110(4):510–6.
15. Lufkin R, Teresi L, Hanafee W. New needle for MR-guided aspiration cytology of the head and neck. AJR Am J Roentgenol. 1987;149(2):380–2.
16. Lufkin R, Teresi L, Chiu L, Hanafee W. A technique for MR-guided needle placement. AJR Am J Roentgenol. 1988;151(1):193–6.
17. Lufkin R, Duckwiler G, Spickler E, Teresi L, Chang M, Onik G. MR body stereotaxis: an aid for MR-guided biopsies. J Comput Assist Tomogr. 1988;12(6):1088–9.
18. Lewin JS, Duerk JL, Jain VR, Petersilge CA, Chao CP, Haaga JR. Needle localization in MR-guided biopsy and aspiration: effects of field strength, sequence design, and magnetic field orientation. AJR Am J Roentgenol. 1996;166(6):1337–45.
19. Nour SGL, Lewin JS. MRI-guided RF ablation in the kidney. In: Kahn TB H, editor. Interventional magnetic resonance imaging, medical radiology. Berlin: Springer; 2012. p. 319–39.
20. Uppot RN, Silverman SG, Zagoria RJ, Tuncali K, Childs DD, Gervais DA. Imaging-guided percutaneous ablation of renal cell carcinoma: a primer of how we do it. AJR Am J Roentgenol. 2009;192(6):1558–70.
21. Brenner DJ, Hall EJ. Computed tomography – an increasing source of radiation exposure. N Engl J Med. 2007;357(22):2277–84.
22. Fazel R, Krumholz HM, Wang Y, Ross JS, Chen J, Ting HH, et al. Exposure to low-dose ionizing radiation from medical imaging procedures. N Engl J Med. 2009;361(9):849–57.
23. Nguyen PK, Wu JC. Radiation exposure from imaging tests: is there an increased cancer risk? Expert Rev Cardiovasc Ther. 2011;9(2):177–83.
24. Lewin JS, Connell CF, Duerk JL, Chung YC, Clampitt ME, Spisak J, et al. Interactive MRI-guided radiofrequency interstitial thermal ablation of abdominal tumors: clinical trial for evaluation of safety and feasibility. J Magn Reson Imaging. 1998;8(1):40–7.
25. Lewin JS, Nour SG, Connell CF, Sulman A, Duerk JL, Resnick MI, et al. Phase II clinical trial of interactive MR imaging-guided interstitial radiofrequency thermal ablation of primary kidney tumors: initial experience. Radiology. 2004;232(3):835–45.
26. Boss A, Clasen S, Kuczyk M, Schick F, Pereira PL. Image-guided radiofrequency ablation of renal cell carcinoma. Eur Radiol. 2007;17(3):725–33.
27. Boss A, Clasen S, Kuczyk M, Anastasiadis A, Schmidt D, Graf H, et al. Magnetic resonance-guided percutaneous radiofrequency ablation of renal cell carcinomas: a pilot clinical study. Invest Radiol. 2005;40(9):583–90.
28. Fennessy FM, Tuncali K, Morrison PR, Tempany CM. MR imaging-guided interventions in the genitourinary tract: an evolving concept. Radiol Clin North Am. 2008;46(1):149–66. vii.
29. Kunkle DA, Egleston BL, Uzzo RG. Excise, ablate or observe: the small renal mass dilemma–a meta-analysis and review. J Urol. 2008;179(4):1227–33; discussion 1233–4.
30. Ljungberg B, Cowan NC, Hanbury DC, Hora M, Kuczyk MA, Merseburger AS, et al. EAU guidelines on renal cell carcinoma: the 2010 update. Eur Urol. 2010;58(3):398–406.
31. Zagoria RJ, Traver MA, Werle DM, Perini M, Hayasaka S, Clark PE. Oncologic efficacy of CT-guided percutaneous radiofrequency ablation of renal cell carcinomas. AJR Am J Roentgenol. 2007;189(2):429–36.
32. Gervais DA, McGovern FJ, Arellano RS, McDougal WS, Mueller PR. Radiofrequency ablation of renal cell carcinoma: part 1, Indications, results, and role in patient management over a 6-year period and ablation

of 100 tumors. AJR Am J Roentgenol. 2005; 185(1):64–71.
33. Zagoria RJ, Hawkins AD, Clark PE, Hall MC, Matlaga BR, Dyer RB, et al. Percutaneous CT-guided radiofrequency ablation of renal neoplasms: factors influencing success. AJR Am J Roentgenol. 2004; 183(1):201–7.
34. Lusch A, Fujimoto S, Findeiss LK, Liss MA, Okhunov Z, Juncal S, et al. Anthropometric renal anatomic alterations between supine and prone positions in percutaneous renal ablation for renal cortical neoplasms. J Endourol. 2013;27:845.
35. Dempsey MF, Condon B. Thermal injuries associated with MRI. Clin Radiol. 2001;56(6):457–65.
36. Dempsey MF, Condon B, Hadley DM. Investigation of the factors responsible for burns during MRI. J Magn Reson Imaging. 2001;13(4):627–31.
37. Nitz WR, Oppelt A, Renz W, Manke C, Lenhart M, Link J. On the heating of linear conductive structures as guide wires and catheters in interventional MRI. J Magn Reson Imaging. 2001;13(1):105–14.
38. Levinson AW, Su LM, Agarwal D, Sroka M, Jarrett TW, Kavoussi LR, et al. Long-term oncological and overall outcomes of percutaneous radio frequency ablation in high risk surgical patients with a solitary small renal mass. J Urol. 2008;180(2):499–504; discussion 504.
39. McDougal WS, Gervais DA, McGovern FJ, Mueller PR. Long-term follow-up of patients with renal cell carcinoma treated with radio frequency ablation with curative intent. J Urol. 2005;174(1):61–3.
40. Best SL, Park SK, Yaacoub RF, Olweny EO, Tan YK, Trimmer C, et al. Long-term outcomes of renal tumor radio frequency ablation stratified by tumor diameter: size matters. J Urol. 2012;187(4):1183–9.
41. Young EE, Castle SM, Gorbatiy V, Leveillee RJ. Comparison of safety, renal function outcomes and efficacy of laparoscopic and percutaneous radio frequency ablation of renal masses. J Urol. 2012;187(4):1177–82.
42. Shingleton WB, Sewell Jr PE. Percutaneous renal tumor cryoablation with magnetic resonance imaging guidance. J Urol. 2001;165(3):773–6.
43. Miki K, Shimomura T, Yamada H, Kishimoto K, Ohishi Y, Harada J, et al. Percutaneous cryoablation of renal cell carcinoma guided by horizontal open magnetic resonance imaging. Int J Urol. 2006;13(7):880–4.
44. Gupta A, Allaf ME, Kavoussi LR, Jarrett TW, Chan DY, Su LM, et al. Computerized tomography guided percutaneous renal cryoablation with the patient under conscious sedation: initial clinical experience. J Urol. 2006;175(2):447–52; discussion 452–3.
45. Atwell TD, Farrell MA, Leibovich BC, Callstrom MR, Chow GK, Blute ML, et al. Percutaneous renal cryoablation: experience treating 115 tumors. J Urol. 2008;179(6):2136–40; discussion 2140–1.
46. Goldberg SN, Gazelle GS. Radiofrequency tissue ablation: physical principles and techniques for increasing coagulation necrosis. Hepatogastroenterology. 2001;48(38):359–67.
47. Gage AA, Baust J. Mechanisms of tissue injury in cryosurgery. Cryobiology. 1998;37(3):171–86.
48. Permpongkosol S, Link RE, Kavoussi LR, Solomon SB. Percutaneous computerized tomography guided cryoablation for localized renal cell carcinoma: factors influencing success. J Urol. 2006;176(5):1963–8; discussion 1968.
49. Littrup PJ, Ahmed A, Aoun HD, Noujaim DL, Harb T, Nakat S, et al. CT-guided percutaneous cryotherapy of renal masses. J Vasc Interv Radiol. 2007;18(3):383–92.
50. Tacke J, Speetzen R, Heschel I, Hunter DW, Rau G, Gunther RW. Imaging of interstitial cryotherapy–an in vitro comparison of ultrasound, computed tomography, and magnetic resonance imaging. Cryobiology. 1999;38(3):250–9.
51. Saliken JC, McKinnon JG, Gray R. CT for monitoring cryotherapy. AJR Am J Roentgenol. 1996;166(4):853–5.
52. Sandison GA, Loye MP, Rewcastle JC, Hahn LJ, Saliken JC, McKinnon JG, et al. X-ray CT monitoring of iceball growth and thermal distribution during cryosurgery. Phys Med Biol. 1998;43(11):3309–24.
53. Silverman SG, Tuncali K, van Sonnenberg E, Morrison PR, Shankar S, Ramaiya N, et al. Renal tumors: MR imaging-guided percutaneous cryotherapy – initial experience in 23 patients. Radiology. 2005;236(2):716–24.
54. Weiss CR, Nour SG, Lewin JS. MR-guided biopsy: a review of current techniques and applications. J Magn Reson Imaging. 2008;27(2):311–25.
55. Nour SG, Derakhshan JJ, Akhtar NJ, Ayres MA, Clampitt ME, Stellato TA, et al. A technique for MRI-guided transrectal deep pelvic abscess drainage. AJR Am J Roentgenol. 2008;191(4):1182–5.
56. Derakhshan JJ, Griswold MA, Nour SG, Sunshine JL, Duerk JL. Characterization and reduction of saturation banding in multiplanar coherent and incoherent steady-state imaging. Magn Reson Med. 2010;63(5):1415–21.
57. White MK, Kaouk JH. Ablative therapy for renal tumors. In: Wein AJ, Kavoussi LR, Novick AC, Partin AW, Peters CA, editors. Campbell-Walsh urology. 10th ed. Philadelphia: Elsevier Saunders; 2012. p. 1670–82.
58. Breda A, Anterasian C, Belldegrun A. Management and outcomes of tumor recurrence after focal ablation renal therapy. J Endourol. 2010;24(5):749–52.
59. Janzen NK, Perry KT, Han KR, Kristo B, Raman S, Said JW, et al. The effects of intentional cryoablation

and radio frequency ablation of renal tissue involving the collecting system in a porcine model. J Urol. 2005;173(4):1368–74.
60. Herts BR, Baker ME. The current role of percutaneous biopsy in the evaluation of renal masses. Semin Urol Oncol. 1995;13(4):254–61.
61. Lokken RP, Gervais DA, Arellano RS, Tuncali K, Morrison PR, Tatli S, et al. Inflammatory nodules mimic applicator track seeding after percutaneous ablation of renal tumors. AJR Am J Roentgenol. 2007;189(4):845–8.
62. Boss A, Clasen S, Kuczyk M, Anastasiadis A, Schmidt D, Claussen CD, et al. Thermal damage of the genitofemoral nerve due to radiofrequency ablation of renal cell carcinoma: a potentially avoidable complication. AJR Am J Roentgenol. 2005;185(6):1627–31.

# Part IV

# On the Horizon

# Augmented Reality for Percutaneous Renal Interventions

17

Jens Rassweiler, Marie-Claire Rassweiler, Michael Müller, Estevao Lima, Bogdan Petrut, Johannes Huber, Jan Klein, Manuel Ritter, Ali S. Gözen, Phillipe Pereira, Axel Häcker, Hans-Peter Meinzer, Ingmar Wegner, and Dogu Teber

For percutaneous renal interventions, optimal access represents the key factor of success [1–4]. Initially sonography and 2D fluoroscopy were used as imaging modalities to assist percutaneous procedures [1–6]. The use of stereofluoroscopy did not prove to be advantageous [7]. Another example of the application of imaging modalities is stone localisation for extracorporeal shock wave lithotripsy (ESWL) (Table 17.1) [7–13]. Some authors tried to apply mechanical and robotic systems based on fluoroscopy or even computed tomography to enhance precision of percutaneous renal access [14–19]. Several groups have published their experience with the use of augmented reality (AR) for different percutaneous renal procedures [19–33]. A recent review summarised the status of kidney targeting and puncturing during percutaneous nephrolithotomy [19].

Based on significant improvement of imaging techniques and information technology (IT), the ability of surgeons can be significantly enhanced by integration of preexisting images on screen during video-assisted procedures. Data of 3D

J. Rassweiler, MD (✉)
Department of Urology, SLK Kliniken Heilbronn, Heidelberg, Germany
e-mail: jens.rassweiler@slk-kliniken.de

M.-C. Rassweiler, MD • M. Ritter, MD
A. Häcker, MD
Department of Urology, Medical School Mannheim, University of Heidelberg, Heidelberg, Germany
e-mail: mc_rassweiler@web.de; manuel.ritter@medma.uni-heidelberg.de; axel.haecher@medma.uni-heidelberg.de

M. Müller, PhD • I. Wegner, PhD • H.-P. Meinzer, PhD
Division of Medical and Biological Informatics, German Cancer Research Center, Heidelberg, Germany
e-mail: michael.mueller@dkfz-heidelberg.de; iwegner@gmx.de; h.p.meinzer@dkfz-heidelberg.de

E. Lima, MD
Department of Urology, Medical School Braga, University of Braga, Braga, Portugal
e-mail: estevaolima@ecsaude.uminho.pt

B. Petrut, MD
Department of Urology and Oncology, Medical School Cluj, University of Cluj, Cluj-Napoca, Romania
e-mail: petrutbogo@yahoo.com

J. Huber, MD
Department of Urology, Medical School, Technical University of Dresden, Dresden, Germany
e-mail: johannes.huber@uniklinikum-dresden.de

J. Klein, MD • A.S. Gözen, MD
Department of Urology, SLK Kliniken Heilbronn, University of Heidelberg, Heidelberg, Germany
e-mail: jan.klein@slk-kliniken.de; asgozen@yahoo.com

P. Pereira, MD
Department of Radiology, SLK Kliniken Heilbronn, University of Heidelberg, Heidelberg, Germany
e-mail: phillipe.pereira@slk-kliniken.de

D. Teber, MD
Department of Urology, Medical School Heidelberg, University of Heidelberg, Heidelberg, Germany
e-mail: dogu.teber@med.uni-heidelberg.de

J.C. Liao, L.-M. Su (eds.), *Advances in Image-Guided Urologic Surgery*,
DOI 10.1007/978-1-4939-1450-0_17, 

**Table 17.1** The impact of imaging and navigation on minimally invasive techniques with renal access

| Procedure [Ref] | Target of navigation | Imaging modalities | Tracking systems | Modifications of navigation | Comments |
|---|---|---|---|---|---|
| Extracorporeal shock wave lithotripsy (ESWL) [8–13] | Urinary stone | Fluoroscopy (two, in-line, iso-centric) | Mechanical | Ultrasound arm | All tested modifications work real time |
| | | Ultrasound (lateral, in-line) | Optical | Two cameras | |
| | | | Acoustic | Four piezoelectric sources | |
| Percutaneous nephrolithotomy (PCNL) [1–7, 14–30] | Collecting system | Fluoroscopy (2D, C-arm, 3D) | Mechanical | Mechanical arm with C-arm (locator) | (3D) Fluoroscopy real time |
| | | Ultrasound | US-guided | Robotic arm with fluoroscopy (PAKY) | EM real time |
| | | CT-based | Laser light | Robotic arm with CT (AcuBot) | CT not real time |
| | | Uro Dyna-CT | Electromagnetic | 3D laser system | Dyna-CT/laser light not real time |
| | | | Marker-based (inside out) | EM catheter | |
| | | | | iPad-assisted | |
| Percutaneous renal biopsy [30–34] | Renal parenchyma | Ultrasound | Attitude tracking | US-guided | CT not real time |
| | | CT | Marker-based | iPad-assisted | |
| | | MRI | | | |

*CT* computed tomography, *MRI* magnetic resonance imaging, *2D* two-dimensional, *3D* three-dimensional

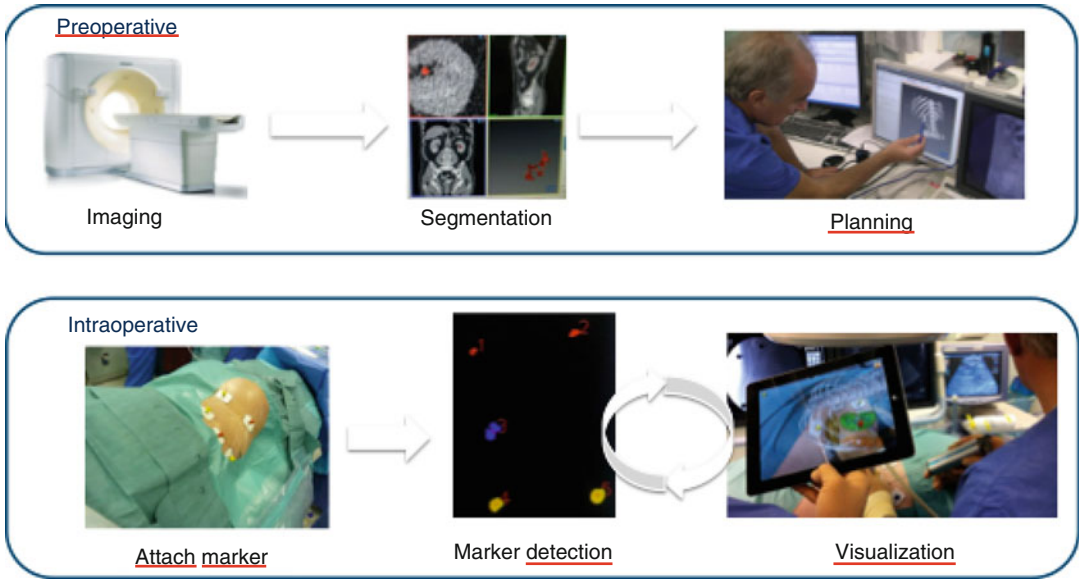


**Fig. 17.1** The basic steps of imaging-guided surgery: using the example of marker-based navigation using the iPad

ultrasound, computed tomography (CT), or magnetic resonance imaging (MRI) can be recorded, segmented, and then displayed on the screen not only for the purpose of an exact diagnosis but also to augment surgeons' spatial orientation [20, 21]. Image-guided surgery (IGS) correlates pre- or intraoperative images to the operative field in real time (Fig. 17.1). IGS aims to increase precision by providing a constant flow of information on a target area and its surrounding anatomical structures. One possibility to provide this information represents the use of augmented reality (AR). AR superimposes computer-generated models on a real video stream by aligning real with virtual image [35, 36].

We present an overview about important projects on surgical navigation supported by the EAU Section of Uro-Technology (ESUT) focussing on AR-assisted percutaneous renal access (Table 17.2) starting with a short update on surgical navigation basics.

## Basics of Surgical Navigation for Percutaneous Renal Access

The main steps of image-guided surgery include (1) preoperative imaging and planning, (2) intraoperative imaging, and (3) tracking (Fig. 17.1).

### Preoperative Imaging

*Preoperative imaging* is usually based on a multidetector row CT or MRI (Table 17.1). In the case of nephrolithiasis requiring percutaneous renal access, according to EAU guidelines computed tomography is indicated as a preoperative diagnostic option to plan the procedure [37]. AR-based techniques, like iPad-assisted marker-based navigation, can use CT for segmentation and image-guided surgery (Fig. 17.1). Special software programs allow the display of data in three dimensions and fusing images of different modalities. The information from different modalities regarding the same anatomical region (kidney) can then be displayed on a single image. These images (augmented reality) represent the basis for *planning of the procedure*, but intraoperative image acquisition is mandatory for any surgical navigation tool [20, 21, 35, 36].

### Intraoperative Imaging

The most popular *image acquisition modalities used intraoperatively* for percutaneous renal access are ultrasound and 2D fluoroscopy (Table 17.1) [1–6]. Actually, these imaging modalities are used mainly under manual control

**Table 17.2** Summary of experimental results of ESUT projects on percutaneous renal access

| Centre | Study [Ref] | Tracking system | Model | Puncturing time (median) | Comments |
|---|---|---|---|---|---|
| Heilbronn/Heidelberg[a] | iPad-assisted marker-based percutaneous access for renal interventions [24, 25] | Marker-based with CT segmentation (+fluoroscopy) | Porcine kidneys embedded in ballistic gel (*ex vivo*) | 1.7 min (trainees)<br>2.5 min (experts) | 20 % reduction of radiation exposure for trainees |
| | Electromagnetic tracking for puncturing the renal collecting system [22, 23] | Electromagnetic (+fluoroscopy) | Porcine kidneys put in swine groin (*ex vivo*) | 15 s | Median distance to sensor 1.8 mm<br>91 % single attempt access<br>Learning phase 30 punctures |
| Mannheim[b] | Laser-assisted percutaneous access to renal collecting system using Dyna-CT [28, 29] | Laser-assisted tracking (+3D fluoroscopy) | Porcine kidneys put in chicken body (*ex vivo*) | 3.2 min | Longer times due to reassessment by Uro Dyna-CT during puncture (fluoro-time 0.35 min)<br>80 % single attempt |
| Braga[c] | Electromagnetic tracking for percutaneous access to renal collecting system [26] | Electromagnetic (+ureteroscopy) | Porcine kidney and ureter (in vivo) | 24 s (plus planning time of 13 s) | 47 s for resident (plus 16 s planning)<br>Longer times for ureter access (51 s) |
| Cluj | Attitude tracking for percutaneous renal biopsy/ focal therapy [31] | Attitude tracking (for ultrasound) | Gel model with sonographical visible target | 7 s | Higher accuracy by attitude tracking (1.0 mm vs. 3 mm distance to centre) |

[a]Supported by Graduiertenkolleg (GRK 1126) of Deutsche Forschungsgemeinschaft (DFG) (Project N3)
[b]Supported by Alfred Kürten-Stiftung
[c]Supported by Foundation for Science and Technology – Portugal (SFRH/BD/74276/2010)

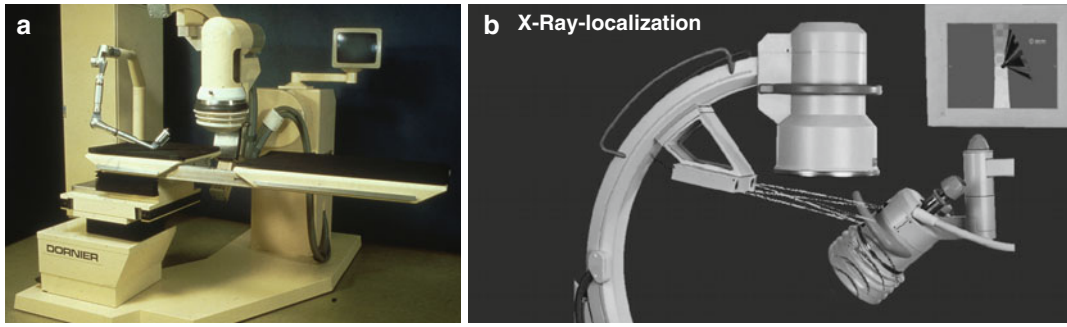


**Fig. 17.2** Navigation in lithotripters for extracorporeal shock wave lithotripsy. (**a**) Dornier MPL 9000: articulated robot arm with integrated ultrasound probe for microprocessor-controlled positioning of the patient based on potentiometers in the joints of the arm (electromagnetic tracking). (**b**) Modulith SLK: combination of fluoroscopic localisation and 3D navigation using a camera system determining the position of the shock wave source in relationship to the stone seen on fluoroscopy (optical tracking)

to guide instruments or needles. In contrast, computed navigation requires 3D data. Apart from ultrasound and 2D fluoroscopy, open MRI, 3D ultrasound, iso-centric 3D C-arm, and Uro Dyna-CT may be useful for intraoperative image acquisition for percutaneous renal surgery (Table 17.1) [15, 17–19, 24, 25, 27–29, 32, 33].

The major challenge of soft tissue navigation is *registration and fusion of preoperative image data on intraoperative patient images*, because the constellation and shape of unconstrained organs may change since planning and also during intervention. A nonrigid image-to-image registration of pre- and intraoperative image data may resolve the issue. Some authors superimposed 3D visualisation of the kidney on the endoscopic image with manual overlapping of the organ boundaries [35, 38, 39], but accuracy is limited because 3D reconstruction and endoscopic image are still displayed on a 2D screen. Point-to-point registration – as used with the iPad – may provide optimal accuracy as long as landmarks or fiducial markers can be spotted exactly in both image systems (Fig. 17.1). Percutaneous renal access entails the advantage that correct correspondence of AR and real view (i.e. on iPad) can be checked easily using the ribs as landmarks.

## Tracking

*Tracking devices* link spatial information from imaging modalities, surgical instruments, or endoscope/ nephroscope by representing these actors in a single coordinate system. Various lithotripters have used different types of tracking modes to enable stone localisation (Fig. 17.2) [10–13]. Technical options include (1) optical tracking, (2) electromagnetic tracking, (3) attitude tracking, (4) acoustic tracking, and (5) marker-based tracking.

*Optical tracking* is based on visual registration of the position of tracking bodies or sensors attached to an endoscope, instrument, or ultrasound probe usually using two or three cameras (Fig. 17.2b). This determines the exact position of the tip of a rigid instrument/endoscope/ultrasound probe in the OR room or accordingly inside the patient [20, 21, 40].

E*lectromagnetic tracking* measures the position of small coils inside the patient without the need of direct line of sight. A magnetic field has to be generated around the patient. The sensor coil is attached to the tip of an instrument, endoscope, or ultrasound transducer [20, 21]. For percutaneous renal access, it has been fixed at the end of a steerable 5-DOF ureteral catheter [22, 23, 26]. The EMT sensor analyses the position of the coil and tracks the puncturing needle accordingly to facilitate a rendezvous manoeuvre (Fig. 17.3). Another possibility of EMT is the use of potentiometers placed at the joints of articulated arms (Fig. 17.2a). Magnetic tracking may be interfered by ferromagnetic objects like surgical table, instruments, or electrical-powered devices [20, 26, 41].

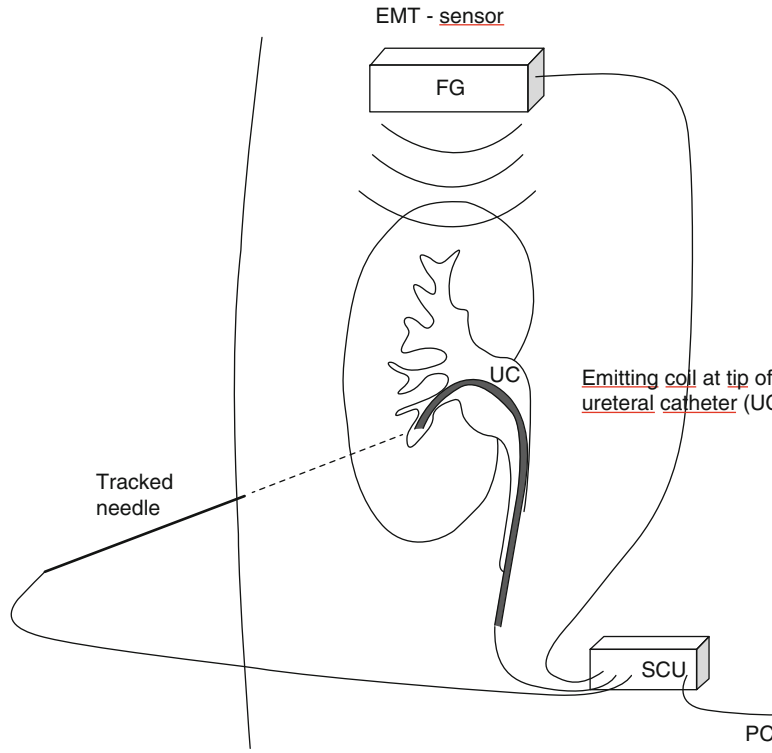


**Fig. 17.3** Navigation used for percutaneous access to the kidney: electromagnetic tracking based on analysis of the position of the electromagnetic emitter attached to tip of ureteral catheter (UC) by EMT sensor at bedside who also tracks the puncturing needle

*Attitude tracking* or motion tracking uses an accelerometer to determine the actual spatial position of an ultrasound probe. Based on this, the lateral extension of a defined movement (attitude) can be determined and calculated [31, 42]. This allows the device to indicate precisely the specific position of the tracked device, such as the exact mid-position as indicated by the two blue LED lights (Fig. 17.4).

*Acoustic tracking* uses supersonic piezoelectric emitters and sensors. These can be placed at rigid imaging devices (ultrasound probe, fluoroscopic C-arm) and at the patient site respectively the shock wave source coupled to the skin of the patient [13]. Similar to optical tracking, the relative position of emitters and sound receivers can be calculated to determine the exact position of stone and focal zone of the shock wave source.

*Marker-based tracking* utilises the information of the monocular video for tracking (Fig. 17.5). Based on the placement of navigation aids, the position and orientation of the tip of the endoscope or rear camera of the iPad in relation to the target organ can be calculated. Prior to image acquisition, navigation aids are attached near the anatomical target region [24, 25]. A surgical planning step localises these navigation aids in the computerised imaging data (CT).

*Post-processing segmentation* includes definition of anatomical structures of interest providing important additional information, such as surgical trajectory, access, or stone localisation. Immediately prior to surgery, the navigation system is set up in the operating room (Fig. 17.1). During intraoperative patient-to-image registration, the respective tracking device is used to localise the navigation aids. Transformation for mapping objects of the image to the tracking device space is calculated, thus enabling visualisation of arbitrary anatomical structures in relation to puncturing needle respectively instruments [24, 25].

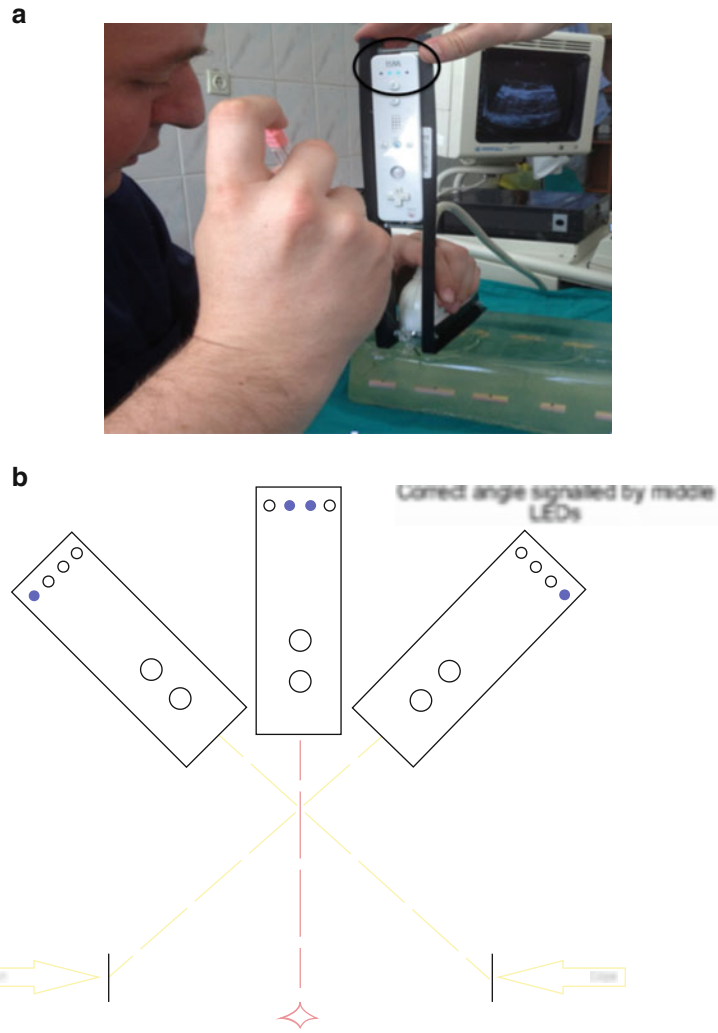


**Fig. 17.4** Navigation used for percutaneous access to the kidney: attitude tracking by attaching an accelerometer (Nintendo WiiMote) to the ultrasound probe mounted in a special chassis. (**a**) Position of the probe can be displayed in real time on a computer. Manipulating ultrasound probe, landmark points (lateral rim of target) can be determined. Based on this the direction to targeted points (exact midline) are calculated and displayed by the tracking device (two *blue* central LED lights = *black circle*). (**b**) Schematic drawing of principle

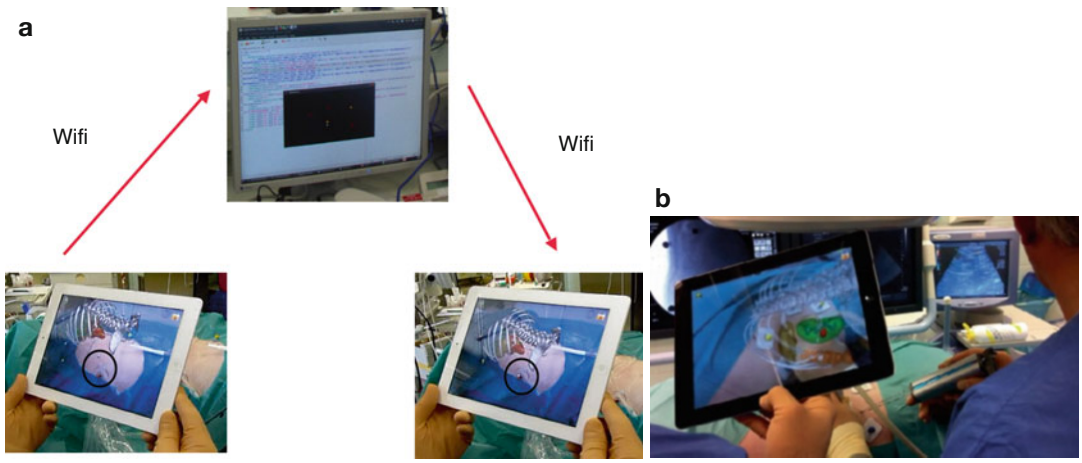


**Fig. 17.5** Navigation used for percutaneous access to the kidney: marker-based tracking based on computed tomography carried out with patient in prone position with markers attached around the target area for puncturing a renal tumour. (**a**) Following segmentation of data, the server/laptop communicates with the iPad via WiFi. (**b**) Exact overlay of virtual pins and real navigation markers on the fused image on iPad indicates correct navigation process (here with demonstration of renal tumour for biopsy). Ultrasound is used as a real-time imaging modality

## European Studies Using AR for Percutaneous Renal Interventions

### Marker-Based iPad-Assisted Puncture of the Collecting System

A marker-based tracking principle previously described during laparoscopic radical prostatectomy [36, 43] was modified to puncture the collecting system prior to percutaneous nephrolithotripsy [24, 25]. Instead of placing navigation aids on the target organ (prostate), we placed coloured markers on the skin around the puncture area. Preoperative imaging consisted of multi-slice CT with the patient in prone position on a PCNL cushion exactly as during surgery (Fig. 17.1). The iPad is used as a camera, computer, and display; data are transferred to the central server/laptop through WiFi (Fig. 17.5a). As real-time imaging mode, we use 2D digital fluoroscopy. Based on experimental studies using porcine kidneys embedded in ballistic gel (Fig. 17.6), we applied this technique in a feasibility study of 19 patients focusing on success,

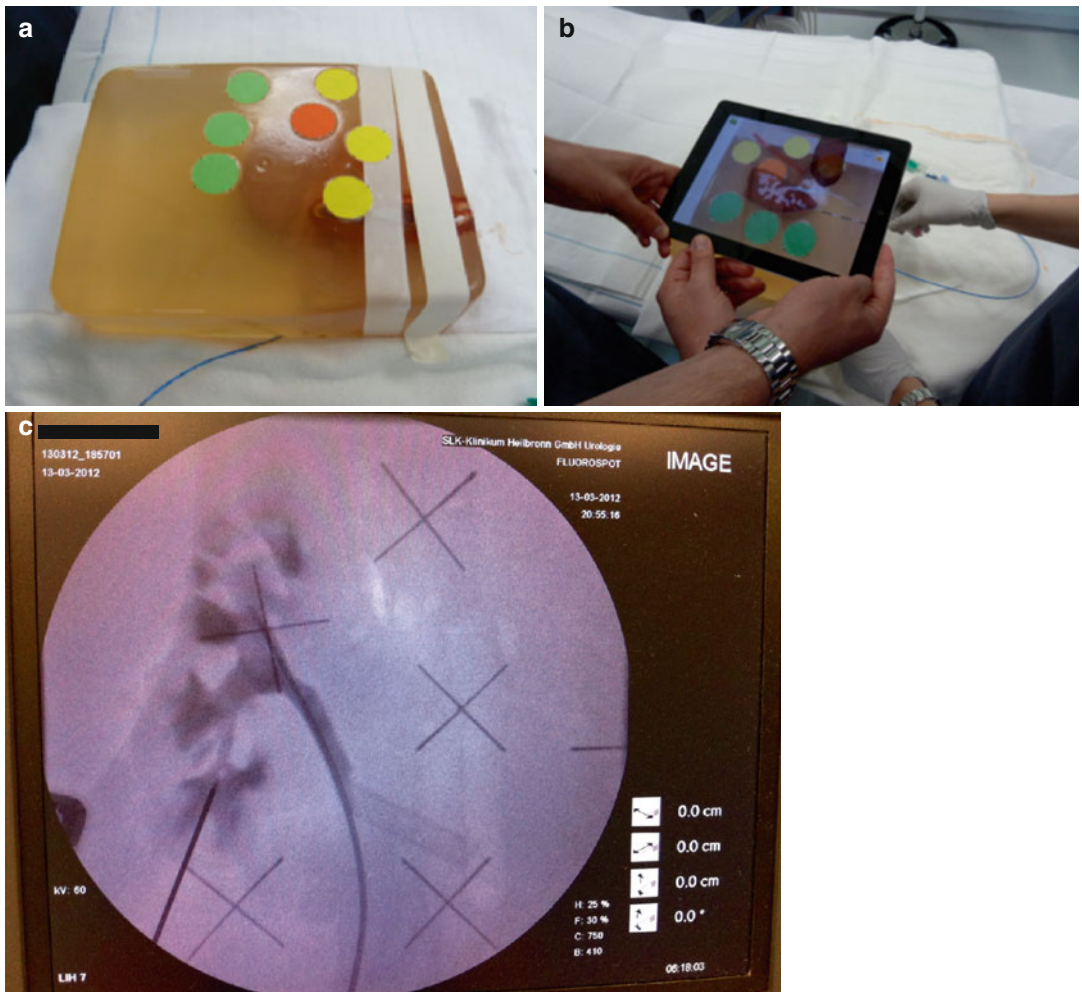


**Fig. 17.6** Marker-based iPad-assisted puncture of the renal collecting system – experimental setup. (**a**) New model of porcine kidney embedded in dark-coloured ballistic gel. (**b**) Segmentation of the kidney and collecting system after multi-slice CT. (**c**) Puncture of the kidney with iPad assistance and verification of successful puncture by fluoroscopy. (**d**) Comparison of puncture times using iPad, ultrasound, or fluoroscopy. Shortest puncture times with iPad performed by trainees

**Fig. 17.6** (continued)

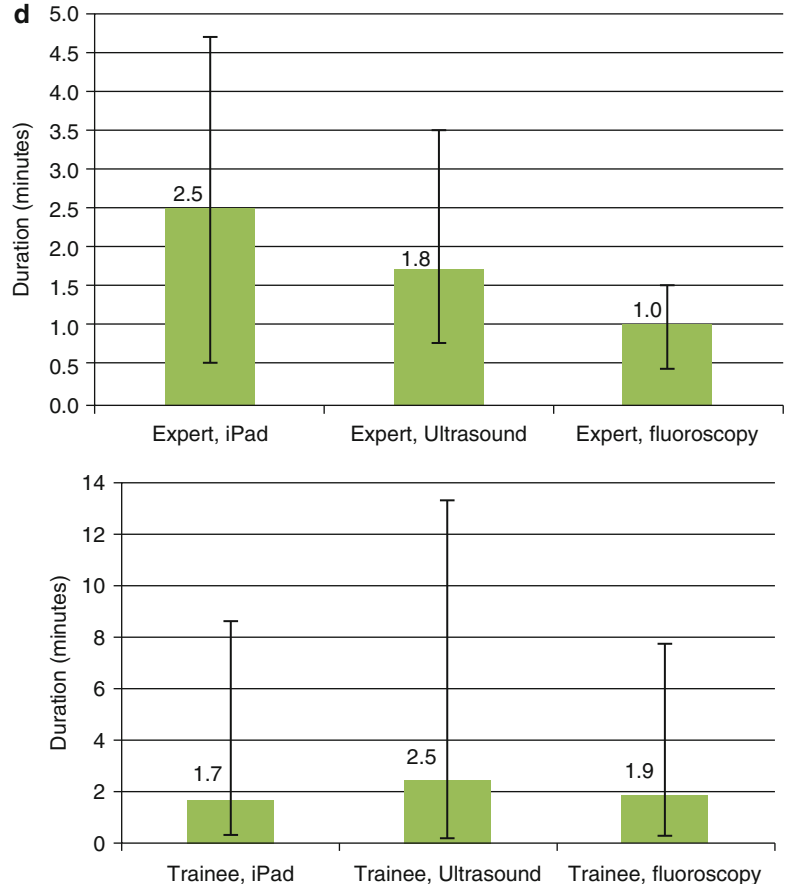


time to puncture the collecting system, and radiation exposure of the patients.

In the in vitro study, image preparation time was 12 min and segmentation time 8 min. Puncture times for experts with iPad were longer compared to ultrasound or fluoroscopy (2.5 min. vs. 1.8 min. vs. 1.0 min.), whereas the trainees significantly benefited from the use of the iPad (1.7 min. vs. 1.9 vs. 2.5 min.) with 20 % reduction of radiation exposure (Fig. 17.6d, Table 17.2). For clinical use, improvements included, smaller radiopaque stickers instead of pins, iPad arm enabling single-surgeon use, and LED light at the back face of the iPad to guarantee optical visibility of all markers (Fig. 17.7c). In 13 of 19 cases, the collecting system was entered in a single attempt (average 1.5) with a radiation exposure of 377.5 μGym$^2$. A matched-pair study which compares standard imaging (US + fluoroscopy) versus iPad-assisted puncture has been initiated (approved by Ethical commission, University of Heidelberg).

## 3D Computer Tomography Using Uro Dyna-CT for Laser-Assisted Puncture of the Renal Collecting System

Uro Dyna-CT (Siemens Medical Solutions, Erlangen, Germany) represents a modified angiography unit [28, 29, 32, 44], which allows the fluoroscopic unit to be rotated around the patient, thereby creating an image similar to computed tomography (Fig. 17.8a). Segmentation of the data allows 3D reconstruction of target structures like the collecting system (filled with contrast dye). An in vitro model of porcine kidney was used to perform a Dyna-CT with Artis Zee® Ceiling to gain multiplanar reconstructions (Fig. 17.8b). Using "bull's eye" technology, a laser light (syngo iGuide® laser guidance system) is directed based on the 3D reconstruction simulating the puncture line. The head of the puncture needle and incision site on the skin have to be in-line to guarantee puncture with correct angles

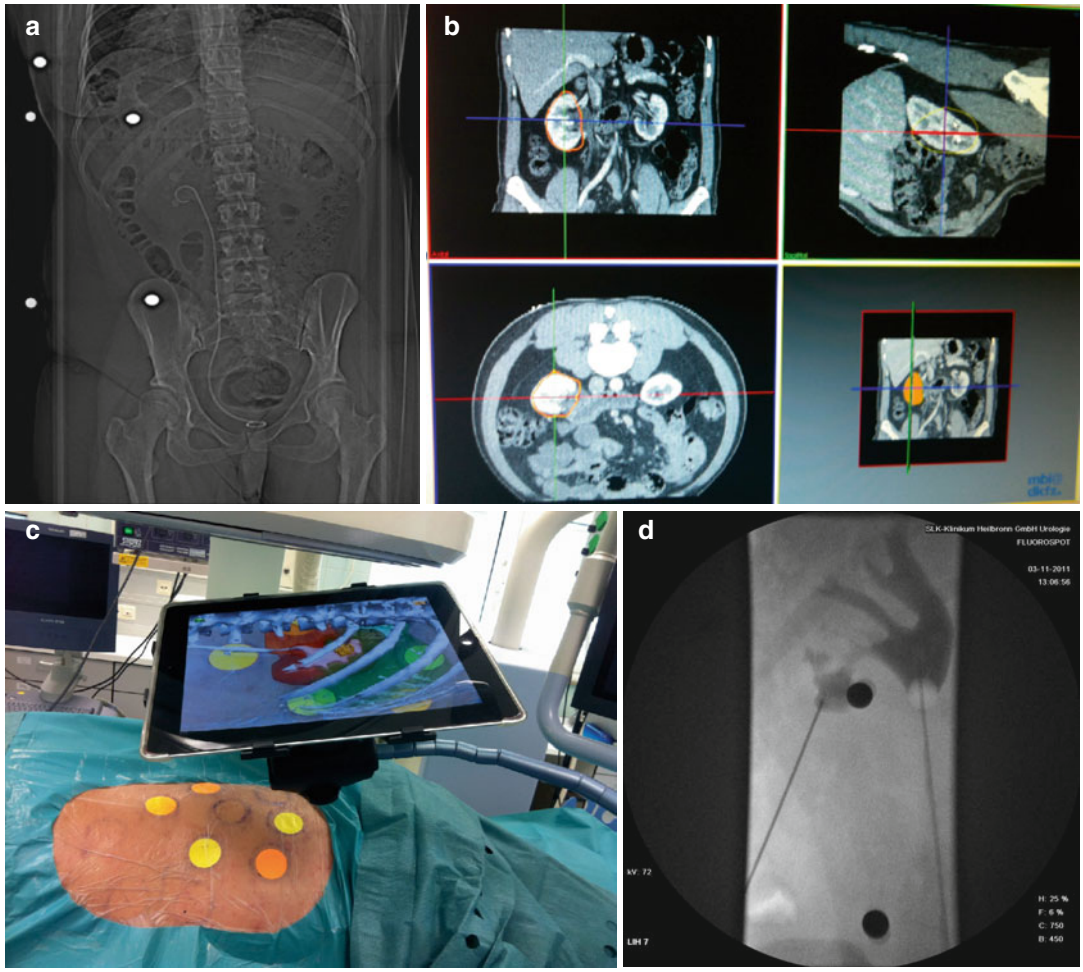


**Fig. 17.7** Clinical experience with marker-based iPad-assisted puncture of the collecting system. (**a**) Preoperative prone multi-slice CT patient with complicated nephrolithiasis on the left kidney with markers placed around target area. (**b**) Semiautomated 3D segmentation of CT (performed by urologist). (**c**) Use of iPad during puncture with display of AR (ribs, kidney, colon, collecting system with stone). The iPad is fixed on a special arm with mounted LED light to enable optimal visualisation of the coloured markers. (**d**) Verification of successful puncture by 2D fluoroscopy

(Fig. 17.8c). Ten punctures were performed and puncture success was depicted by antegrade contrast filling of the collecting system under fluoroscopic control (Fig. 17.8d). Puncture time, tract length, and fluoroscopy time was documented [28].

Data acquisition (8 s) and 3D rendering (48 s) was possible in approximately 1 min. Median time for planning the punctures was 7 [5–15] min. Median puncture time was 4.6 [2–10.2] min. Median tract length was 4.96 [4.33–6.5] cm. Median fluoroscopy time was 0.4 [0.2–1] min. Nine of ten punctures were successful (Table 17.2). A second puncture to gain access to the collecting system was necessary in one case, and one puncture has to be abandoned.

## Electromagnetic Tracking-Based Real-Time Puncture of the Renal Collecting System

Two groups worked on the experimental realisation of real-time electromagnetic tracking [22, 26].

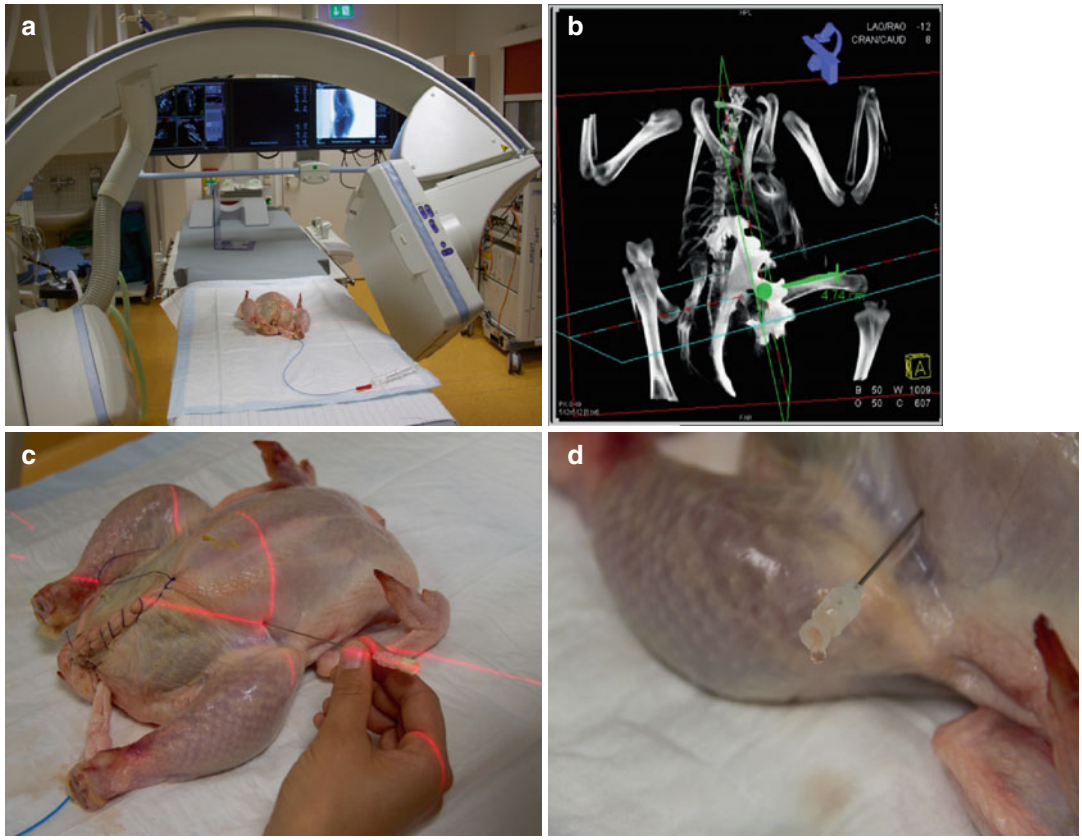


**Fig. 17.8** Experimental evaluation of laser-guided navigation with the Uro Dyna-CT. (**a**) Setup of experiment using *ex vivo* model of porcine kidney embedded in chicken body. Uro Dyna-CT consists of a rotatable digital fluoroscopic unit and a urological carbon intervention table. (**b**) Uro Dyna-CT-segmented images of the porcine kidney model with artificial stones, 3D demonstration of the collecting system, and determination of puncture site (performed by urologist). (**c**) Laser-guided puncture of the kidney. The laser cross indicates the point of needle insertion according to bull's eye view. (**d**) Verification of successful puncture

For this purpose an EMT sensor is put on the tip of a 5-DOF steerable ureteral catheter (UC) tracking the puncture needle electromagnetically (Fig. 17.4). Both groups used a commercially available EMT system (AURORA; NDI, Waterloo, Ontario, Canada) to track the needle. This device features a field generator which builds up an alternating electromagnetic field used either as a cube-shaped or dome-shaped measurement volume. The electromagnetic field-induced voltage in the coil, which is connected to the AURORA interface unit be lead wire. The interface unit calculates spatial information for all connected sensors in real time and transmit it to a computer. The EMT tracking system was connected to a standard laptop running a navigation software implemented using the open-source Medical Imaging Interaction Toolkit (MITK). The distance between the two sensors is calculated and displayed via a graphical user interface: Three widgets are provided to assist placement. Widgets I and II display the position and orientation of both sensors in 3D from different angles and widget III shows the UC sensor as a sphere from the position of the sensor tip. To adopt the rendezvous approach, the field generator is placed alongside a porcine *ex vivo* model and the sensor fitted into the distal end of the UC (Fig. 17.9a). Then the insertion point can be chosen with the tracked needle by centring the virtual representation of the UC sensor in widget III.

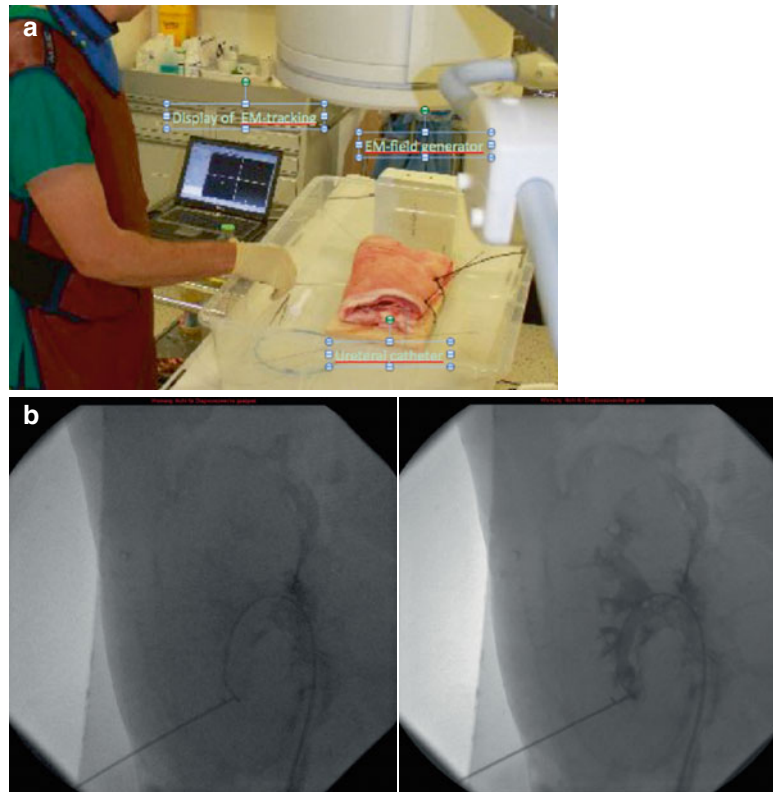


**Fig. 17.9** Experimental evaluation of electromagnetic tracking used for puncturing of the renal collecting system using an *ex vivo* model. (**a**) Setup of the experiment consisting of EM-field generator, steerable ureteral catheter (*UC*), needle and laptop with display of needle, and EN-sensor position at tip of UC. (**b**) Verification of successful puncture by 2D fluoroscopy

### EMT Tracking Using a Porcine *Ex Vivo* Model

Fifteen porcine kidney punctures were performed using three *ex vivo* models with two renal units measuring the puncture time from needle-skin contact until position of needle tip proved to be satisfactory according to the information from the user interface (Fig. 17.9a). Anatomical suitability of the puncture line is checked by fluoroscopy. Next the needle is guided to the tip of the ureteral catheter by viewing widgets I–III. Fine-tuning of insertion depth is assisted by calculating the distances. Success was verified by fluoroscopy (Fig. 17.9b). One hundred percent success was obtained after a maximum of two punctures (92 % after single attempt). Median distance to sensor was 1.8 mm; median duration of puncture was 15 s (Table 17.2). Learning phase required 30 punctures [22].

### EMT Tracking Using a Porcine In Vivo Model

Six anaesthetised female pigs underwent ureterorenoscopies to ascertain endoscopically the success of puncture (Fig. 17.10). Four punctures were performed by two surgeons in each pig: one in the kidney and one in the middle ureter, bilaterally. The number of attempts and time needed to evaluate the virtual trajectory and to perform the puncture were evaluated [26].

Overall, 24 punctures were performed without any complications. Surgeons required more time to evaluate the trajectory during ureteral puncture than the kidney (median 15 vs. 13 s, range 14–18 and 11–16 s, respectively, $p=0.1$). Median renal and ureteral puncture times were 19 and 51 s, respectively (range 14–45 and 45–67; $p=0.003$). Two attempts were needed to achieve a successful ureteral puncture (Table 17.2).

### Attitude Tracking for Ultrasound-Guided Puncture of a Renal Tumour

The idea of this technique is to use a motion tracking device to exactly determine the axis/localisation of the ultrasound probe in relation to the renal tumour. For this purpose the Nintendo WiiMote device is used which has incorporated an accelerometer with 3° of freedom (ADXL330)

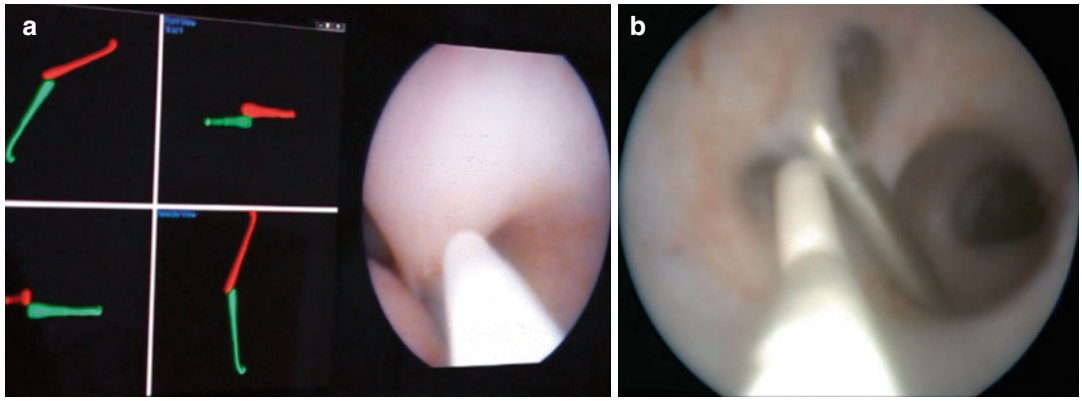


**Fig. 17.10** Experimental evaluation of electromagnetic tracking used for puncturing of the renal collecting system using an *ex vivo* model. (**a**) Control of the needle on the triple monitor which displays the position of needle (*red*) and ureteral catheter equipped with an electromagnetic sensor (*green*) in 3D. (**b**) Ureterorenoscopic verification of the successful puncture

(± 3 g with 10 % sensitivity), a wireless connection with other devices (Bluetooth system BCM2042), and an LED array-guiding device for visualisation of puncture angle: middle light = correct angle (Fig. 17.4). Using GlovePie software for programming the device and a self-made rigid plastic chassis for ultrasound probe enabled the surgeon to apply the attitude tracking to puncture a phantom and renal tumour: With the device, the position of the ultrasound scanner when showing the lateral borders of the target can be determined. Attitude tracking indicates the position of the probe when scanning exactly the middle of the target. The feasibility was evaluated in a phantom model and during central biopsy of 28 renal tumours prior to nephrectomy [31].

In the phantom, 40 punctures were performed revealing a mean distance from centre of 1.0 mm (SD 0.743 mm) with attitude tracking (average time – 7.2 s) compared to 3.20 mm (SD 2.38 mm) without tracking (average time – 5.3 s) (Table 17.2). In the biopsy study, precision evaluated by the pathologist showed a mean error of 1.8 mm with attitude tracking ($n = 16$) compared to a mean error of 4.7 mm in the controls ($n = 12$).

## Discussion

One of the most critical steps for various endourologic procedures in the upper urinary tract represents the ability to obtain an appropriate renal tract. Although fluoroscopy and ultrasound guidance provide well-established ways of percutaneous renal access, these interventions can be demanding, especially in unfavourable settings such as complex anatomy or in sophisticated surgery. Moreover, operator experience and routine have a significant impact on success and complication rates [1, 2, 4, 22, 26]. Several technical modifications have been developed to ease the procedure including optimised handling, use of mechanical arm [24], robot assistance [15, 16], or retrograde endoscopy-guided approaches [45, 46]. However, until now, none of these ideas has become routine, mainly because of high costs [19, 22].

All described projects underline the potential of navigation in percutaneous renal interventions. Actually, there are two main fields, puncture of the collecting system and renal biopsy. However, navigated focal therapy may be a further indication [34, 47]. Interestingly, surgical navigation has been already implemented in different lithotripters (Fig. 17.2) using either electromagnetic, optical, or acoustic tracking. All these systems are highly sophisticated and proven to be safe and effective in clinical use [10–13]. However, the requirements for adequate percutaneous renal access differ completely. For ESWL, respiratory movement of the kidney represents the main problem for effectively targeting the calculus, and it is generally accepted that about 10–20 % of the shock waves

will not hit the target. Percutaneous access to the kidney has to be as exact as possible, e.g. the puncture needle should enter the calyx at the fornix/papilla to minimise any trauma to the surrounding vasculature. Ideally, this should be accomplished in a single attempt. Organ shift and tissue deformation may significantly affect the puncture even under fluoroscopic or ultrasound guidance.

## Problems of Organ Shift and Tissue Deformation

Apart from neurosurgery and orthopaedic surgery, which are well suited due to the fixed anatomy, surgical navigation is mainly limited by the problems of organ shift and tissue deformation. For rigid organ interventions, target structures are assumed to be not deformable and to have constant spatial relationship to anatomical landmarks. In *soft tissue navigation*, all post-imaging changes of surgical anatomy due to organ shift and tissue deformation may add up directly to a target visualisation error. Continuous intraoperative navigation may overcome the constraints of organ shift and tissue deformation during surgery. However, it requires a constant recalculation of the recorded data for reliable accuracy. Soft tissue modelling methods, such as spline-based mathematical approaches or by use of biomechanical models, could be used for compensation of motion caused by heartbeat and respiration, which are most problematic concerning renal interventions [48]. However, at present systems this has not been realised.

Accordingly all navigation technologies have in common, that they deal with soft tissue deformation respectively with mobile organs due to respiratory movements. Even for rigid anatomy, errors of marker-based navigation systems may occur such as (i) fiducial localisation errors, (ii) fiducial registration errors, and (iii) target registration errors (TRE). TRE is the most important type of error, as it reflects the distance between an arbitrary point and its corresponding point in the registered space [20, 49].

## Real Requirements of the Surgeon on Navigation

On the other side, it has to be defined as to what type of information the surgeon needs at what step of the procedure. Moreover, it has to be clarified as to where the real problems lie during puncture. The following are some basic problems:

1. All real-time systems are not suitable to image and thus guide the needle continuously on its way to the target: *Ultrasound* shows the needle and target only, if the scanner, target, and needle are in-line. However, this ideal situation is limited by the fact that the ultrasound image of the target is impaired by overlying rib shadows or even bowel. Identification of the needle tip in the retroperitoneal space is difficult; it is only when the needle has entered the renal parenchyma is its visibility good, provided that the needle and ultrasound probe are in-line. *Fluoroscopy* shows the needle on its entire way to the kidney, however, only in 2D. Therefore, either ultrasound or rotation of the C-arm using bull's eye technique has been recommended. However, the oblique fluoroscopic beam results in a completely unusually image of the collecting system, making handling of the needle difficult for the surgeon.
2. All real-time systems lack the capability of showing anatomical details during puncture: *Ultrasound* may visualise the renal parenchyma and adjacent organs like the liver and spleen, but the renal collecting system can only be demonstrated in case of a dilated renal pelvis. The exact dimension and localisation of stones cannot be visualised. Fluoroscopy may visualise the entire collecting system if a retrograde pyelography with placement of a balloon-ureteral catheter has been performed. But the renal parenchyma remains invisible. The same applies to any adjacent organ and radiolucent calculi, whereas radiopaque calculi can be ideally displayed.
3. There is usually a significant amount of organ shift during puncture, which has to be visualised and thus compensated by the surgeon. Evidently, respiratory movement is

problematic in *extracorporeal shock wave lithotripsy* and can only be minimally compensated by use of a respiratory belt or respiratory-based shock wave application [8]. In *percutaneous puncture of the kidney*, a real-time imaging mode (2D fluoroscopy) is necessary to estimate the actual amount of movement of the kidney, but here again the movement can be kept minimal by stopping the respiration in end inspiration/expiration during the puncture.

4. All this results, even for an experienced surgeon, in the problem that regardless which imaging modality he uses, at a certain point of the puncture, the needle has to be advanced without adequate imaging of the anatomy/tissue. Based on his routine, this usually has no significant impact on the course of the case, but sometimes may result in severe problems, such as bleeding and transcolonic puncture. Apart from ultrasound and 2D fluoroscopy, there is no real-time 3D imaging mode available, since stereofluoroscopy could not be clinically established.

The ideal situation would be that like in laparoscopy, the surgeon could monitor the needle on its entire way to the target and be able to see the adjacent tissue. Evidently, this can only be accomplished by the implementation of augmented reality. However, there is also the *problem of real-time imaging*. Marker-based 3D segmentation using the iPad is based on CT, which cannot be obtained repeatedly during the case [24, 25]. However, the same applies to the use of a 3D C-arm and Uro Dyna-CT, even if both imaging modalities could be obtained repeatedly during the case [28, 29]. Since the organ is only minimally deformed when starting the puncture and organ shift can be monitored by 2D fluoroscopy, the need for continuous reevaluation may be limited. This applies also to robotic systems particularly when CT or MRI data are used [15, 16, 50]. In contrast, EMT tracking has the advantage to be a real-time mode but without imaging of the surrounding anatomy [22, 23, 26]. Based on this, the future may lie in the combination of different AR technologies.

## User Interface: Which Monitor, Which Device

3D visualisation is mandatory for adequate preoperative imaging and planning. Segmentation of data can offer more features such as volume or surface rendering. For percutaneous access to the kidney, such data are very helpful, particularly, when the anatomical structure cannot be directly identified by the standard real-time imaging mode, such as the colon during fluoroscopy or the entire collecting system during sonography.

In laparoscopy, such images can be directly superimposed on the video image. Ukimura et al. superimposed the course of the neurovascular bundle imaged by Duplex-TRUS on a 2D endoscopic image [40]. However, this was limited by the fact that usually a 2D video image is used and the superimposed image (=augmented reality) may disturb the view on anatomical detail. Based on this, we actually prefer during laparoscopy a two-screen navigation rather than the image-in-image technique.

In case of percutaneous renal access, the situation is different: A tablet (i.e. iPad) offers the unique advantage that virtual anatomy can be directly projected over the target area, and due to the camera function of the device, the surgeon can still watch his hands respectively the puncture needle (Fig. 17.7c). Attitude tracking just controls the position of the scanner, while EMT tracking uses a completely different VR monitor to display the position of the needle and EMT sensor (Fig. 17.10a). We anticipate that the combined use of image-guided systems would be ideal to navigate the needle to the target (Fig. 17.11).

## Specific Advantages of Image-Guided Surgery

Exact placement of percutaneous access is most important for a successful ergonomic procedure with minimal risk of complications. Ideally, in percutaneous nephrolithotripsy, this should result

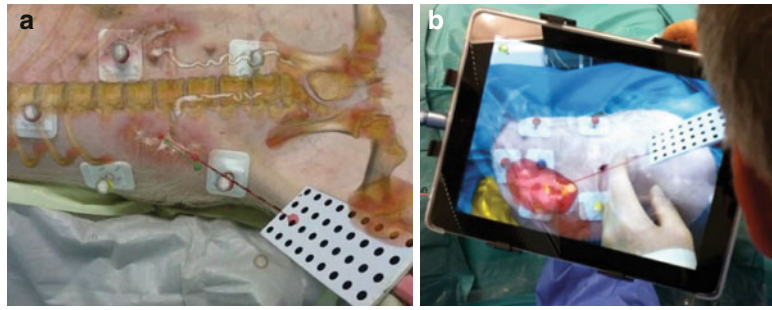


**Fig. 17.11** Combination of iPad-assisted marker-based navigation with tracking of puncture needle. (**a**) Experimental setup: The ideal puncture line (*green*) is displayed on the screen together with the real one (*red*). (**b**) Clinical pilot study showing the problem to get all markers (navigation aids and tablet attached to the needle) on the screen of the iPad without deteriorating the image quality of the CT data

in decrease of blood loss and together with the miniaturising of instruments to a reduction of nephrostomy time. Until now, intraoperative imaging is restricted to ultrasound or fluoroscopy, which could definitively not exactly display the papilla as target nor show anatomical details of surrounding organs. Direct endoscopy using miniaturised needle scopes also is not able to show any anatomical detail during puncturing [19]. Surgical navigation using AR, however, should be able to visualise for the surgeon the exact position of the needle/instruments/nephroscope in relation to the renal parenchyma, collecting system, stones, and organs. Moreover, in more complex cases of nephrolithiasis requiring multiple access points, the optimal position and orientation of puncture sites can be simulated and intraoperatively calculated. Of course, there are several restrictions; for example, the movement of bowel depending on the positioning of the patient might be difficult to assess and to simulate by tissue modelling models.

## Perspectives

The early applications of new imaging systems for soft tissue navigation are promising. However, these are all only first steps in the direction of image-guided surgery. With respect to marker-based navigation and tracking, anatomical landmarks can be spotted in both medical image and tracking device data or the characteristic surface of organs or body parts (i.e. kidney, face). In such cases preoperatively attached navigation aids may be omitted. Moreover, attitude tracking may be also used to evaluate the performance of the trainee (skill assessment [42, 51]).

The next steps may include the use of hybrid techniques of navigation such as (1) the combination of marker-based iPad navigation with marker-based navigation of the puncture needle (Fig. 17.11) or electromagnetic tracking, (2) the combination of optical with marker-based endoscopic tracking, and (3) the combination of Uro Dyna-CT with marker-based endoscopic navigation. Evidently, much more options of tracking combinations might be tested in the future.

### Conclusions

Navigation and tracking techniques have been already used in various indications in the last century, mainly pioneered in Europe. However, recent improvement in information technology substantially alleviated the implementation of pre- and intraoperative imaging on the screen during minimally invasive surgery in urology. Intraoperative navigation can be very helpful during percutaneous puncture of the collecting system and biopsy of a renal tumour using various tracking techniques. The combination of different tracking techniques may further improve this interesting addition to percutaneous renal surgery.

## References


1. Michel MS, Trojan L, Rassweiler JJ. Complications in percutaneous nephrolithotomy. Eur Urol. 2007;51: 899–906.
2. Alken P, Hutschereiter G, Günther R, Marberger M. Percutaneous stone manipulation. J Urol. 1981;125: 463–6.
3. Rassweiler J, Gumpinger R, Miller K, Hölzermann F, Eisenberger F. Multimodal treatment (Extracorporeal shock wave lithotripsy and endourology) of complicated renal stone disease. Eur Urol. 1986;12:294–304.
4. Rassweiler JJ, Renner C, Eisenberger F. Management of staghorn calculi analysis after 250 cases. Braz J Urol. 2000;26:463–78.
5. Desai M. Ultrasonography-guided punctures – with and without puncture guide. J Endourol. 2009;23: 1641–3.
6. Frede T, Hatzinger M, Rassweiler J. Ultrasound in endourology. J Endourol. 2001;15:3–16.
7. Eisenberger F, Gumpinger R, Miller K, Horbaschek H, Sklebitz H. Stereoroentgenology in endourology. Urologe A. 1985;24:342–5.
8. Chaussy C, Schmiedt E, Jocham D, Brendel W, Forssmann B, Walther V. First clinical experience with extracorporeally induced destruction of kidney stones by shock waves. J Urol. 1982;127:417–20.
9. Fuchs G, Miller K, Rassweiler J, Eisenberger F. Extracorporeal shock wave lithotripsy: one-year experience with the Dornier lithotripter. Eur Urol. 1985;11:145–9.
10. Rassweiler J, Westhauser A, Bub P, Eisenberger F. Second-generation lithotripters: a comparative study. J Endourol. 1988;2:193–203.
11. Rassweiler J, Köhrmann KU, Alken P. ESWL, including imaging. Curr Opin Urol. 1992;2:291–9.
12. Rassweiler J, Henkel TO, Köhrmann KU, Potempa D, Jünemann KP, Alken P. Lithotripter technology: present and future. J Endourol. 1992;6:1–13.
13. Rassweiler JJ, Knoll T, Köhrmann KU, McAteer JA, Cleveland RO, Bailey MR, Chaussy C. Shock wave technology and application: an update. Eur Urol. 2011; 59:784–96.
14. Lazarus J, Williams J. The locator: novel percutaneous nephrolithotomy apparatus to aid collecting system puncture – a preliminary report. J Endourol. 2011;25:747–50.
15. Su LM, Stoianovici D, Jarrett TW, Patriciu A, Roberts WW, Cadeddu JA, Ramakumar S, Solomon SB, Kavoussi LR. Robotic percutaneous access to the kidney: comparison with standard manual access. J Endourol. 2002;16:471–5.
16. Pollok R, Mozer P, Guzzo TJ, Marx J, Matlaga B, Petrisor D, Vigaru B, Badaan S, Stoianovici D, Allaf ME. Prospects in percutaneous ablative targeting: comparison of a computer-assisted navigation system and the AcuBot robotic system. J Endourol. 2010; 24:1269–72.
17. Bale R, Widmann G. Navigated CT-guided interventions. Minim Invasive Surg. 2007;16:196–204.
18. Ghani KR, Patel U, Anson K. Computed tomography for percutaneous renal access. J Endourol. 2009;23: 1633–9.
19. Rodrigues PL, Rodrigues NF, Fonseca J, Lima E, Vilaca JL. Kidney targeting and puncturing during percutaneous nephrolithotomy: recent advances and future perspectives. J Endourol. 2013;27:826–34.
20. Baumhauer M, Feuerstein M, Meinzer HP, Rassweiler J. Navigation in endoscopic soft tissue surgery – perspectives and limitations. J Endourol. 2008;22:751–66.
21. Teber D, Baumhauer M, Guven EO, Rassweiler J. Robotics and imaging in urological surgery. Curr Opin Urol. 2009;19:108–13.
22. Huber J, Wegner I, Meinzer HP, Hallscheidt P, Hadaschick B, Pahernik S, Hohenfellner M. Navigated renal access using electromagnetic tracking: an initial experience. Surg Endosc. 2011;25:1307–12.
23. Wegner I, Teber D, Hadaschick B, Pahernik S, Hohenfellner M, Meinzer H-P, Huber J. Pitfalls of electromagnetic tracking in clinical routine using multiple or adjacent sensors. Int J Med Robot Comput Assist Surg. 2013;9(3):268–73.
24. Rassweiler JJ, Müller M, Fangerau M, Klein J, Goezen AS, Pereira P, Meinzer HP, Teber D. iPad-assisted percutaneous access to the kidney using marker-based navigation: initial clinical experience. Eur Urol. 2011;61:628–31.
25. Müller M, Rassweiler M-C, Klein J, Seitel A, Gondam M, Baumhauer M, Teber D, Rassweiler JJ, Meinzer H-P, Maier-Hein L. Mobile augmented reality for computer-assisted percutaneous nephrolithotomy. Int J Comput Assist Radiol Surg. 2013;8(4): 663–75.
26. Rodrigues PL, Vilaça JL, Oliveira C, Cicione A, Rassweiler J, Fonseca J, Rodrigues NF, Correia-Pinto J, Lima E. Collecting system percutaneous access using real-time tracking sensors: first pig model in vivo experience. J Urol. 2013;190(5):1932–7.
27. Kroeze SG, Huisman M, Verkoojen HM, van Diest PJ, Ruud Bosch JL, van den Bosch MA. Real time 3D fluoroscopy-guided large core needle biopsy of renal masses: a critical early evaluation according to the IDEAL recommendations. Cardiovasc Intervent Radiol. 2012;35(3):680–5.
28. Ritter M, Rassweiler MC, Häcker A, Michel MS. Laser-guided percutaneous kidney access with the Uro Dyna-CT: first experience of three-dimensional puncture planning with an ex vivo model. World J Urol. 2013;31(5):1147–51.
29. Rassweiler MC, Ritter M, Michel MS, Häcker A. Influence of endourological devices on 3D reconstruction image quality using Uro-Dyna-CT. World J Urol. 2013;31(5):1291–5.
30. Mozer P, Conort P, Leroy A, Baumann M, Payan Y, Troccaz J, Chartier-Kastler E, Richard F. Aid to percutaneous renal access by virtual projection of the

ultrasound puncture tract onto fluoroscopic images. J Endourol. 2007;21:460–5.
31. Petrut B, Hogea M, Schitcu V. Attitude tracking device for improving precision of ultrasound-guided percutaneous procedures. J. Endourol. 2012;26(Suppl): Abstract No. VP-04-08.
32. Meyer BC, Peter O, Nagel M, Hoheisel M, Frericks BB, Wolf K-J, Wacker FK. Electromagnetic field-based navigation for percutaneous procedures on C-arm CT: experimental evaluation and clinical application. Eur Radiol. 2008;18:2855–64.
33. Braak SJ, van Strijen MJL, van Leersum M, van Es HW, van Heesewijk JPM. Real-time 3D fluoroscopy guidance during needle interventions: technique, accuracy, and feasibility. AJR Am J Roentgenol. 2010;194:W445–51.
34. Sommer CM, Lemm G, Hohenstein E, Stampfl U, Bellemann N, Teber D, Rassweiler J, Kauczor HU, Radeleff BA, Pereira PL. Bipolar versus multipolar radiofrequency (RF) ablation fort the treatment of renal cell carcinoma: differences in technical and clinical parameters. Int J Hyperthermia. 2013;29:21–9.
35. Teber D, Guven S, Simpfendörfer T, Baumhauer M, Guven EO, Yencilek F, Gözen AS, Rassweiler J. Augmented reality: a new tool to improve surgical accuracy during laparoscopic partial nephrectomy? Preliminary in vitro and in vivo results. Eur Urol. 2009;56:332–8.
36. Simpfendörfer T, Baumhauer M, Müller M, Gutt CN, Meinzer HP, Rassweiler JJ, Guven S, Teber D. Augmented reality visualization during laparoscopic radical prostatectomy. J Endourol. 2011;2011(25):1841–5.
37. Türk C, Knoll T, Petrik A, Sarica K, Skolarikos A, Straub M, Seitz C. EAU-guidelines on urolithiasis 2013. In: Presented at EAU-congress, Milan, Mar 2013.
38. Parekattil S, Yeung LL, Su LM. Intraoperative tissue characterization and imaging. Urol Clin North Am. 2009;36:213–21.
39. Su L-M, Vagvolgyi BP, Agarwal R, Reiley CE, Taylor RH, Hager GD. Augmented reality during robot-assisted laparoscopic partial nephrectomy: toward real-time 3D-CT to stereoscopic video registration. Urology. 2009;73:896–900.
40. Ukimura O, Gill IS. Image-fusion, augmented reality and predictive surgical navigation. Urol Clin North Am. 2009;36:115–23.
41. Kindratenko VV. A survey of electromagnetic position tracker calibration techniques. Virtual Reality. 2000;5:169–82.
42. Chmarra MK, Gimbergen CA, Dankelman J. Systems for tracking minimally invasive surgical instruments. Minim Invasive Ther Allied Technol. 2007;16:320–40.
43. Teber D, Simpfendörfer T, Guven S, Baumhauer M, Gözen AS, Rassweiler J. In-vitro evaluation of a soft tissue navigation system for laparoscopic prostatectomy. J Endourol. 2010;24:1487–91.
44. Nozaki T, Fujiuchi Y, Komiya A, Fuse H. Efficacy of DynaCT for surgical navigation during complex laparoscopic surgery: an initial experience. Surg Endosc. 2013;27:903–9.
45. Wynberg JB, Borin JF, Vicena JZ, Hannosh V, Salmon SA. Flexible ureteroscopy directed retrograde nephrostomy for percutaneous nephrolithotomy: description of a technique. J Endourol. 2012;26:1268–74.
46. Kawahara T, Ito H, Terao H, Yoshida M, Ogawa T, Uemura H, Kubota Y, Matsuzaki J. Ureteroscopy assisted retrograde nephrostomy: a new technique for percutaneous nephrolithotomy (PCNL). BJU Int. 2011;110:588–90.
47. Young JL, Khanifar E, Narula N, Ortiz-Vanderdys CG, Kolla SB, Pick DL, Sountoulides PG, Kaufmann OG, Osann KE, Huynh VB, Kaplan AG, Andrade LA, Louie MK, McDougall EM, Clayman RV. Optimal freeze cycle length for renal cryotherapy. J Urol. 2011; 186:238–88.
48. Carter TJ, Sermesant M, Cash DM, Barratt DC, Tanner C, Hawkes DJ. Application of soft tissue modelling to image-guided surgery. Med Eng Phys. 2005;27: 893–909.
49. Rassweiler J, Baumhauer M, Weickert U, Meinzer HP, Teber D, Su LM, Patel VR. The role of imaging and navigation for natural orifice translumenal endoscopic surgery. J Endourol. 2009;23:793–802.
50. Kim C, Chang D, Petrisor D, Chirikjian G, Han M, Stoianovici D. Ultrasound probe and needle guide calibration for robotic ultrasound scanning and needle targeting. IEEE Trans Biomed Eng. 2013;60:1728–34.
51. De la Rosette JJ, Laguna MP, Rassweiler JJ, Conort P. Training in percutaneous nephrolithotomy – a critical review. Eur Urol. 2008;54:994–1003.

# Image Guidance in Robotic-Assisted Renal Surgery

18

S. Duke Herrell, Robert L. Galloway Jr., and Michael I. Miga

The field of urologic surgery has been at the forefront of the adoption of new technology that lessens the invasiveness of surgery and improves patient outcomes over the past several decades. Important surgical paradigm changes include the replacement of open stone surgery with extracorporeal shock wave lithotripsy and endoscopic stone treatment; replacement of open prostate, bladder, and kidney surgeries for both benign and malignant disease with endoscopic and laparoscopic minimally invasive techniques; and the defining role of the field of urology in leading the adoption of surgical robotics to both advance the performance of and widespread adoption of minimally invasive surgery. In each of these cases, new technology and surgical device engineering combined with visionary urologic surgeons served to benefit patients, advance the field, and revolutionize, augment, or in some cases eliminate what had been a dominant "gold standard" surgical approach. At present, we stand as a field on the edge of another potential paradigm shift, the incorporation of advances in intraoperative imaging technologies, which in many cases may be combined with the advances in robotic surgical and interventional platforms, to allow for reductions in invasiveness and improvements in outcomes the likes of which our surgical predecessors could only dream.

For urologic surgeons, new modalities such as minimally invasive surgery, percutaneous and laparoscopic ablation, and robotics are revolutionizing the treatment of the majority of urologic procedures. Image-guided surgery (IGS) incorporates active or "interactive" preoperative imaging to augment the surgeon's knowledge, understanding, and guidance and may permit increased accuracy, precision, and safety. IGS should soon augment the "reality" of the majority of these procedures. IGS has the potential to add additional safety and comfort for the surgeon

S.D. Herrell, MD FACS (✉)
Department of Urologic Surgery,
Vanderbilt University Medical Center,
MCN A 1302, Nashville, TN 37232-2765, USA

Department of Biomedical Engineering,
Vanderbilt University, MCN A 1302,
Nashville, TN 37232-2765, USA
e-mail: duke.herrell@vanderbilt.edu

R.L. Galloway Jr., PhD
Department of Biomedical Engineering,
Vanderbilt University Medical Center,
MCN A 1302, Nashville, TN 37232-2765, USA

Department of Urologic Surgery, Vanderbilt
University Medical Center, Nashville, TN, USA

Department of Neurosurgery,
Vanderbilt University Medical Center,
Nashville, TN, USA

M.I. Miga, PhD
Department of Biomedical Engineering,
Vanderbilt University, Nashville, TN, USA

Department of Neurological Surgery,
Vanderbilt University, Nashville, TN, USA

Department of Radiology and Radiological Sciences,
Vanderbilt University, Nashville, TN, USA
e-mail: michael.i.miga@vanderbilt.edu

J.C. Liao, L.-M. Su (eds.), *Advances in Image-Guided Urologic Surgery*,
DOI 10.1007/978-1-4939-1450-0_18, 

and improve outcomes for the patient. This chapter will examine the basic methodology, current research, and potential applications of image-guided surgery and the potential for intersection with urologic robotic surgery.

## Principles of Image-Guided Surgery (IGS): Overview

IGS can be divided into two broad categories: Type 1, which uses active intraoperative imaging with the real-time production of imaging (e.g., fluoroscopy, ultrasound, CT, or MRI) requiring OR-based scanners, special instrumentation, and auxiliary personnel. While ultrasound and fluoroscopy are quite familiar to the practicing urologic surgeon, intraoperative CT and MRI are mainly present in other surgical disciplines and have been in limited to primarily research use. High-definition-quality axial imaging, such as CT and MRI, is typically preferred by surgeons as an anatomical guide map and basis for three-dimensional reconstructions for guidance and reference. Units such as intraoperative MRI (iMRI) or intraoperative CT scan (iCT) have been studied and have grown in popularity in some fields such as neurosurgery and orthopedics. Active intraoperative scanning, which originally appeared as intraoperative MRI for neurosurgery, has been studied extensively at some centers, but is cost prohibitive for widespread development and requires specialized operating room construction and instrumentation. However, other types of intraoperative imaging, such as CT, may be showing a surge in interest for a variety of fields. Scanner technologies, especially CT, have reduced in cost and portable small footprint units have emerged. Uses include minimally invasive spine surgery, endovascular techniques, assessment of cranial and neurosurgical intraoperative brain surgical field changes, and ablation planning and performance. Investigators at our university have shown that the current limitations for portable CT units include a lack of comparable soft tissue discrimination for the kidney and a lack of optimal spatial accuracy due to design for slice acquisition [1].

The alternative type of image guidance uses preoperatively obtained images for that specific patient, which are then actively and accurately incorporated into the workflow and the visual display of the operation. We refer to this as Type 2 IGS. The images are segmented to show critical structure mapping spatially and are used to map surgical tool position, location, and orientation actively during the procedure and are not used simply as a typical "reference atlas." This type of surgical navigation includes concepts such as image registration, virtual reality/augmented reality, and deformation correction. Images are registered or coordinated with the specific patient's intraoperative anatomy to actively display organ, instrumentation, and vital structure location, potentially including deep anatomy, vascular structures, and tumor margins prior to both standard optical visualization and incision or penetration.

## Principles of IGS: Registration, Localization, Targets, and Error

### Registration

The use of preoperative imaging for IGS requires a coordination (determining mathematical relationship transformation) of three-dimensional (3D) image space to three-dimensional patient anatomy called *registration* [2]. This may be done based on points, surfaces, or volumes. While many engineering concepts are beyond the scope of this chapter, an understanding of some basic terminology and technologies is necessary.

Basic registration is based on aligning imaging and true physical spatial anatomy into one all encompassing three-dimensional coordinate system space. Using the preoperatively obtained axial images, key structures, such as vascular and internal organ structures, tumor margins, and surfaces, have typically been identified, mapped, and color-coded based on the data from the axial imaging (segmentation). These critical structure maps of the patient's specific anatomy are then reassembled into a tomographic three-dimensional display form which highlights the geometric

interrelations and spatial locations based on the original imaging data (3D reconstruction). Alignment of the three-dimensional imaging map and the three-dimensional patient physical anatomical space can be performed utilizing specific exact intrinsic anatomical landmarks (points) or markers (fiducials) that are seen precisely on both the image study and can be localized on or in the patient. Once three-dimensional image map to patient anatomy alignment (registration) is performed, typically by high-speed computer algorithm, the subsurface anatomy and location of important surrounding structures can be displayed to the surgeon on a video screen or as a virtual projected overlay onto the patient (the so-called augmented virtual reality). If the fiducials are in a rigid geometric position, this mathematical transformation is relatively simple (rigid registration). A well-known early example of this would include stereotactic brain biopsy and needle intervention.

Central to any image-guided surgery system is the process of registration, which is the determination of the mathematical relationship between objects in the tomograms and their physical locations in the operating room. Point-based registration has the critical advantage of known correspondence, which each point in imaging space is matched to its location in the physical space. This allows both the use of closed form least square error solutions [3, 4] and the ability to assess the quality of the registration by designating selected points as targets. The points used in the creation of the transformation matrix are known as fiducials. If they are native to the anatomy, they are intrinsic fiducials; if they are attached to the patient, they are extrinsic fiducials. A target is a point with known locations in both spaces, which is not used in the creation of the transformation matrix, such as the center of a tumor or in the research arena another known defined point in both the imaging and patient anatomy. The difference between the transformed location of a target into the second space and its actual location in that space is the target registration error (TRE) and is a true assessment of registration quality.

The second form of image space to physical space registration is to designate a surface in one space (generally physical space) and then match it to a second surface which has been extracted from preoperative images. While a number of techniques have been used for establishing the mathematical match, they are almost all based on the iterative closest point (ICP) method put forth by Besl and McKay [5]. As the title suggests, this is a computer-based repetitive iterative process, and the focus of the majority of the development of algorithm has been to speed the convergence (best fit for the limits of number of iterations/time).

Soft tissue organs, such as abdominal and thoracic, provide a large number of engineering challenges for IGS. First, these organs typically do not possess easily identifiable specific point landmarks on their surface to allow for simple point-to-point-based registration as they tend to be smooth and rounded. As such, more advanced methods of registration alignment are required such as using a captured topographic surface and then matching to the surface which has been extracted from preoperative images (*segmentation*). In this scenario, large numbers of surface point coordinates are necessary. Such surfaces (clouds of points) can be captured by sweeping a tracked tool over the surface or assembling a surface utilizing a reflected laser beam geometry (laser range scanner). This captured surface is sometimes referred to as a surface "patch." These two surfaces – one from image space and one from physical space – can be registered using more advanced surface registration techniques. Complicating matters, these organs are subject to marked *deformation* from a variety of sources including respiratory and patient motion, changes to perfusion, operative manipulation of exposure and dissection, and even penetration with a needle such as for biopsy or ablation.

## Localization and Tracking Techniques

In many instances, the surgeon would also like to display surgical tool tip location(s) (*localization*) within this display and this requires 3D tool tracking (localizers). The first two image-guided surgery systems [6, 7] used different classes of

localizers: triangulation and articulated arms. Both have been used in abdominal surgery.

An articulated arm generally uses fixed length members mounted on revolute joints. By knowing the length of the members and measuring the angles, the end tip position and orientation can be geometrically calculated. The articulated arm most in use in modern surgery is the da Vinci patient side manipulator arm. Well-known advantages of the da Vinci include the ability to potentially enable complex minimally invasive approaches, the presence of wristed instrumentation which eases the complexities of suturing and dissecting angles, a stereoscopic camera system, tremor dampening, and placing control of an additional manipulation and retraction arm as well as the camera under surgeon control. The disadvantages are large purchase and operating costs as well as the limitations of any minimally invasive approach. Some of these limitations are common to both open surgery and MIS and are due to the nature of the visualization. The user cannot see beyond the imaging cone of the laparoscope or their own vision and cannot preemptively see inside a solid organ to locate internal structures. Integration of image guidance has begun in da Vinci surgery [8–10].

There are two types of localization and tracking systems for tools at present, optical and electromagnetic. The dominant choice for localizer systems in the past has been optical triangulation systems such as those from Northern Digital Inc. (NDI, Waterloo, Ontario, CA) and Image Guided Technologies (now owned by Stryker, Kalamazoo, MI). These devices locate either optical sources or optical reflectors placed on the proximal end of a rigid tool. Optical tracking utilizes a specialized camera system which can repetitively determine the tool tip position utilizing the recording of geometric alignment of special "trackers" (geometrically arranged optical sources or optical reflectors) placed on the proximal end of a rigid tool. These systems have a high accuracy (submillimeter) but require line of sight between the camera and trackers, which can be difficult to obtain in the busy operating room environment. By measuring the optical tracker geometric alignment and size from two angles and known length of the tool and tip, the tool's position and orientation and the location of the tip of a rigid tool can be calculated. Optical localizers have been used in both liver surgery [11, 12] and kidney surgery [13].

Electromagnetic triangulation systems such as the Aurora (NDI) have an appeal of not requiring line of sight between localizer and tool and thus are amenable to use with flexible tools. Electromagnetic (EM) tracking utilizes a magnetic field sensor device and wire-based electromagnetic tracker on the patient and instruments allowing tracking actively by the system. Advantages of the system include no need for line of sight and good accuracy; however, variations in electromagnetic field strength and the presence of large metallic (ferromagnetic) objects can result in error. The challenge with such systems is that their accuracy falls off quickly as tool moves from the ideal center of localization [14]. However, for applications not needing millimeter-scale accuracy, the advantages may outweigh the difficulties. Magnetically tracked applications have been tried in the liver [15] and applications for the kidney may soon emerge.

## Target and Registration Error

A "target" is a point with known locations in both spaces, which is not used in the creation of the transformation matrix. The difference between the transformed location and its actual location in that space is the *target registration error* (*TRE*) and is a true assessment of registration quality [16]. However, this metric is only available where points can be unambiguously identified in both spaces. An example would be the rigid registration of the skull for neurosurgical IGS. Because the external surface of the head is available to the surgeon and stable fiducials such as screws can be inserted and visualized in the imaging prior to bringing the patient to the OR, point-based fiducials were the norm. Other approaches include using known bony landmarks, skin adhesive fiducials, or facial surface scanning. This is not possible in abdominal organs although a group of German researchers

has tried using tracked ultrasound imaging systems to determine the location of vascular features such as vessel bifurcations as fiducials [17, 18]. Therefore, most of the image-guided liver and kidney surgery work has been based on surface registrations [19, 20]. With surface-based registration techniques, considerable challenges remain for the assessment of registration quality. These challenges cluster around the concepts of exposure, deformation, and validation [21].

Intuitively, the more complete the surface description, the greater confidence one would have in the quality of the expected registration. However, even in open organ surgery, examples of which are open approach kidney surgery and liver IGS, it is difficult to get access to the whole anterior surface of the organ especially if one uses a laser surface scanner [22] in the attempt to get a high-density spatial sample. Because surface registrations lack point correspondence, they use a metric such as the distance between a point on one surface to the closest point on the other surface. This makes them vulnerable to surfaces with high-rotational symmetries, i.e., the fit can "slide" between locations which generate similar metrics. Given that the biology of organs produces rounded structures, this is an ongoing challenge. One approach is to use some a priori knowledge about the surfaces to provide additional metrics to help "lock in" the registration. One approach for this has been the designation of structures which can be guaranteed to be visible in surgery as "salient features" [23]. This methodology either by itself or in conjunction with a surface can provide similar quality registrations while reducing the chances for error.

In the kidney, there are two exposure problems. The kidney is veiled with perirenal fat which must be removed to capture the kidney surface cloud of points in physical patient space. This is true in either open or minimally invasive cases. The second exposure problem is rapid adoption of minimally invasive approaches as current devices to rapidly capture a large surface patch with the limits of MIS access for registration are limited, but under intense investigation in our laboratory. Benincasa et al. [24] explored the relationship between the registration accuracy and the percentage of exposed surface in kidney registration.

The second challenge to surface-based registration is the deformation of organs during the surgical process. While these deformations may arise from patient pose (position) and organ motion due to breathing, most are caused by the surgical intervention. In kidney surgery, the organ is generally mobilized prior to the surgical intervention into the parenchyma. The act of mobilization is the removal of surrounding attachments of structures, such as overlying bowel and fat and supporting structures. The intent of this process is to free the kidney to both ease of surgical approach and allow access to the major vessels. However, at the start of a surgical tumor removal procedure in the kidney, the renal artery is often clamped to minimize blood loss during the surgery. This results in a loss of turgor in the kidney and a small shape change [25]. Solutions to this are discussed in the Correction section below.

The final challenge in surface-based organ registration is that of validation. As mentioned earlier, surface-based registrations lack one-to-one correspondence and are sensitive to rotationally symmetric surfaces. Therefore the value on which the ICP regresses, mean closest point distance, provides no information on the quality of the registration. Additionally, the lack of a one-to-one correspondence means that a target registration error (TRE) cannot be calculated. Some ongoing work centers on finding a single intrinsic point to be used as a target for assessment. Other works include a statistical analysis to provide a confidence interval based on surface characteristics such as changes in surface curvature.

## Intraoperative IGS Display

One of the most underappreciated challenges of surgical guidance is the intraoperative display of surgical position and orientation during the case, similar to the challenges faced by pilots to incorporate both visual and complex

electronic informational display during active control of flight. The display is attempting to provide seven-dimensional information (X, Y, Z, yaw, pitch, roll, and time) on 2D temporally active display. If the data is presented as a binocular pairing, some idea of the relative positions of objects can be realized but at the cost of the information bandwidth, with potential stress to the operator. An additional hurdle is how to convey meaningful and accurate information to the surgeon in a distracting and potentially stressful environment. Since the exact information needed cannot be displayed, then the image-guided surgical displays are assistive and complement surgical knowledge and intuition. Two of the earliest image-guided surgery systems used a two-over-two display of the three cardinal image slice directions (transverse, sagittal, and coronal) linked to the tracked neurosurgical surgical tool tip. This allowed surgeons to see where motion in one of those planes would take them. By using cardinal planes, the images were presented in a manner familiar to the surgeon allowing for rapid mental processing. Other techniques included reslicing the tomographic images along the plane perpendicular to the point tool or providing the information as cut planes in a rendered image. Having multiple image modalities and image sets (e.g., CT, MRI, PET, and SPECT) increases the complexity. Various fusion techniques have been tried but are rarely adopted by surgeons over concerns regarding intraoperative confusion [26].

## Intraoperative Imaging

As stated earlier, intraoperative imaging can range from MRI, fluoroscopy, and cone beam CT to ultrasound and standard visual endoscopy. No single intraoperative imaging modality has proven to be the answer to operative guidance as each has strengths and weaknesses. Intraoperative MRI provides impressive imaging, but is both costly and a major intrusion into the surgical process, necessitating huge OR construction, specialized non-ferromagnetic instrumentation and equipment, etc. Most current fluoroscopy is low cost and familiar to urologists and surgeons, but fails to provide soft tissue discrimination and has radiation risk. New developments such as flat panel detector digital C-arms allow for some axial slice imaging and three-dimensional reconstructions but seem limited for soft tissue applications and discrimination at present. CT is the most familiar and high quality for urologic surgeons, but intraoperative CT involves significant cost, radiation risk to the patient and OR staff, as well as difficulties with intraoperative workflow. Ultrasound is familiar and growing in application for robotic and laparoscopic use; however, US natively a two-dimensional imaging format, requires extra ports and personnel, can be difficult to identify and maintain key structures in accurate relations and may fail for isoechoic lesions. Endoscopy provides real-time color information but only in a cone directed from the tip of the "scope," cannot "seen" inside solid organs, and can be obscured by a bloody surgical field.

By combining real-time intraoperative visual imaging (optical/camera) with high-resolution 3D preoperative tomographic imaging information presented in an accurately registered and surgeon friendly context, the strengths of both can be preserved and the weaknesses mitigated. As minimally invasive approaches decrease in access and field of vision, such as LESS and NOTES, such surgical navigation techniques may be critical.

There is a final form of surgical display which does not require a new form of image, rather it uses a derived type of image and that is a rendered display. In such a display, the structures of surgical interest, organ outlines, tumor margins, and vascular structures, are localized in the gray-scale tomograms and their image values are replaced with structure labels. Standard computer graphic routines can then take these mapped labels and display them as interactive structures. Visual clues can be provided by changing the color and opacity of the display. Figure 18.1 shows a rendered IGS liver case with tumors, vascular structures, and a preoperatively planned surgical resection plane.

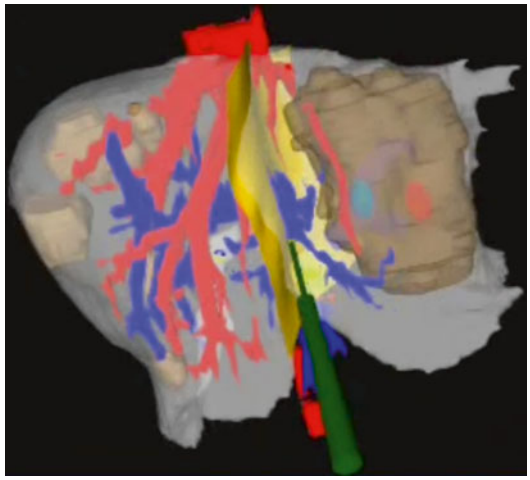

**Fig. 18.1** Rendered liver in intraoperative display. In a fully realized abdominal image-guided system such as the one shown here, the relative position of a surgical tool (shown in *green*) can be interactively displayed along with anatomical structures (*red* arteries, *blue* veins, and *gray* liver parenchyma); lesions (shown in *brown*) and preoperative planning such as the gold preplanned resection plane (Courtesy of Pathfinder Technologies, Nashville, TN, USA)

Such displays are compelling, they are easy to understand, they can be rotated to the surgeon's desired or optimal viewpoint, and structures can be displayed or not as required by the case. In addition, they not only provide location but orientation information and depth information via shading. However, such displays are dependent on the validity of the segmentation algorithm used to define the outline of the structures and thus can provide both potential benefit and risk.

## Correcting Positional Display Errors due to Perioperative Deformation

In the past, the translation of image-guided surgery techniques to the abdominal environment has been limited due to the presence of perioperative deformation. As a result, the most widely used intraoperative guidance approaches for abdominal have been active imaging with the use of ultrasound (US) or visual laparoscopic imaging. The integration of preoperative imaging and planning data for active intraoperative guidance has only recently begun to be commercialized.

In recent reports, soft tissue deformation during liver resection has been documented with intraoperative computed tomography (iCT) and has demonstrated significant effects [27]. While intraoperative magnetic resonance (iMR) and iCT are available, these approaches are cumbersome, incur radiation dose in the latter, and are not economically scalable for many medical centers. A CT-to-ultrasound (US) vessel-based nonrigid registration system for providing the link between image and physical space has been described [28]. While successful, the OR workflow would seem to be a challenge as it requires the identification of as many vascular targets as possible with tracked ultrasound and then determination of corresponding targets within the CT. While the subsurface information would be valuable for nonrigid deformation correction, there is a significant likelihood of misidentification in highly vascularized organs such as the liver and kidney, and the encumbrance of the technique may challenge adoption.

Given the nature of abdominal procedures, the need to compensate for deformation is evident and the requirements for compensation need to be balanced with workflow and accuracy needs. As an example, presentation for open kidney and liver surgery (and even laparoscopic to a degree) involves significant organ distortion prior to the ability to resect or even collect geometric data. However, considerable exposure of the organ (as opposed to intracranial neurosurgery) is afforded for understanding surgical presentation. In partial nephrectomy, the renal artery and potentially the renal vein are clamped to prevent excessive blood loss during resection. This creates a state of turgor within the organ that is different than the preoperative image counterpart. Upon resection, significant drainage from the cortex and medulla regions can ensue and cause significant shape changes. In both of these examples, the surgical characteristics serve as constraints to data acquisition and guidance procedure execution. As the field of image guidance moves forward, it will be

continually evolving to solve new challenges in nonrigid registration.

Over the past several years, approaches to deformation correction for abdominal procedures are being achieved that use sparse intraoperative surface data followed by controlled extrapolative predictions based on computer models [29].

The basic approaches begin with an initial rigid body registration usually performed using traditional [30] or weighted surface registration methods [23]. Once achieved, early correction methods focused at calculating a correspondence between surfaces acquired intraoperatively and their CT/MRI segmented counterparts, and these would be used as boundary conditions in a finite element model derived from the segmented organ in image space [22, 31]. The result could then be used to modify the shape of the CT/MRI organ to match the intraoperative state. While this does provide some improvement, in the "boundary" regions that immediately flank the intraoperative surface, the deformations often look somewhat distorted. In more recent work, efforts to extrapolative methods have been investigated involving iteratively fitting an average shape model to the intraoperatively deformed organ, a shape-based method called the iterative closest atlas (ICAt) technique, and systematically fit a constructed shape by extracting a weighted combination of precomputed shapes [32]. This method precomputes the shapes associated with deformation using a finite element model which allowed for rapid registration intraoperatively. While preliminary results were encouraging, the atlas shape models were challenging to generate for surgical data. There are still powerful aspects to this work we are investigating and such methods proposed must be thoughtfully designed with respect to surgical workflow and speed of translation. Solutions that do not accommodate workflow and are overly encumbered require too much attention from the surgeon and as a result are not easily adopted.

One of the noted drawbacks to an ICP-driven surface registration is that they are sensitive to rotational symmetries and biology tends to create smoothly curved surfaces. Thus, an ICP-driven surface registration can "slide" to incorrect location reducing the robustness of the registration methodology. To address this issue we elected to capture rough designations of important and identifiable "salient" features such as the renal hilum. In the clinical open liver surgery, "salient features" were weighted with the surface to add information to the registration process. Mean error dropped from 24 to 3.6 mm and the standard deviation from 23 to 1.0 mm [23].

## Intraoperative Image-Guided Kidney Partial Nephrectomy

Bringing image guidance to the kidney poses some specific challenges. Recent studies have demonstrated that a partial nephrectomy, either open or MIS, is an effective procedure for renal cell carcinoma and is especially applicable for tumors less than 4–7 cm. In addition to providing equivalent oncologic outcomes, improved patient morbidity and mortality, as compared to complete kidney removal, have been noted. Nephron-sparing procedures are imperative when the contralateral kidney is functionally impaired or has been surgically removed in many cases.

Unlike any previous image-guided surgery target, the kidney is covered in perirenal fat, which hinders access to the surface of the kidney and to localization of specific anatomical surface targets. The fat also results in mechanical coupling to the abdomen and diaphragm resulting in significant movement with respiration. Since a significant fraction of kidney tumors protrude from the kidney, "locating" the tumor is often not the challenge. Rather it is the localization of the parenchymal deep margin point of the tumor while maintaining a clear surgical field, avoiding excessive blood

loss, and performing meticulous repair that is the surgical challenge. Hopefully, by interactively showing the surgeon the location of his or her tools during the surgery in relationship to the critical deep tumor, vascular and collecting system image guidance could minimize excess nephron removal and risk of positive margin and aid in identification of critical structure for avoidance if possible or repair if needed.

## Preliminary Data

We have conducted a number of preliminary studies using a porcine animal model. Swine were chosen as their kidneys closely approximate the size and structure of human kidneys. The first experiment assessed the effect of the loss of perfusion associated with standard kidney vessel clamping and a body force similar to the $CO_2$ insufflation pressure in an MIS application.

The kidneys were obtained from anesthetized or newly euthanized pigs under an IACUC-approved protocol. Heparin was administered intravenously to prevent blood clotting, and the renal artery and vein were closed to retain turgor before resection. Between 15 and 20 glass beads with 2 mm radii and holes through the center were sutured onto the kidney surface in a roughly even distribution over the entire kidney. CT scans of the kidney (160 or 300 mAs, 90 keV, 0.8 mm slice spacing, Philips human CT scanner) were taken before and after the renal artery and vein were cut and the kidney decompressed. We then assessed the kidney changes due to fluid loss by comparison of the CT scans and by tracked fiducial location (Fig. 18.2).

We performed similar experiments incorporating the effect of turgor loss due to an incision. In Fig. 18.3, the incision can be seen. We placed 30 fiducials distributed across the surface of the kidney. Fiducial motion ranged from near zero to 1.1 cm. After applying a correction algorithm, the errors drop dramatically showing a maximum of 0.8 cm at the site of incision but a mean of less than 2 mm. It should be noted at this point that the model is not designed to deal with incisions; therefore the residual error at the opening is to be expected.

## Human Studies: Preliminary Data

We have progressed to human studies for kidney guidance. In the human while we get the additional challenge of the perirenal fat, we

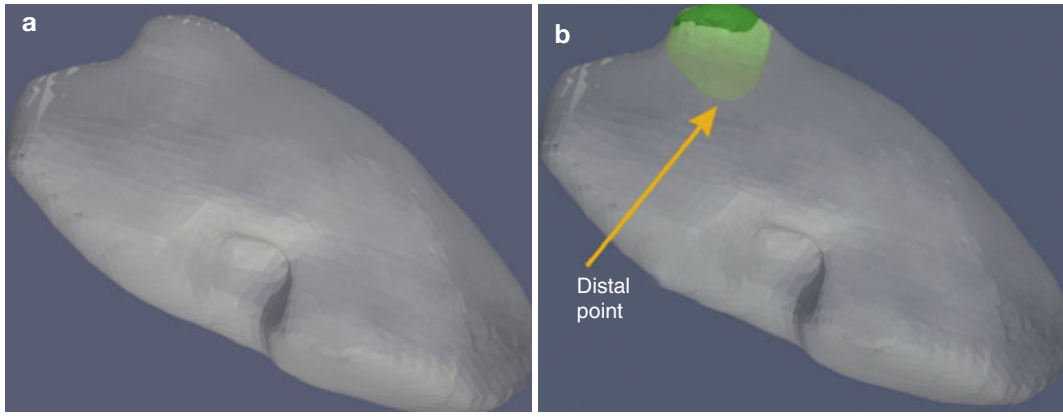


**Fig. 18.2** (**a**) External segmented kidney surface from CT scan – note bulge lateral of tumor from surface. (**b**) External segmented kidney surface showing colored segmentation of tumor margin (*green*) and internal deep margin location of tumor from the surface (*yellow arrow*) (From Galloway et al. [26], with permission)

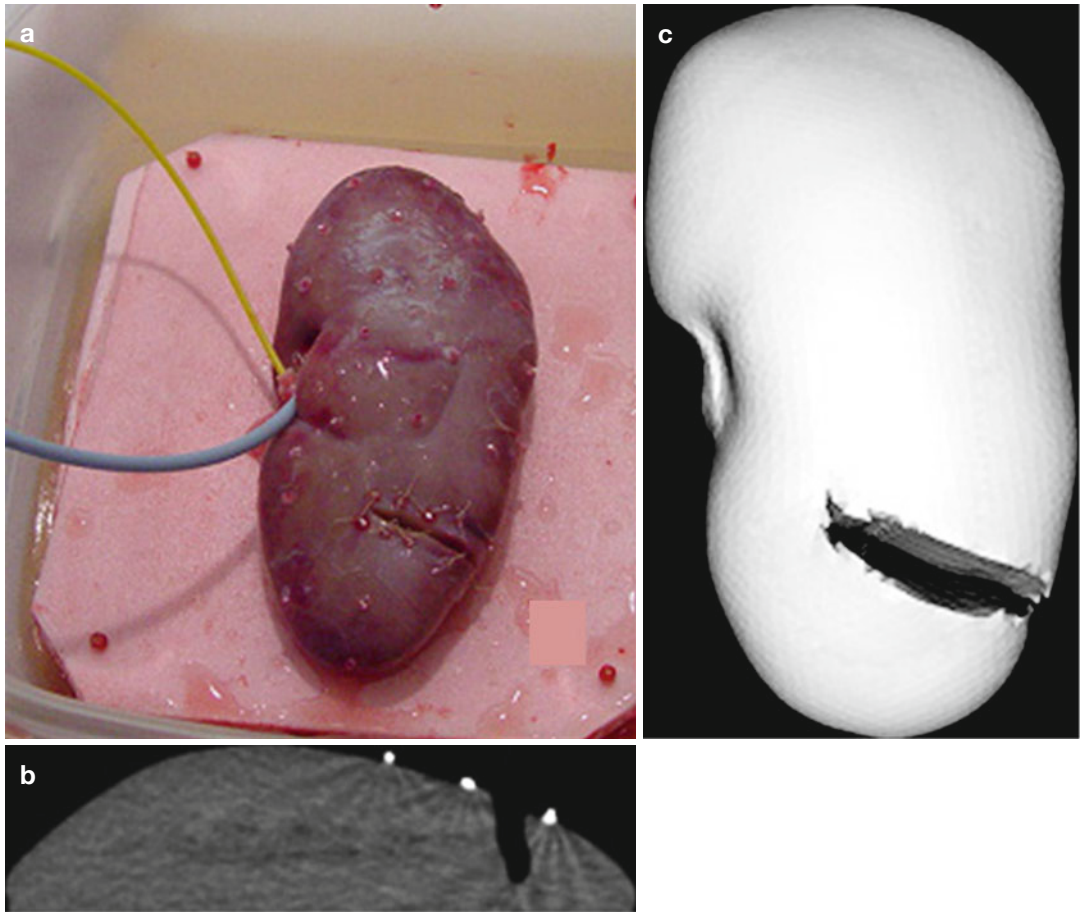


**Fig. 18.3** Measuring deformation in the incised kidney. Kidney turgor is maintained by saline perfusion and drainage via catheters. (**a**) Resected and saline perfused kidney and the fiducial positions (*red beads* sutured on surface). (**b**) Subtraction CT scan showing the depth of the incision and bead fiducials (*white*). (**c**) CT rendering of the surface and incision from the full CT scan (From Galloway et al. [26], with permission)

gain an advantage in that a significant number of human kidney tumors are exophytic. This provides a change in surface curvature (a salient feature) that is ideal for surface registrations (Fig. 18.4).

In our preliminary human studies, we obtained LRS surfaces of a kidney during open nephron-sparing surgical procedures. Since we cannot place extrinsic objects in the kidney prior to surgery, we implemented a unique new solution. Once the kidney was exposed, six surface marker dots were placed on the kidney using a surgical marker. We then performed an LRS scan of the kidney. As the LRS obtains a color image which can be mapped onto the 3D surface, the dots can be localized as "virtual fiducials." The kidney was clamped and iced as a standard step, and after 10 min a second LRS scan was obtained. Finally, the surgery proceeded and the tumor was resected. A final LRS scan was obtained. Our results were encouraging. After clamping and icing the mean TRE for the virtual fiducials is 0.95 mm (max = 1.33 mm). After the resection, the surface had a significant resection crater

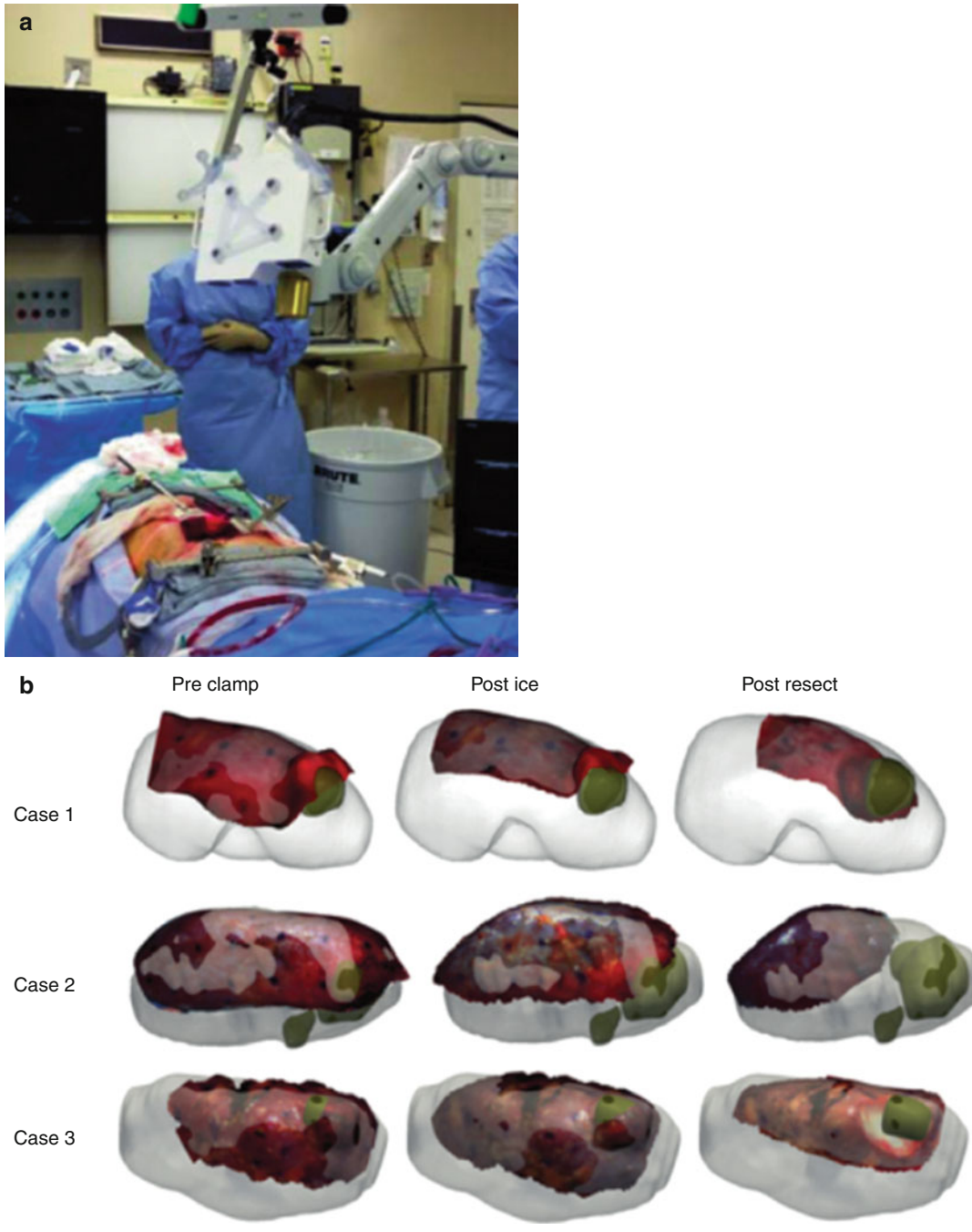


**Fig. 18.4** Laser range scanner capturing kidney surface during open partial nephrectomy case. (**a**) Laser range scanner unit with optical tracking deployed for IRB-approved intraoperative data gathering (no active navigation) in OR during partial nephrectomy cases. (**b**) Post hoc registered laser range scanner surfaces (*red*) shown over corresponding preoperative segmented computed tomography surfaces (*white*), tumors (*green*). Scans were obtained before clamping and were registered via surface-based methods, while subsequent scans were registered to preclamp by "virtual fiducial" point-based methodology

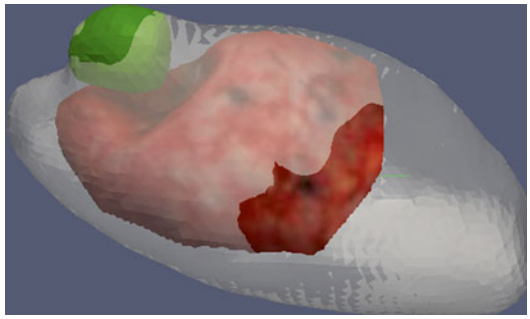

**Fig. 18.5** Postresection display showing former tumor location (*green*), the LRS surface (*red*), and the preoperative CT (*gray*)

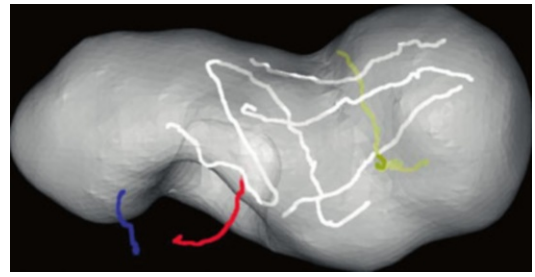

**Fig. 18.6** Surface capture of the kidney registered to segmented computed tomography of kidney and mass. *White lines* represent surface tracking done with tracked da Vinci tool tip obtained actively during partial nephrectomy case; *blue* and *red* represent hilar structures. *Gray* surface model represents segmented kidney surface from preoperative computed tomography scans including large lower pole tumor (*right side* of figure). *Gold line* represents held out data for registration accuracy. Mean closest point distance 1.2 mm

which impeded the surface registration (mean TRE 7.33 and 9.53 mm max). However, we know that an accurate registration could still be performed even after the resection due to the use of the virtual fiducials in a point-based registration (Fig. 18.5).

## Robotic Image-Guided Surgery (RIGS): Vanderbilt University Experience

The current robotic da Vinci technology platform (Intuitive Surgical, Sunnyvale, CA, USA) functions as an "enabling" technology, allowing multiple arm/camera control and intricate maneuvers such as suturing, thus allowing many laparoscopic naïve and even advanced MIS surgeons to perform more complex operative interventions. Starting in 2003, we sought to incorporate the potential benefits of IGS as an "augmenting" technology in combination with the robot's spatial accuracy, tracking, steadiness, and informational data input. We selected the partial nephrectomy procedure with its challenges (hemostasis, ischemia limits, oncologic margins, deformation, etc.) and potential benefits (high-resolution preoperative CT imaging, need for renal functional preservation).

Initially we analyzed the potential for using both intrinsic and extrinsic tracking and a variety of localizers after characterizing the kinematic chain and tracking capabilities of the da Vinci [33]. The desire to place multiple arms in the coordinate space resulted in a hybrid tracking approach incorporating optical tracking (Polaris Spectra, Northern Digital Inc., Waterloo, Canada) and intrinsic localizers in the "robot" [10]. Analysis showed acceptable error (<2 mm).

The RIGS system was then validated in a simulated surgical task of subsurface lesion resection from a gel phantom using both standard visual and IGS augmented guidance, showing benefit in improved resection metrics [9].

Intraoperative performance of surface acquisition with da Vinci during IRB-approved bystander study revealed acceptable registration error estimations (mean closest point distance 1.4 mm) [25]. While surface capture through a tracked tool is feasible, error and the lack of rapid ability to recapture and reregister have led us to explore alternatives (Fig. 18.6).

A common method of noncontact scanning is the use of a laser range scanner (LRS). LRS systems work by triangulating the location of a projected laser point. With the knowledge of the direction of projected laser light and an observation of where it appears in a camera image, one can determine the location of the illuminated point in 3D space. Rapidly panning the laser allows the LRS to acquire a large number of points without moving the sensor physically. LRS has been applied to intraoperative surgical registration during open approaches, but is not compatible or available for an MIS environment at present.

We have incorporated the LRS into complex open partial nephrectomies and a new composite rapid point registration "virtual fiducials" methodology has been developed. Data regarding "real-case" operative deformations is being gathered and analyzed for predictive modeling [20].

We are investigating and characterizing technology known as conoscopic holography to provide rapid and accurate surface capture and registration (Fig. 18.7) [34]. The conoprobe tracks using an optical tracking system and provides distance measurements to points on the tissue. As the laser point is traced over the organ surface by appropriate manual manipulation, a cloud of surface points on the organ is produced. The principles by which conoscopic holography measures distance were proposed by Sirat and coworkers [35]. The system illuminates an area of interest with a collimated light source. The cone of light returning from the illuminated area is filtered and then enters a birefringent crystal. Inside the crystal, constructive and destructive interference occurs, which results in a Fresnel pattern from which distance can be deduced. Conoscopic holography is currently used for distance measurement in industrial profilometers, where it is combined with a motorized X–Y stage. This enables highly accurate measurements of dimensions on machined components and is useful for manufacturing process control.

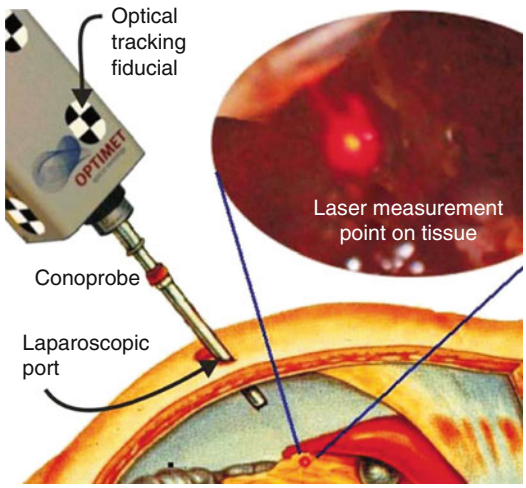


**Fig. 18.7** Conceptual art of MIS access scanning of solid intra-abdominal organ via conoscopic holography. The tracked conoprobe returns distance measurements, which are converted to a point cloud that defines the shape of the tissue surface (From Lathrop et al. [34], with permission)

Working with us in our engineering school, Lathrop and Webster have described experiments exploring the feasibility of using a conoscopic holography-based scanner as a method for obtaining minimally invasive surface scans for soft tissue registration [34]. A scanning system based on conoscopic holography promises the ability to scan through a laparoscopic port without requiring wide exposure of the organ of interest. The facts that conoscopic holography is a proven technique for high-precision distance measurements, the underlying device is readily available commercially in inexpensive packages, can be adopted for use in a minimally invasive sterile manner, and can deliver high-quality distance measurements to biological tissues, making it a compelling technology for laparoscopic surface scanning.

We recently conducted experiments examining the potential use of a conoscopic holography unit adapted for use in the OR. Moving this technique from concept to clinical use requires a rigorous accuracy evaluation, which is the purpose of our paper [36]. We adapted recent nonhomogeneous and anisotropic point-based registration results to provide a theoretical framework for predicting the accuracy of tracked distance measurement systems. Experiments conducted were complex objects of defined geometry, an anthropomorphic kidney phantom, and a human cadaver kidney (Fig. 18.8). Experiments agree with model predictions, producing point RMS errors consistently of <1 mm, surface-based registration with mean closest point error of <1 mm in the phantom, and an RMS target registration error of 0.8 mm in the human cadaver kidney. Tracked conoscopic holography is clinically viable; it enables minimally invasive surface scan accuracy comparable to current clinical methods that require open surgery.

Our work provided a comprehensive accuracy evaluation and experiments with an optically tracked conoscopic holography sensor for application in image-guided surgery. The system

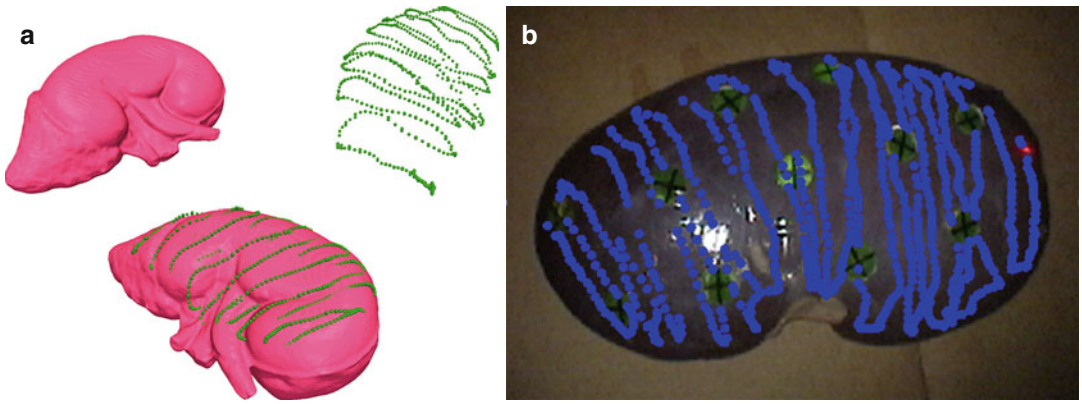


**Fig. 18.8** (**a**) Surface model of the anthropomorphic kidney phantom in the image coordinate system I (*left*) and the conoscopic surface measurement acquired in the patient coordinate system P (*right*). After successful surface-based registration, the measured point can be transformed into the image coordinate system using (*bottom*) (**b**) scanned conoprobe points (*blue dots*) taken from an excised human kidney. The *circles with crosses* serve as assessment fiducials (**a**, From Burgner et al. [36], with permission)

acquires 3D surface measurements of objects of medical interest, which can be used to register preoperative images to anatomy. Our accuracy evaluation experiments show RMS errors that are consistently <1 mm for point measurements. Surface-based registrations performed using the system show a mean closest point error of <1 mm after registration. The average $RMS_{TRE}$ in our human ex vivo cadaver kidney trials was 0.8 mm. These results suggest that conoprobe-enabled surface scans can be useful in extending surface-based registration techniques to the MIS setting for image-guided surgery; they enable accuracy comparable to the existing methods used in open surgery such as LRS. We are currently investigating surface acquisition with the conoprobe in place of the laser range scanner in our deformation correction framework. Thus, this approach has the potential to bring the advantages of image guidance to minimally invasive human surgeries in the near-term future.

## Kidney IGS Navigation (Other Approaches)

Work by Ukimura and Gill described a manual registration augmented reality video overlay of the renal tumor for laparoscopic partial nephrectomy [37]. Data regarding accuracy and error measurement were not provided and limit analysis. More recently these investigators have discussed implanting commercially available EM transponders into described initial ex vivo animal experiments [37].

Teber et al. have described several different potential approaches for kidney IGS including the use of 3D cone beam imaging with the insertion of needle-shaped 1.5 cm navigation fiducials into ex vivo porcine kidneys [38]. Registration after segmentation is then performed as described in our original paper [24]. As would be expected with large numbers of inserted fiducials, error was low ("error margin" of 0.5 mm) (0.2–0.7 mm). However, in human cases, a simple manual registration of segmented anatomical overlays was performed onto video endoscopic images. While the fiducial insertion technique is valid in the laboratory, the insertion of up to five 1.5 cm barbed needles and need for intraoperative scanning will likely limit clinical application.

Su et al. published the initial potential for use of *robotic vision-based IGS* by creating an augmented reality overlay for partial nephrectomy [39]. They used reconstructed, segmented, preoperative, three-dimensional CT data and post hoc manual registration to record video feeds from the binocular robotic endoscope system (Fig. 18.9). Once a manual alignment had been

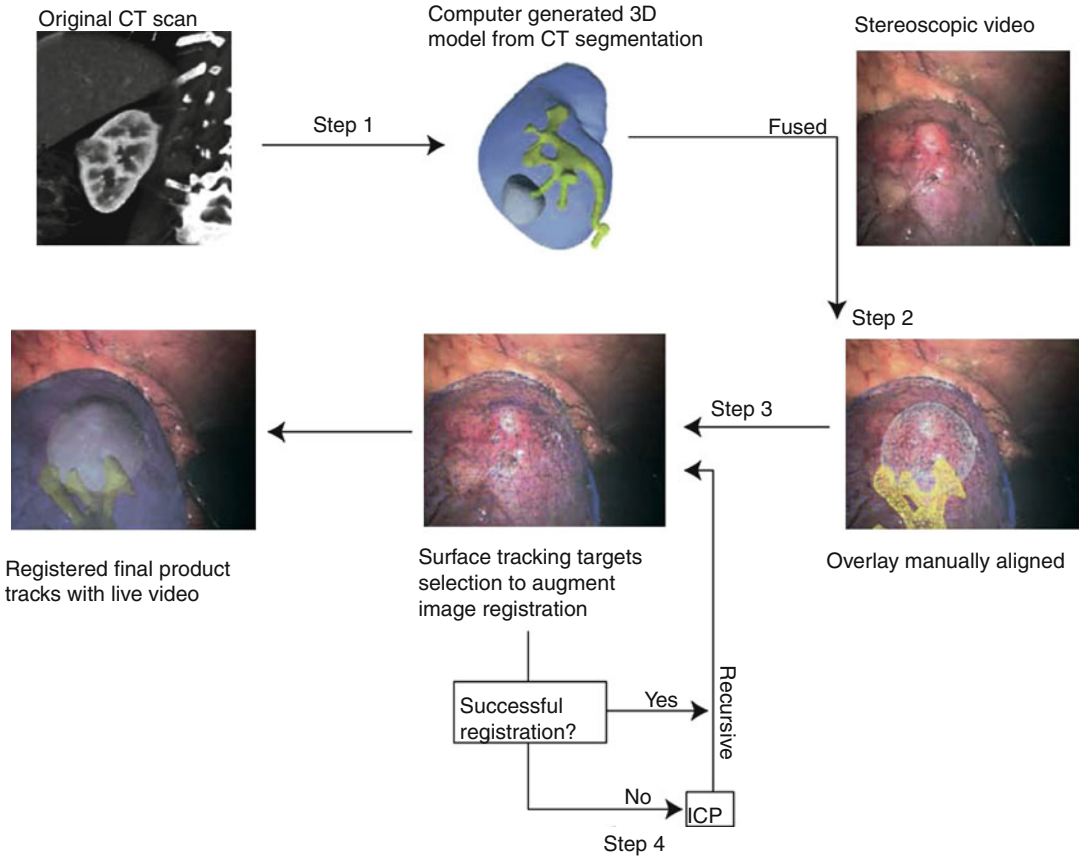


**Fig. 18.9** Stereoscopic video overlay registration algorithm. Flow chart displaying intermediary steps needed to achieve successful three-dimensional manual registration of preoperative computed tomography image to live stereoscopic video. Step 3 implements tracking of manual overlay with live video (From Su et al. [39], with permission)

carried out on the video, the three-dimensional reconstructed mesh model was anchored to identifiable kidney surface points on the video allowing a repetitive "tracking" of the overlay with the kidney using a complex computer algorithm called iterative closest point. Given the post hoc creation, manual registration, and limitations of this approach, no true analysis of registration error or use was feasible, but the potential of the demonstration was obvious and spurred marked interest.

Manual registration overlay is potentially an improvement over surgeon "mental co-registration," i.e., looking at the x-rays and then at the field, but falls short of the true idea of IGS navigation and does not allow error calculation. More recently, Mirota et al. have extensively reviewed vision-based navigation and the progress made in a variety of surgical fields [40].

## Robotic IGS Potential Role in Percutaneous Ablation and Biopsy

Ablative technology has been growing in popularity for a variety of urologic disease processes including small renal masses and prostate cancer. Focal therapies, especially those based on needles, are highly dependent for success on accurate localization and targeting and a thorough understanding of tissue effect geometry and intraoperative monitoring. However, meta-analysis of existing literature has shown concern for increased local recurrence rates versus extirpative proce-

dures [41]. The underlying causation for these rates is not defined and could include such varied sources as targeting, modality, monitoring, tissue effects, and type of interventionalist.

Leveillee recently published an excellent review of technology involved in optimization of image-guided targeting and renal focal therapy [42]. IGS technologies are being increasingly incorporated into needle ablative procedures. Examples include combined real-time ultrasound fused with high-quality preoperative axial imaging and a variety of computer-assisted commercially developed navigation systems for needle tracking systems to augment the intraprocedural placement of needles and potentially increase accuracy during CT-guided needle biopsy and ablative procedures (Koelis, La Tronche, France; Traxtal, Philips Healthcare, Andover, USA; Veran Medical Technologies, St. Louis, USA) [43, 44]. The potential use of MRI thermometry, allowing indirect temperature measurement within tissue, is being actively explored both for needle ablative tissue and other modalities such as high-intensity focused ultrasound [45, 46].

## Robotic-Guided Needle Ablations

Robotic advantages include high spatial accuracy and precision, non-fatigability, and tolerance of hazardous or difficult environments such as the CT and MRI scanner bore. Robotic devices that will orient and actively drive needles for biopsy and ablation during scanning are an active area of research. Robots compatible with fluoroscopy, CT scanner, and MRI have been developed [47].

CT-compatible robots have been developed and may soon be integrated into CT-guided renal mass ablation, hopefully reducing physician and patient exposure to radiation during CT fluoroscopy. One recent study compared a preoperative CT computer-assisted optical needle tracking navigation system (Koelis, France) with a CT-mounted robotic needle driver system (AcuBot, Johns Hopkins University) and found improved accuracy (mean target distance 1.2 vs. 5.8 mm, $p<0.0001$) and reduced targeting time (37 vs. 108 s., $p<0.0001$) for the CT robotic needle driver system [48].

MRI-compatible robots have been developed despite their significant engineering challenges and are continuing to be investigated for prostate biopsy utilizing the potential advantages of multiparametric MRI. There may also be a future role improving accuracy and precision of radiation seed placement for prostate cancer [49].

Even newer robotic-based image-guided procedures are in development including specialized robotically controlled "steerable" needles which may allow for access to previously inaccessible anatomical structures for improved biopsy access and drug and therapy delivery by avoidance of the straight line path of normal linear needles [50].

## IGS and Robotic Prostatectomy

Image guidance during radical prostatectomy could be of immense value as to location of critical structures such as neurovascular bundles and benign and malignant margins. Initial description of a real-time intraoperative transrectal ultrasound guided (TRUS) as an adjunct to laparoscopic prostatectomy was made by Ukimura et al. They were able to perform intraoperative TRUS, and this was felt by the authors to improve dissection around the neurovascular bundle, using vascular flow as a surrogate for bundle preservation. However, documentation of improvements in outcomes and adoption of the procedural adjunct have not occurred [51]. Further development of the technique was challenged by the requirement for a human assistant for manipulation and has not been forthcoming. More recently, the urology robotics laboratory at Johns Hopkins University has described a novel robotic transrectal ultrasound probe robotic manipulator coupled with 3D reconstruction software used for a tandem robot-assisted laparoscopic radical prostatectomy (T-RALP) (Fig. 18.10) [52]. The robotic arm supports and manipulates the transrectal ultrasound probe under joystick control by the da Vinci surgeon and can be positioned despite the da Vinci in the field.

Positional tracking and reconstruction software allows three-dimensional reconstructions for display within the da Vinci surgeon console.

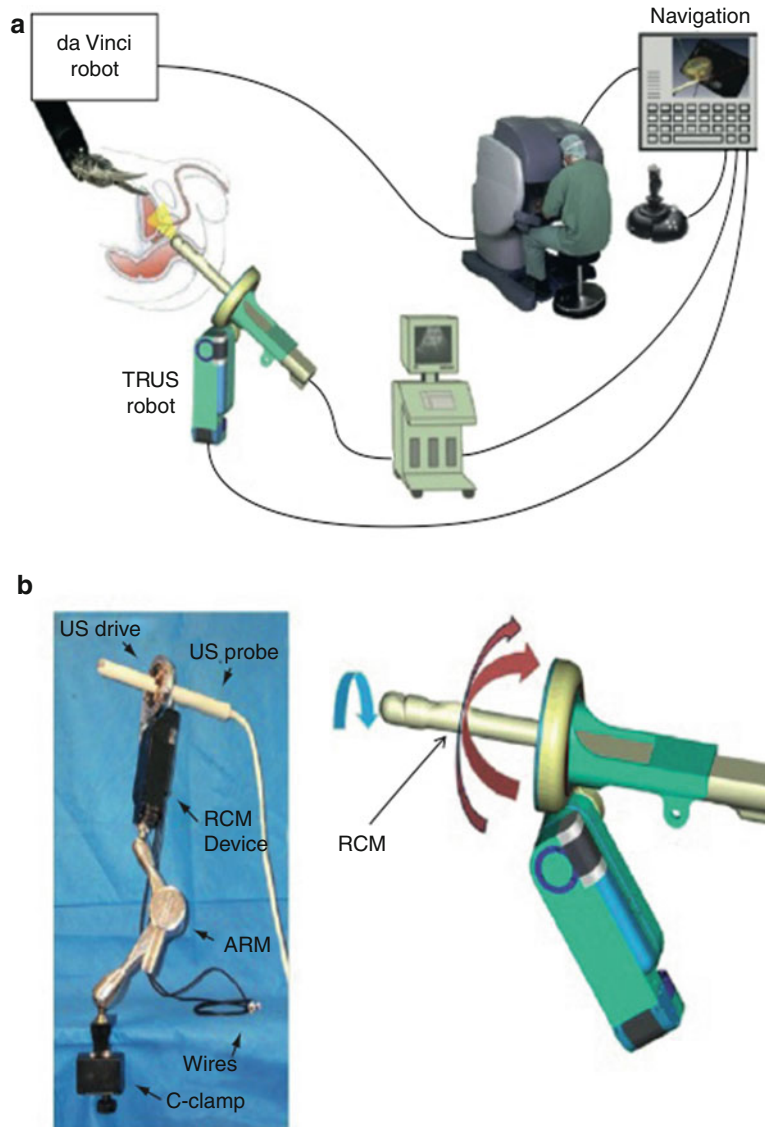


**Fig. 18.10** Tandem robot-assisted robotic prostatectomy schematic and transrectal ultrasound robot. (**a**) Schematic of tandem robot-assisted laparoscopic radical prostatectomy procedure (T-RALP) with robotically controlled transrectal ultrasound manipulator (**b**) with multidirectional control. T-RALP is controlled by surgeon at console with visualization via TilePro™ in da Vinci console (From Han et al. [52], with permission)

Questions as to whether or not preservation of vascular bundle structures truly correlates with nerve preservation and potency and the complexity of neural anatomy remain unanswered. No formal overlay image or virtual reality display is as of yet possible; however, this work truly meets criteria for *robotic image-guided surgery*. Lastly, multiparametric functional MRI of the prostate (dynamic contrast enhancement, diffusion weighted, MR spectroscopy) capitalizes on physiologic differences between cancer and benign cells and has gained increasing attention with the promise of improved diagnostic accuracy of cancer localization within the prostate [53, 54]. As such, imaging technologies such as these may play a future role in image-guided prostate interventions such as targeted biopsies and focal therapy.

## Conclusion

Image guidance has already revolutionized the performance of surgery and interventions in a variety of fields including neurosurgery and orthopedics, but remains in its infancy in urologic surgery. Current research into the combined application of IGS and robotics to

the complexities of soft tissue registration, operative navigation, and surgical use continues and presents unique engineering challenges and a new knowledge requirement for surgeons. Urologic surgeons should continue to research and explore the potential advantages of these advanced technologies and their potential roles to improve standard surgery as well as ablative modalities. Future advances in surgical disease management will likely incorporate a variety of emerging information technologies such as intraoperative image guidance along with advanced computing and robotics. Figures 18.11 and 18.12 show the potential of IGS to be applied to robotic partial nephrectomy.

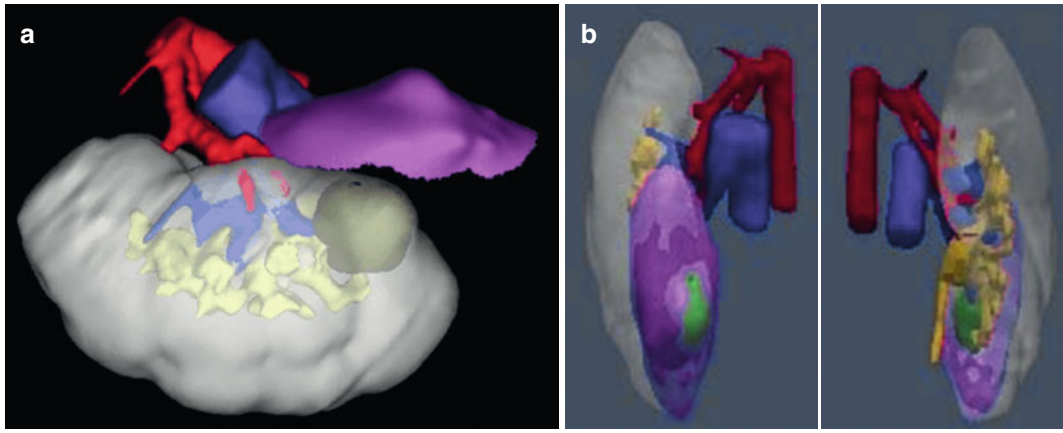


**Fig. 18.11** Segmented renal mass computed tomography with surface capture and registration. (**a**) Segmentation of lower pole tumor case. *Gray* represents kidney surface. *Green* is tumor with margins (subsurface). Collecting system (*yellow*), vena cava and venous anatomy (*blue*), arterial anatomy (*red*) have all been segmented from high-quality preoperative scanning. *Pink* surface represents captured surface. This will be aligned via surface alignment algorithm to perform final registration. (**b**) Visual representation of final registration

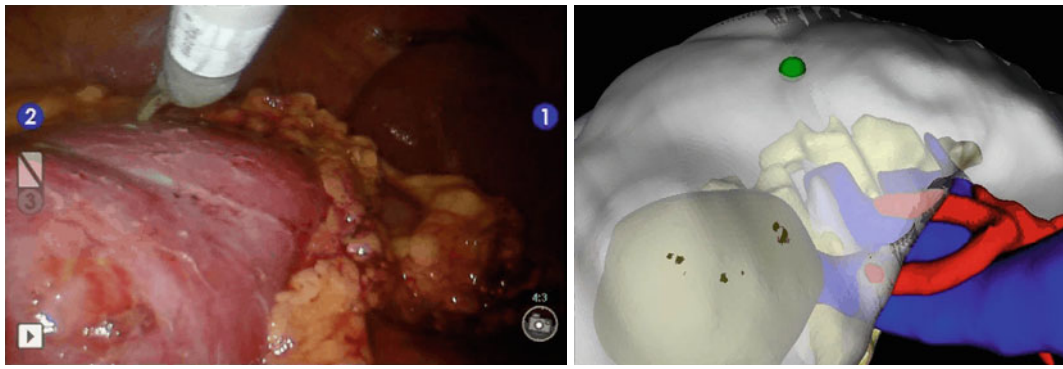


**Fig. 18.12** Intraoperative display of kidney image-guided surgery with tool, critical structure, and tumor location. Once registration is completed, movement of the tracked tool across the surface will enable both visual standard navigation (*left screen*) and location of tracked tool tip (*green dot*) in relationship to potential subsurface critical vascular and tumor margin anatomy segmented from the preoperative scans (*right screen*). Figure represents post hoc registration of data from real case (IRB-approved study VUMC)

## References


1. Balachandran R, Schurzig D, Fitzpatrick JM, Labadie RF. Evaluation of portable CT scanners for otologic image-guided surgery. Int J Comput Assist Radiol Surg. 2011;7:315–321.
2. Galloway RL. The process and development of image-guided procedures. Annu Rev Biomed Eng. 2001;3:83–108.
3. Arun KSK, Huang TST, Blostein SDS. Least-squares fitting of two 3-d point sets. Pattern Anal Mach Intell IEEE Trans. 1987;9(5):698–700. Available from: http://eutils.ncbi.nlm.nih.gov/entrez/eutils/elink.fcgi?dbfrom=pubmed&id=21869429&retmode=ref&cmd=prlinks.
4. Horn BKP. Relative orientation revisited. J Opt Soc Am A. 1991;8(10):1630. Available from: http://www.opticsinfobase.org/abstract.cfm?URI=josaa-8-10-1630.
5. Besl PJ, McKay ND. IEEE Transactions on Pattern Analysis and Machine Intelligence - Special issue on interpretation of 3-D scenes—part II archive. IEEE Computer Society Washington, DC, USA table of contents. 1992;14(2):239–56. doi: 10.1109/34.121791.
6. Roberts DWD, Strohbehn JWJ, Hatch JFJ, Murray WW, Kettenberger HH. A frameless stereotaxic integration of computerized tomographic imaging and the operating microscope. J Neurosurg. 1986;65(4):545–9. Available from: http://thejns.org/doi/abs/10.3171/jns.1986.65.4.0545@sup.2010.112.issue-2.
7. Watanabe EE, Watanabe TT, Manaka SS, Mayanagi YY, Takakura KK. Three-dimensional digitizer (neuronavigator): new equipment for computed tomography-guided stereotaxic surgery. Surg Neurol. 1987;27(6):543–7. Available from: http://eutils.ncbi.nlm.nih.gov/entrez/eutils/elink.fcgi?dbfrom=pubmed&id=3554569&retmode=ref&cmd=prlinks.
8. Herrell SD, Galloway RL, Su L-M. Image-guided robotic surgery: update on research and potential applications in urologic surgery. Curr Opin Urol. 2012;22(1):47–54.
9. Herrell SD, Kwartowitz DM, Milhoua PM, Galloway RL. Toward image guided robotic surgery: system validation. J Urol. 2009;181(2):783–9; discussion 789–90.
10. Kwartowitz DM, Miga MI, Herrell SD, Galloway RL. Towards image guided robotic surgery: multi-arm tracking through hybrid localization. Int J Comput Assist Radiol Surg. 2009;4(3):281–6.
11. Herline AJ, Stefansic JD, Debelak JP, Hartmann SL, Pinson CW, Galloway RL, et al. Image-guided surgery: preliminary feasibility studies of frameless stereotactic liver surgery. Arch Surg (Chicago, Ill: 1960) [Internet]. 1999;134(6):644–9; discussion 649–50. Available from: http://eutils.ncbi.nlm.nih.gov/entrez/eutils/elink.fcgi?dbfrom=pubmed&id=10367875&retmode=ref&cmd=prlinks.
12. Beller S, Hünerbein M, Lange T, Eulenstein S, Gebauer B, Schlag PM. Image-guided surgery of liver metastases by three-dimensional ultrasound-based optoelectronic navigation. Br J Surg. 2007;94(7):866–75. Available from: http://doi.wiley.com/10.1002/bjs.5712.
13. Baumhauer M, Simpfendörfer T, Müller-Stich B, Teber D, Gutt C, Rassweiler J, et al. Soft tissue navigation for laparoscopic partial nephrectomy. Int J Comput Assist Radiol Surg. 2008;3(3):307–14. Available from: http://link.springer.com/article/10.1007/s11548-008-0216-7.
14. Atuegwu NC, Galloway RL. Volumetric characterization of the Aurora magnetic tracker system for image-guided transorbital endoscopic procedures. Phys Med Biol. 2008;53(16):4355–68. Available from: http://eutils.ncbi.nlm.nih.gov/entrez/eutils/elink.fcgi?dbfrom=pubmed&id=18660560&retmode=ref&cmd=prlinks.
15. Clifford MAM, Banovac FF, Levy EE, Cleary KK. Assessment of hepatic motion secondary to respiration for computer assisted interventions. Comput Aided Surg. 2002;7(5):291–9. Available from: http://onlinelibrary.wiley.com/doi/10.1002/igs.10049/full.
16. West JB, Fitzpatrick JM, Toms SA, Maurer CR, Maciunas RJ. Fiducial point placement and the accuracy of point-based, rigid body registration. Neurosurgery. 2001;48(4):810–6; discussion 816–7.
17. Porter BC, Rubens DJ, Strang JG, Smith J, Totterman S, Parker KJ. Three-dimensional registration and fusion of ultrasound and MRI using major vessels as fiducial markers. IEEE Trans Med Imaging. 2001;20(4):354–9. Available from: http://ieeexplore.ieee.org/xpls/abs_all.jsp?arnumber=921484.
18. Nowatschin S, Markert M, Weber S, Lueth TC. A system for analyzing intraoperative B-Mode ultrasound scans of the liver. Conf Proc IEEE Eng Med Biol Soc. 2007;2007:1346–9. Available from: http://ieeexplore.ieee.org/xpls/abs_all.jsp?arnumber=4352547.
19. Rauth TP, Rauth TP, Bao PQ, Bao PQ, Galloway RL, Galloway RL, et al. Laparoscopic surface scanning and subsurface targeting: implications for image-guided laparoscopic liver surgery. Surgery. 2007;142(2):207–14. Available from: http://eutils.ncbi.nlm.nih.gov/entrez/eutils/elink.fcgi?dbfrom=pubmed&id=17689687&retmode=ref&cmd=prlinks.
20. Ong RE, Glisson C, Altamar H, Viprakasit D, Clark P, Herrell SD, et al. Intraprocedural registration for image-guided kidney surgery. IEEE ASME Trans Mechatron. 2010;15(6):847–52.
21. Dimaio S, Kapur T, Cleary K, Aylward S, Kazanzides P, Vosburgh K, et al. Challenges in image-guided therapy system design. Neuroimage. 2007;37 Suppl 1:S144–51.

22. Miga MIM, Sinha TKT, Cash DMD, Galloway RLR, Weil RJR. Cortical surface registration for image-guided neurosurgery using laser-range scanning. IEEE Trans Med Imaging. 2003;22(8):973–85.
23. Clements LWL, Chapman WCW, Dawant BMB, Galloway RLR, Miga MIM. Robust surface registration using salient anatomical features for image-guided liver surgery: algorithm and validation. Med Phys. 2008;35(6):2528–40.
24. Benincasa ABA, Clements LWL, Herrell SDS, Galloway RLR. Feasibility study for image-guided kidney surgery: assessment of required intraoperative surface for accurate physical to image space registrations. Med Phys. 2008;35(9):4251–61.
25. Altamar HO, Ong RE, Glisson CL, Viprakasit DP, Miga MI, Herrell SD, et al. Kidney deformation and intraprocedural registration: a study of elements of image-guided kidney surgery. J Endourol. 2011;25(3): 511–7.
26. Galloway RL, Herrell SD, Miga MI. Image-guided abdominal surgery and therapy delivery. J Healthcare Eng. 2012;3(2):203–28.
27. Heizmann O, Zidowitz S, Bourquain H, Potthast S, Peitgen H-O, Oertli D, et al. Assessment of intraoperative liver deformation during hepatic resection: prospective clinical study. World J Surg. 2010;34(8): 1887–93.
28. Lange T, Wenckebach TH, Lamecker H, Seebass M, Hünerbein M, Eulenstein S, et al. Registration of different phases of contrast-enhanced CT/MRI data for computer-assisted liver surgery planning: evaluation of state-of-the-art methods. Int J Med Robot. 2005; 1(3):6–20.
29. Dumpuri P, Clements LW, Dawant BM, Miga MI. Model-updated image-guided liver surgery: preliminary results using surface characterization. Prog Biophys Mol Biol. 2010;103(2–3):11–1.
30. Herline AJ, Herring JL, Stefansic JD, Chapman WC, Galloway RL, Dawant BM. Surface registration for use in interactive, image-guided liver surgery. Comput Aided Surg. 2000;5(1):11–7.
31. Miga MI, Cash DM, Cao Z, Galloway RL, Dawant B, Chapman WC. Intraoperative registration of the liver for image-guided surgery using laser range scanning and deformable models, Medical Imaging 2003: Visualization, Image-guided Procedures, and Display. Proc. of the SPIE. 2003;5029:350–9.
32. Clements LW, Dumpuri P, Chapman WC, Galloway RL, Miga MI. Atlas-based method for model updating in image-guided liver surgery. In: Cleary KR, Miga MI, editors. Medical imaging. Bellingham: SPIE; 2007. p. 650917.
33. Kwartowitz DM, Herrell SD, Galloway RL. Update: toward image-guided robotic surgery: determining the intrinsic accuracy of the daVinci-S robot. Int J Comput Assist Radiol Surg. 2007;1(5):301–4.
34. Lathrop RA, Hackworth DM, Webster RJ. Minimally invasive holographic surface scanning for soft-tissue image registration. IEEE Trans Biomed Eng. 2010; 57(6):1497–506.
35. Sirat BY, Paz F, Agronik G, Wilner K. Conoscopic holography. In: Iancu O, Manea A, Schiopu P, Cojoc D, editors. SPIE proceedings. Bellingham: SPIE; 2005;5972:376. ISBN: 9780819459916.
36. Burgner J, Simpson AL, Fitzpatrick JM, Lathrop RA, Herrell SD, Miga MI, et al. A study on the theoretical and practical accuracy of conoscopic holography-based surface measurements: toward image registration in minimally invasive surgery. Int J Med Robot. 2012;9:190–203.
37. Ukimura O, Gill IS. Image-fusion, augmented reality, and predictive surgical navigation. Urol Clin North Am. 2009;36(2):115–23, vii.
38. Teber D, Guven S, Simpfendörfer T, Baumhauer M, Güven EO, Yencilek F, et al. Augmented reality: a new tool to improve surgical accuracy during laparoscopic partial nephrectomy? Preliminary in vitro and in vivo results. Eur Urol. 2009;56(2):332–8.
39. Su L-M, Vagvolgyi BP, Agarwal R, Reiley CE, Taylor RH, Hager GD. Augmented reality during robot-assisted laparoscopic partial nephrectomy: toward real-time 3D-CT to stereoscopic video registration. Urology. 2009;73(4):896–900.
40. Mirota DJ, Ishii M, Hager GD. Vision-based navigation in image-guided interventions. Annu Rev Biomed Eng. 2011;13:297–319.
41. Campbell SC, Novick AC, Belldegrun A, Blute ML, Chow GK, Derweesh IH, et al. Guideline for management of the clinical T1 renal mass. J Urol. 2009; 182(4):1271–9.
42. Leveillee RJ, Ramanathan R. Optimization of image-guided targeting in renal focal therapy. J Endourol. 2010;24(5):729–44.
43. Wood BJ, Locklin JK, Viswanathan A, Kruecker J, Haemmerich D, Cebral J, et al. Technologies for guidance of radiofrequency ablation in the multimodality interventional suite of the future. J Vasc Interv Radiol. 2007;18(1 Pt 1):9–24.
44. Krücker J, Xu S, Venkatesan A, Locklin JK, Amalou H, Glossop N, et al. Clinical utility of real-time fusion guidance for biopsy and ablation. J Vasc Interv Radiol. 2011;22(4):515–24.
45. Roujol S, Ries M, Quesson B, Moonen C, Denis de Senneville B. Real-time MR-thermometry and dosimetry for interventional guidance on abdominal organs. Magn Reson Med. 2010;63(4):1080–7.
46. Rieke V, Butts Pauly K. MR thermometry. J Magn Reson Imaging. 2008;27(2):376–90.
47. Mozer P, Troccaz J, Stoianovici D. Urologic robots and future directions. Curr Opin Urol. 2009;19(1): 114–9.
48. Pollock R, Mozer P, Guzzo TJ, Marx J, Matlaga B, Petrisor D, et al. Prospects in percutaneous ablative targeting: comparison of a computer-assisted navigation system and the AcuBot robotic system. J Endourol. 2010;24(8):1269–72.
49. Bonekamp D, Jacobs MA, El-Khouli R, Stoianovici D, Macura KJ. Advancements in MR imaging of the prostate: from diagnosis to interventions. Radiographics. 2011;31(3):677–703.

50. Rucker DC, Jones BA, Webster RJ. A geometrically exact model for externally loaded concentric-tube continuum robots. IEEE Trans Robot. 2010;26(5):769–80.
51. Ukimura O, Magi-Galluzzi C, Gill IS. Real-time transrectal ultrasound guidance during laparoscopic radical prostatectomy: impact on surgical margins. J Urol. 2006;175(4):1304–10.
52. Han M, Kim C, Mozer P, Schäfer F, Badaan S, Vigaru B, et al. Tandem-robot assisted laparoscopic radical prostatectomy to improve the neurovascular bundle visualization: a feasibility study. Urology. 2011;77(2):502–6.
53. Turkbey B, Mani H, Shah V, Rastinehad AR, Bernardo M, Pohida T, et al. Multiparametric 3T prostate magnetic resonance imaging to detect cancer: histopathological correlation using prostatectomy specimens processed in customized magnetic resonance imaging based molds. J Urol. 2011;186(5):1818–24.
54. Krieger A, Iordachita II, Guion P, Singh AK, Kaushal A, Ménard C, et al. An MRI-compatible robotic system with hybrid tracking for MRI-guided prostate intervention. IEEE Trans Biomed Eng. 2011;58(11):3049–60.

# Urologic Surgery Training Using Computer-Assisted Simulators

19

Jason Cheng-En Sea and Chandru P. Sundaram

Surgical training has been traditionally taught as a hands-on apprenticeship. The old adage of surgical training throughout the centuries has been the Halstedian motto of *see one, do one, teach one*. Although the Halstedian motto reflects the importance of hands-on experience, the medical environment that trainees are facing today has changed radically, and this has called into question the viability of continuing with the traditional model of training. As we enter into a modern age, patient safety and the steep learning curves associated with complex instruments have become a few of the many factors that must be overcome to successfully train a urologist. Operating time is seen as an expensive and very limited commodity. Furthermore, studies have shown an increased cost associated with the training of residents in the operating room as the staff surgeon could perform the procedure more efficiently on their own. These external pressures such as cost [1], patient safety, and limitations in resident hours of training have contributed to the need for alternative methods for teaching contemporary urologic procedures. The use of computer-assisted simulators is one such tool that has been examined in order to aid the dissemination of urologic surgical skills. In the era where surgeons are evaluated for their complication rates, simulation may also allow a surgeon to practice the procedure prior to attempting the actual surgery. Finally, simulators have been proposed not only as teaching tools but also as methods for certification.

Simulation in medicine is a relatively new concept considering its extensive use in other fields such as aviation. In order to discuss simulation, it is important to first define the various types of simulation that are available. Simulation can be divided into low-fidelity and high-fidelity simulations. Low fidelity refers to simplified tasks and skills, whereas a high-fidelity simulation refers to simulation of a complete procedure, also known as simulation at a *full scale*. Simulators may also be divided into physical simulators, virtual reality (computer-assisted) simulators, and hybrid simulators. Physical simulators can range from simple box trainers for laparoscopy to complex animal/cadaveric models which approximate the procedure with high fidelity. The advent of virtual simulation began after adequate advances were made in computers and computing power to support the graphics required to make surgical simulators realistic. Virtual reality simulators will be the focus of this chapter and refer to those simulators that are based on computer-generated environments or situations intended to simulate a physical environment. Hybrid simulation, as the name implies, involves a combination of inanimate simulation with an overlay of the virtual components.

J.C.-E. Sea, MD (✉) • C.P. Sundaram, MD
Department of Urology, Indiana University,
535 Barnhill Dr., Suite 420, Indianapolis, IN
46202-5289, USA
e-mail: jason.sea@gmail.com; sundaram@iupui.edu

J.C. Liao, L.-M. Su (eds.), *Advances in Image-Guided Urologic Surgery*,
DOI 10.1007/978-1-4939-1450-0_19, © Springer Science+Business Media New York 2015

Simulation has been identified as an important tool in medicine for a variety of reasons. Major advantages discussed in the literature regarding simulation in medicine include reduction of learning curves, improved safety of patients, ease of accessibility of the simulator to trainees, and avoidance of operating room costs. The validity of simulators and the establishment of their applicability to each type of surgical procedure are also a major focus of research in simulation and will be discussed within this chapter. Although we have herein only discussed simulators as a teaching tool for urology trainees, there have also been suggestions that simulation can also be used to examine the acquisition and maintenance of those same skills to ensure proficiency. This idea of minimal technical expertise and standards for graduating residency has already been applied in some surgical specialties with the integration of the FLS requirements as criteria for graduation [2].

## Education and the Importance of Simulation

The evolution of urology has introduced increasingly complex procedures in the areas of endoscopic and laparoscopic surgery [3]. These procedures have been shown to decrease pain and improve patient recovery times. However, the skills required for these procedures remain some of the most technically difficult and can require years of training to achieve proficiency. One of the most recent developments to affect the landscape of urology has been the introduction of robotic-assisted urologic surgery. Numerous studies have shown the rapid adoption of robotics to an expanding number of urologic procedures [4–6].

A number of authors have published articles to address the issues associated with robotics training and the optimal methods to train and credential future urologists [7–9]. These authors agree on the need of a structured method; however, the exact recommendations vary. The traditional Halstedian method is generally seen as limited in the era of robotics. While traditional surgeries—performed open or laparoscopic—allowed the lead surgeon to stand next to the trainee and have immediate access to the patient, robotics has physically separated the surgeon and the trainee. Even if the surgeon is at the bedside assisting, there is no direct access to the robotic console. Some of these issues may be alleviated by the dual console robot but at substantial costs for purchase of the additional equipment and the requirement of additional staffing.

The majority of educational papers regarding robotics training describe the training of novices in residency programs; in addition, there is also literature detailing the training of novices at the postgraduate urologist levels [9]. Mirheydar et al. and McDougal et al. described a high rate of take to their respective programs with regard to participants performing robotic surgery on follow-up [9, 10]. A look at how most authors describe their approach to robotics training reveals that the majority divide the steps into preclinical and clinical phases. In general, the methodology of a training education program consists of introductory sessions to the robot followed by gaining experience as a bedside assist. The bedside assist allows familiarization with the equipment and the steps of the procedure. Finally, trainees are allowed on the console and are allowed to perform more and more difficult portions of the procedure in a graduated manner [11]. Throughout the literature, the authors emphasize the importance of simulators as a stress-free and safe environment in which skills can be acquired.

The concept of learning curves is central to the discussion of education and the acquisition of new surgical skills. A fundamental concept tied to the learning curve is that training and practice are required for a surgeon to become proficient at a given surgical technique or procedure. Because a trainee must begin at the start of a learning curve, patient safety and outcomes can be an issue as the trainee's skills are still undergoing improvement during this period. Various authors have published their experience regarding the learning curve associated with RALP with the number of cases to reach proficiency being estimated anywhere from 25 to 150 cases [12–15]. Although studies have

demonstrated that robotics can be taught safely and without adverse outcomes [16], the question remains whether there are even better ways to decrease the learning curve so as to hasten the rate that a surgeon achieves proficiency. Simulation may be one way to decrease the learning curve and improve surgical outcomes.

A number of studies have advocated for the integration of robotic simulators into urologic surgical training programs [3, 17–19]. A survey of program directors in the United Kingdom indicated that the majority of program directors believed that the use of simulation would lead to improved surgical training [20]. The authors went on to suggest that all trainees should have access to simulators and furthermore should undergo training through a formalized curriculum. A survey of program directors in the United States yielded similar results as Le et al. concluded that program directors believed laparoscopic simulators were a useful education tool [21]. Additional evidence supporting the integration of simulation into surgical training exists as surveys across other surgical specialties including neurosurgery, plastic surgery, orthopedic surgery, and gynecological surgery. These surveys have yielded similar views regarding the importance of simulators for training purposes [22–26].

## Types of Validity in Simulation

In order for a simulator to be useful in the education of surgical trainees, it must first have validation studies performed. The relevant types of validity that have been described include face, content, construct, concurrent, and predictive validity [19, 27]. Face validity is described as the realism of the exercises compared to the real procedure or task. Content validity is defined as whether a simulation teaches the skills it was intended to impart. Construct validity is the ability of the simulation to differentiate between skill levels of the participants and subjects being tested. For example, a group of novices should score lower than a group of expert surgeons performing the same exercise. Concurrent validity is a comparison of the simulator to the gold standard of teaching the skills. Using these different types of validity, comparisons can be made to other simulations or teaching methodologies. Finally, predictive validity is determined by the ability of the simulation to predict the future performance of the trainee.

## History of Simulators in Surgery

In order to understand the benefits of simulation in surgery, we need not look further than the work completed in *Fundamentals of Laparoscopic Surgery* (FLS)—a comprehensive program utilized in the training for laparoscopic surgery. With the advent of laparoscopy, and the recognition that the universal transfer of laparoscopic skills to their trainees was critical for competency, the general surgeons developed a skills curriculum to ensure uniform standards were met. Extensive validation studies with the FLS exercises allowed the establishment of a general surgery curriculum and eventually allowed the integration of the program into the accreditation process [2].

In order for a simulation to be useful, there must be proof that training in the simulated environment makes a difference in regard to outcomes in real surgery. Warm-up time on virtual simulators prior to performing tasks on the robotic console is a situation that has been studied as a possible benefit of simulation [28]. Studies support the hypothesis that a warm-up session in virtual reality or with inanimate tasks prior to performing laparoscopic surgery improves performance during the following surgery. Calatayud et al. demonstrated this skill transfer when trainees were assessed with or without warm-up sessions prior to performing laparoscopic cholecystectomies [29]. Do et al. demonstrated this with a laparoscopic box trainer with warm-up before laparoscopic tasks [30]. Warm-up benefits were also demonstrated in urology studies looking at performance during laparoscopic surgery [31]. Virtual simulation was used as a warm-up exercise prior to completion of a laparoscopic nephrectomy. The authors studied the outcomes of the surgery and found that

the take down of the white line of Toldt was improved in those who underwent the warm-up session prior to the actual nephrectomy [31]. However, there are no studies looking at VR warm-up in relation to performance during actual robotic-assisted surgery.

## Laparoscopic Simulators

Laparoscopic simulators are available for low-fidelity tasks, as well as for the high-fidelity simulation of procedures. The high-fidelity simulations include simulation of a complete laparoscopic cholecystectomy and laparoscopic nephrectomy. Commercially available laparoscopic trainers include the MISTELS (McGill University, Montreal, Canada), MIST-VR (Mentice AB, Gothenburg, Sweden), LAP Mentor (Simbionix, Lod, Israel), and LapSim (Surgical Science Ltd, Gothenburg, Sweden).

MISTELS is a physical simulator which was developed at McGill University in Montreal, Canada. Although it is not a virtual simulator, it is important to discuss briefly because it is the most studied of the laparoscopic simulators and serves as a standard as to which the virtual reality simulators are compared. It consists of five exercises which are performed within a box trainer. The trainee utilizes either a 0° laparoscope or fixed camera in conjunction with instruments inserted through two working ports. The tasks are described as transfer, cutting, ligating loop, and suturing with intracorporeal or extracorporeal technique [32]. Metrics for each exercise include time and efficiency. Penalties are applied to the score for inaccuracy and errors. Construct validity [33–35], concurrent validity [36, 37], face validity, and predictive validity [32] have been demonstrated for the MISTELS simulator. The Fundamentals of Laparoscopic Surgery (FLS) curriculum is a validated set of exercises that is based on the MISTELS program. McCluney et al. found that FLS was able to predict the performance of subjects in the operating room as assessed by GOALS [38]. Of note, the FLS program is integrated into the general surgery training curriculum and is being used for the credentialing of new graduates.

The LAP Mentor (Simbionix, Lod, Israel) simulator consists of nine tasks performed on a VR terminal with haptic feedback. Face, construct, and content validity have been verified for this simulator [39]. The nine exercises differ in the metrics that they measure, but this is handled by an algorithm within the software that generates a composite score. A total score available upon completion of the exercise reflects the overall performance of the trainee. The exercises were described as manipulation of a 0° scope, manipulation of a 30° scope, eye-hand coordination, clipping leaking hoses, grasping and clipping leaking hoses, two-handed maneuvers, cutting, fulguration, and objection translocation. Face validity was verified as 89 % of participants found the simulator to be realistic. Content validity was assessed by the expert participants in the study of whom 91 % found it to be useful for teaching laparoscopic skills. Construct validity was demonstrated as the non-camera skills of the simulator were able to differentiate between the laparoscopic naïve and the expert group.

LapSim (Surgical Science Ltd, Gothenburg, Sweden) consists of nine tasks, including camera navigation, instrument navigation, coordination, grasping, list and grasp, cutting, clip applying, fine dissection, and suturing [40]. A study was carried out across eight centers in Europe studying the LapSim for validity. They attempted to establish the levels that corresponded to novices and experts and used the data to establish minimum proficiency levels. Construct validity was demonstrated in 21 of the 32 metrics recorded across the nine tasks. The authors noted that the suturing task was found to have low construct validity and given this outcome hypothesized that the exercise may not be useful for trainees.

MIST-VR (Mentice AB, Goteborg, Sweden) was one of the first virtual reality simulators available for education within laparoscopic surgery. The simulator consisted of a box trainer with a computer-generated virtual environment projected onto a video screen. Movement of the physical tools was translated into movements within the virtual space. A total of six training tasks are available on this particular system. In studies of this simulator, a noted drawback was

the lack of haptic feedback. It has been found to have poor face and content validity, construct validity [41], and concurrent validity [42, 43]. Sickle et al. published scores on the MIST-VR that corresponded to varying levels of expertise as established by testing surgeons across the nation. That data was proposed to be used for setting proficiency levels utilizing the MIST-VR as an evaluation tool.

The Procedicus MIST Nephrectomy simulator (Mentice, Gothenburg, Sweden) is the only simulator currently described in literature that simulates a urologic procedure at the high-fidelity level [44]. It was described as a joint venture between Mentice and Guy's Hospital and King's College London. With this simulator, both transperitoneal and retroperitoneal approaches to laparoscopic nephrectomy are possible. The simulation itself is divided into three tasks, which include identification/division of the ureter, isolation of the renal vessels, and finally the complete mobilization of the kidney from surrounding structures. In one study, there were eight experts, ten immediate trainees, and ten novice trainees enrolled for validity testing [44]. Both face and content validity were verified by survey of the expert participants. Construct validity was demonstrated as the experts outperformed the novices. This was seen in the metrics, such as time for completion, travel, hemorrhage, and number of errors.

A number of studies have examined the transfer of skills from virtual reality simulators to the operating room in laparoscopic surgery [36, 37, 42, 45–52]. Studies examining this aspect of simulator education looked at skill transfer during real operations in the OR and with the swine model. Results from these studies have demonstrated that operative time was reduced when training was carried out on the virtual simulator. Other metrics that were assessed include instrument path, number of movements of the instruments, global rating of performance, and error scores. A pair of studies investigating the correlation of simulator practice to outcomes in the operating room with laparoscopic cholecystectomy were conducted by Schijven et al. and Seymour et al. [43, 53]. The use of a virtual reality simulator over the course of 4 days was demonstrated to improve surgical skills in the operating room during real surgery [53]. Seymour et al. had participants complete training on the MIST-VR until expert levels were achieved on the simulator assessments. The study found that VR-trained residents were faster and made fewer errors during the actual OR. Grantcharov et al. performed a study in which 16 trainees were randomized to complete exercises on the MIST-VR versus no training. The subjects then performed laparoscopic cholecystectomy and the outcomes were assessed. Faster operative times and fewer errors were observed in those who underwent virtual simulator training versus those who did not. Overall, the literature supports the hypothesis that virtual reality simulation improves the performance of trainees within the operating room [54].

Virtual reality has been shown to be beneficial in laparoscopic surgery as a warm-up task immediately prior to the operation [29]. A study involving general surgeons performing cholecystectomies demonstrated a benefit derived from completion of three tasks requiring approximately 15 min. Performance of the cholecystectomy was blinded and rated by OSAT rating scale. A significant difference was seen favoring the group undergoing preoperative warm-up exercises.

## Simulators in Endourology

Simulators are available for the various technical procedures encountered in the realm of endourology including urethrocystoscopy, ureterorenoscopy, transurethral resection of the prostate (TURP), percutaneous nephrolithotomy, and transurethral resection of bladder tumor (TURBT).

Duke University Medical Center developed a VR simulation for ureterorenoscopy which has been validated for content validity [55]. Some of the simulators are used to simulate multiple types of procedures. URO Mentor (Simbionix, Tel Aviv, Israel) allows for simulation of urethrocystoscopy and semirigid/flexible ureteroscopy. It has been validated for face [56, 57], content [56–58], and construct [59–61] validity. A study conducted by

Schout et al. involving 100 interns randomized to either training with the simulator or control demonstrated that practice on the URO Mentor translated to improved performance in cystourethroscopy in the operating room [62]. George Washington University developed a VR simulator for lower urinary tract procedures that included a hardware interface device. They were able to integrate this device with the endoscopic instruments inserted through the urethra and into the bladder, with the benefit of haptic feedback. This simulator has been validated for content validity [63].

Although new procedures such as GreenLight™ laser therapy are becoming more popular, there is still a lack of validated simulators for those procedures. However, there are a number of simulators available for TURP—the gold standard procedure for prostate resection in the setting of benign prostatic hyperplasia. The University of Washington VR TURP simulator (George Washington University, Washington, DC, USA) has been validated for face [64], content, and construct [65] validity. This simulator attempts to incorporate bleeding and hemostasis into the exercise to emulate realistic environments. In addition, a haptic interface is available allowing force feedback on the instruments to increase the realism of the simulation. Uro Trainer (Karl Storz GmbH, Tuttlingen, Germany) is a VR simulator that can be used for TURBT and TURP simulation. Four endoscopes are simulated in the trainer, and this hardware also includes haptics for force feedback. The simulation allows for diagnosis of bladder tumors as well as resection and coagulation of the tumor. Mishra et al. and Reich et al. performed face and content validation on the simulator [66, 67]. PelvicVision (Melerit Medical, Linkoping, Sweden) is a VR simulator for TURP procedures that was studied by Kallstrom et al. [68]. In that study, 24 residents underwent practice sessions with the simulator before performing TURPS in the operating room. The investigators found that 75 % of residents were able to complete the TURP after using the simulator, which was improvement from 10 % prior to simulator training.

The PERC Mentor simulator (Simbionix, Lod, Israel) is used for the teaching of skills required for successful completion of a percutaneous nephrolithotomy. This simulator has a needle that is passable through a simulated abdominal wall, and fluoroscopy is simulated with a cumulative radiation dose calculation available during the exercise. PERC Mentor has been validated for construct validity in two separate studies [69, 70]. In one of the studies, the PERC Mentor was compared to a live porcine model. Twenty-four experts completed the exercises and then rated their experiences. The live model was found to be more realistic, but the PERC Mentor had the advantages of being easier to set up and allowing for continued repetition of the task. The authors concluded that both the PERC Mentor and the animal model were useful as training tools.

## Robotic Simulators

### Available Robotic Simulation Systems

At least four platforms for robotic surgical simulation have been described in literature. These include the Mimic dV-Trainer (Mimic Technologies Inc, Seattle, Washington), SimSurgery Education Platform (SimSurgery, Oslo, Norway), Robotic Surgical Simulator System (Simulated Surgical Systems, Williamsville, NY), and the da Vinci Skills Simulator (Intuitive Surgical, Sunnyvale, CA). As the application of robotic-assisted urologic surgery has grown, there has been a concurrent increase in the interest of robotic simulators as reflected by the increasing number of publications over the past few years. Validation studies have been performed for all of the simulators individually, but only a limited number of comparisons between types of simulators have been conducted (Table 19.1). Other topics that are addressed in the literature are the applicability of these simulators to trainees of more advanced levels, the cost versus benefit of purchasing these simulators, and the need for a validated curriculum to be adopted by urology training programs. The next section will discuss each robotic simulator platform, its advantages/disadvantages, and some of the general issues seen in robotic simulation (Table 19.2).

**Table 19.1** Summary of validation studies on robotic surgical simulators

| Authors | Year published | Simulator studied | Exercises performed in study | Number of participants in study | Validity assessed |
|---|---|---|---|---|---|
| Brinkman et al. | 2013 | dVSSS | Ring and rail 2 | 17 novices | Repetitions required |
| Colaco et al. | 2013 | RoSS | Ball drop | Current urology residents at Robert Wood Johnson University Hospital | Construct |
| Hung et al. | 2013 | dVSSS | Pegboard 2, ring and rail 2, suture sponge 3, tubes | 38 novices, 11 experts | Construct |
| Stegemann et al. | 2013 | dVSSS | Ball placement, suture pass, fourth arm manipulation | 65 novices | Attempted curriculum validity |
| Brinkman et al. | 2012 | dVSSS | Ring and rail 2 | 17 novices, 3 experts | Repetitions required |
| Finnegan et al. | 2012 | dVSSS | 24 exercises | 27 attendings, 3 fellows, 9 residents | Construct |
| Hung et al. | 2012 | dVSSS | 17 exercises | 24 novices, 3 experts | Concurrent, predictive |
| Kang et al. | 2012 | Mimic dvT | Tube 2 | 20 novices (medical students) | Repetitions required |
| Kelly et al. | 2012 | dVSSS | Camera targeting, energy switching, threading rings, dots and needles, ring and rail | 19 novices, 9 intermediates, 10 experts | Face, content, construct |
| Lee et al. | 2012 | Mimic dvT | Pegboard ring transfer, ring transfer, matchboard, threading of rings, rail task | 10 attendees, 2 fellows, 4 senior residents, 4 junior residents | Face, content, construct, concurrent |
| Liss et al. | 2012 | dVSSS and Mimic dvT | Pegboard 1, pegboard 2, tubes | 6 students, 7 attendees, 7 junior residents, 6 senior residents, 6 fellows | Content, construct |
| Perrenot et al. | 2012 | dVSSS and Mimic dvT | Pick and place, pegboard, ring and rail, match board, camera targeting | 5 experts, 6 intermediate, 8 beginners, 37 residents, 19 nurses/medical students | Face, content |
| Gavazzi et al. | 2011 | SEP | Arrow manipulation, surgeon's knot | 18 novices, 12 experts | Face, content, construct |
| Hung et al. | 2011 | dVSSS and Mimic dvT | 10 virtual reality exercises | 16 novices, 32 intermediates | Face, content, construct |
| Jonsson et al. | 2011 | ProMIS | Pull/loosen elastic bands, cutting a circle, suture tying, vesicourethral anastomosis | 5 experts, 19 novices | Construct |
| Korets et al. | 2011 | Mimic dvT | 15 exercises | 16 residents | Concurrent |

(continued)

**Table 19.1** (continued)

| Authors | Year published | Simulator studied | Exercises performed in study | Number of participants in study | Validity assessed |
|---|---|---|---|---|---|
| Lerner et al. | 2010 | Mimic dvT | Letter board, pick and place, ring walk, clutching cavity | 12 medical students, 10 residents, 1 fellow | Concurrent |
| Seixas-Mikelus et al. | 2010 | RoSS | Clutch control, ball place, needle removal, fourth arm tissue removal | 31 experts, 11 novices | Content |
| Seixas-Mikelus et al. | 2010 | RoSS | Basic ball pick and place, advanced ball pick and place | 24 experts, 6 novices | Face |
| Kenney et al. | 2009 | Mimic dvT | Pick and place, pegboard, dots and numbers, suture sponge | 19 novices, 7 experts | Face, content, construct |
| Sethi et al. | 2009 | Mimic dvT | Ring and cone, string walk, letter board | 5 experts, 15 novices | Content, construct |

**Table 19.2** Advantages/disadvantages and confirmed validation of available robotic surgical simulators

| Simulator | Pros | Cons | Validation |
|---|---|---|---|
| Mimic da Vinci Trainer (dVT) | 1. Stand-alone unit<br>2. 3D viewer | 1. Instruments not as robust as dVSSS<br>2. Does not use actual console | 1. Face<br>2. Content<br>3. Construct<br>4. Concurrent |
| Intuitive Surgical da Vinci Surgical Skills Simulator (dVSSS) | 1. Use of actual surgical console<br>2. 3D viewer<br>3. Potentially able to use as warm-up just prior to surgery | 1. Not available when console used for surgery | 1. Face<br>2. Content<br>3. Construct<br>4. Concurrent |
| RoSS | 1. Stand-alone unit<br>2. 3D viewer | 1. Does not use actual console | 1. Face<br>2. Content<br>3. Construct |
| SEP | 1. Stand-alone unit | 1. Lack of 3D viewer | 1. Face<br>2. Content<br>3. Construct |

## Robotic Surgical Simulator System (RoSS)

The Robotic Surgical Simulator System (Simulated Surgical Systems, Williamsville, NY) is described as a stand-alone robotic simulator that includes a 3D display and hardware simulating the da Vinci surgical system console (Fig. 19.1). The software includes an algorithm that captures various metrics which in turn are used to generate a score that reflects the outcome of the completed exercises. The RoSS has had face validity [71] as well as content validity studied [72]. Seixas-Mikelus et al. recruited 42 subjects to use the simulator and complete surveys regarding their experience. The respondents indicated that 94 % thought the RoSS would be useful for training purposes. A high percentage of respondents were also in favor of using the RoSS for testing residents before OR experience and were also in favor of use in the certification of robotic surgery. Face validity was assessed in a separate study also authored by Seixas-Mikelus et al. [71]. Thirty participants answered questionnaires regarding the realism of the simulator, and the results indicated that 33 % of novices, 78 % of intermediates, and 50 % of experts thought the simulator were somewhat close. Sixty-seven percent of novices, 22 % of intermediates, and 40 % of experts thought it was very close. Ten percent


**Fig. 19.1** Robotic Surgical Simulator System (*RoSS*) (Courtesy of SimSurgery, Norway)

of experts rated the simulator not close. Colaco et al. published a study in 2013 demonstrating construct validity of the RoSS [73]. In their study, it was found that training time, performance, and rating of the simulator by the participant were correlated.

## SimSurgery Education Platform (SEP)

SEP robotic trainer (SimSurgery, Oslo, Norway) is described as a stand-alone system with 21 exercises designed to train robotic surgical skills. Exercises are broadly divided into tissue manipulation, basic suturing, and advanced suturing. The face validity and content validity of this system have been verified in a study by Gavazzi et al. [74]. One noted drawback of the SEP compared to other available simulators was that it lacked the 3D viewer that is integrated into the da Vinci console. Thirty participants performing tasks involving arrow manipulation and tying a surgeon's knot were studied to prove face, content, and construct validity. Participants rated the realism "highly" (90 %), confirming face validity. Construct validity was also verified as the expert group outperformed the novice group. It was noted that more metrics were seen to differ between the novices and experts in the knot-tying exercise compared to the place-an-arrow exercise. This was suggested to be due to the difficulty of the exercise, with the observation that it was easier to distinguish between novices and experts when the task complexity was increased.

## Mimic da Vinci Trainer (dVT)

Mimic dV-Trainer (Mimic Technologies Inc., Seattle, Washington) became available in 2007 and is a stand-alone unit for simulation of the da Vinci surgical system (Fig. 19.2). The unit includes

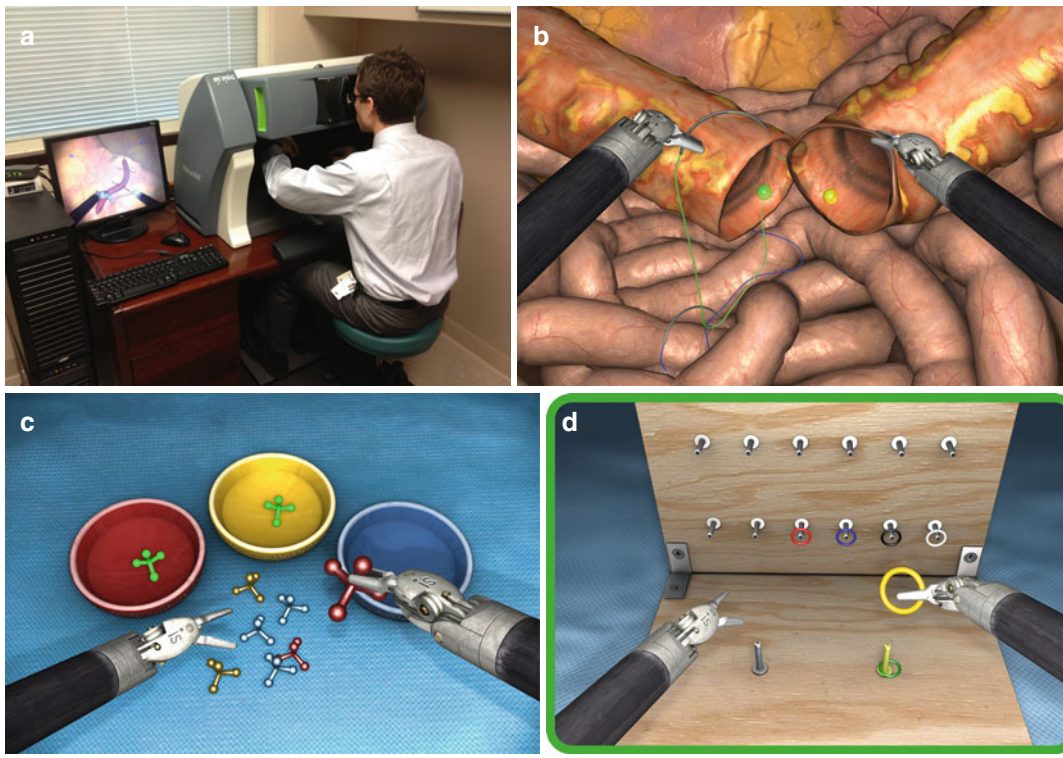


**Fig. 19.2** (**a**) Mimic da Vinci Trainer (dVT) in use at Indiana University Urology residents' office, (**b**) tube exercise, (**c**) pick and place exercise, (**d**) pegboard exercise (**b**–**d** Courtesy of Mimic Technologies, Park Ridge, IL, USA)

foot pedals to simulate the equipment on an Intuitive Surgical da Vinci S or Si system. The scoring of the exercises is performed with an internal algorithm that generates a total score as well as separate scores for 11 other metrics. The face, construct, and content validity have been validated in various studies [75, 76]. In a study by Sethi et al., 20 participants underwent three repetitions of three separate exercises and completed questionnaires regarding the use of the simulator. The 15 novices were differentiated from the experts by their performance, thereby confirming the construct validity. Participants rated the realism of the simulator above average to high in all parameters investigated, confirming the face validity. Content was assessed by the expert surgeons and the conclusion was that exercises were valid for the training of residents. Kenney et al. demonstrated face, content, and construct validity on the Mimic dV-Trainer but utilizing a different set of exercises than Sethi et al. In their study, 24 participants underwent training with four exercises [77]. Experienced surgeons were again found to outperform novices for face validity. The simulator was rated as useful for training by the expert surgeons and the virtual reality representation of the instruments was found to be acceptable, but some of the exercises involving needle suturing into a sponge were found to be less than ideal.

The concurrent validity of the Mimic dVT has also been validated [78, 79]. Lerner et al. and Korets et al. both looked at concurrent validity of the Mimic trainer compared to inanimate exercises on the da Vinci console. Korets et al. had three groups of participants. One group completed 15 exercises in the Mimic curriculum and was considered to pass when all exercises had a minimal score of 80 %. The second group had a 90 min personalized session with an endourology fellow serving as mentor. The third group had no additional training. The results demonstrate improvement of performance for the two groups who had training over the control group (no training). The difference in improvement comparing the Mimic and the da Vinci training group was insignificant, leading Korets et al. to conclude that either method (VR or inanimate training) was acceptable in improving skills.

## da Vinci Surgical Skills Simulator (dVSSS)

The da Vinci Skills Simulator (Intuitive Surgical, Sunnyvale, CA) is a backpack unit that attaches to the da Vinci Si or Si-e surgical system and allows the user to perform virtual reality exercises on the robotic console (Fig. 19.3). The exercises were developed in collaboration with Mimic Technologies and Simbionix. Broad categories of training exercises include camera/clutching, fourth arm integration, system settings, needle control/driving, energy/dissection, EndoWrist manipulation, and knot tying.

Finnegan et al. published an industry-sponsored study demonstrating the construct validity of the dVSSS in 2012 [80]. In their study, the participants completed all 24 exercises within the Mimic software on the dVSSS. Their statistical analysis demonstrated that within certain exercises construct validity was present. The participants were divided into three groups according to the number of robotic cases previously performed. Significant differences were seen within certain metrics in 15 of the exercises that they studied. The authors suggested that certain exercises were better than others at distinguishing between groups of trainees and that this would have to be optimized in the future with further studies. Exercises that were not valid could be removed from a potential curriculum.

Groups out of University of Southern California (USC) and Thomas Jefferson University have published studies on the validity of the dVSSS [81, 82]. Both groups confirm that the simulator has face, content, and construct validity. Hung et al. commissioned their study as a prospective study with involvement of experts from urology, cardiothoracic surgery, and gynecology. Participants in both studies rated the realism of the simulator highly with scores of 8/10 in Hung's study [82] and 4.1–4.3 out of 5 in Kelly's study [81]. Content validity was confirmed in the USC study, with the experts outperforming the rest of the participants in the study in nearly all measures. In contrast to this, the group out of Thomas Jefferson University found that content validity was present only when their intermediate and


**Fig. 19.3** (**a**) da Vinci Surgical Systems Simulator (dVSSS) at Indiana University main operating room, (**b**) dVSSS attached to console, example of ring walk exercise, and associated metrics (**b**, Courtesy of Intuitive Surgical, Inc., Sunnyvale, CA, USA)

expert participants were combined into a single group. They reasoned that this was due to differences in study design, including sample size, number of repeats of each exercise, exercises studied, and method of defining experience levels (grouping). Content validity was established in both studies as the experts determined that the simulator was a good tool for training residents and fellows.

## Other Methods of Education for Robotics Training and Comparison Between Available Robotic Simulators

Although there is research data on each robotic simulator individually, limited data is available comparing the simulators to each other. This makes it difficult to decide on what the standard should be in robotic surgery simulation [83]. Whereas laparoscopic surgery has a validated curriculum involving the FLS, there still remains work to be completed in the domain of robotic surgical simulation to achieve the same end point. In this vein, some studies on robotic simulation have begun to look at how the simulators compare to validated training exercises. Hung et al. studied three options for robotic surgery education, which included inanimate tasks, virtual reality simulation, and surgery on a live porcine model. Each method was identified to have a different set of advantages and disadvantages. The inanimate task is cost-effective, but requires the availability of an extra robot or the use of an existing robot during off-hours. The virtual reality simulator is currently costly but can be made more readily available for trainees if it is a stand-alone unit. The porcine model is considered high fidelity since it models the tissues most similarly to the real surgery but is also very costly, requires a lot of additional preparation, and requires that the robot be available for trainees to use. Despite differences within each method of education, Hung et al. demonstrated that there was correlation of performance across the three modalities. Both the VR exercises (four selected exercises) and the inanimate exercises used in the study were previously validated for construct validity. The results of this study also demonstrated construct validity as the experts outperformed the novices in the tasks evaluated. The authors concluded that all modalities were useful and targeted the same skill sets.

One of the few studies that examine differences between the simulators is by Liss et al. who conducted their study to compare the construct validity and the correlation between the Mimic dVT and the dVSSS [84]. Participants including

medical students, residents, fellows, and staff urologists were instructed to perform exercises first on the dVSSS and then on the dVT. Exercises included the pegboard 1, pegboard 2, and tubes. They were evaluated by metrics provided within the software that had been previously validated. Results indicated that there was a correlation between the simulators in the suturing task, which was deemed as the most difficult and relevant task. Both simulators were identified to have good construct validity, as they were able to distinguish between the participants of various skill levels. The authors discussed the advantages and disadvantages of each system, finding that the Mimic dVT was easier to access because it is a stand-alone system. Both systems had a similar cost at an estimated $100,000. The dVSSS was found to have better face and content validity as rated by the study participants. Another benefit identified for the dVSSS was that since the system is attached to the console used for the actual surgery, it can serve as a warm-up just prior to surgery. Conversely, a drawback of the simulator being attached to the actual console is that it also precludes use of the system for practice when a surgery is being performed. Hung et al. suggested that the limitations of the Mimic dVT are such that it does not utilize the actual da Vinci console and therefore lacks the same realism compared to the dVSSS [82].

At the Indiana University urology department, Lerner et al. studied participants undergoing training with the Mimic dVT and assessed improvements in task completion on the da Vinci surgical system while performing inanimate exercises [78]. Results demonstrated that the novice learners utilizing the dVT improved their baseline scores in pattern cutting and pegboard times. Compared to a group consisting of novice residents, the medical students were seen to make similar improvements in time and accuracy between the initial and final sessions. The virtual training was seen to be beneficial in improving outcomes for exercises that were similar in the inanimate exercise set on the dVSSS. The Mimic trainer was therefore identified as a tool for novices to familiarize themselves with the basic mechanics of robotic surgery. Through simulator practice, a decrease in instrument collisions and an increase in comfort with the use of the foot pedals/console controls were derived and thought to result in improved performance on the actual console.

Hung et al. demonstrated the benefit of virtual simulation with the da Vinci Skills Simulator on the performance of wet lab skills that mimicked surgery [85]. Tasks included bowel resection, cystotomy and repair, and partial nephrectomy in wet lab. Evaluation was carried out by experts utilizing the GOALS metrics which were described by Vassilou et al. as a rating scale for evaluation of technical skills in laparoscopy [86]. Simulation involved the completion of 17 selected tasks. The trainees with the lowest baseline scores on the da Vinci Skills Simulator were found to have the most benefits in improvement. This suggested that the trainees that require remedial work may benefit the most from additional simulator time. Furthermore, they found correlation between the trainees' scores in the virtual simulation and the wet lab exercises. Excessive tissue pressure, collisions, and time were also found to have correlation.

## Robotic Surgery Training Curves and Applicability of Simulator to Expert Robotic Surgeons

Although it is generally agreed upon that simulator training is safe and helps novice trainees attain the basic skills required to operate the robotic console, there is less documented benefit when the simulator is assessed in the context of educating expert surgeons. In order to better understand these phenomena, we look at studies that have identified the shape and duration of learning curves of trainees on the simulator. A number of recent studies have also delved into the reasons why certain metrics on the robotic simulators may not be appropriate for assessing the expert robotic surgeon.

Kang et al. studied the number of repetitions required for a novice to train in a given exercise on the Mimic dV-Trainer [87]. They selected "Tube 2" program which is representative of the

urethral anastomosis in a robotic-assisted prostatectomy. The participants consisted of 20 medical students who were considered naïve of the surgical procedure. No comparison to expert performance was included in this exercise. Analysis was carried out to identify the number of repetitions required for the slope to plateau, indicating a stable performance level of the exercise. Seventy-four repetitions were identified as the number that was required for a plateau. The authors concluded that the participants could start at a naïve level and spend 4 h to complete the 74 repetitions required to reach mastery of the exercise. A caveat noted was that mastery of the exercise in the simulator was not necessarily indicative of performance in real surgery. A drawback of the study was that the primary factor that was assessed was time for completion of the task, which is not necessarily the best metric. Real surgery involves more than quick completion of a procedure and may also involve careful dissection to achieve dissection in appropriate tissue planes. Studies or exercises only assessing time may be overlooking other critical metrics. Jonsson et al. also commented on the applicability of tasks to the intermediate trainee and expert surgeon. They recommended that sufficiently complex training exercises be included as the construct validity may not be valid on simple tasks [88].

Brinkman et al. also studied the number of repetitions needed for skills acquisition on a robotic simulator [89]. Similar to Kang et al. they looked at repetitions of a single exercise. Ring and Rail II was utilized in the da Vinci Skills Simulator. Utilizing a similar cohort comprised solely of medical students, they examined the effect of exercise repetition on performance and attempted to find the number of trials to reach expert level. Expert performance was determined by having three participants that had greater than 150 robotic cases perform the exercises. The results support that of Kang et al. in that ten exercises were not sufficient for the novices to reach an expert level of performance. The study looked at multiple variables, not just time, for task completion, and the authors concluded that certain metrics were better suited to assess novices versus experts. Furthermore, they noted that some metrics such as time could be negated by poor instrument use involving the clashing of arms and excessive tension. In other words, the simulator could provide basic assessment of skills, but this may not necessarily transfer directly to real surgical performance, since a real surgery is multifaceted. Interestingly, not all metrics were seen as applicable to experts.

Kelley et al. also commented on the differing degrees of complexity of the exercises and surmised that certain exercises may be more applicable to experts [81]. This is further supported by Hung et al. who surveyed experts and found them to be in agreement that the simulator was limited in relevance for the expert in robotic surgery [82]. In regard to why certain metrics may not be applicable, Perrenot et al. identified the "camera out of view" metric as something that may not be applicable to experts who are used to having instruments out of camera view but are still aware of their exact location within the abdomen or working field [75].

## Curriculum in Robotics Training

The University of Texas Southwestern Medical Center is one group that has proposed a curriculum for robotics training. Of note, their curriculum involves inanimate exercises and not virtual reality simulators. Dulan et al. and Arain et al. published papers on the validity of the curriculum as well as the feasibility of implementing the curriculum [90, 91]. In their initial description of the curriculum, it was presented as 2 months in duration and involving three components. The first of the components was online material, including a test at the end of the material. Trainees were then given a tutorial on the basic use and positioning/docking of the robot followed by mentoring in a series of nine inanimate tasks [92]. The inanimate skills included peg transfer, clutch and camera movement, rubber band transfer, simple suture, clutch camera peg, stair rubber band transfer, running and cutting rubber band, pattern cut, and running suture. These tasks are described as being similar to and designed based on the previously validated FLS.

Arain et al. further assessed the robotics curriculum at University of Texas Southwestern by examining the feasibility of implementation [91]. Residents, fellows, and staff from general surgery, urology, and gynecology were enrolled into the program. Participants were required to practice exercises until the predetermined level of proficiency had been reached. Similar to other reports, the authors found that numerous repetitions were required to reach a baseline of proficiency. Results demonstrated increased confidence with robotic skills after completion of the program. Proficiency was seen to be reached at 72 repetitions. Performance in the tests was seen to increase in all nine exercises, demonstrating educational benefit based on comparisons of the pretest and posttest results. Inter-rater reliability was seen to be adequate for all exercises except the suture-running, which was explained by the fact that the exercise was complicated in nature. The conclusions from the authors were that the robotics training curriculum proposed was feasible from an economic standpoint, demonstrated educational benefits, and was reliable in terms of its measures.

Lucas et al. described a robotics training curriculum at Indiana University [8]. The curriculum consisted of introductory sessions performed online through the intuitive surgical website which included modules to familiarize the trainee with basic controls. The trainee then graduated to one-on-one sessions which were held on the console during off-peak hours in the operating room. The trainee was able to become familiar with the operation of the console, as well as the procedures involved with bedside assisting. Docking, instrument changes, arm placement, and troubleshooting tips were taught. After obtaining adequate experience as a bedside assistant, the trainees were allowed to proceed to console time during live surgeries. As the trainees gained experience and confidence, they were gradually allowed to perform more difficult parts of the surgery. This method of graduated increases in difficulty has been shown to be successful in training novices as reported by Rashid et al. who broke down the robotic-assisted radical prostatectomy (RALP) into five distinct steps [11]. Lucas et al. concluded that the data showed a statistically significant trend of improving overall score and decreasing time required for each step as the trainee progressed in their training course.

In the assessment of their curriculum, Lucas et al. found that the performance in selected metrics of the inanimate training tasks improved over the duration of the curriculum. The five inanimate tasks included pegboard, checkerboard, sting running, pattern cutting, and suturing. These tasks were designed or selected based on prior validation of similar tasks in the FLS curriculum. The basic tasks were thought to serve as the foundation on which more advanced robotic skills could be developed. At the end of the training, there were no statistical differences between residents defined as inexperienced and those defined as experienced. A proposed use of the inanimate portion of the curriculum was to ensure that all trainees were at an adequate minimum level of skills before proceeding to live surgery.

The Fundamentals of Robotic Surgery (FRS) is an ongoing collaboration that aims to provide a validated curriculum for the training of surgeons with robotic surgery [93]. The FRS is currently preparing to undergo validation as of 2013 and will hopefully be available in the near future as an additional tool for the training of future robotic surgeons. In contrast to prior attempts, the effort is multi-institutional and multispecialty in its efforts to create a universal curriculum. A total of 25 outcome measures were convened upon by the participants involved in the design of the curriculum. The curriculum was subdivided into didactic-based learning, psychomotor skills training, and team-based training/communication training.

For the didactic portion of the curriculum, tasks were divided into three phases that included the preoperative, intraoperative, and postoperative phases of patient care. In the preoperative phase, the learner would be expected to demonstrate proficiency in the setup of equipment and positioning of staff in preparation to perform robotic surgery. Intraoperative skills training would focus on the actual use of the robotic console and the robotic tools used in the surgery. Finally, a postoperative phase includes steps for

undocking and removal of the robot. The curriculum is currently undergoing validation at this time.

The psychomotor component of the FRS curriculum was proposed to include seven exercises. Tasks included docking and instrument insertion, ring tower transfer, knot tying, railroad track, fourth arm cutting, cloverleaf dissection, and vessel dissection/division. A team training and communication component to the curriculum was thought to be important given the cooperation required for a robotic surgery to be successfully accomplished. Focus was placed towards preoperative preparation, robotic docking, intraoperative communication, and undocking the robot/debriefing of the team.

In an alternate effort, Stegemann et al. have proposed the Fundamental Skills of Robotic Surgery (FSRS) as a validated curriculum [18]. This curriculum involving 16 tasks was based on the RoSS. In their study, 53 participants were divided into groups that completed tasks with the dVSSS either with or without prior training in the robotics curriculum. A crossover group was additionally tested. Participants included medical students, residents, fellows, and staff urologists. They found that the group undergoing curriculum training and the crossover group had improved scores in certain metrics within each task.

## Future Directions and Uses

FLS is now used for assessment of competency with laparoscopic skills prior to graduation of general surgery residents. Along similar veins of discussion, there have been proposals to test competency in robotic-assisted surgery prior to graduation of urology trainees/novices. Although no assessments currently exist, multiple groups have proposed that the robotic simulator could play a central role in this [17, 19, 81, 94]. A simulator could also be used at the beginning of residency to determine minimal competency prior to beginning the clinical phase of learning on patients. Another phase in urologic training that the simulator could be applicable is for competency assessment of the graduating resident. Along similar lines, the simulator could be employed to assess competency of the newly trained postgraduate urologist. Steps must still be taken to determine the appropriate tool for assessment by determining the validity of the simulator and setting minimal levels for proficiency on that particular platform. This would have to involve a large-scale analysis of experts' scores to determine the validity of the minimal proficiency levels [19].

Another scenario in which robotic simulators may play a crucial role is in that of skill maintenance in low-volume robotic surgeons. Jenison et al. found that the skills required for robotic surgery can degrade in as little as 4 weeks [95]. In that study, a total of 25 attending surgeons and 29 residents were enrolled and underwent initial training, repeating the exercise until a predetermined proficiency level had been met. After meeting the proficiency goal, the participants did not perform robotic surgery for 12 weeks, but were tested at 4, 8, and 12 weeks to assess their skill retention levels. A significant increase in time and errors within the task completion was seen across the participants. This poses as problem for the low-volume roboticist who may only encounter or perform a robotic-assisted case a few times per year. Suggestions have been made that these low-volume surgeons may be able to improve upkeep of their robotic skills with access to a simulator through which they can practice on a regular basis [80].

### Conclusions

In summary, the direction that urology is advancing towards involves more and more complex procedures and surgical techniques. The advent of endourology, laparoscopy, and robotic-assisted laparoscopy has brought changes to the way in which urology trainees are educated. In order for urology novices to become competent in surgery, they must overcome many barriers including operating room costs, patient safety, limited working hours, and other factors. The simulator is but one tool in the armamentarium for training residents in endoscopy, laparoscopy, and robotics. Its cost

and benefits must be weighed against other available methods of training. What is known is that the simulator provides a safe environment for novices to acquire skills, and studies have validated the transfer of these skills towards performance on the robotic console. Studies are still needed to demonstrate direct correlation of simulator use to outcomes in surgeries performed on actual patients.

Although much work has been invested into the use of simulators for teaching urologic surgery, there is still much to be done. One of the major obstacles that must be addressed in order for training to become more standardized and consistent across programs is the development of a curriculum. The future of simulation in urology training is advancing at a fast pace and many possibilities exist. Given the results seen thus far, expanding the use of simulators to include even wider applications, such as credentialing in the field of urology, is a promising possibility.

## References


1. Steinberg PL, Merguerian PA, Bihrle 3rd W, Seigne JD. The cost of learning robotic-assisted prostatectomy. Urology. 2008;72(5):1068–72.
2. Okrainec A, Soper NJ, Swanstrom LL, Fried GM. Trends and results of the first 5 years of Fundamentals of Laparoscopic Surgery (FLS) certification testing. Surg Endosc. 2011;25(4):1192–8.
3. Gohil R, Khan RS, Ahmed K, Kumar P, Challacombe B, Khan MS, et al. Urology training: past, present and future. BJU Int. 2012;109(10):1444–8.
4. Lowrance WT, Eastham JA, Savage C, Maschino AC, Laudone VP, Dechet CB, et al. Contemporary open and robotic radical prostatectomy practice patterns among urologists in the United States. J Urol. 2012;187(6):2087–92. PubMed PMID: 22498227: Pubmed Central PMCID: PMC3407038. Epub 2012/04/14. eng.
5. Ahmed K, Khan MS, Vats A, Nagpal K, Priest O, Patel V, et al. Current status of robotic assisted pelvic surgery and future developments. Int J Surg Lond Engl. 2009;7(5):431–40. PubMed PMID: 19735746. Epub 2009/09/09. eng.
6. Monn MF, Bahler CD, Schneider EB, Whittam BM, Misseri R, Rink RC, et al. Trends in robot-assisted laparoscopic pyeloplasty in pediatric patients. Urology. 2013;81(6):1336–41. PubMed PMID: 23522294. Epub 2013/03/26. eng.
7. Guzzo TJ, Gonzalgo ML. Robotic surgical training of the urologic oncologist. Urol Oncol. 2009; 27(2):214–7. PubMed PMID: 19285237. Epub 2009/03/17. eng.
8. Lucas SM, Gilley DA, Joshi SS, Gardner TA, Sundaram CP. Robotics training program: evaluation of the satisfaction and the factors that influence success of skills training in a resident robotics curriculum. J Endourol. 2011;25(10):1669–74. PubMed PMID: 21815825. Epub 2011/08/06. eng.
9. Mirheydar H, Jones M, Koeneman KS, Sweet RM. Robotic surgical education: a collaborative approach to training postgraduate urologists and endourology fellows. JSLS. 2009;13(3):287–92. PubMed PMID: 19793464. Pubmed Central PMCID: PMC3015961. Epub 2009/10/02. eng.
10. McDougall EM, Corica FA, Chou DS, Abdelshehid CS, Uribe CA, Stoliar G, et al. Short-term impact of a robot-assisted laparoscopic prostatectomy 'mini-residency' experience on postgraduate urologists' practice patterns. Int J Med Robot. 2006;2(1):70–4. PubMed PMID: 17520615. Epub 2007/05/24. eng.
11. Rashid HH, Leung YY, Rashid MJ, Oleyourryk G, Valvo JR, Eichel L. Robotic surgical education: a systematic approach to training urology residents to perform robotic-assisted laparoscopic radical prostatectomy. Urology. 2006;68(1):75–9. PubMed PMID: 16844450. Epub 2006/07/18. eng.
12. Menon M, Tewari A, Peabody JO, Shrivastava A, Kaul S, Bhandari A, et al. Vattikuti Institute prostatectomy, a technique of robotic radical prostatectomy for management of localized carcinoma of the prostate: experience of over 1100 cases. Urol Clin North Am. 2004;31(4):701–17. PubMed PMID: 15474597. Epub 2004/10/12. eng.
13. Patel VR, Tully AS, Holmes R, Lindsay J. Robotic radical prostatectomy in the community setting–the learning curve and beyond: initial 200 cases. J Urol. 2005;174(1):269–72. PubMed PMID: 15947662. Epub 2005/06/11. eng.
14. Ahlering TE, Skarecky D, Lee D, Clayman RV. Successful transfer of open surgical skills to a laparoscopic environment using a robotic interface: initial experience with laparoscopic radical prostatectomy. J Urol. 2003;170(5):1738–41. PubMed PMID: 14532766. Epub 2003/10/09. eng.
15. Herrell SD, Smith Jr JA. Robotic-assisted laparoscopic prostatectomy: what is the learning curve? Urology. 2005;66(5 Suppl):105–7. PubMed PMID: 16194715. Epub 2005/10/01. eng.
16. Schroeck FR, de Sousa CA, Kalman RA, Kalia MS, Pierre SA, Haleblian GE, et al. Trainees do not negatively impact the institutional learning curve for robotic prostatectomy as characterized by operative time, estimated blood loss, and positive surgical margin rate. Urology. 2008;71(4):597–601. PubMed PMID: 18387389. Epub 2008/04/05. eng.
17. Lee JY, Mucksavage P, Sundaram CP, McDougall EM. Best practices for robotic surgery training and

credentialing. J Urol. 2011;185(4):1191–7. PubMed PMID: 21334030. Epub 2011/02/22. eng.
18. Stegemann AP, Ahmed K, Syed JR, Rehman S, Ghani K, Autorino R, et al. Fundamental skills of robotic surgery: a multi-institutional randomized controlled trial for validation of a simulation-based curriculum. Urology. 2013;81(4):767–74. PubMed PMID: 23484743. Epub 2013/03/15. eng.
19. Vlaovic PD, McDougall EM. New age teaching: beyond didactics. Sci World J. 2006;6:2370–80. PubMed PMID: 17619704. Epub 2007/07/11. eng.
20. Forster JA, Browning AJ, Paul AB, Biyani CS. Surgical simulators in urological training – views of UK Training Programme Directors. BJU Int. 2012;110(6):776–8. PubMed PMID: 22233327. Epub 2012/01/12. eng.
21. Le CQ, Lightner DJ, VanderLei L, Segura JW, Gettman MT. The current role of medical simulation in American urological residency training programs: an assessment by program directors. J Urol. 2007;177(1):288–91. PubMed PMID: 17162066. Epub 2006/12/13. eng.
22. Rosen JM, Long SA, McGrath DM, Greer SE. Simulation in plastic surgery training and education: the path forward. Plast Reconstr Surg. 2009;123(2):729–38. PubMed PMID: 19182636. discussion 39–40; Epub 2009/02/03. eng.
23. Malone HR, Syed ON, Downes MS, D'Ambrosio AL, Quest DO, Kaiser MG. Simulation in neurosurgery: a review of computer-based simulation environments and their surgical applications. Neurosurgery. 2010;67(4):1105–16. PubMed PMID: 20881575. Epub 2010/10/01. eng.
24. Schreuder HW, Wolswijk R, Zweemer RP, Schijven MP, Verheijen RH. Training and learning robotic surgery, time for a more structured approach: a systematic review. BJOG. 2012;119(2):137–49. PubMed PMID: 21981104. Epub 2011/10/11. eng.
25. Modi CS, Morris G, Mukherjee R. Computer-simulation training for knee and shoulder arthroscopic surgery. Arthroscopy. 2010;26(6):832–40. PubMed PMID: 20511043. Epub 2010/06/01. eng.
26. Mabrey JD, Reinig KD, Cannon WD. Virtual reality in orthopaedics: is it a reality? Clin Orthop Relat Res. 2010;468(10):2586–91. PubMed PMID: 20559765. Pubmed Central PMCID: 3049630. Epub 2010/06/19. eng.
27. McDougall EM. Validation of surgical simulators. J Endourol. 2007;21(3):244–7. PubMed PMID: 17444766. Epub 2007/04/21. eng.
28. Lendvay TS, Brand TC, White L, Kowalewski T, Jonnadula S, Mercer LD, et al. Virtual reality robotic surgery warm-up improves task performance in a dry laboratory environment: a prospective randomized controlled study. J Am Coll Surg. 2013;216(6):1181–92. PubMed PMID: 23583618. Epub 2013/04/16. eng.
29. Calatayud D, Arora S, Aggarwal R, Kruglikova I, Schulze S, Funch-Jensen P, et al. Warm-up in a virtual reality environment improves performance in the operating room. Ann Surg. 2010;251(6):1181–5. PubMed PMID: 20485133. Epub 2010/05/21. eng.
30. Do AT, Cabbad MF, Kerr A, Serur E, Robertazzi RR, Stankovic MR. A warm-up laparoscopic exercise improves the subsequent laparoscopic performance of Ob-Gyn residents: a low-cost laparoscopic trainer. JSLS. 2006;10(3):297–301. PubMed PMID: 17212883. Pubmed Central PMCID: PMC3015706. Epub 2007/01/11. eng.
31. Lee JY, Mucksavage P, Kerbl DC, Osann KE, Winfield HN, Kahol K, et al. Laparoscopic warm-up exercises improve performance of senior-level trainees during laparoscopic renal surgery. J Endourol. 2012;26(5):545–50. PubMed PMID: 22192095. Pubmed Central PMCID: PMC3552180. Epub 2011/12/24. eng.
32. Fried GM, Feldman LS, Vassiliou MC, Fraser SA, Stanbridge D, Ghitulescu G, et al. Proving the value of simulation in laparoscopic surgery. Ann Surg. 2004;240(3):518–25. discussion 25–8. PubMed PMID: 15319723. Pubmed Central PMCID: PMC1356442. Epub 2004/08/21. eng.
33. Derossis AM, Antoniuk M, Fried GM. Evaluation of laparoscopic skills: a 2-year follow-up during residency training. Can J Surg J Can Chir. 1999;42(4):293–6. PubMed PMID: 10459330. Epub 1999/08/25. eng.
34. Derossis AM, Fried GM, Abrahamowicz M, Sigman HH, Barkun JS, Meakins JL. Development of a model for training and evaluation of laparoscopic skills. Am J Surg. 1998;175(6):482–7. PubMed PMID: 9645777. Epub 1998/06/30. eng.
35. Dauster B, Steinberg AP, Vassiliou MC, Bergman S, Stanbridge DD, Feldman LS, et al. Validity of the MISTELS simulator for laparoscopy training in urology. J Endourol. 2005;19(5):541–5. PubMed PMID: 15989441. Epub 2005/07/02. eng.
36. Feldman LS, Hagarty SE, Ghitulescu G, Stanbridge D, Fried GM. Relationship between objective assessment of technical skills and subjective in-training evaluations in surgical residents. J Am Coll Surg. 2004;198(1):105–10. PubMed PMID: 14698317. Epub 2003/12/31. eng.
37. Fried GM, Derossis AM, Bothwell J, Sigman HH. Comparison of laparoscopic performance in vivo with performance measured in a laparoscopic simulator. Surg Endosc. 1999;13(11):1077–81. discussion 82. PubMed PMID: 10556441. Epub 1999/11/11. eng.
38. McCluney AL, Vassiliou MC, Kaneva PA, Cao J, Stanbridge DD, Feldman LS, et al. FLS simulator performance predicts intraoperative laparoscopic skill. Surg Endosc. 2007;21(11):1991–5. PubMed PMID: 17593434. Epub 2007/06/27. eng.
39. McDougall EM, Corica FA, Boker JR, Sala LG, Stoliar G, Borin JF, et al. Construct validity testing of a laparoscopic surgical simulator. J Am Coll Surg. 2006;202(5):779–87. PubMed PMID: 16648018. Epub 2006/05/02. eng.
40. van Dongen KW, Ahlberg G, Bonavina L, Carter FJ, Grantcharov TP, Hyltander A, et al. European consensus on a competency-based virtual reality training program for basic endoscopic surgical psychomotor

skills. Surg Endosc. 2011;25(1):166–71. PubMed PMID: 20574856. Epub 2010/06/25. eng.
41. Chaudhry A, Sutton C, Wood J, Stone R, McCloy R. Learning rate for laparoscopic surgical skills on MIST VR, a virtual reality simulator: quality of human-computer interface. Ann R Coll Surg Engl. 1999;81(4):281–6. PubMed PMID: 10615201. Pubmed Central PMCID: PMC2503263. Epub 2000/01/01. eng.
42. Grantcharov TP, Kristiansen VB, Bendix J, Bardram L, Rosenberg J, Funch-Jensen P. Randomized clinical trial of virtual reality simulation for laparoscopic skills training. Br J Surg. 2004;91(2):146–50. PubMed PMID: 14760660. Epub 2004/02/05. eng.
43. Seymour NE, Gallagher AG, Roman SA, O'Brien MK, Bansal VK, Andersen DK, et al. Virtual reality training improves operating room performance: results of a randomized, double-blinded study. Ann Surg. 2002;236(4):458–63. discussion 63–4. PubMed PMID: 12368674. Pubmed Central PMCID: PMC1422600. Epub 2002/10/09. eng.
44. Brewin J, Nedas T, Challacombe B, Elhage O, Keisu J, Dasgupta P. Face, content and construct validation of the first virtual reality laparoscopic nephrectomy simulator. BJU Int. 2010;106(6):850–4. PubMed PMID: 20128776. Epub 2010/02/05. eng.
45. Youngblood PL, Srivastava S, Curet M, Heinrichs WL, Dev P, Wren SM. Comparison of training on two laparoscopic simulators and assessment of skills transfer to surgical performance. J Am Coll Surg. 2005;200(4):546–51. PubMed PMID: 15804468. Epub 2005/04/05. eng.
46. Scott DJ, Bergen PC, Rege RV, Laycock R, Tesfay ST, Valentine RJ, et al. Laparoscopic training on bench models: better and more cost effective than operating room experience? J Am Coll Surg. 2000;191(3):272–83. PubMed PMID: 10989902. Epub 2000/09/16. eng.
47. Hyltander A, Liljegren E, Rhodin PH, Lonroth H. The transfer of basic skills learned in a laparoscopic simulator to the operating room. Surg Endosc. 2002;16(9):1324–8. PubMed PMID: 11988802. Epub 2002/05/04. eng.
48. Andreatta PB, Woodrum DT, Birkmeyer JD, Yellamanchilli RK, Doherty GM, Gauger PG, et al. Laparoscopic skills are improved with LapMentor training: results of a randomized, double-blinded study. Ann Surg. 2006;243(6):854–60. discussion 60–3. PubMed PMID: 16772789. Pubmed Central PMCID: PMC1570578. Epub 2006/06/15. eng.
49. Aggarwal R, Ward J, Balasundaram I, Sains P, Athanasiou T, Darzi A. Proving the effectiveness of virtual reality simulation for training in laparoscopic surgery. Ann Surg. 2007;246(5):771–9. PubMed PMID: 17968168. Epub 2007/10/31. eng.
50. Hamilton EC, Scott DJ, Fleming JB, Rege RV, Laycock R, Bergen PC, et al. Comparison of video trainer and virtual reality training systems on acquisition of laparoscopic skills. Surg Endosc. 2002;16(3):406–11. PubMed PMID: 11928017. Epub 2002/04/03. eng.
51. Ahlberg G, Enochsson L, Gallagher AG, Hedman L, Hogman C, McClusky 3rd DA, et al. Proficiency-based virtual reality training significantly reduces the error rate for residents during their first 10 laparoscopic cholecystectomies. Am J Surg. 2007;193(6):797–804. PubMed PMID: 17512301. Epub 2007/05/22. eng.
52. Larsen CR, Soerensen JL, Grantcharov TP, Dalsgaard T, Schouenborg L, Ottosen C, et al. Effect of virtual reality training on laparoscopic surgery: randomised controlled trial. BMJ. 2009;338:b1802. PubMed PMID: 19443914. Pubmed Central PMCID: PMC3273782. Epub 2009/05/16. eng.
53. Schijven MP, Jakimowicz JJ, Broeders IA, Tseng LN. The Eindhoven laparoscopic cholecystectomy training course – improving operating room performance using virtual reality training: results from the first E.A.E.S. accredited virtual reality trainings curriculum. Surg Endosc. 2005;19(9):1220–6.
54. Larsen CR, Oestergaard J, Ottesen BS, Soerensen JL. The efficacy of virtual reality simulation training in laparoscopy: a systematic review of randomized trials. Acta Obstet Gynecol Scand. 2012;91(9):1015–28. PubMed PMID: 22693954. Epub 2012/06/15. eng.
55. Preminger GM, Babayan RK, Merril GL, Raju R, Millman A, Merril JR. Virtual reality surgical simulation in endoscopic urologic surgery. Stud Health Technol Inform. 1996;29:157–63. PubMed PMID: 10172841. Epub 1995/12/09. eng.
56. Shah J, Montgomery B, Langley S, Darzi A. Validation of a flexible cystoscopy course. BJU Int. 2002;90(9):833–5. PubMed PMID: 12460341. Epub 2002/12/04. eng.
57. Dolmans VE, Schout BM, de Beer NA, Bemelmans BL, Scherpbier AJ, Hendrikx AJ. The virtual reality endourologic simulator is realistic and useful for educational purposes. J Endourol. 2009;23(7):1175–81. PubMed PMID: 19530899. Epub 2009/06/18. eng.
58. Michel MS, Knoll T, Kohrmann KU, Alken P. The URO mentor: development and evaluation of a new computer-based interactive training system for virtual life-like simulation of diagnostic and therapeutic endourological procedures. BJU Int. 2002;89(3):174–7. PubMed PMID: 11856093. Epub 2002/02/22. eng.
59. Gettman MT, Le CQ, Rangel LJ, Slezak JM, Bergstralh EJ, Krambeck AE. Development of a standardized curriculum for teaching cystoscopic skills using a computer-based endourologic simulator. Simul Healthc. 2009;4(2):92–7. PubMed PMID: 19444046. Epub 2009/05/16. eng.
60. Watterson JD, Beiko DT, Kuan JK, Denstedt JD. Randomized prospective blinded study validating acquisition of ureteroscopy skills using computer based virtual reality endourological simulator. J Urol. 2002;168(5):1928–32. PubMed PMID: 12394678. Epub 2002/10/24. eng.
61. Jacomides L, Ogan K, Cadeddu JA, Pearle MS. Use of a virtual reality simulator for ureteroscopy training. J Urol. 2004;171(1):320–3. discussion 3. PubMed PMID: 14665905. Epub 2003/12/11. eng.

62. Schout BM, Ananias HJ, Bemelmans BL, d'Ancona FC, Muijtjens AM, Dolmans VE, et al. Transfer of cysto-urethroscopy skills from a virtual-reality simulator to the operating room: a randomized controlled trial. BJU Int. 2010;106(2):226–31. discussion 31. PubMed PMID: 19912184. Epub 2009/11/17. eng.
63. Manyak MJ, Santangelo K, Hahn J, Kaufman R, Carleton T, Hua XC, et al. Virtual reality surgical simulation for lower urinary tract endoscopy and procedures. J Endourol. 2002;16(3):185–90. PubMed PMID: 12028630. Epub 2002/05/25. eng.
64. Sweet R, Kowalewski T, Oppenheimer P, Weghorst S, Satava R. Face, content and construct validity of the University of Washington virtual reality transurethral prostate resection trainer. J Urol. 2004;172(5 Pt 1):1953–7. PubMed PMID: 15540764. Epub 2004/11/16. eng.
65. Rashid HH, Kowalewski T, Oppenheimer P, Ooms A, Krieger JN, Sweet RM. The virtual reality transurethral prostatic resection trainer: evaluation of discriminate validity. J Urol. 2007;177(6):2283–6. PubMed PMID: 17509340. Epub 2007/05/19. eng.
66. Mishra S, Kurien A, Ganpule A, Veeramani M, Sabnis RB, Desai M. Face and content validity of transurethral resection of prostate on Uro trainer: is the simulation training useful? J Endourol. 2010;24(11):1839–43. PubMed PMID: 20653419. Epub 2010/07/27. eng.
67. Reich O, Noll M, Gratzke C, Bachmann A, Waidelich R, Seitz M, et al. High-level virtual reality simulator for endourologic procedures of lower urinary tract. Urology. 2006;67(6):1144–8. PubMed PMID: 16765168. Epub 2006/06/13. eng.
68. Kallstrom R, Hjertberg H, Svanvik J. Impact of virtual reality-simulated training on urology residents' performance of transurethral resection of the prostate. J Endourol. 2010;24(9):1521–8. PubMed PMID: 20677993. Epub 2010/08/04. eng.
69. Mishra S, Kurien A, Ganpule A, Muthu V, Sabnis R, Desai M. Percutaneous renal access training: content validation comparison between a live porcine and a virtual reality (VR) simulation model. BJU Int. 2010;106(11):1753–6. PubMed PMID: 20950308. Epub 2010/10/19. eng.
70. Knudsen BE, Matsumoto ED, Chew BH, Johnson B, Margulis V, Cadeddu JA, et al. A randomized, controlled, prospective study validating the acquisition of percutaneous renal collecting system access skills using a computer based hybrid virtual reality surgical simulator: phase I. J Urol. 2006;176(5):2173–8. PubMed PMID: 17070287. Epub 2006/10/31. eng.
71. Seixas-Mikelus SA, Kesavadas T, Srimathveeravalli G, Chandrasekhar R, Wilding GE, Guru KA. Face validation of a novel robotic surgical simulator. Urology. 2010;76(2):357–60. PubMed PMID: 20299081. Epub 2010/03/20. eng.
72. Seixas-Mikelus SA, Stegemann AP, Kesavadas T, Srimathveeravalli G, Sathyaseelan G, Chandrasekhar R, et al. Content validation of a novel robotic surgical simulator. BJU Int. 2011;107(7):1130–5. PubMed PMID: 21029316. Epub 2010/10/30. eng.
73. Colaco M, Balica A, Su D, Barone J. Initial experiences with RoSS surgical simulator in residency training: a validity and model analysis. J Robot Surg. 2013;7(1):71–5.
74. Gavazzi A, Bahsoun AN, Van Haute W, Ahmed K, Elhage O, Jaye P, et al. Face, content and construct validity of a virtual reality simulator for robotic surgery (SEP Robot). Ann R Coll Surg Engl. 2011;93(2):152–6. PubMed PMID: 22041146. Pubmed Central PMCID: PMC3293312. Epub 2011/11/02. eng.
75. Perrenot C, Perez M, Tran N, Jehl JP, Felblinger J, Bresler L, et al. The virtual reality simulator dV-trainer((R)) is a valid assessment tool for robotic surgical skills. Surg Endosc. 2012;26(9):2587–93. PubMed PMID: 22476836. Epub 2012/04/06. eng.
76. Sethi AS, Peine WJ, Mohammadi Y, Sundaram CP. Validation of a novel virtual reality robotic simulator. J Endourol. 2009;23(3):503–8. PubMed PMID: 19265469. Epub 2009/03/07. eng.
77. Kenney PA, Wszolek MF, Gould JJ, Libertino JA, Moinzadeh A. Face, content, and construct validity of dV-trainer, a novel virtual reality simulator for robotic surgery. Urology. 2009;73(6):1288–92. PubMed PMID: 19362352. Epub 2009/04/14. eng.
78. Lerner MA, Ayalew M, Peine WJ, Sundaram CP. Does training on a virtual reality robotic simulator improve performance on the da Vinci surgical system? J Endourol. 2010;24(3):467–72. PubMed PMID: 20334558. Epub 2010/03/26. eng.
79. Korets R, Mues AC, Graversen JA, Gupta M, Benson MC, Cooper KL, et al. Validating the use of the Mimic dV-trainer for robotic surgery skill acquisition among urology residents. Urology. 2011;78(6):1326–30. PubMed PMID: 22001096. Epub 2011/10/18. eng.
80. Finnegan KT, Meraney AM, Staff I, Shichman SJ. da Vinci skills simulator construct validation study: correlation of prior robotic experience with overall score and time score simulator performance. Urology. 2012;80(2):330–5. PubMed PMID: 22704177. Epub 2012/06/19. eng.
81. Kelly DC, Margules AC, Kundavaram CR, Narins H, Gomella LG, Trabulsi EJ, et al. Face, content, and construct validation of the Da Vinci skills simulator. Urology. 2012;79(5):1068–72. PubMed PMID: 22546387. Epub 2012/05/02. eng.
82. Hung AJ, Zehnder P, Patil MB, Cai J, Ng CK, Aron M, et al. Face, content and construct validity of a novel robotic surgery simulator. J Urol. 2011;186(3):1019–24. PubMed PMID: 21784469. Epub 2011/07/26. eng.
83. Hung AJ, Jayaratna IS, Teruya K, Desai MM, Gill IS, Goh AC. Comparative assessment of three standardized robotic surgery training methods. BJU Int. 2013;112(6):864–71. PubMed PMID: 23470136. Epub 2013/03/09. Eng.
84. Liss MA, Abdelshehid C, Quach S, Lusch A, Graversen J, Landman J, et al. Validation, correlation, and comparison of the da Vinci trainer(™) and the da

Vinci surgical skills simulator(™) using the mimic(™) software for urologic robotic surgical education. J Endourol. 2012;26(12):1629–34. PubMed PMID: 22845173. Epub 2012/08/01. eng.

85. Hung AJ, Patil MB, Zehnder P, Cai J, Ng CK, Aron M, et al. Concurrent and predictive validation of a novel robotic surgery simulator: a prospective, randomized study. J Urol. 2012;187(2):630–7. PubMed PMID: 22177176. Epub 2011/12/20. eng.
86. Vassiliou MC, Feldman LS, Andrew CG, Bergman S, Leffondre K, Stanbridge D, et al. A global assessment tool for evaluation of intraoperative laparoscopic skills. Am J Surg. 2005;190(1):107–13. PubMed PMID: 15972181. Epub 2005/06/24. eng.
87. Kang SG, Yang KS, Ko YH, Kang SH, Park HS, Lee JG, et al. A study on the learning curve of the robotic virtual reality simulator. J Laparoendosc Adv Surg Tech A. 2012;22(5):438–42. PubMed PMID: 22401588. Epub 2012/03/10. eng.
88. Jonsson MN, Mahmood M, Askerud T, Hellborg H, Ramel S, Wiklund NP, et al. ProMIS can serve as a da Vinci(R) simulator – a construct validity study. J Endourol. 2011;25(2):345–50. PubMed PMID: 21114413. Epub 2010/12/01. eng.
89. Brinkman WM, Luursema JM, Kengen B, Schout BM, Witjes JA, Bekkers RL. da Vinci skills simulator for assessing learning curve and criterion-based training of robotic basic skills. Urology. 2013;81(3):562–6.
90. Dulan G, Rege RV, Hogg DC, Gilberg-Fisher KK, Tesfay ST, Scott DJ. Content and face validity of a comprehensive robotic skills training program for general surgery, urology, and gynecology. Am J Surg. 2012;203(4):535–9. PubMed PMID: 22326049. Epub 2012/02/14. eng.
91. Arain NA, Dulan G, Hogg DC, Rege RV, Powers CE, Tesfay ST, et al. Comprehensive proficiency-based inanimate training for robotic surgery: reliability, feasibility, and educational benefit. Surg Endosc. 2012;26(10):2740–5. PubMed PMID: 22538678. Epub 2012/04/28. eng.
92. Dulan G, Rege RV, Hogg DC, Gilberg-Fisher KM, Arain NA, Tesfay ST, et al. Developing a comprehensive, proficiency-based training program for robotic surgery. Surgery. 2012;152(3):477–88. PubMed PMID: 22938907. Epub 2012/09/04. eng.
93. Smith R, Patel V, Satava R. Fundamentals of robotic surgery: outcomes measures and curriculum development. 2013. [cited 2013]. Available from: https://www.nicholsoncenter.com/sites/default/files/research/Fundamentals%20of%20Robotic%20Surgery%20Outcomes%20Measures%20and%20Curriculum%20Development.pdf.
94. Lee JY, Mucksavage P, Kerbl DC, Huynh VB, Etafy M, McDougall EM. Validation study of a virtual reality robotic simulator – role as an assessment tool? J Urol. 2012;187(3):998–1002. PubMed PMID: 22264455. Epub 2012/01/24. eng.
95. Jenison EL, Gil KM, Lendvay TS, Guy MS. Robotic surgical skills: acquisition, maintenance, and degradation. JSLS. 2012;16(2):218–28. PubMed PMID: 23477169. Pubmed Central PMCID: PMC3481234. Epub 2013/03/13. eng.

# Molecular Imaging in Urology

# 20

Ying Pan, Mark Hsu, and Joseph C. Liao

Imaging plays an integral role in urology by providing anatomical detail and diagnostic insight of urologic diseases. Cross-sectional imaging technologies including computed tomography (CT), magnetic resonance imaging (MRI), and ultrasound (US) are used primarily for initial diagnosis, surgical planning, and disease surveillance. In the operating room setting, optical imaging based on white light has provided the illumination for endourologic procedures of the upper and lower urinary tracts, as well as complex abdominal and pelvic surgeries increasingly performed through the laparoscopic/robotic approach. Nevertheless, current imaging technologies still carry limitations such as inadequate sensitivity in early detection of metastases (CT and MRI) [1, 2] and suboptimal diagnostic accuracy (e.g., white-light cystoscopy) [3]. As early diagnosis and accurate staging are particularly critical in the management of urologic malignancies [4], innovative imaging methodologies are needed to improve patient outcomes in urology.

Y. Pan, PhD • M. Hsu, MD
Department of Urology, Stanford University School of Medicine, Stanford, CA, USA
e-mail: yingpan@stanford.edu; markhsu@stanford.edu

J.C. Liao, MD (✉)
Department of Urology, Stanford University School of Medicine, Stanford, CA, USA

VA Palo Alto Heath Care System, Palo Alto, CA, USA
e-mail: jliao@stanford.edu

Molecular imaging is defined as the visualization, characterization, and measurement of biologic processes at the molecular and cellular levels in human and other living systems [5]. It involves a combination of imaging technologies along with molecular imaging agents which target disease-specific genetic and cellular alternations that enhance the differentiation between benign and neoplastic processes. Thus, molecular imaging is capable of real-time visualization of biochemical events at the cellular and molecular level in living cells, tissues, and/or intact subjects [6]. By tagging neoplastic areas with cancer-selective imaging agents, molecular imaging provides not only anatomical but also functional evaluation of diseased organs [7].

Molecular imaging can be broadly classified into anatomical imaging techniques (e.g., CT, MRI, US) and functional imaging with radionucleotide labeling [positron emission tomography (PET) and single-photon emission CT (SPECT)] and optical imaging. Hybrid imaging incorporating anatomical and functional imaging modalities is also becoming more widely available. The imaging systems themselves can be grouped by the energy used (X-rays, positrons, photons, sound waves), the spatial resolution (macroscopic, microscopic), and the type of information that is attained (anatomical, physiological, cellular, or molecular) [8] (Table 20.1). At the smallest scale on the molecular level, specific cell targets implicated in pathogenesis can be visualized for diagnostics and image-guided

J.C. Liao, L.-M. Su (eds.), *Advances in Image-Guided Urologic Surgery*,
DOI 10.1007/978-1-4939-1450-0_20, © Springer Science+Business Media New York 2015

resection intraoperatively or for therapeutic targeting in the clinical arena.

Although still in its infancy, molecular imaging has clinical applications ranging widely from diagnostic uses in disease detection and tumor characterization, real-time guidance in surgery [9], to clinical outcomes such as treatment response and prognosis. In this chapter, we will discuss the urologic applications of existing molecular imaging in clinical practice as well as emerging technologies currently in the preclinical setting.

## Molecular Imaging Agents

While some molecular imaging techniques can visualize the intrinsic differences, such as Raman scattering and autofluorescence, between normal and diseased tissues [9, 10], an exogenous molecular imaging agent is generally required [6] and administrated systematically or topically. In general, molecular imaging agents should have high selectivity, minimal background from nonspecific binding, suitable pharmacokinetics, excellent in vivo stability, and good safety profile [6]. While for topical application, the imaging agents are delivered to target organ directly thus smaller amount of imaging agents are required, which together reduce potential toxicity and blood clearance issues from intravenous injection [10]. This is of special importance for endoscopy-based molecular imaging of urothelial malignancies where imaging agents are introduced intravesically. Translational and clinical examples of molecular imaging though topical administration can be found for imaging of gastrointestinal cancer, another epithelial malignancy [11].

An exogenous molecular imaging agent is typically comprised of a targeting molecule and a signaling conjugate, which should not interfere with the function of the targeting molecule. Targeting molecules can be categorized based on size, ranging from small molecules, peptides, engineered proteins (e.g., affibody), aptamers, and monoclonal antibodies (mAb)—each of which possesses different pharmacokinetic and binding properties (Fig. 20.1) [6].

Small molecules (usually <500 Da) have the smallest size among all molecular imaging agent, which allows them to access and image intracellular targets. Unlike other molecular imaging agents that enable imaging by direct binding to specific target, small molecules can also visualize alternations in protein or cellular functions including metabolism, hypoxia, enzyme activity, and protein synthesis [6]. One clinical example is fluorodeoxyglucose (FDG) that targets increased glucose metabolism found commonly in cancer cells. $^{18}$F-FDG has been the most commonly used PET molecular probe for penile, bladder, prostate, and kidney cancer [12]. On the other hand, due to the small size, there are very limited numbers of signaling conjugates, and small molecules can be attached without altering their pharmacokinetic and targeting properties [6].

Peptides (~15 amino acids) are intermediate in size between small molecules and mAb and engineered proteins. Thus, peptides provide increased flexibility in signaling conjugates and generally offer superior selectivity and specificity than small molecules. While peptides generally have lower affinity compared to mAbs, the relatively smaller size makes them less immunogenic and allows penetration to deep tissue where mAbs are not accessible. The biggest limitation of peptide as targeting molecule is the in vivo stability, and strategies such as adding prosthetic group is mostly required for radiolabeling of peptides. An example of peptide-based molecular imaging agent for SPECT is $^{111}$In-DTPA-octreotide, a somatostatin analog originally developed for scintigraphy of neuroendocrine tumors. More peptide imaging agents are under clinical trial or preclinical investigations [13]. One preclinical example of peptide-based molecular imaging is bombesin (BBN) analogs targeting the gastrin-releasing peptide receptor (GRPR) as molecular probes for PET imaging of prostate cancer. In vivo imaging results on animal models are promising [14].

Monoclonal antibodies can recognize tumor-associated antigens including adhesion molecules and cell surface proteins with ultrahigh affinity and specificity [15]. However, their utilization as molecular imaging agents are limited

**Table 20.1** Overview of molecular imaging systems

| Technique | Resolution[a] | Depth | Time[b] | Quantitative[c] | Multichannel | Imaging agents | Target | Cost[d] | Main small animal use | Clinical use |
|---|---|---|---|---|---|---|---|---|---|---|
| MRI | 10–100 µm | No limit | Minutes to hours | Yes | No | Paramagnetic chelates, magnetic particles | Anatomical, physiological, molecular | $$$ | Versatile imaging modality with high soft tissue contrast | Yes |
| CT | 50 µm | No limit | Minutes | Yes | No | Iodinated molecules | Anatomical, physiological | $$ | Imaging lungs and bone | Yes |
| Ultrasound | 50 µm | cm | Seconds to minutes | Yes | No | Microbubbles | Anatomical, physiological | $$ | Vascular and interventional imaging[e] | Yes |
| PET | 1–2 mm | No limit | Minutes to hours | Yes | No | 18 F-, 64Cu-, or 11C-labeled compounds | Physiological, molecular | $$$ | Versatile imaging modality with many tracers | Yes |
| SPECT | 1–2 mm | No limits | Minutes to hours | Yes | No | 99mTc- or 11In-labeled compounds | Physiological, molecular | $$ | Imaging labeled antibodies, proteins and peptides | Yes |
| Fluorescence | 2–3 mm | <1 cm | Seconds to minutes | No | Yes | Photoproteins, fluorochromes | Physiological, molecular | $ | Rapid screening of molecular events in surface-based disease | Yes |
| FMT | 1 mm | <10 cm | Minutes to hours | Yes | Yes | Near-infrared fluorochromes | Physiological, molecular | $ | Quantitative imaging of fluorochrome reporters | In development |
| Bioluminescence imaging | Several mm | cm | Minutes | No | Yes | Luciferins | Molecular | $$ | Gene expression, cell and bacteria tracking | No |
| Intravital microscopy[f] | 1 µm | <400–800 µm | Seconds to hours | No | Yes | Photoproteins, fluorochromes | Anatomical, physiological, molecular | $$$ | All of the above at higher resolutions but limited depths and coverage | In development[g] |

From Weissleder and Pittet [8], with permission from Nature Publishing Group

[a]For high resolution, small animal imaging systems (Clinical imaging systems differ)

[b]Time for image acquisition

[c]Quantitative here means inherently quantitative. All approaches allow relative quantification

[d]Cost is based on purchase price of imaging systems in the United States. $, <US$100,000; $$, $100,000 to 300,000; $$$, >US$300,000

[e]Interventional means used for interventional procedures such as biopsies or injection of cells under ultrasound guidance

[f]Laser-scanning confocal or multiphoton microscopy.

[g]For microendoscopy and skin imaging

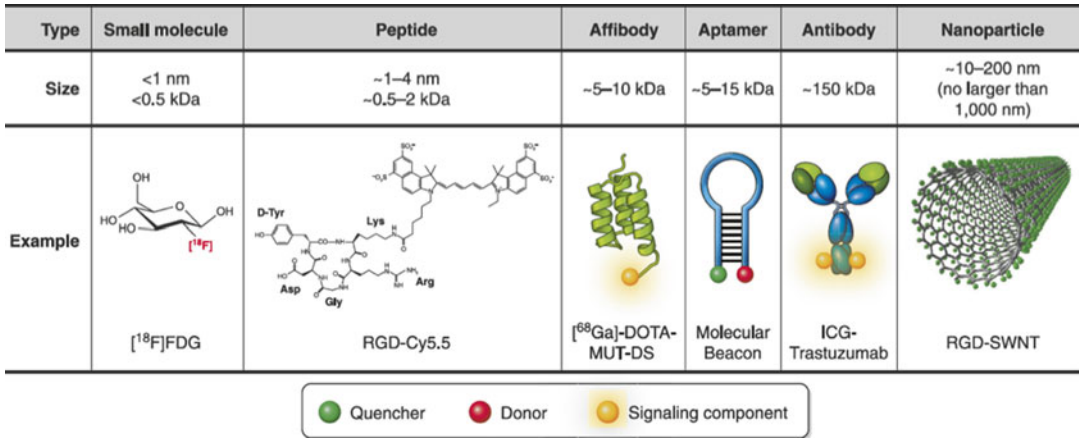


**Fig. 20.1** Overview of molecular imaging agents. $^{18}$F-FDG is a small molecule PET imaging agent for visualizing activity and levels of hexokinase type II and glucose transporter I. RGD peptide labeled with cyanine 5.5 (*RGD-Cy5.5*) is a fluorescent peptide imaging agent for imaging alpha-v beta-3 ($\alpha_v\beta_3$) integrins. Affibody PET agent gallium-68-labeled DOTA-MUT-DS ($^{68}$Ga-DOTA-MUT-DS) and fluorescent mAb agent ICG-trastuzumab are both used to image human epidermal growth factor receptor type 2 (HER2). A general representation of an aptamer molecular beacon (also known as smart/activatable probe) is shown as an example of an aptamer imaging agent. Lastly, RGD-SWNT is depicted as an example of a nanoparticle imaging agent (From James and Gambhir [6], with permission from The American Physiological Society)

by high immunogenicity from murine origin, restricted tissue penetration, and slow clearance from blood associated with big size (150 kDa) [6, 16]. The immunogenicity issue can be overcome by production of chimeric and humanized mAb [15]. mAb derivatives with smaller size have also been developed to improve the pharmacokinetics of mAb while maintaining the specificity and affinity [17]. While single-chain variable fragment (scFv, ~25 kDa), which contains one antigen-binding site of mAb, clears too quickly to generate adequate accumulation on target, mAb derivatives with intermediate size such as diabodies (scFc dimer, ~55 kDa) and minibodies (scFv fused to single Fc domain, ~80 kDa) have shown promising imaging results on animal models [17]. Currently, there are at least 8 mAbs approved for SPECT molecular imaging [16]. Among them, $^{111}$In-capromabpendetide (ProstaScint) in particular is approved for molecular imaging of prostate cancer [18].

Affibodies are emerging molecular imaging agents with significant potential for clinical translation [6]. Affibodies are small non-immunoglobulin affinity ligands capable of binding to a wide range of protein targets. They are selected from combinatorial libraries based on a 58-amino acid, three-alpha-helical Z-domain scaffold [17]. Affibodies have fast clearance from the blood with adequate tumor uptake [16]. There are growing interests in using affibodies as alternative to mAb and mAb derivatives. One example is affibody molecules that target epidermal growth factor receptor 2 as molecular probe for SPECT. A clinical study on breast cancer patients with $^{111}$In- or $^{68}$Ga-labeled ABY-002 has shown great potential to localize metastatic lesions [19]. Variants of ABY-002 also have been investigated on prostate cancer xenografts [20].

Aptamers are single-stranded DNA or RNA oligonucleotides that are activated upon binding to their targets. While aptamers offer high affinity and specificity comparable to mAbs, their application as molecular imaging agent is limited by low in vivo stability and short half-life associated with their small size [6]. Molecular imaging with aptamers in general is still in its infancy and needs further investigation [6]. Recently, a novel nucleolin-targeted DNA aptamer (AS1411) has been evaluated as therapeutic drug for metastatic renal cell carcinoma in a phase II trial study [21]. Low toxicity was observed in patients, indicating

AS1411 may potentially be translated for molecular imaging purpose.

Targeting molecules can be conjugated to radioisotopes, fluorescent dyes, or nanoparticles to enable visualization. Molecular imaging with targeted nanoparticles is emerging as an exciting diagnostic tool. Nanoparticles can vary largely in size, shape, and material they can be composed of, with unique surface properties and reactivates [6, 22]. The large variety offers nanoparticles great flexibility in terms of imaging techniques they are compatible with, thus enabling multimodality molecular imaging [6, 22]. Nanoparticles are designed to be intrinsically near-infrared fluorescent [e.g., single-wall carbon nanotubes (SWNTs), quantum dots (Qdots)], or have magnetic properties [e.g., superparamagnetic iron oxide nanoparticles (SPIOs)] [23]. By surface modification [24] or additional radiolabeling [25], dual-labeled nanoparticles targeting the same ligands can therefore be recognized simultaneously by two or even three imaging techniques. In general, different imaging techniques are complementary rather than competitive [23], and the multimodality capacity of nanoparticles will facilitate the cross-talk between the whole-body scan imaging techniques (e.g., PET, CT) and optical imaging techniques (e.g., photoacoustic imaging, Raman spectroscopy), opening up the opportunity of tumor staging and characterization with single-molecular imaging agent.

The flexibility of nanoparticles also enables the capacity for multiplexed imaging. Many nanoparticles [e.g., quantum dots (Qdots) and surface-enhanced Raman scattering (SERS) gold nanoparticles] are tunable for different emission wavelength or Raman spectrum by alternation of size or structure. Same type of nanoparticles with different characteristics can be functionalized for simultaneous imaging of different tumor targets. In vivo studies on small animals have demonstrated simultaneous detection and separation of ten different types of SERS particles [26]. The Raman spectroscopy feature for detecting SERS nanoparticles has been incorporated into endoscopy [27], and molecular imaging of bladder cancer with targeted SERS particles is currently under active investigation.

The large surface area-to-volume ratio of many nanoparticles allows substantial payloads of targeting molecules, contributing to their ultrahigh sensitivity [6, 28], thereby minimizing the quantity of the imaging agent required and enabling molecular imaging with insensitive conventional imaging techniques such as CT [29] and MRI [30]. Nanocrystals such as Qdots offer additional benefits including 20-fold greater brightness and 100-fold greater stability to photobleaching than organic fluorophores [31], which is ideal for optical imaging.

While promising, in vivo application of nanoparticles can be challenging due to general pharmacokinetic issues associated with their large size (10 ~ 200 nm). While toxicity can also be an issue for nanoparticles such as Qdots with a core made of cadmium, Qdot-based molecular imaging may still have a role in evaluation of urogenital malignancies through topical (e.g., intravesical) administration, which could potentially minimize the toxicity and other limitations from systematic use. On the other hand, gold nanoparticles (AuNP) could be a safer alternative and have been approved for therapeutic use in humans [32]. Efficacy of therapeutic gold nanoparticles has also been demonstrated for treatment of prostate cancer on mouse xenograft [33], accelerating the clinical translation of molecular imaging of urological malignancies with targeted nanoparticles.

## Molecular Imaging with Conventional Imaging Modalities

Current investigations of molecular imaging platforms incorporating conventional CT and MRI have emerged in recent years, which promise to add molecular information such as with PET and SPECT. PET and SPECT are radionuclide imaging techniques that trace whole-body distribution of intravenously administrated radiolabeled imaging agents [6], delivering excellent sensitivity along with unlimited depth of penetration and quantitative capability. As biochemical changes often precede anatomical ones in disease, PET and SPECT are able to detect such changes

before CT and MRI. A limitation of PET and SPECT, however, is the lack of an anatomical reference frame (addressed by combining with CT/MRI). On the other hand, US is efficient in detecting vascular structures with high resolution and sensitivity [34], with transrectal US being the current standard for real-time guidance of prostate biopsy [35]. While it is relatively cost-effective and has a good safety profile, it is limited in its ability to image bone or air-containing structures and by its limited depth of penetration [6].

## CT and MRI

Currently, CT and MRI rely on iodinated and gadolinium (Gd)-based nonspecific imaging agents to provide tissue contrast [6]. While routinely used in detection of urologic malignancies [35], the application of CT and MRI in molecular imaging is constrained by low sensitivity since large amounts of imaging agents are needed to produce an adequate readout. These considerations are clinically relevant given the risks of radiation exposure and contrast nephropathy for CT scan and nephrogenic systemic fibrosis for MRI. However, multiple examples of CT and MRI molecular imaging have begun to emerge recently. Gastrin-release peptide (GRP) fragments targeting GRPR have been chelated to Gd for in vivo MRI of prostate cancer [30, 36]. GRPR, a member of the BBN receptor family, is consistently overexpressed in prostate cancer [37] but absent or very low on normal and hyperplastic prostate tissues [38].

A AuNP dual loaded with RNA aptamer targeting prostate-specific membrane antigen (PSMA) and doxorubicin has shown preferential binding to PSMA-expressing prostate cancer cells in vitro by CT scan [39]. PSMA is a type II transmembrane glycoprotein with folate hydrolase activity [40, 41] whose expression in normal tissues is highly restricted to prostate epithelium [42–44]. Given its high-level expression in all prostate cancers [43–47], PSMA has been a well-established biomarker for prostate cancer diagnosis and immunotherapy [48].

## US

In recent years, an intravascular contrast agent using gas-filled microbubbles coated with lipids or biopolymers has been studied for the imaging of cancer-associated neovascularity indicative of angiogenesis. This contrast-based US technique has shown significant benefits for detecting high-grade/high-volume prostate cancer in clinical trials [49–51] and is under active investigation for diagnosis of renal masses [52–54]. The microbubbles have exhibited an acceptable safety profile and can be attached with disease-specific targeting molecules, thus adding a molecular imaging dimension to ultrasound [55, 56]. While most of molecular imaging studies with contrast-enhanced US are under preclinical development [56–60], a phase 0 clinical trial completed in 2012 in prostate cancer patient for microbubbles (BR55) targeting human vascular epidermal growth factor receptor 2 (VEGFR2) (Available online: http://www.clinicaltrials.gov/ct2/show/NCT01253213).

## PET/SPECT

A panel of clinical-grade, molecular imaging agents has been clinically used with PET to image prostate cancer, among them $^{18}$F-FDG (glucose metabolism), $^{11}$C-acetate, $^{18}$F-fluoroacetate, $^{11}$C/$^{18}$F-choline (lipogenesis), anti-1-amino-3-18F-fluorocyclobutane-1-carboxylic acid (anti-$^{18}$F-FACBC) and $^{11}$C-methionine (amino acid transportation), 18F-fluoro-5a-dihydrotestosterone (18F-FDHT) (androgen receptor), and $^{64}$Cu-CB-TE2A-AR06 (GRPR) [12, 61–63].

While $^{18}$F-FDG has been most commonly used in imaging urological malignancies by targeting increased glucose metabolism in cancer cells, FDG PET/CT has limited applicability in detecting primary prostate cancer and local recurrence due to the generally low avidity of FDG for primary prostate cancer, uptake in cases of prostatitis and benign prostatic hypertrophy, and interference from nearby bladder excretion [12, 61, 62]. However, FDG uptake has been shown to be higher in untreated patients with advanced-

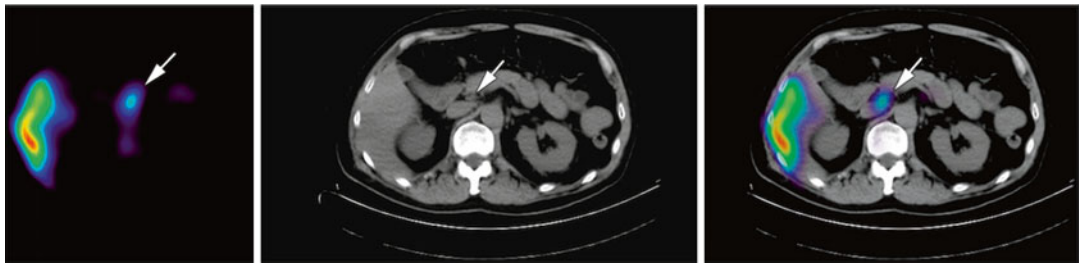

**Fig. 20.2** SPECT/CT case of showing a 1.5×0.7 cm peripancreatic lymph node with correlative $^{111}$In-capromab pendetide uptake. Images of SPECT alone (*left*); CT alone (*middle*); SPECT/CT fusion (*right*). *Arrows* indicate where the lymph node uptake was identified (From Aparici et al. [131], with permission from e-Century Publishing Corporation)

stage prostate cancer [64] and aggressive poorly differentiated tumors than in well-differentiated tumors [65]. Cumulative evidences have shown FDG PET/CT may be useful in the subset of patients with greater than intermediate risk (Gleason sum score ≥7), increased serum prostate surface antigen (PSA) level at initial diagnosis [66], and restaging patients with PSA relapse after treatment for localized prostate cancer [67–69]. The most useful application of FDG PET/CT may be providing prognostic information in patients with castration-sensitive and castration-resistant metastatic disease [12, 64, 70, 71].

In addition, by using a diuretic followed by oral hydration, this strategy may facilitate the FDG PET/CT detection of recurrent or residual bladder lesions for invasive bladder cancer [72]. Overall, FDG PET/CT may indeed have a major impact on the clinical management of up to 41 % of prostate cancer patients, 33 % with kidney cancer patients, and 36 % with bladder cancer patients older than 65 years [73, 74].

$^{111}$In-capromab pendetide (ProstaScint®) is the only approved radioimmunoscintigraphy agent for molecular imaging of prostate cancer. ProstaScint consists of a radiolabeled murine mAb (7E11-C5.3) to PSMA. The clinical utilities of ProstaScint scan with SPECT include: (1) detecting occult lymph node metastasis in patients with high PSA level prior to treatment [75, 76], (2) identifying early recurrence after treatment [77, 78], and (3) stratifying patients for salvage radiation therapy [79, 80]. While the recent technical advance with fusion of SPECT with CT/MRI has revolutionized ProstaScint scan with doubled diagnostic accuracy and reduced false-positive rate (Fig. 20.2) [80], ProstaScint has limited use in detecting bone metastases, and the intracellular epitope recognition of ProstaScint also remains controversial. ProstaScint binds to intracellular epitope of the transmembrane PSMA protein, raising concerns of its limited accumulation in viable cells [12]. Another mAb (J591) against PSMA that recognizes extracellular epitope of PSMA has been developed and studied in phase II trial for imaging metastatic castration-resistant prostate cancer [81]. Also, two novel small molecule PSMA inhibitors (MIP-1095 and MIP-1072) have been studied in phase I trial, in which the $^{123}$I-labeled compounds localized to metastatic lesions in both soft tissue and bone at as early as 1–4 h after intravenous administration [82]. A multifunctional nanoparticle functionalized with bladder cancer-specific ligand (PLZ4) also demonstrated both fluorescent imaging and therapeutic potential in mouse orthotopic model of dog bladder cancer [83]. Their clinical utility requires further validation in larger clinical studies.

## Molecular Optical Imaging

Optical imaging utilizes visible, ultraviolet, and infrared light to interrogate tissues of interest, with its advantages including superior resolution and relatively facile integration into the operating room setting. By integrating features such as

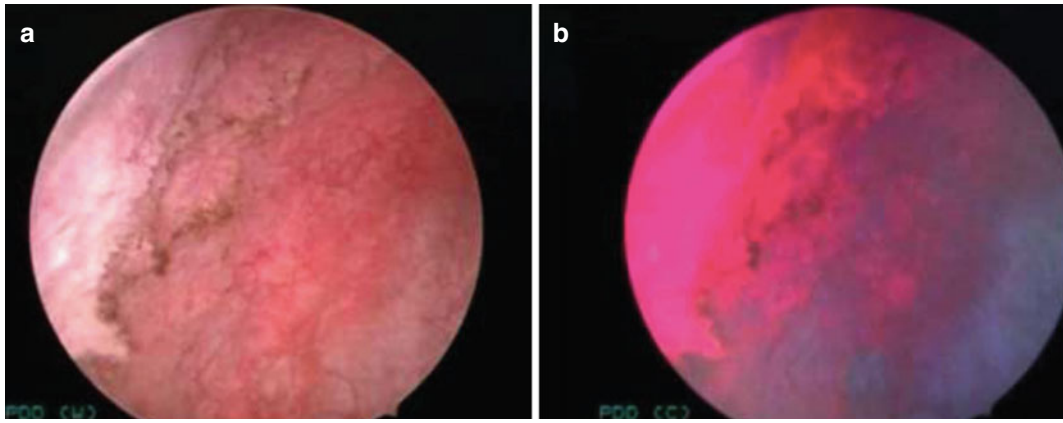


**Fig. 20.3** PDD for bladder cancer. WLC (**a**) of the right lateral bladder wall demonstrated a diffuse area of nonpapillary tumor. Under PDD (**b**), pink fluorescence outlines the extent of the neoplastic region that was pathologically confirmed to be carcinoma in situ (CIS) (From Hsu et al. [24], with permission from Wolters Kluwer Health)

fluorescence imaging into standard white-light endoscopic and laparoscopic procedures, the visual contrast between normal/benign and tumor tissues is enhanced, enabling real-time, intraoperative visualization and characterization of tumor tissues [84]. The advent of fluorescence-guided surgery has been a novel paradigm for cancer diagnostics and treatment [9].

Several promising optical imaging modalities have entered the urologic clinical arena, ranging on a macroscopic [i.e., photodynamic diagnosis (PDD), near-infrared fluorescence (NIRF)] to microscopic [i.e., optical coherence tomography (OCT), confocal laser endomicroscopy (CLE)] scale. PDD, NIRF, and CLE all require an exogenous fluorescent imaging agent. The potential in-human application of fluorescent molecular imaging has been presented in ovarian cancer [85] and colon cancer [86], adding promise for future application to urologic malignancies.

## PDD

PDD (Fig. 20.3) is considered a molecular imaging modality by detecting increased metabolism of photosensitive protoporphyrin analogs [5-aminolevulinic acid (5-ALA), or its more strongly fluorescent ester analog, hexaminolevulinate (HAL)] in tumor cells. PDD provides macroscopic examination of tissues by inducing pink-colored fluorescence from selective accumulation of 5-ALA or HLA using a blue light source (375 ~ 440 nm). PDD has been applied principally in bladder cancer through intravesical contrast administration under an integrated blue fluorescence cystoscope setting, with more limited experience in penile, prostate, and kidney cancers. This is in part due to the limited penetration depth of light [34] and established bladder accessibility with intravesical endoscopy [5]. Nevertheless, PDD with 5-ALA has been used to guide Nd:YAG laser coagulation in penile surgery for carcinoma [87], to assess margin status in laparoscopic partial nephrectomy [88], and to assess margin status during prostatectomy [89, 90]. For bladder cancer, PDD has a potential role in addressing white-light cystoscopy (WLC)'s shortcomings with incomplete resection of suspicious lesions that can subsequently lead to tumor recurrence/progression [3]. In human studies, PDD has been shown to improve initial detection of carcinoma in situ (CIS) compared to WLC [91–93].

Despite the above benefits, PDD still suffers from up to 30 % false-positive rate, particularly in patients with prior bacillus Calmette-Guérin (BCG) treatment, the standard immunotherapy for bladder cancer [3]. Preliminary studies are ongoing with

combining the PDD concept with molecular imaging agents targeting tumor-specific antigens. CD47, for example, is a marker that is widely distributed in various malignancies including bladder cancer. Antibodies to this marker have demonstrated therapeutic effect for bladder cancer in mouse xenograft [94] and may be used for molecular imaging. This provides potential in improving specificity using molecular markers to differentiate cancerous lesions as opposed to relying on metabolic differences.

### NIRF

NIRF has revolutionized optical imaging by providing extended depth of penetration and minimal tissue autofluorescence at near-infrared spectrum (800 ~ 2,500 nm) [95]. As NIRF imaging systems used in conjunction with open, laparoscopic, and robotic-assisted surgery have been developed, NIRF has been used with non-tumor-specific NIRF dye [indocyanine green (ICG)] and nanoparticle (99mTc-nanocolloid) to facilitate intraoperative imaging during nephrectomy to locate the hilar vessels [96, 97] and robotic prostatectomy to highlight the sentinel lymph nodes draining the prostate [98].

Molecular imaging of prostate cancer with NIRF is currently under active preclinical investigation. An Alexa Fluor 680-conjugated bombesin (BBN) peptide targeting BBN receptors has shown 90 % accuracy in detecting metastatic prostate cancer [99]. To facilitate clinical translation, BBN peptide [100] and epithelial cell adhesion molecule (EpCAM) mAb [101] were coupled with IRDye®800CW (IR800CW), a NIRF dye with good safety profile [102]. Recently, multimodality and quantitative molecular imaging with NIRF have been demonstrated to improve prostate cancer detection and resection. Monoclonal antibody against PSMA has been dual labeled with $^{111}$In and IR800CW to enable SPECT/CT and NIFR imaging, with SPECT/CT for preoperative tumor detection and NIFR for surgery guidance [103]. A panel of EpCAM mAbs dual labeled with $^{64}$Cu and IR800CW was also evaluated by PET/CT and NIRF to enhance the sensitivity and specificity of lymph nodes metastases detection [104].

### CLE

CLE allows for real-time in vivo microscopy with cellular level resolution using a miniaturized fiberoptic imaging probe with a 488 nm laser and nonspecific fluorescein as the imaging agent. The clinical system (Cellvizio, Mauna Kea Technologies) uses probes ranging from 0.85 to 2.6 mm in diameter, which fit through working channels of standard cystoscopes. In vivo application of CLE with fluorescein in urological operations has been reported in the lower urinary tract, particularly with bladder cancer [105–108]. While visualization of benign versus low- and high-grade tumors with respect to cellular organization and vascularization were shown, diagnosis with CLE is largely based on cell architecture and morphology, making real-time analysis of confocal images challenging in the operating room.

A fluorescein isothiocyanate (FITC)-labeled bladder cancer-specific molecular imaging agent may improve the clinical application of CLE. FITC has a well-approved safety profile and is capable of protein conjugation. The signaling molecule may be adapted from clinically approved therapeutic mAb or peptides to facilitate clinical translation. CLE molecular imaging agent for bladder cancer is currently under investigation. On the other hand, in-human application of targeted imaging with CLE has been demonstrated for other epithelial diseases including colonic dysplasia [109] and esophageal neoplasia [86] using FITC-labeled peptide, confirming the feasibility of molecular imaging with CLE. Future investigation may allow combined molecular imaging of CLE with macroscopic endoscopic technique such as PDD to enable simultaneous tumor detection and characterization.

## Emerging Molecular Imaging Modalities

Several emerging molecular imaging modalities [i.e., photoacoustic imaging (PAI), Raman spectroscopy (RS), and multiphoton microscopy (MPM)] hold great promise in preclinical studies. PAI detects ultrasound transmission resulting

from optical absorption by tissues. Imaging agents such as SWNT and AuNP emit strong photoacoustic signals via light absorption and can be used to enhance tissue contrast or functionalized with signaling molecules to enable molecular imaging with PAI [110, 111]. The advantages of PAI include superior depth of penetration (up to 5 cm) compared to optical imaging, significantly lower doses of imaging agent required (picograms to micrograms), and minimal background noise compared to traditional US [6]. The urologic application of PAI has been explored, with preliminary results of an ex vivo study on human prostate tissues suggesting that PAI can differentiate between normal, benign, and malignant tissues by detecting the intrinsic differences in photoacoustic signals [112]. In vivo visualization of prostate tumors has been shown in mouse models [113, 114], with a transrectal probe combining US and PAI under development to facilitate image-guided prostate biopsy. In a pilot study on ex vivo porcine bladders, PAI successfully visualized simulated tumors of injected biomaterials containing varying degrees of pigment, suggesting PAI can potentially visualize tumor depth in the bladder and provide complimentary staging information to diagnostic cystoscopies [115]. Photoacoustic endoscopy has been developed recently [116, 117], and PAI platforms contrasted with non-targeted non-ionizing imaging agents have been investigated for in vivo visualization of the bladder in small animals [27, 118, 119] to facilitate clinical translation. While PAI molecular imaging agents for urological malignancies are still under investigation, the feasibility of molecular imaging with PAI has been demonstrated in tumor-bearing mice for identifying breast cancer lesions using SWNT functionalized with Arg-Gly-Asp (RGD) peptide targeting tumor overexpressed integrin [120].

RS detects alternation in vibrational state of molecules in biological tissues under near-infrared light illumination (785–845 nm), which is known as a Raman shift [121]. Detection of multiple Raman peaks from the target tissue is plotted to create a spectrum of peaks, achieving a molecular "fingerprint" of the tissue examined without the need for exogenous contrast agent [121, 122]. RS's drawbacks include time to obtain a spectrum (1–5 s), weak signals, and limited field of view. SERS gold nanoparticles have been demonstrated to augment relatively weak signals from Raman scattering to improve sensitivity. These nanoparticles, when conjugated with tumor-specific ligands, have been used for in vivo tumor detection in small animals [123]. Targeted SERS particles also have the potential to enable multiplexed targeted imaging during endoscopy [124]. The feasibility of in vivo bladder cancer diagnosis was demonstrated using a fiberoptic Raman endoscopic probe that could differentiate cancerous tissue from normal urothelium in near real time during cystoscopy [122]. Bladder cancer-specific SERS particles are currently under investigation. On the other hand, RS has also been considered for implications in prostate cancer with pathologic diagnosis, margin status, and diagnostic biomarkers [125].

MPM uses simultaneous absorption of 2–3 near-infrared photon to cause nonlinear excitation equivalent to that created by a single photon of blue light and allows for both in vivo imaging and ex vivo imaging of fresh, unprocessed, and unstained tissue via distinct intrinsic tissue emissions (ITEs). Imaging capabilities include submicron resolution and up to 0.5 mm depth of penetration. Urologic investigations using MPM have been done with periprostatic nerves in a rat model [126], visualization and quantification of renal uptake [127, 128], differentiating normal and pathologic human bladder biopsies [129], and testicular biopsies distinguishing normal from abnormal spermatogenesis in patients being worked up for nonobstructive azoospermia [130].

## Conclusion

Molecular imaging offers the promise to transform urologic diagnostic and therapeutic paradigm from conventional imaging based on anatomic features to functional characterization of urological diseases with unprecedented resolutions. As our understanding of urological disease pathogenesis continues to improve, imaging technology is able to

exploit the inherent differences between benign and disease processes via biochemical processes, optical properties, and molecular targeting. Implementation of these technologies holds the potential to improve patient outcome and reduce morbidity, provided that they are well tolerated and cost-effective. Well-designed, prospective trials will continue to be needed to document our clinical experience with these modalities and further validate and refine the roles of imaging in the urology patient for diagnostic and therapeutic benefit.

## References


1. Taneja SS. Imaging in the diagnosis and management of prostate cancer. Rev Urol. 2004;6(3):101–13.
2. Vikram R, Sandler CM, Ng CS. Imaging and staging of transitional cell carcinoma: part 2, upper urinary tract. AJR Am J Roentgenol. 2009;192(6):1488–93. doi:10.2214/ajr.09.2577.
3. Liu JJ, Droller MJ, Liao JC. New optical imaging technologies for bladder cancer: considerations and perspectives. J Urol. 2012;188(2):361–8. doi:10.1016/j.juro.2012.03.127.
4. Brawer MK. Early diagnosis and staging of prostate cancer. Rev Urol. 2003;5 Suppl 6:S17–22.
5. Greco F, Cadeddu JA, Gill IS, Kaouk JH, Remzi M, Thompson RH, van Leeuwen FW, van der Poel HG, Fornara P, Rassweiler J. Current perspectives in the use of molecular imaging to target surgical treatments for genitourinary cancers. Eur Urol. 2013. doi:10.1016/j.eururo.2013.07.033.
6. James ML, Gambhir SS. A molecular imaging primer: modalities, imaging agents, and applications. Physiol Rev. 2012;92(2):897–965. doi:10.1152/physrev.00049.2010.
7. Ukimura O. Image-guided surgery in minimally invasive urology. Curr Opin Urol. 2010;20(2):136–40. doi:10.1097/MOU.0b013e3283362610.
8. Weissleder R, Pittet MJ. Imaging in the era of molecular oncology. Nature. 2008;452(7187):580–9. doi:10.1038/nature06917.
9. Nguyen QT, Tsien RY. Fluorescence-guided surgery with live molecular navigation–a new cutting edge. Nat Rev Cancer. 2013;13(9):653–62. doi:10.1038/nrc3566.
10. Hellebust A, Richards-Kortum R. Advances in molecular imaging: targeted optical contrast agents for cancer diagnostics. Nanomedicine (Lond). 2012;7(3):429–45. doi:10.2217/nnm.12.12.
11. Atreya R, Goetz M. Molecular imaging in gastroenterology. Nat Rev Gastroenterol Hepatol. 2013;10(12):704–12. doi:10.1038/nrgastro.2013.125.
12. Jadvar H. Molecular imaging of prostate cancer: PET radiotracers. AJR Am J Roentgenol. 2012;199(2):278–91. doi:10.2214/AJR.12.8816.
13. Lee S, Xie J, Chen X. Peptides and peptide hormones for molecular imaging and disease diagnosis. Chem Rev. 2010;110(5):3087–111. doi:10.1021/cr900361p.
14. Liu Y, Hu X, Liu H, Bu L, Ma X, Cheng K, Li J, Tian M, Zhang H, Cheng Z. A comparative study of radiolabeled bombesin analogs for the PET imaging of prostate cancer. J Nucl Med. 2013;54(12):2132–8. doi:10.2967/jnumed.113.121533.
15. Malviya G, Conti F, Chianelli M, Scopinaro F, Dierckx RA, Signore A. Molecular imaging of rheumatoid arthritis by radiolabelled monoclonal antibodies: new imaging strategies to guide molecular therapies. Eur J Nucl Med Mol Imaging. 2010;37(2):386–98. doi:10.1007/s00259-009-1272-0.
16. Olafsen T, Wu AM. Antibody vectors for imaging. Semin Nucl Med. 2010;40(3):167–81. doi:10.1053/j.semnuclmed.2009.12.005.
17. Feldwisch J, Tolmachev V. Engineering of affibody molecules for therapy and diagnostics. Methods Mol Biol. 2012;899:103–26. doi:10.1007/978-1-61779-921-1_7.
18. Turkbey B, Mena E, Aras O, Garvey B, Grant K, Choyke PL. Functional and molecular imaging: applications for diagnosis and staging of localised prostate cancer. Clin Oncol. 2013;25(8):451–60. doi:10.1016/j.clon.2013.05.001.
19. Baum RP, Prasad V, Muller D, Schuchardt C, Orlova A, Wennborg A, Tolmachev V, Feldwisch J. Molecular imaging of HER2-expressing malignant tumors in breast cancer patients using synthetic 111In- or 68Ga-labeled affibody molecules. J Nucl Med. 2010;51(6):892–7. doi:10.2967/jnumed.109.073239.
20. Malmberg J, Perols A, Varasteh Z, Altai M, Braun A, Sandstrom M, Garske U, Tolmachev V, Orlova A, Karlstrom AE. Comparative evaluation of synthetic anti-HER2 Affibody molecules site-specifically labelled with 111In using N-terminal DOTA, NOTA and NODAGA chelators in mice bearing prostate cancer xenografts. Eur J Nucl Med Mol Imaging. 2012;39(3):481–92. doi:10.1007/s00259-011-1992-9.
21. Rosenberg JE, Bambury RM, Van Allen EM, Drabkin HA, Lara Jr PN, Harzstark AL, Wagle N, Figlin RA, Smith GW, Garraway LA, Choueiri T, Erlandsson F, Laber DA. A phase II trial of AS1411 (a novel nucleolin-targeted DNA aptamer) in metastatic renal cell carcinoma. Invest New Drugs. 2014;32(1):178–87. doi:10.1007/s10637-013-0045-6.
22. Xia Y. Nanomaterials at work in biomedical research. Nat Mater. 2008;7(10):758–60. doi:10.1038/nmat2277.
23. Ferro-Flores G, Ocampo-Garcia BE, Santos-Cuevas CL, Morales-Avila E, Azorin-Vega E. Multifunctional radiolabeled nanoparticles for targeted therapy. Curr Med Chem. 2014;21(1):124–38.
24. Kircher MF, de la Zerda A, Jokerst JV, Zavaleta CL, Kempen PJ, Mittra E, Pitter K, Huang R, Campos C, Habte F, Sinclair R, Brennan CW, Mellinghoff IK, Holland EC, Gambhir SS. A brain tumor molecular

imaging strategy using a new triple-modality MRI-photoacoustic-Raman nanoparticle. Nat Med. 2012;18(5):829–34. doi:10.1038/nm.2721.
25. Kim YH, Jeon J, Hong SH, Rhim WK, Lee YS, Youn H, Chung JK, Lee MC, Lee DS, Kang KW, Nam JM. Tumor targeting and imaging using cyclic RGD-PEGylated gold nanoparticle probes with directly conjugated iodine-125. Small. 2011;7(14):2052–60. doi:10.1002/smll.201100927.
26. Zavaleta CL, Smith BR, Walton I, Doering W, Davis G, Shojaei B, Natan MJ, Gambhir SS. Multiplexed imaging of surface enhanced Raman scattering nanotags in living mice using noninvasive Raman spectroscopy. Proc Natl Acad Sci U S A. 2009;106(32):13511–6. doi:10.1073/pnas.0813327106.
27. Zavaleta CL, Garai E, Liu JT, Sensarn S, Mandella MJ, Van de Sompel D, Friedland S, Van Dam J, Contag CH, Gambhir SS. A Raman-based endoscopic strategy for multiplexed molecular imaging. Proc Natl Acad Sci U S A. 2013;110(25):E2288–97. doi:10.1073/pnas.1211309110.
28. Lee JH, Huh YM, Jun YW, Seo JW, Jang JT, Song HT, Kim S, Cho EJ, Yoon HG, Suh JS, Cheon J. Artificially engineered magnetic nanoparticles for ultra-sensitive molecular imaging. Nat Med. 2007;13(1):95–9. doi:10.1038/nm1467.
29. Reuveni T, Motiei M, Romman Z, Popovtzer A, Popovtzer R. Targeted gold nanoparticles enable molecular CT imaging of cancer: an in vivo study. Int J Nanomedicine. 2011;6:2859–64. doi:10.2147/ijn.s25446.
30. Wei L, Li S, Yang J, Ye Y, Zou J, Wang L, Long R, Zurkiya O, Zhao T, Johnson J, Qiao J, Zhou W, Castiblanco A, Maor N, Chen Y, Mao H, Hu X, Yang JJ, Liu ZR. Protein-based MRI contrast agents for molecular imaging of prostate cancer. Mol Imaging Biol. 2011;13(3):416–23. doi:10.1007/s11307-010-0342-9.
31. Walling MA, Novak JA, Shepard JR. Quantum dots for live cell and in vivo imaging. Int J Mol Sci. 2009;10(2):441–91. doi:10.3390/ijms10020441.
32. McNeil SE. Nanoparticle therapeutics: a personal perspective. Wiley Interdiscip Rev Nanomed Nanobiotechnol. 2009;1(3):264–71. doi:10.1002/wnan.6.
33. Shukla R, Chanda N, Zambre A, Upendran A, Katti K, Kulkarni RR, Nune SK, Casteel SW, Smith CJ, Vimal J, Boote E, Robertson JD, Kan P, Engelbrecht H, Watkinson LD, Carmack TL, Lever JR, Cutler CS, Caldwell C, Kannan R, Katti KV. Laminin receptor specific therapeutic gold nanoparticles (198AuNP-EGCg) show efficacy in treating prostate cancer. Proc Natl Acad Sci U S A. 2012;109(31):12426–31. doi:10.1073/pnas.1121174109.
34. Abeloff MD. Abeloff's clinical oncology. 4th ed. Philadelphia: Churchill Livingstone/Elsevier; 2008.
35. Wein AJ, Kavoussi LR, Campbell MF. Campbell-Walsh urology. 10th ed. Philadelphia: Elsevier Saunders; 2012.
36. Xue S, Qiao J, Jiang J, Hubbard K, White N, Wei L, Li S, Liu ZR, Yang JJ. Design of ProCAs (Protein-Based Gd MRI Contrast Agents) with high dose efficiency and capability for molecular imaging of cancer biomarkers. Med Res Rev. 2014. doi:10.1002/med.21313.
37. Jensen RT, Battey JF, Spindel ER, Benya RV. International Union of Pharmacology. LXVIII. Mammalian bombesin receptors: nomenclature, distribution, pharmacology, signaling, and functions in normal and disease states. Pharmacol Rev. 2008;60(1):1–42. doi:10.1124/pr.107.07108.
38. Markwalder R, Reubi JC. Gastrin-releasing peptide receptors in the human prostate: relation to neoplastic transformation. Cancer Res. 1999;59(5):1152–9.
39. Kim D, Jeong YY, Jon S. A drug-loaded aptamer-gold nanoparticle bioconjugate for combined CT imaging and therapy of prostate cancer. ACS Nano. 2010;4(7):3689–96. doi:10.1021/nn901877h.
40. Pinto JT, Suffoletto BP, Berzin TM, Qiao CH, Lin S, Tong WP, May F, Mukherjee B, Heston WD. Prostate-specific membrane antigen: a novel folate hydrolase in human prostatic carcinoma cells. Clin Cancer Res. 1996;2(9):1445–51.
41. Ghosh A, Heston WD. Tumor target prostate specific membrane antigen (PSMA) and its regulation in prostate cancer. J Cell Biochem. 2004;91(3):528–39. doi:10.1002/jcb.10661.
42. Israeli RS, Powell CT, Corr JG, Fair WR, Heston WD. Expression of the prostate-specific membrane antigen. Cancer Res. 1994;54(7):1807–11.
43. Silver DA, Pellicer I, Fair WR, Heston WD, Cordon-Cardo C. Prostate-specific membrane antigen expression in normal and malignant human tissues. Clin Cancer Res. 1997;3(1):81–5.
44. Sokoloff RLNKC, Gasior CL, Marker KM, Grauer LS. A dual-monoclonal sandwich assay for prostate-specific membrane antigen- levels in tissues, seminal fluid and urine. Prostate. 2000;43(2):150–7.
45. Wright GL, Haley C, Beckett ML, Schellhammer PF. Expression of prostate-specific membrane antigen in normal, benign, and malignant prostate tissues. Urol Oncol. 1995;1:18–28.
46. Schmittgen TD, Teske S, Vessella RL, True LD, Zakrajsek BA. Expression of prostate specific membrane antigen and three alternatively spliced variants of PSMA in prostate cancer patients. Int J Cancer J Int Cancer. 2003;107(2):323–9. doi:10.1002/ijc.11402.
47. Perner S, Hofer MD, Kim R, Shah RB, Li H, Moller P, Hautmann RE, Gschwend JE, Kuefer R, Rubin MA. Prostate-specific membrane antigen expression as a predictor of prostate cancer progression. Hum Pathol. 2007;38(5):696–701. doi:10.1016/j.humpath.2006.11.012.
48. Olson WCHW, Rajasekaran AK. Clinical trials of cancer therapies targeting prostate-specific membrane antigen. Rev Recent Clin Trials. 2007;2(3).
49. Halpern EJ. Contrast-enhanced ultrasound imaging of prostate cancer. Rev Urol. 2006;8 Suppl 1:S29–37.
50. Halpern EJ, Gomella LG, Forsberg F, McCue PA, Trabulsi EJ. Contrast enhanced transrectal ultrasound for the detection of prostate cancer: a randomized, double-blind trial of dutasteride pretreatment. J Urol. 2012;188(5):1739–45. doi:10.1016/j.juro.2012.07.021.

51. Smeenge M, Mischi M, Laguna Pes MP, de la Rosette JJ, Wijkstra H. Novel contrast-enhanced ultrasound imaging in prostate cancer. World J Urol. 2011;29(5):581–7. doi:10.1007/s00345-011-0747-3.
52. Houtzager S, Wijkstra H, de la Rosette JJ, Laguna MP. Evaluation of renal masses with contrast-enhanced ultrasound. Curr Urol Rep. 2013;14(2):116–23. doi:10.1007/s11934-013-0309-x.
53. Barr RG, Peterson C, Hindi A. Evaluation of indeterminate renal masses with contrast-enhanced US: a diagnostic performance study. Radiology. 2013;271(1):133–42. doi:10.1148/radiol.13130161.
54. Ignee A, Straub B, Schuessler G, Dietrich CF. Contrast enhanced ultrasound of renal masses. World J Radiol. 2010;2(1):15–31. doi:10.4329/wjr.v2.i1.15.
55. Kiessling F, Fokong S, Koczera P, Lederle W, Lammers T. Ultrasound microbubbles for molecular diagnosis, therapy, and theranostics. J Nucl Med. 2012;53(3):345–8. doi:10.2967/jnumed.111.099754.
56. Kaneko OF, Willmann JK. Ultrasound for molecular imaging and therapy in cancer. Quant Imaging Med Surg. 2012;2(2):87–97. doi:10.3978/j.issn.2223-4292.2012.06.06.
57. Wang L, Li L, Guo Y, Tong H, Fan X, Ding J, Huang H. Construction and in vitro/in vivo targeting of PSMA-targeted nanoscale microbubbles in prostate cancer. Prostate. 2013;73(11):1147–58. doi:10.1002/pros.22663.
58. Weller GE, Wong MK, Modzelewski RA, Lu E, Klibanov AL, Wagner WR, Villanueva FS. Ultrasonic imaging of tumor angiogenesis using contrast microbubbles targeted via the tumor-binding peptide arginine-arginine-leucine. Cancer Res. 2005;65(2):533–9.
59. Haag P, Frauscher F, Gradl J, Seitz A, Schafer G, Lindner JR, Klibanov AL, Bartsch G, Klocker H, Eder IE. Microbubble-enhanced ultrasound to deliver an antisense oligodeoxynucleotide targeting the human androgen receptor into prostate tumours. J Steroid Biochem Mol Biol. 2006;102(1–5):103–13. doi:10.1016/j.jsbmb.2006.09.027.
60. Deelman LE, Decleves AE, Rychak JJ, Sharma K. Targeted renal therapies through microbubbles and ultrasound. Adv Drug Deliv Rev. 2010;62(14):1369–77. doi:10.1016/j.addr.2010.10.002.
61. Jadvar H. Molecular imaging of prostate cancer with PET. J Nucl Med. 2013;54(10):1685–8. doi:10.2967/jnumed.113.126094.
62. Cho SY, Szabo Z. Molecular Imaging of urogenital diseases. Semin Nucl Med. 2014;44(2):93–109. doi:10.1053/j.semnuclmed.2013.10.008.
63. Wieser G, Mansi R, Grosu AL, Schultze-Seemann W, Dumont-Walter RA, Meyer PT, Maecke HR, Reubi JC, Weber WA. Positron Emission Tomography (PET) imaging of prostate cancer with a gastrin releasing peptide receptor antagonist – from mice to men. Theranostics. 2014;4(4):412–9. doi:10.7150/thno.7324.
64. Oyama N, Akino H, Suzuki Y, Kanamaru H, Sadato N, Yonekura Y, Okada K. The increased accumulation of [18F]fluorodeoxyglucose in untreated prostate cancer. Jpn J Clin Oncol. 1999;29(12):623–9.
65. Jadvar H. Imaging evaluation of prostate cancer with 18F-fluorodeoxyglucose PET/CT: utility and limitations. Eur J Nucl Med Mol Imaging. 2013;40 Suppl 1:S5–10. doi:10.1007/s00259-013-2361-7.
66. Minamimoto R, Uemura H, Sano F, Terao H, Nagashima Y, Yamanaka S, Shizukuishi K, Tateishi U, Kubota Y, Inoue T. The potential of FDG-PET/CT for detecting prostate cancer in patients with an elevated serum PSA level. Ann Nucl Med. 2011;25(1):21–7. doi:10.1007/s12149-010-0424-4.
67. Chang CH, Wu HC, Tsai JJ, Shen YY, Changlai SP, Kao A. Detecting metastatic pelvic lymph nodes by 18F-2-deoxyglucose positron emission tomography in patients with prostate-specific antigen relapse after treatment for localized prostate cancer. Urol Int. 2003;70(4):311–5, 70141.
68. Schoder H, Herrmann K, Gonen M, Hricak H, Eberhard S, Scardino P, Scher HI, Larson SM. 2-[18F] fluoro-2-deoxyglucose positron emission tomography for the detection of disease in patients with prostate-specific antigen relapse after radical prostatectomy. Clin Cancer Res. 2005;11(13):4761–9. doi:10.1158/1078-0432.CCR-05-0249.
69. Desai B, Elatre W, Quinn DI, Jadvar H. FDG PET/CT demonstration of pancreatic metastasis from prostate cancer. Clin Nucl Med. 2011;36(10):961–2. doi:10.1097/RLU.0b013e3182291d1a.
70. Sharma P, Karunanithi S, Singh Dhull V, Jain S, Bal C, Kumar R. Prostate cancer with lytic bone metastases: 18F-fluorodeoxyglucose positron emission tomography-computed tomography for diagnosis and monitoring response to medical castration therapy. Indian J Nucl Med. 2013;28(3):178–9. doi:10.4103/0972-3919.119545.
71. Meirelles GS, Schoder H, Ravizzini GC, Gonen M, Fox JJ, Humm J, Morris MJ, Scher HI, Larson SM. Prognostic value of baseline [18F] fluorodeoxyglucose positron emission tomography and 99mTc-MDP bone scan in progressing metastatic prostate cancer. Clin Cancer Res. 2010;16(24):6093–9. doi:10.1158/1078-0432.CCR-10-1357.
72. Anjos DA, Etchebehere EC, Ramos CD, Santos AO, Albertotti C, Camargo EE. 18F-FDG PET/CT delayed images after diuretic for restaging invasive bladder cancer. J Nucl Med. 2007;48(5):764–70. doi:10.2967/jnumed.106.036350.
73. Hillner BE, Siegel BA, Shields AF, Liu D, Gareen IF, Hunt E, Coleman RE. Relationship between cancer type and impact of PET and PET/CT on intended management: findings of the national oncologic PET registry. J Nucl Med. 2008;49(12):1928–35. doi:10.2967/jnumed.108.056713.
74. Hillner BE, Siegel BA, Hanna L, Shields AF, Duan F, Gareen IF, Quinn B, Coleman RE. Impact of 18F-FDG PET used after initial treatment of cancer: comparison of the National Oncologic PET Registry 2006 and 2009 cohorts. J Nucl Med. 2012;53(5):831–7. doi:10.2967/jnumed.112.103911.
75. Hinkle GH, Burgers JK, Neal CE, Texter JH, Kahn D, Williams RD, Maguire R, Rogers B, Olsen JO, Badalament RA. Multicenter radioimmunoscinti-

graphic evaluation of patients with prostate carcinoma using indium-111 capromab pendetide. Cancer. 1998;83(4):739–47.
76. Manyak MJ, Hinkle GH, Olsen JO, Chiaccherini RP, Partin AW, Piantadosi S, Burgers JK, Texter JH, Neal CE, Libertino JA, Wright Jr GL, Maguire RT. Immunoscintigraphy with indium-111-capromab pendetide: evaluation before definitive therapy in patients with prostate cancer. Urology. 1999;54(6):1058–63.
77. Schuster DM, Savir-Baruch B, Nieh PT, Master VA, Halkar RK, Rossi PJ, Lewis MM, Nye JA, Yu W, Bowman FD, Goodman MM. Detection of recurrent prostate carcinoma with anti-1-amino-3-18F-fluorocyclobutane-1-carboxylic acid PET/CT and 111In-capromab pendetide SPECT/CT. Radiology. 2011;259(3):852–61. doi:10.1148/radiol.11102023.
78. Raj GV, Partin AW, Polascik TJ. Clinical utility of indium 111-capromab pendetide immunoscintigraphy in the detection of early, recurrent prostate carcinoma after radical prostatectomy. Cancer. 2002;94(4):987–96.
79. Kahn D, Williams RD, Haseman MK, Reed NL, Miller SJ, Gerstbrein J. Radioimmunoscintigraphy with In-111-labeled capromab pendetide predicts prostate cancer response to salvage radiotherapy after failed radical prostatectomy. J Clin Oncol. 1998;16(1):284–9.
80. Manyak MJ. Indium-111 capromab pendetide in the management of recurrent prostate cancer. Expert Rev Anticancer Ther. 2008;8(2):175–81. doi:10.1586/14737140.8.2.175.
81. Tagawa ST, Milowsky MI, Morris M, Vallabhajosula S, Christos P, Akhtar NH, Osborne J, Goldsmith SJ, Larson S, Taskar NP, Scher HI, Bander NH, Nanus DM. Phase II study of lutetium-177-labeled anti-prostate-specific membrane antigen monoclonal antibody J591 for metastatic castration-resistant prostate cancer. Clin Cancer Res. 2013;19(18):5182–91. doi:10.1158/1078-0432.CCR-13-0231.
82. Barrett JA, Coleman RE, Goldsmith SJ, Vallabhajosula S, Petry NA, Cho S, Armor T, Stubbs JB, Maresca KP, Stabin MG, Joyal JL, Eckelman WC, Babich JW. First-in-man evaluation of 2 high-affinity PSMA-avid small molecules for imaging prostate cancer. J Nucl Med. 2013;54(3):380–7. doi:10.2967/jnumed.112.111203.
83. Lin TY, Zhang H, Luo J, Li Y, Gao T, Lara Jr PN, de Vere WR, Lam KS, Pan CX. Multifunctional targeting micelle nanocarriers with both imaging and therapeutic potential for bladder cancer. Int J Nanomedicine. 2012;7:2793–804. doi:10.2147/ijn.s27734.
84. Hsu M, Gupta M, Su LM, Liao JC. Intraoperative optical imaging and tissue interrogation during urologic surgery. Curr Opin Urol. 2014;24(1):66–74. doi:10.1097/mou.0000000000000010.
85. van Dam GM, Themelis G, Crane LM, Harlaar NJ, Pleijhuis RG, Kelder W, Sarantopoulos A, de Jong JS, Arts HJ, van der Zee AG, Bart J, Low PS, Ntziachristos V. Intraoperative tumor-specific fluorescence imaging in ovarian cancer by folate receptor-alpha targeting: first in-human results. Nat Med. 2011;17(10):1315–9. doi:10.1038/nm.2472.
86. Sturm MB, Joshi BP, Lu S, Piraka C, Khondee S, Elmunzer BJ, Kwon RS, Beer DG, Appelman HD, Turgeon DK, Wang TD. Targeted imaging of esophageal neoplasia with a fluorescently labeled peptide: first-in-human results. Sci Transl Med. 2013;5(184):184ra161. doi:10.1126/scitranslmed.3004733.
87. Schlenker B, Gratzke C, Seitz M, Bader MJ, Reich O, Schneede P, Hungerhuber E, Stief CG, Tilki D. Fluorescence-guided laser therapy for penile carcinoma and precancerous lesions: long-term follow-up. Urol Oncol. 2011;29(6):788–93. doi:10.1016/j.urolonc.2009.10.001.
88. Hoda MR, Popken G. Surgical outcomes of fluorescence-guided laparoscopic partial nephrectomy using 5-aminolevulinic acid-induced protoporphyrin IX. J Surg Res. 2009;154(2):220–5. doi:10.1016/j.jss.2008.12.027.
89. Adam C, Salomon G, Walther S, Zaak D, Khoder W, Becker A, Reich O, Blana A, Ganzer R, Denzinger S, Popken G, Sroka R, Knuchel-Clarke R, Kollermann J, Sauter G, Hartmann A, Bertz S, Graefen M, Huland H, Wieland W, Stief CG. Photodynamic diagnosis using 5-aminolevulinic acid for the detection of positive surgical margins during radical prostatectomy in patients with carcinoma of the prostate: a multicentre, prospective, phase 2 trial of a diagnostic procedure. Eur Urol. 2009;55(6):1281–8. doi:10.1016/j.eururo.2009.02.027.
90. Ganzer R, Blana A, Denzinger S, Wieland WF, Adam C, Becker A, Khoder W, Walther S, Stief CG, Zaak D, Salomon G, Hartmann A, Knuechel R, Bertz S, Popken G. Intraoperative photodynamic evaluation of surgical margins during endoscopic extraperitoneal radical prostatectomy with the use of 5-aminolevulinic acid. J Endourol Soc. 2009;23(9):1387–94. doi:10.1089/end.2009.0374.
91. Schumacher MC, Holmang S, Davidsson T, Friedrich B, Pedersen J, Wiklund NP. Transurethral resection of non-muscle-invasive bladder transitional cell cancers with or without 5-aminolevulinic acid under visible and fluorescent light: results of a prospective, randomised, multicentre study. Eur Urol. 2010;57(2):293–9. doi:10.1016/j.eururo.2009.10.030.
92. Stenzl A, Burger M, Fradet Y, Mynderse LA, Soloway MS, Witjes JA, Kriegmair M, Karl A, Shen Y, Grossman HB. Hexaminolevulinate guided fluorescence cystoscopy reduces recurrence in patients with nonmuscle invasive bladder cancer. J Urol. 2010;184(5):1907–13. doi:10.1016/j.juro.2010.06.148.
93. Grossman HB, Gomella L, Fradet Y, Morales A, Presti J, Ritenour C, Nseyo U, Droller MJ, Group PBS. A phase III, multicenter comparison of hexaminolevulinate fluorescence cystoscopy and white light cystoscopy for the detection of superficial papillary lesions in patients with bladder cancer. J Urol. 2007;178(1):62–7. doi:10.1016/j.juro.2007.03.034.

94. Willingham SB, Volkmer JP, Gentles AJ, Sahoo D, Dalerba P, Mitra SS, Wang J, Contreras-Trujillo H, Martin R, Cohen JD, Lovelace P, Scheeren FA, Chao MP, Weiskopf K, Tang C, Volkmer AK, Naik TJ, Storm TA, Mosley AR, Edris B, Schmid SM, Sun CK, Chua MS, Murillo O, Rajendran P, Cha AC, Chin RK, Kim D, Adorno M, Raveh T, Tseng D, Jaiswal S, Enger PO, Steinberg GK, Li G, So SK, Majeti R, Harsh GR, van de Rijn M, Teng NN, Sunwoo JB, Alizadeh AA, Clarke MF, Weissman IL. The CD47-signal regulatory protein alpha (SIRPa) interaction is a therapeutic target for human solid tumors. Proc Natl Acad Sci U S A. 2012;109(17):6662–7. doi:10.1073/pnas.1121623109.
95. Keereweer S, Kerrebijn JD, van Driel PB, Xie B, Kaijzel EL, Snoeks TJ, Que I, Hutteman M, van der Vorst JR, Mieog JS, Vahrmeijer AL, van de Velde CJ, Baatenburg de Jong RJ, Lowik CW. Optical image-guided surgery–where do we stand? Mol Imaging Biol. 2011;13(2):199–207. doi:10.1007/s11307-010-0373-2.
96. Tobis S, Knopf JK, Silvers CR, Marshall J, Cardin A, Wood RW, Reeder JE, Erturk E, Madeb R, Yao J, Singer EA, Rashid H, Wu G, Messing E, Golijanin D. Near infrared fluorescence imaging after intravenous indocyanine green: initial clinical experience with open partial nephrectomy for renal cortical tumors. Urology. 2012;79(4):958–64. doi:10.1016/j.urology.2011.10.016.
97. Manny TB, Krane LS, Hemal AK. Indocyanine green cannot predict malignancy in partial nephrectomy: histopathologic correlation with fluorescence pattern in 100 patients. J Endourol Soc. 2013;27(7):918–21. doi:10.1089/end.2012.0756.
98. van der Poel HG, Buckle T, Brouwer OR, Valdes Olmos RA, van Leeuwen FW. Intraoperative laparoscopic fluorescence guidance to the sentinel lymph node in prostate cancer patients: clinical proof of concept of an integrated functional imaging approach using a multimodal tracer. Eur Urol. 2011;60(4):826–33. doi:10.1016/j.eururo.2011.03.024.
99. Cai QY, Yu P, Besch-Williford C, Smith CJ, Sieckman GL, Hoffman TJ, Ma L. Near-infrared fluorescence imaging of gastrin releasing peptide receptor targeting in prostate cancer lymph node metastases. Prostate. 2013;73(8):842–54. doi:10.1002/pros.22630.
100. Shrivastava A, Ding H, Kothandaraman S, Wang SH, Gong L, Williams M, Milum K, Zhang S, Tweedle MF. A high-affinity near-infrared fluorescent probe to target bombesin receptors. Mol Imaging Biol. 2014. doi:10.1007/s11307-014-0727-2.
101. Zhu B, Wu G, Robinson H, Wilganowski N, Hall MA, Ghosh SC, Pinkston KL, Azhdarinia A, Harvey BR, Sevick-Muraca EM. Tumor margin detection using quantitative NIRF molecular imaging targeting EpCAM validated by far red gene reporter iRFP. Mol Imaging Biol. 2013;15(5):560–8. doi:10.1007/s11307-013-0637-8.
102. Marshall MV, Draney D, Sevick-Muraca EM, Olive DM. Single-dose intravenous toxicity study of IRDye 800CW in Sprague-Dawley rats. Mol Imaging Biol. 2010;12(6):583–94. doi:10.1007/s11307-010-0317-x.
103. Lutje S, Rijpkema M, Franssen GM, Fracasso G, Helfrich W, Eek A, Oyen WJ, Colombatti M, Boerman OC. Dual-modality image-guided surgery of prostate cancer with a radiolabeled fluorescent anti-PSMA monoclonal antibody. J Nucl Med. 2014. doi:10.2967/jnumed.114.138180.
104. Hall MA, Pinkston KL, Wilganowski N, Robinson H, Ghosh P, Azhdarinia A, Vazquez-Arreguin K, Kolonin AM, Harvey BR, Sevick-Muraca EM. Comparison of mAbs targeting epithelial cell adhesion molecule for the detection of prostate cancer lymph node metastases with multimodal contrast agents: quantitative small-animal PET/CT and NIRF. J Nucl Med. 2012;53(9):1427–37. doi:10.2967/jnumed.112.106302.
105. Sonn GA, Jones SN, Tarin TV, Du CB, Mach KE, Jensen KC, Liao JC. Optical biopsy of human bladder neoplasia with in vivo confocal laser endomicroscopy. J Urol. 2009;182(4):1299–305. doi:10.1016/j.juro.2009.06.039.
106. Adams W, Wu K, Liu JJ, Hsiao ST, Jensen KC, Liao JC. Comparison of 2.6- and 1.4-mm imaging probes for confocal laser endomicroscopy of the urinary tract. J Endourol Soc. 2011;25(6):917–21. doi:10.1089/end.2010.0686.
107. Wu K, Liu JJ, Adams W, Sonn GA, Mach KE, Pan Y, Beck AH, Jensen KC, Liao JC. Dynamic real-time microscopy of the urinary tract using confocal laser endomicroscopy. Urology. 2011;78(1):225–31. doi:10.1016/j.urology.2011.02.057.
108. Chang TC, Liu JJ, Hsiao ST, Pan Y, Mach KE, Leppert JT, McKenney JK, Rouse RV, Liao JC. Interobserver agreement of confocal laser endomicroscopy for bladder cancer. J Endourol Soc. 2013;27(5):598–603. doi:10.1089/end.2012.0549.
109. Hsiung PL, Hardy J, Friedland S, Soetikno R, Du CB, Wu AP, Sahbaie P, Crawford JM, Lowe AW, Contag CH, Wang TD. Detection of colonic dysplasia in vivo using a targeted heptapeptide and confocal microendoscopy. Nat Med. 2008;14(4):454–8. doi:10.1038/nm1692.
110. Wilson KE, Wang TY, Willmann JK. Acoustic and photoacoustic molecular imaging of cancer. J Nucl Med. 2013;54(11):1851–4. doi:10.2967/jnumed.112.115568.
111. Zackrisson S, van de Ven SM, Gambhir SS. Light in and sound out: emerging translational strategies for photoacoustic imaging. Cancer Res. 2014;74(4):979–1004. doi:10.1158/0008-5472.can-13-2387.
112. Dogra VS, Chinni BK, Valluru KS, Joseph JV, Ghazi A, Yao JL, Evans K, Messing EM, Rao NA. Multispectral photoacoustic imaging of prostate cancer: preliminary ex-vivo results. J Clin Imaging Sci. 2013;3:41. doi:10.4103/2156-7514.119139.
113. Kumon RE, Deng CX, Wang X. Frequency-domain analysis of photoacoustic imaging data from prostate adenocarcinoma tumors in a murine model. Ultrasound Med Biol. 2011;37(5):834–9. doi:10.1016/j.ultrasmedbio.2011.01.012.

114. Bauer DR, Olafsson R, Montilla LG, Witte RS. 3-D photoacoustic and pulse echo imaging of prostate tumor progression in the mouse window chamber. J Biomed Opt. 2011;16(2):026012. doi:10.1117/1.3540668.
115. Kamaya A, Vaithilingam S, Chung BI, Oralkan O, Khuri-Yakub BT. Photoacoustic imaging of the bladder: a pilot study. J Ultrasound Med. 2013;32(7):1245–50. doi:10.7863/ultra.32.7.1245.
116. Yang JM, Maslov K, Yang HC, Zhou Q, Shung KK, Wang LV. Photoacoustic endoscopy. Opt Lett. 2009;34(10):1591–3.
117. Yang JM, Favazza C, Chen R, Yao J, Cai X, Maslov K, Zhou Q, Shung KK, Wang LV. Simultaneous functional photoacoustic and ultrasonic endoscopy of internal organs in vivo. Nat Med. 2012;18(8):1297–302. doi:10.1038/nm.2823.
118. Koo J, Jeon M, Oh Y, Kang HW, Kim J, Kim C, Oh J. In vivo non-ionizing photoacoustic mapping of sentinel lymph nodes and bladders with ICG-enhanced carbon nanotubes. Phys Med Biol. 2012;57(23):7853–62. doi:10.1088/0031-9155/57/23/7853.
119. Jeon M, Jenkins S, Oh J, Kim J, Peterson T, Chen J, Kim C. Nonionizing photoacoustic cystography with near-infrared absorbing gold nanostructures as optical-opaque tracers. Nanomedicine (Lond). 2013. doi:10.2217/nnm.13.103.
120. De la Zerda A, Zavaleta C, Keren S, Vaithilingam S, Bodapati S, Liu Z, Levi J, Smith BR, Ma TJ, Oralkan O, Cheng Z, Chen X, Dai H, Khuri-Yakub BT, Gambhir SS. Carbon nanotubes as photoacoustic molecular imaging agents in living mice. Nat Nanotechnol. 2008;3(9):557–62. doi:10.1038/nnano.2008.231.
121. Rao AR, Hanchanale V, Javle P, Karim O, Motiwala H. Spectroscopic view of life and work of the Nobel Laureate Sir C.V. Raman. J Endourol Soc. 2007;21(1):8–11. doi:10.1089/end.2006.9998.
122. Draga RO, Grimbergen MC, Vijverberg PL, van Swol CF, Jonges TG, Kummer JA, Ruud Bosch JL. In vivo bladder cancer diagnosis by high-volume Raman spectroscopy. Anal Chem. 2010;82(14):5993–9. doi:10.1021/ac100448p.
123. Qian X, Peng XH, Ansari DO, Yin-Goen Q, Chen GZ, Shin DM, Yang L, Young AN, Wang MD, Nie S. In vivo tumor targeting and spectroscopic detection with surface-enhanced Raman nanoparticle tags. Nat Biotechnol. 2008;26(1):83–90. doi:10.1038/nbt1377.
124. Vendrell M, Maiti KK, Dhaliwal K, Chang YT. Surface-enhanced Raman scattering in cancer detection and imaging. Trends Biotechnol. 2013;31(4):249–57. doi:10.1016/j.tibtech.2013.01.013.
125. Kast RE, Tucker SC, Killian K, Trexler M, Honn KV, Auner GW. Emerging technology: applications of Raman spectroscopy for prostate cancer. Cancer Metastasis Rev. 2014. doi:10.1007/s10555-013-9489-6.
126. Yadav R, Mukherjee S, Hermen M, Tan G, Maxfield FR, Webb WW, Tewari AK. Multiphoton microscopy of prostate and periprostatic neural tissue: a promising imaging technique for improving nerve-sparing prostatectomy. J Endourol Soc. 2009;23(5):861–7. doi:10.1089/end.2009.0221.
127. Molitoris BA, Sandoval RM. Quantifying dynamic kidney processes utilizing multi-photon microscopy. Contrib Nephrol. 2007;156:227–35. doi:10.1159/0000102088.
128. Caplanusi A, Parreira KS, Lima WR, Marien B, Van Der Smissen P, de Diesbach P, Devuyst O, Courtoy PJ. Intravital multi-photon microscopy reveals several levels of heterogeneity in endocytic uptake by mouse renal proximal tubules. J Cell Mol Med. 2008;12(1):351–4. doi:10.1111/j.1582-4934.2007.00192.x.
129. Jain M, Robinson BD, Scherr DS, Sterling J, Lee MM, Wysock J, Rubin MA, Maxfield FR, Zipfel WR, Webb WW, Mukherjee S. Multiphoton microscopy in the evaluation of human bladder biopsies. Arch Pathol Lab Med. 2012;136(5):517–26. doi:10.5858/arpa.2011-0147-OA.
130. Najari BB, Ramasamy R, Sterling J, Aggarwal A, Sheth S, Li PS, Dubin JM, Goldenberg S, Jain M, Robinson BD, Shevchuk M, Scherr DS, Goldstein M, Mukherjee S, Schlegel PN. Pilot study of the correlation of multiphoton tomography of ex vivo human testis with histology. J Urol. 2012;188(2):538–43. doi:10.1016/j.juro.2012.03.124.
131. Aparici CM, Carlson D, Nguyen N, Hawkins RA, Seo Y. Combined SPECT and multidetector CT for prostate cancer evaluations. Am J Nucl Med Mol Imaging. 2012;2(1):48–54.

# Index



J.C. Liao, L.-M. Su (eds.), *Advances in Image-Guided Urologic Surgery*,
DOI 10.1007/978-1-4939-1450-0, © Springer Science+Business Media New York 2015